Copyright is owned by the Author of the thesis. Permission is given for a copy to be downloaded by an individual for the purpose of research and private study only. The thesis may not be reproduced elsewhere without the permission of the Author.

Asymmetric Catalysis *via* Spatially Separated Chiral and Catalytic Motifs in Multicomponent Metal-Organic Frameworks

A thesis presented in partial fulfilment of the requirements of the degree of

Doctor of Philosophy

in

Chemistry

at Massey University, Manawatū, New Zealand

Ludwig Petters

2025

For Regina and Franz

Abstract

Modern life without catalysis is inconceivable. Asymmetric catalysts are a special type of catalyst that preferentially produce one of two possible enantiomers over the other. The ability to selectively obtain exclusively one of the possible enantiomers is of highest importance for modern synthetic chemistry. To enable the transfer of chiral information from the catalyst to the reaction substrates, asymmetric catalysts must be chiral. In conventional asymmetric catalysts, the catalytic and chiral motifs are held close together within one single molecule.

In this work, we break the design limitation of conventional asymmetric catalysts with a strategy we call 'remote asymmetric induction' (RAI). In RAI catalysts, the catalytic and chiral motifs are independent of each other in their design and synthesis. To achieve this, we use the multicomponent metal-organic framework MUF-77 (MUF = Massey University Framework). MUF-77 consists of three chemically distinct linkers that each occupy a specific position in the framework without disorder or randomness. To create RAI catalysts, the catalytic and chiral motifs are individually anchored to the different building blocks of MUF-77. By virtue of the MUF-77 structure, the catalytic and chiral motifs are in close proximity to one another in a catalytic pore, which creates an active site. This enables the transfer of chiral information to the reaction participants.

Initially the reaction scope of the RAI catalyst was expanded by screening a variety of RAI-MOFs incorporating different catalytic and chiral functionalities across a range of model reactions. A promising catalyst for one model reaction was identified and investigated in depth. Through systematic modification of important reaction variables, the variation in enantioselectivity of this system was explored. After parameter optimisation, very good to excellent enantioselectivity was achieved. Control experiments confirmed that the origin of enantioselectivity arises from remote cooperative interactions between the functionalities in the active site. The catalysts were then tested for classical performance metrics and a hypothetical transition state within the MOF pore was proposed. This work establishes RAI as an alternative platform to develop high-performing asymmetric catalysts.

Contributions

All the work in this thesis was completed by Ludwig Petters

Except:

- Dr. Seok June Lee synthesised H_2bpdc-gua.
- The syntheses of H_2bdc-OX-(*S*)-5-MeCl, H_2bdc-^{5}N-(*S*)-CH_2OH-cycloHex, Me_2bpdc-NH_2, benzaldehydes **24** and **33** were performed by Cara Bosman under the supervision of the author.
- The syntheses of H_3hbtt, H_3hptt and H_3hott were performed by prior group members.
- The synthetic protocol for H_2bpdc-^{7}N-Boc was provided by Dr. Bernhard Auer.
- Parts of the synthetic protocol to H_2bpdc-urea-Ph were established by Dr. Jose Quinsaat.
- High-resolution mass spectrometry data were collected by Dave Lun.
- NMR spectra measured on the 700 MHz spectrometer were measured by Dr. Patrick Edwards.
- The TLC and HPLC conditions for the Friedel-Crafts reaction were developed by Dr. Jose Quinsaat.
- The TLC and HPLC conditions for the Pictet-Spengler reaction were developed by Mohana Arul.

Acknowledgements

First and foremost, I want to thank my supervisor Professor Shane Telfer for giving me the opportunity to do this PhD project. Thank you for your guidance, support and the chance to grow as a researcher. I would also like to thank my two co-supervisors: Dr. Gareth J. Rowlands, for the advice whenever I needed a second opinion about organic synthesis; and Dr. Tyson Dais, for helping with any issues related to the XRD device and for stepping up as a co-supervisor when needed.

I would like to acknowledge the Marsden Fund and Massey University for their financial support. Further, I want to thank the MacDiarmid institute and especially MESA for the great opportunities to grow beyond just my research with workshops, symposia and networking opportunities.

I also want to thank everyone who supported my daily research in any form. Dr. Pat Edwards for his continuous support with NMR-related questions. Dave Lun for all the technical support with HPLC and other lab equipment. All past and present group members who assisted in any way. A special thank you goes to Subo, for starting the project, helping me become familiar with all the instruments at the beginning, and for the continued support over the years. Additionally, I want to thank Mohana for all the discussions and for working on this ambitious project alongside me. Ghadir, for overcoming synthetic challenges together and sharing synthesis procedures. Cara, for synthesising shared linker precursors.

I would also like to take this opportunity to thank all my friends and family that made life colourful. Everyone in Germany and all over the world that kept in touch, even though time zones can make that difficult. Marco for making me more mindful and being the friend I needed when I did. Calum for the motivation to become stronger. Nick for all the fish we caught together (or didn't). Maddy and Ryan for all the walks, games nights and shared meals we had. And most importantly, Sam. Thank you for being my cornerstone. Without all of you, life would have been grey.

Lastly, I want to thank my parents, Regina and Franz. Your unwavering support and trust in me give me the strength to overcome every challenge I face.

Publications and thesis structure

Publications relevant to this thesis

Not applicable.

Additional publications

1. Cheng, L.; De Leon-Rodriguez, L. M.; Gilbert, E. P.; Loo, T.; Petters, L.; Yang, Z. Self-assembly and hydrogelation of a potential bioactive peptide derived from quinoa proteins. *Int. J. Biol. Macromol.* **2024**, *259*, 129296.

Table of Contents

List of abbreviations

AIBN	Azobisisobutyronitrile
bdc	1,4-Benzene dicarboxylic acid
BINAP	2,2′-Bis(diphenylphosphino)1,1′-binapthyl
BINOL	1,1′-Bi-2-naphthol
Boc	*tert*-Butyloxycarbonyl
BPin	Bis(pinacolato)diboron
bpdc	Biphenyl-4,4′-dicarboxylic acid
btb	1,3,5-Benzene tricarboxylic acid
DCM	Dichloromethane
DEF	*N*,*N*′-Diethylformamide
DMF	*N*,*N*-Dimethylformamide
DMEDA	*N*,*N*-Dimethyl ethylenediamine
ee	Enantiomeric excess
eq.	Equivalents
HBD	Hydrogen bond donor
HKUST	Hong Kong University of Science and Technology
hmtt	5,5,10,10,15,15-hexamethyltruxene-2,7,12-tricarboxylate
HPLC	High-performance liquid chromatography
Hz	Hertz
MOF	Metal-organic framework
MUF	Massey University framework
Mes	Mesylate
NBS	*N*-Bromosuccinimide
NMP	*N*-Methylpyrrolidine
NMR	Nuclear Magnetic Resonance Spectroscopy
ppm	Parts per million
PXRD	Powder X-ray diffraction

RAI	Remote asymmetric induction
R_f	Retention factor
r.t.	Room temperature
SCXRD	Single crystal X-ray diffraction
TEA	Triethylamine
TFA	Trifluoroacetic acid
TGA	Thermogravimetric analysis
THF	Tetrahydrofuran
TLC	Thin layer chromatography
TOF	Turnover frequency
TON	Turnover number
Ts	Tosylate
UV	Ultraviolet
ZIF	Zeolitic imidazolate frameworks

Chapter 1 – Introduction

1.1 Asymmetric catalysis: the conventional approach

1.1.1 Importance of asymmetric catalysis and its measure of success

Imagining a world without the influence of catalysis is nearly impossible.[1] Catalysts are molecules that alter a reaction's pathway by decreasing the activation energy needed to form a desired product.[2] At the same time, the catalyst itself is not consumed and can participate in many reaction cycles. The importance of catalysis becomes particularly obvious when applied to chiral molecules, where the preferential formation of one of the two possible mirror-image molecules is often critical.[3] Many organic molecules like sugars and amino acids are chiral, meaning that they have at least one stereogenic element: typically a carbon atom bound to four chemically different partners.[4, 5] Formally, molecules are also chiral if they lack an improper axis of rotation.[5] This lack of symmetry means the molecule exists as a pair of non-superimposable mirror images, known as enantiomers.[6]

Reactions catalysed by achiral catalysts generally produce both enantiomers in equal amounts (provided that the product is chiral), resulting in a racemic mixture (**Figure 1.1 A**). In contrast, asymmetric catalysts direct the reaction towards the preferential formation of one enantiomer (**Figure 1.1 B**).[4] The ultimate goal is to obtain specifically just one of the two enantiomers. This is central to life[3, 7, 8] and consequently also for modern synthetic chemistry, especially in regards to the production of pharmaceuticals.[9]

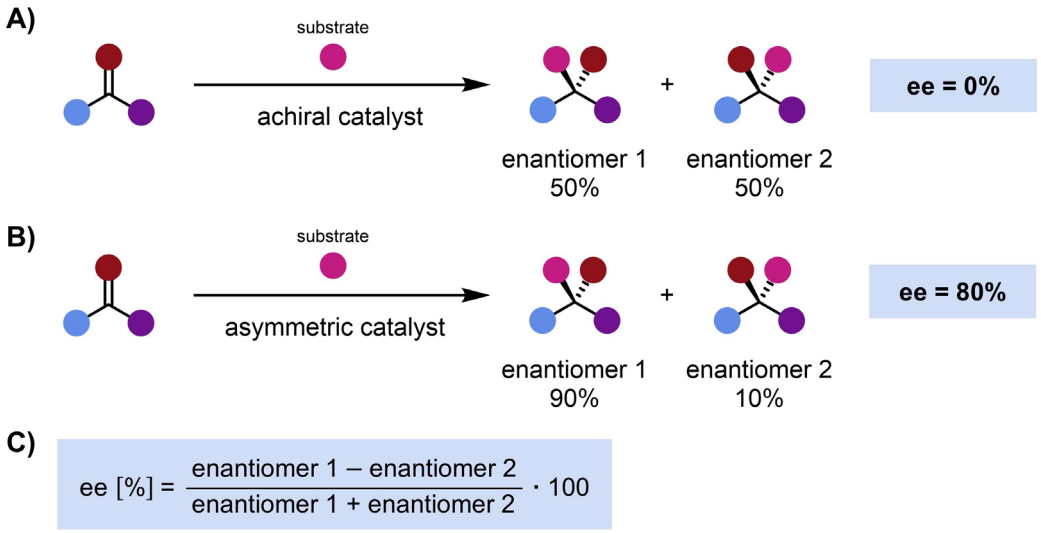

Figure 1.1 Schematic representation of the reaction outcome using **A)** an achiral catalyst and **B)** an asymmetric catalyst. **C)** The equations for calculating the ee from enantiomer mixtures is shown.

The success of preferentially producing one enantiomer is typically quantified using enantiomeric excess (ee) (**Figure 1.1 C**). Alternative metrics such as the enantiomer ratio (er) have also been proposed. This expresses enantiomer proportions as a ratio (**Figure 1.1 B**: er = 90:10).[10, 11] While ee was originally assessed by optical rotation measurements, modern analytical techniques, particularly chromatographic methods, allow direct quantification of enantiomers.[12] Despite recommendations to adopt er as the main metric, ee remains the predominant measure in the asymmetric catalysis literature for reporting enantioselectivity.[10, 12, 13]

Enzymes, metal complexes, and organocatalysts have emerged as the three most widely used platforms for the creation of efficient asymmetric catalysts.[14] They are commonly referred to as the 'three pillars of asymmetric catalysis' (**Figure 1.2**).[15-17] Although other approaches, such as heterogeneous asymmetric catalysts, have been investigated, they remain comparatively rare and often less successful.[18]

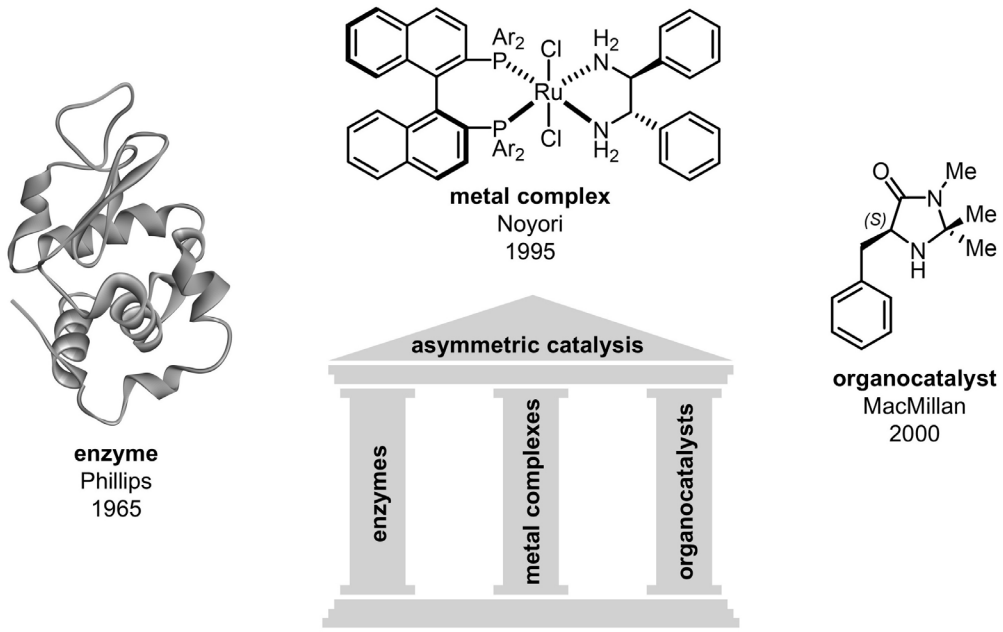

Figure 1.2 The three pillars of asymmetric catalysis, each illustrated with a representative example.[19-21]

1.1.2 Enzyme catalysis

Enzymes, nature's catalysts, have been unknowingly used by humanity for centuries as biocatalysts in food production, for example by the use of yeast in bread making or bacterial strains in cheese production.[22] Today, enzymes are widely applied in both research and industrial contexts.[23, 24]

Enzymes comprise long amino acid chains that fold into intricate three-dimensional structures through non-covalent interactions (**Figure 1.3**).[25, 26] The catalytically-active part of

an enzyme is referred to as the active site, which is often deeply buried within the structure.[27] Within the active site, multiple amino acid residues, often remote from one another in sequence space, come together to cooperatively achieve the chemical transformation, while also providing the chiral environment needed to exclusively form one enantiomer.[27-29] This cooperative architecture is often built from three amino acid residues and called a catalytic triad. A classic example is the catalytic triad of serine, histidine, and aspartic acid found in serine proteases (**Figure 1.3**).[30]

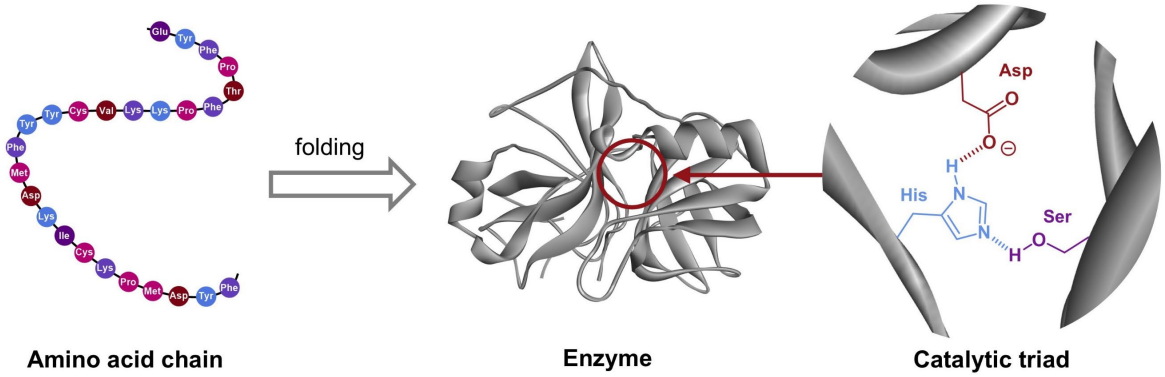

Figure 1.3 Schematic depiction of an amino acid chain folding into a three-dimensional enzyme.[31] The enzyme's active site, consisting of a catalytic triad of serine, histidine, and aspartic acid, is illustrated schematically.

Enzymes catalyse a diverse range of reactions, including carbon-carbon bond-forming and redox reactions, that are relevant to asymmetric synthesis particularly for the production of pharmaceuticals.[32-36] Many of these reactions use prochiral or racemic substrates, yet enzymes are capable of exclusively producing one enantiomer of the product (ee > 99.9%), making them invaluable tools in stereoselective synthesis.[37]

Beyond their exceptional enantioselectivity, enzymes are environmentally friendly and energy efficient.[38] As they are derived from biological systems, they usually operate under mild conditions: aqueous media, ambient temperatures, and physiological pH.[22, 39] Enzymes can also show outstandingly high reaction rates.[40]

However, enzymatic catalysis often faces one fundamental limitation: they are highly specific for a single substrate. Their catalytic efficiency is generally not transferable across a broad range of substrates, especially unnatural ones.[41-43] This limitation has been partially addressed through advances in directed evolution and protein engineering.[42, 44]

1.1.3 Chiral metal complexes

Following the pioneering work of Noyori, Knowles, and Sharpless in the mid-1960s, who were jointly awarded the Nobel Prize in Chemistry in 2001, chiral metal complexes have been firmly established as the second pillar of asymmetric catalysis.[45-47] Chiral metal complexes consist of a metal ion stabilised by the coordination of multiple chiral and/or achiral organic ligands (**Figure 1.4 A**).[2, 4] The metal centre is responsible for driving the chemical transformation, and is typically a transition metal such as palladium, rhodium, ruthenium, iridium, manganese or copper.[45, 48, 49] Main-group metal and metalloid complexes have been reported, yet they remain comparatively underexplored.[50, 51] The ligands stabilising the metal centre often feature bidentate or multidentate coordination sites, primarily based on phosphine, oxygen and nitrogen-donor ligands, that form chelates to enhance the overall stability of the complex.[52]

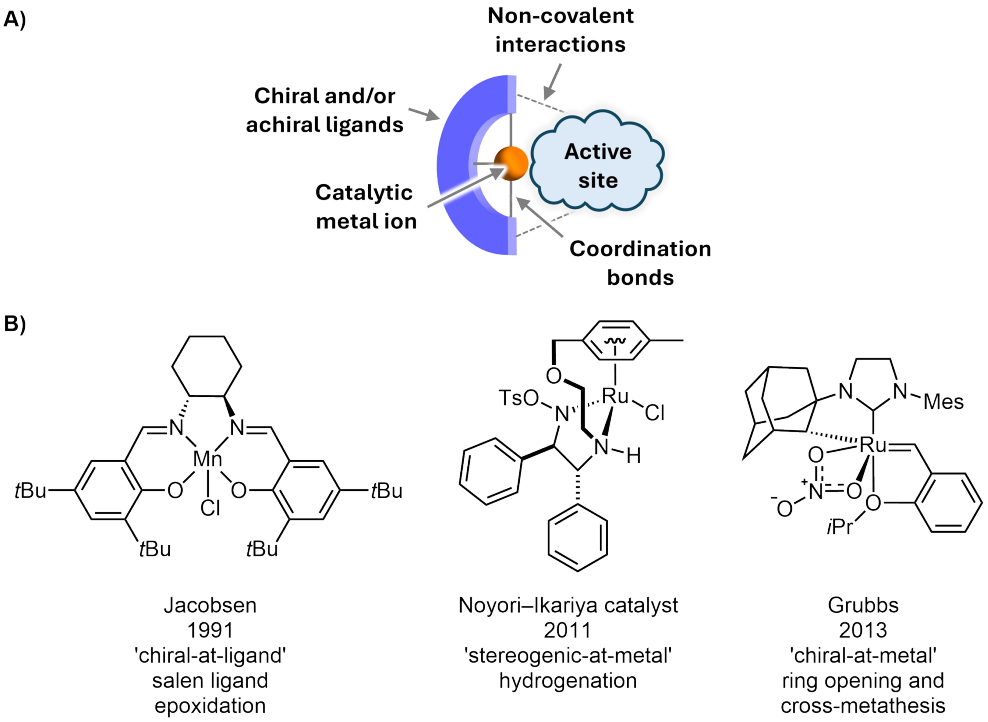

Figure 1.4 A) Schematic depiction of the general structure of asymmetric metal complex catalysts and **B)** depiction of examples of chiral metal complexes.[53-55]

The chirality of metal complexes is generally achieved by using one of two strategies: (i) the 'chiral-at-ligand' or (ii) the 'stereogenic-at-metal' approach.[14, 49] Most research efforts have focused on the first strategy, where the overall chirality of the complex arises from the chiral ligands alone.[16, 50] This led to the development of a wide variety of such ligands, with many high-performing catalysts featuring 'privileged' ligands, such as BINAP, BINOL, or salen (**Figure 1.4 B** first example).[56-58] The term 'privileged' was earned because of their broad applicability across numerous reactions and mechanistic classes.[14] In contrast, the 'stereogenic-at-metal' approach was historically underexplored but has gained increasing attention in the last

two decades.[59] In this strategy, the metal ion itself serves as the stereogenic centre, with chirality arising from the asymmetric spatial arrangement of both chiral and/or achiral ligands around the metal.[59] Complexes in which the chirality originates from a stereogenic metal centre coordinated exclusively by achiral ligands are referred to as 'chiral-at-metal' complexes (**Figure 1.4 B** third example).[49, 60] This is typically achieved using multidentate ligands that coordinate to the metal centre in an asymmetric fashion and thus create a defined chiral geometry at the metal centre.[49]

Asymmetric hydrogenation has become one of the most successful applications, with prominent examples such as the Noyori-type ruthenium complexes (**Figure 1.2** and **Figure 1.4 B** second example) demonstrating high activity and enantioselectivity (ee ≥ 98%) across diverse substrates.[61] These reactions are widely utilised in the synthesis of chiral pharmaceuticals, agrochemicals, and fine chemicals.[62] Besides hydrogenations, asymmetric metal complexes catalyse a range of synthetically important transformations, including C–C bond-forming reactions, isomerisations, epoxidations, and many more, often with excellent enantioselectivities commonly exceeding ee = 95%.[14, 46, 49]

This broad applicability is arguably their greatest strength over enzymatic and organocatalysts: a single 'privileged' chiral metal complex can achieve excellent enantioselectivities across mechanistically different reactions and a wide substrate range.[14] Small and synthetically easy to achieve modifications to these 'privileged' ligands further make it possible to tailor the catalysts to fit challenging substrates.[58, 63] Additionally, they show high catalytic efficiency, typically requiring catalyst loadings of less than 1 mol%, while maintaining high reaction rates.[64, 65]

Despite their strengths, some limitations exist. The inherent toxicity of certain transition metals presents challenges for pharmaceutical synthesis, as residual catalyst contamination must be rigorously avoided.[66] In addition, their homogeneous nature complicates catalyst recovery and recycling, and combined with the high cost of noble metals can limit scalability in cost-sensitive settings.[67]

Nevertheless, the combination of their broad applicability and high enantioselectivity firmly establishes chiral metal complexes as one of the 'three pillars' of asymmetric catalysis.[14]

1.1.4 Asymmetric organocatalysis

Asymmetric organocatalysts, recognised as the third pillar of asymmetric catalysis, emerged in the early 2000s as a feasible alternative to enzymes or chiral metal complexes.[17, 68, 69] These catalysts are low molecular weight, metal-free, organic molecules that catalyse chemical transformations through substrates interacting with their functional groups.[70] Some notable mentions are amines,[71] carboxylic/phosphoric acids,[72] guanidines[73, 74] and ureas/thioureas,[75, 76] but the list is ever growing (**Figure 1.5 B**). Some systems even feature two catalytic sites, often a Brønsted or Lewis base together with a hydrogen bond donor catalyst, that operates cooperatively as a bifunctional catalyst.[75, 77] The organic scaffold that possesses the catalytically active groups must itself be chiral. This creates an ideal environment for the transfer of stereochemical information during the reaction (**Figure 1.5 A**).[2]

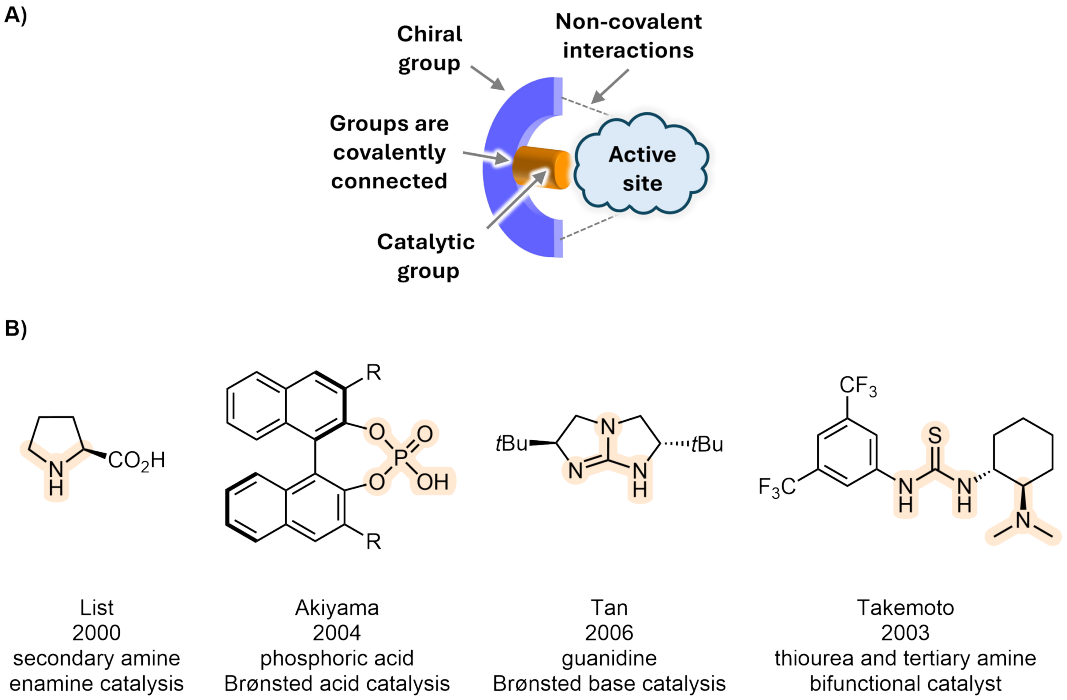

Figure 1.5 A) Schematic depiction of the general structure of asymmetric organocatalysts and **B)** depiction of examples of asymmetric organocatalysts featuring various catalytic functional groups.[77-80]

Arguably the most famous example of an asymmetric organocatalyst is the naturally occurring amino acid L-proline. It is capable of catalysing a range of reactions *via* enamine catalysis, achieving exceptional enantioselectivities of > 95% ee.[71] L-Proline became famous through the work of Benjamin List, who received the Nobel Prize in Chemistry in 2021 for his work using the amino acid as an asymmetric organocatalyst for aldol reactions.[78, 81] Benjamin List shared the Nobel Prize with David MacMillan, who independently developed imidazolidinone-based catalysts (**Figure 1.2**).[20] These MacMillian catalysts activate α,β-unsaturated aldehydes *via* iminium ion formation toward nucleophilic addition reactions such

as Diels-Alder reactions, or Michael additions, achieving high enantioselectivities across a broad substrate range.[20, 82]

Building on these landmark contributions, nearly all reaction classes previously dominated by enzymatic or metal-based catalysis have since been explored using organocatalysts.[16, 17, 70, 83] Compared to enzymes and chiral metal complexes, asymmetric organocatalysts offer several key advantages. Being metal-free, they generally show lower toxicity than transition metal-based catalysts, an important consideration for the synthesis of pharmaceuticals.[9, 69] They usually are stable under atmospheric conditions and compatible with aqueous media, making them more universally applicable than sensitive metal complexes that must be handled under inert conditions.[69] They are also readily modified using standard synthetic methods, and unlike enzymes, do not require lengthy evolution processes. However, their reaction rates are typically slower, and relatively high catalyst loadings, often up to 30 mol% are required to achieve acceptable conversions.[84]

1.1.5 Heterogeneous asymmetric catalysts

The three classes of asymmetric catalysts discussed thus far — enzymes, chiral metal complexes, and organocatalysts — are generally homogeneous, operating in solution.[4] In contrast, heterogeneous asymmetric catalysts, typically solids used in solvent or gas-phase reactions, remain comparatively underdeveloped,[85] as they often struggle to achieve enantioselectivities comparable to their homogeneous counterparts.[18, 86] The motivation behind their development is to combine the high enantioselectivity of asymmetric catalysts with the recyclability and easy separation of heterogeneous catalysts. Two main strategies have been developed:

(i) immobilisation of a homogeneous asymmetric catalyst onto a solid support (**Figure 1.6 A**),[87] and

(ii) generation of a chiral environment on a metal surface through the adsorption of chiral modifiers (**Figure 1.6 B**).[88]

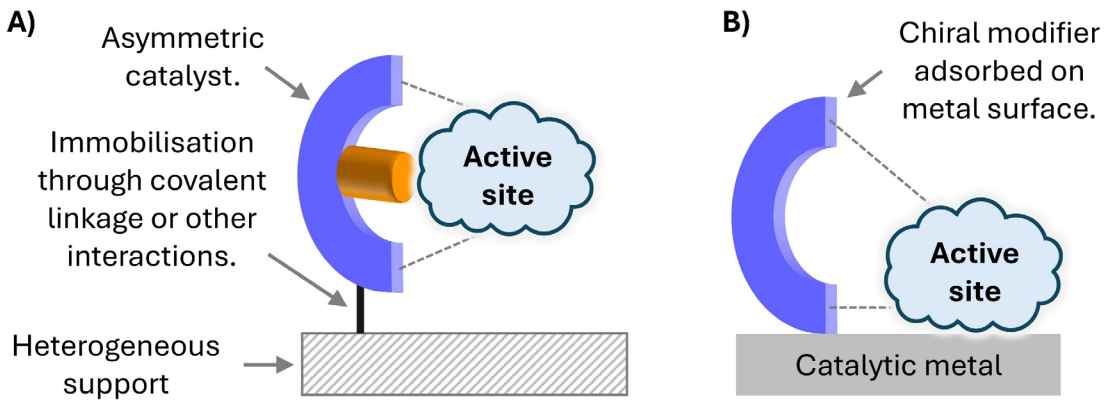

Figure 1.6 Schematic illustration of two approaches to heterogeneous asymmetric catalysis: **A)** immobilisation of an asymmetric homogeneous catalyst on a solid support, and **B)** surface modification of a metal catalyst by adsorption of a chiral modifier.

Immobilisation of a homogeneous asymmetric catalyst is the most widely applied method and can be achieved either through covalent linkage to a solid support or by non-covalent interactions (**Figure 1.6 A**).[18, 87] Covalent immobilisation usually requires additional functionalisation of the catalyst, which can be synthetically challenging and/or reduce its effectiveness. Immobilisation through non-covalent interactions such as van der Waals interactions, hydrogen bonding or electrostatic forces has the benefit that often no extensive modification of the catalyst is required.[89] However, as the catalyst–support interaction is comparatively weak, catalyst leaching becomes a major concern.[86, 90] This raises the possibility that the observed enantioselectivity may actually originate from the leached species acting in solution, rather than from the heterogeneous catalyst. For individual systems, immobilisation has proven effective, and high enantioselectivities have been reported. One example is the use of immobilised BINAP–Ru complexes on magnetite (Fe_3O_4) nanoparticles, used in the asymmetric hydrogenation of ketones.[91] In this case, comparable enantioselectivities (ee = ~85-98%) to the homogeneous analogue were observed, while catalyst recyclability was also enabled. Yet, in most cases, enantioselectivities are lower than those observed with the corresponding homogeneous catalysts.[18, 85, 88]

The second strategy, adsorbing chiral modifiers onto metal surfaces, or inversely, depositing metals onto chiral supports (**Figure 1.6 B**), remains comparatively underdeveloped, as it suffers significantly from site heterogeneity.[88, 92] For example, the adsorption of chiral molecules onto a metal surface is difficult to control, resulting in inconsistent chiral environments across the surface. This leads to differences in active site accessibility, which ultimately causes diminished or unreliable enantioselectivities.[18, 85, 88]

1.1.6 Achieving high enantioselectivity: a non-trivial challenge

Reactions that produce chiral molecules but are catalysed by an achiral catalyst result in a racemic mixture. This is because the energy, $\Delta G^{\ddagger}$, of the transition states leading to each stereoisomer is inherently identical.[4] Asymmetric catalysts achieve selectivity for the preferred enantiomer by lowering the energy of the transition state leading to it.[93] This produces a free energy difference ($\Delta\Delta G^{\ddagger}$) between the transition states leading to the two enantiomers (**Figure 1.7 A**).[11, 93-95] The magnitude of $\Delta\Delta G^{\ddagger}$ defines the ee of the product. As such, $\Delta\Delta G^{\ddagger}$ and ee are interchangeable, with a specific ee correlating to a precise $\Delta\Delta G^{\ddagger}$ at that temperature.[93, 95] Noteworthy, the temperature is an important factor influencing $\Delta\Delta G^{\ddagger}$. The same $\Delta\Delta G^{\ddagger}$ that correlates to a high ee at low temperatures correlates to lower ee at high temperatures.[95]

$$ee[\%] = \frac{1-e^{\frac{-\Delta\Delta G^{\ddagger}_{R/S}}{RT}}}{1+e^{\frac{-\Delta\Delta G^{\ddagger}_{R/S}}{RT}}} \cdot 100 \qquad \text{or} \qquad \Delta\Delta G^{\ddagger}_{R/S} = -RTln\left(\frac{100+ee}{100-ee}\right)$$

The non-linear relationship between ee and $\Delta\Delta G^{\ddagger}$ means that moderate $\Delta\Delta G^{\ddagger}$ values are sufficient to attain good ee values (**Figure 1.7 B**). Exceptionally high ee values (≥99%) require much greater energetic discrimination between the two transition states.[95] As a result, achieving such levels of enantioselectivity remains a non-trivial challenge.

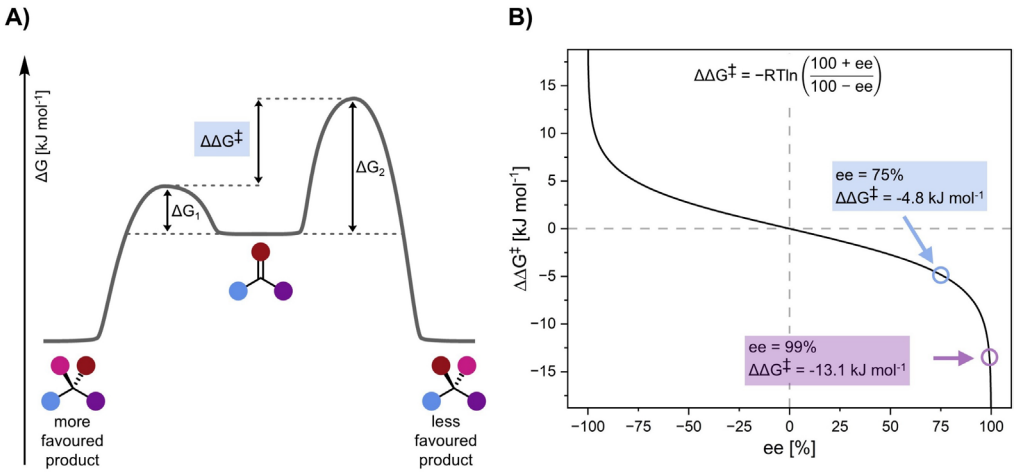

Figure 1.7 A) Schematic depiction of the potential free energy surface of a reaction catalysed by an asymmetric catalyst, producing one enantiomer preferentially. The difference in free energy ($\Delta\Delta G^{\ddagger}$) between the corresponding transition states is highlighted. **B)** Graphical representation of the non-linear correlation between ee and $\Delta\Delta G^{\ddagger}$ at 25 °C.

A 'perfect' asymmetric catalyst would simultaneously deliver both excellent enantioselectivity and broad applicability across different substrates and reaction types. In practice, however, most catalysts fall short in at least one of these two areas. To improve performance and get closer to the 'perfect' case, two main strategies are typically employed:

(i) modification of the catalyst structure to improve enantioselectivity for a defined set of substrates and/or

(ii) screening a diverse reaction and substrate range to identify suitable matches.

Both strategies aim to optimise catalyst enantioselectivity and scope, but they also require considerable experimental effort.

Strategy (i) commonly leads to increasingly complex catalysts, which require more sophisticated synthetic methods.[52, 58, 96] However, since the catalyst is simultaneously responsible for both activation of the reaction and induction of chirality, its optimisation typically has the most significant impact. As a result, this approach is often the first step in attempts to achieve high enantioselectivity, and considerable effort has been devoted over the decades to the rational design of catalysts.[61, 68]

A strong example of this strategy was reported by Rein *et al.*, who investigated a generality-oriented optimisation of aminoxyl radical catalysts for the enantioselective desymmetrisation of meso-diols to obtain chiral lactones.[97] They synthesised over 70 distinct chiral aminoxyl radical catalysts featuring small peptide chains (**Figure 1.8 A**) aiming to improve the general enantioselectivity for a defined set of 15 model substrates (**Figure 1.8 B**). The result was the remarkable progression from low and substrate-specific ee values to a broadly effective catalyst with excellent enantioselectivities (ee > 90%) for almost the entire substrate set. However, with over 70 catalysts synthesised, this was extremely labour intensive.

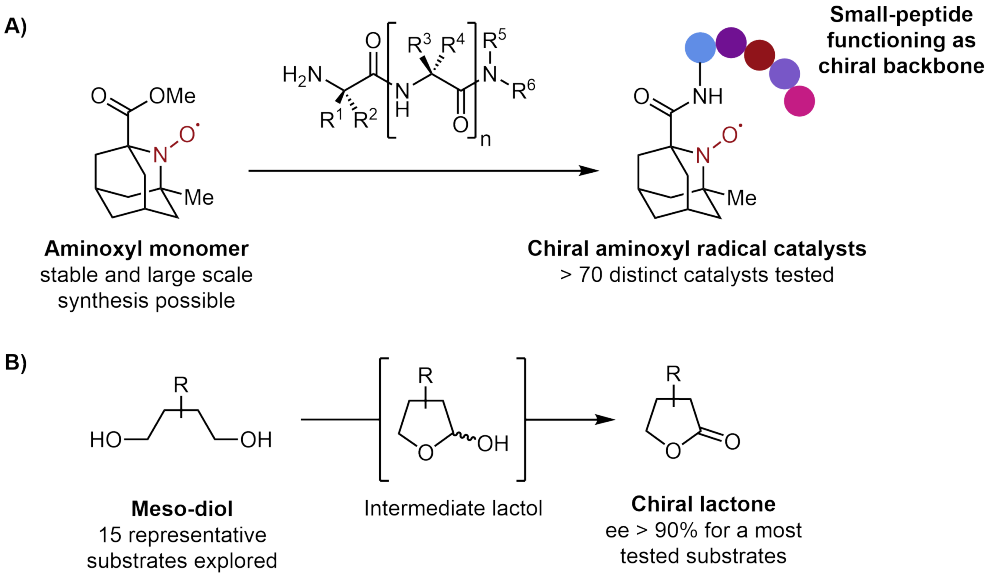

Figure 1.8 A) Reaction scheme for the synthesis of chiral aminoxyl radical catalysts. Small peptides are coupled with an aminoxyl monomer to create a library of >70 catalysts. **B)** Reaction scheme for the enantioselective desymmetrisation of meso-diols to chiral lactones.

The second strategy (ii) typically requires little synthetic effort but demands perseverance, as it involves performing numerous reactions during condition screening and optimisation. While this can greatly enhance enantioselectivity for a specific catalyst, improvements rarely translate across different catalysts, especially with differing activation modes.[98] Condition

optimisation usually includes solvent and substrate screening, with the substrate scope often being limited by commercial availability. A deliberate structural modification of the substrate is rare but can in certain cases be highly fruitful.

The strength of this strategy was beautifully demonstrated by Huang *et al.,* who investigated the chiral phosphoric acid-catalysed synthesis of amino acids *via* the decarboxylative protonation of aminomalonic acids (**Figure 1.9**).[99] Initially they attempted strategy (i) and screened over 45 different chiral phosphoric acids for their enantioselectivity for a small set of model substrates. However, even after this extensive effort only unsatisfactory enantioselectivities (ee < 60%) were achieved. In response, they shifted to strategy (ii), selecting a single catalyst (**Figure 1.9**, catalyst shown) and focusing on substrate screening. By introducing an 'anchoring group' to enhance catalyst-substrate interactions, they observed significant improvements: ee values between 90-98% were obtained across a diverse substrate range, without the need for further catalyst modifications.

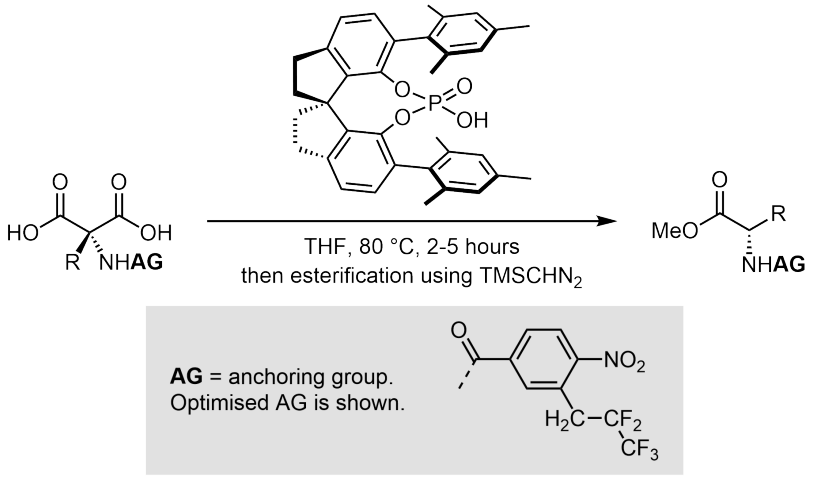

Figure 1.9 Reaction scheme for the chiral phosphoric acid-catalysed synthesis of amino acids *via* the decarboxylative protonation of aminomalonic acids. The amine is shown functionalised with an anchoring group.

Both examples beautifully illustrate the extensive effort required to master the non-trivial challenge of achieving excellent enantioselectivities across a broad substrate scope. Regardless of whether catalyst modification or substrate screening is pursued, the optimisation process demands significant time and resources.

This raises a fundamental question: is it possible to reimagine the approach to catalyst design to make their development simpler and less labour intensive? This ambitious goal lies at the core of the presented work.

1.2 Asymmetric catalysis: the novel approach of remote asymmetric induction

1.2.1 The concept of remote asymmetric induction: breaking design limitations of conventional asymmetric organocatalysts

When attempting to reimagine the design of asymmetric catalysts, the key feature that must be retained in any alternative design is the ability to induce chirality - that is, to transfer stereochemical information from a chiral source to the reaction substrates. For this to occur, the catalytic unit and the chiral element must simultaneously interact with the reaction substrates during the stereo-controlling reaction step. This requires their close spatial proximity.

The fundamental design limitation shared by all conventional asymmetric organocatalysts is that the catalytic unit and the chiral element are connected by covalent bonds (**Figure 1.10 A**).[2, 48] This is due to synthetic practicality: it is exceedingly difficult to prepare catalysts where these motifs are disconnected and repositioned at will. However, a catalyst platform in which the catalytic and chiral motifs are not covalently connected but still engage simultaneously with the substrates would represent a major conceptual advance and offer unprecedented flexibility. Such a catalyst design would allow the independent synthesis and optimisation of both motifs, creating a highly modular and adaptable catalyst platform. In comparison with conventional catalysts, this could accelerate catalyst development and optimisation.

Translating this concept to actual catalyst design, one possible strategy to achieve full synthetic independence of the catalyst and chiral unit is by anchoring them individually to 'backbone' molecules (**Figure 1.10 B**). The backbone self-assembles through weak interactions bringing the catalyst and chiral unit into close spatial proximity. This positions the functionalities to form an active site where they interact simultaneously with the reaction substrates resulting in chiral induction (**Figure 1.10 C**). As the chiral induction occurs remotely through space, we define this new, unprecedented concept of asymmetric catalysis as 'remote asymmetric induction' (RAI) catalysis.

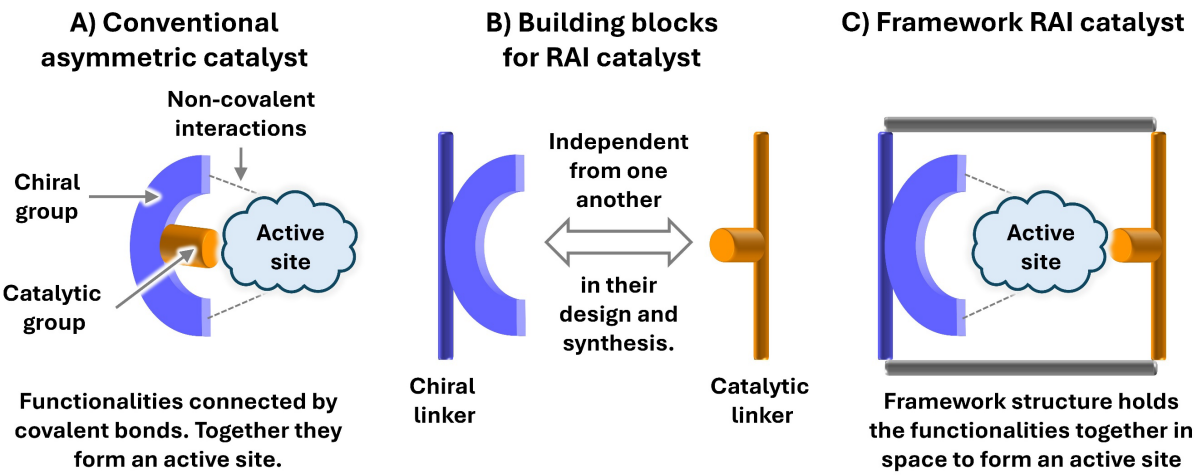

Figure 1.10 Schematic representation of **A)** a conventional asymmetric catalyst, **B)** independently synthesised catalytic and chiral building blocks of **C)** an assembled RAI catalyst framework.

One potential platform for RAI catalyst design are polymers, which can theoretically co-assemble and fold to form proximity-based active sites. However, the inherent difficulty of controlling polymer folding and assembly limits this strategy. This would most likely result in random rather than cooperative arrangements of the catalyst and chiral moieties.

Alternative platforms for catalyst design that avoid this limitation are structurally defined scaffolds, such as molecular cages or metal-organic frameworks (MOFs). The building blocks (linkers) of these architectures self-assemble through coordinative interactions with metal ions to form highly ordered and symmetrical structures. Due to the inherent spatial precision of these architectures, the pre-determined positioning of attached functional motifs becomes possible by selecting materials with appropriate framework geometries. This enables the deliberate construction of active sites that potentially facilitate asymmetric catalysis *via* remote, but spatially controlled interaction of catalytic and chiral functionalities.

Using MOFs as the platform for the development of RAI catalysis presents distinct advantages over molecular cages. MOFs are solids, and therefore catalysis in solution is heterogeneous. This makes separation and recycling of the catalyst after the reaction feasible, unlike in homogeneous catalysis (e.g., molecular cages), where catalyst separation can be difficult.[18, 100, 101] Additionally, a defining strength of MOFs — particularly multicomponent MOFs (MC-MOFs) — is their modularity. Each linker is synthesised independently, typically by simple or literature-known routes, and framework assembly is reliably tolerant to variations in linker functionality.[102] This robustness enables tuning of catalyst properties through small, targeted changes to a single linker, without altering the overall structure. For example, replacing the catalyst linker allows a completely different reaction to be carried out using the same platform. This modularity combined with their robustness to various solvents and temperatures makes the MC-MOFs an ideal platform for RAI catalysts.

1.2.2 Multicomponent metal-organic frameworks: the ideal platform for the implementation of the RAI-concept

MOFs are porous, crystalline, 3D coordination networks built of organic linkers and metal ions or clusters.[103] The linkers are typically *exo*-bidentate or multidentate carboxylate or nitrogen-donor molecules that connect the metal nodes through coordination bonds. Since the first reported MOF, MOF-5, introduced by Yaghi *et al.* in 1999,[104] the number of publications reporting new structures or applications of existing ones is ever growing (**Figure 1.11**). Most MOFs are binary systems, consisting of a single type of linker and metal node. Their characteristics such as permanent porosity, high surface area and tunable pore environment make them a sought after platform for applications like gas absorption and separation,[105-107] sensing[108, 109] or catalysis.[110-113] Notable examples such as HKUST-1,[114] UIO-67,[115] and ZIF-8[116] have become widely studied due to their exceptional chemical stability.

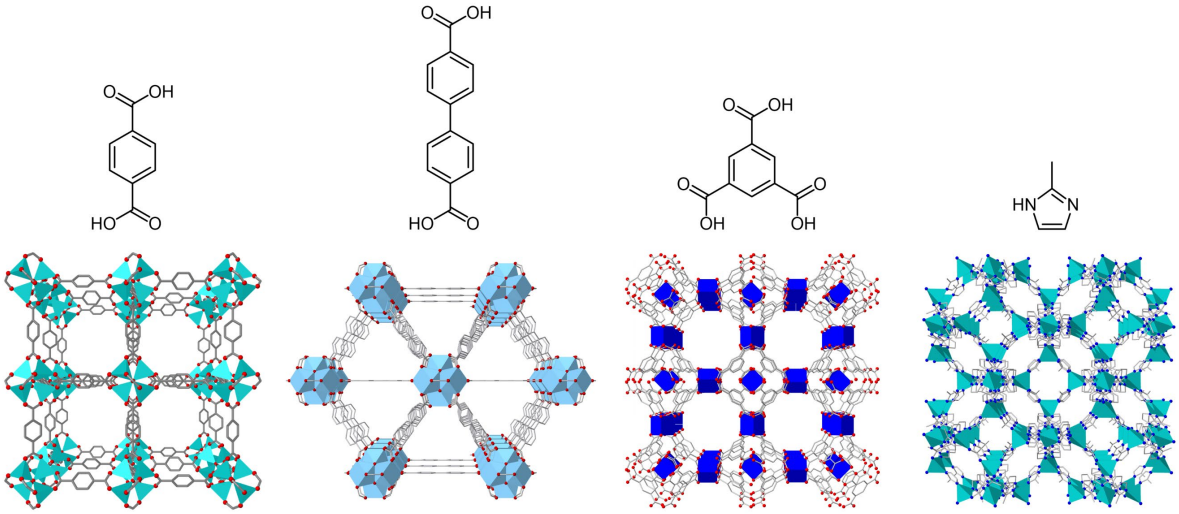

Figure 1.11 Overview of prominent and extensively studied MOFs. Their respective linkers are shown. Hydrogen atoms and solvent molecules are omitted for clarity.

The key characteristic that makes MOFs especially suitable to be the platform for RAI catalysis is that they follow the isoreticular principle.[102] This principle allows the modification of the size or functionality of the building blocks while retaining the original framework topology. Although conventional binary MOFs, such as MOF-5, allow for functional diversity in their framework, they are not suitable for the development of the RAI concept. In these systems, catalytic and chiral groups can be introduced by separately functionalising the same linker backbone. Upon co-assembly, the indistinguishable nature of the backbone results in a random distribution of the functionalities throughout the framework, yielding a multivariate MOF[117] (**Figure 1.12**). This lack of positional control makes it impossible to control whether

both functionalities occupy the same pore, limiting the efficiency of cooperative catalysis within a shared confined space.

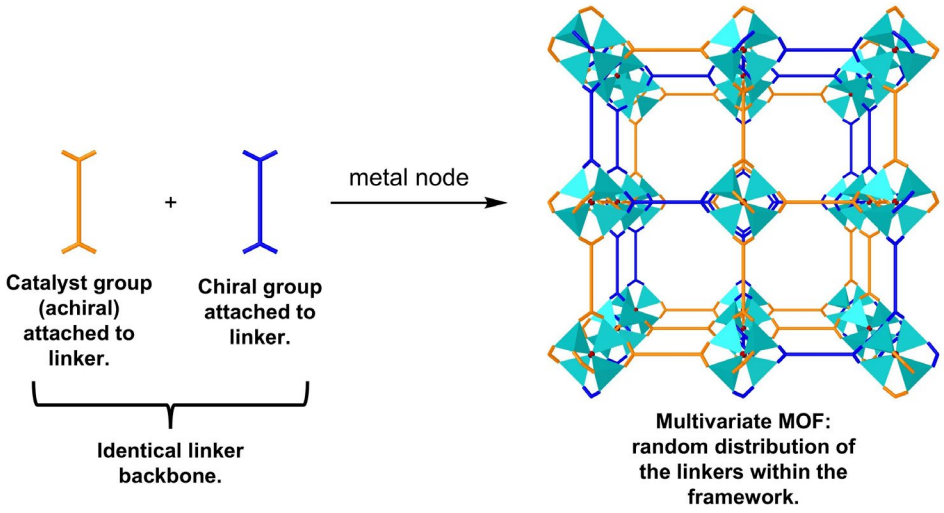

Figure 1.12 Binary, multivariate MOF as the platform for RAI catalysis leads to a random distribution of functionalised linkers throughout the framework, with no control over the position of the functionalities.

This limitation can be avoided by using a special class of MOFs, multicomponent MOFs (MC-MOFs). MC-MOFs are built from several linkers with distinct topologies that co-assemble into the same lattice. Each distinct linker occupies a specific position within the framework without disorder or randomness. Therefore, if one linker is functionalised with a catalyst moiety and a second distinct linker with a chiral group, they will not occupy the same position in the framework and the location of the groups will be known.

The first MC-MOF with three distinct organic ligands, MUF-7 (MUF = Massey University Framework) was reported in 2013.[118] MUF-7 is a quaternary MC-MOF, built up from Zn_4O clusters and three distinct linkers: a 1,4-benzenedicarboxylic acid (bdc), a biphenyl-4,4′-dicarboxylic acid (bpdc), and a tritopic tricarboxylic acid, 1,3,5-benzenetricarboxylic acid (btb) (**Figure 1.13**). MUF-7 is described by the formula, $[Zn_4O(btb)_{1.33}(bpdc)_{0.5}(bdc)_{0.5}]$. Four distinct pores are defined by the network: three tetrahedral micropores and one dodecahedral mesopore. All three tetrahedral micropores are constructed from four tritopic linkers connecting two linear linkers orthogonally facing each other. Each tetrahedral pore is host to a different linker pair, bpdc-bdc in **B**, bdc-bdc in **C** and bpdc-bpdc in **D**, resulting in different environments for each pore. The dodecahedral mesopore **A** is composed of eight tritopic linkers connecting three pairs of bpdc and bdc, facing each other across the pore void space. Since the linear likers that face each other in the pore have different lengths, the mesopore is slightly jagged.

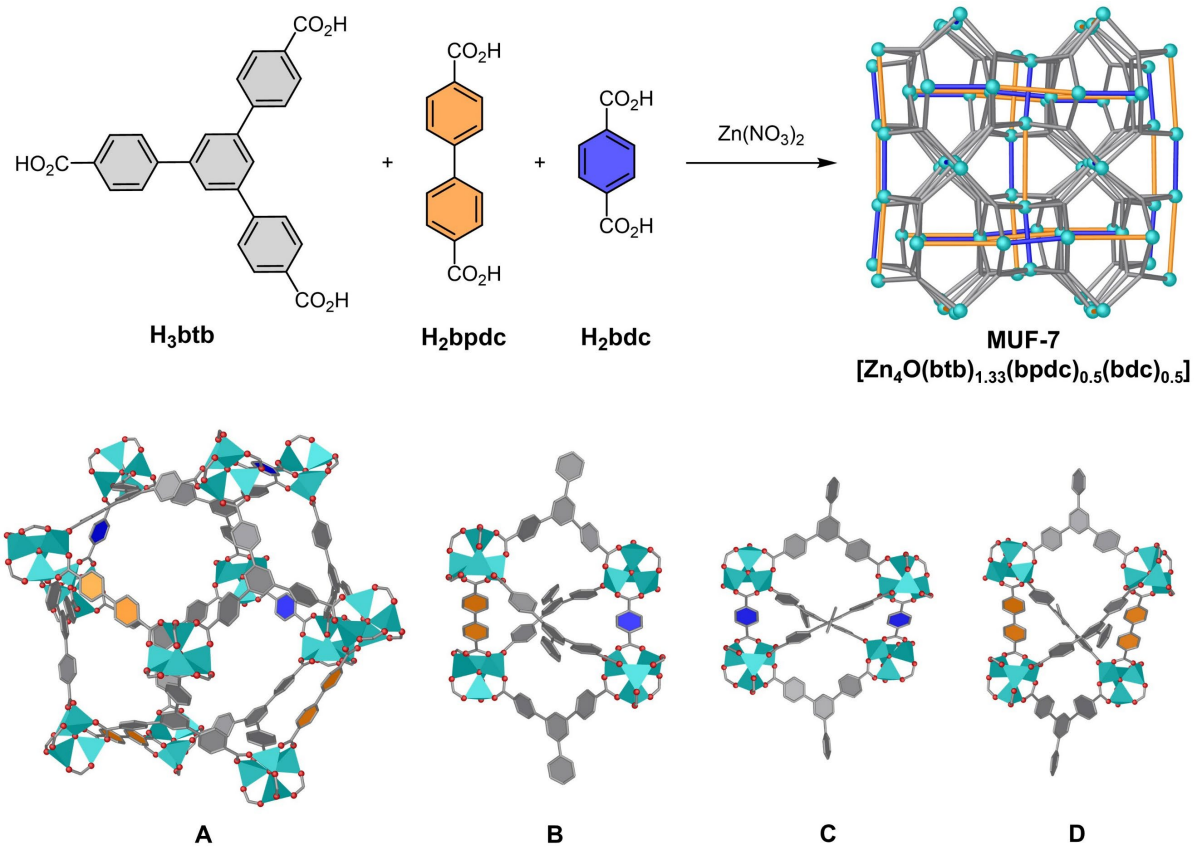

Figure 1.13 Schematic representation of the synthesis of MUF-7 (top). The four distinct pores found in MUF-7 are shown (bottom).

As the successor to MUF-7, the MUF-77 series was reported in 2015.[119] MUF-77 is majorly built of the same building blocks as MUF-7, but differs in that the tritopic ligand is not btb, but a tritopic truxene tricarboxylic acid, for example 5,5,10,10,15,15-hexamethyltruxene-2,7,12-tricarboxylate (hmtt) (**Figure 1.14**). This difference makes MUF-77 superior in its stability against atmospheric moisture.[119] The structure is defined by the formula, $[Zn_4O(hmtt)_{1.33}(bpdc)_{0.5}(bdc)_{0.5}]$. MUF-77 has one type of tetrahedral micropore and two dodecahedral mesopores. The tetrahedral micropore **III** is built of four tritopic linkers connecting one bdc and bpdc orthogonally facing each other. Both dodecahedral mesopores are constructed of eight tritopic linkers connecting six linear linkers facing each other across the pore void in pairs of two. The pairs of linear linkers in the mesopores are of the same kind. In pore **I** only bpdc linkers are incorporated, while pore **II** is host to only bdc linkers. This difference in length of the linear linkers leads to a slight pore size difference of the two mesopores.

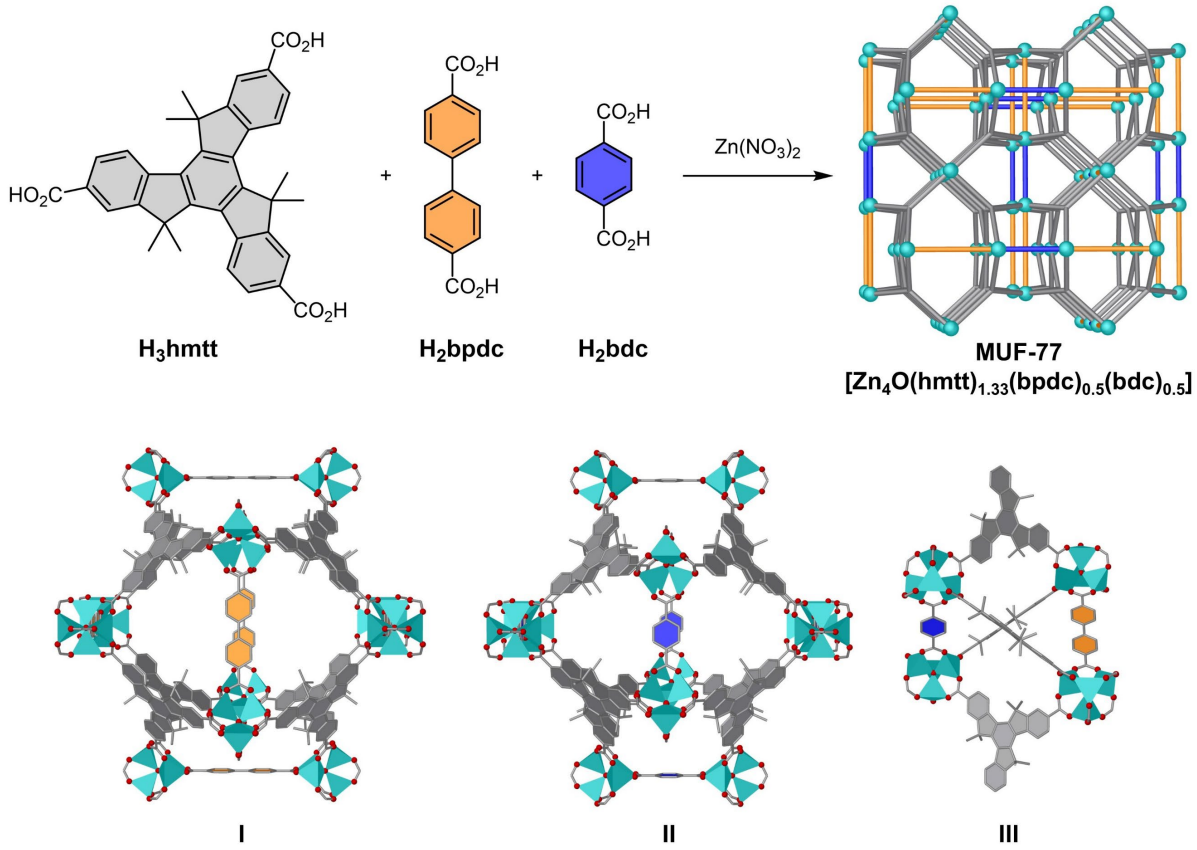

Figure 1.14 Schematic representation of the synthesis of MUF-77 (top). The three distinct pores found in MUF-77 are shown (bottom).

Transferring the RAI-concept to these quaternary MC-MOFs, achiral catalysts and chiral moieties can be individually attached to the distinct linkers to be integrated together into the framework. Due to synthetic practicability, the focus is set on attaching them to the linear linkers, bdc and bpdc, instead if the tritopic truxene. Owing to the precision of framework assembly, these functionalised linear linkers reliably frame the same pore, such as tetrahedral micropore **III** in MUF-77 (**Figure 1.15**), effectively defining a spatially confined active site. Substrates infiltrate the framework channels, reach the active sites, and interact with the catalyst, promoting a chemical transformation. Simultaneously, the remote chiral element will orient the substrates using noncovalent interactions to achieve chiral induction. Accomplishing chiral induction in this way is unprecedented. Yet it is feasible: noncovalent interactions are capable of enhancing stereochemical effects in conventional catalysts.[120-125]

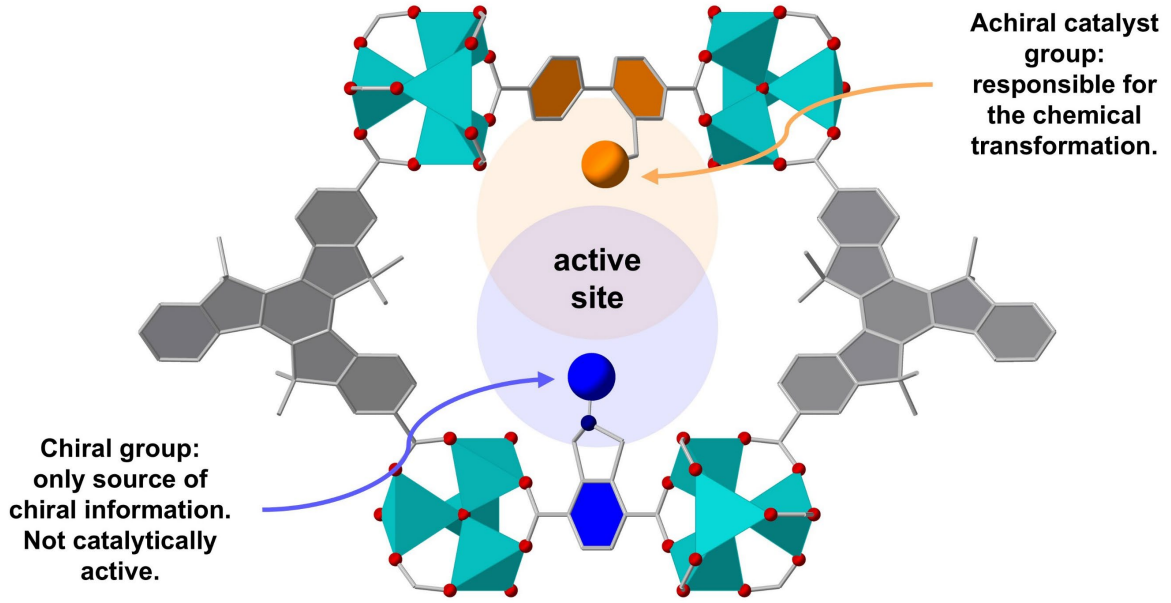

Figure 1.15 Schematic representation of an RAI active site in the tetrahedral micropores present in MUF-77.

1.2.3 Proof of principle: The RAI-concept works!

A series of MUF-77 catalysts were reported in 2017.[126] In this study, the established chiral organocatalyst L-proline was attached to either one of the linear linkers (bdc or bpdc) as the catalyst for aldol reactions with acetone (**Figure 1.16**). To change the chemical environment of the prolinyl group, a set of bulky achiral functional groups (shown as a white sphere in **Figure 1.16**) were attached to the other linear linker, acting as modulators. Noticeable changes in both ee and reaction rate were observed, depending on the size of the achiral functional group. The change in reaction rate is easily explained by the size differences of the functionalities as increasing the filling of the pores slows the rate of diffusion. Yet, the huge change, and in some cases even the complete reversal in ee, was hard to explain, given that the prolinyl group was the only source of chiral information and was not changed during the experiments. This finding highlighted that modulating the chemical environment in close proximity to the catalyst centre has a major influence on the chiral information of the product.

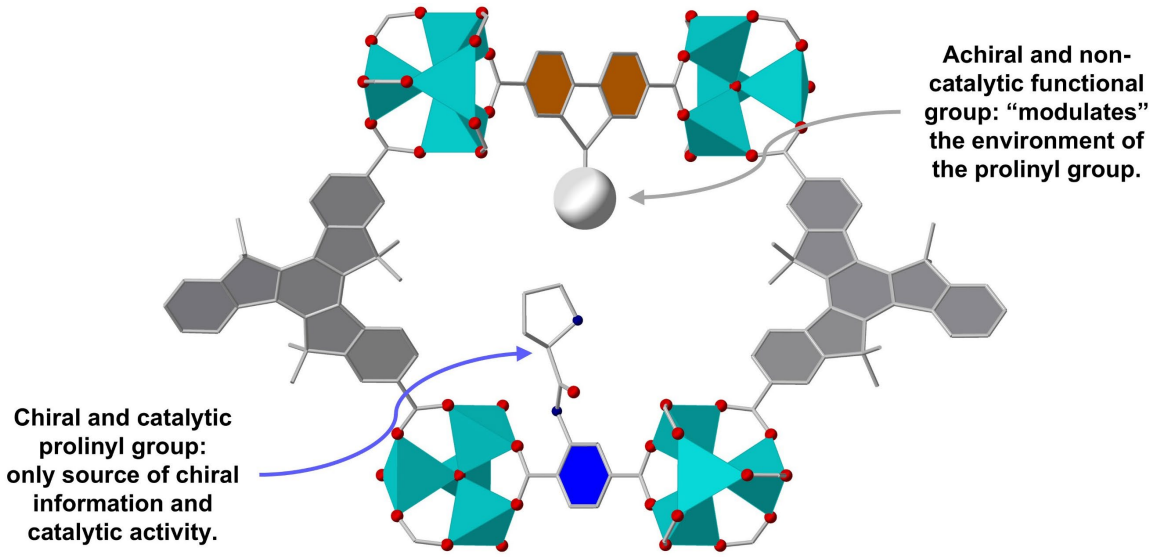

Figure 1.16 Schematic representation of a tetrahedral micropore present in MUF-77 equipped with a chiral and catalytic prolinyl group and an achiral and non-catalytic functional group that "modulates" the environment of the pore.

Inspired by these findings, the concept of RAI was first developed and tested by former PhD student and postdoctoral fellow Dr Seok June Lee. Dr Lee attached an achiral guanidine moiety (**Figure 1.17**, highlighted in orange) to the longer linear linker, bpdc, and integrated this achiral catalyst linker into the MUF-77 structure. The resulting achiral MOF catalyst showed catalytic activity for the Henry reaction of functionalised benzaldehydes with nitromethane. As no chiral information was present within the MOF structure, a racemic product mixture (ee = 0%) was obtained. Subsequently, by attaching a chiral - but not catalytically active - oxazolidinone functionality (**Figure 1.17**, highlighted in blue) onto the small linear linker, bdc, a distinct ee was observed. Reversing the stereochemistry of the chiral linker also reversed the ee of the product. These experiments provide a clear proof of concept for the approach of RAI in MUF-77 and form the foundation of this work. Building on these results, Dr Lee expanded the family of chiral oxazolidinone linkers and explored the effect of different solvents, alongside the substrate scope of benzaldehydes, on the ee of the Henry reactions. The highest ee values observed were ±35%.

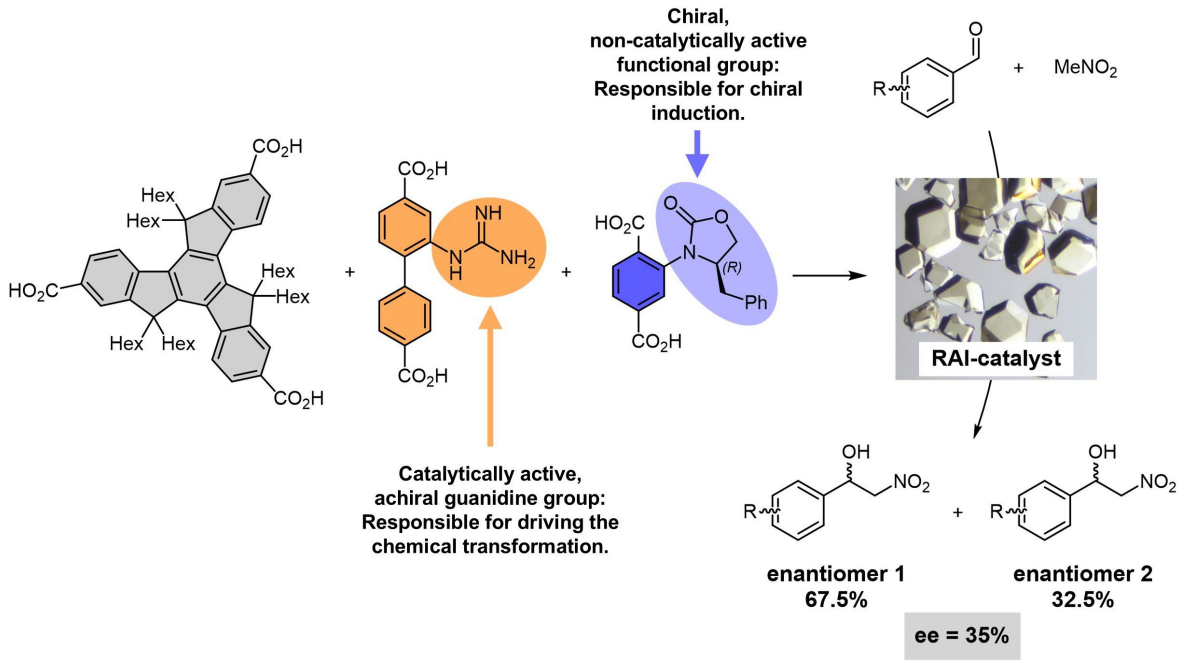

Figure 1.17 Schematic illustration of the synthesis of an RAI catalyst used for the Henry reaction between functionalised benzaldehydes and nitromethane, yielding an ee of up to 35%.

A particularly noteworthy finding from these experiments was that the linker combination of truxenes, the achiral guanidine-functionalised bpdc, and different chiral oxazolidinone-functionalised bdc's did not only form the expected MUF-77 topology but also a MUF-7 type structure or mixtures of both topologies simultaneously (**Figure 1.18**). Extensive experience within the Telfer research group has previously shown that MOFs constructed from truxene-based linkers typically adopt the MUF-77 topology. Yet, in exceptionally rare cases, specific linker combinations lead to the formation of a MUF-7 topology, despite the presence of the more rigid truxene instead of the more flexible btb that is present in the original MUF-7. These MOFs represent an intermediate between MUF-7 and MUF-77, maintaining the linker combination associated with MUF-77 while adopting the MUF-7 topology. In the context of RAI catalysis, this structural variation had a significant impact on the catalytic performance. MOFs constructed from the same linker set but existing in the different topologies produced notably different enantioselectivities. For the Henry reactions tested with these linker combinations, the MUF-7-type topology consistently yielded higher enantioselectivities than the corresponding MUF-77 structure. Although the underlying reasons for the observed differences and the precise stereo control mechanisms associated with each topology remained unclear at the time, these findings nonetheless demonstrated that the RAI concept is functionally viable within both network topologies. This provided significant validation for the robustness and adaptability of the RAI concept across different MOF architectures.

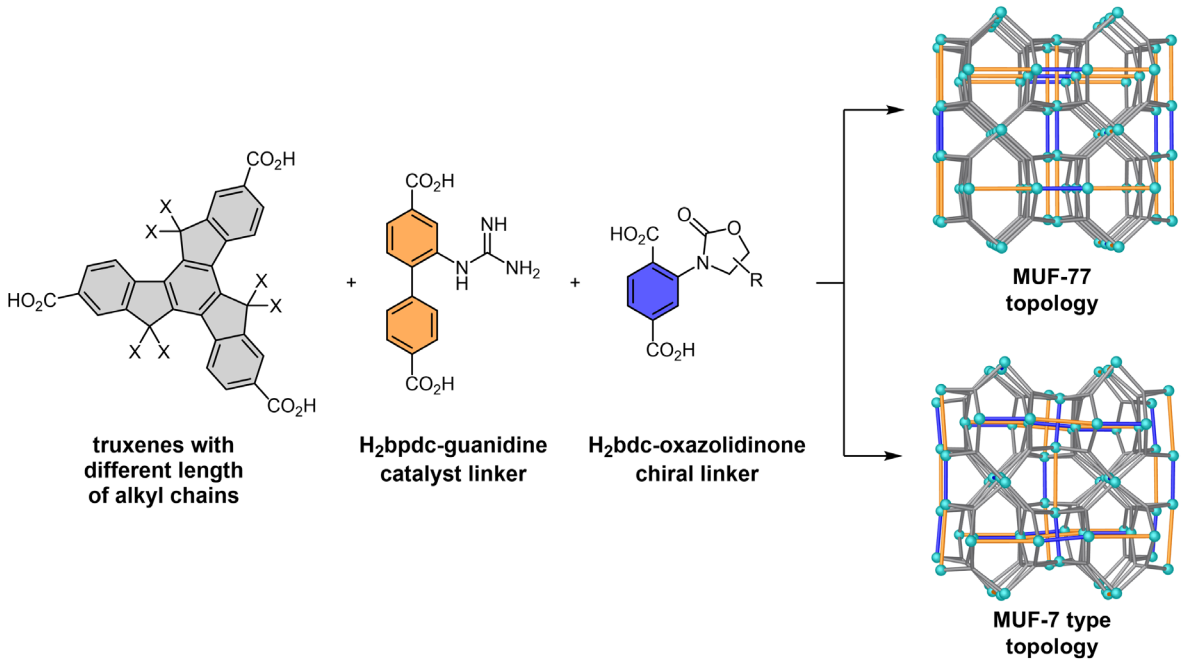

Figure 1.18 Schematic illustration of the synthesis of RAI catalysts showing the MUF-77 or MUF-7 type topology formed using the identical combination of linkers.

Dr. Jose Quinsaat contributed to the development of MUF-77 RAI catalysts by focusing on the incorporation of hydrogen-bond donor motifs to broaden the reaction scope. His primary target was the Friedel-Crafts reaction of β-nitrostyrene with indole.[127] Catalysts featuring squaramide and urea functionalities were synthesised and systematically evaluated for their activity in this transformation. No significant differences in activity between urea and squaramide-based catalysts could be observed in these initial experiments. However, the size of the functional group was found to significantly influence activity, with larger groups reducing performance attributed to overcrowding within the MOF pores. The MUF-77 catalysts demonstrated catalytic performance across a wide temperature range (–18 °C to 50 °C) and retained their activity over at least five reaction cycles, indicating good recyclability without significant loss of activity. This work provided the experimental foundation for their application as RAI catalysts.

A noteworthy clarification:

The term ‘remote asymmetric induction’ (RAI) has been used in the literature, although in contexts that differ significantly from the present work. RAI has been used to refer to either:

(i) reactions where the stereo information is controlled by a chiral centre within the substrate itself, located multiple bonds away from the reactive site;[128, 129] or

(ii) catalysts, for example short peptides, where a distant chiral centre interacts with the substrate and thus modulates reactivity at the catalytic site.[130]

In all examples, the chiral centre is an inherent part of either the substrate or the catalyst. In contrast, we propose a redefinition of the term RAI, wherein the stereochemical information is introduced to prochiral substrates by a chiral element that is not covalently connected with the catalyst moiety or the substrate.

1.2.4 Goal of this work

The overarching goal of this work is to develop a RAI catalyst that is as effective an asymmetric catalyst as possible. This includes:

(i) Achieving ee values as close to 100% as possible.
(ii) Being effective across a broad scope of substrates.
(iii) Showing sufficient activity to operate under mild conditions without the need for elevated temperatures.
(iv) Being robust and not requiring handling under inert conditions.

Chapter 2 – Expanding the scope of RAI catalysis

2.1 Introduction

2.1.1 Goal and experimental strategy

Achieving high enantioselectivity with RAI-MOF catalysts is a multidimensional and complex challenge. Many variables influence the transfer of chiral information to the products (**Figure 2.1**). As these can be modified simultaneously, an almost infinite number of potential experiments exists. Our challenge is to identify the important variables and optimise them to bring about high ee's.

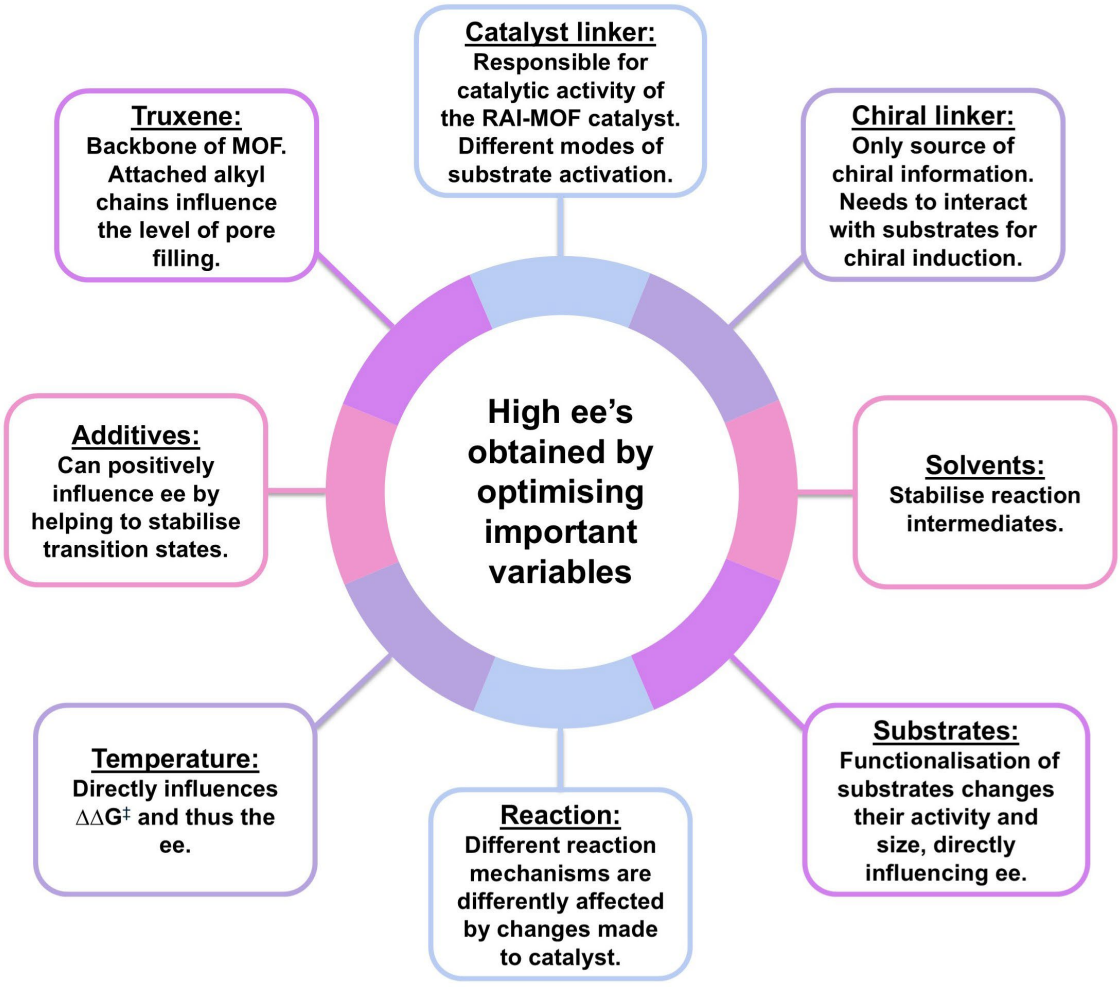

Figure 2.1 Variables that influence the successful transfer of chiral information during catalysis.

To roughly quantify the number of possible unique experiments, one can consider that three achiral catalyst linkers paired with 10 chiral linkers and four truxenes yield 120 distinct MUF-77 RAI catalysts. Testing these catalysts across five different reactions in five solvents would require 3,000 individual experiments. Functionalised substrates, variations in reaction conditions and additives would further increase this number. This highlights the necessity of a strategic approach to obtaining high ee's *via* a reasonable number of experiments.

This chapter has two main goals:

(i) To identify a promising combination of a reaction type, catalyst, and chiral linker that demonstrates good selectivity and, most importantly, high variation in ee with minor modifications. The selected system should also allow for variables to be changed easily in future experiments to enhance the ee.

(ii) To identify 'dead ends' that will not be explored further. This is essential for reducing the experimental workload and maintaining focus.

To achieve these objectives, a targeted, step-by-step screening method, comprising seven individual steps, was developed (**Figure 2.2**). These steps can be grouped into three overarching categories: catalyst linker only (**step 1**–**3**), chiral linker only (**step 4** and **5**) and implementing the RAI concept by combining both linkers (**step 6** and **7**).

In **step 1**, effective organocatalytic motifs that potentially can be attached to one of the three ligands of MUF-77 were identified. To build on the work of former group members, it was decided to exclusively attach the catalyst moieties onto the longer linear ligand, bpdc. This reserves the bdc for incorporating the chiral functionality. These achiral catalyst linkers were then designed and synthesised.

In **Step 2** MUF-77 syntheses were performed with the achiral H_2bpdc-catalyst ligands. The primary focus was to confirm that the MUF-77 structure formed without any side products ('phase pure') and that the catalyst moiety remained intact under the MOF synthesis conditions. This was confirmed *via* PXRD (powder X-ray diffraction) and NMR (nuclear magnetic resonance) spectroscopy. If a linker failed to form the MUF-77 structure, it was considered a 'dead end' and was not explored further.

In **step 3**, the achiral MUF-77 catalysts were tested for their activity against a variety of reactions. To streamline this process, TLC (thin layer chromatography) and HPLC (high-performance liquid chromatography) conditions for the selected model reactions were developed. MUF-77 catalysts that showed a 'hit' for a particular reaction (or set of reactions) were further investigated in **step 6** and **step 7**. Reactions where no activity was observed were excluded ('dead ends'), significantly reducing the experimental workload.

Step 4 was to identify chiral but non-catalytically active motifs that could be attached to the bdc linkers. The chiral motifs were selected based on insights from asymmetric catalysis and enzymes, with consideration of commercial availability.

Step 5 was used to confirm that the chiral H_2bdc linkers reliably formed the MUF-77 structure without undergoing any side reactions under MOF synthesis conditions or forming

unwanted phases. If a linker failed to form the MUF-77 structure, it was considered a 'dead end' and was not explored further. Additionally, the chiral MOFs without a catalyst unit were tested for catalytic activity against the reactions identified in **step 3**. This ensured that they did not show catalytic activity themselves. Only chiral bdc linkers that were not catalytically active were used for the reactions in later steps.

Step 6 paired the bdc-chiral with the achiral bpdc-catalyst linkers in MUF-77 to form MUF-77 RAI catalysts. The phase purity of the RAI-MOFs was confirmed to ensure that the functionalised linkers were compatible and could be combined in MUF-77.

In **step 7** the MUF-77 RAI catalysts, synthesised in **step 6**, were used to catalyse the reactions identified in **step 3**. The ee of the reaction mixtures were analysed using chiral HPLC. The variation in ee was explored by changing parameters such as the solvent or using functionalised substrates. If a significant variation in ee was observed, the respective variable was further investigated. However, if only modest ee's or insignificant variation in the ee could be observed despite changing many parameters, the MUF-77 RAI catalyst and reaction system were not investigated further since it was deemed unlikely the ee could be boosted into the >90% target range.

Step 6 and **step 7** together are considered the heart of the project. They form a loop process where each experiment is guided by the findings from previous catalyses. Ultimately, one system - consisting of a RAI-MOF catalyst family catalysing one reaction - was identified that demonstrated good ee but, more importantly, showed high variation in ee with small modifications of parameters and still had the potential for easy expansion. This system was selected for detailed exploration in the following chapter.

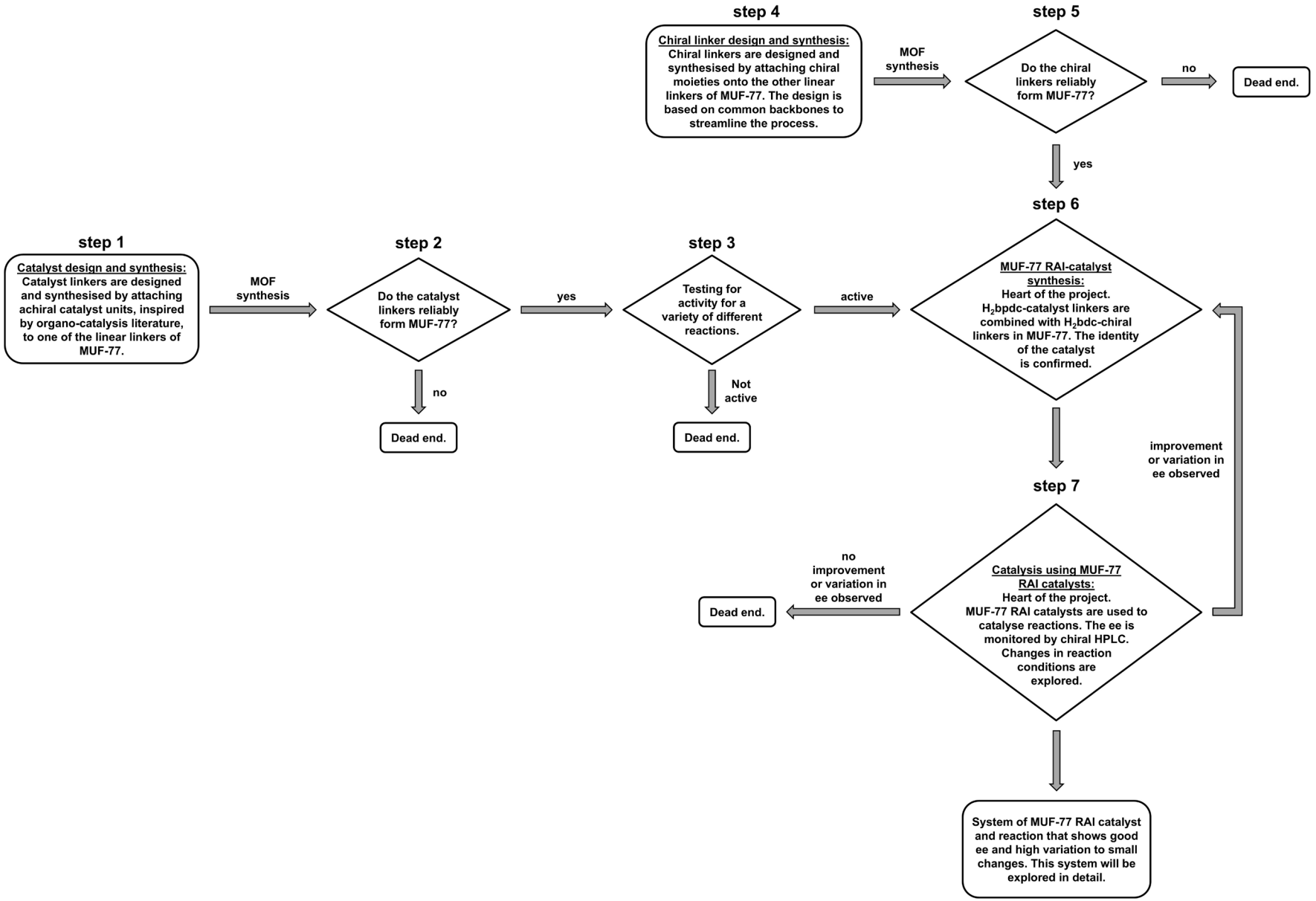

Figure 2.2 Flow chart depicting the targeted, step-by-step screening method used to identify effective RAI catalysts.

2.1.2 MOF linker nomenclature

This thesis refers to a large number of ligands. To ensure clarity, each ligand is given a simplified abbreviation.

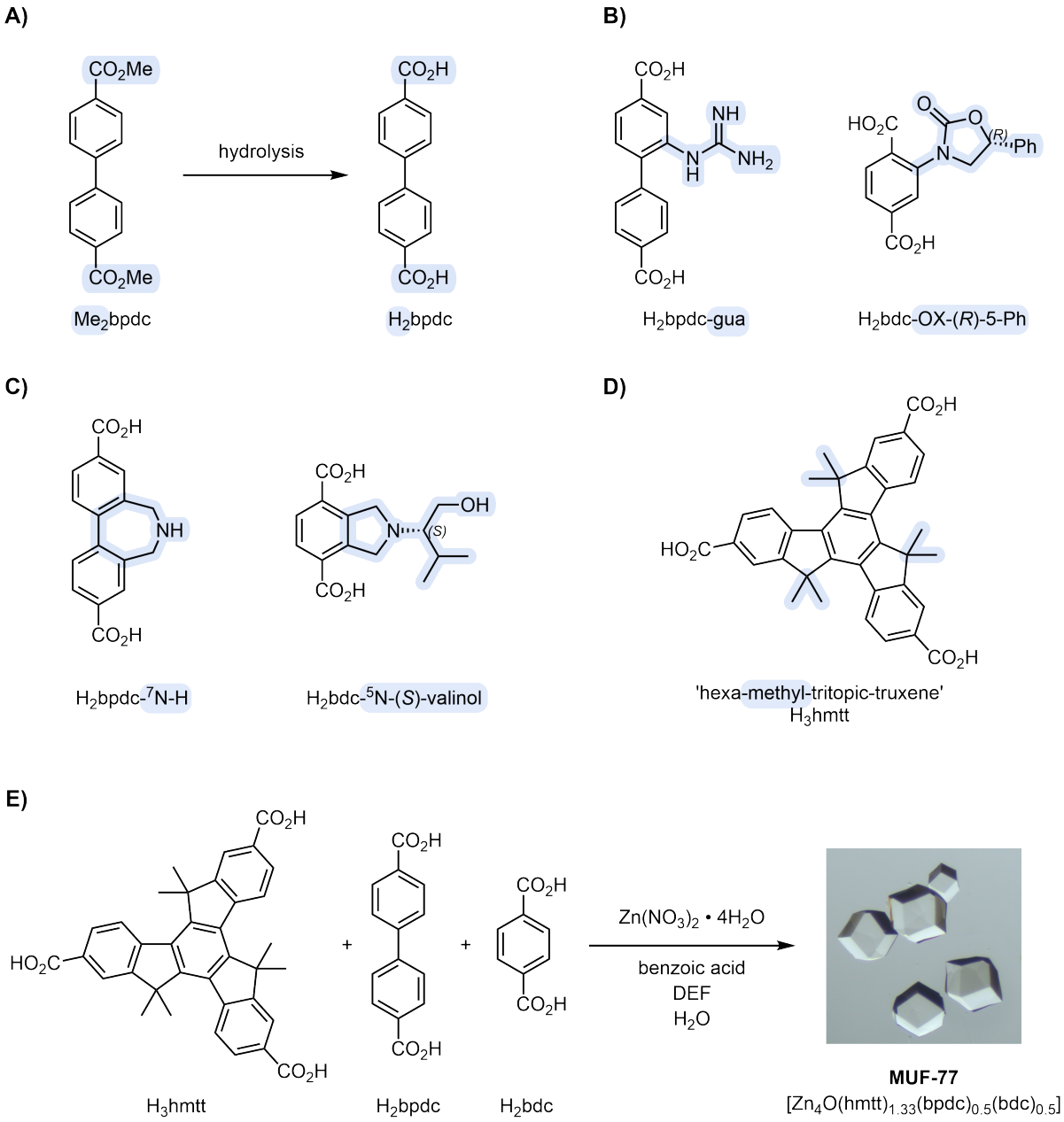

Figure 2.3 A-D) Representative examples of linkers and their corresponding nicknames used in this thesis. Key functionalities relevant to the naming process are highlighted in light blue. **E)** Reaction scheme showing the synthesis of MUF-77 crystals with the chemical formula $[Zn_4O(hmtt)_{1.33}(bpdc)_{0.5}(bdc)_{0.5}]$.

Abbreviations commonly used in the literature for the two linear linkers are 'bpdc' for [1,1′-biphenyl]-4,4′-dicarboxylic acid and 'bdc' for benzene-1,4-dicarboxylic acid.[131] During ligand synthesis, the carboxylic acids are typically protected as methyl esters, and the ligand name receives the prefix 'Me_2' (e.g. Me_2bpdc). The final ligands with the unprotected carboxylic acids hold the prefix 'H_2' (e.g. H_2bpdc, **Figure 2.3 A**). When a functional group is

attached to the ligand backbone, an abbreviation descriptive of that functionality is added to the name separated by a dash. For example, if a guanidine group is attached to one of the phenyl rings of H_2bpdc, the abbreviation 'gua' is added, giving the ligand the name H_2bpdc-gua (**Figure 2.3 B**). The same approach is taken for all bdc ligands with the addition that the stereochemistry of the attached functional group is also specified. For example, a bdc ligand with a chiral oxazolidinone-based functionality attached to the backbone, is referred to as H_2bdc-OX-(*R*)-5-Ph (**B**).

The bpdc and the bdc ligands often have additional appended rings. In this thesis, these rings contain a nitrogen atom to which additional functionality is attached (**Figure 2.3 C**). A superscript is used to indicate the number of atoms in the ring and an abbreviation for the attached functionality is added. For instance, if the functionality attached to a five-membered ring with nitrogen as the central atom on the H_2bdc backbone is derived from the amino alcohol valinol, the name of the resulting ligand is H_2bdc-^{5}N-(*S*)-ValOH (**Figure 2.3 C**).

During this project, the tritopic truxenes were solely modified by changing the alkyl chain length attached to the planar backbone. Each truxene features six alkyl chains of equal length and the number of carbon atoms is indicated. For example, the truxene ligand with six methyl groups is referred to as H_3hmtt, where 'm' is for 'methyl' (**Figure 2.3 D**).

MUF-77 syntheses are typically represented as illustrated in **Figure 2.3 E**. The chemical formula of MUF-77, $[Zn_4O(hmtt)_{1.33}(bpdc)_{0.5}(bdc)_{0.5}]$, details the incorporated linkers, their functional groups (as relevant), and relative stoichiometry.

2.1.3 MUF-77 RAI catalysis: the heart of the project

This section outlines the practical steps involved in preparing the RAI-MOF catalysts, preparing and performing the reaction and measuring ee for catalytic reaction products (**Figure 2.4**). Detailed information for each step is provided in **section 2.4**.

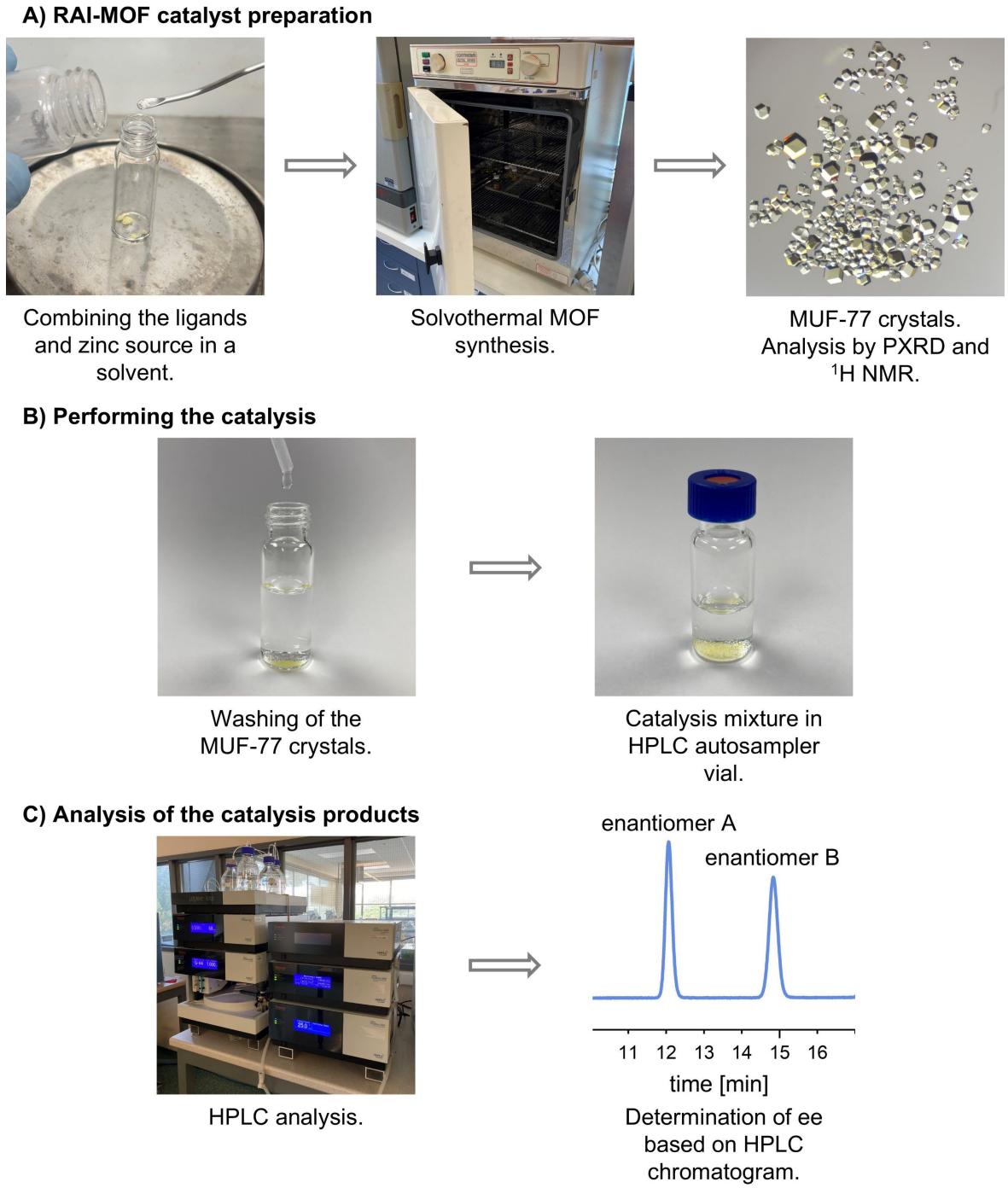

Figure 2.4 Stepwise procedure for performing catalysis with MUF-77 RAI catalysts.

The first step in the process is the synthesis and analysis of the RAI-MOF catalyst (**Figure 2.4 A**). This is achieved by combining the three relevant linkers, a zinc source and solvent in a vial and placing the MOF synthesis mixture in an isothermal oven until MUF-77 crystals are obtained. The identity and phase purity of the RAI-MOF sample is confirmed by PXRD and

^{1}H NMR analysis. PXRD measurements provide information about the identity of the framework structure of the bulk sample. By comparison of the PXRD pattern with the calculated PXRD pattern of MUF-7/ MUF-77, the structure is confirmed. The absence of additional reflections in the experimental pattern highlights the phase purity. The ^{1}H NMR spectra of digested MOF samples provide information on whether the ligands are present in the correct stoichiometry, as derived from the MOF formula. This further confirms the phase purity. Additionally, the identity of the ligands is validated, showing that no linker degradation or side reactions occurred during MOF synthesis.

A noteworthy clarification:

To maintain clarity and reduce redundancy, the confirmation of the phase purity of the synthesised MOF samples by PXRD and ^{1}H NMR is discussed only three times within the main sections of this work:

(i) for one achiral catalyst MOF (**section 2.2.2**; **Figure 2.9**),
(ii) for one chiral, non-catalytic MOF (**section 2.2.5**; **Figure 2.14**) and,
(iii) for one RAI catalyst MOF (**section 2.2.6**; **Figure 2.17**).

However, the phase purity of all discussed MOFs was confirmed. The remaining data are provided in the appendix.

The second step is to perform catalysis using the RAI-MOF crystals (**Figure 2.4 B**). Prior to catalysis, the crystals are washed sequentially with acetone, followed by the solvent used for the desired reaction. Washing is performed by decanting the old solvent and adding fresh solvent in multiple steps. The washed crystals are then transferred into a HPLC autosampler vial and, depending on the quantity of crystals, may be split into multiple batches. Catalysis stock solutions with standardised concentrations are prepared separately. Before starting the catalysis, the solvent covering the pre-washed crystals is decanted and the prepared catalysis stock solution is added. The catalysis reaction mixture is stored at room temperature between 1-5 days until analysis. It is important to note that the reaction mixture is not stirred, as stirring would crush the MUF-77 crystals, leading to small particles floating in the solvent rather than intact crystals settling at the bottom of the vial. This would introduce the need for an additional purification step before analysis thus slow down the screening procedure.

The third step is the analysis of the reaction mixture by chiral HPLC (**Figure 2.4 C**). The HPLC autosampler vial containing the catalysis mixture, with the MUF-77 crystals settled at the bottom of the vial, is directly placed into the HPLC autosampler. A small amount of solution (0.1-3 µL) is injected on to the column and the eluent monitored *via* absorption at a selected

UV (Ultraviolet) wavelength. The resulting HPLC chromatogram typically displays peaks corresponding to unreacted reagents and two distinct peaks for the two product enantiomers (**Figure 2.5**). The enantiomer that elutes first from the column is designated as 'enantiomer A.' The peak areas of the enantiomers are determined by integration, and the ee is calculated as:

$$ee[\%] = \frac{\text{enantiomer A - enantiomer B}}{\text{enantiomer A + enantiomer B}} \cdot 100$$

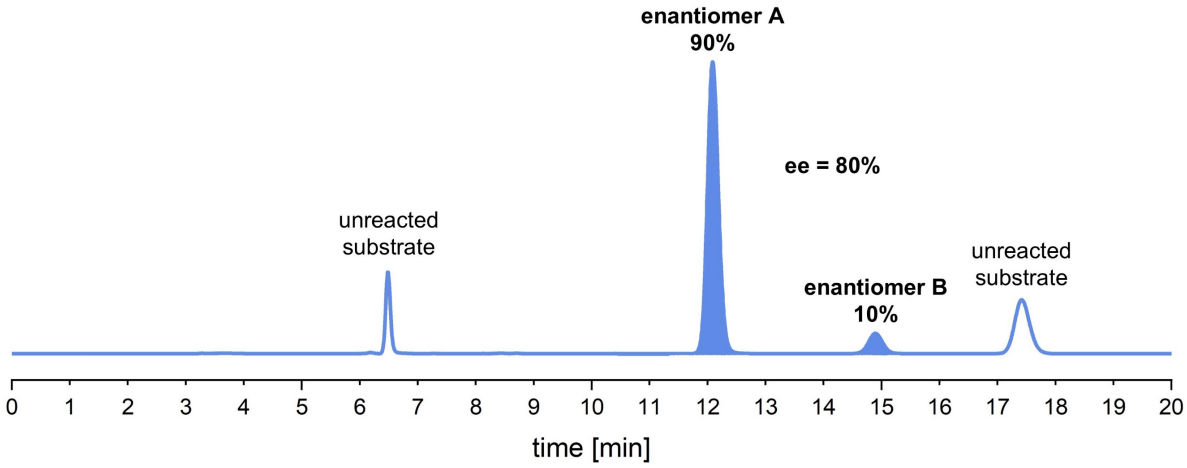

Figure 2.5 Depiction of a representative chiral HPLC chromatogram. The peaks of the unreacted substrates and the two product peaks are labelled. The integration of the product peaks (highlighted by blue shading) is used to calculate the ee.

2.2 Results and discussion

2.2.1 Catalyst design and synthesis

Inspiration for the design of catalyst linkers is not hard to find as the number of published organocatalysts seems endless.[70, 83, 132] The real challenge lies in the identification of motifs that are synthetically feasible for attachment to one of the linkers and, most importantly, do not impede the formation of the MUF-77 structure. The selection of the catalyst moieties as well as the respective MOF ligand design and synthesis is discussed here. The goal was to have a small collection of active organocatalyst linkers on hand to enable testing of the RAI concept across a broad range of reactions.

2.2.1.1 Secondary amine organocatalysts: enamine and iminium ion catalysis

The 2021 Nobel Prize in chemistry was awarded to Benjamin List[78] and David MacMillan[20] for their pioneering work in enamine and iminium ion catalysis (**Figure 2.6 A**). This milestone highlighted the importance this branch of asymmetric organocatalysis has had in the development of the field. Since then, many examples of asymmetric secondary amine catalysts have been reported, showing excellent activity and enantioselectivity for aldol reactions,[133] Mannich reactions,[134] Michael reactions[135] and many others.[71, 136] Moreover, enamine catalysis is found in nature, as for example in aldolase enzymes that catalyse aldol reactions between aldehydes and ketones.[137, 138]

Secondary amines catalyse C–C bond forming reactions by first reacting with aldehydes or ketones to form an iminium ion and, if possible, an enamine intermediate (**Figure 2.6 B**). The iminium ion or enamine then acts as a nucleophile, attacking an electrophile. Finally, the desired product is obtained after cleavage of the secondary amine. The covalent bonding between the catalyst and substrate in the activated intermediate elicits the excellent enantioselectivity observed in these reactions.[68, 71, 139]

These characteristics make secondary amine catalysts highly desirable for exploration with the RAI concept. Accordingly, the symmetrical, achiral secondary amine linker, H_2bpdc-^{7}N-H, was identified as a promising candidate (**Figure 2.6 C**). However, as secondary amines are prone to undergo unwanted side reactions under MOF synthesis conditions, the procatalyst, H_2bpdc-^{7}N-Boc was designed featuring a Boc-protecting group (*tert*-butyloxycarbonyl).[126, 140, 141] The Boc-protecting group prevents side reactions during MOF synthesis and can be removed after framework formation by thermolytic cleavage.[142]

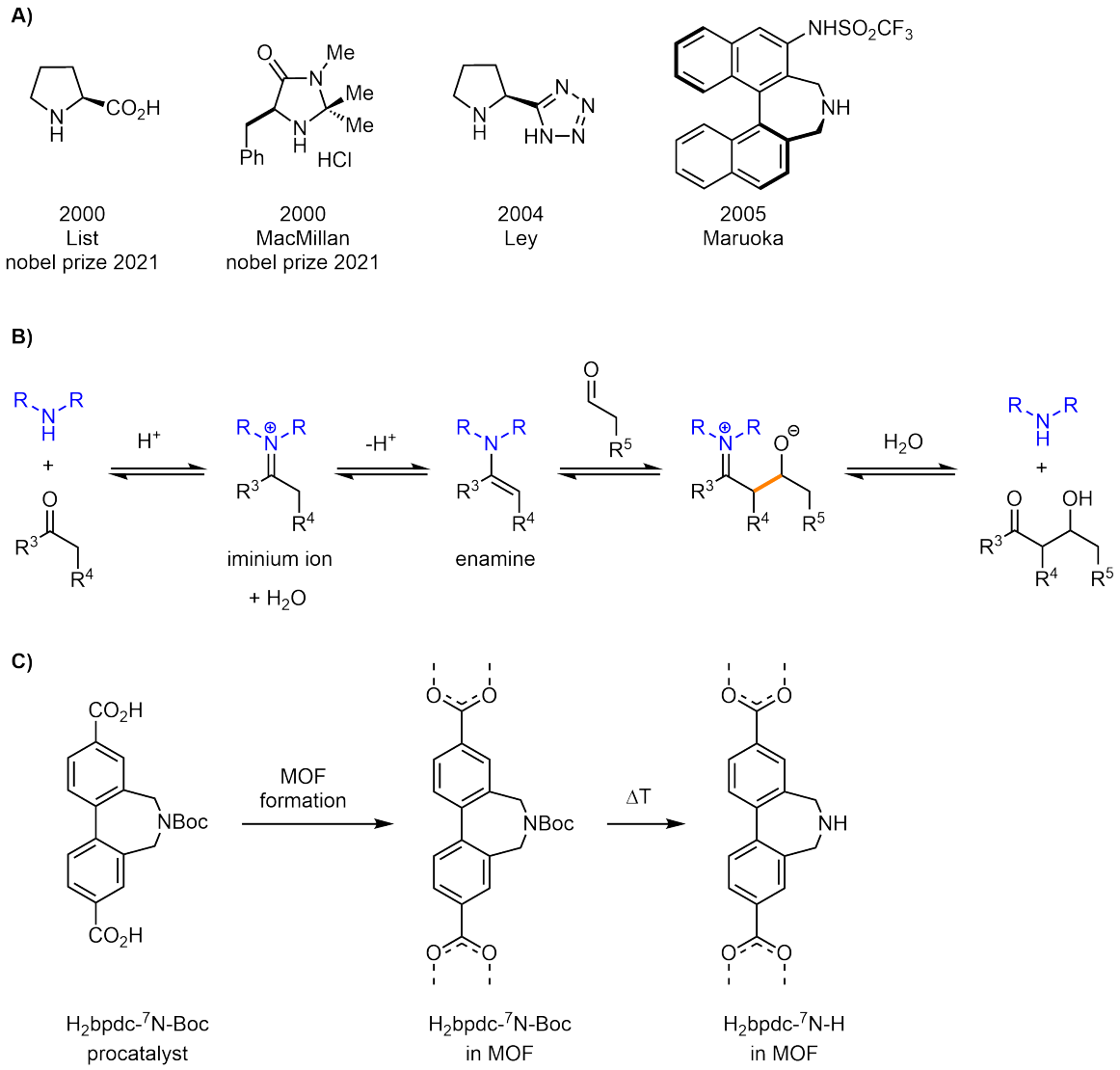

Figure 2.6 A) Depiction of literature examples of asymmetric secondary amine organocatalysts,[20, 78, 134, 143] **B)** the mechanism of an amine-catalysed aldol reaction between a ketone and an aldehyde and **C)** the secondary amine functionalised ligand H_2bpdc-^{7}N-H as present in MUF-77 and its Boc-protected procatalyst.

The procatalyst linker H_2bpdc-^{7}N-Boc was successfully synthesised following group internal protocols (**Scheme 2.1**). First, the carboxyl group of 4-bromo-3-methylbenzoic acid was converted to the corresponding methyl ester. Subsequently, two equivalents of methyl 4-bromo-3-methylbenzoate were coupled under Suzuki conditions to form Me_2bpdc-$(Me)_2$. The benzylic methyl groups were then brominated with NBS (*N*-Bromosuccinimide) to yield Me_2bpdc-$(MeBr)_2$. Substitution with allylamine produced Me_2bpdc-^{7}N-allylamine, from which the allyl group was cleaved to yield Me_2bpdc-^{7}N-H. The secondary amine was Boc-protected to yield Me_2bpdc-^{7}N-Boc. Lastly, the methyl esters were hydrolysed under basic conditions to produce the final Boc-protected procatalyst linker, H_2bpdc-^{7}N-Boc.

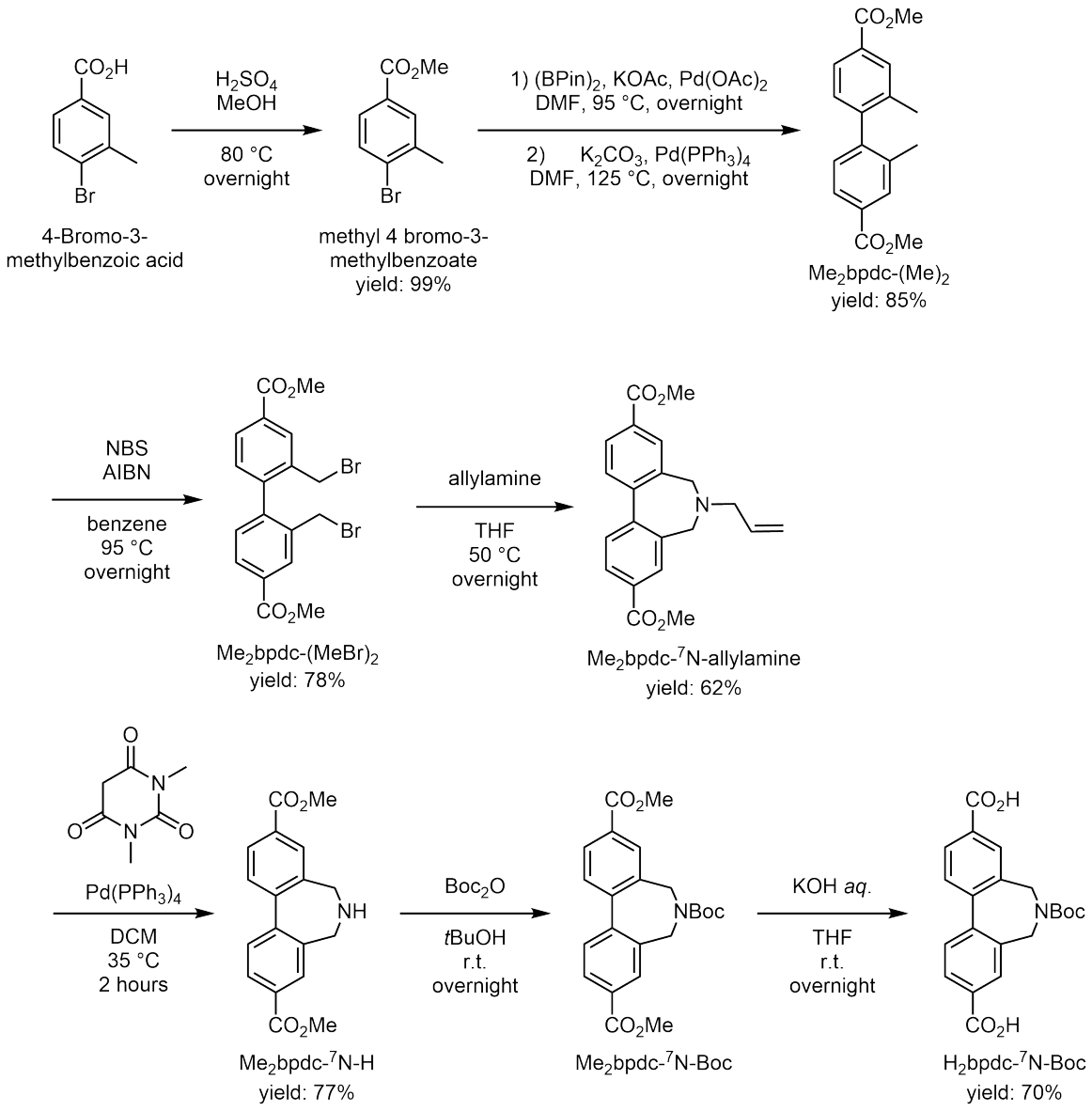

Scheme 2.1 Reaction scheme for the synthesis of the procatalyst H_2bpdc-^{7}N-Boc.

2.2.1.2 Guanidine organocatalysts: Brønsted base catalysts with hydrogen bond donor capacity

Recognised as one of the strongest organo-Brønsted bases with a pK_a of 13.7, the guanidine group has attracted significant attention as an efficient organocatalyst since the mid-1990's (**Figure 2.7 A**).[74, 144, 145] Beyond its strong basicity, the delocalised guanidinium cation shows remarkable hydrogen bond donor capacity. This is often considered to significantly influence the enantioselectivity of the catalyst (**Figure 2.7 B**).[74, 146-148] Structurally, the guanidine motif can exist as acyclic, monocyclic and bicyclic forms, allowing for diverse catalyst designs with varying steric demands and flexibility.[74] Guanidine catalysts – either alone, or in tandem with thioureas[149] or amides[150] – have successfully been used as enantioselective catalysts for Henry[146, 151], aldol[152, 153], Michael,[154, 155] Mannich[156, 157] and other reactions.[158, 159] More recently,

guanidine groups have also been introduced into MOF-based catalysts *via* post-synthetic modification.[160, 161]

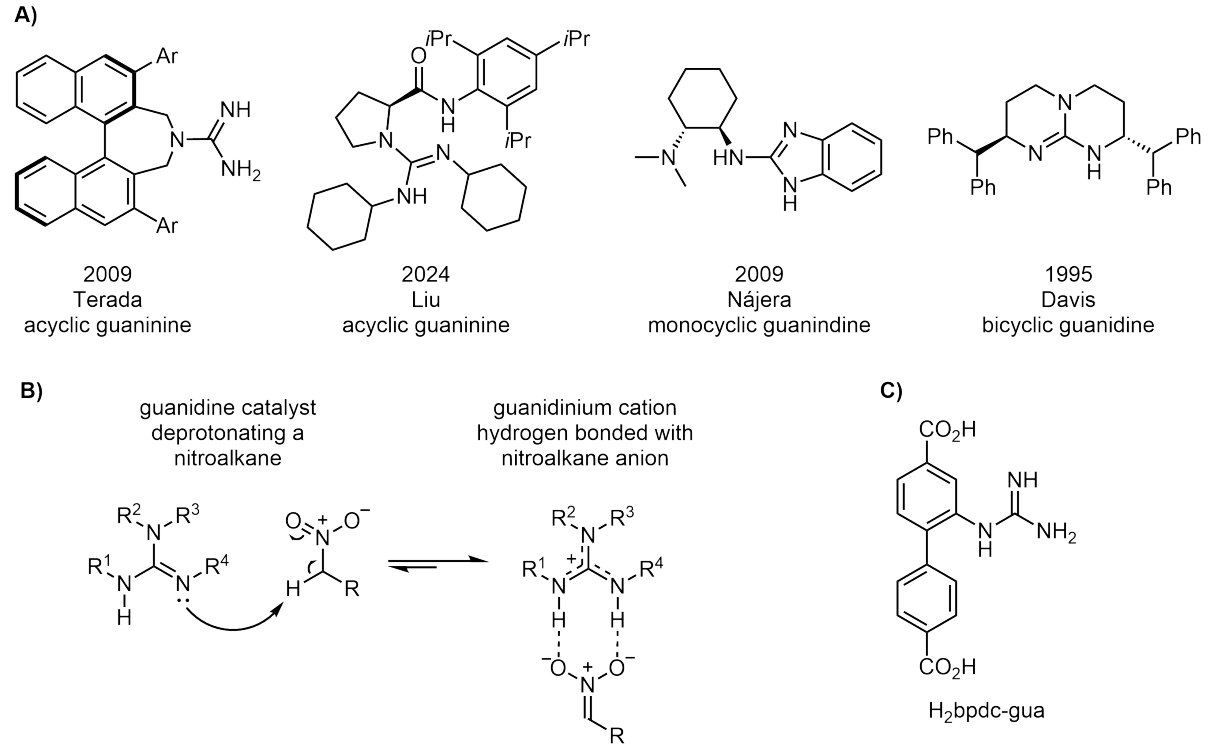

Figure 2.7 A) Depiction of literature examples[146, 162-164] of chiral guanidine organocatalysts, **B)** a guanidine catalyst deprotonating a nitroalkane and subsequently hydrogen bonding with its anion, and **C)** the achiral guanidine functionalised MUF-77 linker, H_2bpdc-gua.

All this considered, the guanidine functionality is highly desirable for exploration in MUF-77 RAI catalysis. The achiral guanidine functionalised linker, H_2bpdc-gua (**Figure 2.7 C**), was identified as the ideal candidate. As discussed in **Chapter 1.2.3**, this linker was previously designed, synthesised and used for the proof of principle study of the RAI concept. However, the earlier work exclusively focused on the Henry reaction of functionalised benzaldehydes with nitromethane, with other reactions remaining unexplored.

The guanidine catalyst linker, H_2bpdc-gua, was successfully synthesised as shown in **Scheme 2.2**. The group-established precursor, Me_2bpdc-NH_2, was coupled with the Boc-protected guanidine precursor 1,3-bis(*tert*-butoxycarbonyl)-2-methylisothiourea to yield Me_2bpdc-gua$(Boc)_2$. The Boc-protecting groups were then removed under acidic conditions to produce Me_2bpdc-gua. Finally, the methyl esters were hydrolysed under basic conditions to yield the target linker H_2bpdc-gua.

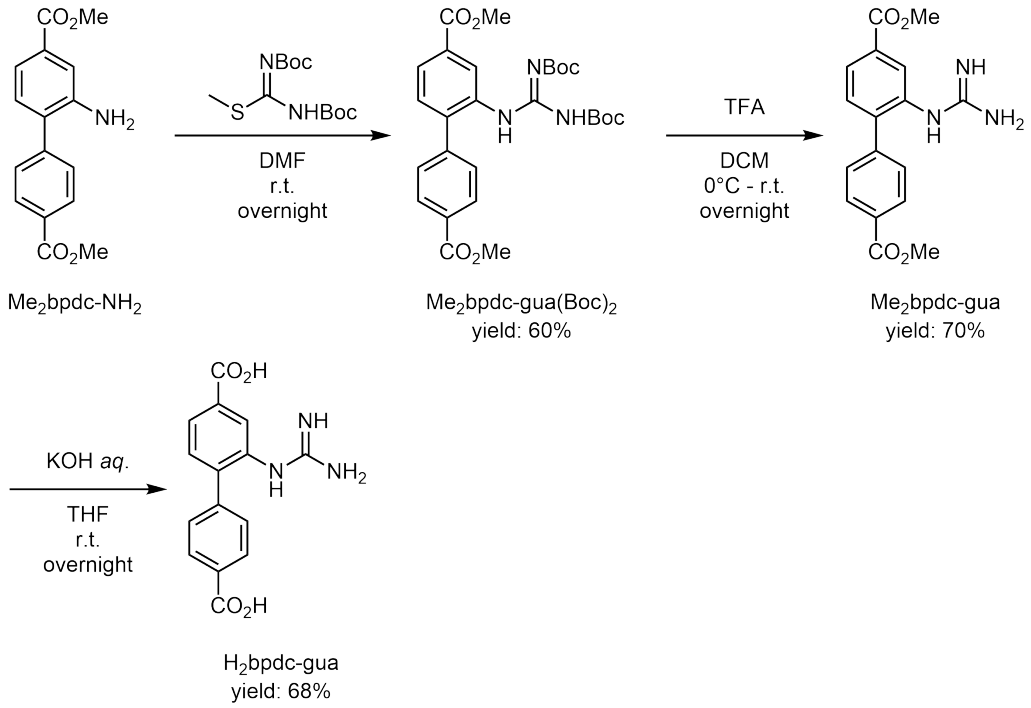

Scheme 2.2 Reaction scheme for the synthesis of H_2bpdc-gua.

2.2.1.3 Urea, thiourea and squaramide organocatalysts: hydrogen bond donor catalysis

Hydrogen-bond donor (HBD) catalysts (**Figure 2.8 A**) have attracted growing interest for their ability to recognise and activate functional groups through dual hydrogen bond interactions (**Figure 2.8 B**).[165, 166] Building on the first urea-based HBD catalyst - reported in 1994 by Curran - thiourea and squaramide catalysts have been developed, offering stronger H-bond donors with higher acidity and enhanced catalytic performance. [165, 167] Recent trends focus on bifunctional catalysts, combining HBDs with, for example Brønsted bases to activate nucleophiles, enhancing efficiency and enantioselectivity.[168] These catalysts have proven effective in Strecker,[169] Michael,[170, 171] or the aza-Henry reactions,[172] demonstrating excellent enantioselectivities. HBD catalysts have also been integrated into MOFs, boosting catalytic efficiency in Henry[173] and Friedel-Crafts reactions.[127, 174-177]

These features made them attractive candidates to be used as catalysts in RAI catalysis. The urea-functionalised linker, H_2bpdc-urea-Ph (**Figure 2.8 C**), was identified as a promising initial HBD catalyst linker. This linker design was selected based on initial experiments, which indicated that urea-based bpdc linkers exhibited comparable activity to their squaramide counterparts, while also offering a more accessible synthesis and higher yields **(Chapter 1.2.3)**.

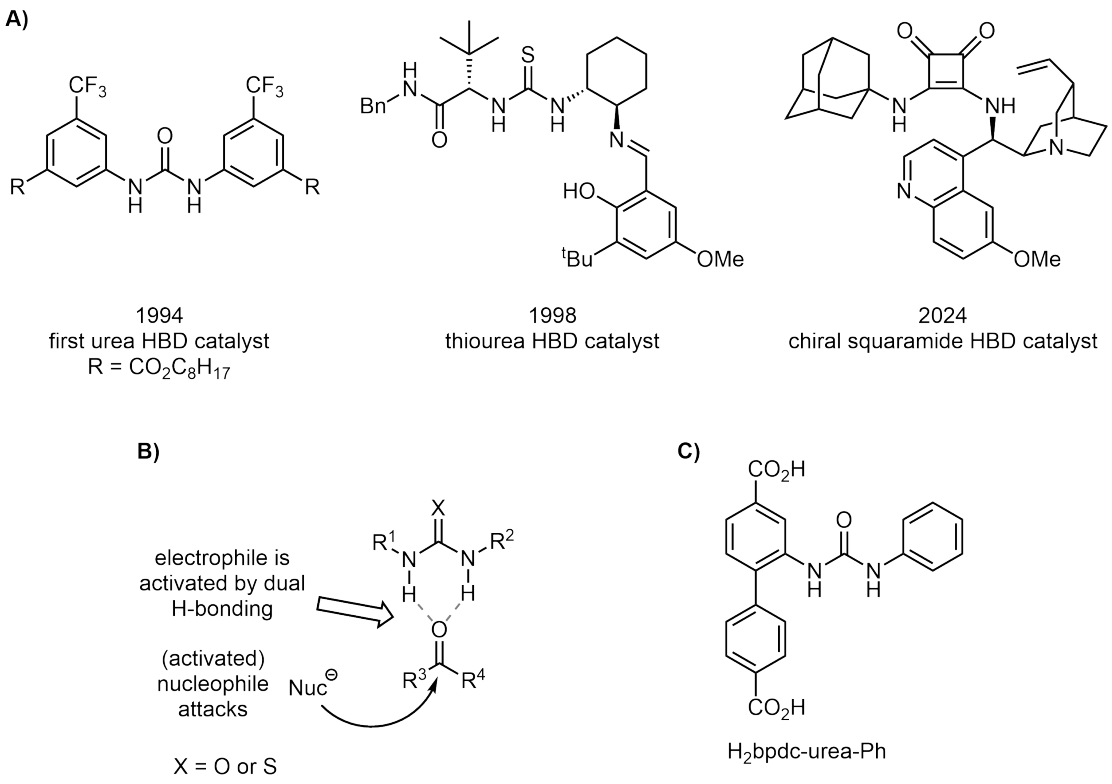

Figure 2.8 A) Depiction of literature examples of achiral and chiral hydrogen-bond-donor organocatalysts[167, 169, 170], **B)** the mode of activation of electrophiles by dual hydrogen bonding[166] and **C)** the achiral urea functionalised MUF-77 linker, H_2bpdc-urea-Ph.

H_2bpdc-urea-Ph was successfully synthesised using a combination of group-internal procedures and adapted literature-reported methods (**Scheme 2.3**).[173] The group-established precursor, Me_2bpdc-NH_2, was coupled with phenyl isocyanate to yield the urea-functionalised intermediate Me_2bpdc-urea-Ph. Subsequently, the methyl esters were hydrolysed under basic conditions to yield the target linker, H_2bpdc-urea-Ph.

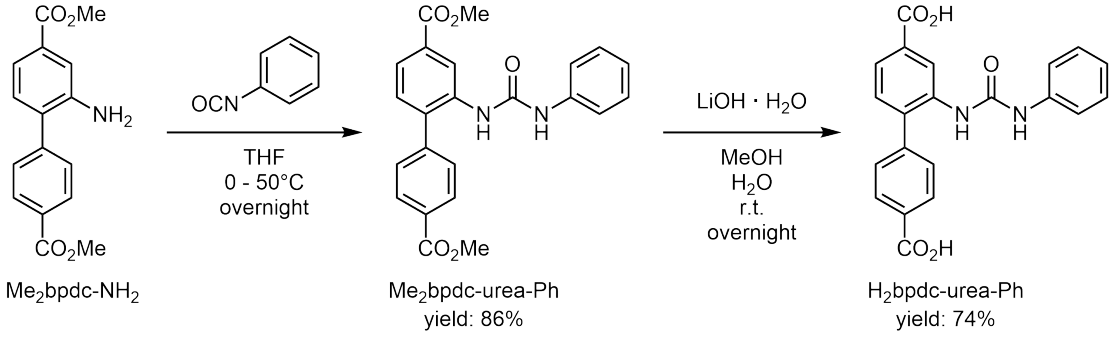

Scheme 2.3 Reaction scheme for the synthesis of H_2bpdc-urea-Ph.

2.2.2 Achiral MUF-77 catalyst synthesis

With the three catalytic bpdc linkers in hand, the respective achiral MUF-77 catalysts were prepared (**step 2** of **Figure 2.2**). Unfunctionalised H_2bdc was used for MOF formation to ensure the MUF-77 catalysts were achiral. H_3hmtt was chosen due to its minimal pore filling, which reduced the likelihood of reaction suppression caused by overcrowding. An example MOF synthesis for the achiral MUF-77 catalyst [$Zn_4O(hmtt)_{1.33}$(bpdc-gua)$_{0.5}$(bdc)$_{0.5}$] is shown in **Figure 2.9 A**. The other achiral MUF-77 catalysts with H_2bpdc-urea-Ph and H_2bpdc-^{7}N-Boc were synthesised using the same conditions.

All three achiral MUF-77 catalysts were obtained phase pure, without side reactions or formation of different phases detected. The representative PXRD and ^{1}H NMR data for [$Zn_4O(hmtt)_{1.33}$(bpdc-gua)$_{0.5}$(bdc)$_{0.5}$] are shown in **Figure 2.9 B** and **C**. In the measured PXRD diffractogram, the observed reflection positions match those of the calculated MUF-77 pattern, with no additional reflections present. This is supported by the ^{1}H NMR spectrum of a digested MOF sample of [$Zn_4O(hmtt)_{1.33}$(bpdc-gua)$_{0.5}$(bdc)$_{0.5}$], which shows the expected signals for the three linkers in the correct ratio (hmtt:bpdc-gua:bdc = 1.33:0.5:0.5). No additional peaks are present that would indicate side reactions or impurities. Together, these results confirm the phase purity and identity of the achiral catalyst MOF.

Since H_2bpdc-gua and H_2bpdc-urea-Ph were the final catalyst linkers as designed for catalysis, the successful MUF-77 syntheses implied that they passed **step 2** (**Figure 2.2**) and were ready to be screened for their activity in **step 3** (**Figure 2.2**).

H_2bpdc-^{7}N-Boc, however, was a procatalyst, meaning that the Boc-protecting group first needed to be removed while maintaining MOF crystallinity and ligand identity. To determine the required temperature for thermolytic cleavage of the Boc-group within the MOF, thermogravimetric analysis (TGA) was performed on the free linker, H_2bpdc-^{7}N-Boc (**Figure 2.10 A**). A weight loss of 24% was observed between 50-250 °C, with an onset temperature of 162 °C. This weight loss correlates well with the theoretical mass reduction of 26%, expected for the thermolytic cleavage of the Boc-group as CO_2 and isobutylene.[142]

After identifying the temperature range for thermolytic cleavage, trials were conducted to develop a streamlined process for Boc removal in a fume hood. Until now, the thermolytic cleavage of Boc-groups performed by the Telfer research group was done either using a TGA device or a heating mantle of the activation port of a gas sorption device. However, both methods suffer from considerable limitations. Using a TGA is gas and time intensive since the sample is heated under a N_2 atmosphere rather than vacuum, resulting in slower deprotection. Separately, access to the activation port of the gas sorption device was very limited, due to high

sample throughput of the group. Both techniques also allow deprotection of only one MUF-77 sample at a time, making them highly time inefficient, especially considering the number of different RAI-MOFs that require deprotection in **step 6**.

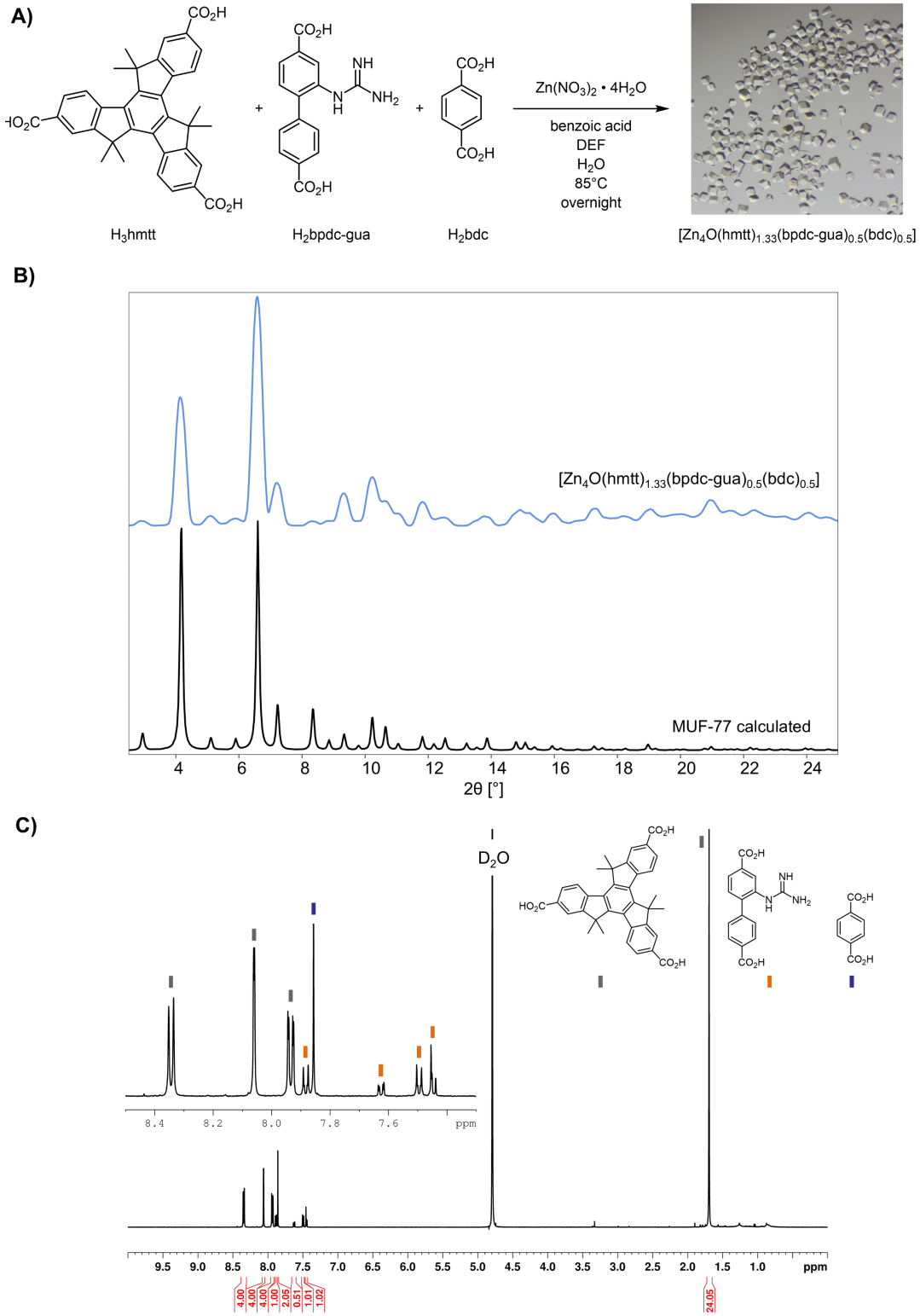

Figure 2.9 A) Reaction scheme showing the solvothermal MOF synthesis of the achiral MUF-77 catalysts $[Zn_4O(hmtt)_{1.33}(bpdc\text{-}gua)_{0.5}(bdc)_{0.5}]$. **B)** Experimental PXRD pattern (blue) and calculated pattern of MUF-77 (black). **C)** ^{1}H NMR spectra of the digested MUF-77 in a D_2O - NaOD mixture. The peaks are labelled by colour to highlight the corresponding linker.

With these concerns in mind, a streamlined bench-top deprotection method was developed, using a standard high vacuum oil pump connected to a Schlenk line for vacuum and a dry bath as the heating source (**Figure 2.10 B**). This allowed deprotection of up to three samples simultaneously, while also not depending on availability of special equipment. The achiral MUF-77 procatalyst $[Zn_4O(hmtt)_{1.33}(bpdc\text{-}^{7}N\text{-}Boc)_{0.5}(bdc)_{0.5}]$ was successfully deprotected using this setup, yielding $[Zn_4O(hmtt)_{1.33}(bpdc\text{-}^{7}N\text{-}H)_{0.5}(bdc)_{0.5}]$ as the final catalyst. This was confirmed by NMR of a digested MOF sample. All three ligands had therefore successfully passed **step 2** and the achiral MUF-77 catalysts were ready for screening in **step 3**.

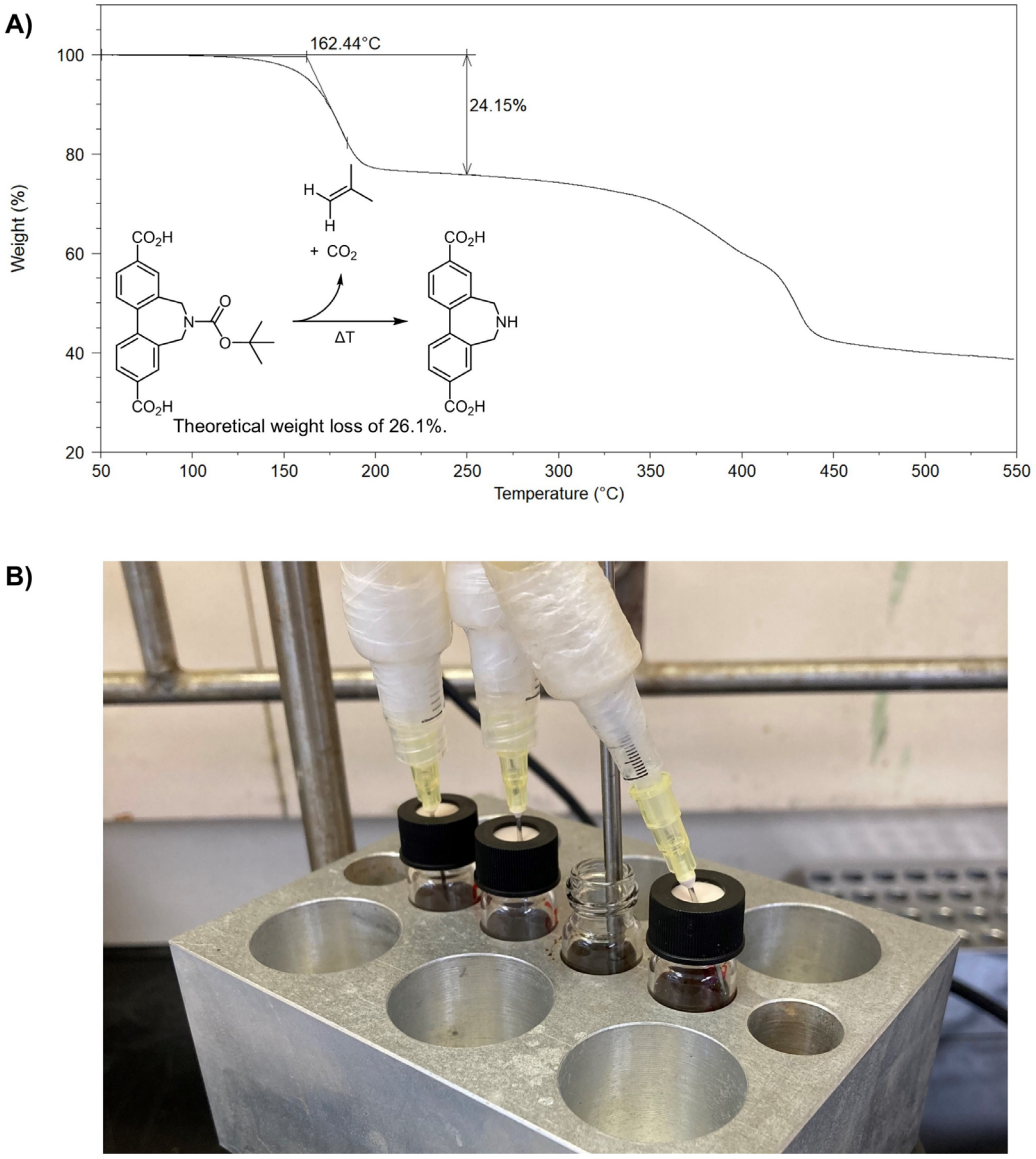

Figure 2.10 A) TGA trace of H_2bpdc-^{7}N-Boc. The thermolytic cleavage of the Boc-group can be observed before 250 °C with a weight loss of 24%. The onset point is labelled. **B)** Setup for Boc-deprotection of three samples simultaneously in the fume hood.

2.2.3 Screening for activity

Following the successful installation of the potentially catalytically active groups in MUF-77, the catalyst MOFs were screened for their activity across a variety of model reactions (**step 3** of **Figure 2.2**). The goal was to identify which class(es) of reaction(s) each catalyst is active for. This is important as only reactions for which the catalyst groups are active for will be investigated with RAI-MOFs in **step 6** and **step 7**.

The potentially catalytically active MOFs are:

(i) $[Zn_4O(hmtt)_{1.33}(bpdc\text{-}^{7}N\text{-}H)_{0.5}(bdc)_{0.5}]$

(ii) $[Zn_4O(hmtt)_{1.33}(bpdc\text{-}gua)_{0.5}(bdc)_{0.5}]$

(iii) $[Zn_4O(hmtt)_{1.33}(bpdc\text{-}urea\text{-}Ph)_{0.5}(bdc)_{0.5}]$

It is reiterated that the MOFs are achiral at this point.

The model reactions were selected by identifying reactions catalysed by secondary amino, guanidine, urea, and thiourea functional groups in the literature.[71, 158, 166, 174, 178] To broaden the reaction scope, additional model reactions of synthetic relevance were included to probe for unanticipated catalytic activity. Model reactions with small or medium sized substrates were selected to enhance diffusion within the MOF pores.

TLC and HPLC conditions for the model reactions were first developed. This was achieved by isolating catalysis products using generic homogeneous catalysts. One example is the Michael reaction of β-nitrostyrene with cyclohexanone catalysed by L-proline.[179] TLC conditions were established for the reactants and products, allowing catalysis reaction progress to be carefully monitored. Chiral HPLC conditions using either reverse phase or normal phase were developed to separate and quantify the two product enantiomers.

Before screening for activity, the MOFs were washed using a standard procedure (**Section 2.4.6**). Catalysis was then started by addition of a stock solution containing the catalysis substrates to the MOF crystals. The heterogeneous MOF catalysis reaction mixtures were left to stand at room temperature. If no product formation was detected by TLC after two days, the reaction mixtures were heated to 50 °C (provided the temperature remained below the boiling point of the solvent) for an additional three days. If no product formation could be observed at this stage, the experiment was considered ‘not active’. If the product spot was observed by TLC, the experiment was considered ‘active’.

The catalyst loading was not measured precisely but was estimated to be between 5-15 mol% in each case. The loading is defined as the ratio between the number of moles of the limiting substrate and the number of moles of catalytic linkers in the MOF. The amount of

conversion was not of interest in these screening experiments. The outcome of the experiments was classified as either 'active' or 'inactive' as summarised in **Table 2.1**.

The MUF-77 catalyst featuring bpdc-gua showed good activity for the Henry and aldol reactions. Activity for the Henry reaction was expected, as this reaction is commonly catalysed by guanidines. Guanidines are basic enough to deprotonate nitromethane ($pK_a \sim 10.2$).[180] Its activity for the aldol reaction was also expected as guanidine organocatalysts are known to catalyse various aldol reactions,[78, 138] and these generally proceed *via* an enolate intermediate.[181]

Similarly, the bpdc-^{7}N-H catalyst MOF was active for both the Henry and the aldol reactions. Its activity for the aldol reaction was anticipated, as amines are well known to catalyse this reaction *via* an imine intermediate.[78, 138] Its activity for the Henry reaction was relatively unexpected, as secondary amines are not commonly used to catalyse Henry reactions.

The bpdc-urea-Ph catalyst MOF showed good activity for the Friedel-Crafts reaction and a faint TLC product spot was observed for the aldol reaction after one day at 50 °C. Its activity for the Friedel-Crafts reaction was expected, as very similar linkers had been shown to be catalytically active for this reaction in MOFs.[173, 177] However, its activity for the aldol reaction was quite surprising. Tandem catalysts combining an HBD catalyst with a second catalyst group, such as an amine, are known to catalyse aldol reactions,[181] but there is little (if any) literature on HBD-catalysts being active for aldol reactions without a co-catalyst.

In total, six catalyst-reaction combinations were identified during the screening experiments. The fact that none of the catalyst MOFs showed activity for the Baylis-Hillman, the Pictet Spengler and both Michael reactions, rendered them 'dead ends' and they were not pursued further.

Table 2.1. Heatmap illustrating the results of screening the activity of three potentially catalytic MUF-77 frameworks against seven model reactions. The general formula of the frameworks is $[Zn_4O(hmtt)_{1.33}(X)_{0.5}(bdc)_{0.5}]$, where X is the bpdc ligand in the first row of the table. Green indicates catalytic activity and red indicates inactivity.

	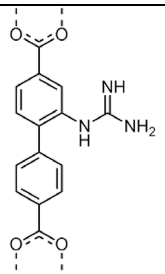	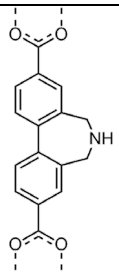	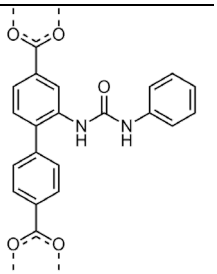
Aldol 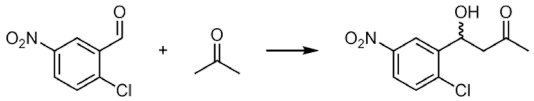			
Michael_1 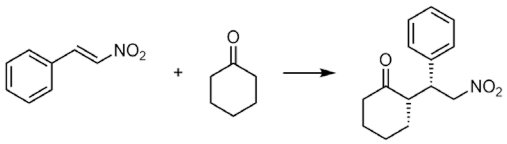			
Michael_2 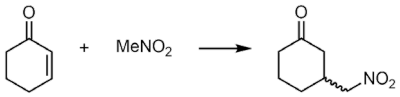			
Henry 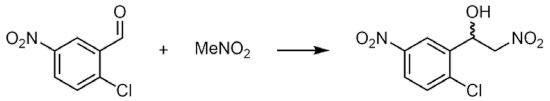			
Baylis Hillman 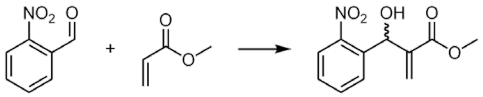			
Friedel-Crafts 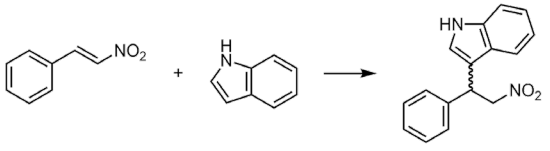			
Pictet Spengler 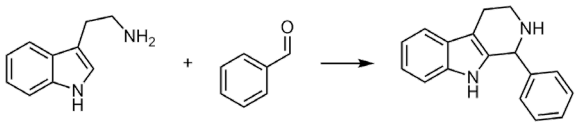			

2.2.4 Design and synthesis of chiral linkers

Alongside the catalyst linkers (**step 1-3**), the chiral linkers were of utmost importance to the RAI concept as they provide the only source of chiral information in the frameworks. This section outlines the selection of chiral moieties as well as the MOF linker design, synthesis and testing (**step 4** and **5** of **Figure 2.2**). The central aim was to build a diverse library of chiral linkers featuring various motifs and spatial orientations. All chiral linkers were based on the bdc linker.

When designing these chiral linkers, three criteria had to be met:

(i) The synthetic route for attachment of the chosen chiral precursor must be feasible.

(ii) The chiral precursor must be commercially available in enantiomerically pure form.

(iii) The final linker is unlikely to be catalytically active itself.

Chiral linkers derived from functionalised oxazolidinones

One promising approach was to expand on the successful work developed in the proof of principle study of the RAI concept, and to use chiral oxazolidinones as a platform for chiral bdc linker design (**Chapter 1.2.3**). This functional group had proven to meet all chiral linker design criteria, and a standardised synthetic route was already established. Four chiral oxazolidinone linkers were selected for testing during this project (**Figure 2.11 A**). These linkers were chosen based on their different functionalities, spatial orientations and the commercial availability of the chiral oxazolidinone precursor.

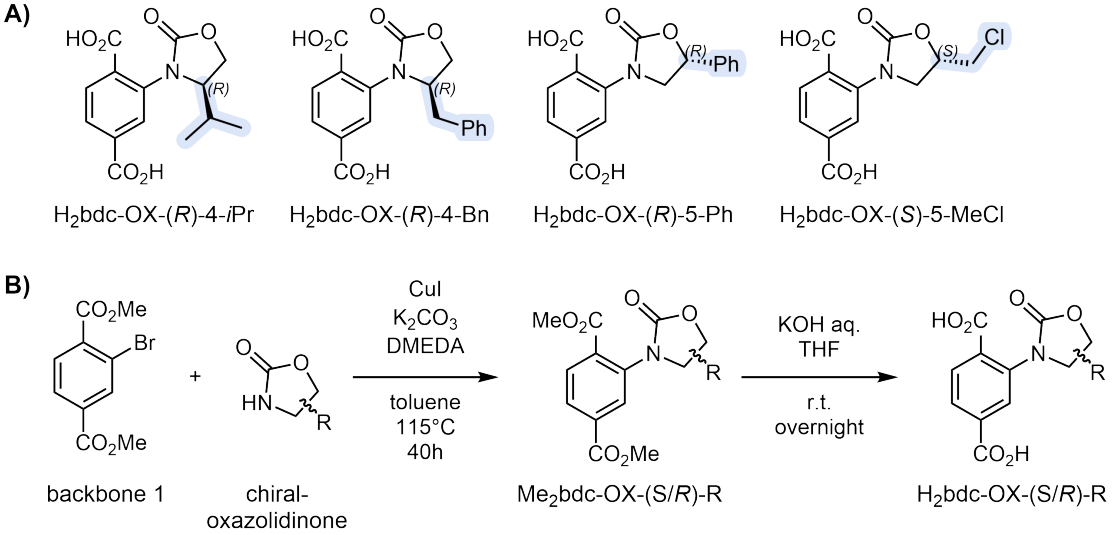

Figure 2.11 A) Depiction of the chiral oxazolidinone-based bdc linkers selected for testing in RAI catalysts. The functional groups on the asymmetric carbon atom are highlighted. **B)** Synthetic route to the chiral bdc-oxazolidinone linkers.

The synthesis of this family of linkers was performed starting from a common precursor, backbone 1, following a standardised two-step synthetic protocol (**Figure 2.11 B**). The first step was coupling of backbone 1 with the respective chiral oxazolidinone functionality to yield Me_2bdc-OX-(*S*/*R*)-R. Subsequently, the methyl esters were hydrolysed under basic conditions to yield the target linker, H_2bdc-OX-(*S*/*R*)-R. All linkers were obtained in high yield and purity, which satisfied **step 4** of **Figure 2.2**.

(i) H_2bdc-OX-(*R*)-4-*i*Pr: *Iso*-propyl functionality serves as relatively rigid aliphatic steric bulk. It is attached at the 4-position of the oxazolidinone, positioning it close to the bdc-backbone in the final linker.

(ii) H_2bdc-OX-(*R*)-4-Bn: Benzyl functionality serves as relatively flexible aromatic steric bulk. It is attached at the 4-position of the oxazolidinone, positioning it close to the bdc-backbone in the final linker.

(iii) H_2bdc-OX-(*R*)-5-Ph: Phenyl functionality serves as rigid aromatic steric bulk. It is attached at the 5-position of the oxazolidinone, orienting it away from bdc-backbone in the final linker.

(iv) H_2bdc-OX-(*S*)-5-MeCl: Chloromethyl group serves as small but polarisable steric bulk. It is attached at the 5-position of the oxazolidinone, orienting it away from bdc-backbone in the final linker.

Chiral linkers derived from primary amines

To broaden the scope of the chiral linkers beyond oxazolidinone moieties, alternative options were considered. A key source of inspiration came from nature's most successful catalysts, enzymes. In the active sites of enzymes, multiple amino acid residues come together in a catalytic pocket to cooperatively catalyse reactions while simultaneously creating the ideal chiral environment for nearly perfect enantiocontrol.[182, 183] While some of the amino acid residues are directly responsible for the catalytic activity, others solely provide the chiral environment.[27, 183] This inspired the idea of attaching amino acids with likely non-catalytically active residues onto the bdc-backbone. Enantiomerically pure amino acids and their derivatives are inexpensive and structurally diverse, making them an ideal platform for building a large family of chiral linkers

Attachment of amino acids and their derivatives to the bdc backbone *via* the amino groups was identified as the most feasible synthetic approach. To minimise the risk of the chiral linkers showing unintended catalytic activity themselves – for example for aldol reactions through

enamine catalysis mediated by secondary amines – linker designs were explored that would yield tertiary amines, which are typically inert towards such catalytic pathways. An additional design concern was that if the carboxyl group of amino acids was left exposed, it could potentially compete with the carboxyl groups of the bdc-backbone during MOF synthesis and impede framework formation. To avoid this issue, the linker design was centred around amino alcohol derivatives, which retain the same chiral centre but replace the carboxyl group with a hydroxyl group. In addition to amino alcohols, several simple primary amines were identified as potential chiral motifs.

All this considered, a series of four chiral linkers was designed (**Figure 2.12 A**) and their synthesis developed (**Figure 2.12 B**). The synthetic route was based on a common precursor, backbone 2, which can be synthesised in bulk in four steps. Its functionalisation with primary amines delivers a symmetric five-membered ring attached to the bdc-backbone. The chiral residue is pointing vertically away from the backbone. Hereafter, this family of linkers will be referred to as the "family of bdc-^{5}N-chiral linkers" or simply "^{5}N-chiral linkers," with "^{5}N" referring to the five-membered ring attached to the bdc-backbone.

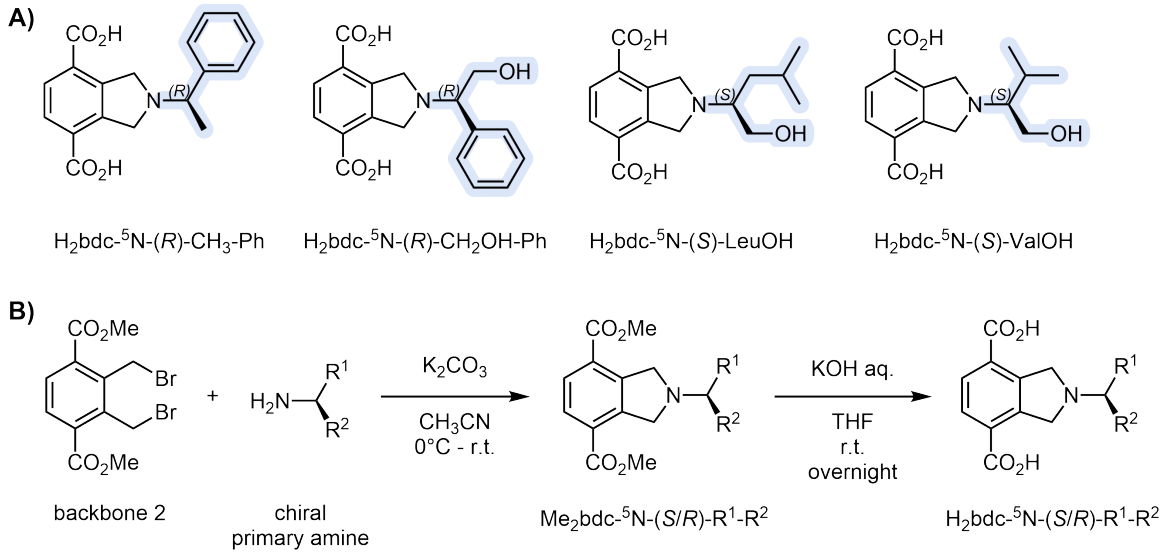

Figure 2.12 A. Symmetrical chiral linkers derived from simple primary amines and amino alcohols that have been synthesised with their functional groups highlighted.
B. Standardised synthesis of various chiral linkers based on backbone 2.

The four designed linkers featuring diverse functional groups (**Figure 2.12 A**) were successfully synthesised with good yields and purity following the standardised procedure. Therefore, all linkers satisfied **step 4** of **Figure 2.2**.

(i) H_2bdc-^{5}N-(*R*)-Ph-CH_3: Derived from the primary amine (*R*)-1-phenylethylamine, the two functional groups on the chiral carbon atom provide steric bulk and the possibility of π–π interactions.

(ii) H_2bdc-^{5}N-(*R*)-Ph-CH_2OH: Derived from the amino alcohol (*R*)-phenylglycinol, R^1 is a hydroxymethyl group, which has the capacity for hydrogen bonding.

(iii) H_2bdc-^{5}N-(*S*)-LeuOH: Derived from the amino alcohol, leucinol, R^1 is a hydroxymethyl group, which has the capacity for hydrogen bonding.

(iv) H_2bdc-^{5}N-(*S*)-ValOH: Derived from the amino alcohol, valinol, R^1 is a hydroxymethyl group, which has the capacity for hydrogen bonding.

2.2.5 MUF-77 synthesis with chiral linkers and control experiments

After successfully synthesising the two families of chiral linkers, the next step was to incorporate them into MUF-77 and to perform control experiments (**step 5** of **Figure 2.2**). This was important to confirm that the chiral linkers were compatible with the MUF-77 synthesis conditions and to ensure that they did not endow the framework with catalytic activity.

Initially, MOF synthesis was performed using the simplest truxene, H_3hmtt, and the unfunctionalised H_2bpdc (**Figure 2.13**). Since all chiral linkers within each family share a common backbone, one representative example from each group was selected for these experiments: H_2bdc-OX-(*R*)-5-Ph and H_2bdc-^{5}N-(*S*)-ValOH. It was assumed that if these representatives were compatible with MUF-77 synthesis conditions and if the chiral MOF showed no catalytic activity, the remainder of the linker family would behave similarly.

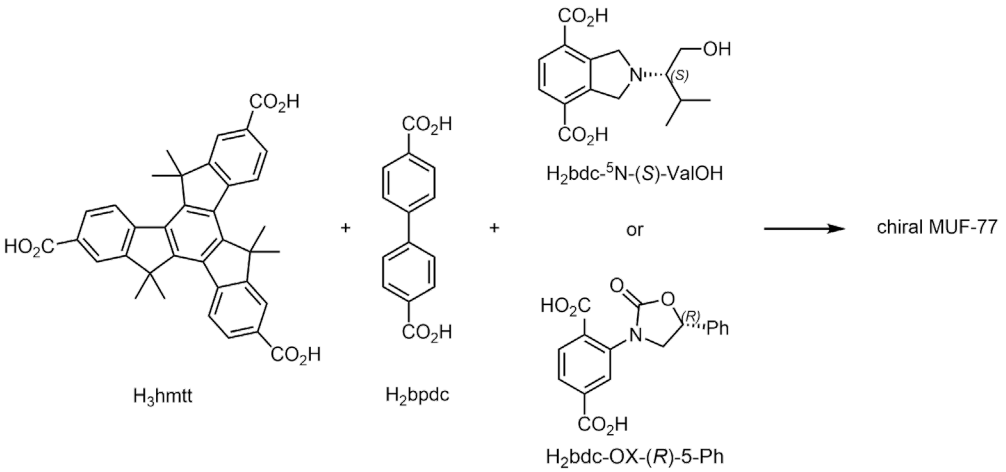

Figure 2.13 Schematic diagram showing the synthesis of representative chiral MUF-77's with the formula $[Zn_4O(hmtt)_{1.33}(bpdc)_{0.5}(bdc\text{-}OX\text{-}(R)\text{-}5\text{-}Ph)_{0.5}]$ and $[Zn_4O(hmtt)_{1.33}(bpdc)_{0.5}(bdc\text{-}^5N\text{-}(S)\text{-}ValOH)_{0.5}]$.

H_2bdc-OX-(*R*)-5-Ph and H_2bdc-^{5}N-(*S*)-ValOH were successfully incorporated into MUF-77 as confirmed by PXRD and ^{1}H NMR measurements. This established that both families of chiral linkers were compatible with the MUF-77 synthesis conditions.

The representative analytical data for $[Zn_4O(hmtt)_{1.33}(bpdc)_{0.5}(bdc\text{-}^5N\text{-}(S)\text{-}ValOH)_{0.5}]$ are shown in **Figure 2.14 A** and **B**. In the measured PXRD diffractogram, the observed reflection positions match those of the calculated MUF-77 pattern, with no additional reflections being observed. This is supported by the ^1H NMR spectrum of a digested MOF sample, which shows the expected signals for the three linkers in the correct ratio (hmtt:bpdc:bdc-^{5}N-(*S*)-ValOH = 1.33:0.5:0.5) with no additional peaks present that would indicate side reactions or impurities. Together, these results confirm the phase purity of the achiral catalyst MOF.

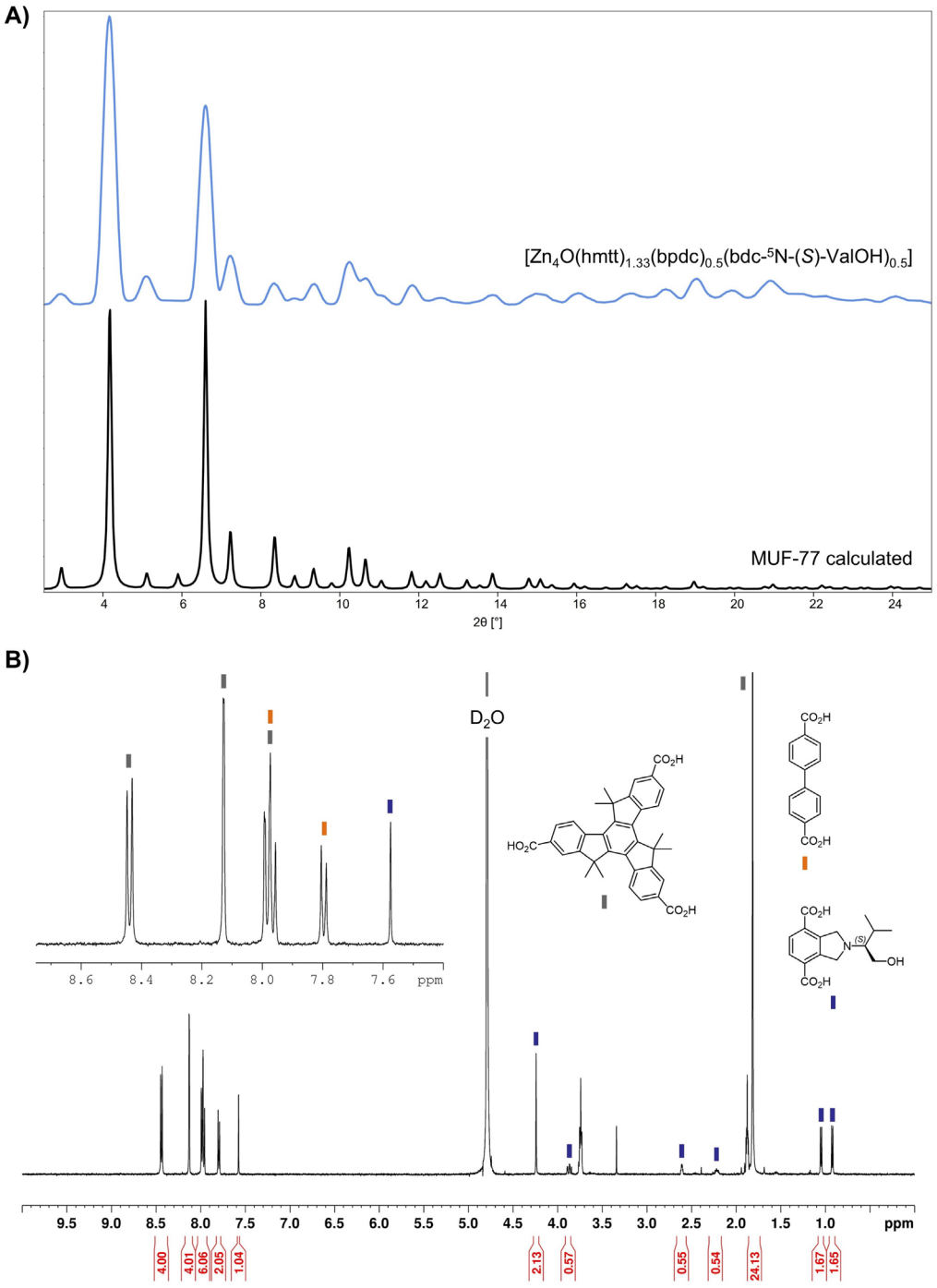

Figure 2.14 A) Experimental PXRD pattern (blue) and calculated pattern of MUF-77 (black). **B)** ^1H NMR spectra of the digested MUF-77 in a D_2O - NaOD mixture. The peaks are labelled by colour to highlight the corresponding linker.

The two chiral MOFs, $[Zn_4O(hmtt)_{1.33}(bpdc)_{0.5}(bdc\text{-}OX\text{-}(R)\text{-}5\text{-}Ph)_{0.5}]$ and $[Zn_4O(hmtt)_{1.33}(bpdc)_{0.5}(bdc\text{-}^5N\text{-}(S)\text{-}ValOH)_{0.5}]$ were washed following the standard washing procedure and then tested for their catalytic activity for the Henry, aldol and Friedel-Crafts reactions (**Table 2.2**). No catalytic activity was observed for the Henry and aldol reaction after three days at room temperature, as determined by TLC and HPLC analysis. However, unexpectedly, both MOFs showed catalytic activity for the Friedel-Crafts reaction. HPLC analysis revealed that the reaction mixture showed an ee of 24.7% when catalysed by $[Zn_4O(hmtt)_{1.33}(bpdc)_{0.5}(bdc\text{-}OX\text{-}(R)\text{-}5\text{-}Ph)_{0.5}]$ and 6.3% when catalysed by $[Zn_4O(hmtt)_{1.33}(bpdc)_{0.5}(bdc\text{-}^5N\text{-}(S)\text{-}ValOH)_{0.5}]$. These results revealed that the chiral linkers themselves acted as asymmetric catalysts within the MOFs, rather than being exclusively passive. This finding violated the fundamental principle of the RAI concept, where the chiral source needs to be passive and solely responsible for providing the chiral information. Therefore both families of linkers were considered unsuitable for exploring the RAI concept when catalysing the Friedel-Crafts reaction. The exact origin and mechanism of this unexpected catalytic activity remains unknown, but since this combination was classified as a 'dead end' in the stepwise screening approach, it was not explored further.

Table 2.2 Results of the testing for activity of the two chiral MOFs $[Zn_4O(hmtt)_{1.33}(bpdc)_{0.5}(bdc\text{-}OX\text{-}(R)\text{-}5\text{-}Ph)_{0.5}]$ and $[Zn_4O(hmtt)_{1.33}(bpdc)_{0.5}(bdc\text{-}^5N\text{-}(S)\text{-}ValOH)_{0.5}]$. Reactions were performed using the standard catalysis conditions and were monitored for three days.

	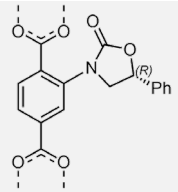 bdc-OX-(*R*)-5-Ph	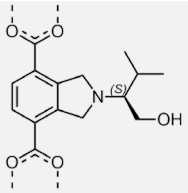 bdc-^{5}N-(*S*)-ValOH
Aldol 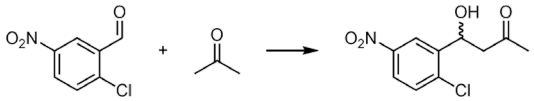	no activity observed	no activity observed
Henry 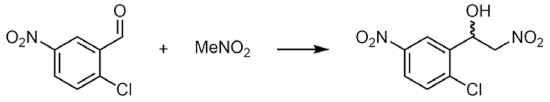	no activity observed	no activity observed
Friedel-Crafts 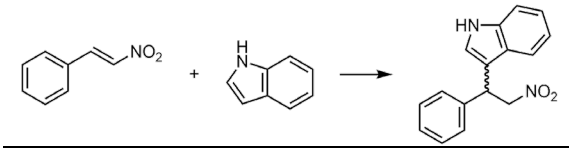	active ee = 24.7%	active ee = 6.3%

To verify the compatibility of the two families of chiral linkers with the temperature that is required for thermally cleaving the Boc group from the H_2bpdc-^{7}N-Boc procatalyst linker, TGA measurements were performed on the free linkers H_2bdc-OX-(*R*)-5-Ph and H_2bdc-^{5}N-(*S*)-ValOH as the representative examples. H_2bdc-OX-(*R*)-5-Ph showed its first significant weight loss at an onset temperature of ~262 °C (**ESI Figure 2.74**). This temperature is well above the 165-190 °C range required for Boc-deprotection. Consequently, this family of chiral linkers could be reliably used in conjunction with the H_2bpdc-^{7}N-Boc procatalyst linker.

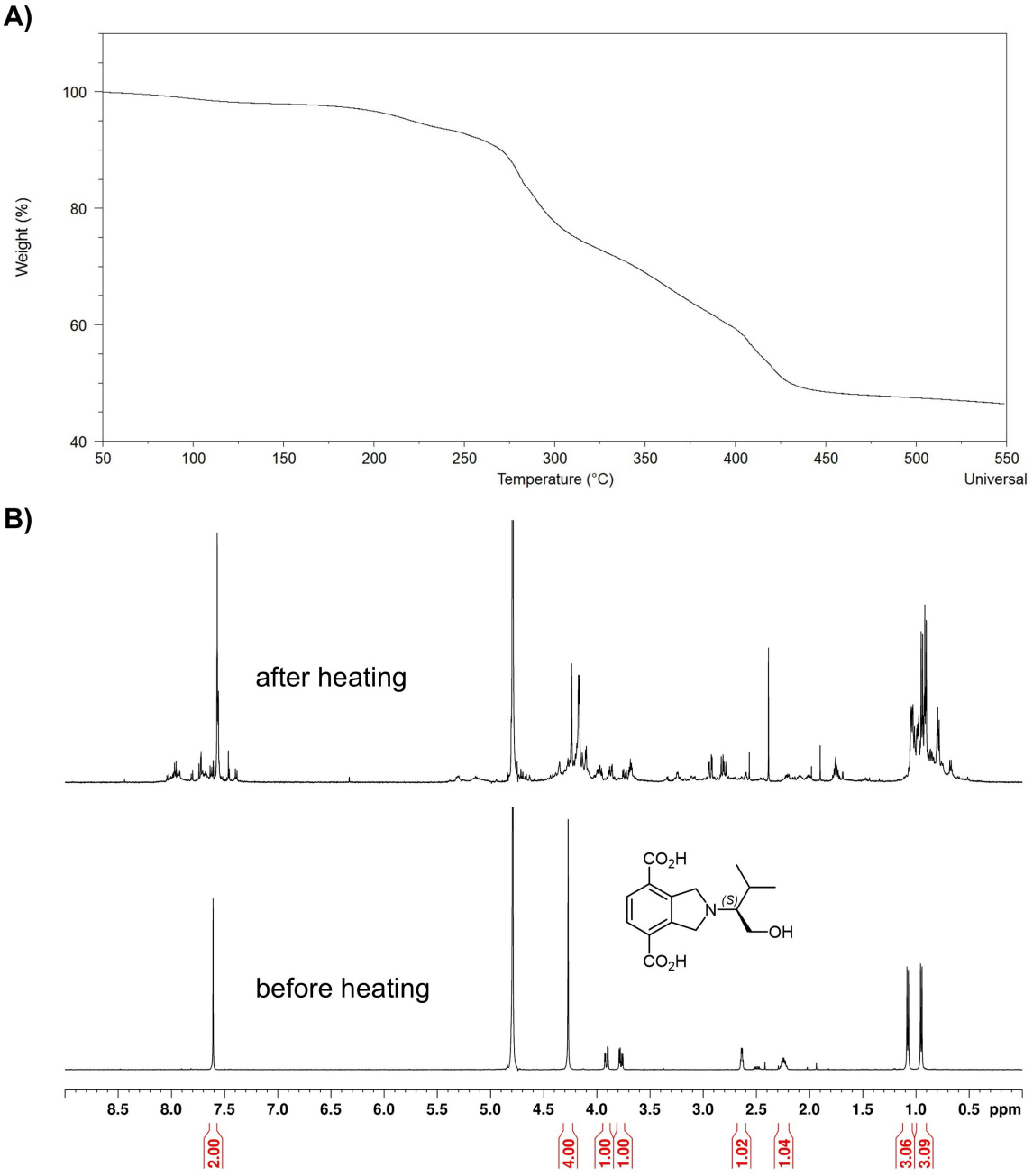

Figure 2.15 A) TGA trace of H_2bdc-^{5}N-(S)-ValOH and **B)** ^{1}H-NMR spectra of H_2bdc-^{5}N-(*S*)-ValOH in a D_2O - NaOD mixture. The lower spectrum is of the pure ligand The upper spectrum was measured after heating the linker at 160 °C for one hour.

TGA measurements performed on H_2bdc-^{5}N-(*S*)-ValOH as the representative example were not as decisive. Between 100-250 °C, a gradual weight loss of 6.0% was observed without a clear onset point (**Figure 2.15 A**). Beyond 250 °C, the sample decomposed with a significant weight loss. The early weight loss and low decomposition temperature suggested limited thermal stability of H_2bdc-^{5}N-(*S*)-ValOH, which was independently confirmed by ^{1}H NMR spectroscopy (**Figure 2.15 B**). Therefore, the family of ^{5}N-chiral linkers is incompatible with thermolytic Boc-deprotection conditions, meaning that they cannot be used in combination with the procatalyst H_2bpdc-^{7}N-Boc.

2.2.6 Synthesis and testing of RAI-MOF catalysts

The project now entered its most crucial phase: the synthesis and testing of RAI-MOF catalysts (**step 6** and **step 7** of **Figure 2.2**). This discussion is divided into three sections, corresponding to the three catalytic linkers. Each catalytic linker was paired with the families of chiral linkers, and the resulting RAI-MOFs were examined for their enantioselectivity in the identified reactions. Several key parameters were varied and their influence on the enantioselectivity assessed. The ultimate goal was to identify a system – comprising one model reaction catalysed by a class of RAI-MOFs, built from a single catalyst linker and a family of chiral linkers – that not only demonstrated good ee (above 50%) but, more importantly, showed high variation in ee with small modifications of parameters. The identified system is explored in depth in the following chapters.

It is worth noting that:

(i) The focus of this work was exclusively on the enantioselectivity of the RAI-MOF catalysts, measured in the ee. Low ee values of ee = ± 1% are considered to be 0%, as this falls into the error margin observed between the individual MOF batches.

(ii) The goal of this section was not to perform every theoretically possible experiment. Instead, the focus was on screening broadly for high variation (15-30%) in the ee with fairly dramatic changes to conditions. A high variation indicated that additional changes may boost the ee towards 100%. On the other hand, parameters that induced little variation in the ee were at this point not considered worthy of further investigation.

(iii) When a system of model reaction and RAI-MOF catalyst family is found that meets the objective – good ee and high variation in response to modifications – any ongoing efforts in other systems will be stopped to focus on the identified system. This has the potential to leave these other systems not fully explored.

(iv) The effective catalyst loading was not precisely determined before each catalysis. Precise determination of effective catalyst loading requires thorough drying of the MOF crystals. The exposure to atmospheric conditions during weighing leads to a complete loss of crystallinity. Consequently, the MOF crystals were kept in suspension at all times and were divided by eye so that the effective catalyst loading was roughly 5-15 % (**section 2.4.6**). Examples where the catalyst loading was retrospectively determined are discussed in **Chapter 4.2.2.3**.

(v) The conversion of the individual catalyses was only of secondary concern as long as sufficient product formation allowed for reliable integration of the product peaks during HPLC analysis. The reliability of the ee measurements by HPLC is high, even at low conversion (**Chapter 4.2.2.3**). In general, higher conversions were observed when a greater amount of MOF crystals was used or when the reaction time was extended before HPLC analysis. Since catalyst loading was not measured and reaction times were not fully standardised, conversion was not quantified but instead assessed qualitatively by comparing product and substrate integrals. Conversions were categorised as 'low,' 'medium,' 'high,' or 'quantitative' based on these comparisons.

For the sake of readability and clarity, the RAI-MOFs are assigned abbreviations and numbered systematically. The general abbreviation follows the structure:

MOF-topology_catalyst_chiral_number

The term 'MOF-topology' refers to the topology of the MOF, as confirmed by PXRD. It is distinguished between the MUF-77 and the MUF-7 type topology (**Chapter 1.2.3**). 'Catalyst' represents the catalyst linker of the RAI-MOF, with the following shortened abbreviations used: 'gua' for bpdc-gua, 'urea' for bpdc-urea-Ph and '^{7}N-H' for bpdc-^{7}N-H. The term 'chiral' refers to the family of chiral linkers rather than a specific linker itself, with 'Ox' used for oxazolidinone-based chiral linkers and '^{5}N' representing chiral linkers featuring a five-membered ring. Within each discussion, the MOFs are then assigned a number, starting from one. For example, the RAI-MOF with the chemical formula of $[Zn_4O(hmtt)_{1.33}(bpdc\text{-}^{7}N\text{-}H)_{0.5}(bdc\text{-}OX\text{-}(R)\text{-}5\text{-}Ph)_{0.5}]$ would be abbreviated as: MUF-77_^{7}N-H_Ox_1.

2.2.6.1 RAI-MOFs with bpdc-^{7}N-H as the catalyst linker

In this section, the enantioselectivity of RAI-MOF catalysts based on the secondary amine catalyst linker, bpdc-^{7}N-H, were explored. As this linker previously demonstrated activity in the aldol and Henry reactions, the focus is placed on these two transformations (**section 2.2.3**). The catalyst linker was exclusively combined with the family of oxazolidinone-based chiral linkers, as the family of bdc-^{5}N-chiral linkers were previously found to be incompatible with the conditions required for thermolytic Boc-deprotection of the procatalyst bpdc-^{7}N-Boc (**section 2.2.5**).

Five RAI-MOFs were synthesised, consisting of the procatalyst H_2bpdc-^{7}N-Boc, different oxazolidinone-based chiral linkers and two distinct truxenes (**Figure 2.16** and **Table 2.3**). The three oxazolidinone-based chiral linkers were selected to compare vastly different functional groups: alkyl, aromatic and halogen, as well as to explore the effect of the chiral functionality's position on the backbone.

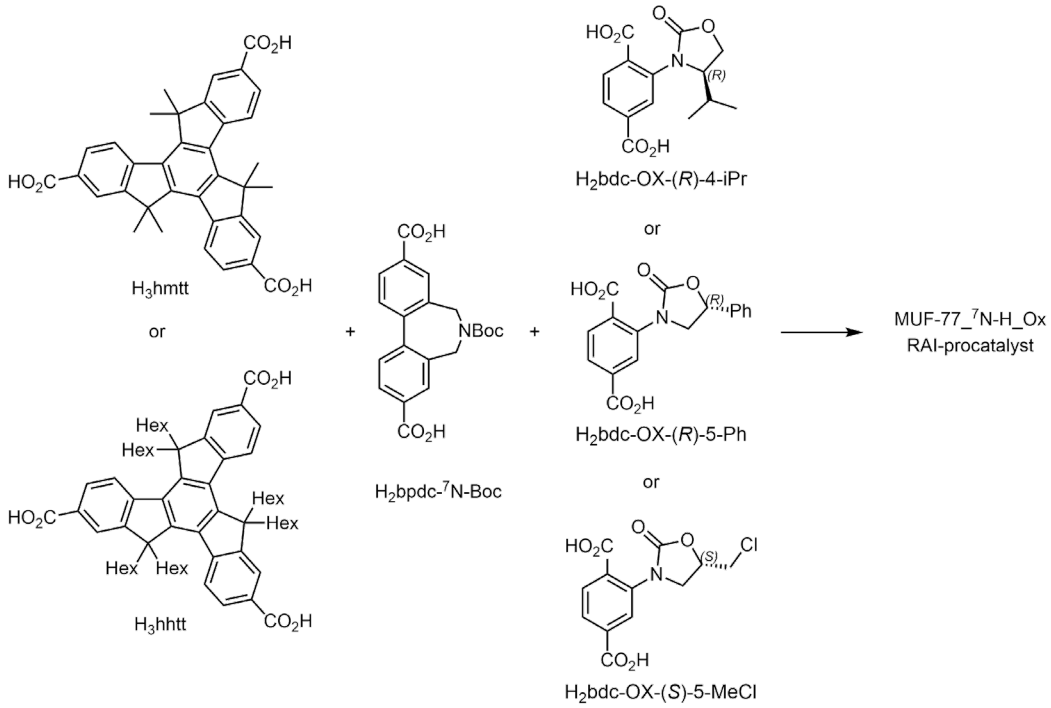

Figure 2.16 Schematic diagram showing the RAI-MOF procatalyst synthesis using H_2bpdc-^{7}N-Boc, different truxenes and oxazolidinone-based chiral linkers. The RAI-MOF procatalysts were activated by Boc-removal before being used as catalysts.

All RAI-MOF procatalysts were activated by thermolytic Boc-deprotection using the standard procedure (**Section 2.4.4**). After Boc-removal, the crystallinity of the catalysts was confirmed by PXRD (**Figure 2.17 A**), and the identity of the linkers was evaluated by ^{1}H NMR spectroscopy of digested samples (representative example in **Figure 2.17 B**).

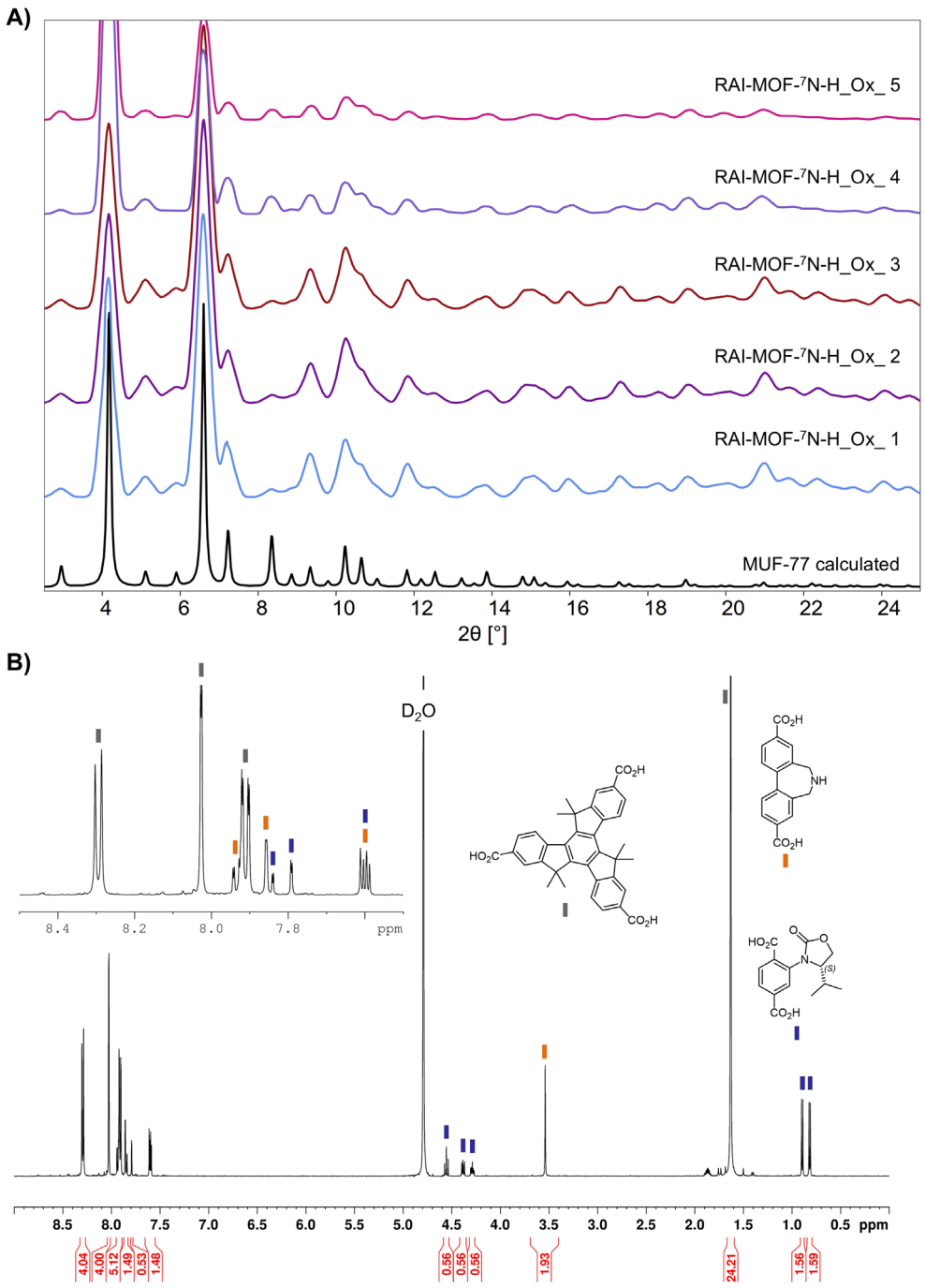

Figure 2.17 A) PXRD pattern of MUF-77_^{7}N-H_Ox_1-5 compared to the calculated pattern of MUF-77. **B)** ^{1}H NMR spectrum of digested MUF-77_^{7}N-H_Ox_1 in D_2O/ NaOD. The peaks are labelled by colour to highlight the corresponding linker.

The PXRD pattern confirmed that all samples maintained high crystallinity during Boc-removal. No other phases besides the MUF-77 topology were detected. This is supported by the ^{1}H NMR spectrum of the digested MOF samples, which shows the expected signals for the three linkers in the correct ratio (hmtt:bpdc-^{7}N-H:bdc-OX-(*R*)-4-iPr = 1.33:0.5:0.5) with no additional peaks present that would indicate side reactions or linker degradation during heating. Together, these results confirm the phase purity and linker identities of the RAI-MOF catalysts.

Table 2.3 Abbreviations and ligand combination for the five different RAI-MOF catalysts synthesised using H_2bpdc-^{7}N-Boc, different truxenes and chiral oxazolidinone-based linkers. The generalised MUF-77 formula after Boc-removal is: $[Zn_4O(\textbf{truxene})_{1.33}(bpdc\text{-}^7N\text{-}H)_{0.5}(\textbf{chiral-bdc})_{0.5}]$.

RAI-MOF	truxene	chiral bdc
MUF-77_^{7}N-H_Ox_1	hmtt	bdc-OX-(*R*)-4-*i*Pr
MUF-77_^{7}N-H_Ox_2	hmtt	bdc-OX-(*R*)-5-Ph
MUF-77_^{7}N-H_Ox_3	hmtt	bdc-OX-(*S*)-5-MeCl
MUF-77_^{7}N-H_Ox_4	hhtt	bdc-OX-(*R*)-4-*i*Pr
MUF-77_^{7}N-H_Ox_5	hhtt	bdc-OX-(*R*)-5-Ph

Aldol reaction

The influence of different reaction substrates on the ee of the acetone aldol reaction was first explored. All five MUF-77-^{7}N-H_Ox catalysts were used and the functional groups attached to the benzaldehyde were varied (**Table 2.4**). Four benzaldehydes featuring nitro groups were chosen, as their HPLC conditions were known and the position of a nitro group on the ring had previously been shown to affect enantioselectivity. However, in this set of experiments, no significant ee was observed for any of the four tested aldehydes.

Table 2.4 Measured ee values for the aldol reaction of different benzaldehydes with acetone, catalysed by the different MUF-77_^{7}N-H_Ox catalysts.

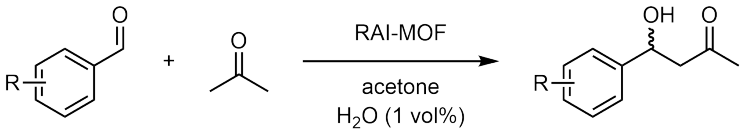

RAI-MOF	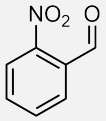	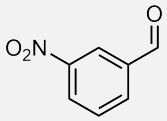	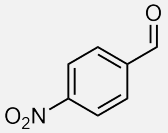	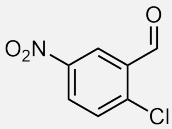
MUF-77_^{7}N-H_Ox_1	-1.5%	-1.0%	0 %	0%
MUF-77_^{7}N-H_Ox_2	0%	0%	2.0%	0%
MUF-77_^{7}N-H_Ox_3	0%	0%	0%	0%
MUF-77_^{7}N-H_Ox_4	1.4%	0%	0%	0%
MUF-77_^{7}N-H_Ox_5	0%	0 %	0%	0%

Next, the influence of the reaction solvent on the ee of the aldol reaction was explored using a common pair of substrates: 2-chloro-5-nitrobenzaldehyde and 50 equivalents of acetone (**Table 2.5**). For solvents that were miscible with water, 1 vol% of water was added, which has

been shown to increase the reaction rate of aldol reactions catalysed by secondary amine catalysts.[126]

In 1,2-dichloroethane, no conversion was observed. This may be due to the exclusion of water due to immiscibility. Acetonitrile produced similar results to acetone itself. However, 1,4-dioxane led to noticeable ee values of between +1.6% and -3.2%. This indicates that the solvent can influence reaction ee, albeit to a very modest degree.

Taken together, the MUF-77-^{7}N_Ox catalysts did not produce promising ee values, nor did they show significant variation in response to changes in the reaction substrate or solvent for the acetone aldol reaction. Consequently, no further studies were conducted on this system.

Table 2.5 Measured ee values for the aldol reaction of 2-chloro-5-nitrobenzaldehyde with acetone in different solvents, catalysed by the different MUF-77_^{7}N-H_Ox catalysts. If no conversion was observed, it is labelled as 'N.R.' (no reaction). If a combination was not explored, it is labelled as 'N.D.' (not determined).

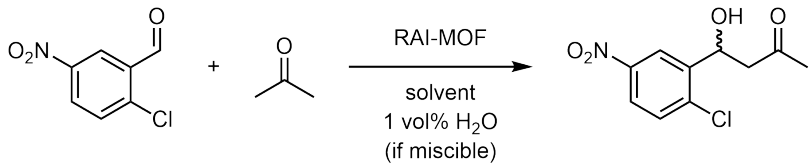

RAI-MOF	acetone	1,4-dioxane	acetonitrile	1,2-dichloroethane
MUF-77_^{7}N-H_Ox_1	0%	1.3%	0%	N.R.
MUF-77_^{7}N-H_Ox_2	0%	-2.6%	0%	N.R.
MUF-77_^{7}N-H_Ox_3	0%	-3.1%	0%	N.R.
MUF-77_^{7}N-H_Ox_4	0%	-3.2%	N.D.	N.D.
MUF-77_^{7}N-H_Ox_5	0%	1.6%	N.D.	N.D.

Henry reaction

To evaluate the performance of the MUF-77-^{7}N_Ox catalysts for the Henry reaction, the first set of experiments focused on assessing how different reaction substrates influenced the ee. The Henry reaction was catalysed using the five MUF-77-^{7}N_Ox catalysts while systematically varying the functional groups attached to the aldehyde (**Table 2.6**). All reactions were performed in 1,4-dioxane as the standard solvent with 50 equivalents of nitromethane. MUF-77-^{7}N_Ox_1 did not produce any measurable ee, while MUF-77-^{7}N_Ox_2-5 showed low ee values. The highest was 5.1% for the Henry reaction of 2-chloro-5-nitrobenzaldehyde and nitromethane catalysed by MUF-77-^{7}N_Ox_2. However, no clear trend emerged regarding

either the influence of different chiral linkers or truxenes on enantioselectivity, nor the effect of different positions of substituents on the reaction substrates.

Table 2.6 Measured ee values for the Henry reaction of different aldehydes with nitromethane in 1,4 dioxane, catalysed by MUF-77_^{7}N-H_Ox catalysts.

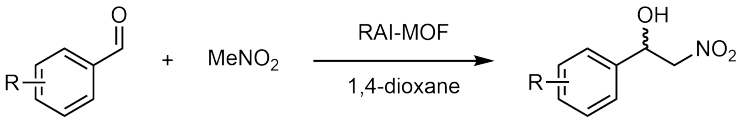

RAI-MOF	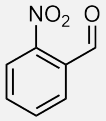	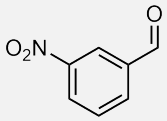	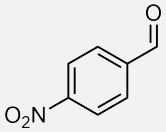	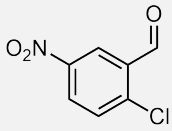
MUF-77_^{7}N-H_Ox_1	0%	0%	0%	0%
MUF-77_^{7}N-H_Ox_2	0%	3.4%	1.4%	5.1%
MUF-77_^{7}N-H_Ox_3	1.7%	1.2%	1.7%	4.1%
MUF-77_^{7}N-H_Ox_4	2.0%	3.3%	-4.4%	-1.0%
MUF-77_^{7}N-H_Ox_5	-3.0%	0%	2.2%	1.1%

Secondly, the effect of solvent on the ee of the Henry reaction was examined (**Table 2.7**). The solvents were selected to cover a range of polarity and protic properties. All experiments were performed using 2-chloro-5-nitrobenzaldehyde as the aldehyde and 50 equivalents of nitromethane. 1,4-Dioxane showed the best performance, with the results suggesting that the choice of solvent has only a minor influence on the enantioselectivity.

Table 2.7 Measured ee values for the Henry reaction of 2-chloro-5-nitrobenzaldehyde with nitromethane in different solvents catalysed by MUF-77_^{7}N-H_Ox catalysts. N.R. = no reaction; N.D. = not determined.

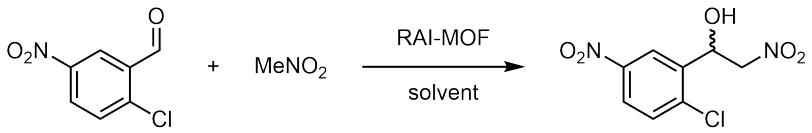

RAI-MOF	methanol	1,4-dioxane	acetonitrile	1,2-dichloroethane
MUF-77_^{7}N-H_Ox_1	-1.0%	0%	-3.8%	N.R.
MUF-77_^{7}N-H_Ox_2	1.9%	5.1%	0%	N.R.
MUF-77_^{7}N-H_Ox_3	1.2%	4.1%	0%	N.R.
MUF-77_^{7}N-H_Ox_4	N.D.	-1.0%	N.D.	N.D.
MUF-77_^{7}N-H_Ox_5	N.D.	1.1%	N.D.	N.D.

Considering all these experiments for the Henry reaction, the MUF-77-^{7}N_Ox catalysts did not produce high ee values and showed little variation in response to changes in either the reaction substrate or solvent. As a result, further studies on this system were not pursued.

2.2.6.2 RAI-MOFs with bpdc-urea-Ph as the catalyst linker

In this section, the enantioselectivity of RAI-MOF catalysts featuring the urea-HBD catalyst linker, bpdc-urea-Ph, were explored. This catalyst linker has previously demonstrated activity in the Friedel-Crafts and the aldol reaction (**section 2.2.3**). However, as both families of chiral linkers were themselves active and enantioselective for the Friedel-Crafts reaction (**section 2.2.5**), only aldol reactions were tested with the RAI-MOF catalysts.

Three RAI-MOF catalysts were synthesised using the catalyst linker H_2bpdc-urea-Ph, the truxene H_3hmtt, and different oxazolidinone-based chiral linkers (**Figure 2.18** and **Table 2.8**). These three oxazolidinone-based chiral linkers were selected to compare the influence of different functional groups: alkyl, aromatic and halogen, as well as to examine how the position of the chiral functionality in relation to the backbone affects the enantioselectivity.

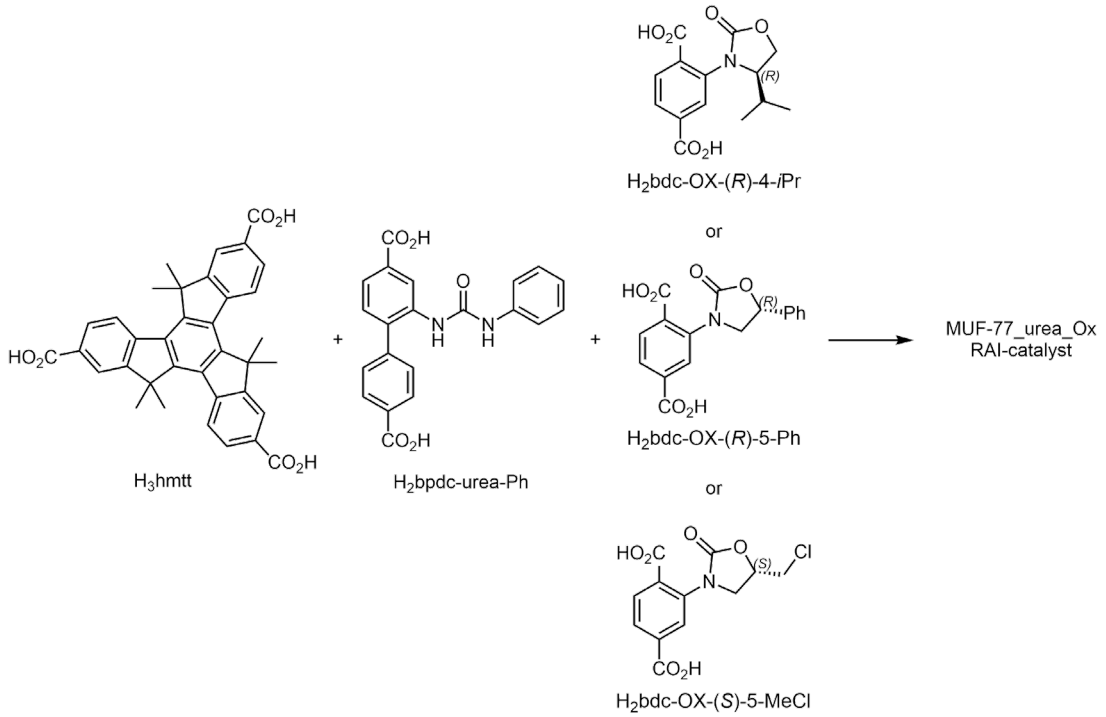

Figure 2.18 Schematic diagram showing the RAI-MOF synthesis using H_2bpdc-urea-Ph, H_3hmtt and different oxazolidinone-based chiral linkers.

Table 2.8 Abbreviations and ligand combination for the three different RAI-MOFs synthesised using H_2bpdc-urea-Ph, H_3hmtt and different chiral oxazolidinone-based linkers. The generalised MUF-77 formula is: $[Zn_4O(hmtt)_{1.33}(bpdc\text{-}urea\text{-}Ph)_{0.5}(\textbf{chiral bdc})_{0.5}]$.

RAI-MOF	chiral bdc
MUF-77_urea_Ox_1	H_2bdc-OX-(*R*)-4-*i*Pr
MUF-77_urea_Ox_2	H_2bdc-OX-(*R*)-5-Ph
MUF-77_urea_Ox_3	H_2bdc-OX-(*S*)-5-MeCl

Once the catalyst identity was verified, the MUF-77_urea_Ox catalysts were tested for their enantioselectivity in aldol reactions. The first set of experiments was performed to explore differently functionalised aldehydes (**Table 2.9**).

MUF-77_urea_Ox_2, which features a relatively large aromatic group on its chiral linker, produced only near racemic product mixtures. In contrast, MUF-77_urea_Ox_1 and MUF-77_urea_Ox_3, which contain smaller functional groups at the four- and five-positions of the oxazolidinone yielded higher ee values. The highest ee observed was 8.3%, achieved with MUF-77_urea_Ox_1 in the acetone-aldol reaction of *meta*-nitrobenzaldehyde. Determining a clear trend in how the identity and position of the chiral linker or aldehyde functionalisation influenced enantioselectivity proved challenging. Due to the generally low ee values, the differences between systems were too small to draw reliable conclusions.

Table 2.9 Measured ee values for the aldol reaction of different aldehydes with acetone, catalysed by the different MUF-77_urea_Ox catalysts.

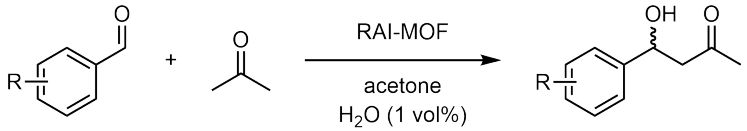

RAI-MOF	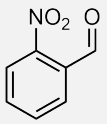	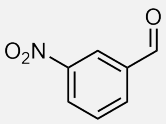	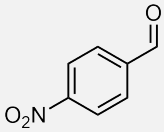	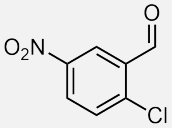
MUF-77_urea_Ox_1	5.1%	8.3%	1.5%	2.0%
MUF-77_urea_Ox_2	0%	1.4%	0%	0%
MUF-77_urea_Ox_3	-2.3%	-4.2%	0%	-7.3%

Despite the ee being too low for reliable conclusions to be drawn, these initial screening experiments were promising, as distinct non-zero ee values were obtained. This indicated that the RAI concept was fundamentally viable for this combination of model reaction and MUF-77_urea_Ox catalysts.

However, at that stage, a more promising combination of model reaction and RAI-MOF catalyst for in-depth investigation had been identified using a different class of RAI catalyst. As a result, all efforts on the MUF-77_urea_Ox catalysts were stopped, even though several key variables remained unexplored.

2.2.6.3 RAI MOFs with bpdc-gua as the catalyst linker

2.2.6.3.A Combination of bpdc-gua with oxazolidinone-based chiral linkers

In this section, the enantioselectivity of various RAI-MOF catalysts based on the guanidine catalyst linker, bpdc-gua, combined with oxazolidinone based chiral bdc linkers were examined. This RAI-MOF catalyst combination was previously explored during the proof of principle study (**Chapter 1.2.3**). From these results it is known that the linker combination of truxene, bpdc-gua and oxazolidinone-based chiral bdc linkers is unique in its ability to form not only the MUF-77 but also a MUF-7 topology. This is an exceptionally rare occurrence and has been observed in only a handful of cases throughout the extensive experience of the Telfer research group working with MUF-77. Notably, across all RAI-MOF catalyst syntheses performed in this study, both in earlier sections and later chapters, the MUF-7 topology has only been observed with this exact linker combination and no other.

It had been found that for the Henry reaction catalysed by RAI-MOFs built from this linker combination, the MUF-7 structure consistently outperformed the MUF-77 topology, yielding superior enantioselectivity (**Chapter 1.2.3**). This discovery introduced an additional layer of complexity for this combination of linkers, as it effectively doubled the number of potential experiments worth exploring. It further raised two questions: (i) which factors influence the framework growth to preferentially form one over the other topology and (ii) how the different topologies affect the enantioselectivity of the catalyst for other reactions besides the Henry reaction.

Directing framework formation between the MUF-77 and MUF-7 topology

The network topology formed during MOF synthesis is highly sensitive to conditions such as linker identity and attached functionality, metal-to-linker ratios, concentration of substrates, solvent, temperature, and the presence of modulators.[184] This principle applies equally to MC-MOFs.[131] While most truxene-containing systems exclusively form the MUF-77 topology, RAI-MOF catalysts based on bpdc-gua, combined with oxazolidinone chiral bdc linkers are an exception, as they can yield both the MUF-77 and MUF-7 type topology. Even within a single MOF synthesis batch, mixtures of both topologies have been found. These observations suggested that while specific linker combinations may show a natural preference towards one topology over the other, the outcome is not predictable. However, obtaining each topology in phase-pure form is of high importance for RAI catalysis, as the two topologies possess different pore environments (**Chapter 1.2.2** and **Figure 2.19 A**) and are therefore expected to show differences in enantioselectivity. To reliably compare the enantioselectivity of RAI-MOF catalysts with the same combination of linkers but different network topologies, MOF synthesis conditions were developed to direct framework growth toward a single topology.

Differentiating between the two topologies is not trivial. As both topologies share the same stoichiometry ($[Zn_4O(truxene)_{1.33}(bpdc)_{0.5}(bdc)_{0.5}]$), NMR spectroscopy does not provide information about the framework identity. Visually, the crystals are also indistinguishable, as they show identical crystal morphology (**Figure 2.19 B** and **C**). Instead, XRD measurements are required to differentiate them. SCXRD measurements can precisely determine the framework type of an individual crystal (**Figure 2.19 D**). However, as the samples were needed for catalysis and the average topology of all crystals within the sample was of interest, PXRD was used to differentiate them. The reflections of interest indicating the presence of the MUF-7 topology are at $2\theta = 3.6°$ and 5.5°. For the MUF-77 structure, the reflections of interest are found at $2\theta = 2.9°$, 5.1° and 5.9°.

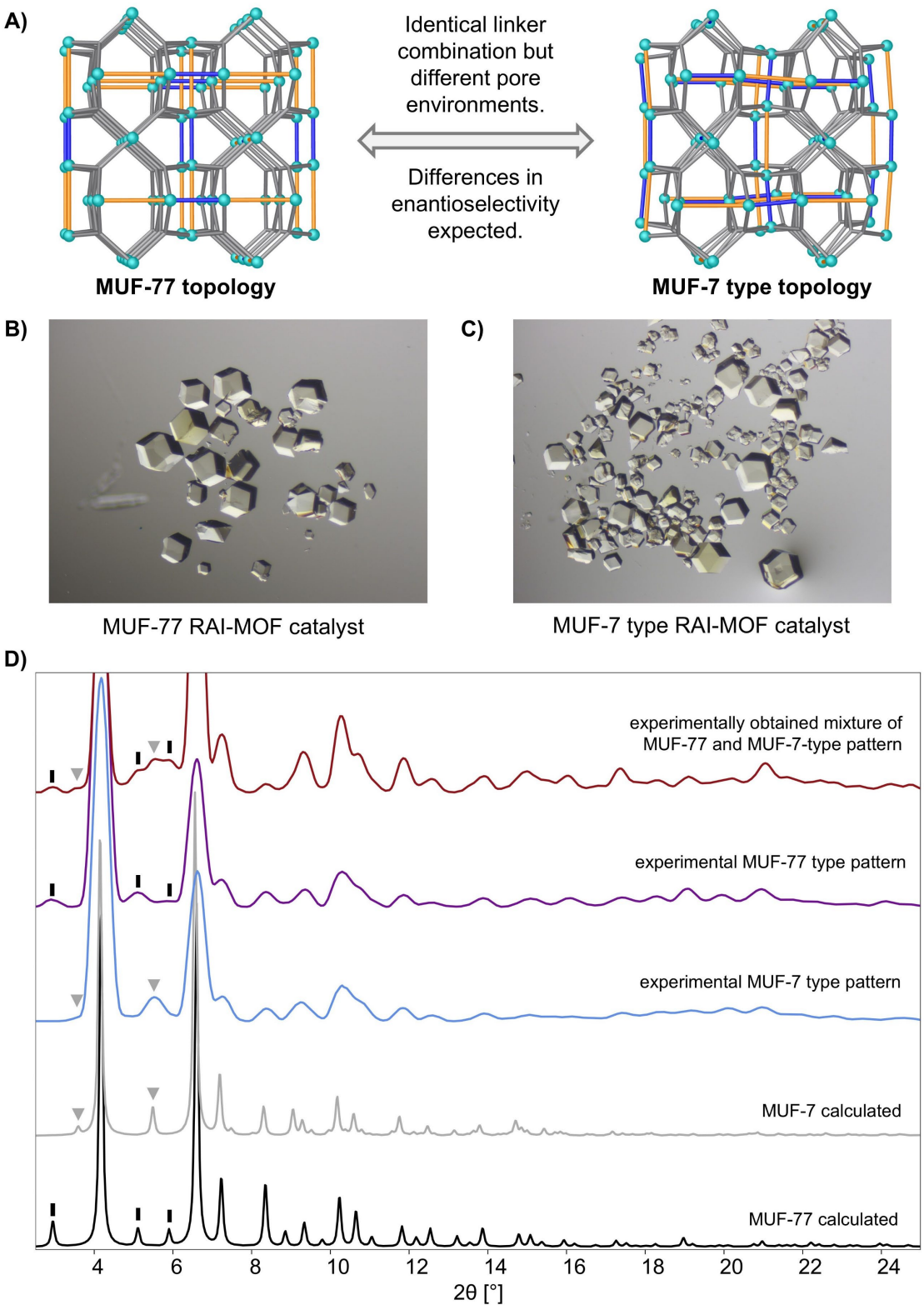

Figure 2.19 A) Schematic depiction of the MUF-77 and MUF-7 type topology. **B)** Photomicrograph of crystals with MUF-77 topology. **C)** Photomicrograph of crystals with MUF-7 type topology. **D)** Representative experimental and calculated PXRD pattern to highlight the minor differences between the MUF-77 and MUF-7 type topology. The reflections of interest for MUF-77 are highlighted by black rectangles. The reflections of interest for MUF-7 are highlighted by grey triangles.

MOF synthesis conditions were explored to determine if framework formation could be guided to preferentially yield the MUF-77 or MUF-7 type topology. Three representative linker combinations were chosen for this: MUF-X_gua_OX_1-3 (**Figure 2.20** and **Table 2.10**). Through systematically changing the MOF synthesis conditions (**Table 2.10**), it was identified that two main factors influenced the type of framework formed: the reaction temperature and the concentration of $Zn(NO_3)_2{\cdot}4H_2O$ (**Figure 2.20**). The key results from systematically adjusting these MOF synthesis parameters are summarised in **Table 2.10**.

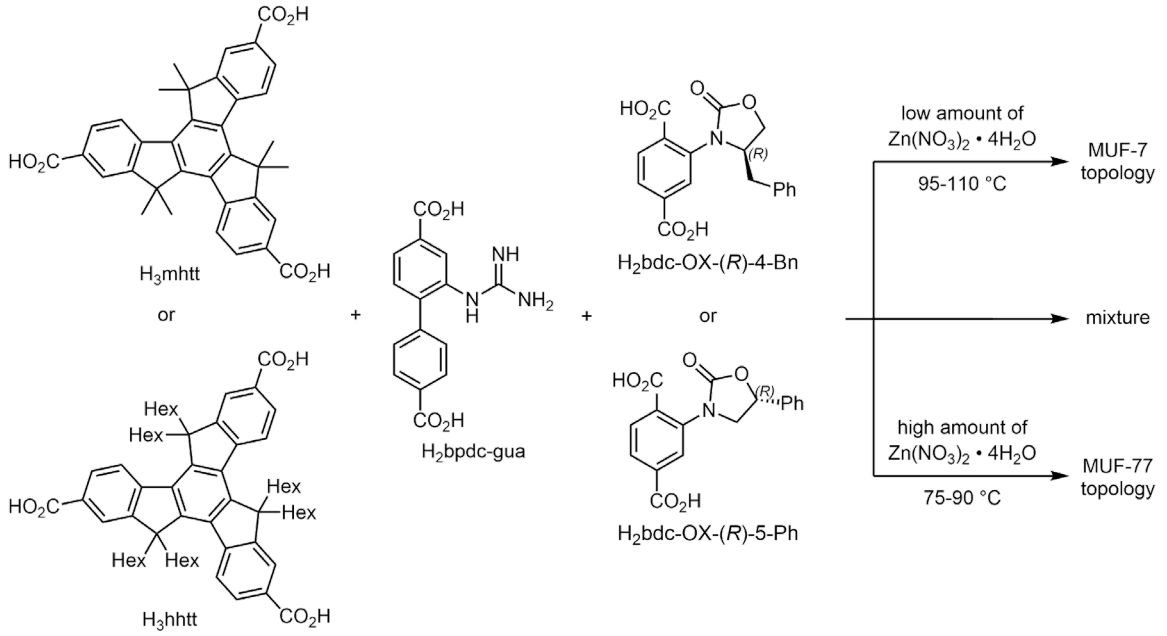

Figure 2.20 Schematic diagram showing the RAI-MOF catalyst synthesis with the MUF-77 or MUF-7 topology using H_2bpdc-gua, different truxenes and oxazolidinone-based chiral linkers.

The linker combination used in MUF-X_gua_Ox_3 naturally favoured the MUF-7 topology, as this structure was obtained across the entire temperature range (75-110 °C) with the standard $Zn(NO_3)_2{\cdot}4H_2O$ concentrations of 16.5 mg/mL. Significantly increasing the $Zn(NO_3)_2{\cdot}4H_2O$ concentration successfully shifted the MOF formation towards the MUF-77 topology. In contrast, the topology of MUF-X_gua_Ox_2 was strongly influenced by variations of the MOF synthesis temperature while maintaining the standard $Zn(NO_3)_2{\cdot}4H_2O$ concentration of 16.5 mg/mL throughout. At 110 °C, the MOF preferentially adopted the MUF-7 topology, whereas at lower temperatures (75–85 °C), the MUF-77 topology was favoured. For MUF-X_gua_Ox_1, neither temperature nor the $Zn(NO_3)_2{\cdot}4H_2O$ concentration variation alone resulted in a phase-pure formation of one topology. However, a combination of both leverages proved effective in directing the synthesis predominantly toward either the MUF-7 or MUF-77 topology.

Table 2.10 Overview of MOF syntheses conditions. The variables of interest were the truxene and the chiral bdc for the linker and the amount of $Zn(NO_3)_2 \cdot 4H_2O$ as well as the temperature for the reaction conditions. The observed framework topology is stated.

RAI-MOF (X = 77 or 7 topology)	truxene	chiral bdc	MOF synthesis conditions	framework topology
MUF-X_gua_Ox_1	hmtt	bdc-OX-(*R*)-4-Bn	8.8 mg/mL of $Zn(NO_3)_2 \cdot 4H_2O$ 100 °C	Mostly MUF-7
			44.0 mg/mL of $Zn(NO_3)_2 \cdot 4H_2O$ 75 °C	MUF-77
			16.5 mg/mL of $Zn(NO_3)_2 \cdot 4H_2O$ 75-110 °C	mixture
			8.8-79.4 mg/mL of $Zn(NO_3)_2 \cdot 4H_2O$ 85 °C	mixture
MUF-X_gua_Ox_2	hhtt	bdc-OX-(*R*)-4-Bn	16.5 mg/mL of $Zn(NO_3)_2 \cdot 4H_2O$ 110 °C	MUF-7
			16.5 mg/mL of $Zn(NO_3)_2 \cdot 4H_2O$ 75-85 °C	MUF-77
MUF-X_gua_Ox_3	hhtt	bdc-OX-(*R*)-5-Ph	16.5 mg/mL of $Zn(NO_3)_2 \cdot 4H_2O$ 75-110 °C	MUF-7
			77.4 mg/mL of $Zn(NO_3)_2 \cdot 4H_2O$ 85 °C	MUF-77

Overall, a general trend was observed: higher temperatures (95-110 °C) and/or lower concentrations of $Zn(NO_3)_2 \cdot 4H_2O$ preferentially yielded the MUF-7 topology, while lower temperatures (75–95 °C) and/or higher $Zn(NO_3)_2 \cdot 4H_2O$ concentrations led to the preferential formation of the MUF-77 structure.

MUF-77 vs. MUF-7 RAI-MOF catalysis: Differences in enantioselectivity

As outlined earlier, the MUF-77 and MUF-7-type topologies show vastly different pore environments. As a consequence, different enantioselectivities are expected when catalysing the same reaction with catalysts possessing identical linker combinations, but different topologies. This had been observed previously by Dr. Lee during his work with the Henry reaction. To explore this further, RAI-MOF-gua catalyst with either MUF-77 or MUF-7 type topology were synthesised and tested for both the Henry and aldol reaction. MUF-X_gua_Ox_1-3 catalysts were used (**Figure 2.20** and **Table 2.11**) for these experiments,

as conditions had already been developed to preferentially obtain both topologies. The better performing topology was then explored in more detail in subsequent experiments.

Table 2.11 Ligand combination for MUF-77_gua_Ox and MUF-7_gua_Ox catalysts synthesised with H_2bpdc-gua, different truxenes and chiral oxazolidinone-based linkers. The generalised MOF formula is: $[Zn_4O(\textbf{truxene})_{1.33}(\text{bpdc-gua})_{0.5}(\textbf{chiral-bdc})_{0.5}]$.

RAI-MOF (X = 77 or 7 topology)	truxene	chiral bdc
MUF-X_gua_Ox_1	hmtt	bdc-OX-(*R*)-4-Bn
MUF-X_gua_Ox_2	hhtt	bdc-OX-(*R*)-4-Bn
MUF-X_gua_Ox_3	hhtt	bdc-OX-(*R*)-5-Ph

Henry reaction

To ensure comparability, all MUF-77 and MUF-7 catalysts were used to catalyse the same Henry reaction of 2-chloro-5-nitrobenzaldehyde with nitromethane in 1,4-dioxane. The observed ee values are listed in **Table 2.12**.

For the linker combination of MUF-X_gua_Ox_1, the network topology did not play a significant role, as the measured ee vale was zero for MUF-77 and very low for MUF-7. However, MUF-7_gua_Ox_2 and MUF-7_gua_Ox_3 outperformed their MUF-77 counterparts. A difference of 10.0% for MUF-X_gua_Ox_2 and 12.7% for MUF-X_gua_Ox_3 was observed when comparing the measured ee values achieved by the two topologies. This indicated that, for these linker combinations the MUF-7 topology was superior. The differences between MUF-7_gua_Ox_1 and MUF-7_gua_Ox_2, which feature the same chiral linker, were attributed to the varying levels of pore filling between the truxenes hmtt and hhtt.

Overall, the experiments suggested that for the MUF-77/7_gua_Ox catalysts, the MUF-7 topology provides superior enantioselectivities compared to the MUF-77 analogues. The exact mechanism behind the transfer of chiral information in both topologies with this linker combination remains unclear and was not further investigated at this screening stage.

Table 2.12 Measured ee values for the Henry reaction of 2-chloro-5-nitrobenzaldehyde with nitromethane in 1,4-dioxane, catalysed by MUF-77_gua_Ox and MUF-7_gua_Ox catalysts.

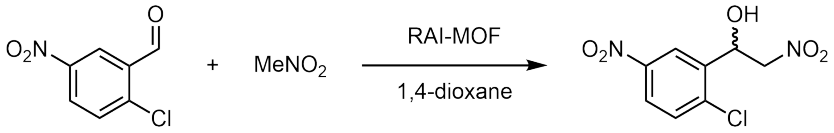

RAI-MOF (X = 77 or 7 topology)	MUF-77	MUF-7
MUF-X_gua_Ox_1	-2.7%	0%
MUF-X_gua_Ox_2	4.3%	14.3%
MUF-X_gua_Ox_3	-5.8%	-18.5%

Aldol reaction

To compare the differences in enantioselectivity of the two topologies in the acetone-aldol reaction, it was decided to solely use MUF-X_gua_Ox_2, which had shown good results in the Henry reaction with the MUF-7 topology, while screening multiple functionalised aldehydes and solvents. The measured ee values for the first set of experiments, the variation of the reaction substrates, are shown in **Table 2.13**.

Table 2.13 Measured ee values for the aldol reaction of different aldehydes with acetone, catalysed by MUF-77_gua_Ox_2 and MUF-7_gua_Ox_2.

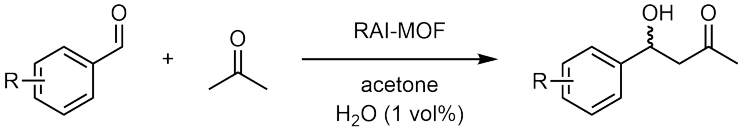

MUF-X_gua_Ox_2 (X = 77 or 7 topology)	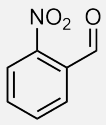	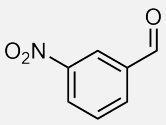	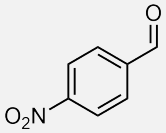	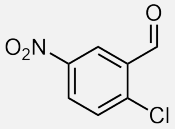
MUF-77	1.9%	3.1%	2.6%	3.1%
MUF-7	-1.0%	0%	0%	2.9%

It was observed that both network topologies for MUF-X_gua_Ox_2 produced only racemic product mixtures or small ee values of about 3%. This indicated that regardless of the network topology RAI-MOF catalysts with this linker combination were inefficient at transferring chiral information during the acetone-aldol reaction.

This was further explored in the second set of experiments, where the acetone-aldol reaction of 2-chloro-5-nitrobenzaldehyde was performed in three additional solvents (**Table 2.14**).

Performing the reaction in 1,4-dioxane instead of acetone slightly increases the ee by 4.7%, reaching 7.6% for the MUF-7 topology, while not significantly affecting the performance of the MUF-77 topology. Acetonitrile and 1,2-dichloroethane both minimally reduced the ee. These findings indicated that the catalytic performance of the topologies is solvent dependent. However, no huge variation in ee was observed that would have justified further screening efforts.

Table 2.14 Measured ee values for the aldol reaction of 2-chloro-5-nitrobenzaldehyde with acetone in different solvents, catalysed by MUF-77_gua_Ox_2 and MUF-7_gua_Ox_2.

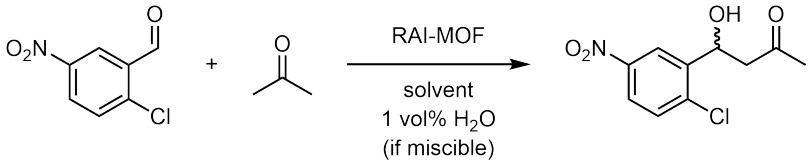

MUF-X_gua_Ox_2 (X = 77 or 7 topology)	acetone	1,4-dioxane	acetonitrile	1,2-dichloroethane
MUF-77	3.1%	3.9%	1.4%	2.1%
MUF-7	2.9%	7.6%	2.2%	2.2%

Considering these results for both the Henry and aldol reactions, it became apparent that the MUF-X_gua_Ox catalysts produced the highest ee values when showing the MUF-7 topology and catalysing the Henry reaction. No further experiments were conducted to differentiate the catalytic performance of the two topologies. However, these experiments showed that topology manipulation could be a potential method to alter the enantioselectivity in these systems in future work.

2.2.6.3.B Combination of bpdc-gua with bdc-^{5}N-chiral linkers

In this section, the enantioselectivity of various RAI-MOF catalysts based on the guanidine catalyst linker, bpdc-gua, combined with ^{5}N-chiral linkers were examined. This linker combination yielded exclusively the MUF-77 topology, regardless of the MOF synthesis conditions.

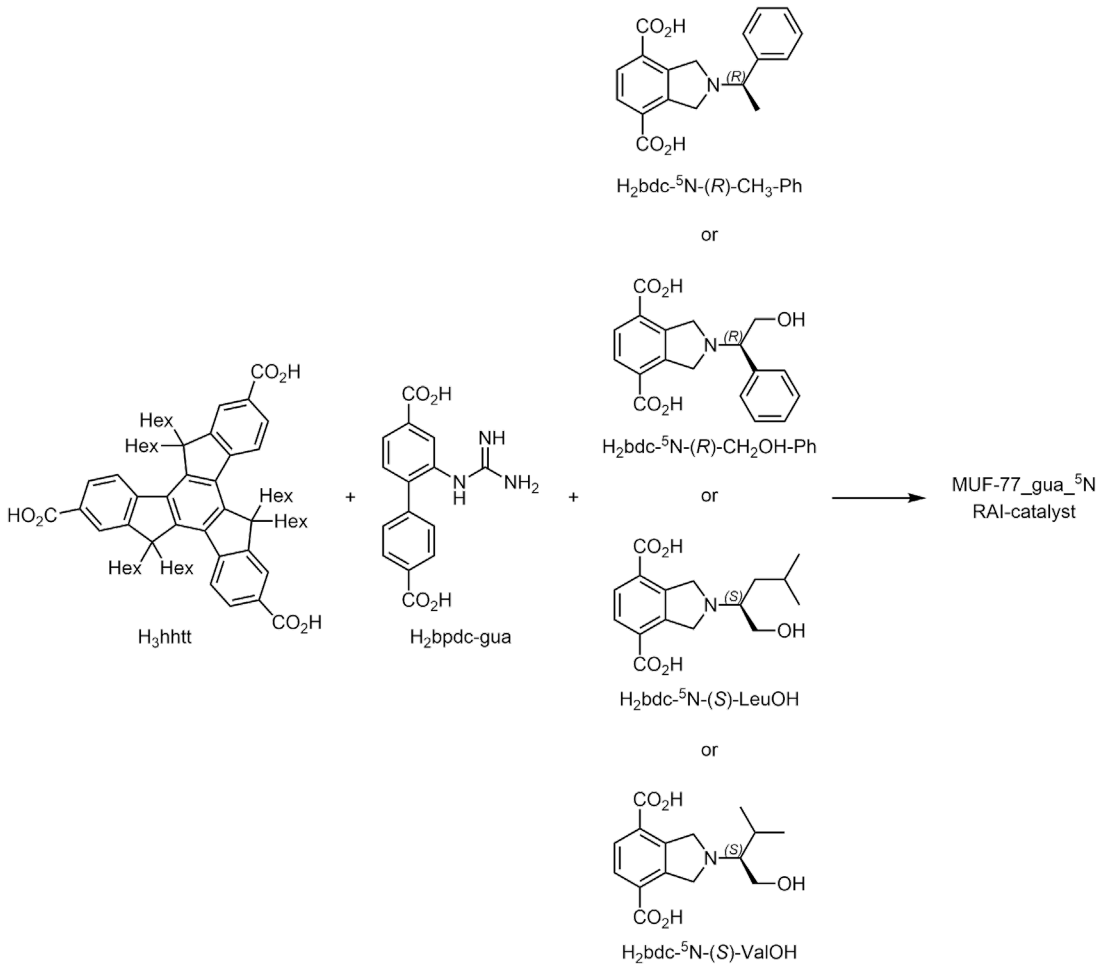

Figure 2.21 Schematic diagram showing the MUF-77_gua_^{5}N catalyst synthesis using H_2bpdc-gua, H_3hhtt and bdc-^{5}N-chiral linkers.

Table 2.15 Ligand combination for the RAI-MOF catalysts synthesised using H_2bpdc-gua, H_3hhtt and different bdc-^{5}N-chiral linkers. The generalised RAI-MOF formula is $[Zn_4O(hhtt)_{1.33}(bpdc\text{-}gua)_{0.5}(\textbf{chiral-bdc})_{0.5}]$.

RAI-MOF	chiral bdc
MUF-77_gua_^{5}N_1	bdc-^{5}N-(*R*)-CH_3-Ph
MUF-77_gua_^{5}N_2	bdc-^{5}N-(*R*)-CH_2OH-Ph
MUF-77_gua_^{5}N_3	bdc-^{5}N-(*S*)-LeuOH
MUF-77_gua_^{5}N_4	bdc-^{5}N-(*S*)-ValOH

Four MUF-77_gua_^{5}N catalysts were synthesised (**Figure 2.21** and **Table 2.15**). As an initial screening experiment, the Henry reaction of 2-chloro-5-nitrobenzaldehyde with nitromethane in 1,4-dioxane was performed with these RAI catalysts (**Table 2.16**). MUF-77_gua_^{5}N_1 and MUF-77_gua_^{5}N_2 displayed negligible enantioselectivity. However, MUF-77_gua_^{5}N_3 and MUF-77_gua_^{5}N_4 yielded ee values of 18.1% and -35.8%, respectively. The pronounced difference in enantioselectivity arising from simple changes in chiral linker functionality indicated that this system showed high variation. Notably, the ee of −35.8% achieved by MUF-77_gua_^{5}N_4 ([$Zn_4O(hhtt)_{1.33}(bpdc\text{-}gua)_{0.5}(bdc\text{-}^5N\text{-}(S)\text{-}ValOH)_{0.5}$]) was also the highest ee observed to that date with the RAI concept.

Table 2.16 Measured ee values for the Henry reaction of 2-chloro-5-nitrobenzaldehyde with nitromethane in 1,4-dioxane, catalysed by MUF-77_gua_^{5}N catalysts.

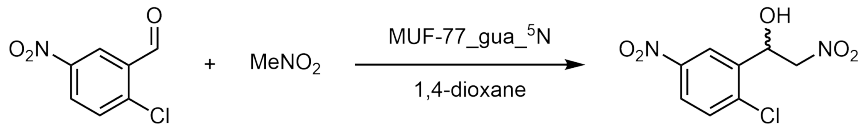

RAI-MOF	ee
MUF-77_gua_^{5}N_1	1.5%
MUF-77_gua_^{5}N_2	-1.4%
MUF-77_gua_^{5}N_3	18.1%
MUF-77_gua_^{5}N_4	-35.8%

Encouraged by these findings, MUF-77_gua_^{5}N_4 was selected for further investigation to assess further variation in the ee. This RAI-MOF catalyst was used to catalyse the Henry reaction with a variety of different benzaldehydes to determine how modest changes in substrate influenced enantioselectivity (**Table 2.17**). It became apparent that the ee was highly sensitive to the reaction substrate. The observed ee values ranged from 2.5% with 4-nitrobenzaldehyde to −65.2% and −65.1% with 5-chloro-2-nitrobenzaldehyde and 3-methyl-5-nitrobenzaldehyde, respectively. The HPLC trace of the catalysis mixture from the Henry reaction of 5-chloro-2-nitrobenzaldehyde with nitromethane is shown in **Figure 2.22**.

Table 2.17 Measured ee values for the Henry reaction of different benzaldehydes with nitromethane in 1,4-dioxane, catalysed by MUF-77_gua_^{5}N_4.

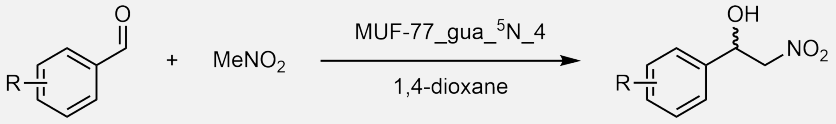

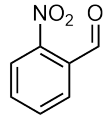	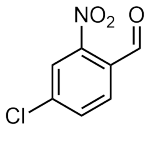	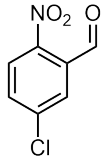	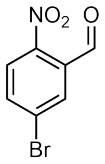	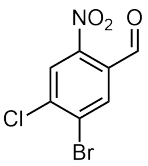
-21.3%	-19.4%	-65.2%	-64.4%	-60.1%
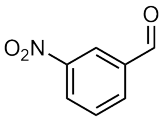	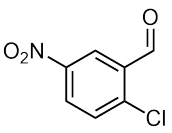	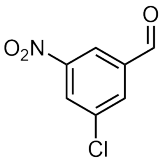	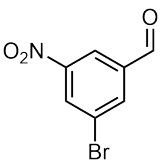	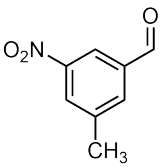
-12.9%	-35.8% -38.3%*	-62.2%	-58.9%	-65.1%
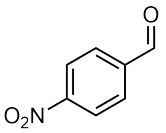	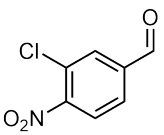			
2.5%	-25.3%			

* Reproduced experimental value.

Several key findings could be extracted from this set of experiments.

(i) The position of the nitro-group relative to the aldehyde played a crucial role for the enantioselectivity in the Henry reaction catalysed by MUF-77_gua_^{5}N_4. *Ortho*- and *meta*-substituted benzaldehydes yielded significantly higher ee values compared to with *para*-substitution.

(ii) The influence of an additional functional group on the ee was highly dependent on its position within the aromatic ring. The most prominent example for this was the striking 45.8% difference in ee between 5-chloro-2-nitrobenzaldehyde and 4-chloro-2-nitrobenzaldehyde, even though they differ by only a single position of the chloro-substituent.

(iii) The nature of the additional substituent – whether being different halogens or a methyl group – had only a minor influence on the ee, provided they were attached at the same position on the aromatic ring. This suggested that steric and electronic effects from these groups were less significant than their positional effects.

(iv) The Henry reaction with 2-chloro-5-nitrobenzaldehyde was repeated, yielding an ee of −38.3%, closely matching the −35.8%. This indicated high reproducibility of the RAI-MOF catalysis with this linker combination and the MUF-77 topology.

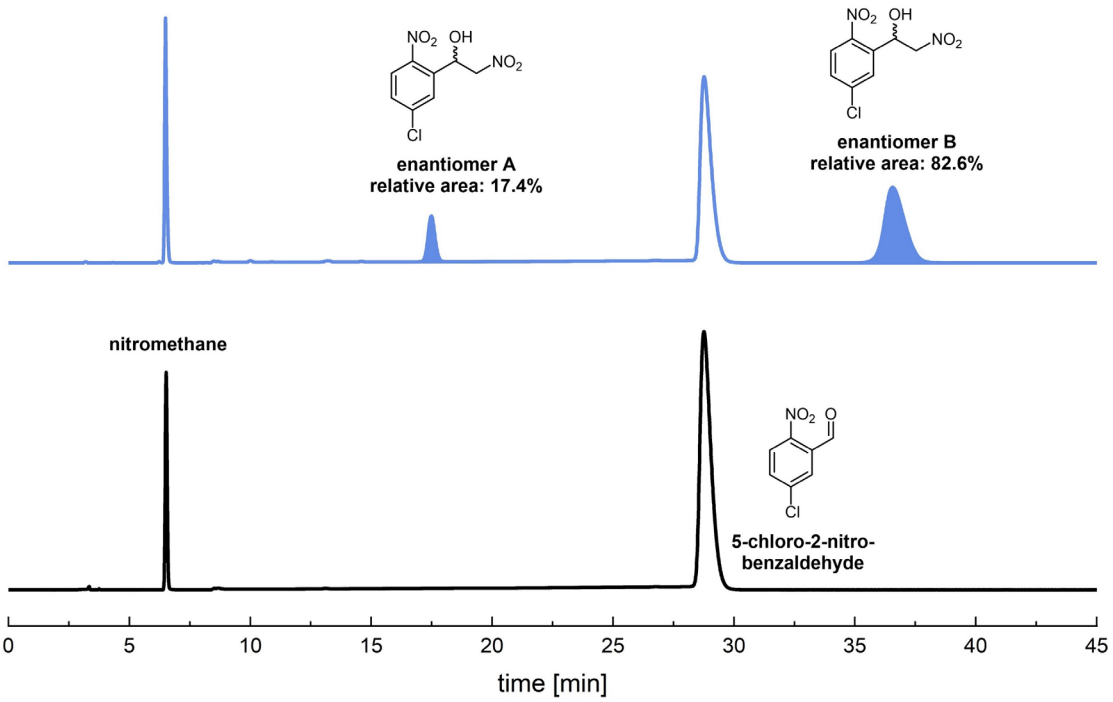

Figure 2.22 HPLC trace of the catalysis mixture from the Henry reaction of 5-chloro-2-nitrobenzaldehyde with nitromethane, catalysed by MUF-77_gua_^{5}N_4. The peaks corresponding to the reaction substrates and the two Henry-product enantiomers are labelled.

It is important to emphasise that these findings were preliminary and highly specific to this particular RAI-MOF catalyst, MUF-77_gua_^{5}N_4. It was unknown if the same trends would be observed for related catalysts. However, these initial results clearly demonstrated the significant variation of enantioselectivity in response to small changes in the reaction substrates. This matched the main objective of this chapter: identifying a system of RAI-MOF catalyst family for a model reaction that showed high variation in ee in response to small changes. The highest ee of −65.2% was by far the best result obtained with the RAI concept to date and suggested that exceptional ee values of >90% are possible with this new approach to asymmetric catalysis.

2.2.7 Choosing the system with the greatest potential to focus the experimental work

This phase of research aimed to identify a family of RAI-MOF catalysts and model reaction that showed the greatest potential for in depth investigation in the following chapters. A model system was selected based on the individual experimental results from each system discussed above.

The first group of RAI-MOF catalysts were based on the achiral secondary amine catalyst linker bpdc-^{7}N-H. This linker was combined with three chiral oxazolidinone linkers and two truxenes to form five catalysts. These catalysts showed only modest enantioselectivity for both the aldol and Henry reaction (**Section 2.2.6.1**). The highest ee observed was 5.1%. The chiral linkers based on the ^{5}N-chiral structure were not compatible with the secondary amine catalyst due to their instability towards the Boc-deprotection conditions required to reveal the active catalyst. The limited enantioselectivity and lack of variation in ee in response to changes in reaction conditions makes this an unattractive system to pursue further.

The second group of RAI-MOF catalysts possessed the achiral hydrogen bond donor catalyst linker bpdc-urea-Ph. This linker was combined with three oxazolidinone chiral linkers and H_3hmtt to form three catalysts. These catalysts could only be tested for the aldol reaction and produced modest enantioselectivities of up to 8.3% (**Section 2.2.6.2**). Work on this system was stopped to prioritise a higher-performing RAI-MOF catalyst identified with a different catalyst linker.

The third group of RAI-MOF catalysts consisted of the achiral guanidine catalyst linker bpdc-gua, combined with two oxazolidinone chiral linkers and two different truxenes. These provided promising ee values of up to 18% for the Henry reaction (**Section 2.2.6.3.A**). One major drawback of this system was its tendency to form both the MUF-77 and MUF 7 type topologies. Since both topologies feature distinct pore environments that give different enantioselectivities, it was crucial to obtain only one topology phase purely. While synthesis conditions could be adjusted to favour a single topology, this required a time-consuming optimisation process for each linker combination. It also remained uncertain if future oxazolidinone-based chiral bdc linkers would behave similarly, particularly given the rarity of the formation of the MUF-7 type topology with truxene-based MOFs. Linker development for this system was also limited to a small selection of commercially available chiral oxazolidinones. Additionally, this system had already been investigated by Dr. Lee, leaving only minor variables such as additive addition left to explore, that are unlikely to majorly shift the ee.

Finally, the fourth group of RAI-MOF catalysts also consisted of the bpdc-gua linker but were combined with four bdc-^{5}N-chiral linkers and H_3hhtt. Unlike the RAI-MOF featuring oxazolidinone-based linkers, this linker combination exclusively formed the MUF-77 structure, significantly reducing the experimental workload and complexity. This system produced high ee values of up to –65.2% in first screening experiments for the Henry reaction, which was by far the highest performing system to date. Substantial variation of enantioselectivity in response to small changes in reaction substrates was also observed. This was particularly encouraging as it suggested that small modifications could potentially increase the ee to higher values. This combination of model reaction and catalyst has not been previously investigated beyond this work and remains largely unexplored. This leaves great room for further optimisation of all reaction parameters.

Another major advantage of this RAI-MOF system was the availability and affordability of the precursors needed for the synthesis of the chiral linkers. The chiral linkers are derived from simple primary amines and amino alcohols, which are inexpensive (often less than $10 per gram) and available in numerous structural variations. The Henry reaction also proved to be an excellent model reaction, as benzaldehydes with diverse functional groups are often very inexpensive, allowing for a broad screening of reaction substrates.

The RAI-MOF catalysts consisting of bpdc-gua and the bdc-^{5}N-chiral linkers, and the Henry reaction (**Figure 2.23**) was chosen for in depth exploration in the following chapters.

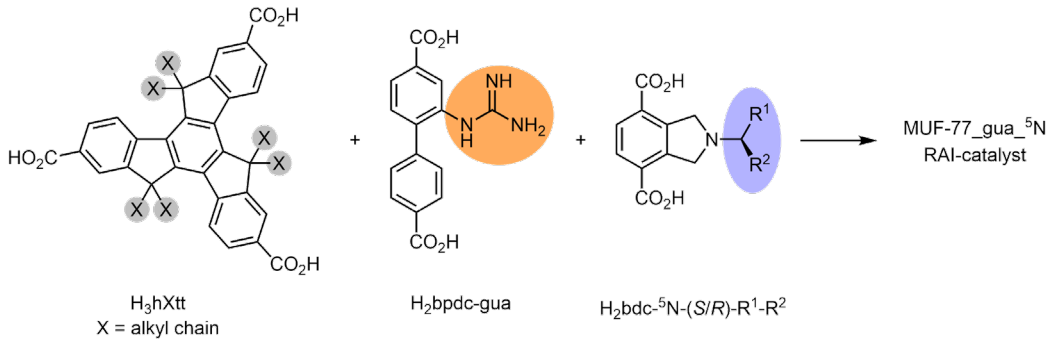

Figure 2.23 Schematic diagram showing the RAI-MOF catalyst synthesis using H_2bpdc-gua, truxenes with different alkyl chain lengths and the family of H_2bdc-^{5}N-chiral linkers. The generalised RAI-MOF formula is $[Zn_4O(hXtt)_{1.33}(bpdc\text{-}gua)_{0.5}(bdc\text{-}^{5}N\text{-}(S/R)\text{-}R^{1}\text{-}R^{2})_{0.5}]$.

2.3 Conclusion

In this chapter, the scope of the RAI concept was expanded, and a highly promising system consisting of one reaction, one catalyst linker and a family of chiral linkers was identified for future exploration in the following chapters. This was achieved through the development and execution of a structured step-by-step screening method. The major milestones of this structured screening method included:

(i) Design and synthesis of three achiral catalyst linkers inspired by conventional asymmetric organocatalysis literature.
(ii) Synthesis of achiral MUF-77 catalysts incorporating these linkers.
(iii) Screening the achiral MUF-77 catalysts for catalytic activity across seven model reactions.
(iv) Design and synthesis of two families of chiral linkers: chiral oxazolidinone based and simple chiral primary amine (amino alcohol) based.
(v) Validation of chiral linker compatibility with MUF-77 synthesis conditions.
(vi) The synthesis of various RAI-MOF catalysts built from different combinations of truxenes, achiral catalyst linkers and chiral linkers.
(vii) Using these RAI-MOF catalysts to explore factors influencing enantioselectivity. The highest ee obtained was −65.2%.

The system of model reaction and RAI-MOF catalyst ultimately selected for detailed investigation in the following chapters was the Henry reaction catalysed by RAI-MOFs consisting of the achiral guanidine catalyst linker bpdc-gua and the bdc-^{5}N-chiral linker family. This combination proved particularly promising, as it already produced high enantioselectivity after minimal condition optimisation and that the enantioselectivity was sensitive to small modifications in conditions.

2.4 Experimental section

2.4.1 General

All starting materials and solvents were used as received from commercial sources without further purification unless otherwise noted. Solvents were dried over 4 Å molecular sieves. Column chromatography was performed on silica gel (grade 60, mesh size 230-400, Scharlau).

NMR spectra were collected at room temperature using Bruker 500 MHz or Bruker 700 MHz spectrometers. The solvent protons were used as an internal standard for calibration.

High resolution mass spectrometry data were collected on a ThermoScientific Q Exactive Focus Hybrid Quadripole-Orbitrap Mass Spectrometer using either an APCI or an EI probe head.

Thermogravimetric analyses were performed on a TA Instruments Q50 device.

The HPLC measurements were performed on Thermo Fisher Dionex Ultimate 3000 systems equipped with UV detectors. The Chromeleon^{TM} Chromatography Data System (CDS) Software was used for data processing.

X-ray diffraction data (PXRD and SCXRD) were collected using a Bruker D8 Venture diffractometer with Cu_{α} radiation (1.54178 Å) generated by a IμS microfocus Diamond sealed tube and equipped with a Photon III 28 detector. The PXRD data were measured with phi 360°/min for 1 min. For SCXRD measurements, low temperature cooling was achieved using an Oxford Cryostream 800. Data were collected, integrated, scaled, and averaged using the APEX3 or APEX4 software package. Single crystal data were refined using the SHELX[185] package under Olex2.[186] PXRD data were processed into 1D diffractograms using APEX3 and Diffrac.Eva. Predicted PXRD patterns were generated from cif files using Mercury.

2.4.2 Linker synthesis and characterisation

All truxenes used in this work were prepared using established methods.[119] One representative, fully descriptive synthesis is available in the Electronic Appendix to **Chapter 3**.

This section presents the synthesis and characterization of one representative example from each family of chiral linkers. The syntheses and characterisation of all other chiral linkers are available in the Electronic Appendix to **Chapter 2**.

The NMR and XRD data for all linkers and MOFs are provided in the Electronic Appendix to **Chapter 2**.

2.4.2.1 H_2bpdc-catalyst linkers

H_2bpdc-^{7}N-Boc

The synthesis of H_2bpdc-^{7}N-Boc was performed as depicted in **Scheme 2.1**, following group established and literature reported procedures.

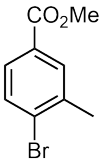

Methyl 4-bromo-3-methylbenzoate

The solution of 4-bromo-3-methylbenzoic acid (10.0 g, 46.5 mmol, 1.0 eq.) in MeOH (150 mL) and H_2SO_4 (1 mL) was refluxed at 80 °C overnight. The solvent was removed under reduced pressure and the residue was dissolved in CH_2Cl_2 (150 mL). The organic phase was washed with H_2O (3 × 50 mL), dried over $MgSO_4$, and the solvent was removed under reduced pressure to yield methyl 4-bromo-3-methylbenzoate as a white solid (10.5 g, 46.0 mmol, 99%). The ^{1}H NMR spectrum agrees with literature data.[187]

^{1}H NMR (500 MHz, $CDCl_3$) δ (ppm) 7.90 (d, J = 1.4 Hz, 1H), 7.69 (dd, J = 8.3, 1.5 Hz, 1H), 7.60 (d, J = 8.3 Hz, 1H), 3.90 (s, 3H), 2.44 (s, 3H).

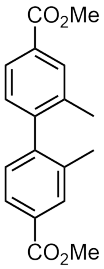

Me_2bpdc-$(Me)_2$

Methyl 4-bromo-3-methylbenzoate (1.1 g, 4.7 mmol, 1.0 eq.), bis(pinacolato)diboron ($(BPin)_2$) (1.4 g, 5.4 mmol, 1.2 eq.), KOAc (1.5 g, 14.7 mmol, 3.2 eq.) and $Pd(OAc)_2$ (39.9 mg, 177.7 μmol, 4 mol%) were suspended in dry DMF (30 mL) under an argon atmosphere and the reaction mixture was stirred at 95 °C overnight. After cooling to room temperature 4-bromo-3-methylbenzoic acid methyl ester (1.1 g, 4.7 mmol, 1.0 eq.), K_2CO_3 (990.0 mg, 7.2 mmol, 1.5 eq.) and $Pd(PPh_3)_4$ (162.0 mg, 140.2 μmol, 3 mol%) were added and the reaction mixture was stirred at 125 °C overnight. After cooling to room temperature, solids were removed by filtration through celite. The reaction mixture was extracted with EtOAc (2 × 100 mL) and the combined organic phase was washed with water (5 × 50 mL), dried over $MgSO_4$ and the solvent was removed under reduced pressure. The crude

product was recrystalised in MeOH to yield Me_2bpdc-$(Me)_2$ as a white solid (1.2 g, 4.0 mmol, 85%). The ^{1}H NMR spectrum agrees with literature data.[188]

^{1}H NMR (500 MHz, $CDCl_3$) δ (ppm) 7.97 (s, 2H), 7.90 (dd, *J* = 7.9, 1.3 Hz, 2H), 7.15 (d, *J* = 7.9 Hz, 2H), 3.94 (s, 6H), 2.08 (s, 6H).

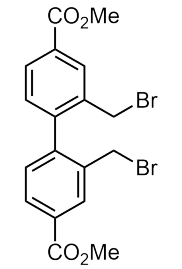

Me_2bpdc-$(MeBr)_2$

Me_2bpdc-$(Me)_2$ (1.0 g, 3.4 mmol, 1.0 eq.), *N*-bromosuccinimide (NBS) (1.2 g, 6.7 mmol, 2.0 eq.) and azobisisobutyronitrile (AIBN) (56.0 mg, 341.0 µmol, 0.1 eq.) were suspended in dry benzene (20 mL) under an argon atmosphere and the reaction mixture was refluxed at 95 °C overnight. The solvent was removed under reduced pressure and the residue was dissolved in CH_2Cl_2 (75 mL). The organic phase was washed with H_2O (3 × 20 mL), dried over $MgSO_4$, and the solvent was removed under reduced pressure to yield the crude product as a yellow oil. After passing through a plug of silica (cyclohexane/EtOAc; 3/2) Me_2bpdc-$(MeBr)_2$ was obtained as a slightly yellow solid (1.2 g, 2.6 mmol, 78%). The ^{1}H NMR spectrum agrees with literature data.[189]

^{1}H NMR (500 MHz, $CDCl_3$) δ (ppm) 8.24 (d, *J* = 1.5 Hz, 2H), 8.06 (dd, *J* = 8.2, 1.6 Hz, 2H), 7.36 (d, *J* = 7.9 Hz, 2H), 4.33 (d, *J* = 10.3 Hz, 2H), 4.17 (d, *J* = 10.3 Hz, 2H), 3.97 (s, 6H).

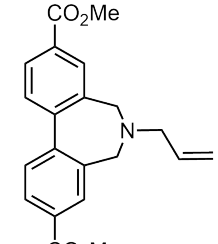

Me_2bpdc-^{7}N-allylamine

Me_2bpdc-$(MeBr)_2$ (1.5 g, 3.20 mmol, 1.0 eq.) was dissolved in 25 mL dry THF under an argon atmosphere and the solution was heated at 50 °C. Four aliquots of allylamine (240 µL, 3.20 mmol, 1.0 eq.) was added over 8 hours, totalling 4.0 equivalents. The reaction solution was stirred at 50 °C overnight. The solvent was removed under reduced pressure and the residue was dissolved in CH_2Cl_2 (75 mL). The organic phase was washed with H_2O (3 × 20 mL), dried over $MgSO_4$, and the solvent was removed under reduced pressure to yield the crude product as a yellow oil. The crude product was purified by silica-gel column chromatography (cyclohexane/EtOAc gradient from 5:1 to 2:1), followed by recrystallisation in diethyl ether, to yield Me_2bpdc-^{7}N-allylamine as a white solid (702.0 mg, 2.0 mmol, 62%).

^{1}H NMR (500 MHz, DMSO-*d6*) δ (ppm) 8.06 (dd, *J* = 8.0, 2.0 Hz, 2H), 7.96 (d, *J* = 2.0 Hz, 2H), 7.72 (d, *J* = 8.0 Hz, 2H), 5.97-5.89 (m, 1H), 5.26 (dd, *J* = 17.2, 1.6 Hz, 1H), 5.21 (dd, *J* = 10.2, 1.5 Hz, 1H), 3.89 (s, 6H), 3.34 (s, 4H), 3.16 (d, *J* = 6.6 Hz, 2H). ^{13}C NMR (126 MHz, DMSO-*d6*) δ (ppm) 165.94, 144.21, 136.07, 135.10, 130.25, 129.50, 128.94, 128.21, 117.70,

57.89, 53.89, 52.28. HRMS (FTMS + p ESI Full) calculated for $[M+H]^+$ $(C_{21}H_{22}N_1O_4)^+$ m/z 352.1543, found m/z 352.1540.

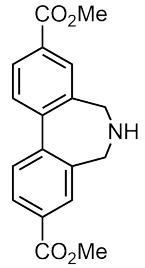

Me2bpdc-7N-H

The de-allylation procedure was adapted from a general procedure reported by F. Guibe *et al.*[190] The solution of Me2bpdc-7N-allylamine (857.0 mg, 2.4 mmol, 1.0 eq.) in dry, degassed CH_2Cl_2 (5 mL) under an argon atmosphere was stirred at room temperature. Tetrakis(triphenylphosphine)palladium(0) (64.5 mg, 1.5 mol%) and N,N′-dimethylbarbituric acid (NDMBA, 1.22 g, 7.8 mmol, 3.2 eq.) were added and the reaction mixture was stirred at 35 °C for two hours. The suspension was diluted with CH_2Cl_2 (50 mL) and washed with saturated K_2CO_3 solution (2 × 10 mL) and H_2O (3 × 20 mL). The organic phase was dried over $MgSO_4$, and the solvent was removed under reduced pressure to yield a brown solid as the crude product. The crude solid was suspended in diethyl ether (10 mL) and sonicated for 30 minutes. The solid was isolated by filtration, washed with diethyl ether (10 mL) and dried under vacuum to yield Me2bpdc-7N-H as a slightly beige solid (584.0 mg, 1.9 mmol, 77%).

^{1}H NMR (500 MHz, DMSO-*d6*) δ (ppm) 8.04 (dd, *J* = 7.9, 1.8 Hz, 2H), 7.99 (d, *J* = 1.6 Hz, 2H), 7.68 (d, *J* = 8.0 Hz, 2H), 3.89 (s, 6H), 3.50 (s, 4H). ^{13}C NMR (126 MHz, DMSO-*d6*) δ (ppm) 165.97, 144.42, 137.64, 129.89, 129.70, 128.59, 128.14, 52.22, 47.80. HRMS (FTMS + p ESI Full) calculated for $[M+H]^+$ $(C_{18}H_{18}N_1O_4)^+$ m/z 312.1230, found m/z 312.1225.

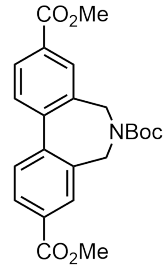

Me2bpdc-7N-Boc

Me2bpdc-7N-H (715.3 mg, 2.3 mmol, 1.0 eq.) was suspended in dry *tert*-butanol (15 mL) under an argon atmosphere. A solution of di-*tert*-butyl decarbonate (1.0 g, 4.6 mmol, 2.0 eq.) in *tert*-butanol (2 mL) was added and the reaction mixture was stirred at 30 °C overnight. The solvent was removed under reduced pressure to yield the crude product as a yellow oil. After passing through a plug of silica (CH_2Cl_2), Me2bpdc-7N-Boc was obtained as a beige solid (857.6 mg, 2.1 mmol, 91%).

^{1}H NMR (500 MHz, $CDCl_3$) δ (ppm) 8.14 (dd, *J* = 7.9, 1.3 Hz, 2H), 8.11 (brs, 2H), 7.60 (d, *J* = 7.9 Hz, 2H), 4.29 (brs, 4H), 3.96 (s, 6H), 1.53 (s, 9H).

The ^{1}H NMR spectra showed the presence of unreacted di-*tert*-butyl decarbonate. The product was used without further purification for ester hydrolysis.

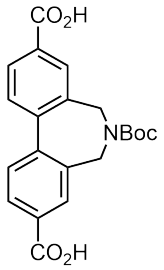

H2bpdc-7N-Boc

Me2bpdc-7N-Boc (422.5 mg) was dissolved in THF (3 mL), and a 1 M KOH solution (3 mL) was added. The reaction mixture was stirred at room temperature overnight, after which the THF was removed under reduced pressure. The aqueous phase was cooled to 0 °C and the pH was adjusted to 4.0 with dilute HCl, resulting in the formation of a precipitate. The solid was isolated by filtration, washed with water (2 × 5 mL) and dried under reduced pressure to yield H2bpdc-7N-Boc as a slightly beige solid (276.0 mg, 719.9 μmol, 70%).

^{1}H NMR (500 MHz, D2O/NaOD) δ (ppm) 7.82 (dd, *J* = 7.9, 1.6 Hz, 2H), 7.74 (d, *J* = 1.6 Hz, 2H), 7.40 (d, *J* = 7.9 Hz, 2H), 4.00 (s, 4H), 1.33 (s, 9H). ^{13}C NMR (126 MHz, D2O/NaOD) δ (ppm) 174.60, 155.76, 142.13, 136.46, 133.59, 129.98, 129.22, 128.26, 82.09, 47.39, 27.68. HRMS (FTMS + p ESI Full) calculated for $[M]^-$ $(C_{21}H_{20}N_1O_6)^-$ m/z 382.1285, found m/z 382.1298. The identity of the ^{13}C signal at 47.39 ppm was confirmed by HMQC spectroscopy.

H2bpdc-gua

H2bpdc-gua was synthesised by a former member of the research group, as outlined in **Scheme 2.2**. The identity and purity were confirmed prior to its use in this work. The following data were obtained by Ludwig Petters.

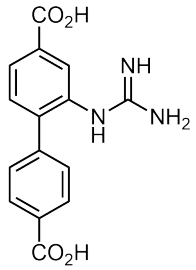

H2bpdc-gua

^{1}H NMR (500 MHz, D2O/NaOD) δ (ppm) 7.82 (d, *J* = 8.1 Hz, 2H), 7.56 (d, *J* = 7.8 Hz, 1H), 7.43 (d, *J* = 8.1 Hz, 2H), 7.38-7.37 (m, 2H). ^{13}C NMR (126 MHz, D2O/NaOD) δ (ppm) 175.55, 175.34, 155.17, 145.14, 142.61, 138.36, 136.92, 134.83, 130.48, 128.66, 125.55, 124.00. HRMS (FTMS + p ESI Full) calculated for $[M]^-$ $(C_{15}H_{12}N_3O_4)^-$ m/z 298.0822, found m/z 298.0833.

HMQC spectroscopy was used to confirm that the intense ^{13}C signal at 128.66 ppm corresponds to four individual carbons.

H_2bpdc-urea-Ph

The synthesis of H_2bpdc-urea-Ph was performed as depicted in **Scheme 2.3**.

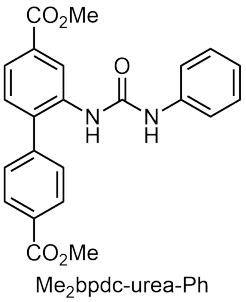

Me_2bpdc-urea-Ph

Me_2bpdc-urea-Ph was synthesised following a general procedure as reported by Siu *et. al.*.[191] A solution of Me_2bpdc-NH_2 (501.5 mg, 1.8 mmol, 1.0 eq.) in dry THF (15 mL) was stirred at 0 °C under a nitrogen atmosphere. Phenyl isocyanate (400.0 µL, 3.7 mmol, 2.1 eq.) was added, and the reaction mixture was stirred at 50 °C overnight. The reaction suspension was concentrated to about 5 mL, the solid isolated by filtration, washed with toluene (2 × 3 mL) and Et_2O (2 × 3 mL) and dried *in vacuo*. Me_2bpdc-urea-Ph was obtained as a white powdery solid (612.8 mg, 1.5 mmol, 86%).

^{1}H NMR (500 MHz, $CDCl_3$) δ (ppm) 8.69 (s, 1H), 7.96 (d, J = 8.1 Hz, 2H), 7.79, (dd, J = 7.9, 1.1 Hz, 1H), 7.70 (s, 1H), 7.41 (d, J = 8.9 Hz, 2H), 7.24-7.17 (m, 6H), 7.03-7.01 (m, 1H), 3.87 (s, 3H), 3.83 (s, 3H). ^{13}C NMR (126 MHz, $CDCl_3$) δ (ppm) 167.06, 166.73, 153.32, 142.84, 138.18, 135.99, 135.68, 130.75, 130.27, 129.99, 129.35, 129.27, 129.16, 129.02, 124.85, 123.81, 123.36, 120.34, 52.47, 52.36. HRMS (FTMS + p ESI Full) calculated for $[M+Na]^+$ $(C_{23}H_{20}N_2O_5Na)^+$ m/z 427.1264, found m/z 427.1261.

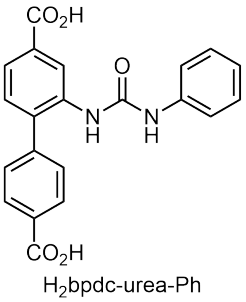

H_2bpdc-urea-Ph

The suspension of Me_2bpdc-urea-Ph (315.8 mg, 780.9 µmol, 1.0 eq.) in MeOH (13 mL) and H_2O (5 mL) was stirred at room temperature. Solid LiOH · H_2O was added, and the reaction mixture was stirred overnight. The MeOH was removed under reduced pressure, and the aqueous solution was acidified to pH 1 with 3 M aqueous HCl, resulting in the formation of a white precipitate. The solid was isolated by centrifugation, washed with H_2O (2 × 10 mL) and MeOH (2 × 10 mL) and dried *in vacuo* to yield H_2bpdc-urea-Ph as a white powdery solid (217.9 mg, 579.0 µmol, 74%).

^{1}H NMR (500 MHz, D_2O/NaOD) δ (ppm) 7.88 (d, *J* = 1.3 Hz, 1H), 7.86 (d, *J* = 8.2 Hz, 2H), 7.76 (dd, *J* = 7.9, 1.3 Hz, 1H), 7.40 (d, *J* = 8.2 Hz, 2H), 7.37 (d, *J* = 8.0 Hz, 1H), 7.23 (t, *J* = 7.8 Hz, 2H), 7.07 (t, *J* = 7.4 Hz, 1H), 6.97 (d, *J* = 7.8 Hz, 2H). ^{13}C NMR (126 MHz, D_2O/NaOD) δ (ppm) 175.11, 174.58, 156.40, 141.08, 139.26, 137.25, 136.66, 135.36, 133.83, 130.34, 129.13, 129.02, 128.51, 126.93, 126.76, 124.51, 122.08. HRMS (FTMS + p ESI Full) calculated for $[M]^-$ $(C_{21}H_{15}N_2O_5)^-$ m/z 375.0975, found m/z 375.0984.

2.4.2.2 Backbones for chiral linker synthesis

Backbone 1

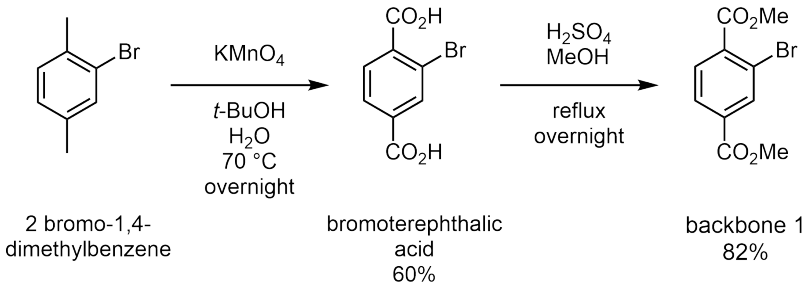

Scheme 2.4 Reaction scheme for the two-step synthesis of backbone 1.

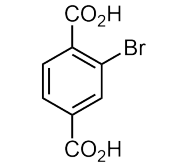

bromoterephthalic acid

The synthesis of bromoterephthalic acid was performed as reported by Qiao *et. al*.[192] 2-Bromo-1,4-dimethylbenzene (15.8 g, 85.4 mmol, 1.0 eq.) was dissolved in a mixture of *tert*-butanol (75 mL) and H_2O (75 mL). $KMnO_4$ (33.5 g, 212.0 mmol, 2.5 eq.) was added and the reaction solution was stirred at 70 °C for 2 hours. After cooling down to room temperature, a second batch of $KMnO_4$ (33.5 g, 212.0 mmol, 2.5 eq.) was added and the mixture was stirred at 70 °C overnight. The hot reaction mixture was filtered through a glass frit and the solids were washed with water (2 × 250 mL). The filtrate was concentrated to about 200 mL and acidified with concentrated HCl resulting in the formation of a white precipitate. The suspension was extracted with EtOAc (2 × 250 mL). The combined organic phases were washed with water (3 × 100 mL), dried over $MgSO_4$ and after removal of the solvent under reduced pressure, the product, bromoterephthalic acid was obtained as a white solid (12.5 g, 50.9 mmol, 60%). The ^{1}H NMR spectrum agrees with literature data.[192]

^{1}H NMR (500 MHz, *d6*-DMSO) δ (ppm) 13.50 (br, 2H), 8.14 (d, J = 1.4 Hz, 1H), 7.98 (dd, J = 7.9 Hz, J = 1.4 Hz, 1H), 7.82 (d, J = 8.2 Hz, 1H).

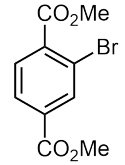

backbone 1

Bromoterephthalic acid (12.5 g, 50.9 mmol, 1.0 eq.) was dissolved in a mixture of MeOH (200 mL) and H_2SO_4 (5 mL), and the reaction solution was refluxed at 80 °C overnight. After cooling to room temperature, the solvent was removed under reduced pressure. The residue was dissolved in CH_2Cl_2 (100 mL), washed with H_2O (3 × 25 mL) dried over $MgSO_4$ and the solvent was removed under reduced pressure. After passing through a plug of silica (EtOAc/cyclohexane; 1/9), backbone 1 was obtained as a white solid (11.4 g, 41.8 mmol, 82%). The ^{1}H NMR spectrum agrees with literature data.[193]

^{1}H NMR (500 MHz, $CDCl_3$) δ (ppm) 8.28 (s, 1H), 7.97 (dd, *J* = 8.2, 1.7 Hz, 1H), 7.78 (d, *J* = 8.1 Hz, 1H), 3.93 (s, 3H), 3.92, (s, 3H).

Backbone 2

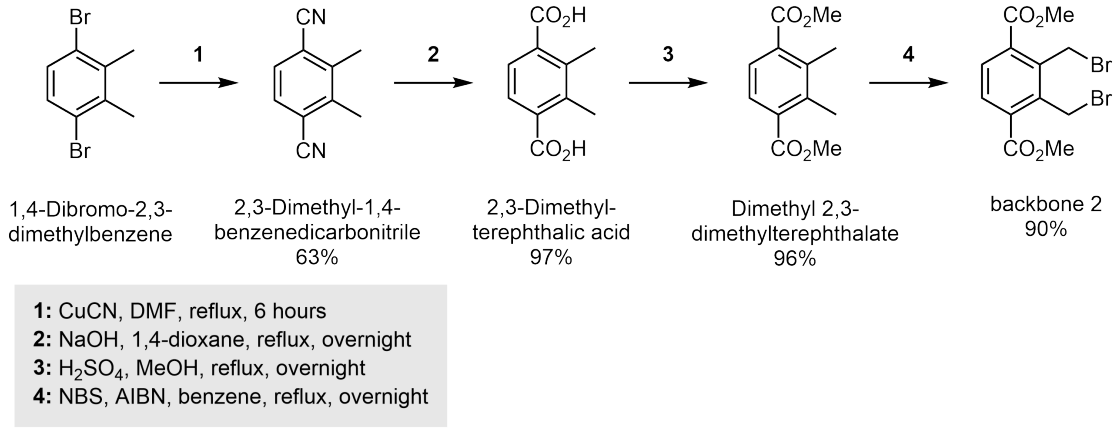

Scheme 2.5 Reaction scheme for the four-step synthesis of backbone 2.

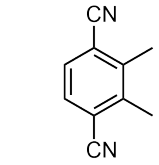

2,3-Dimethyl-1,4-benzenedicarbonitrile

The synthesis of 2,3-dimethyl-1,4-benzenedicarbonitrile was performed as reported by Lai *et. al.*[194] 1,4-Dibromo-2,3-dimethylbenzene (9.1 g, 29.3 mmol, 1.0 eq.) and CuCN (7.9 g, 88.0 mmol, 3.0 eq.) were suspended in dry DMF (30 mL) under an argon atmosphere and the reaction mixture was refluxed at 170 °C for 4 hours. After cooling to room temperature, the solution of $FeCl_3 \cdot 6H_2O$ (10.0 g, 37.0 mmol, 1.3 eq.) in H_2O (20 mL) and concentrated HCl (4 mL) was added, and the mixture was stirred overnight. H_2O (100 mL) and EtOAc (200 mL) were added, the suspension was vigorously mixed, and all solids were removed *via* filtration through celite. The organic phase was isolated, washed with water (3 × 50 mL), dried over $MgSO_4$ and the solvent was removed under reduced pressure to yield 2,3-dimethyl-1,4-benzenedicarbonitrile as a white solid (2.9 g, 18.6 mmol, 63%). The ^{1}H NMR spectrum agrees with literature data.[194]

^{1}H NMR (500 MHz, $CDCl_3$) δ (ppm) 7.55 (s, 2H), 2.56 (s, 6H).

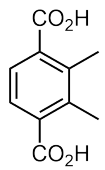

2,3-Dimethyl-terephthalic acid

2,3-Dimethyl-1,4-benzenedicarbonitrile (2.9 g, 18.6 mmol, 1.0 eq.) was suspended in a NaOH solution (35 mL, 20 wt%) and 1,4-dioxane (3 mL) and refluxed at 115 °C overnight. After cooling to room temperature, the reaction mixture was acidified to pH 1 using concentrated HCl, resulting in the formation of a fine, white precipitate. The precipitate was isolated by filtration,

washed with water (3 × 10 mL) and dried in *vacuo* to yield 2,3-dimethyl-terephthalic acid as a white powder (3.5 g, 18.0 mmol, 97%).

^{1}H NMR (500 MHz, *d6*-DMSO) δ (ppm) 13.09 (brs, 2H), 7.51 (s, 2H), 2.39 (s, 6H). ^{13}C NMR (126 MHz, *d6*-DMSO) δ (ppm) 170.05, 137.38, 135.34, 126.38, 17.13.

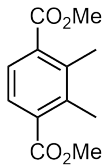

Dimethyl 2,3-dimethylterephthalate

2,3-Dimethyl-terephthalic acid (3.5 g, 18.0 mmol, 1.0 eq.) was dissolved in a mixture of MeOH (50 mL) and H_2SO_4 (1 mL), and the rection solution was refluxed at 80 °C overnight. After cooling to room temperature, the solvent was removed under reduced pressure. The residue was dissolved in CH_2Cl_2 (100 mL), washed with H_2O (3 × 25 mL) dried over $MgSO_4$ and the solvent was removed under reduced pressure to yield dimethyl 2,3-dimethylterephthalate as a white solid (3.9 g, 17.4 mmol, 96%). The ^{1}H NMR spectrum agrees with literature data.[195]

^{1}H NMR (500 MHz, $CDCl_3$) δ (ppm) 7.57 (s, 2H), 3.91 (s, 6H), 2.46 (s, 6H).

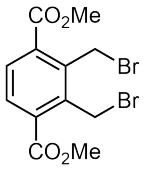

backbone 2

Dimethyl 2,3-dimethylterephthalate (1.0 g, 4.7 mmol, 1.0 eq.), *N*-bromosuccinimide (NBS) (1.9 g, 10.6 mmol, 2.2 eq.) and azobisisobutyronitrile (AIBN) (82.7 mg, 503.6 µmol, 0.1 eq.) were suspended in dry benzene (20 mL) under an argon atmosphere and the reaction mixture was refluxed at 95 °C overnight. The solvent was removed under reduced pressure and the residue was dissolved in CH_2Cl_2 (100 mL). The organic phase was washed with H_2O (3 × 20 mL), dried over $MgSO_4$, and the solvent was removed under reduced pressure to yield the crude product as a yellow oil. After passing through a plug of silica (CH_2Cl_2), backbone 2 was obtained as a slightly yellow solid (1.6 g, 4.2 mmol, 90%).

^{1}H NMR (500 MHz, $CDCl_3$) δ (ppm) 7.89 (s, 2H), 5.12 (s, 4H), 3.97 (s, 6H). ^{13}C NMR (126 MHz, $CDCl_3$) δ (ppm) 166.66, 139.14, 134.18, 130.84, 52.97, 25.15.

2.4.2.3 Chiral linkers based on the structure: H_2bdc-OX-(*S*/*R*)-R

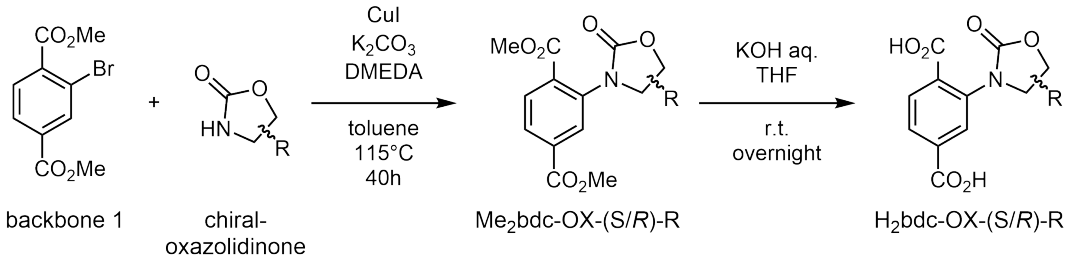

Scheme 2.6 Schematic reaction scheme for the two-step synthesis of H_2bdc-OX-(*S*/*R*)-R chiral linkers starting from backbone 1.

All Me_2bdc-OX-(*S*/*R*)-R intermediates were synthesised following a generalised procedure adapted from the reported method by Kaskel *et al*.[196, 197]

Backbone 1 (1.0 eq.), CuI (0.2 eq.), K_2CO_3 (3.0 eq.) and the respective chiral oxazolidinone (1.3 eq.) were suspended in dry toluene under an argon atmosphere. *N,N'*-Dimethylethylenediamine (DMEDA) (0.4 eq.) was added, and the reaction mixture was stirred at 115 °C for 35 hours. After cooling to room temperature, the solvent was removed under reduced pressure. The residue was dissolved in CH_2Cl_2 (200 mL), the solids removed, and the organic phase was washed with H_2O (3 × 50 mL). The solvent was removed under reduced pressure to yield the crude product as a yellow oil. The product was purified by silica-gel column chromatography.

The final H_2bdc-OX-(*S*/*R*)-R linkers were obtained by basic hydrolysis of the corresponding Me_2bdc-OX-(*S*/*R*)-R intermediates, following a generalised procedure inspired by reported methods and group established protocols.[196]

To a solution of Me_2bdc-OX-(*S*/*R*)-R (1.0 eq.) in THF (25 mL), 1 M KOH (25 mL) was added dropwise at 0 °C. The reaction solution was stirred at 0 °C for one hour and then warmed to room temperature overnight. The reaction mixture was cooled to 0 °C and acidified with 1M HCl to pH 3.0, resulting in the formation of a precipitate. The suspension was extracted with EtOAc (3 × 50 mL), the combined organic phase was washed with water (3 × 20 mL) and dried over $MgSO_4$. The solvent was removed under reduced pressure to yield the crude product, which was recrystalised in acetonitrile to yield the final linker.

One representative example for the linker synthesis is shown below. The remaining data are provided in the Appendix to **Chapter 2**.

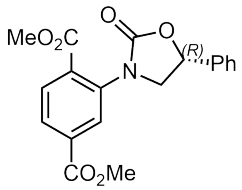

Me_2bdc-OX-(*R*)-5-Ph

The title compound was prepared from backbone 1 (1.2 g, 4.4 mmol, 1.0 eq.) and (*R*)-5-phenyl-2-oxazolidinone (704.0 mg, 4.3 mmol, 1.0 eq.) according to the general procedure. Me_2bdc-OX-(*R*)-5-Ph (1.1 g, 3.2 mmol, 72%) was obtained as a slightly yellow oil after silica-gel column chromatography (cyclohexane/EtOAc gradient from 9:1 to 7:3).

^{1}H NMR (500 MHz, $CDCl_3$) δ (ppm) 8.01-7.97 (m, 2H), 7.94 (d, *J* = 1.1 Hz, 1H), 7.53-7.39 (m, 5H), 5.73 (t, *J* = 8.2 Hz, 1H), 4.41 (t, *J* = 8.5 Hz, 1H), 4.04 (t, *J* = 8.2 Hz, 1H), 3.94 (s, 3H), 3.93 (s, 3H). ^{13}C NMR (126 MHz, $CDCl_3$) δ (ppm) 165.95, 165.51, 156.33, 138.02, 137.31, 134.14, 131.89, 131.59, 129.28, 129.13, 128.15, 127.48, 126.20, 75.64, 55.18, 52.92, 52.77. HRMS (FTMS + p ESI Full) calculated for $[M+H]^+$ $(C_{19}H_{18}N_1O_6)^+$ m/z 356.1129, found m/z 356.1126.

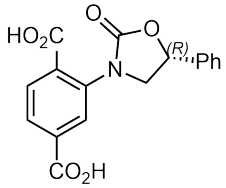

H_2bdc-OX-(*R*)-5-Ph

The title compound was prepared from Me_2bdc-OX-(*R*)-5-Ph (1.1 g, 3.2 mmol, 1.0 eq.) according to the general ester hydrolysis procedure. H_2bdc-OX-(*R*)-5-Ph was obtained as a slightly yellow, powdery solid (935.4 mg, 2.9 mmol, 91%).

^{1}H NMR (500 MHz, D_2O/NaOD) δ (ppm) 7.85-7.83 (m, 2H), 7.66-7.62 (m, 3H), 7.56-7.48 (m, 3H), 5.87 (t, *J* = 8.2 Hz, 1H), 4.51 (t, *J* = 8.9 Hz, 1H), 4.13 (dd, *J* = 8.9, 7.7 Hz, 1H). ^{13}C NMR (126 MHz, D_2O/NaOD) δ (ppm) 174.56, 174.05, 158.48, 138.49, 138.19, 137.87, 133.31, 129.43, 129.12, 128.81, 128.24, 126.84, 126.62, 76.53, 54.91. HRMS (FTMS + p ESI Full) calculated for $[M]^-$ $(C_{17}H_{12}N_1O_6)^-$ m/z 326.0659, found m/z 326.0672.

2.4.2.4 Chiral linkers based on the structure: H_2bdc-^{5}N-(*S*/*R*)-R^1-R^2

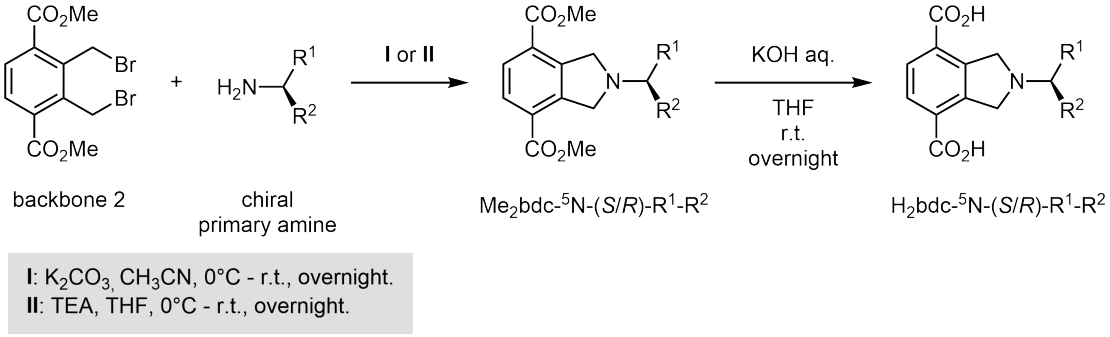

Scheme 2.7 Schematic reaction scheme for the two-step synthesis of H_2bdc-^{5}N-(*S*/*R*)-R^1-R^2 chiral linkers starting from backbone 2.

All Me_2bdc-^{5}N-(*S*/*R*)-R^1-R^2 intermediates were prepared following one of two procedures:

General procedure I: A suspension of backbone 2 (1.0 eq.) and K_2CO_3 (2.8 eq.) in dry CH_3CN (15.0 mL) was stirred at 0 °C, and a solution of the respective chiral primary amine (NH_2-(*S*/*R*)-R^1-R^2) (1.3-1.5 eq.) in dry CH_3CN (1.0 mL) was added to the reaction mixture in four aliquots over 8 hours. After the complete addition, the reaction mixture was allowed to warm to room temperature and stirred overnight. The solid was removed by filtration, washed with CH_3CN (20 mL) and the combined solvent was removed under reduced pressure. The crude product was purified by silica-gel column chromatography.

General procedure II: A solution of backbone 2 (1.0 eq.) and TEA (triethylamine) (2.8 eq.) in dry THF (15.0 mL) was stirred at 0 °C, and a solution of the respective chiral primary amine (NH_2-(*S*/*R*)-R^1-R^2) (1.3-1.5 eq.) in dry THF (1.0 mL) was added to the reaction mixture in four aliquots over 8 hours. After the complete addition, the reaction mixture was allowed to warm to room temperature and stirred overnight. The solvent was removed under reduced pressure. The crude product was purified by silica-gel column chromatography.

All H_2bdc-^{5}N-(*S*/*R*)-R^1-R^2 linkers were prepared by standard basic ester hydrolysis.

Me_2bdc-^{5}N-(*S*/*R*)-R^1-R^2 (1.0 eq.) was dissolved in THF (3 mL), and a 1 M KOH solution (3 mL) was added. The reaction mixture was stirred at room temperature overnight, after which the THF was removed under reduced pressure. The aqueous phase was cooled to 0 °C and the pH was adjusted to 3.5-5.5 with dilute HCl, resulting in the formation of a precipitate. The solid was isolated by filtration, washed with water (2 × 5 mL) and dried under reduced pressure.

One representative example for the linker synthesis is shown below. The remaining data are provided in the Appendix to **Chapter 2**.

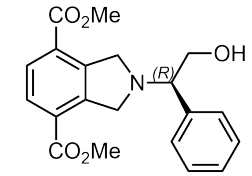

Me_2bdc-^{5}N-(*R*)-CH_2OH-Ph

The title compound was prepared from backbone 2 (496.1 mg, 1.3 mmol, 1.0 eq.) and (*R*)-(-)-2-phenylglycinol (253.0 mg, 1.8 mmol, 1.4 eq.) according to general procedure **I**. Me_2bdc-^{5}N-(*R*)-CH_2OH-Ph (369.7 mg, 1.0 mmol, 80%) was obtained as a slightly yellow oil after silica-gel column chromatography (cyclohexane/EtOAc; 2/1; v/v; 0.5% TEA).

^{1}H NMR (500 MHz, *d6*-DMSO) δ (ppm) 7.86 (s, 2H), 7.38-7.26 (m, 5H), 4.79 (t, J = 5.2 Hz, 1H), 4.21 (d, J = 15.7 Hz, 2H), 4.12 (d, J = 14.5 Hz, 2H), 3.86-3.82 (m, 1H) 3.81 (s, 6H), 3.70-3.67 (m, 2H). ^{13}C NMR (126 MHz, *d6*-DMSO) δ (ppm) 165.79, 144.13, 142.01, 128.73, 128.62, 128.19, 127.53, 70.88, 65.46, 57.76, 52.77. MS (ESI) calculated for $[M+H]^+$ $(C_{20}H_{22}N_1O_5)^+$ m/z 356.2, found m/z 355.9.

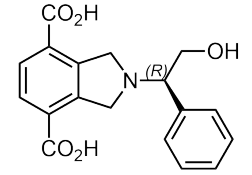

H_2bdc-^{5}N-(*R*)-CH_2OH-Ph

The title compound was prepared from Me_2bdc-^{5}N-(*R*)-CH_2OH-Ph (369.7 mg, 1.0 mmol, 1.0 eq.) according to the general ester hydrolysis procedure. H_2bdc-^{5}N-(*R*)-CH_2OH-Ph precipitated at pH 5.5 as a fine, slightly beige solid (265.4 mg, 810.8 µmol, 78%).

^{1}H NMR (500 MHz, *d6*-DMSO) δ (ppm) 7.83 (s, 2H), 7.39-7.26 (m, 5H), 4.73 (s, 1H), 4.22 (d, J = 14.4 Hz, 2H), 4.14 (d, J = 14.5 Hz, 2H), 3.83-3.79 (m, 1H), 3.70-3.66 (m, 2H). ^{13}C NMR (126 MHz, *d6*-DMSO) δ (ppm) 167.20, 143.62, 142.00, 129.33, 128.85, 128.76, 128.65, 127.56, 71.00, 65.44, 58.03. HRMS (FTMS) calculated for $[M]^-$ $(C_{18}H_{16}N_1O_5)^-$ m/z 326.1023, found m/z 326.1028.

2.4.3 General solvothermal MOF synthesis procedure

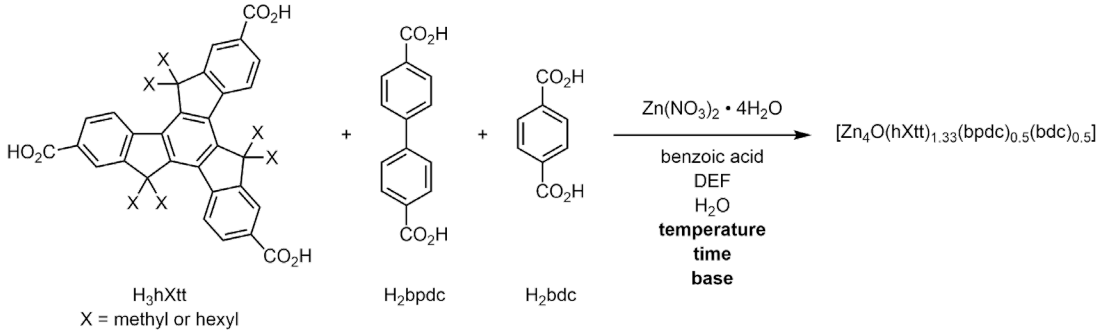

Scheme 2.8 Schematic reaction scheme showing the solvothermal MOF synthesis of the representative example $[Zn_4O(hXtt)_{1.33}(bpdc)_{0.5}(bdc)_{0.5}]$. The reaction parameters varied in the three methods used throughout this work are highlighted.

All syntheses were performed in 4 mL vials fitted with septum caps. H_3hXtt (4.0 μmol), the H_2bpdc derivative (4.8-6.8 μmol), the H_2bdc derivative (8.0-11.0 μmol), benzoic acid (8.0 mg if H_3hmtt was used and 14.0 mg if other truxene derivatives were used) and $Zn(NO_3)_2 \cdot 4H_2O$ (16.5 mg) were weighed into the reaction vessels. DEF (1.0 mL) and H_2O (50.0 μL) were added, and the mixture was sonicated for one minute. The vials were then heated to achieve MOF formation. Three different methods were used:

Method 1: The vial was heated at 85 °C in an isothermal oven. MOF formation was observed within 12-24 hours.

Method 2: The vial was heated at 110 °C in a dry bath. MOF formation was observed within 2-4 hours.

Method 3: The vial was heated for 15 minutes at 85 °C in an isothermal oven. TEA (2.5-4.5 μL) was added, the MOF synthesis mixture was briefly sonicated, and then placed back into the oven. Within the next 30 minutes, a small amount of fine white solid precipitated, which was removed by filtration through a syringe filter. MOF formation was observed within 2-5 hours after filtration.

Once MOF crystals were obtained in satisfactory amounts, the mother liquid was decanted, and the crystals were washed sequentially with DMF (1 × 1 mL) and acetone (5 × 1 mL). Each MOF synthesis yields approximately 5-15 mg of MOF crystals.

Table 2.18 Linkers, weights and molar amounts used for the MOF synthesis of this work. The applied MOF synthesis method (#) and the measured linker ratio of the digested MOF as determined by NMR are stated.

MOF name code	#	truxene	H_2bpdc-R	H_2bdc-R	NMR ratio
$[Zn_4O(hmtt)_{1.33}(bpdc\text{-}^7N\text{-}Boc)_{0.5}(bdc)_{0.5}]$	1	H_3hmtt 2.2 mg 4.0 µmol	-^{7}N-Boc 2.1 mg 5.5 µmol	-H 1.3 mg 7.8 µmol	1.33/ 0.5/ 0.5
$[Zn_4O(hmtt)_{1.33}(bpdc\text{-}gua)_{0.5}(bdc)_{0.5}]$	1	H_3hmtt 2.2 mg 4.0 µmol	-gua 1.4 mg 4.7 µmol	-H 1.3 mg 7.8 µmol	1.33/ 0.5/ 0.5
$[Zn_4O(hmtt)_{1.33}(bpdc\text{-}urea\text{-}Ph)_{0.5}(bdc)_{0.5}]$	1	H_3hmtt 2.2 mg 4.0 µmol	-urea-Ph 2.3 mg 6.1 µmol	-H 1.3 mg 7.8 µmol	1.33/ 0.5/ 0.5
$[Zn_4O(hmtt)_{1.33}(bpdc)_{0.5}(bdc\text{-}OX\text{-}(R)\text{-}5\text{-}Ph)_{0.5}]$	1	H_3hmtt 2.2 mg 4.0 µmol	-H 1.2 mg 5.0 µmol	-OX-(*R*)-5-Ph 2.7 mg 8.3 µmol	1.33/ 0.5/ 0.5
$[Zn_4O(hmtt)_{1.33}(bpdc)_{0.5}(bdc\text{-}^5N\text{-}(S)\text{-}ValOH)_{0.5}]$	3	H_3hmtt 2.2 mg 4.0 µmol	-H 1.2 mg 5.0 µmol	-(*S*)-ValOH 2.6 mg 8.9 µmol	1.33/ 0.5/ 0.5
MUF-77_^{7}N-H_Ox_1	2	H_3hmtt 2.2 mg 4.0 µmol	-^{7}N-Boc 2.1 mg 5.5 µmol	-OX-(*R*)-4-*i*Pr 2.4 mg 8.2 µmol	1.33/ 0.5/ 0.5
MUF-77_^{7}N-H_Ox_2	2	H_3hmtt 2.2 mg 4.0 µmol	-^{7}N-Boc 2.1 mg 5.5 µmol	--OX-(*R*)-5-Ph 2.7 mg 8.3 µmol	1.33/ 0.5/ 0.5
MUF-77_^{7}N-H_Ox_3	2	H_3hmtt 2.2 mg 4.0 µmol	-^{7}N-Boc 2.1 mg 5.5 µmol	-OX-(*S*)-5-MeCl 2.4 mg 8.0 µmol	1.33/ 0.5/ 0.5
MUF-77_^{7}N-H_Ox_4	2	H_3hhextt 3.9 mg 4.0 µmol	-^{7}N-Boc 2.1 mg 5.5 µmol	-OX-(*R*)-4-*i*Pr 2.4 mg 8.2 µmol	1.33/ 0.5/ 0.5
MUF-77_^{7}N-H_Ox_5	2	H_3hhextt 3.9 mg 4.0 µmol	-^{7}N-Boc 2.1 mg 5.5 µmol	-OX-(*R*)-5-Ph 2.7 mg 8.3 µmol	1.33/ 0.5/ 0.5
MUF-77_urea_Ox_1	2	H_3hmtt 2.2 mg 4.0 µmol	-urea-Ph 2.3 mg 6.1 µmol	-OX-(*R*)-4-*i*Pr 2.4 mg 8.2 µmol	1.33/ 0.5/ 0.5
MUF-77_urea_Ox_2	2	H_3hmtt 2.2 mg 4.0 µmol	-urea-Ph 2.3 mg 6.1 µmol	-OX-(*R*)-5-Ph 2.7 mg 8.3 µmol	1.33/ 0.5/ 0.5
MUF-77_urea_Ox_3	2	H_3hmtt 2.2 mg 4.0 µmol	-urea-Ph 2.3 mg 6.1 µmol	-OX-(*S*)-5-MeCl 2.4 mg 8.0 µmol	1.33/ 0.5/ 0.5
MUF-77/7_gua_Ox_1	2	H_3hmtt 2.2 mg 4.0 µmol	-gua 1.4 mg 4.7 µmol	-OX-(*R*)-4-Bn 2.8 mg 8.2 µmol	1.33/ 0.5/ 0.5
MUF-77/7_gua_Ox_2	2	H_3hhextt 3.9 mg 4.0 µmol	-gua 1.4 mg 4.7 µmol	-OX-(*R*)-4-Bn 2.8 mg 8.2 µmol	1.33/ 0.5/ 0.5
MUF-77/7_gua_Ox_3	2	H_3hhextt 3.9 mg 4.0 µmol	-gua 1.4 mg 4.7 µmol	-OX-(*R*)-5-Ph 2.7 mg 8.3 µmol	1.33/ 0.5/ 0.5
MUF-77_gua_^{5}N_1	3	H_3hhextt 3.9 mg 4.0 µmol	-gua 1.4 mg 4.7 µmol	-(*R*)-CH_3-Ph 2.7 mg 8.7 µmol	1.33/ 0.5/ 0.5
MUF-77_gua_^{5}N_2	3	H_3hhextt 3.9 mg 4.0 µmol	-gua 1.4 mg 4.7 µmol	-(*R*)-CH_2OH-Ph 2.9 mg 8.9 µmol	1.33/ 0.5/ 0.5
MUF-77_gua_^{5}N_3	3	H_3hhextt 3.9 mg 4.0 µmol	-gua 1.4 mg 4.7 µmol	-(*S*)-LeuOH 2.6 mg 8.5 µmol	1.33/ 0.5/ 0.5
MUF-77_gua_^{5}N_4	3	H_3hhextt 3.9 mg 4.0 µmol	-gua 1.4 mg 4.7 µmol	-(*S*)-ValOH 2.6 mg 8.9 µmol	1.33/ 0.5/ 0.5

A comment on MOF NMRs

To confirm the linker identity and the correct linker ratio, the ^{1}H NMR of digested MOF samples was recorded. Before digestion, the MOF crystals were washed with acetone (5 × 1 mL) and dried *in vacuo* for a minimum of one hour. All MOFs featuring the truxene functionalised with methyl groups (hmtt) were digested in a D_2O/NaOD (550.0 µL/6.0 µL) mixture aided by sonication. All MOFs featuring truxenes functionalised with longer alkyl chains than methyl, for example hexyl chains in hhtt, were digested in a DMSO-*d6*/DCl (550.0 µL/4.0 µL) mixture aided by sonication.

Integration and calibration of the linker signals were performed in one of two ways. According to the MOF formula, $[Zn_4O(truxene)_{1.33}(bpdc)_{0.5}(bdc)_{0.5}]$, the linkers are present in a 1.33:0.5:0.5 molar ratio. One of the three truxene aromatic signals – each corresponding to three protons – was calibrated to either 4H (as 1.33 × 3H = 4H) or 8H (as 2.66 × 3H = 8H). When calibrated to 4H, the bpdc and bdc signals are expected to show half the true integration. In contrast, when calibrated to 8H, the bpdc and bdc signals are expected to match their true integrals.

2.4.4 Generalised thermolytic cleavage of Boc-protection groups in a fume hood

Before Boc-deprotection, the MOFs were washed with acetone (5 × 1 mL). The thermolytic cleavage of the Boc-protecting group was carried out in 4 mL vials sealed with septum caps. A syringe connected to a Schlenk line was carefully used to pierce the septum, allowing the application of vacuum. The vials were then placed in a dry bath and heated at 190 °C for eight hours or overnight. After heating, the vials were gradually cooled to room temperature while maintaining vacuum. Subsequently, the MOF crystals were placed under an inert atmosphere of nitrogen or argon before the punctured septum caps were removed. The crystals were then immediately suspended in fresh acetone. Minimizing exposure to atmospheric conditions was critical during this process. Once suspended, the crystals were ready for use in catalysis.

2.4.6 Preparation of catalysis stock solutions

All catalysis stock solutions were prepared on a 1.0 mL scale. For all reactions a standard concentration of 4.0×10^{-2} M was chosen for the reaction limiting substrate (**Table 2.19**). For stock solutions with substrates featuring different functional groups, identical molar quantities and ratios were used to ensure consistency. Stock solutions were stored at room temperature for up to two weeks without any observed side reactions.

Table 2.19 The quantities of representative reaction substrates required to prepare 1 mL of catalysis stock solution for all model reactions.

reaction	substrate 1	substrate 2	solvent
Aldol	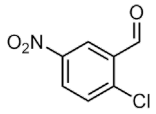 2-chloro-5-nitrobenzaldehyde 7.4 mg, 40.0 µmol, 1.0 eq.	 acetone 148 µL, 2.0 mmol, 50.0 eq.	842 µL, 10 µL of H_2O
Michael_1	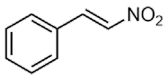 β-nitrostyrene 6.0 mg, 40.0 µmol, 1.0 eq.	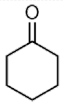 cyclohexanone 82.8 µL, 800.0 µmol, 20.0 eq.	917.2 µL
Michael_2	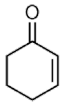 2-cyclohexen-1-one 3.9 µL, 40.0 µmol, 1.0 eq.	nitromethane 21.4 µL, 400.0 µmol, 10.0 eq.	974.7 µL
Henry	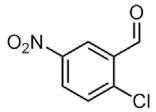 2-chloro-5-nitrobenzaldehyde 7.4 mg, 40.0 µmol, 1.0 eq.	nitromethane 107.0 µL, 2.0 mmol, 50.0 eq.	893 µL
Baylis Hillman	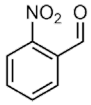 *o*-nitrobenzaldehyde 6.0 mg, 40.0 µmol, 1.0 eq.	 methyl acrylate 36.3 µL, 400.0 µmol, 10.0 eq.	963.7 µL
Friedel Crafts	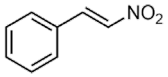 β-nitrostyrene 6.0 mg, 40.0 µmol, 1.0 eq.	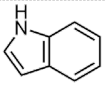 indole 9.4 mg, 80.0 µmol, 2.0 eq.	1.0 mL
Pictet Spengler	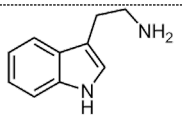 tryptamine 6.4 mg, 40.0 µmol, 1.0 eq.	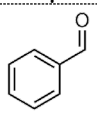 benzaldehyde 40.8 µL, 400.0 µmol, 10.0 eq.	959.2 µL

2.4.7 Generalised RAI catalysis procedure

Approximately 1.0-2.0 mg of RAI-MOF catalyst crystals were transferred into HPLC autosampler vial inlets (400 μL), which in turn were placed into 1.5 mL HPLC autosampler vials. The crystals were washed (5 × 200 μL) with the same solvent used for the reaction. Each washing step involved decanting the old solvent and adding fresh solvent. After the final washing step, the solvent was decanted, and any residual solvent was removed using a glass capillary. The catalysis reaction was started by adding 100 μL of the pre-prepared catalysis stock solutions, containing the reaction substrates, to the RAI-MOF catalyst crystals. Using this amount of stock solution with approximately 1.0-2.0 mg of MOF crystals resulted in an effective catalyst loading of 5-15% relative to the reaction limiting substrate. The effective catalyst loading refers to the number of catalytically active units within the MOF, rather than the total amount of MOF used. Given the general chemical formula of MUF-77 RAI catalysts, $[Zn_4O(truxene)_{1.33}(bpdc\text{-}catalyst)_{0.5}(bdc\text{-}chiral)_{0.5}]$, the number of catalytically active sites corresponds to 50% of the total amount of MOF present. The heterogeneous catalysis mixtures were stored at room temperature for 16-72 hours before analysis.

For HPLC analysis, the autosampler vials were placed into the HPLC device, and 0.1-3.0 μL of the reaction solution was taken and injected onto the system. The analysis was performed using the pre-determined conditions, including the chiral column, mobile phase and flow rate. The eluting products were detected by UV absorption at four different wavelengths (210 nm, 230 nm, 245 nm and 280 nm). The peaks corresponding to the two product enantiomers were integrated, and the ee for each catalysed reaction was calculated.

Chapter 3 – Catalyst and condition optimisation to maximise the enantioselectivity

3.1 Introduction

The ultimate goal of this thesis is to use the new approach to asymmetric catalysis, remote asymmetric induction in multicomponent MOFs, to achieve as high enantioselectivity as possible. After screening multiple reactions, catalyst motifs and chiral groups in **Chapter 2**, the work presented in this chapter focuses on achieving as high enantioselectivity as possible using the RAI-MOF catalysts. The specific goals for this chapter are:

(i) To systematically optimise variables affecting enantioselectivity,

(ii) To build a knowledge base of the features that are important for high enantioselectivity,

(iii) To combine all optimised variables to achieve the highest possible enantioselectivity.

Experimentally, this is achieved by building on the system of RAI-MUF-77 catalysts and model reaction, identified in **Chapter 2**: MUF-77_gua_^{5}N catalysts (**Figure 3.1 A)**), catalysing the Henry reaction of functionalised benzaldehydes with nitromethane (**Figure 3.1 B)**).

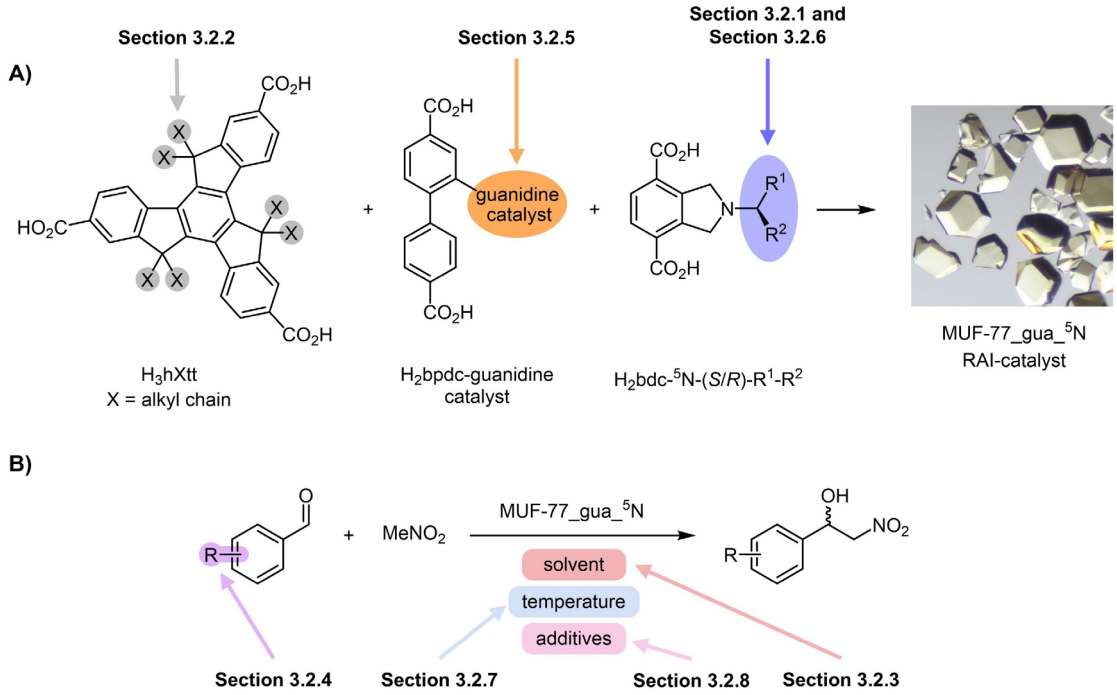

Figure 3.1 A) Schematic diagram showing the MUF-77_gua_^{5}N catalyst synthesis and **B)** the Henry reaction of functionalised benzaldehydes with nitromethane. The variables that are explored throughout the thesis are highlighted.

All experiments reported in this chapter focus on optimising the ee of the Henry reactions, with only a secondary focus on other metrics, such as conversion. Two main experimental strategies were considered: a conventional 'one variable at a time' approach and the statistically driven 'design of experiments' (DoE) approach.[198] While a DoE approach has the potential to significantly reduce the number of required experiments by simultaneously evaluating multiple variables, it requires comprehensive knowledge of all relevant variables at the design stage. However, at the start of this work, only hypotheses existed regarding potentially influential variables, such as solvent, chiral linker, and reaction substrate. Therefore, the traditional approach of varying one variable at a time was chosen to allow for an organic and natural flow of the experiments.

A systematic, iterative process was then developed to implement this strategy. The experimental workflow (**Figure 3.2**) began by designing the initial set of experiments/linkers inspired by the system identified in **Chapter 2**: MUF-77_gua_^{5}N catalysts for the Henry reaction of functionalised benzaldehydes with nitromethane (**Figure 3.1**). The gained insights then inspired the design of subsequent experiments/linkers, allowing for a targeted exploration of the specific variable's influence. This iterative process was repeated multiple times until the experimental possibilities for a given variable were fully explored. Once completed, the focus shifted to the next variable. The variables that showed the greatest influence on the enantioselectivity were revisited multiple times after going through the iterative process for other parameters.

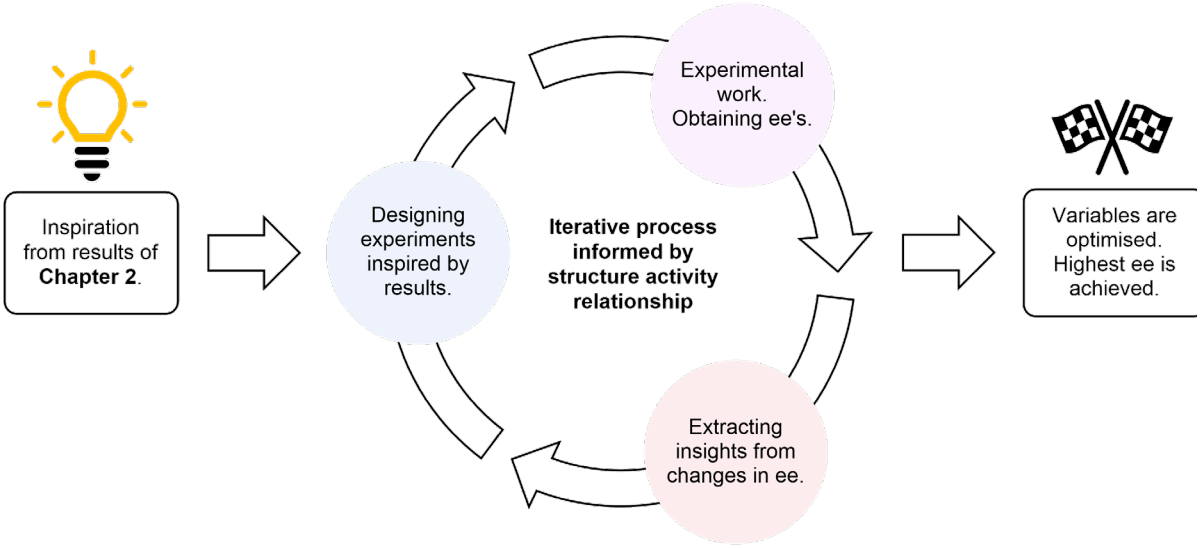

Figure 3.2 Iterative process used to explore the structure activity relationship of the MUF-77_gua_^{5}N catalysts for the Henry reaction to achieve the highest possible ee.

It is worth noting that a potential drawback of this approach is the risk of identifying a false global maximum, as each variable is optimised in isolation without simultaneously considering

the full reaction space.[198] To mitigate this risk, additional experiments were performed during each loop process, intentionally involving a range of lower performing variables.

Each section focuses on one variable before the optimised variables are ultimately combined to achieve the highest ee reported in this thesis. Overall, the emphasis of this chapter is placed on experimental work, with relatively short interpretations. A detailed discussion of the origin of enantioselectivity is deferred to **Chapter 4.2.3**.

3.2 Results and discussion

3.2.1 Chiral linker

The chiral linkers are the exclusive source of chiral information in the RAI-MUF-77 catalysts. This makes them the key component to achieve stereo control. For asymmetric induction to occur, the chiral moiety must interact with the reaction substrates during the reaction. This interaction can potentially involve hydrogen bonding or van der Waals interactions, which can be both attractive and repulsive.

To identify linker features that are important for achieving high enantioselectivity for the Henry reaction, analogues of the four bdc-^{5}N-chiral linkers identified in **Chapter 2.2.4** were synthesised. The chiral precursors were chosen to explore the importance of the presence of a hydrogen bond donor group as well as the overall structure and size of the chiral functionality. To extract how the identity of the chiral linker influences the ee of the product mixture, all other variables were held constant. All MUF-77_gua_^{5}N catalysts were synthesised using H_3hhextt, and H_2bpdc-gua (**Figure 3.3 A)**. As reference reaction, the Henry reaction of 2-chloro-5-nitrobenzaldehyde with nitromethane in 1,4-dioxane was selected (**Figure 3.3 B**).

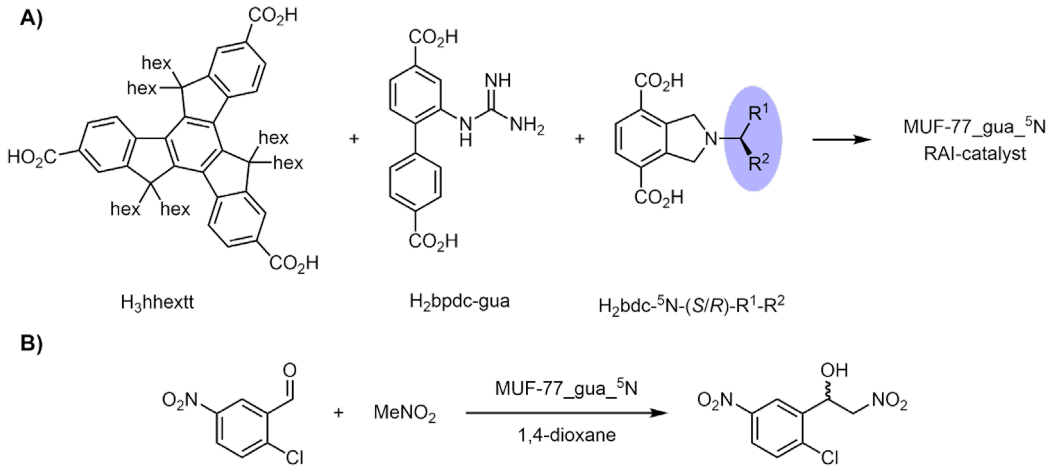

Figure 3.3 A) Reaction scheme showing the MUF-77_gua_^{5}N catalyst synthesis using H_3hhextt, H_2bpdc-gua and H_2bdc-^{5}N-chiral linkers. **B)** Henry reaction of 2-chloro-5-nitrobenzaldehyde with nitromethane.

The library of chiral H_2bdc-^{5}N-(*S*/*R*)-R^1-R^2 linkers was expanded to 15 linkers in total, which were all integrated into their respective MUF-77_gua_^{5}N catalysts (**Table 3.1**) as confirmed by PXRD and ^{1}H NMR spectroscopy on digested MOF samples.

Steric bulk emerged as a crucial factor influencing enantioselectivity. Bulky chiral moieties consistently led to low ee values (MUF-77_gua_^{5}N_1-3 and 5-7). Interestingly, the nature of the steric bulk, whether aromatic (MUF-77_gua_^{5}N_2) or aliphatic (MUF-77_gua_^{5}N_5 and 6), made little difference. Conversely, reducing the steric bulk significantly improved enantioselectivity, provided that a hydroxyl functional group was present (MUF-77_gua_^{5}N_8, 4, 9, 10). The highest ee of -64.4% was observed for MUF-77_gua_^{5}N_10, incorporating bdc-^{5}N-(*S*)-AlaOH, which is a compact, hydroxyl-bearing chiral linker.

Further reducing the steric bulk was contemplated but not explored for practical reasons. For example, replacing the methyl group by a smaller halo group, is not synthetically feasible, and placing hydroxy and amino groups on the same carbon leads to instability. Removing the methyl group altogether would eliminate the chiral centre.

The importance of a hydroxyl group is clear. Replacing it with a methyl group (bdc-^{5}N-(*R*)-CH_2CH_3-CH_3) resulted in a complete loss of enantioselectivity (MUF-77_gua_^{5}N_11). Similarly, replacing it by a methoxy ether (bdc-^{5}N-(*S*)-CH_2OCH_3-CH_3) caused a substantial drop in ee to 6.2% (MUF-77_gua_^{5}N_12). Together, these results suggested that the hydroxyl group was a key structural feature for achieving high enantioselectivity, likely through hydrogen bonding interactions with the reaction substrates.

The positional effect of the hydroxyl group relative to the linker backbone and chiral centre was explored. Introducing a CH_2-spacer to move the OH-group further away from the chiral centre (bdc-^{5}N-(*S*)-$(CH_2)_2$OH-CH_3) decreased the |ee| from 64.4% (MUF-77_gua_^{5}N_10) to 16.2% (MUF-77_gua_^{5}N_13). Moreover, when the position of the hydroxyl group relative to the linker backbone was kept the same as in H_2bdc-^{5}N-(*S*)-AlaOH, but the chiral centre was repositioned to the carbon bearing the hydroxyl group by moving the methyl-group to the same carbon (bdc-^{5}N-CH_2CH-(*R*)-CH_3OH), a significant decrease in |ee| from 64.4% (MUF-77_gua_^{5}N_10) to 21.3% (MUF-77_gua_^{5}N_14) was observed. These results highlighted the importance of the position of the hydroxyl group relative to the chiral centre and simultaneously to the linker backbone. The effect of introducing a second hydroxyl group was tested using the smallest synthetically feasible linker bdc-^{5}N-(*R*)-ThrOH. This linker delivered a low |ee| of 9.0% (MUF-77_gua_^{5}N_15), which can be compared to the 54.4% observed for MUF-77_gua_^{5}N_9.

Table 3.1 The influence of the chiral linker on ee's measured for the Henry reaction of 2-chloro-5-nitrobenzaldehyde with nitromethane using MUF-77_gua_^{5}N RAI catalysts. The carboxylates of the linkers are omitted for clarity.

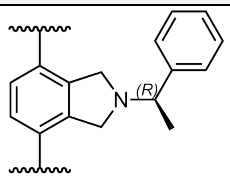	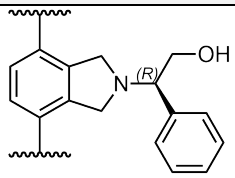	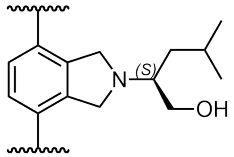
bdc-^{5}N-(*R*)-CH_3-Ph MUF-77_gua_^{5}N_1 **ee = 1.5%**	bdc-^{5}N-(*R*)-CH_2OH-Ph MUF-77_gua_^{5}N_2 **ee = -1.4%**	bdc-^{5}N-(*S*)-LeuOH MUF-77_gua_^{5}N_3 **ee = 18.1%**
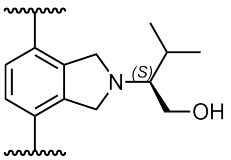	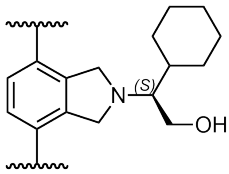	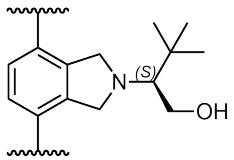
bdc-^{5}N-(*S*)-ValOH MUF-77_gua_^{5}N_4 **ee = -38.3%**	bdc-^{5}N-(S)-CH_2OH-cycloHex MUF-77_gua_^{5}N_5 **ee = -9.8%**	bdc-^{5}N-(*S*)-CH_2OH-*t*Bu MUF-77_gua_^{5}N_6 **ee = -10.0%**
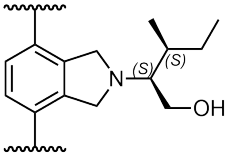	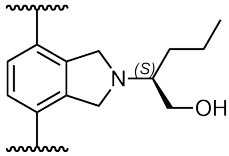	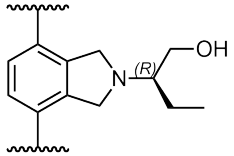
bdc-^{5}N-(*S*)-isoLeuOH MUF-77_gua_^{5}N_7 **ee = -22.0%**	bdc-^{5}N-(*S*)-CH_2OH-$(CH_2)_2CH_3$ MUF-77_gua_^{5}N_8 **ee = -16.2%**	bdc-^{5}N-(*R*)-CH_2OH-CH_2CH_3 MUF-77_gua_^{5}N_9 **ee = 54.4%**
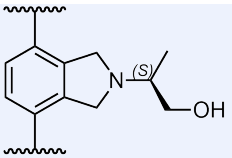	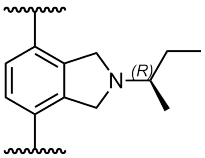	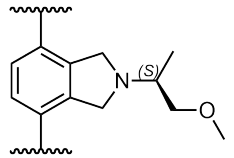
bdc-^{5}N-(*S*)-AlaOH MUF-77_gua_^{5}N_10 **ee = -64.4%**	bdc-^{5}N-(*R*)-CH_2CH_3-CH_3 MUF-77_gua_^{5}N_11 **ee = 0%**	bdc-^{5}N-(*S*)-CH_2OCH_3-CH_3 MUF-77_gua_^{5}N_12 **ee = 6.2%**
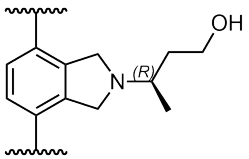	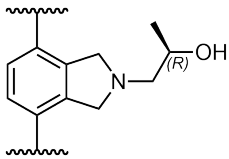	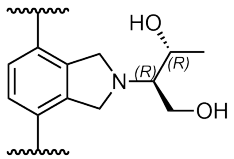
bdc-^{5}N-(*R*)-$(CH_2)_2OH$-CH_3 MUF-77_gua_^{5}N_13 **ee = 16.2%**	bdc-^{5}N-CH_2CH-(*R*)-CH_3-OH MUF-77_gua_^{5}N_14 **ee = -21.3%**	bdc-^{5}N-(*R*)-ThrOH MUF-77_gua_^{5}N_15 **ee = -9.0%**

Overall, these results confirm that the ee was highly sensitive to the structure of the chiral linker. The highest enantioselectivities were achieved with compact linkers featuring a single hydroxyl group at an optimal distance from the chiral centre and the linker backbone. These features are embodied in bdc-^{5}N-(*S*)-AlaOH in MUF-77_gua_^{5}N_10.

3.2.2 Variation of the truxene

The tritopic truxenes form the backbone of the MUF-77 structure. Until now, they were considered a passive building block, essential for framework formation and stability, but not significantly influential on the enantioselectivity of the RAI-MUF-77 catalysts. However, altering the length of the alkyl chains on the truxene backbone changes the pore filling of the MOF, potentially impacting enantioselectivity.

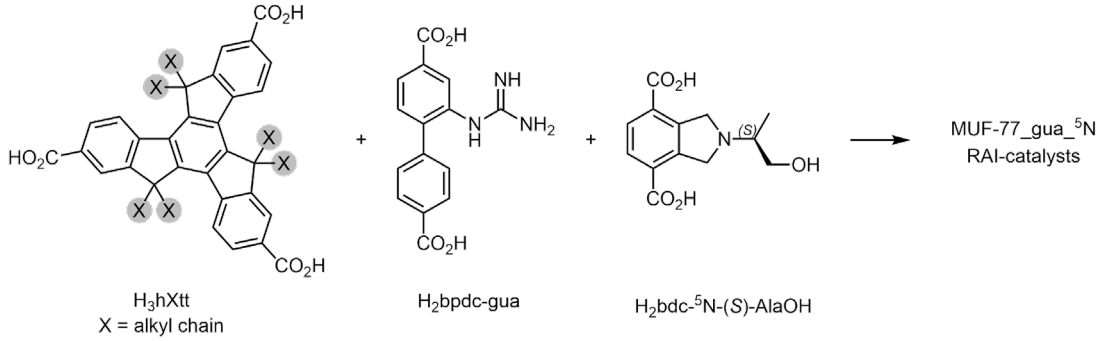

Figure 3.4 Schematic diagram showing the MUF-77_gua_^{5}N catalyst synthesis using H_2bpdc-gua, H_2bdc-^{5}N-(*S*)-AlaOH and truxenes with varying alkyl chain lengths.

The goal of this section was to assess the impact of the truxene functionalisation on the enantioselectivity of the MUF-77_gua_^{5}N catalysts for the Henry reaction. To investigate this, six MUF-77_gua_^{5}N catalysts were synthesised (**Figure 3.4** and **Table 3.2**), each consisting of bdc-^{5}N-(*S*)-AlaOH as the chiral and bpdc-gua as the catalytic linker, differing only in the length of the alkyl chains on the truxene backbone. Alkyl chain lengths from methyl to octyl were tested. For comparability, the Henry reaction of 2-chloro-5-nitrobenzaldehyde with nitromethane was used as a reference reaction for all catalysts (**Figure 3.3 B)**. The RAI-MOF codes and corresponding ee values are listed in **Table 3.2**.

Table 3.2 The influence of the truxene linker on ee's measured for the Henry reaction of 2-chloro-5-nitrobenzaldehyde with nitromethane in 1,4-dioxane using MUF-77_gua_^{5}N RAI catalysts.

hXtt (X = alkyl chain length)	RAI-MOF	|ee|
hmtt (X = 1)	MUF-77_gua_^{5}N_16	9.4%
hbtt (X = 4)	MUF-77_gua_^{5}N_17	25.5%
hptt (X = 5)	MUF-77_gua_^{5}N_18	31.4%
hhextt (X = 6)	MUF-77_gua_^{5}N_10	64.4%
hheptt (X = 7)	MUF-77_gua_^{5}N_19	35.1%
hott (X = 8)	MUF-77_gua_^{5}N_20	8.3%

The catalysis results (**Table 3.2**, column three) demonstrated that although the truxenes are neither catalytically active nor contain a chiral centre, the length of their alkyl chains had a pronounced impact on the enantioselectivity of the MUF-77_gua_^{5}N catalyst. MUF-77_gua_^{5}N_16 featuring the smallest truxene, hmtt, produced a product mixture with a low ee of 9.4%. Extending the alkyl chain length to butyl (MUF-77_gua_^{5}N_17) and pentyl (MUF-77_gua_^{5}N_18) moderately increased the ee to 25.5% and 31.4%, respectively. Further increasing it to hexyl chains (MUF-77_gua_^{5}N_10) led to a large increase in ee to 64.4%. Longer alkyl chains such as heptyl (MUF-77_gua_^{5}N_19) and octyl (MUF-77_gua_^{5}N_20) caused a drop in ee to 35.1% and 8.3%, respectively.

The dependency of the ee on the alkyl chain length of the truxene means that they must influence the catalysed reaction. Analysis of the MUF-77 framework reveals a possible explanation: the alkyl chains occupy the large pores and only allow catalysis to occur in the small pores where the transfer of stereochemical information is maximised.

MUF-77 consists of three distinct pore types (**Chapter 1.2.2**). The small pores are defined by all three linkers and is the core of the RAI concept. The two large pores are constructed from truxenes and only one of the two linear linkers each. The large pores containing bdc as a building block accommodate multiple chiral groups but are not catalytically active. Therefore, these pores do not influence the overall enantioselectivity of the RAI-MUF-77 catalyst. However, the large pores being exclusively built of truxenes and bpdc linkers contain no chiral but multiple catalyst moieties. While they may be catalytically active, the lack of a chiral moiety will yield racemic products. This would lower the overall enantioselectivity of the RAI-MUF-77 catalyst, as the final ee reflects the sum of all catalytic events within the MOF.

SCXRD measurements of functionalised truxene and its precursors showed that the alkyl chains point vertically away from the truxene backbone.[119] This was also confirmed to be the case within the MUF-77 crystals at different temperatures (-100 °C – 60 °C), with usually the first three to four carbon atoms of each chain being resolvable by SCXRD, while the remainder were too disordered to be observed. Therefore, with the alkyl chains pointing vertically away from the truxene backbone, they exclusively orient into the large pores, leaving the small pores unoccupied (**Figure 3.5 B**). Using modelling without energy minimisation to artificially extend the chains following the observable trends suggested that hexyl chains optimally fill the large pores (**Figure 3.5 A**) and physically block catalytic activity within them, thereby restricting the reaction to the small pores.

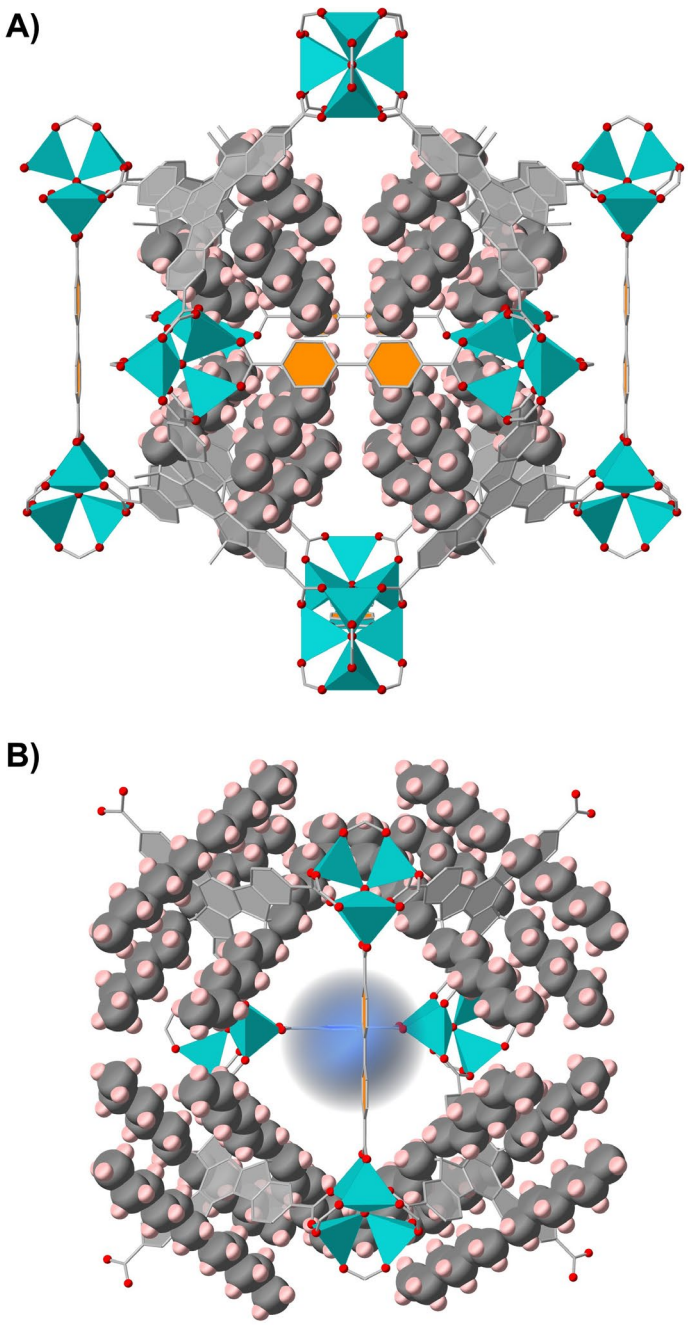

Figure 3.5 A) Hypothetical large pore in MUF-77 built of hhextt and bpdc. The alkyl chains pointing into the pore are shown as space filling, while the chains on the outside of the pore are omitted for clarity. **B)** Hypothetical small pore in MUF-77 built of hhextt, bpdc and bdc. The empty pore is highlighted by a blue sphere. The alkyl chains were modelled based on SCXRD data.

Shorter alkyl chains leave the large pores partially unfilled, allowing racemic catalysis to occur within the large pore. Heptyl and octyl chains exceed the dimensions of the large pore and encroach into the neighbouring small pores, disrupting the transfer of stereochemical information during the catalysis and thus lowering the enantioselectivity (**Figure 3.6**). These findings offer a rationale for the correlation of ee and alkyl chain length on the truxene linkers.

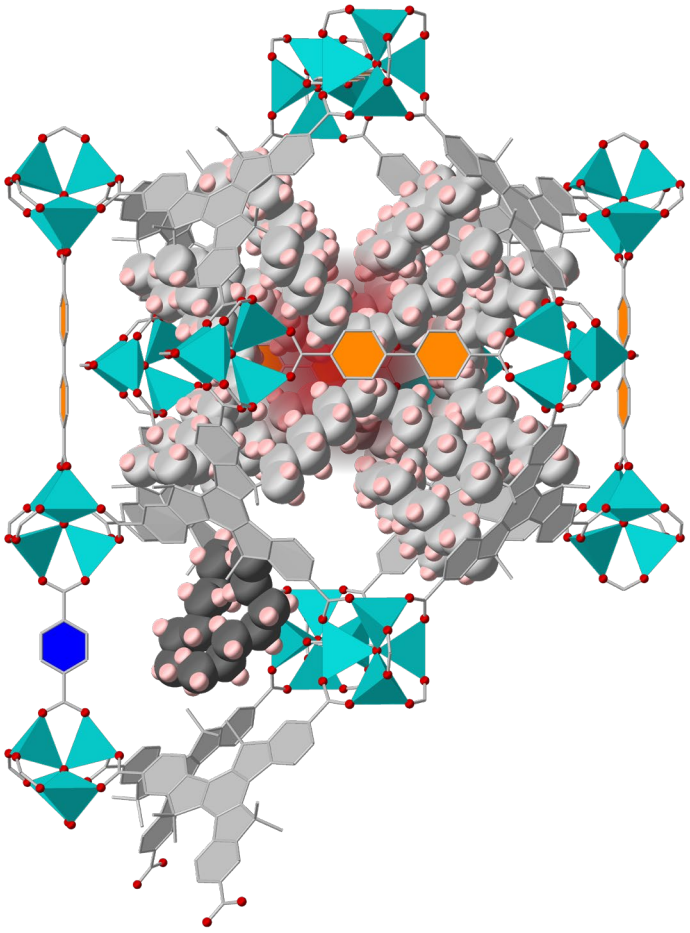

Figure 3.6 Hypothetical large and neighbouring small pore structure with heptyl chains attached to the truxene. The interference of the alkyl chains within the pore centre is highlighted by a red sphere. The alkyl chains that are bent to point into the neighbouring small pores are shown as dark grey.

3.2.3 Solvent

The choice of solvent can dramatically impact reaction rates and enantioselectivity in asymmetric catalysis.[198-200] Through interactions with substrates, catalysts, and reaction intermediates, solvents can significantly alter reaction outcomes. In fact, changes in solvent have been reported to shift ee values from 0% to up to 90% in some cases.[99, 201]

The goal of this section was to explore the impact of different solvents on the enantioselectivity of the MUF-77_gua_^{5}N catalysts for the Henry reaction. To isolate the effect of the solvent, all experiments were performed using MUF-77_gua_^{5}N_10 as the catalyst (**Figure 3.7 A**), exclusively catalysing the Henry reaction of 2-chloro-5-nitrobenzaldehyde with nitromethane (**Figure 3.7 B**).

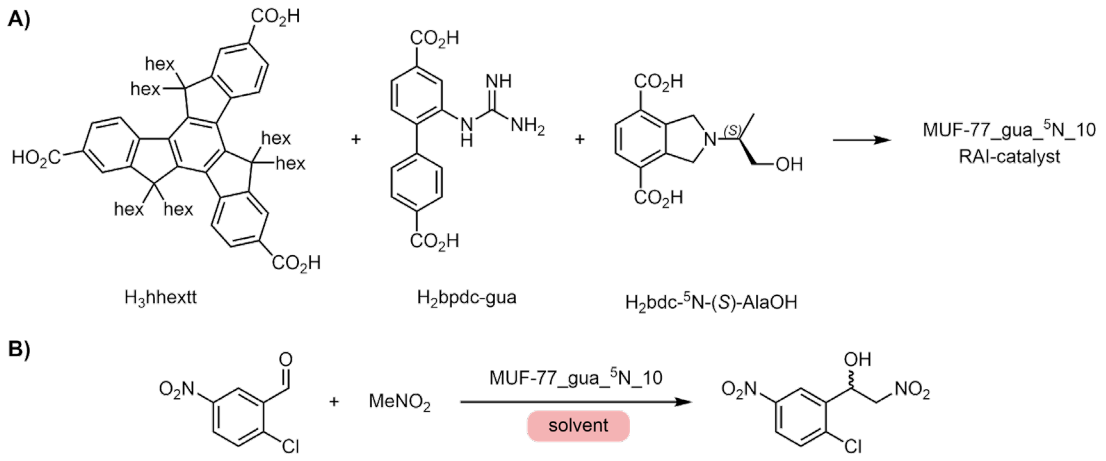

Figure 3.7 A) Schematic diagram showing the synthesis of MUF-77_gua_^{5}N_10 using H_3hhextt, H_2bpdc-gua and H_2bdc-^{5}N-(*S*)-AlaOH. **B)** Henry reaction of 2-chloro-5-nitrobenzaldehyde with nitromethane in various solvents catalysed by MUF-77_gua_^{5}N_10.

Initially, a range of solvents with diverse functional groups and properties were assessed using a non-targeted screening approach (**Table 3.3**). Ethers rapidly emerged as the most promising system. Using other solvents either yielded no reaction (nitromethane and toluene) or produced product mixtures with no or low ee values. Cyclic ethers (tetrahydrofuran and 1,4-dioxane) produced the highest enantioselectivities, while open chain ethers (diethyl ether) showed lower selectivity. This highlighted the substantial variability in ee depending on solvent functional groups and shape (open vs cyclic: diethyl ether vs tetrahydrofuran).

To evaluate the impact of structural variations in open chain ethers on ee, a range of ethers were tested. Symmetrically extending the ether chain by incorporating one or two additional ether linkages (1,2-dimethoxyethane and diglyme) had minimal effect on the enantioselectivity of the catalyst. In contrast, ethers with a methyl group and a second, bulkier group produced larger variability in ee. Methoxybenzene, containing an aromatic ring, led to a nearly racemic product mixture, whereas methoxycyclopentane, featuring a cyclopentane group, achieved the highest ee observed for open chain ethers with just over 20%.

Additionally, different tetrahydrofuran derived solvents were assessed. Adding a methyl group (2-methyltetrahydrofuran) resulted in a slight increase in ee, while the unsaturated analogue (2,5-dihydrofuran) led to a minor decrease in enantioselectivity. Introducing a second ether functionality into the five-membered ring (1,3-dioxolane) did not change the ee significantly. Further modification of the cyclic di-ether by adding a methyl group (2-methyl-1,3-dioxolane) also had minimal impact on the enantioselectivity. In contrast, the addition of a carbonyl group, by using a cyclic carbonate (ethylene or propylene carbonate) resulted in nearly complete loss of enantioselectivity.

Table 3.3 Overview of solvents tested for the Henry reaction of 2-chloro-5-nitrobenzaldehyde and nitromethane, catalysed by MUF-77_gua_^{5}N_10. The structure and name of the solvents as well as the respective measured |ee| is stated. 'N.R.' = no reaction.

nitromethane N.R.	acetonitrile |ee| = 0%[c]	methanol |ee| = 3.6%	isopropanol |ee| = 1.9%
1,2-dichloroethane |ee| = 13.4%	ethyl acetate |ee| = 12.9%	toluene N.R.	[bmim]BF_4 |ee| = 1.4%[b]
diethyl ether |ee| = 6.4%	1,2-dimethoxyethane |ee| = 5.0%	diglyme |ee| = 9.7%	*t*-butyl methyl ether |ee| = 13.1%
methoxybenzene |ee| = 1.3%[b]	methoxycyclopentane |ee| = 20.7%	tetrahydrofuran |ee| = 38.0%	2-methylhydrofuran |ee| = 44.2%
2,5-dihydrofuran |ee| = 34.8%[c]	1,3-dioxolane |ee| = 37.2%	2-methyl-1,3-dioxolane |ee| = 39.4%[c]	ethylene carbonate |ee| = 0%[a]
propylene carbonate |ee| = 5.1%	1,4-dioxane |ee| = 64.4%	1,4-dioxene |ee| = 10.7%	1,4-oxathiane |ee| = 0%[c]
1,4-dioxan-2-one N.R.[a]	1,3-dioxane |ee| = 53.2%	1,3-dioxan-5-ol |ee| = 3.2%[c]	trimethylene carbonate |ee| = 2.2%[a]

[a] Reaction was performed at 5 °C above the melting point of the solvent.
[b] Low level background reaction observed in stock solution.
[c] Low level of side reactions observed in catalysis reaction mixture.

Next, different 1,4-dioxane-derived solvents were explored. Interestingly, changing one of the ether groups to a thio-ether (1,4-oxathiane) resulted in a complete loss of enantioselectivity. This radical change in ee highlighted the large variability in enantioselectivity depending on the identity of the solvent. Introducing a double bond (1,4-dioxene) similarly caused a substantial decrease in ee, while the incorporation of a carbonyl group (1,4-dioxan-2-one)

completely suppressed the reaction. Changing the position of the two ether groups relative to each other within the cyclic system (1,3-dioxane) only slightly reduced the ee. Further modification of the 1,3-dioxane backbone by adding an OH group (1,3-dioxan-5-ol) or a carbonyl group to form a cyclic carbonate (trimethylene carbonate) led to a complete loss of enantioselectivity.

Overall, the experiments confirmed the strong dependency of enantioselectivity on the reaction solvent. Cyclic ethers emerged as the highest performing class of solvents for the Henry reaction catalysed by MUF-77_gua_^{5}N catalysts, with 1,4-dioxane facilitating the highest enantioselectivity.

3.2.4 Functional group on the benzaldehyde

The 'perfect' asymmetric catalyst would display high activity and enantioselectivity across a large range of diverse substrates. However, as catalyst-substrate interactions are highly specific to both the catalyst structure and the functionalities of the reaction substrates, most catalysts are limited in their substrate scope.[99, 202] To identify the optimal fit for a specific catalyst and simultaneously gain essential insights into the structural features of the substrates that most strongly influence enantioselectivity, a common approach is to screen a range of differently functionalised substrates.[98, 203] This was the goal of this section.

The identity and position of functional groups on a benzaldehyde backbone was systematically varied to determine the influence on the ee. Insights were gained into their structure-activity relationships. Other variables were held constant: all reactions were catalysed by MUF-77_gua_^{5}N_10 (**Figure 3.7 A**), using nitromethane as the second substrate and 1,4-dioxane as the solvent for the Henry reaction (**Figure 3.8**). For consistency, a non-IUPAC nomenclature system for the functionalised benzaldehydes is used during the discussion.

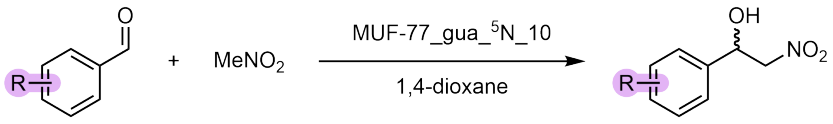

Figure 3.8 Henry reaction of functionalised benzaldehydes with nitromethane in 1,4-dioxane catalysed by MUF-77_gua_^{5}N_10.

Before catalysing the different Henry reactions with the RAI-MUF-77 catalyst, the HPLC conditions for each reaction had to be developed. This was achieved by using the catalyst linker precursor, Me_2bpdc-gua, as a homogeneous catalyst to obtain a racemic product mixture and using previously optimised HPLC methods as a starting point to separate the racemic product on HPLC. The conditions were refined when needed to ensure effective separation of the two product signals from one another and from the reaction substrates. To be certain that the

observed peaks corresponded to the desired product, the catalysis products of three representative benzaldehydes (**11**, **14**, and **22**, **Table 3.6**) were isolated, their identities confirmed by NMR, and the product signals validated by injecting the individual products onto the HPLC (**Figure 3.23**; Appendix **Chapter 3**). In both the homogeneous and RAI-MUF-77 catalysis, the benzaldehydes were typically converted exclusively into the corresponding Henry products, with no side products detected by TLC or HPLC. This is consistent with the asymmetric catalysis literature for the Henry reaction, where yields ≥95% are commonly observed.[172, 204, 205]

Table 3.4 Overview of the measured ee values for the Henry reactions of various mono-functionalised benzaldehydes with nitromethane. 'N.R.' = no reaction.

2-X-benzaldehyde		
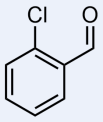	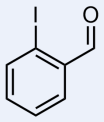	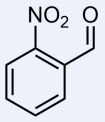
1	**2**	**3**
N.R.	N.R.	ee = 41.8%
3-X-benzaldehyde		
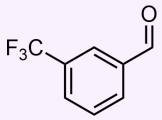	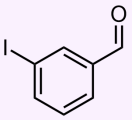	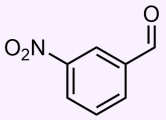
4	**5**	**6**
N.R.	N.R.	ee = 34.4%
4-X-benzaldehyde		
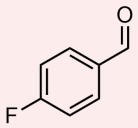	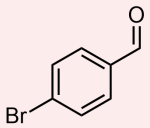	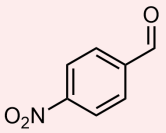
7	**8**	**9**
N.R.	N.R.	ee = 16.8%

Benzaldehydes featuring only halo substituents, or surprisingly a -CF_3 group, did not show any reaction (**Table 3.4**). In contrast, benzaldehydes featuring a nitro group showed conversion and the ee of the product mixture could be determined. These differences in reactivity can be attributed to the varying electron-withdrawing strengths of the substituents, described by their substituent constant (σ) from the Hammett equation.[206, 207] Larger σ values indicate stronger electron-withdrawing effects, with the values differing slightly depending on the substitution position (meta: σ_m, or para: σ_p). Out of the tested substituents, nitro has the strongest electron-withdrawing effect ($\sigma_p = 0.78$), compared to CF_3 ($\sigma_p = 0.54$) or halo groups (for example Cl: $\sigma_p = 0.23$). Comparing the ee for the three nitro-functionalised benzaldehydes (**3**, **6**, and **9**), it is

apparent that the position of the nitro group relative to the aldehyde had a significant effect on the ee. Substitution at the 2-position (*ortho*) delivers the highest ee (41.8%).

Table 3.5 Summary of the measured ee values for the Henry reactions of all possible benzaldehydes featuring a nitro group and a chloro group.

Y-Cl-2-nitrobenzaldehydes				
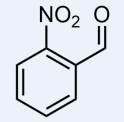	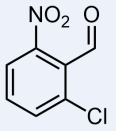	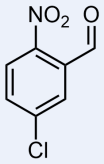	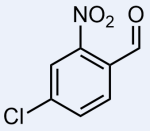	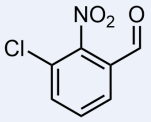
3 ee = 41.8%	**10** ee = 16.0%	**11** ee = 77.1%	**12** ee = 54.5%	**13** ee = 61.2%
Y-Cl-3-nitrobenzaldehydes				
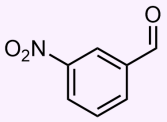	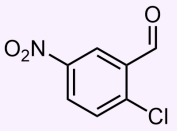	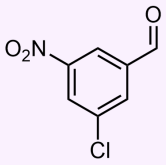	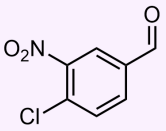	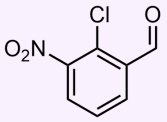
6 ee = 34.4%	**14** ee = 64.4%	**15** ee = 75.4%	**16** ee = 50.4%	**17** ee = 26.9%
Y-Cl-4-nitrobenzaldehydes				
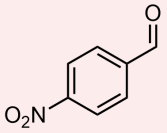	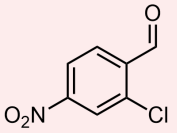	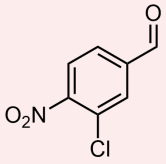		
9 ee = 16.8%	**18** ee = 29.7%	**19** ee = 41.4%		

The impact of the position of a second functional group on the nitrobenzaldehyde was then investigated. All possible isomers of benzaldehydes containing a nitro group and a chloro group were tested (**Table 3.5**). The results revealed that there was up to a five-fold difference in ee between the isomers. For instance, introducing a Cl-group *ortho* to the aldehyde and *meta* to the nitro group (benzaldehyde **10**), resulted in a significant reduction in enantioselectivity, with the ee decreasing by 25.8% to 16.0%, compared to the 41.8% observed for unsubstituted 2-nitrobenzaldehyde. Remarkably, shifting the Cl-group by one position to be *para* to the NO_2-group and *meta* to the aldehyde (benzaldehyde **11**) increased the ee to 77.1%, a **rise of 61.1%** caused by this simple positional change. Similarly, large variations were observed for the *meta*-nitrobenzaldehydes upon altering the chloro group position. In contrast, 3-nitrobenzaldehydes functionalised with a chloro group showed comparatively lower ee values and less variability with positional changes. Overall, these experiments uncovered a high

variation in enantioselectivity based on the position of a second substituent on the benzaldehydes. The highest |ee| values were observed for benzaldehydes **11**, **15** and **14**, with 77.1%, 75.4% and 64.4% respectively.

Following these observations, the impact of the identity of the second substituent on the ee was evaluated. The substitution pattern of the three highest performing chloro-nitrobenzaldehydes **11**, **15**, and **14**, as well as the lower performing chloro-nitrobenzaldehyde **19**, were selected as the starting points for these experiments. The chloro group was exchanged for various other functional groups and the effect on the ee was monitored (**Table** 3.6). Possible explanations for the origin of differences in ee between the functional groups can be extracted.

Changing the chloro (**11**, **15**, **14** and **19**) to a bromo (**21**, **30**, **37** and **40**) or methyl (**22**, **31**, **38** and **41**) group produced similar or slightly higher ee regardless of the substitution pattern. As bromo, methyl, and occasionally chloro groups are considered isosteric while simultaneously showing different electronic effects, the similar ee values suggest that their influence on the ee is contributed by their size rather than their electronic differences.[208-210]

When changing the chloro group to larger substituents, as for example a methoxy or trifluoromethyl group, differences between the substitution pattern were observed. For 5-X-2-nitrobenzaldehydes, substitution with these larger functionalities (**23** and **26**) yielded similar ee as with for example a chloro or methyl group. In contrast, the same change resulted in a considerable drop in ee for the 5-X-3-nitrobenzaldehydes (**32** and **34**). This showed that the different substitution pattern of the benzaldehydes can behave differently to the same change in size of one substituent: 5-X-2-nitrobenzaldehydes tolerate larger second substituents, while for 5-X-3-nitrobenzaldehydes the size of the second substituent has a more pronounced effect. This is likely due to differences in noncovalent van der Waals interactions and/or steric repulsions of these groups with the restricted pore environment during the reaction. This observation agrees with the strong positional effect between the different isomers of benzaldehydes containing a nitro group and a chloro group (**Table 3.5**). The position of the functional group often matters more than their identity. However, even larger phenyl-substituted benzaldehydes **24** and **33** did not produce any reaction, regardless of the substitution pattern. This is likely due to their large size restricting diffusion into the MOF pores.

Changing the chloro group to substituents that have a more pronounced electron withdrawing effect, as for example a fluoro (**20**, **29**, **36** and **39**), a nitrile (**27**) or a second nitro (**35**) group, decreased the ee regardless of the substitution pattern. The effect of these groups on the ee did not follow the discussed size dependency but seemed to be predominantly caused by their stronger electronic effects. The origin of this behaviour remained unknown.

Table 3.6 Summary of the measured ee values for the Henry reactions of double-functionalised benzaldehydes with nitromethane. Each benzaldehyde features one NO_2-group and one additional substituent.

5-X-2-nitrobenzaldehydes

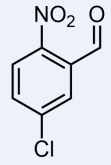

11
ee = 77.1%

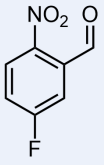

20
ee = 56.7%

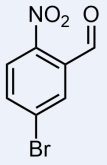

21
ee = 78.1%

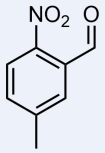

22
ee = 82.4%

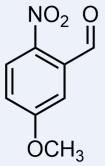

23
ee = 81.8%

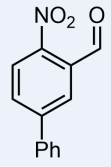

24
N.R.

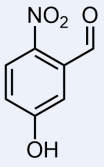

25
ee = 15.4%

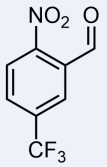

26
ee = 76.4%

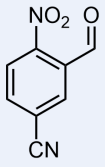

27
ee = 66.6%

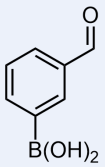

28
side reactions

5-X-3-nitrobenzaldehydes

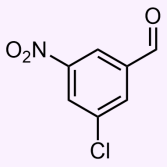

15
ee = 75.4%

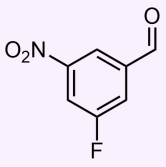

29
ee = 37.0%

30
ee = 77.3%

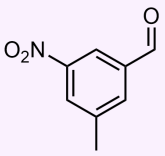

31
ee = 71.4%

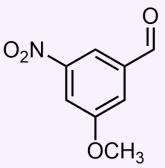

32
ee = 45.6%

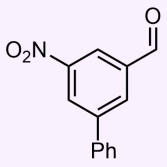

33
N.R.

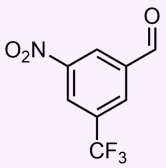

34
ee = 63.8%

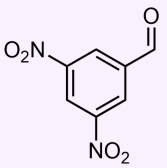

35
ee = 36.4%

6-X-3-nitrobenzaldehydes

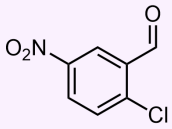

14
ee = 64.4%

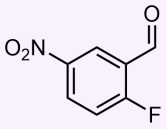

36
ee = 47.2%

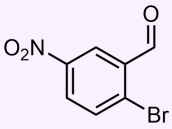

37
ee = 63.5%

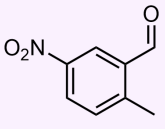

38
ee = 68.1%

5-X-4-nitrobenzaldehydes

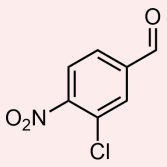

19
ee = 41.4%

39
ee = 4.5%

40
ee = 43.3%

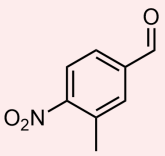

41
ee = 48.7%

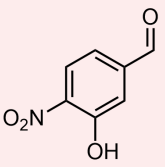

42
ee = 0%

Benzaldehydes **24** and **33** were synthesised.

Introducing a hydroxyl group (**25** and **42**) instead of a chloro group resulted in a very large drop in ee. This was even the case for the 5-X-2-nitrobenzaldehyde substitution pattern, which had previously tolerated the most diverse range of functional groups. Unlike all other tested functionalities, the hydroxyl group can participate in strong hydrogen bonding interactions, acting as either a donor or acceptor. In the absence of a hydroxyl group, any hydrogen bonding interaction from the RAI-MOF functionalities – such as the hydroxy group on the chiral linker, which was previously shown to be critical for stereocontrol (**section 3.2.1**) – is expected to occur *via* the aldehyde oxygen. This is because the aldehyde oxygen typically represents the strongest hydrogen bond acceptor within the substrate. However, the presence of a hydroxyl group is likely to compete with the aldehyde for accepting hydrogen bonds directed from the RAI catalyst, thereby reducing the enantioselectivity.

Boronic acid functionalisation (benzaldehyde **28**) promoted unwanted side reactions and thus was not further explored.

Overall, it could be shown that the RAI-MUF-77 catalyst tolerated various substrate functionalities and yielded similarly high ee values for substrates of comparable sizes and electronic effects. The highest |ee| values were observed for benzaldehydes **21**, **23** and **22** with 78.1%, 81.8% and 82.4% respectively. All three highest performing benzaldehydes were based on the same substitution pattern of 5-X-2-nitrobenzaldehydes with the second substituent *para* to the nitro group and *meta* to the aldehyde.

Lastly, the effect of introducing a third substituent on the benzaldehyde on the ee was explored (**Table 3.7**). The three benzaldehydes tested were all based on 5-X-2-nitrobenzaldehyde with one substituent *para* to the nitro group and *meta* to the aldehyde. Functionalisation with a third substituent at different positions relative to the aldehyde, nitro group or the other substituent, either with the same functionality (**43**) or with a different functional group (**44** and **46**) was performed. This consistently produced the same outcome: the ee of the triple-functionalised nitrobenzaldehyde was close to the comparable higher-performing double-functionalised benzaldehyde. For example, benzaldehyde **46** is a combination of the derivatives **12** and **21** that give 54.5% and 78.1% ee respectively. However, the ee for **46** is most similar to the ee of **21** rather than **12**. It is worth noting that this observation was made for less strongly interacting halo functional groups and may not hold for more influential groups like NO_2 or OH.

Table 3.7 Summary of the measured ee values for the Henry reactions of triple functionalised benzaldehydes with nitromethane. Each benzaldehyde features a nitro group and two additional substituents. The doubly functionalised benzaldehydes showing the same substituents are shown for comparison.

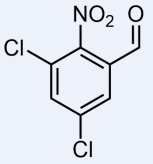 **43** ee = 74.5%	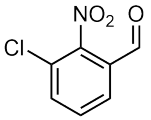 **13** ee = 61.2%	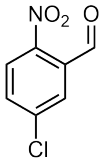 **11** ee = 77.1%
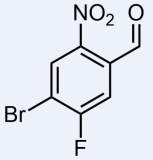 **44** ee = 55.2%	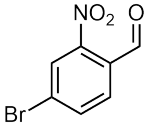 **45** ee = 34.7%	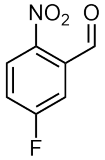 **20** ee = 56.7%
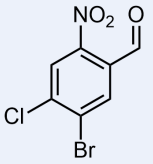 **46** ee = 76.2%	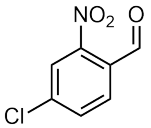 **12** ee = 54.5%	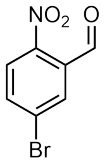 **21** ee = 78.1%

Overall, the experiments highlighted the large variation in ee that was delivered by the benzaldehyde substrate. Functionalisation of the benzaldehyde with a nitro group was necessary to achieve a reaction, and the position of the nitro group relative to the aldehyde around the ring had a significant impact on the ee. Additional substituents either increased or decreased the enantioselectivity depending on their position relative to the nitro group and the aldehyde. Additionally, the identity of the substituents was crucial, with a combination of steric and electronic effects likely responsible for differences in ee between various substituents. Initial experiments also indicated that if two substituents are present on a nitrobenzaldehyde, the ee of the higher-performing single-substituted benzaldehyde is generally maintained.

Overall, these experiments suggested that as long as the additional functional groups do not participate in strong hydrogen bonding (donating or accepting) their effect on the ee is largely attributed to their position and size rather than just their electronic effects.

3.2.5 Catalyst linker: different guanidine catalysts

Within the RAI-MUF-77 frameworks, the guanidine group on the bpdc-gua linker catalyses the Henry reaction. Its high basicity (pK_a of guanidium cations ~ 12 - 14)[144] allows for the deprotonation of nitromethane (pK_a ~ 10.2),[180] initiating the reaction. Additionally, the resulting guanidinium cation shows remarkable hydrogen bonding capacities.[74, 148, 211] This enables the guanidine catalyst to function as a hydrogen bond donor and interact with reaction substrates even after protonation. As such, modifications of the guanidine catalyst linker have the potential to not only influence its activity, by changing its basicity, but also its capacity to engage in hydrogen bonding. The goal of this section was to explore several variations of the bpdc-gua linker to assess their impact.

3.2.5.1 Methylated guanidine catalyst

Methylation of guanidine catalysts is known to have a major impact on their activity and selectivity.[212] This suggested that introducing methyl groups to the guanidine moiety of bpdc-gua has the potential to alter its catalytic activity, while likely not compromising its ability to be incorporated in the MUF-77 framework. The catalyst linker, H_2bpdc-gua$(Me)_2$, was designed and successfully synthesised (**Scheme 3.1**). The amino group of Me_2bpdc-NH_2 was condensed with N,N′-dimethylurea in the presence of phosphorus oxychloride to form Me_2bpdc-gua$(Me)_2$. This was inspired by related literature.[213] Subsequently, Me_2bpdc-gua$(Me)_2$ was converted to H_2bpdc-gua$(Me)_2$ through ester hydrolysis under standard conditions.

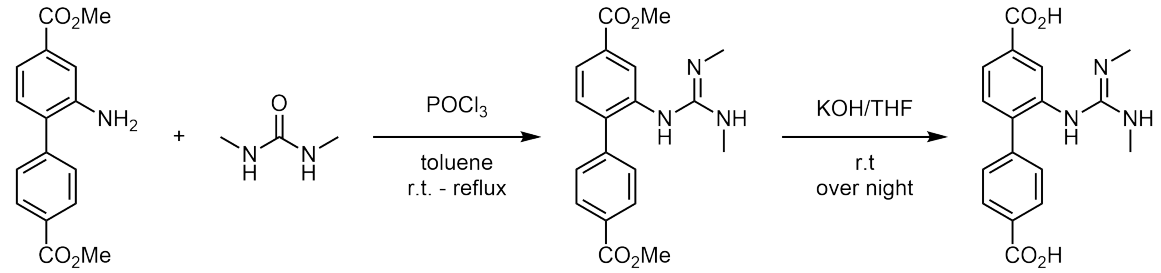

Scheme 3.1 Reaction scheme for the synthesis of the methylated guanidine catalyst linker H_2bpdc-gua$(Me)_2$.

Following the successful synthesis of H_2bpdc-gua$(Me)_2$, its compatibility with MUF-77 synthesis conditions (**step 2** of the screening procedure outlined in **Chapter 2**) had to be verified. Additionally, it was necessary to assess whether the methylated guanidine moiety retained catalytic activity for the Henry reaction (**step 3** of the screening procedure in **Chapter 2**). To address both aspects, the achiral MUF-77 catalyst,

[$Zn_4O(hmtt)_{1.33}(bpdc\text{-}gua(Me)_2)_{0.5}(bdc)_{0.5}$], was synthesised using unfunctionalised H_2bdc and the small truxene H_3hmtt under standard MUF-77 synthesis conditions. PXRD and NMR analysis of a digested MOF sample confirmed successful MOF formation. Pleasingly, its catalytic activity was also confirmed by conducting the standard Henry reaction of 2-chloro-5-nitrobenzaldehyde with nitromethane in 1,4-dioxane, producing a racemic product mixture. These results validated the use of the catalyst linker for assessment in the RAI MUF-77 catalysis.

The RAI catalyst, MUF-77_gua_^{5}N_21, was synthesised (**Figure 3.9**) and its structure confirmed by PXRD and NMR analysis of a digested MOF sample. Subsequently, the catalyst was tested for the Henry reaction of various functionalised benzaldehydes with nitromethane in 1,4-dioxane (**Figure 3.8**). The measured ee values (**Table 3.8**) are compared to those obtained with MUF-77_gua_^{5}N_10 (**Figure 3.7 A**), featuring the non-methylated bpdc-gua catalyst.

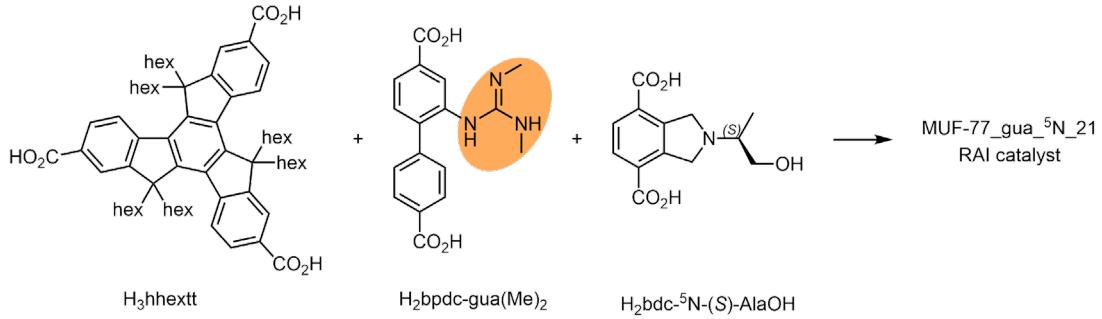

Figure 3.9 Schematic diagram showing the synthesis of MUF-77_gua_^{5}N_21 using H_3hhextt, H_2bpdc-gua(Me)$_2$ and H_2bdc-^{5}N-(*S*)-AlaOH. The MOF formula is [$Zn_4O(hhextt)_{1.33}(bpdc\text{-}gua(Me)_2)_{0.5}(bdc\text{-}^5N\text{-}(S)\text{-}AlaOH)_{0.5}$].

MUF-77_gua_^{5}N_21 produced lower ee values than MUF-77_gua_^{5}N_10. All 5-X-2-nitrobenzaldehyde derivatives (*ortho*-nitrobenzaldehyde with a second substituent *para* to the NO_2-group and *meta* to the aldehyde) showed a consistent reduction in ee of ~16-18% (**Table 3.8**, row 1-4). The 3-nitrobenzaldehydes and 4-nitrobenzaldehyde were proportionally slightly stronger affected by the catalyst methylation with reductions in ee of up to 30% observed (**Table 3.8** row 5-8). Additionally, as expected, the *para*-nitrobenzaldehyde showed the lowest enantioselectivity (**Table 3.8** row 8). Overall, similar ee trends across the differently functionalised benzaldehydes were observed when compared to the non-methylated catalyst, MUF-77_gua_^{5}N_10.

The results showed that methylation of the guanidine moiety led to a consistent reduction in enantioselectivity of the RAI-MUF-77 catalyst, while the substrate-dependent ee trends were retained. This supported the previously observed ee trends for the Henry reaction of functionalised benzaldehydes catalysed by the RAI-MUF-77 catalyst featuring the non-methylated guanidine moiety.

Table 3.8 Measured |ee| values for the Henry reaction of functionalised benzaldehydes with nitromethane, catalysed by MUF-77_gua_^{5}N_21 and MUF-77_gua_^{5}N_10.

	MUF-77_gua_^{5}N_21 (bpdc-gua(Me)$_2$)	**MUF-77_gua_^{5}N_10** (bpdc-gua)
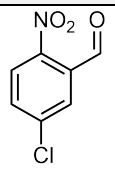	61.1%	77.1%
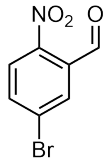	60.3%	78.1%
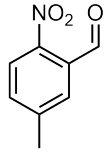	66.1%	82.4%
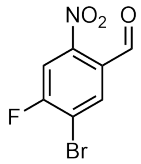	62.2%	78.2%
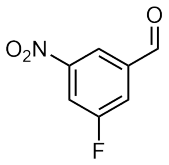	21.1%	37.0%
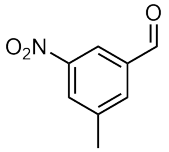	49.8%	71.4%
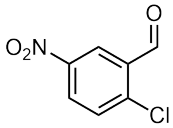	34.1%	64.4%
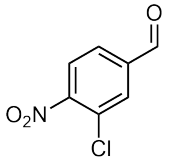	14.1%	41.4%

3.2.5.2 Symmetrical guanidine catalyst

An alternative strategy to modify the guanidine catalyst was to make the linker symmetrical. In the guanidine catalyst linker, H_2bpdc-gua, the guanidine moiety is attached to one of the two aromatic rings, making the linker non-symmetrical. To achieve symmetry, designs were explored that connect the two phenyl rings *via* a bridging connection with the guanidine group being attached in the middle. The previously discussed secondary amine catalyst linker H_2bpdc-^{7}N-H (**Chapter 2.2.1**) was identified as a feasible platform for this linker design.

Accordingly, the symmetrical catalyst linker H_2bpdc-^{7}N-gua was designed and successfully synthesised (**Scheme 3.2**). The first step was the addition of the Boc-protected guanidine group onto the secondary amine of Me_2bpdc-^{7}N-H, to generate Me_2bpdc-^{7}N-gua-Boc_2. Next, the Boc-protection groups were removed *via* acidic cleavage to obtain Me_2bpdc-^{7}N-gua. Subsequently, Me_2bpdc-^{7}N-gua was converted to H_2bpdc-^{7}N-gua *via* basic ester hydrolysis under standard conditions.

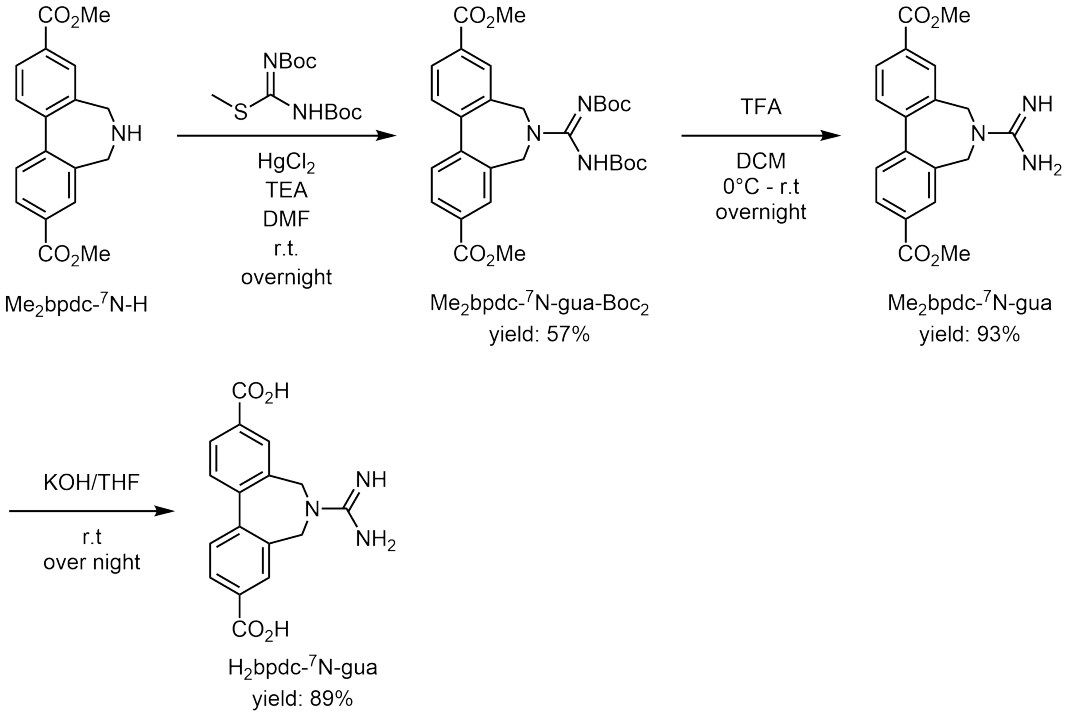

Scheme 3.2 Reaction scheme for the synthesis of the symmetrical guanidine catalyst linker H_2bpdc ^{7}N-gua.

As with all previously developed catalysts linkers, it was necessary to confirm that the newly synthesised linker was compatible with the MUF-77 synthesis conditions and that the guanidine moiety had retained its catalytic activity for the Henry reaction following the structural modification. To address both points, the achiral MUF-77 catalyst, $[Zn_4O(hmtt)_{1.33}(bpdc\text{-}^7N\text{-}gua)_{0.5}(bdc)_{0.5}]$, was synthesised using the unfunctionalised H_2bdc and the truxene H_3hmtt under standard MUF-77 synthesis conditions. PXRD and NMR analysis of a digested MOF sample confirmed successful MOF formation. Additionally, as expected, its

catalytic activity could be confirmed by conducting the Henry reaction of 2-chloro-5-nitrobenzaldehyde with nitromethane in 1,4-dioxane as a reference. These results validated the use of the catalyst linker for assessment in the RAI MUF-77 catalysis.

The RAI catalyst, MUF-77_gua_^{5}N_22, was synthesised (**Figure 3.10**) and its structure confirmed by PXRD and NMR analysis of a digested MOF sample. Subsequently, the catalyst was tested for the Henry reaction of various functionalised benzaldehydes with nitromethane in 1,4-dioxane (**Figure 3.8**). The measured ee values (**Table 3.9**) were compared to those obtained with MUF-77_gua_^{5}N_10 (**Figure 3.7 A**), featuring the non-cyclic bpdc-gua catalyst.

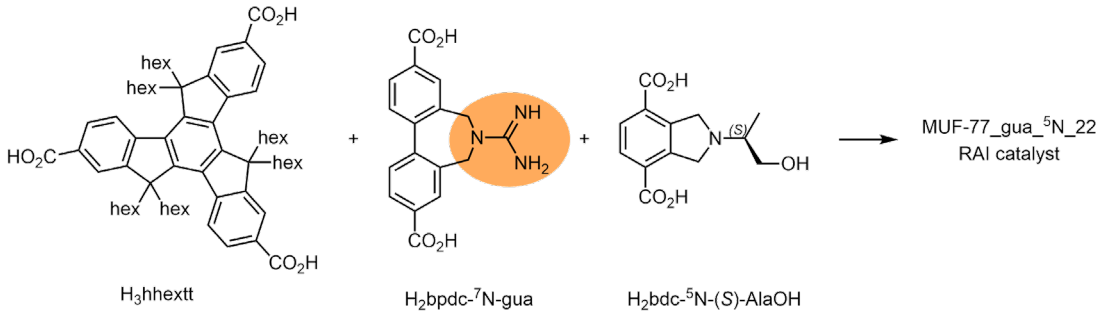

Figure 3.10 Schematic diagram showing the synthesis of MUF 77_gua_^{5}N_22 using H_3hhextt, H_2bpdc-^{7}N-gua and H_2bdc-^{5}N-(*S*)-AlaOH. The MOF formula is $[Zn_4O(hhextt)_{1.33}(bpdc\text{-}^{7}N\text{-}gua)_{0.5}(bdc\text{-}^{5}N\text{-}(S)\text{-}AlaOH)_{0.5}]$.

Across all tested benzaldehydes MUF-77_gua_^{5}N_22 yielded significantly lower ee values compared to MUF-77_gua_^{5}N_10. The highest ee observed was 27.5% for 5-methyl-2-nitrobenzaldehyde, representing a reduction of approximately 55% points from the 82.4% achieved with MUF-77_gua_^{5}N_10. The other benzaldehydes showed similarly large reductions in ee.

The pronounced decrease in ee showed that this specific catalyst linker modification had a detrimental effect on the enantioselectivity of the respective RAI catalyst. This is likely due to the catalyst linker adopting a different spatial orientation within the pore caused by the change in linker geometry. It remains unknown whether this is due to the linker being symmetrical, or rather because the guanidine group is located one carbon spacer further from the bpdc backbone and thus extends further into the pore.

Table 3.9 Measured |ee| values for the Henry reaction of functionalised benzaldehydes with nitromethane, catalysed by MUF-77_gua_^{5}N_22 and MUF-77_gua_^{5}N_10.

	MUF-77_gua_^{5}N_22 (bpdc-^{7}N-gua)	**MUF-77_gua_^{5}N_10** (bpdc-gua)
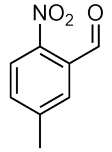	27.5%	82.4%
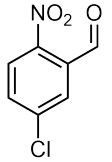	25.2%	77.1%
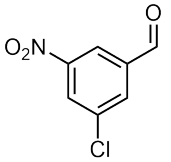	17.0%	75.4%
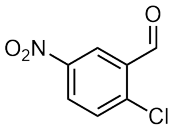	12.1%	64.4%
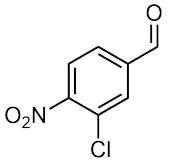	1.1%	41.4%

3.2.6 A linker with chiral groups on both sides

As seen in the exploration of the 15 different H_2bdc-^{5}N-chiral linkers, discussed in **section 3.2.1**, the size and nature of the chiral functionality plays a crucial role in achieving enantioselectivity. A fundamental requirement for the efficient transfer of chiral information is for the catalyst moiety and the chiral group to occupy the same pore and be directed toward one another. This is enabled by the small pores of MUF-77. However, the chiral linkers are able to rotate around their long axes so the chiral group may also be directed elsewhere. This rotation will be dynamic and, broadly speaking, there are four possibilities:

(i) Both the catalyst and the chiral moiety point into the same pore (**Figure 3.11 A)** blue spere). Transfer of stereochemical information is possible, as required by the RAI concept.

(ii) Only the catalyst moiety points into the small pore (**Figure 3.11 A)** red sphere). A racemic product is produced.

(iii) Only the chiral moiety points into the small pore. No reaction is observed.

(iv) Neither the catalyst nor the chiral moiety points into the small pore.

Pore environment (i) represents the core of the RAI concept and (iii) and (iv) do not lower the enantioselectivity as no product is formed. However, pore environment (ii) would produce a racemic product mixture and thus lower the overall enantioselectivity of the catalyst. Eliminating the possibility of pore environment (ii) could therefore enhance the observed enantioselectivity. This can be accomplished through double-functionalisation of the chiral linker (**Figure 3.12**), which means that *all* small pores that contain a catalytic linker also contain a chiral linker (**Figure 3.11 B**).

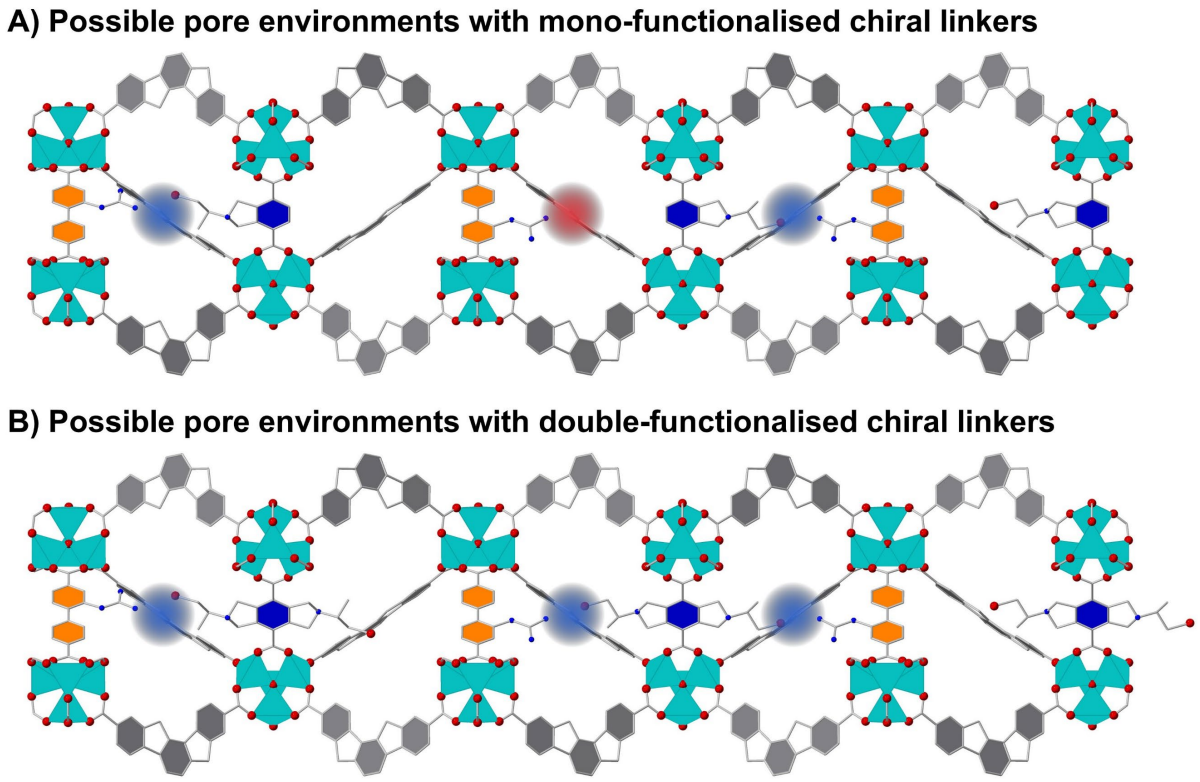

Figure 3.11 A) Possible small pore environments in MUF-77 when using mono-functionalised or **B)** double-functionalised chiral linkers. The pores that contain only a catalyst moiety are highlighted by a red sphere, while pores that contain both a catalyst and a chiral moiety are highlighted by a blue sphere. The front-facing truxenes are not shown for clarity.

Accordingly, the symmetrical, double-functionalised chiral linker H_2bdc-2x-^{5}N-(*S*)-AlaOH was designed inspired by the high-performing linker, H_2bdc-^{5}N-(*S*)-AlaOH (**Figure 3.12**).

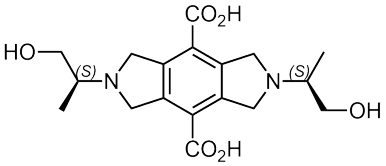

Figure 3.12 Depiction of the symmetrical, double-functionalised chiral linker H_2bdc-2x-^{5}N-(*S*)-AlaOH.

It was anticipated that the synthesis of H_2bdc-2x-^{5}N-(*S*)-AlaOH could be achieved following the established procedures for the mono-functionalised linkers, using the precursor needed for double functionalisation, backbone 3 (**Scheme 3.3**). Thus, the synthesis of

backbone 3 was attempted using the reaction conditions previously established for backbone 2 (conditions labelled with numbers). However, most conditions had to be either slightly adjusted or a completely different route was used (**Scheme 3.3**, conditions labelled with letters). The initial cyanation step was successfully completed by employing a higher boiling solvent at elevated temperatures over an extended reaction time. Conversion of the resulting nitrile to the corresponding acid could not be achieved under standard basic conditions and was instead accomplished *via* the primary amide. Likewise, esterification of the acid failed under typical acidic conditions, but was ultimately successful through formation of the acyl chloride using oxalyl chloride and catalytic DMF. Bromination proceeded under standard conditions with *N*-bromosuccinimide (NBS) and azobisisobutyronitrile (AIBN) but delivered reduced yields compared to the mono-functionalised analogue.

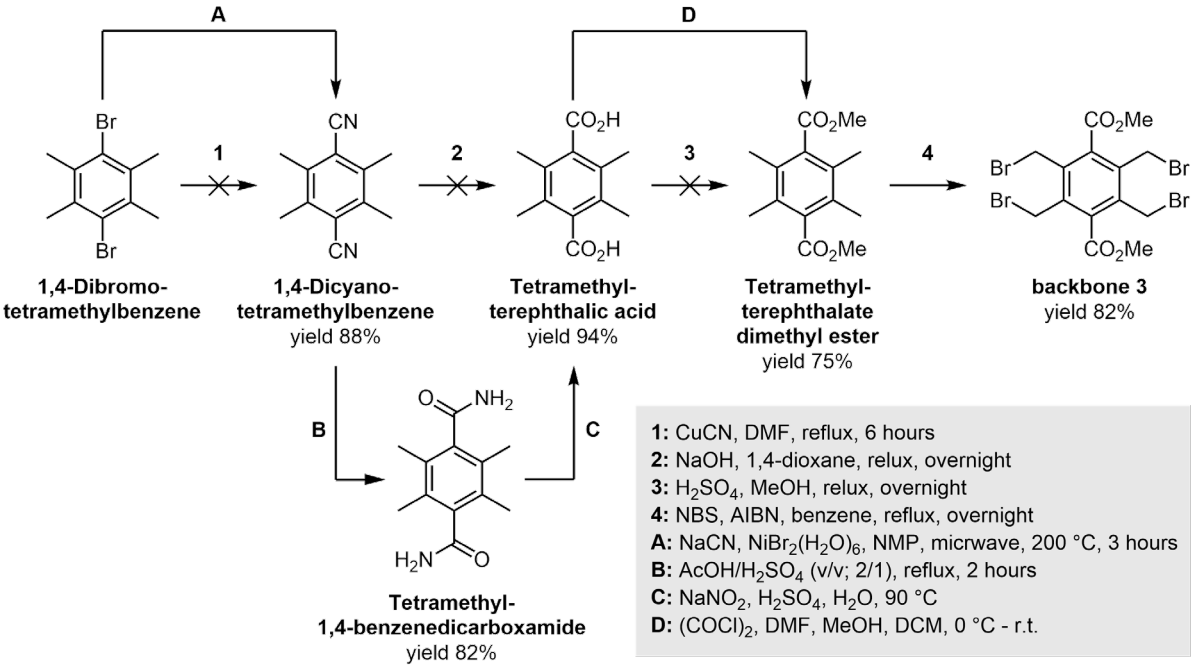

Scheme 3.3 Reaction scheme for the attempted and successful synthesis of backbone 3.

After successful synthesis of backbone 3, the synthesis of Me_2bdc-2x-^{5}N-(*S*)-AlaOH was attempted. Following the previously established procedures for the mono-functionalised linkers (**Figure 3.13**, conditions 1 and 3) no product formation could be achieved. The crude ^{1}H NMR spectrum showed no methyl ester signals, suggesting basic ester hydrolysis had occured. Modified procedures that omitted base (**Figure 3.13**, conditions 2 and 4) or attempting an alternative method inspired by Kreher *et al.*[214] (**Figure 3.13**, condition 5) also failed. However, for all conditions backbone 3 was fully consumed within five hours (judged by TLC), with no desired product formed. The product mixtures displayed unexpectedly high polarity and required highly polar TLC conditions (9.0% MeOH, 90% THF, and 1.0% TEA), compared to those used for the purification of Me_2bdc-^{5}N-(*S*)-AlaOH (10% cyclohexane, 89% EtOAc, and 1% TEA). Preparative TLC allowed isolation of the major product, which showed a strong

HRMS signal at 404.2177 (m/z) (**Figure 3.22**). The ^{1}H NMR revealed two distinct CH_3-signals in a 1:2 ratio, consistent with the methyl groups of alaninol, while no signals corresponding to the methyl ester protecting groups were present (**Figure 3.21**). An explanation that aligns with these observations is the formation of an unwanted side product as depicted in **Figure 3.13**. Two alaninol molecules attach to one side of backbone 3 through nucleophilic substitution at the methyl ester carbonyls rather than exclusively at the alkyl bromide groups. The proposed structure of the side product is supported by both the observed HRMS (**Figure 3.22**) and ^{1}H NMR spectra (**Figure 3.21**).

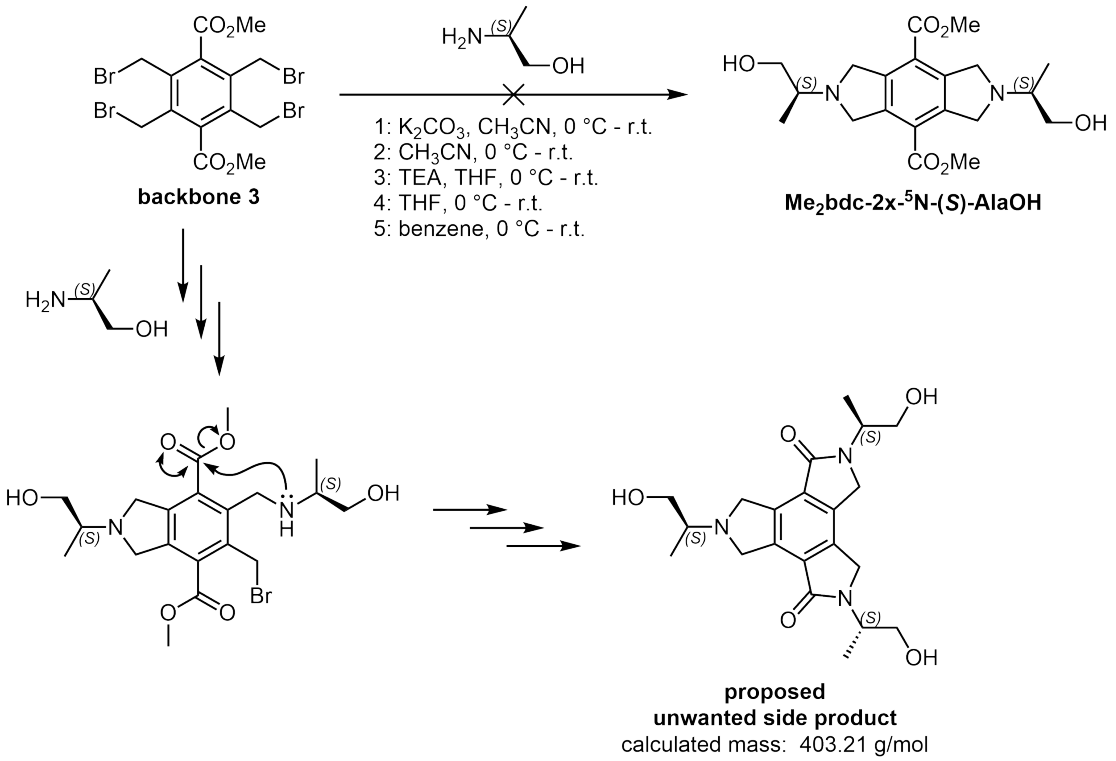

Figure 3.13 Reaction of backbone 3 with alaninol forms an unwanted side-product rather than the desired Me_2bdc-2x-^{5}N-(*S*)-AlaOH.

To avoid this unwanted side reaction, it was opted to change to *tert*-butyl esters for protection of the acids. Backbone 4 was synthesised using the modified conditions developed for backbone 3 (**Section 3.4.1.2**). *t*Bu_2bdc-2x-^{5}N-(*S*)-AlaOH was successfully obtained by reaction with alaninol (**Figure 3.14**). Notably, *t*Bu_2bdc-2x-^{5}N-(*S*)-AlaOH crystallised from the reaction mixture as large block-shaped crystals, and its identity was confirmed by SCXRD (**Figure 3.14**) alongside ^{1}H NMR spectroscopy, ^{13}C NMR spectroscopy, and HRMS. Subsequently, *t*Bu_2bdc-2x-^{5}N-(*S*)-AlaOH was converted to H_2bdc-2x-^{5}N-(*S*)-AlaOH under standard conditions.

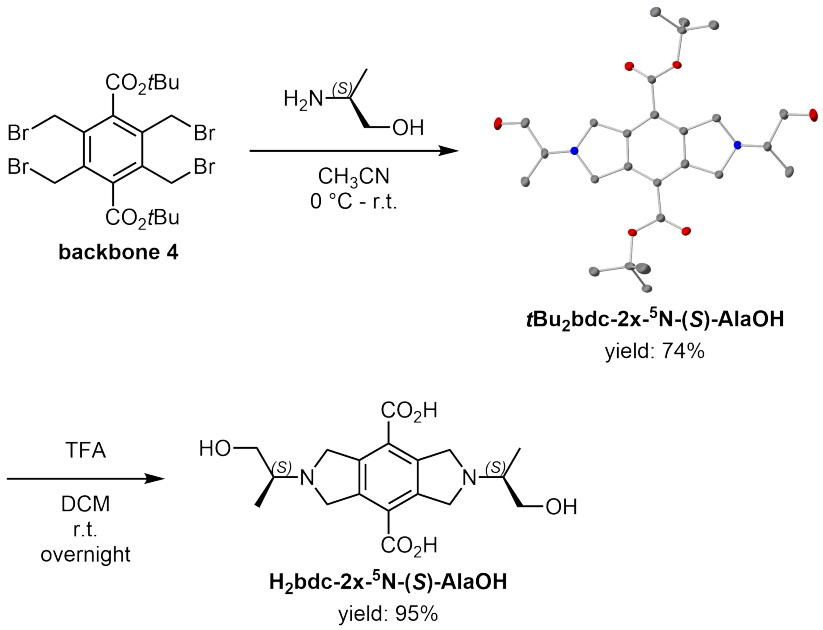

Figure 3.14 Reaction scheme for the synthesis of the double-functionalised chiral linker H_2bdc-2x-^{5}N-(*S*)-AlaOH. The linker precursor, *t*Bu$_2$bdc-2x-^{5}N-(*S*)-AlaOH is shown as the obtained SCXRD structure. The hydrogens are emitted for clarity. C = grey, O = red, N = blue.

The chiral linker H_2bdc-2x-^{5}N-(*S*)-AlaOH was successfully integrated into MUF-77 together with H_2bpdc-gua and H_3hhextt to create the RAI catalyst, MUF-77_gua_^{5}N_23 (**Figure 3.15**). The identity and successful formation of the MOF was confirmed by PXRD and ^{1}H NMR spectroscopic analysis of a digested MOF sample.

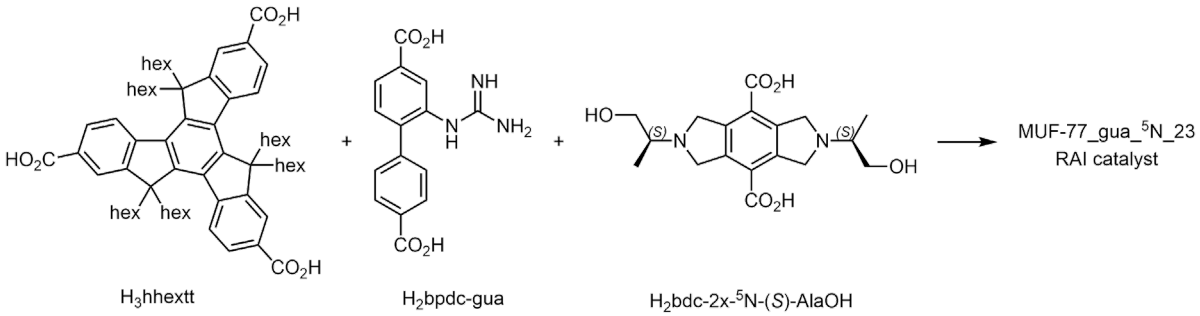

Figure 3.15 Schematic diagram showing the synthesis of MUF 77_gua_^{5}N_23 using H_3hhextt, H_2bpdc-gua and H_2bdc-2x-^{5}N-(*S*)-AlaOH. The MOF formula is $[Zn_4O(hhextt)_{1.33}(bpdc\text{-}gua)_{0.5}(bdc\text{-}2x\text{-}^5N\text{-}(S)\text{-}AlaOH)_{0.5}]$.

The Henry reactions of selected benzaldehydes with nitromethane in 1,4-dioxane (**Figure 3.8**) were catalysed by MUF-77_gua_^{5}N_23 (**Figure 3.15**), and the resulting ee values were compared with those obtained using MUF-77_gua_^{5}N_10 (**Figure 3.7 A**), the analogous mono-functionalised RAI catalyst. The catalysis results showed that the enantioselectivity of the catalyst featuring the double-functionalised chiral linker was consistently lower than its mono-functionalised counterpart (**Table 3.10**). This was unexpected, as the double-functionalisation removes the possibility of only a catalyst moiety being present within the small pores and thus theoretically should yield higher ee values. A potential rationale for this

observation is that the additional steric bulk introduced on the opposing side of the linker lowers its rotational freedom, thereby reducing its ability to adopt an optimal orientation for interacting with the reaction substrates at the catalytic site. Furthermore, a second reaction substrate could simultaneously interact with the chiral linker from the adjacent small pore, which may interfere with the precise alignment required for effective asymmetric induction.

Table 3.10 Measured |ee| values for the Henry reaction of functionalised benzaldehydes with nitromethane, catalysed by MUF-77_gua_^{5}N_23 and MUF-77_gua_^{5}N_10. The RAI-MUF-77 catalysts are represented by their respective chiral linkers.

	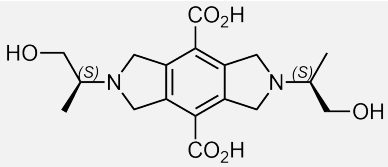	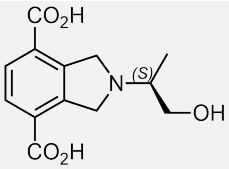
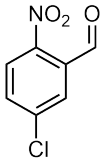	51.4%	77.1%
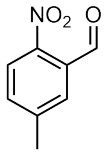	52.1%	82.4%
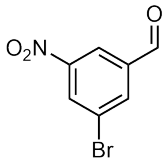	35.1%	77.3%
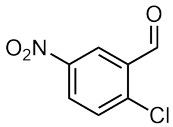	25.5%	64.4%

In summary, the synthetic procedure to obtain double-functionalised bdc-2x-^{5}N-chiral linkers was developed and a representative chiral linker could successfully be synthesised and integrated into the MUF-77 structure. However, it did not produce the same level of enantioselectivity as the respective mono-functionalised chiral linker. Consequently, no further linkers based on this design principle were pursued.

3.2.7 Reaction conditions: temperature, ratio and concentration

This section had two goals:

(i) To explore the influence of the reaction temperature on the enantioselectivity of the MUF-77_gua_^{5}N catalysts.

(ii) To evaluate the influence of the ratio of reaction substrates and their overall concentration on the ee.

MUF-77_gua_^{5}N_10 was chosen for this set of experiments (**Figure 3.7 A**). The reaction of 5-methyl-2-nitrobenzaldehyde with nitromethane in 1,4-dioxane was selected as representative Henry reaction (**Figure 3.16**).

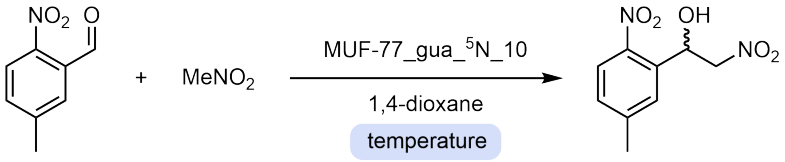

Figure 3.16 Henry reaction of 5-methyl-2-nitrobenzaldehyde with nitromethane in 1,4-dioxane.

3.2.7.1 Influence of the reaction temperature on the enantioselectivity of the RAI-MOF catalysts

It is well established in the field of asymmetric catalysis that lower reaction temperatures often enhance enantioselectivity.[95, 203] To assess whether this principle holds true for the RAI concept, the influence of temperature on enantioselectivity was systematically investigated. Three samples from the same MUF-77_gua_^{5}N_10 synthesis batch were used to catalyse the same Henry reaction at three different temperatures (**Table 3.11**). The reactions at 20 °C and 60 °C were performed using dry baths for temperature control, while the reaction at 4 °C was performed in a refrigerator.

As expected, the ee of the reaction at 20 °C matched the ee so far obtained for reactions at room temperature. The reaction at 60 °C showed a significantly lower ee of 51.7%, while a noticeable increase to 84.6% was observed for the reaction at 4 °C. This confirmed that the reaction temperature is an important factor influencing the enantioselectivity of the catalysts with lower temperatures being beneficial.

Table 3.11 Measured |ee| values for the Henry reaction of 5-methyl-2-nitrobenzaldehyde with nitromethane in 1,4-dioxane, catalysed by three samples from the same MOF synthesis batch of MUF-77_gua_^{5}N_10 at different temperatures.

temperature	|ee|
4 °C	84.6%
20 °C	82.2%
60 °C	51.7%

It is worth noting that the melting point of 1,4-dioxane is 11.8 °C[215] and thus the Henry stock solution containing both reaction substrates froze at 4 °C. However, in the presence of the MOF crystals the catalysis reaction solution remained liquid. Further decreasing the temperature to 0 °C by cooling in an ice/water slurry resulted in freezing of the reaction mixture.

3.2.7.2 Effect of the ratio of reaction substrates and their overall concentration on the ee

Until now, all reactions were performed using the same standard concentrations and ratios of functionalised benzaldehydes and nitromethane. The functionalised benzaldehydes were the limiting reagents with a concentration of 4.0×10^{-2} M and the nitromethane was introduced in a large excess as 50 equivalents with a concentration of 2.0 M. Overall the ratio of the two substrates was 1:50. Those values have been used as the standard so far as they yielded fast and often quantitative reactions of the limiting reagent and allowed good signal to noise ratio in the HPLC analysis with only injecting a low amount of sample.

Yet, the overall concentration and the ratio between the two reaction substrates is expected to have some influence on the performance of the catalyst and the outcome of the reaction. To test this presumption, six Henry reaction stock solutions were prepared, in which either the substrate concentration was varied while keeping their ratio constant, or the ratio of the two reagents was changed, which requires that the concentration of at least one substrate was also changed. The measured |ee| values are listed in **Table 3.12**. The conversion of each reaction was judged qualitatively to get a rough feel for how those changes affect the overall catalyst performance.

Table 3.12 Measured |ee| values and qualitatively assessed conversion for the Henry reaction of 5-methyl-2-nitrobenzaldehyde with nitromethane in 1,4-dioxane catalysed by MUF-77_gua_^{5}N_10. The concentration and ratio of the reaction substrate is stated.

#	benzaldehyde	nitromethane	ratio	|ee|	conversion
1	4.0×10^{-2} M	2.0 M	1:50	83.1%	quantitative
2	8.0×10^{-2} M	4.0 M	1:50	71.0%	trace
3	2.0×10^{-2} M	1.0 M	1:50	84.2%	good
4	4.0×10^{-3} M	0.2 M	1:50	84.8%	good
5	4.0×10^{-2} M	4.0×10^{-2} M	1:1	83.0%	trace
6	4.0×10^{-2} M	0.4 M	1:10	82.9%	low
7	4.0×10^{-2} M	10 M	1:250	-	no reaction

Row 1 in **Table 3.12** provides the benchmark ee for this MOF synthesis batch under previously established standard conditions, serving as the reference for comparison. Keeping the ratio of the reaction substrates constant but increasing their overall concentration (row 2 in **Table 3.12**) resulted in a decrease the ee, while simultaneously suppressing the reaction to only a trace amount of conversion. The drop in conversion could be explained by overcrowding of the MOF pores due to the high amount of benzaldehyde and/or the higher concentration of nitromethane, which has already been shown to negatively influence the conversion (**section 3.2.3**). The decrease in ee might be attributed to a likely lower amount of 1,4-dioxane present in the MOF pores during the reaction, caused by the higher overall substrate concentration. In contrast, reducing the concentration of the reaction substrates (row 3 and 4 in **Table 3.12**) led to improved enantioselectivity while maintaining good conversions. Reducing the benzaldehyde to nitromethane ratio to 1:10 and 1:1 while keeping the benzaldehyde concentration constant (row 5 and 6 in **Table 3.12**), did not result in any significant changes in the ee but did reduce the conversion. Increasing the ratio to 1:250 (row 7 in **Table 3.12**) completely prevented the reaction. This was consistent with the observation made in **section 3.2.3**, where attempting a Henry reaction in pure nitromethane did not yield any reaction product.

In summary, the total concentration of reactants has a more pronounced effect on enantioselectivity, with lower concentrations favouring higher ee values. The reaction substrate ratio has no beneficial impact on ee but influences the conversion.

3.2.8 Effect of additives

Minor variations in reaction conditions can significantly impact the enantioselectivity of asymmetric catalysts. One strategy to utilise this is the use of additives: non-catalytic, substances that themselves are not consumed during the reaction but enhance reaction efficiency and/or enantioselectivity, often by stabilising key reaction intermediates.[125, 216, 217] Common additives include acid/bases, water, aromatics, alcohols and even salts.[125, 216, 217]

The goal for this section was to explore the effect of additives on the performance of the MUF-77_gua_^{5}N catalysts for the Henry reaction. MUF-77_gua_^{5}N_10 was chosen for this set of experiments (**Figure 3.7**). The reaction of 5-methyl-2-nitrobenzaldehyde with nitromethane in 1,4-dioxane was selected as the representative Henry reaction (**Figure 3.16**). Standard concentration and ratios were used.

Table 3.13 Measured |ee| values for the Henry reaction of 5-methyl-2-nitrobenzaldehyde with nitromethane in 1,4-dioxane, catalysed by MUF-77_gua_^{5}N_10 in the presence of 0.6 eq. of different additives in respect to the benzaldehyde.

Additive	Features and additional comments	|ee|
None	Reference sample for comparison of MOF synthesis batch.	83.5%
Water	Good hydrogen bond donor and acceptor. Can be protonated/ deprotonated.	83.2%
Methanol	Hydrogen bond donor and acceptor.	83.3%
Phenol	Hydrogen bond donor and acceptor.	83.1%
Benzoic acid	Weakly acidic (pK_a = 4.2).	83.7%
Acetic acid	Weakly acidic (pK_a = 4.8).	84.0%
Pyridine	Weakly basic (pK_b = 8.8).	86.6%

The additives are added at 0.6 equivalents with respect to the benzaldehyde in the catalysis solution (**Table 3.13**). To eliminate any batch-to-batch variation, all experiments were performed with the MOF crystals form one synthesis batch. One catalysis was performed without the addition of an additive to have a baseline ee of the MOF synthesis batch for comparability. Of all the additives that were tested, only pyridine showed an appreciable influence on the enantioselectivity. Here, the ee rose to 86.6%.

Encouraged by these promising results, further experiments were performed using varying concentrations of pyridine and its derivatives (**Table 3.14**). At 6.0×10^{-2} equivalents, pyridine produced only a minor increase in ee of 0.5%, showing that trace levels are insufficient to cause a significant effect. Increasing the concentration to 6.0 equivalents did not improve the ee beyond the improvement observed with 0.6 equivalents. This suggests a saturation effect in which more additive does not translate to increased catalytic benefit beyond a critical threshold. It is worth noting that no background reaction was observed even at 6.0 equivalents of pyridine, confirming that pyridine alone does not catalyse the Henry reaction. The different methyl pyridines generally had a positive effect with respect to the system without an additive but less so compared to the unfunctionalised pyridine.

Table 3.14 Measured |ee| values for the Henry reaction of 5-methyl-2-nitrobenzaldehyde with nitromethane in 1,4-dioxane, catalysed by MUF-77_gua_^{5}N_10 in the presence of different pyridine derivatives as additives.

Additive	**Additive ratio to benzaldehyde.**	**|ee|**
No additive	Reference sample for comparison of MOF synthesis batch.	83.4%
Pyridine	6.0×10^{-2} eq.	83.9%
Pyridine	0.6 eq.	86.6%
Pyridine	6.0 eq.	86.6%
2-Methylpyridine	0.6 eq.	83.9%
3-Methylpyridine	0.6 eq.	85.3%
4-Methylpyridine	0.6 eq.	85.3%

3.2.9 Combining all insights to achieve the highest ee

The overarching goal for this chapter was to maximise the ee achieved using the RAI concept by building on the lessons of **Chapter 2** and optimising all variables known to influence the enantioselectivity of the RAI-MUF-77 catalysts.

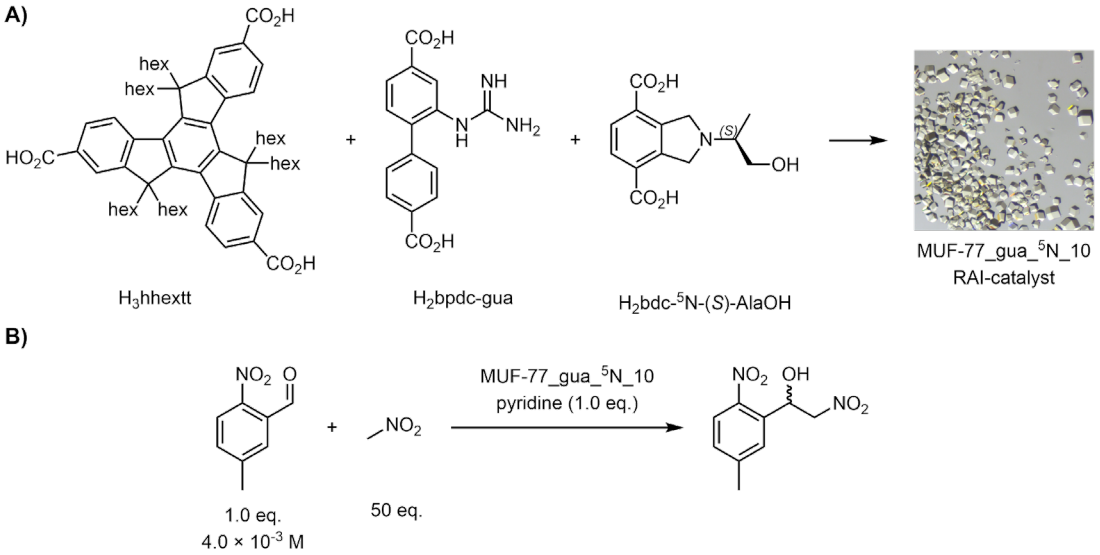

Figure 3.17 A) Reaction scheme for the synthesis of the RAI-MOF catalyst MUF-77_gua_^{5}N_10 and **B)** the Henry reaction of 5-methyl-2-nitrobenzaldehyde with nitromethane in 1,4-dioxane. The reaction conditions are stated.

An experiment was performed using the full set of parameters that had been optimised individually:

- The catalyst MUF-77_gua_^{5}N_10 was selected, as it had previously shown the highest enantioselectivity among all tested RAI-MUF-77 catalysts. MUF-77_gua_^{5}N_10 is built up from the catalyst linker bpdc-gua, the chiral linker bdc-^{5}N-(*S*)-AlaOH and the tritopic truxene hhextt.
- The Henry reaction of 5-methyl-2-nitrobenzaldehyde with nitromethane was chosen as this aldehyde had consistently yielded the highest ee.
- A substrate ratio of 1:50 was used to achieve good conversion, while the concentration of the limiting reagent (benzaldehyde) was reduced from 4.0×10^{-2} M to 4.0×10^{-3} M. As the solvent, 1,4-dioxane was used.
- Pyridine was added to the stock solution as an additive with 1.0 equivalents with respect to the benzaldehyde.
- The catalysis was performed at 4 °C.

Pleasingly, this combination of all optimised parameters delivered an ee of 87.8%, the highest enantioselectivity observed to date (**Figure 3.18**).

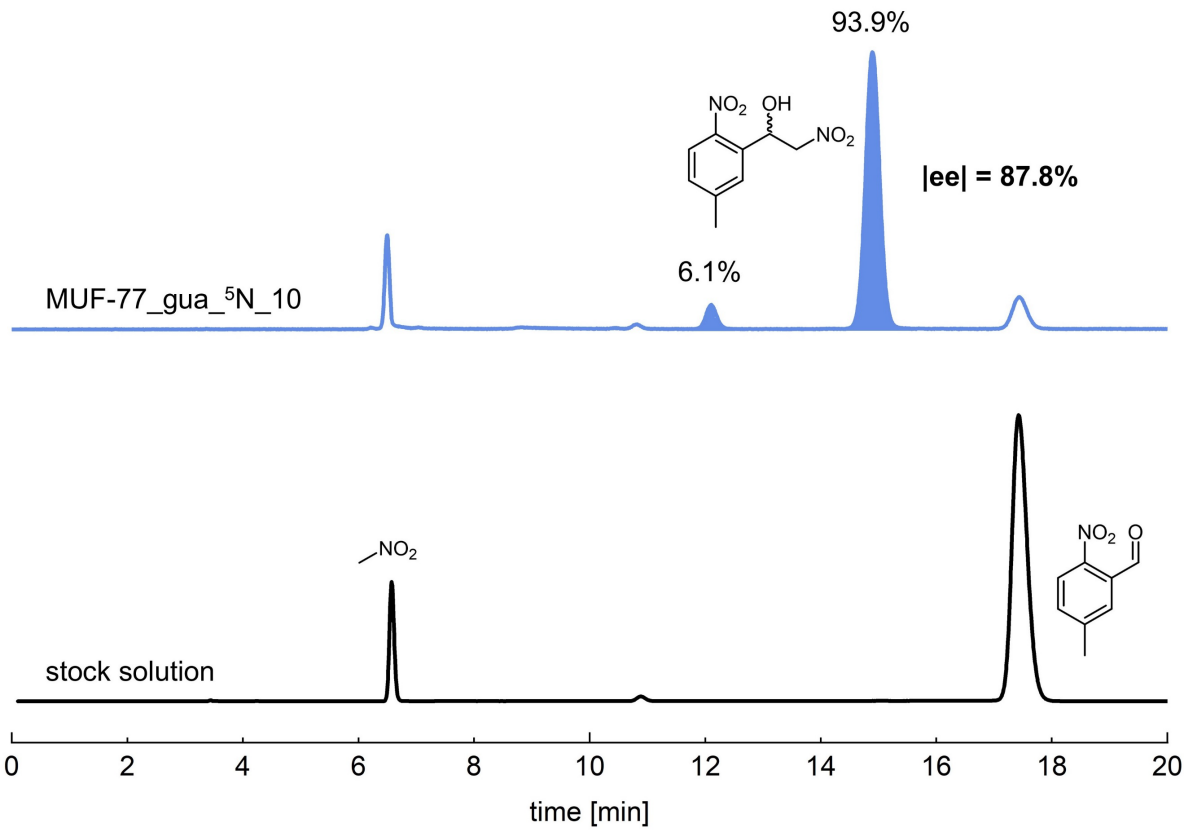

Figure 3.18 HPLC trace of the Henry reaction of 5-methyl-2-nitrobenzaldehyde with nitromethane in 1,4-dioxane, catalysed by MUF-77_gua_^{5}N_10 at 4 °C in the presence of 1.0 equivalents of pyridine as an additive.

3.2.10 Probing for false optima and validation of observed trends

As discussed in **section 3.1**, the 'one variable at a time' approach toward RAI optimisation assumes the variables are independent of one another. However, if the individual variables are strongly correlated, false maxima may be reached and higher peaks in the ee landscape overlooked. To assess this risk, a variety of '2D' experiments were performed, simultaneously changing two variables that were not maxima when examined individually. These variables were selected on the basis of their ability to cause a significant *variation* in the ee. That is, while they did not produce the maximum ee, the variation in ee showed that they were important. Parameters that showed low variation, such as the reaction conditions (temperature and ratios), were excluded from these experiments under the assumption that they inherently have little influence on the ee.

Correlation between chiral linkers and benzaldehydes

In this set of experiments, the potential correlation between the identity of the chiral linker and the functionality of the benzaldehyde substrate was explored. For this, RAI-MUF-77 catalysts featuring different chiral linkers were used to catalyse a variety of Henry reactions using different functionalised benzaldehydes (**Table 3.15**). To extract any correlation between these two variables, all other factors were kept constant. All MUF-77_gua_^{5}N catalysts were synthesised using H_3hhextt, and H_2bpdc-gua. All Henry reactions were performed using the standard concentration and ratios (1:50), in 1,4-dioxane without the addition of an additive and at room temperature.

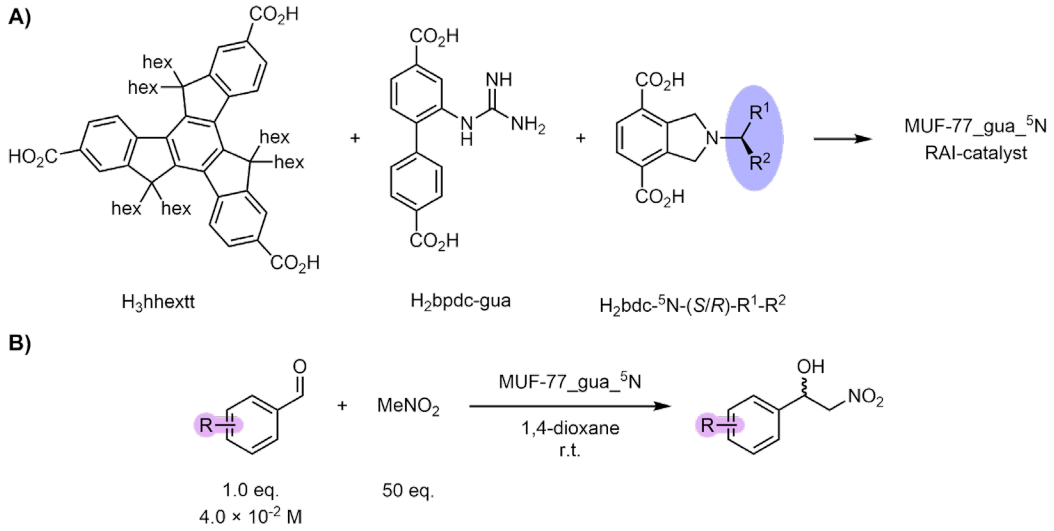

Figure 3.19 A) Reaction scheme showing the MUF-77_gua_^{5}N catalyst synthesis using H_3hhextt, H_2bpdc-gua and H_2bdc-^{5}N-chiral linkers. **B)** Henry reaction of various benzaldehydes with nitromethane in 1,4-dioxane.

The obtained |ee| values are listed in **Table 3.15**. Pleasingly, no new maximum was observed above that identified by the linear screening of individual variables one at a time. The highest ee was still observed for MUF-77_gua_^{5}N_10 catalysing the Henry reaction of 5-methyl-2-nitrobenzadehyde with nitromethane. This supports the assumption that no strong correlation between the chiral linker identity and benzaldehyde functionality exists.

A second important observation is that similar trends in ee were seen across the tested 2D array. The benzaldehydes that yielded higher ee with MUF-77_gua_^{5}N_10, the highest-performing RAI catalyst, also produced higher ee values with the lower performing RAI-MUF-77 catalysts. Consistent trends could also be seen between the different chiral linker functionalities. Across all tested benzaldehydes, the order of highest to lowest enantioselectivity was: MUF-77_gua_^{5}N_10 > 9 > 4 > 8 > 13.

These observations highlight the low correlation between the individual variables.

Table 3.15 Measured |ee| values for the Henry reactions of various benzaldehydes with nitromethane catalysed by different MUF-77_gua_^{5}N catalysts. The functional groups of the chiral linkers are shown. 'N.D.' = not determined.

Chiral group / Substrate	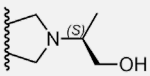 MUF-77_ gua_^{5}N_10	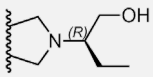 MUF-77_ gua_^{5}N_9	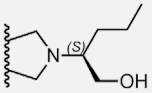 MUF-77_ gua_^{5}N_8	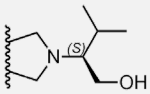 MUF-77_ gua_^{5}N_4	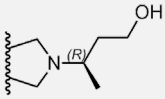 MUF-77_ gua_^{5}N_13
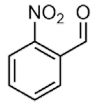	41.8%	35.3%	10.2%	21.3%	2.0%
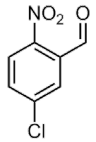	77.1%	N.D.	44.3%	65.2%	25.3%
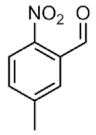	82.4%	73.6%	51.5%	66.8%	32.9%
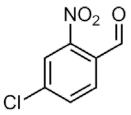	54.5%	N.D.	N.D.	19.4%	3.1%
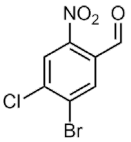	76.2%	N.D.	46.3%	60.1%	25.8%
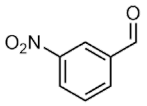	34.4%	22.9%	N.D.	12.9%	7.2%
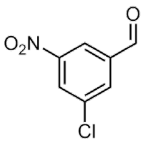	75.4%	N.D.	N.D.	62.2%	32.0%
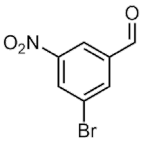	77.3%	65.6%	39.4%	58.9%	N.D.
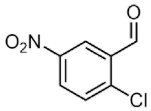	64.4%	54.4%	16.2%	38.3%	16.2%
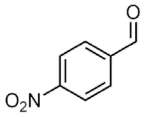	16.8%	N.D.	N.D.	2.5%	1.0%
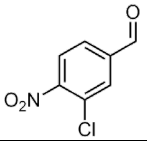	41.4%	N.D.	5.0%	25.3%	N.D.

Correlation between solvent and benzaldehydes

This set of experiments investigated the potential correlation between the reaction solvent and different benzaldehyde substrates (**Figure 3.20**). To ensure comparability, all reactions were performed with the same RAI-MUF-77 catalyst, MUF-77_gua_^{5}N_10 (**Figure 3.7 A**), under standard conditions (4.0×10^{-2} M benzaldehyde; 50 equivalent nitromethane), without additives, and at room temperature.

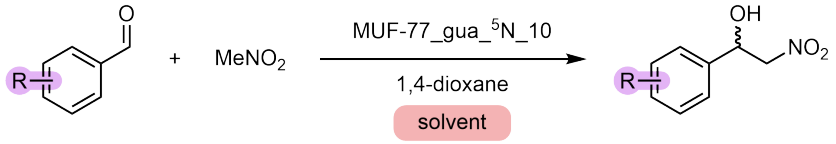

Figure 3.20 Henry reaction of functionalised benzaldehydes with nitromethane in various solvents, catalysed by MUF-77_gua_^{5}N_10. The two variables that are explored are highlighted.

The second and third highest-performing solvents from previous experiments (**section 3.2.3**), 1,3-dioxane and 2-methylhydrofuran, were selected for this study due to them facilitating promising ee values. As shown in **Table 3.16**, both solvents produced lower ee values for all tested benzaldehydes compared to 1,4-dioxane, with 1,3-dioxane outperforming 2-methylhydrofuran. Importantly, the relative enantioselectivity trends across the different benzaldehydes were largely preserved across the tested solvents. A single outlier was observed: the Henry reaction of 5-methyl-2-nitrobenzaldehyde in 2-methylhydrofuran produced an unexpectedly high ee of 64.5% - approximately 10% higher than anticipated based on the previously observed trends among the benzaldehydes - closely matching the 67.0% achieved in 1,3-dioxane.

These results indicate a small correlation between the benzaldehyde functionality and solvent identity in affecting the enantioselectivity of the Henry reaction. However, no new maximum in ee was observed. This supports the conclusion that the previously identified optimum conditions represent global, rather than local, optima.

Table 3.16 Measured |ee| values for the Henry reactions of different benzaldehydes with nitromethane in various solvents, catalysed by MUF-77_gua_^{5}N_10. 'N.D.' = not determined.

	 1,4-dioxane	 1,3-dioxane	 2-methylhydrofuran
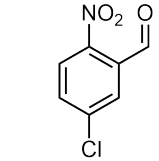	77.1%	64.8%	51.9%
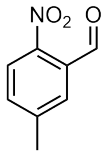	82.4%	67.0%	64.5%
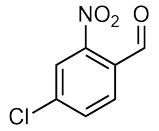	54.5%	25.6%	N.D.
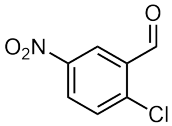	64.4%	53.2%	43.8%
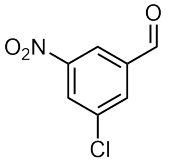	75.4%	59.0%	N.D.
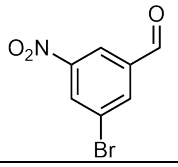	77.3%	60.2%	44.3%

3.3 Conclusion

A comprehensive assessment of the RAI catalyst system identified in **Chapter 2** – MUF-77_gua_^{5}N catalysts for the Henry reaction of functionalised benzaldehydes with nitromethane – has been performed. An approach of iteratively making one change at a time was used to systematically explore the variables that influence the enantioselectivity with the goal of achieving the highest possible ee. Major milestones of this chapter include:

(i) Expansion of the H_2bdc-^{5}N-chiral linker family from four to 15 members. The presence of a hydroxy group at the correct distance to both the linker backbone and the chiral centre was found to be essential for high enantioselectivity. Additionally, sterically less demanding linkers produced higher ee values. The bdc-^{5}N-(*S*)-AlaOH linker delivered the best results.

(ii) Variation in the enantioselectivity upon changing the alkyl chain attached to the truxene backbone was investigated. The hexyl-functionalised truxene, H_3hhextt, showed the best performance in terms of ee. Modelling based on SCXRD data suggested that hexyl chains optimally fill the large framework pores and direct the reaction to the small pores. The catalytic *and* chiral linkers can simultaneously interact with the reaction substrates in these small pores.

(iii) 28 distinct solvents were tested for the Henry reaction. Cyclic ethers emerged as the best solvents with 1,4-dioxane facilitating the highest enantioselectivity.

(iv) The effect of the benzaldehyde substrate on the enantioselectivity of the catalysis was explored by testing 46 distinct benzaldehydes. Functionalisation with a nitro group was essential for achieving activity, and its position with respect to the aldehyde influenced the enantioselectivity. Addition of a second substituent onto the benzaldehyde had the potential to decrease or increase the enantioselectivity drastically, depending on its identity and position in respect to the other functionalities. 5-Methyl-2-nitrobenzaldehyde produced the highest ee.

(v) Two additional guanidine catalysts were synthesised to explore the effect of variations of the catalyst moiety on the enantioselectivity of the RAI-MUF-77 catalysts. H_2bpdc-gua(Me)$_2$ is similar to H_2bpdc-gua but with a methylated guanidine moiety. H_2bpdc-^{7}N-gua featured a symmetrical backbone building on a bridge connecting the two phenyl rings of bpdc. Both modified guanidine catalysts produced lower enantioselectivities showing that these modifications reduced the efficiency of transfer of stereochemical information during catalysis.

(vi) A doubly-functionalised chiral linker H_2bdc-2x-^{5}N-(*S*)-AlaOH was designed and synthesised. RAI-MUF-77 catalysis featuring this linker resulted in lower ee values compared to the respective mono-functionalised counterpart.

(vii) The effect of the reaction conditions, temperature, substrate ratios and concentrations on the ee was explored. Lower temperature and substrate concentrations facilitated higher enantioselectivity of the RAI-MUF-77 catalysts. The ratio of the reaction substrates only had a minor effect on the enantioselectivity but influenced the conversion of the limiting substrate.

(viii) The effect of the addition of additives to the catalysis reaction mixture was explored. Out of nine tested additives, pyridine and its derivatives increased enantioselectivity, with pyridine itself showing the highest improvement.

(ix) All optimised variables were combined to achieve an optimised ee. The catalyst MUF-77_gua_^{5}N_10, consisting of H_3hhextt, H_2bpdc-gua and H_2bdc-^{5}N-(*S*)-AlaOH, was used to catalyse the Henry reaction of 5-methyl-2-nitrobenzaldehyde with nitromethane in 1,4 dioxane at 4 °C with the addition of 1.0 equivalents of pyridine. An |ee| of 87.8% was obtained, the highest achieved to date using the RAI concept.

(x) Additional experiments with high, mid and low performing variables were performed confirming that the optimised ee in (ix) was likely a global optimum. No higher performing system could be identified nor anything close. Additionally, the same ee trends were observed for lower-performing systems, indicating that the variables do not strongly correlate.

3.4 Experimental section

3.4.1 Linker synthesis

All H_2bdc-^{5}N-(*S*/*R*)-R^1-R^2 chiral linkers were synthesised according to the procedures described in **Chapter 2.4.2.4** (**Scheme 2.7**).

The truxene functionalised with heptyl chains, H_3hheptt, was synthesised following group established and reported procedures.[119]

All NMR and PXRD data for both the synthesised linkers and all MOFs are provided in the Appendix to **Chapter 3**.

3.4.1.1 Guanidine catalyst linkers

H_2bpdc-gua(Me)$_2$

The synthesis of H_2bpdc-gua(Me)$_2$ was performed as depicted in **Scheme 3.1**.

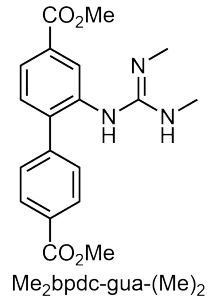

Me$_2$bpdc-gua-(Me)$_2$

The synthesis protocol for Me$_2$bpdc-gua(Me)$_2$ was inspired by a general procedure reported by Shalbaf et al.[213] N,N′-dimethylurea (223.6 mg, 2.5 mmol, 1.3 eq.) was suspended in dry toluene (12 mL) under an argon atmosphere. Under vigorous stirring, $POCl_3$ (622.8 mg, 4.1 mmol, 2.0 eq.) was added dropwise. The reaction mixture was stirred at room temperature overnight. A solution of Me$_2$bpdc-NH_2 (568.2 mg, 2.0 mmol, 1.0 eq.) in 4.0 mL dry toluene was then added, and the mixture was refluxed for 20 hours. After cooling, a viscous oil and a slightly cloudy solution formed. The solution was decanted, and water (20 mL) was added to the residual oil, forming a cloudy white/yellow solid. The pH was adjusted to 13 while stirring in an ice bath. The resulting basic suspension was extracted with DCM (2 × 30 mL). Removal of the organic phase under reduced pressure yielded Me$_2$bpdc-gua(Me)$_2$ as a white solid (110.8 mg, 311.8 µmol, 16% yield).

^{1}H NMR (500 MHz, $CDCl_3$) δ (ppm) 8.01 (d, *J* = 8.2 Hz, 2H), 7.67 (dd, *J* = 8.2, 1.3 Hz, 1H), 7.63 (d, *J* = 1.3 Hz, 1H), 7.59 (d, *J* = 8.2 Hz, 2H), 7.38 (d, *J* = 8.2 Hz, 1H), 3.91 (s, 3H), 3.89 (s, 3H), 3.72-3.71 (m, 2H), 2.65 (s, 3H), 2.64 (s, 3H). ^{13}C NMR (126 MHz, $CDCl_3$) δ (ppm) 167.28, 167.25, 151.93, 148.11, 144.92, 138.78, 130.81, 130.62, 129.18, 129.08, 128.54, 126.02, 123.24, 52.17, 28.61.

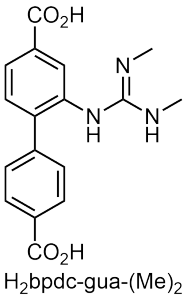

H_2bpdc-gua-$(Me)_2$

Me_2bpdc-gua$(Me)_2$ (101.2 mg, 284.8 μmol, 1.0 eq.) was dissolved in THF (2 mL), and a 1 M KOH solution (2 mL) was added. The reaction mixture was stirred at room temperature overnight, after which the THF was removed under reduced pressure. The aqueous phase was cooled to 0 °C and the pH was adjusted to 3.0 with dilute HCl, resulting in the formation of a slightly yellow precipitate. The solid was isolated by filtration, washed with water (2 × 5 mL) and dried under reduced pressure to yield H_2bpdc-gua$(Me)_2$ as a yellow powder (88.2 mg, 269.4 μmol, 95% yield).

^{1}H NMR (500 MHz, D_2O/NaOD) δ (ppm) 7.91 (d, J = 8.2 Hz, 2H), 7.63 (dd, J = 7.9, 1.4 Hz, 1H), 7.52 (d, J = 8.2 Hz, 2H), 7.46-7.45 (m, 2H), 2.51 (s, 6H). ^{13}C NMR (126 MHz, D_2O/NaOD) δ (ppm) 175.56, 175.53, 156.25, 145.95, 142.85, 138.14, 137.00, 134.67, 130.48, 128.53, 126.01, 123.56, 27.58. HRMS (FTMS + p ESI Full) calculated for $[M+H]^+$ $(C_{17}H_{18}N_3O_4)^+$ m/z 328.1292, found m/z 328.1289.

HMQC spectroscopy was used to confirm that the intense ^{13}C signal at 128.53 ppm corresponds to four individual carbons.

H_2bpdc-^{7}N-gua

The synthesis of H_2bpdc-^{7}N-gua was performed as depicted in **Scheme 3.2.**

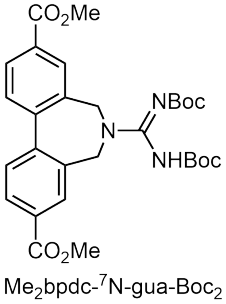

Me_2bpdc-^{7}N-gua-Boc_2

A suspension of Me_2bpdc-^{7}N-H (393.0 mg, 1.3 mmol, 1.0 eq.), 1,3-di-Boc-2-methylisothiourea (467.3 mg, 1.6 mmol, 1.3 eq.), TEA (550 μL) in dry DMF (13 mL) under an argon atmosphere was cooled to 0 °C, and then $HgCl_2$ (435.2 mg, 1.6 mmol, 1.3 eq.) was added to the stirring suspension. The mixture was kept at 0 °C for 30 min and then warmed up to room temperature overnight. The light-yellow mixture was poured into an ice/water slurry and extracted with CH_2Cl_2 (2 × 50 mL). The combined organic layer was washed with water (5 × 20 mL), dried over $MgSO_4$ and removed under reduced pressure. The crude product was purified using silica-gel column chromatography (cyclohexane/EtOAc gradient from 8:1 to 6:1). Me_2bpdc-^{7}N-gua-Boc_2 was obtained as a white solid (401.6 mg, 725.4 μmol, 57%)

^{1}H NMR (500 MHz, DMSO-*d6*) δ (ppm) 9.77 (s, 1H), 8.12 (d, J = 8.0 Hz, 2H), 8.10 (s, 2H), 7.80 (d, J = 8.0 Hz, 2H), 4.25 (brs, 4H), 3.89 (s, 6H), 1.44 (s, 9H), 1.39 (s, 9H). ^{13}C NMR (126 MHz, DMSO-*d6*) δ (ppm) 165.68, 159.60, 151.14, 149.85, 143.62, 133.97, 130.05, 129.69, 128.67, 80.34, 77.49, 52.33, 48.86, 27.99, 27.90. HRMS (FTMS + p ESI Full) calculated for $[M+H]^+$ $(C_{29}H_{36}N_3O_8)^+$ m/z 554.2497, found m/z 554.2492.

HMQC spectroscopy was used to identify the broad signal in the ^{13}C spectrum at 48.86 ppm corresponds to two carbons connected to the four protons associated with the broad singlet at 4.25 ppm in the ^{1}H NMR spectrum.

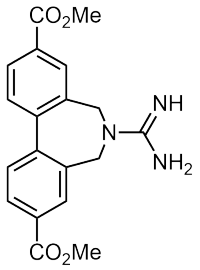

Me$_2$bpdc-^{7}N-gua

Me$_2$bpdc-^{7}N-gua-Boc$_2$ (102.3 mg, 184.8 µmol, 1.0 eq.) was dissolved in CH_2Cl_2 (2 mL), cooled to 0 °C, and TFA (1 mL) was added dropwise. The reaction mixture was allowed to warm to room temperature and stirred overnight. The mixture was then cooled to 0 °C, and saturated K_2CO_3 solution was added until no further gas formation was observed. The pH was adjusted to 8 using dilute HCl. The mixture was extracted with CH_2Cl_2 (3 × 10 mL). The combined organic phase was washed with water (1 × 10 mL), dried over $MgSO_4$. Removal of the solvent under reduced pressure yielded Me$_2$bpdc-^{7}N-gua as a yellow solid (61.0 mg, 172.6 µmol, 93% yield).

^{1}H NMR (500 MHz, DMSO-*d6*) δ (ppm) 8.22 (s, 2H), 8.16 (d, *J* = 8.0 Hz, 2H), 7.84 (d, *J* = 8.0 Hz, 2H), 7.68 (brs, 3H), 4.33 (s, 4H), 3.91 (s, 6H). ^{13}C NMR (126 MHz, DMSO-*d6*) δ (ppm) 165.63, 155.15, 143.41, 132.88, 130.73, 130.24, 130.10, 129.14, 52.42, 47.92. HRMS (FTMS + p ESI Full) calculated for $[M+H]^+$ $(C_{19}H_{20}N_3O_4)^+$ m/z 354.1448, found m/z 354.1443.

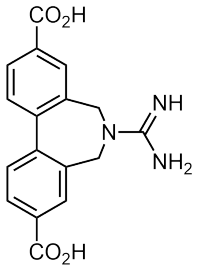

H$_2$bpdc-^{7}N-gua

Me$_2$bpdc-^{7}N-gua (61.0 mg, 172.6 µmol, 1.0 eq.) was dissolved in THF (2 mL), and a 1 M KOH solution (2 mL) was added. The reaction mixture was stirred at room temperature overnight, after which the THF was removed under reduced pressure. The aqueous phase was cooled to 0 °C and the pH was adjusted to 3.0 with dilute HCl, resulting in the formation of a precipitate. The solid was isolated by filtration, washed with water (2 × 5 mL) and dried under reduced pressure to yield H$_2$bpdc-^{7}N-gua as a white powder (49.8 mg, 153.1 µmol, 89% yield).

^{1}H NMR (500 MHz, DMSO-*d6*) δ (ppm) 13.26 (brs, 2H), 8.19 (s, 2H), 8.13 (d, *J* = 7.9 Hz, 2H), 7.86 (brs, 3H), 7.81 (d, *J* = 8.0 Hz, 2H), 4.34 (s, 4H). ^{13}C NMR (126 MHz, DMSO-*d6*) δ (ppm) 166.65, 155.29, 143.15, 132.64, 131.40, 130.87, 130.24, 128.96, 47.99. HRMS (FTMS + p ESI Full) calculated for $[M+H]^+$ $(C_{17}H_{16}N_3O_4)^+$ m/z 326.1135, found m/z 326.1130.

3.4.1.2 Backbones for double functionalised chiral linkers

The synthesis of backbone 3 and backbone 4 was performed as depicted in **Scheme 3.3**.

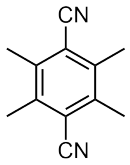

1,4-Dicyano-tetramethylbenzene

1,4-Dibromo-tetramethylbenzene (593.8 mg, 2.0 mmol, 1.0 eq.), sodium cyanide (596.3 mg, 12.2 mmol, 6.0 eq.) and $NiBr_2 \cdot 6H_2O$ (2.0 g, 6.1 mmol, 3.0 eq.) was weighed into a 15 mL microwave vial and suspended in NMP (4 mL). The suspension was heated in the microwave at 200°C for 3 hours. After cooling to room temperature, the reaction mixture was poured into an ice/water slurry (50 mL). The mixture was extracted with EtOAc (100 mL), resulting in the precipitation of a grey solid, which was removed by filtration. The organic phase was washed with water (5 × 25 mL) and dried over $MgSO_4$. Removal of the organic phase under reduced pressure yielded 1,4-dicyano-tetramethylbenzene as a white powder (331.0 mg, 1.8 mmol, 88%). The ^{1}H NMR spectrum agrees with literature data.[218]

^{1}H NMR (500 MHz, $CDCl_3$) δ (ppm) 2.49 (s, 12H). ^{13}C NMR (126 MHz, $CDCl_3$) δ (ppm) 138.61, 118.14, 116.99, 18.64.

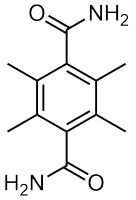

Tetramethyl-1,4-benzene-dicarboxamide

1,4-Dicyano-tetramethylbenzene was suspended in 7.5 mL of an AcOH/H_2SO_4 mixture (2/1; v/v) and refluxed at 120 °C for 2 hours. After cooling to room temperature, the dark solution was poured into an ice/water slurry (25 mL), which resulted in the precipitation of a grey solid. The solid was isolated by filtration, washed with water and dried to yield tetramethyl-1,4-benzenedicarboxamide as a beige solid (313.9 mg, 1.4 mmol, 82%). The ^{1}H NMR spectrum agrees with literature data.[219]

^{1}H NMR (500 MHz, DMSO-*d6*) δ (ppm) 7.68-7.46 (m, 4H), 2.12 (s, 12H). ^{13}C NMR (126 MHz, DMSO-*d6*) δ (ppm) 171.94, 139.11, 128.76, 16.35.

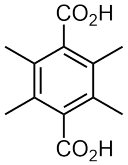

Tetramethyl-terephthalic acid

Tetramethyl-1,4-benzenedicarboxamide (313.9 mg, 1.4 mmol, 1.0 eq.) was suspended in an H_2SO_4/H_2O (2/1; v/v) mixture (7.5 mL) and the suspension was heated at 90 °C for four hours. $NaNO_2$ (1.0 g, 14.5 mmol, 10.2 eq.) was added in small increments over 2 hours. The reaction mixture was cooled down to room temperature and poured into an ice/water slurry (25 mL). The water phase was extracted with EtOAc (5 × 50 mL). The combined organic phase was removed under reduced pressure, yielding a yellow solid. The residue was re-dissolved in 1M NaOH aq. solution (15 mL) and 500 mg of activated charcoal was added. The suspension was stirred for three hours. The charcoal was removed by filtration. The filtrate was acidified

using concentrated HCl to pH < 1, resulting in the formation of a white solid. The solid was isolated by filtration, washed with excess of water and dried *in vacuo* to yield tetramethyl-terephthalic acid as a white solid (298.0 mg, 1.3 mmol, 94%). The ^{1}H NMR spectrum agrees with literature data.[218]

^{1}H NMR (500 MHz, D_2O/NaOD) δ (ppm) 2.14 (s, 12H). ^{13}C NMR (126 MHz, DMSO-*d6*) δ (ppm) 180.26, 140.37, 127.57, 16.12. HRMS (FTMS + p ESI Full) calculated for $[M]^-$ $(C_{12}H_{13}O_4)^-$ m/z 221.0808, found m/z 221.0816.

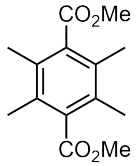

Tetramethyl-terephthalate dimethyl ester

Tetramethyl-terephthalic acid (80.0 mg, 360.0 µmol, 1.0 eq.) was suspended in dry CH_2Cl_2 (2.0 mL) and stirred at 0°C under an argon atmosphere. Oxalyl chloride (182.8 mg, 1.4 mmol, 4.0 eq.) and two drops of catalytic DMF solution (1 drop DMF in 0.5 ml dry CH_2Cl_2) were added to the cooled, stirring suspension. The suspension was allowed to warm up to room temperature. Over the next 45 minutes, the white solid gradually dissolved with slight gas formation. The reaction solution was cooled to 0 °C and dry methanol (2 mL) was added. The mixture was stirred at room temperature for two hours. CH_2Cl_2 (50 mL) was added and the organic phase was washed with water (3 × 15 mL) and dried over $MgSO_4$. The crude product was passed through a short plug of silica (CH_2Cl_2) to yield tetramethyl-terephthalate dimethyl ester as a white solid (67.5 mg, 269.7 µmol, 75%).

^{1}H NMR (500 MHz, $CDCl_3$) δ (ppm) 3.91 (s, 6H), 2.15 (s, 12H). ^{13}C NMR (126 MHz, $CDCl_3$) δ (ppm) 171.14, 136.17, 130.56, 52.19, 16.89.

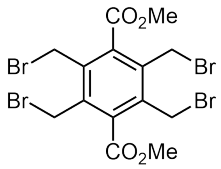

backbone 3

Tetramethyl-terephthalate dimethyl ester (67.5 mg, 269.7 µmol, 1.0 eq.), N-bromosuccinimide (NBS) (285.2 mg, 1.6 mmol, 5.9 eq.) and azobisisobutyronitrile (AIBN) (10.1 mg, 60.9 µmol, 0.2 eq.) were suspended in dry benzene (20 mL) under an argon atmosphere and the reaction mixture was refluxed at 95 °C overnight. The solvent was removed under reduced pressure and the residue was dissolved in CH_2Cl_2 (100 mL). The organic phase was washed with H_2O (3 × 20 mL), dried over $MgSO_4$, and the solvent was removed under reduced pressure to yield the crude product as a yellow oil. The crude product was purified by silica-gel chromatography (cyclohexane/CH_2Cl_2; 1/1) to yield backbone 3 as a white solid (124.5 mg, 220.0 µmol, 82%).

^{1}H NMR (500 MHz, $CDCl_3$) δ (ppm) 4.58 (s, 8H), 4.05 (s, 6H). ^{13}C NMR (126 MHz, $CDCl_3$) δ (ppm) 167.21, 137.98, 135.30, 53.10, 24.59.

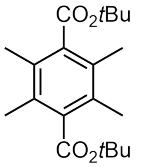

tetramethyl-terephthalate di-*tert*-butyl ester

Tetramethyl-terephthalic acid (216.0 mg, 971.9 µmol, 1.0 eq.) was suspended in dry CH_2Cl_2 (6.0 mL) and stirred at 0 °C under an argon atmosphere. Oxalyl chloride (493.4 mg, 3.9 mmol, 4.0 eq.) and two drops of catalytic DMF solution (1 drop DMF in 0.5 ml dry CH_2Cl_2) were added to the cooled, stirring suspension. The suspension was allowed to warm up to room temperature. Over the next 45 minutes, the white solid gradually dissolved with slight gas formation. The reaction solution was cooled to 0 °C and *tert*-butanol (2 mL) was added. The mixture was stirred at room temperature for two hours. CH_2Cl_2 (50 mL) was added, and the organic phase was washed with water (3 × 15 mL) and dried over $MgSO_4$. The crude product was passed through a short plug of silica (CH_2Cl_2) to yield tetramethyl-terephthalate di-*tert*-butyl ester as a white solid (152.6 mg, 456.3 µmol, 47%).

^{1}H NMR (500 MHz, $CDCl_3$) δ (ppm) 2.19 (s, 12H), 1.60 (s, 18H). ^{13}C NMR (126 MHz, $CDCl_3$) δ (ppm) 169.98, 136.97, 129.87, 82.00, 28.30, 16.40.

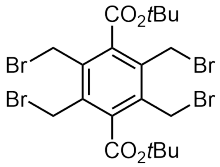

backbone 4

Tetramethyl-terephthalate dimethyl ester (152.6 mg, 456.3 µmol, 1.0 eq.), *N*-bromosuccinimide (NBS) (487.3 mg, 2.7 mmol, 6.0 eq.) and azobisisobutyronitrile (AIBN) (15.0 mg, 91.3 µmol, 0.2 eq.) were suspended in dry benzene (20 mL) under an argon atmosphere and the reaction mixture was refluxed at 95 °C overnight. The solvent was removed under reduced pressure and the residue was dissolved in CH_2Cl_2 (100 mL). The organic phase was washed with H_2O (3 × 20 mL), dried over $MgSO_4$, and the solvent was removed under reduced pressure to yield the crude product as a yellow oil. The crude product was purified by silica-gel chromatography (cyclohexane/CH_2Cl_2; 1/1) to yield backbone 3 as a white solid (152.6 mg, 234.8 µmol, 51%).

^{1}H NMR (500 MHz, $CDCl_3$) δ (ppm) 4.62 (s, 8H), 1.70 (s, 18H). ^{13}C NMR (126 MHz, $CDCl_3$) δ (ppm) 166.15, 139.14, 134.57, 85.24, 28.16, 24.82.

3.4.1.3 Double functionalised chiral linkers

Side product observed during Me$_2$bdc-2x-^{5}N-(*S*)-AlaOH synthesis

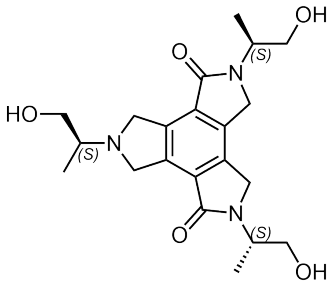

proposed side product

The synthesis described here was performed according to **Figure 3.13** condition 3. Backbone 3 (51.2 mg, 90.5 µmol, 1.0 eq.) was placed in a 4 mL vial, suspended in 2.0 mL dry acetonitrile and stirred at 0 °C. (*S*)-Alaninol (17.0 mg, 226.2 µmol, 2.5 eq.) was diluted in minimum amount of dry acetonitrile and added in three portions over five hours. Backbone 3 was fully consumed 10 minutes after the final addition of (*S*)-alaninol. The solvent was removed under reduced pressure to yield a yellow oil. Preparative TLC (9.5% MeOH, 90% THF, and 0.5% TEA) was used to isolate the main reaction product.

^{1}H NMR (400 MHz, $CDCl_3$) δ (ppm) 4.55-4.32 (m, 10H), 3.90 (dd, *J* = 11.5, 3.7 Hz, 2H), 3.81-3.77 (m, 2H), 3.72 (dd, *J* = 10.9, 4.6 Hz, 1H), 3.53 (dd, *J* = 10.9, 6.8 Hz, 1H), 3.10-3.05 (m, 1H), 1.36 (d, *J* = 7.0 Hz, 6H), 1.16 (d, *J* = 6.6 Hz, 3H). HRMS (FTMS + p ESI Full) calculated for $[M+H]^+$ $(C_{21}H_{30}N_3O_5)^+$ m/z 404.2180, found m/z 404.2177.

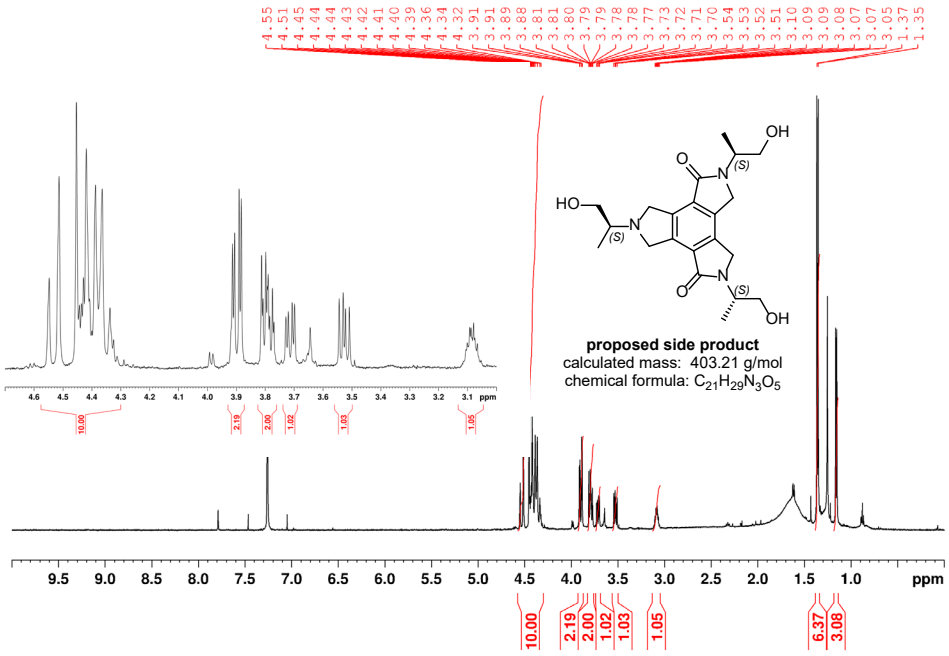

Figure 3.21 ^{1}H NMR spectrum of the side product observed during the synthesis attempt of Me$_2$bdc-2x-^{5}N-(*S*)-AlaOH in $CDCl_3$.

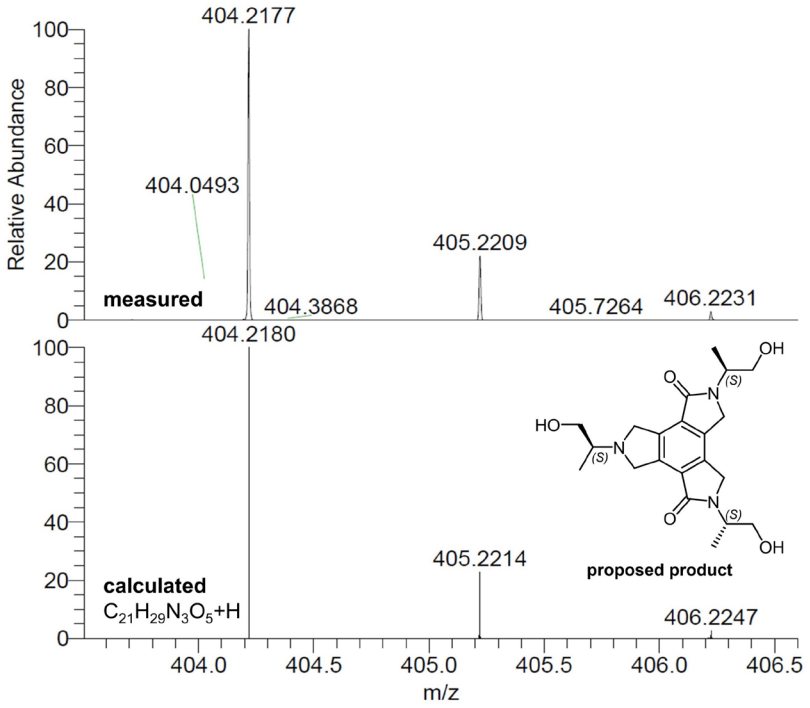

Figure 3.22 HRMS spectrum of side product observed during the synthesis attempt of Me_2bdc-2x-^{5}N-(*S*)-AlaOH and the calculated pattern based on the proposed structure.

H_2bdc-2x-^{5}N-(*S*)-AlaOH

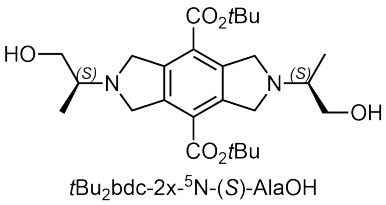

The synthesis was performed according to **Figure 3.14**. Backbone 4 (122.8 mg, 188.9 µmol, 1.0 eq.) was placed in a 4 mL vial, suspended in 3.0 mL dry acetonitrile and stirred at 0 °C. (*S*)-Alaninol (63.7 mg, 848.1 µmol, 4.4 eq.) was added in three portions over seven hours, and the reaction mixture was stirred for five hours during which time colourless block shaped crystals and a slightly beige supernatant formed. The crystals, which were pure product, were isolated by filtration and dried in vacuum. The filtrate was then removed under reduced pressure to yield a beige solid that was purified by silica-gel chromatography (89% EtOAc, 10% MeOH, 1% TEA) to yield *t*Bu_2bdc-2x-^{5}N-(*S*)-AlaOH as a white solid. The two product fractions were combined (66.4 mg, 139.3 µmol, 74% yield).

^{1}H NMR (400 MHz, $CDCl_3$) δ (ppm) 4.30 (d, *J* = 13.5 Hz, 4H), 4.24 (d, *J* = 13.5 Hz, 4H), 3.71 (dd, *J* = 10.4, 2.7 Hz, 2H), 3.49 (dd, *J* = 10.4, 6.6 Hz, 2H), 3.05-2.99 (m, 2H), 2.74 (brs, 2H), 1.59 (s, 18H), 1.17 (d, *J* = 6.5 Hz, 6H). ^{13}C NMR (126 MHz, $CDCl_3$) δ (ppm) 165.02, 142.13, 124.94, 82.48, 64.67, 58.13, 55.71, 28.44, 12.86. HRMS (FTMS + p ESI Full) calculated for $[M+H]^+$ $(C_{26}H_{41}N_2O_6)^+$ m/z 477.2959, found m/z 477.2948.

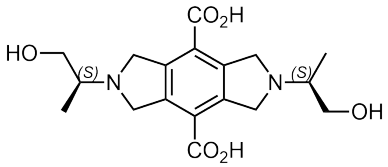

H_2bdc-2x-^{5}N-(*S*)-AlaOH

The synthesis was performed according to **Figure 3.14**. *t*Bu$_2$bdc-2x-^{5}N-(*S*)-AlaOH (24.1 mg, 50.6 µmol, 1.0 eq.) was dissolved in DCM (750 µL), cooled to 0 °C, and TFA (500 µL) was added dropwise. The reaction solution was allowed to warm to room temperature and stirred overnight. The solvent was removed under reduced pressure to yield a white solid. The solid was suspended in DCM, sonicated for 10 minutes, isolated *via* filtration, and dried under vacuum to yield H_2bdc-2x-^{5}N-(*S*)-AlaOH as a white solid (17.5 mg, 48.0 µmol, 95% yield).

^{1}H NMR (500 MHz, D_2O/NaOD) δ (ppm) 4.08 (s, 8H), 3.82 (dd, *J* = 11.3, 4.1 Hz, 2H), 3.55 (dd, *J* = 11.3, 6.7 Hz, 2H), 2.88-2.82 (m, 2H), 1.21 (d, *J* = 6.4 Hz, 6H). ^{13}C NMR (126 MHz, D_2O/NaOD) δ (ppm) 175.19, 136.84, 128.86, 64.33, 59.93, 55.91, 15.09. HRMS (FTMS + p ESI Full) calculated for $[M+H]^+$ $(C_{18}H_{25}N_2O_6)^+$ m/z 365.1707, found m/z 365.1703.

3.4.2 MOF synthesis

All MOFs discussed this chapter were synthesised following MOF synthesis method 3, as described in **Chapter 2.4.3**. The linker weights used for each MOF synthesis, are listed in **Table 3.17**. The linker ratios (truxene/bpdc/bdc) for each digested MOF sample are stated as determined by ^{1}H NMR. All ^{1}H NMR and PXRD data are available in the Appendix for **Chapter 3**.

Table 3.17 Linkers, weights and molar amounts used for the MOF synthesis of this work. The measured linker ratio of digested MOF according to NMR is stated.

MOF name code	truxene	H_2bpdc-R	H_2bdc-^{5}N-R	NMR ratio
MUF-77_gua_^{5}N_5	H_3hhextt 3.9 mg 4.0 µmol	-gua 1.4 mg 4.7 µmol	-(*S*)-CH_2OH-cycloHex 2.7 mg 8.1 µmol	1.33/ 0.5/ 0.5
MUF-77_gua_^{5}N_6	H_3hhextt 3.9 mg 4.0 µmol	-gua 1.4 mg 4.7 µmol	-(*S*)-CH_2OH-*t*Bu 2.8 mg 9.1 µmol	1.33/ 0.5/ 0.5
MUF-77_gua_^{5}N_7	H_3hhextt 3.9 mg 4.0 µmol	-gua 1.4 mg 4.7 µmol	-(*S*)-isoLeuOH 2.7 mg 8.8 µmol	1.33/ 0.5/ 0.5
MUF-77_gua_^{5}N_8	H_3hhextt 3.9 mg 4.0 µmol	-gua 1.4 mg 4.7 µmol	-(*S*)-CH_2OH-$(CH_2)_2CH_3$ 2.7 mg 9.2 µmol	1.33/ 0.5/ 0.5
MUF-77_gua_^{5}N_9	H_3hhextt 3.9 mg 4.0 µmol	-gua 1.4 mg 4.7 µmol	-(*R*)-CH_2OH-CH_2CH_3 2.6 mg 9.3 µmol	1.33/ 0.5/ 0.5
MUF-77_gua_^{5}N_10	H_3hhextt 3.9 mg 4.0 µmol	-gua 1.4 mg 4.7 µmol	-(*S*)-AlaOH 2.5 mg 9.4 µmol	1.33/ 0.5/ 0.5
MUF-77_gua_^{5}N_11	H_3hhextt 3.9 mg 4.0 µmol	-gua 1.4 mg 4.7 µmol	-(*R*)-CH_2CH_3-CH_3 2.4 mg 9.1 µmol	1.33/ 0.5/ 0.5
MUF-77_gua_^{5}N_12	H_3hhextt 3.9 mg 4.0 µmol	-gua 1.4 mg 4.7 µmol	-(*S*)-CH_2OCH_3-CH_3 2.5 mg 9.0 µmol	1.33/ 0.5/ 0.5
MUF-77_gua_^{5}N_13	H_3hhextt 3.9 mg 4.0 µmol	-gua 1.4 mg 4.7 µmol	-(*R*)-$(CH_2)_2$OH-CH_3 2.5 mg 9.0 µmol	1.33/ 0.5/ 0.5
MUF-77_gua_^{5}N_14	H_3hhextt 3.9 mg 4.0 µmol	-gua 1.4 mg 4.7 µmol	-CH_2CH-(*R*)-CH_3-OH 2.5 mg 9.0 µmol	1.33/ 0.5/ 0.5
MUF-77_gua_^{5}N_15	H_3hhextt 3.9 mg 4.0 µmol	-gua 1.4 mg 4.7 µmol	-(*R*)-ThrOH 2.4 mg 8.1 µmol	1.33/ 0.5/ 0.5
MUF-77_gua_^{5}N_16	H_3hmtt 2.2 mg 4.0 µmol	-gua 1.4 mg 4.7 µmol	-(*S*)-AlaOH 2.5 mg 9.4 µmol	1.33/ 0.5/ 0.5
MUF-77_gua_^{5}N_17	H_3hbtt 3.2 mg 4.0 µmol	-gua 1.4 mg 4.7 µmol	-(*S*)-AlaOH 2.5 mg 9.4 µmol	1.33/ 0.5/ 0.5
MUF-77_gua_^{5}N_18	H_3hptt 3.6 mg 4.0 µmol	-gua 1.4 mg 4.7 µmol	-(*S*)-AlaOH 2.5 mg 9.4 µmol	1.33/ 0.5/ 0.5
MUF-77_gua_^{5}N_19	H_3hheptt 4.2 mg 4.0 µmol	-gua 1.4 mg 4.7 µmol	-(*S*)-AlaOH 2.5 mg 9.4 µmol	1.33/ 0.5/ 0.5
MUF-77_gua_^{5}N_20	H_3hott 4.6 mg 4.0 µmol	-gua 1.4 mg 4.7 µmol	-(*S*)-AlaOH 2.5 mg 9.4 µmol	1.33/ 0.5/ 0.5
MUF-77_gua_^{5}N_21	H_3hhextt 3.9 mg 4.0 µmol	-gua(Me)$_2$ 1.6 mg 4.9 µmol	-(*S*)-AlaOH 2.5 mg 9.4 µmol	1.33/ 0.5/ 0.5
MUF-77_gua_^{5}N_22	H_3hhextt 3.9 mg 4.0 µmol	-^{7}N-gua 2.2 mg 6.8 µmol	-(*S*)-AlaOH 2.5 mg 9.4 µmol	1.33/ 0.5/ 0.5
MUF-77_gua_^{5}N_23	H_3hhextt 3.9 mg 4.0 µmol	-gua 1.4 mg 4.7 µmol	-2x-^{5}N-(*S*)-AlaOH 3.9 mg 10.7 µmol	1.33/ 0.5/ 0.5
$[Zn_4O(hmtt)_{1.33}(bpdc\text{-}gua(Me)_2)_{0.5}(bdc)_{0.5}]$	H_3hmtt 2.2 mg 4.0 µmol	-gua(Me)$_2$ 1.6 mg 4.9 µmol	-H 1.3 mg 8.0 µmol	1.33/ 0.5/ 0.5
$[Zn_4O(hmtt)_{1.33}(bpdc\text{-}^7N\text{-}gua)_{0.5}(bdc)_{0.5}]$	H_3hmtt 2.2 mg 4.0 µmol	-^{7}N-gua 2.2 mg 6.8 µmol	-H 1.3 mg 8.0 µmol	1.33/ 0.5/ 0.5

3.4.3 RAI catalysis procedures

All catalyses were performed as described in **Chapter 2.4.7**.

3.4.3.1 Preparation of Henry reaction stock solutions

All Henry reaction stock solutions were prepared on a 1.0 mL scale and stored at room temperature for up to two weeks. Unless otherwise stated, a 1:50 ratio of benzaldehyde to nitromethane was used as the standard. Standard stock solutions were prepared by dissolving the benzaldehyde (40.0 µmol, 1.0 eq.) in a solvent (893 µL) and nitromethane (107.0 µL, 2.0 mmol, 50.0 eq.).

3.4.3.2 HPLC analysis of Henry reaction catalysis mixtures

The HPLC analysis of all Henry reaction mixtures was performed using a reverse-phase HPLC system (Thermo Fisher Dionex Ultimate 3000) equipped with a Lux-Amylose column. Separation of the two product enantiomers was achieved using CH_3CN:H_2O mixtures (50:50 to 60:40) as the mobile phase at a flow rate of 0.5 mL/min. The eluting reaction mixtures were monitored by UV absorption at four different wavelengths (210 nm, 230 nm, 245 nm, and 280 nm). The peaks corresponding to the two product enantiomers were integrated, and the ee for each catalysed reaction was calculated.

3.4.3.3 Verification of peak identity in HPLC for the Henry reaction

The purification of the Henry reaction product is available in the appendix to **Chapter 3**.

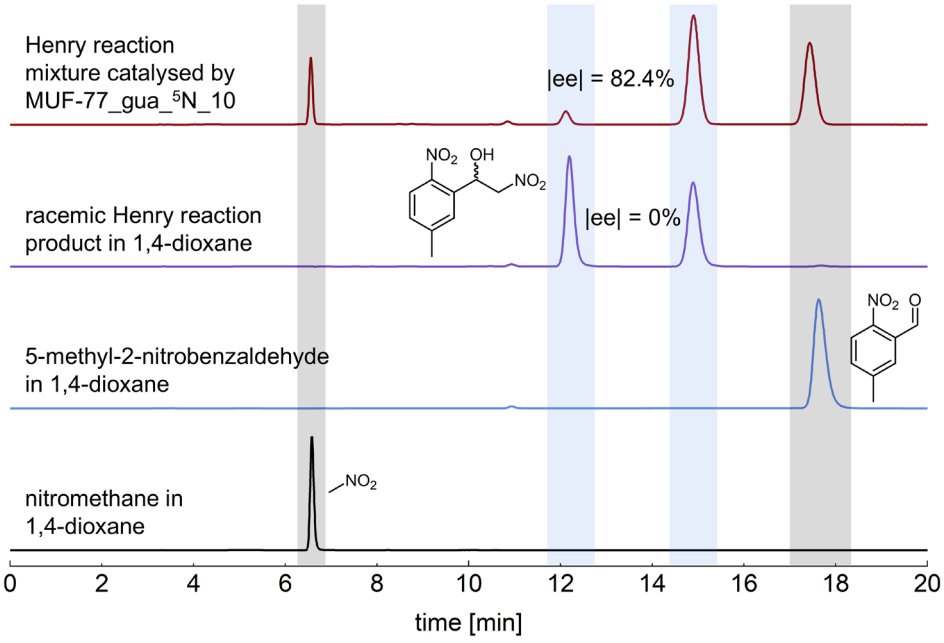

Figure 3.23 HPLC traces of nitromethane, 5-methyl-2-nitrobenzaldehyde, the purified racemic Henry reaction product and a catalysis reaction mixture of MUF-77_gua_^{5}N_10.

3.4.4 SCXRD measurements

All single-crystal X-ray diffraction data were collected on a Bruker D8 Venture diffractometer with temperature control *via* an Oxford Cryostream, where necessary. Data collection and processing were performed using Bruker APEX 3, and the structure was solved and refined using the SHELX package[185] under Olex2.[186]

Table 3.18 Summary of SCXRD data.

Identification code	*t*Bu$_2$bdc-2x-^{5}N-(*S*)-AlaOH
Empirical formula	$C_{52}H_{79}N_4O_{12}$
Formula weight	952.19
Temperature [K]	100
Crystal system	monoclinic
Space group	$P2_1$
a [Å]	9.8801(4)
b [Å]	20.3416(8)
c [Å]	13.1237(6)
α [°]	90
β [°]	103.669(2)
γ [°]	90
Volume [Å^3]	2562.86(19)
Z	2
ρ_{calc} [g cm^{-3}]	1.234
μ [mm^{-1}]	0.708
F(000)	1030.0
Crystal size [mm^3]	1.0 × 0.3 × 0.3
Radiation [Å]	CuKα (λ = 1.54178)
2θ range for data collection [°]	6.932 to 148.986
Index ranges	$-12 \leq h \leq 10$, $-25 \leq k \leq 23$, $-16 \leq l \leq 16$
Completeness	99.9%
Reflections collected	92141
Independent reflections	10022 [R_{int} = 0.0312, R_{sigma} = 0.0162]
Data/restraints/parameters	10022/1/638
Goodness-of-fit on F^2	1.036
Final *R* indexes [*I*>=2σ (*I*)]	R_1 = 0.0301, wR_2 = 0.0799
Final *R* indexes [all data]	R_1 = 0.0312, wR_2 = 0.0809
Largest diff. peak/hole [e Å^{-3}]	0.33/-0.26
Flack parameter	0.05(2)

Chapter 4 – Control experiments, catalyst performance and hypothetical reaction mechanism

4.1 Introduction

The overarching goal of this thesis is to demonstrate that the new approach to asymmetric catalysis, remote asymmetric induction using multicomponent MOFs, is not only possible, but also versatile, high performing and robust. After screening multiple reactions, catalyst motifs and chiral groups in **Chapter 2**, the work presented in **Chapter 3** focused on the deeper understanding and optimisation of one system, resulting in a very good to excellent ee of 87.8%. However, important aspects of the RAI catalyst development that remain to be addressed in detail include

- important control experiments,
- evaluation of the catalyst performance using classical criteria,
- obtaining insights into the reaction mechanism and clues to the origin of the enantioselectivity and the structure of the transition state.

All experiments presented in this chapter involve the highest performing RAI catalyst, MUF-77_gua_^{5}N_10 (**Figure 3.17**), identified in **Chapter 3**.

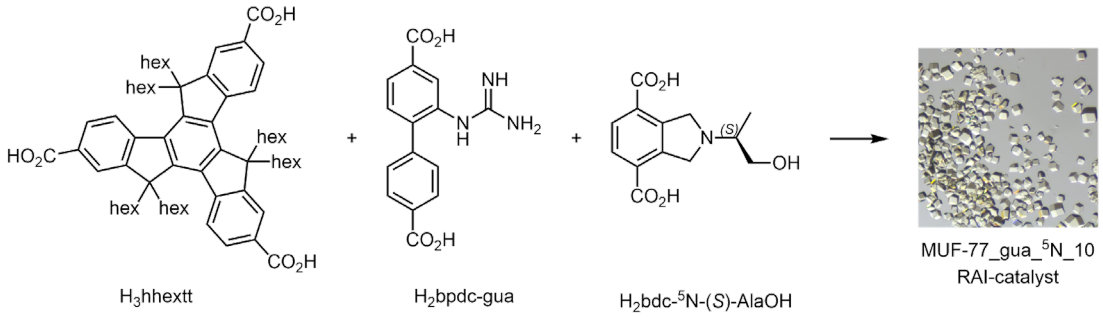

Figure 4.1 Reaction scheme for the synthesis of the RAI-MOF catalyst MUF-77_gua_^{5}N_10.

4.2 Results and discussion

4.2.1 Validation of the RAI process

The transfer of chiral information during a reaction relies on the catalyst unit and the chiral group simultaneously interacting with the reaction substrates to generate the stereochemistry-defining reaction intermediate. This simultaneous interaction is only possible if the catalyst and chiral group are close to one another in space.

In conventional homogeneous asymmetric organocatalysts, the catalytic site is either inherently chiral or positioned close to an element of chirality. Because of this structural connection, the two regions of the catalyst have no choice but to remain in proximity. In fact, separating them into distinct “regions” is mostly not even possible.

In contrast, the RAI concept renders the chiral unit entirely independent from the catalytic group in terms of design, structure and synthesis. This concept is built on a set of hypotheses, all of which must hold true simultaneously:

(i) The chiral linker is the sole source of chiral information within the MOF. If no chiral linker is present, the product should be racemic.

(ii) The catalyst linker is exclusively responsible for any chemical transformations catalysed by the MOF. If no catalyst linker is present, no reaction should be observed.

(iii) An overarching structure must hold the catalyst and chiral components in close spatial proximity. This allows them to interact simultaneously with the reaction intermediates and enables the transfer of chiral information during the reaction. If no structure is built up, the product should be racemic.

(iv) Inverting the chirality of the chiral linker should invert the stereochemistry of the reaction products.

(v) The external surface area of the MOF crystals should have minimal influence on the enantioselectivity. Rapid substrate diffusion ensures that catalysis occurs in the pores throughout the entire MOF crystal. If the external surface area of the MOF crystals is increased, the catalytic process should be unaffected.

The following section presents important control experiments that confirm each of these foundational assumptions to be true.

4.2.1.1 Catalyst and chiral linkers both required simultaneously within framework to build a functional RAI catalyst

This section addresses the hypotheses (i) and (ii) together: Both the catalyst and chiral linker must be present simultaneously within the framework structure to build an effective RAI catalyst (**Figure 4.2**). If the chiral linker is missing in the framework, the catalysis product is expected to be racemic (hypothesis i). In contrast, if the catalyst linker is missing, no reaction should be observed (hypothesis ii).

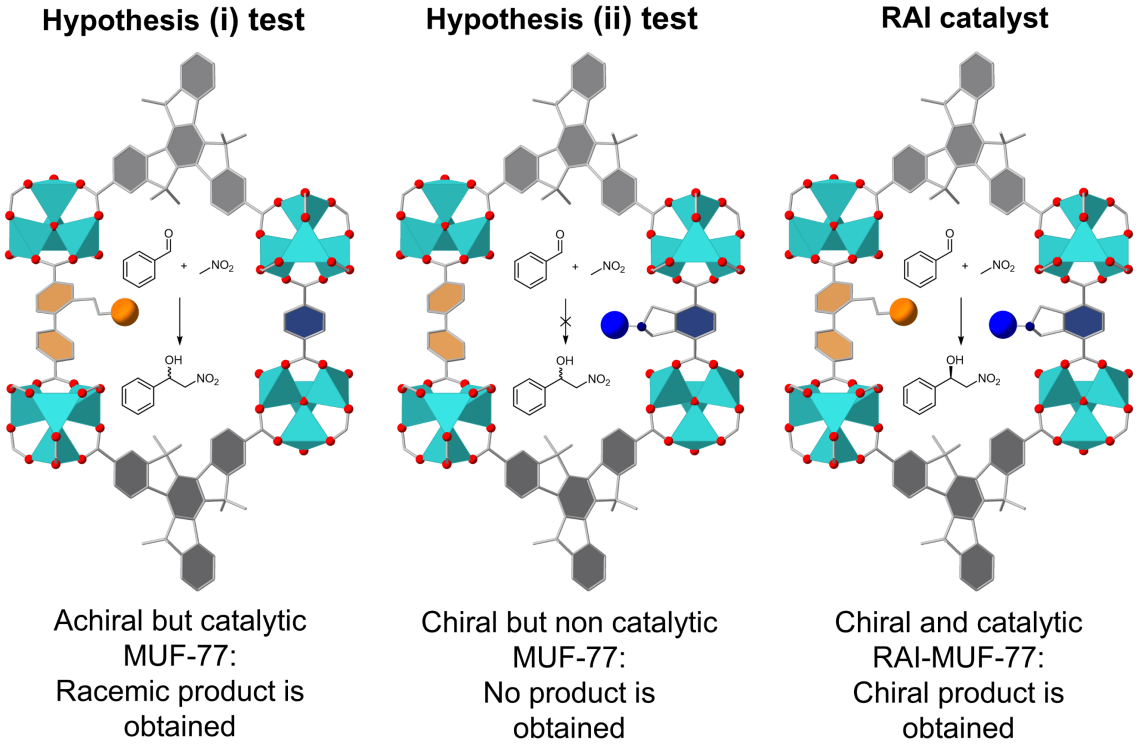

Figure 4.2 Schematic representation of small pores in MUF-77 featuring either only a catalyst linker **A)**, a chiral linker **B)** or both linkers simultaneously **C)**. Catalyst groups are depicted as orange speres. Chiral groups are shown as blue spheres. The expected reaction is shown in the pores

The objective of this section is to verify these assumptions. Therefore, three MOFs were examined:

a. A MOF containing catalyst linker only and no chiral moiety: $[Zn_4O(hhextt)_{1.33}(bpdc\text{-}gua)_{0.5}(bdc)_{0.5}]$

b. A MOF containing a chiral linker only and no catalytic moiety: $[Zn_4O(hhextt)_{1.33}(bpdc)_{0.5}(bdc\text{-}^5N\text{-}(S)\text{-}AlaOH)_{0.5}]$

c. A conventional RAI-MOF that is known to deliver a high ee: MUF-77_gua_^{5}N_10: $[Zn_4O(hhextt)_{1.33}(bpdc\text{-}gua)_{0.5}(bdc\text{-}^5N\text{-}(S)\text{-}AlaOH)_{0.5}]$

The Henry reaction of 5-methyl-2-nitrobenzaldehyde with nitromethane in 1,4-dioxane under standard catalysis conditions was used. The key outputs are HPLC traces (**Figure 4.3**).

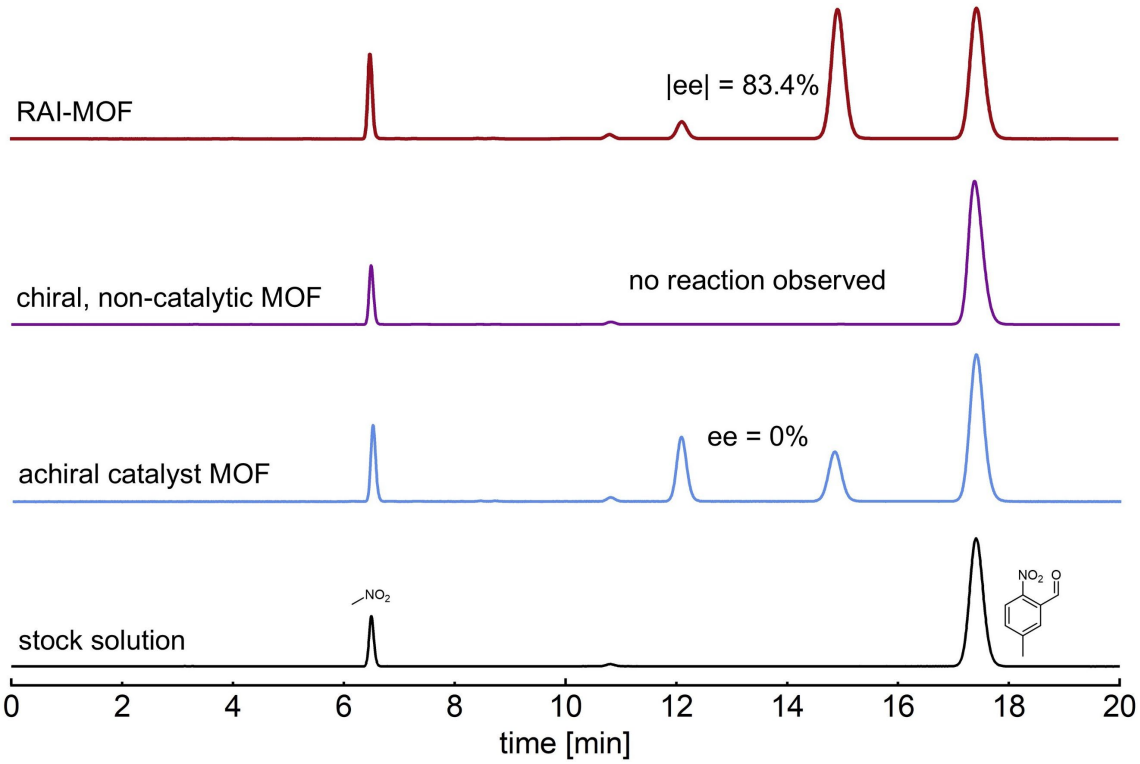

Figure 4.3 HPLC traces of the stock solution for the Henry reaction of 5-methyl-2-nitrobenzaldehyde with nitromethane in 1,4-dioxane (black) and the reaction solutions catalysed by the catalyst MOF with no chiral linker (blue), the chiral MOF with no catalyst linker (purple) and the RAI catalyst MUF-77_gua_^{5}N_10 (red).

An ee of 0% was observed using [Zn_4O(hhextt)$_{1.33}$(bpdc-gua)$_{0.5}$(bdc)$_{0.5}$] where no chiral linker was present in the MOF. This confirms hypothesis (i) that the product enantioselectivity emerges exclusively from the chiral moiety.

No product formation was observed using [Zn_4O(hhextt)$_{1.33}$(bpdc)$_{0.5}$(bdc-^{5}N-(*S*)-AlaOH)$_{0.5}$] where no catalytic linker was present in the MOF. This confirms hypothesis (ii) that the catalytic activity emerges exclusively from the designated catalytic moiety.

As established in **Chapter 3**, MUF-77_gua_^{5}N_10 ([Zn_4O(hhextt)$_{1.33}$(bpdc-gua)$_{0.5}$(bdc-^{5}N-(*S*)-AlaOH)$_{0.5}$]), containing both catalytic and chiral linkers, delivers an ee of 83.4% for this Henry reaction.

4.2.1.2 Catalyst and chiral linkers in solution

This section addresses the RAI concept hypothesis (iii): A framework structure holds the catalyst and chiral linkers in close spatial proximity. This allows them to interact simultaneously with the reaction intermediates and enables the transfer of chiral information during the reaction. If the framework structure is removed and the linkers are not held close to one another in space, no enantioselectivity is observed.

To validate this assumption, the catalyst linker bpdc-gua and chiral linker bdc-^{5}N-(*S*)-AlaOH were combined in solution and their (homogenous) catalytic activity examined. To ensure solubility and to eliminate any possible interference from the carboxylic acid groups required for MOF growth, the methyl ester variants of the linkers (Me_2bpdc-gua and Me_2bdc-^{5}N-(*S*)-AlaOH) were employed. The model Henry reaction of 2-chloro-5-nitrobenzaldehyde with nitromethane in 1,4-dioxane was chosen. Three catalyst experiments were performed using:

a. Me_2bpdc-gua alone.
b. Me_2bdc-^{5}N-(*S*)-AlaOH alone.
c. Me_2bpdc-gua and Me_2bdc-^{5}N-(*S*)-AlaOH together.

For each experiment, the respective linkers were dissolved in the Henry reaction stock solution and sat at room temperature for one day before analysis by HPLC. The loading of each linker was set to 10 mol% relative to 2-chloro-5-nitrobenzaldehyde. The key outputs are HPLC chromatograms (**Figure 4.4**).

Me_2bpdc-gua alone catalysed the reaction to full conversion, yielding a racemic product mixture. Me_2bdc-^{5}N-(*S*)-AlaOH alone showed no catalytic activity. When both linkers were present in solution, full conversion was observed, but the product mixture remained racemic, despite the presence of the chiral linker. In contrast, the RAI-MOF, MUF-77_gua_^{5}N_10, featuring this exact linker combination, yields an ee of 64.9% for this Henry reaction under the same reaction conditions (**Chapter 3.2.1**).

These results confirm that effective transfer of chiral information during catalysis requires the linkers to be fixed in close proximity to one another within an overarching structure, in this case the MUF-77 framework. This validates the RAI concept hypothesis (iii).

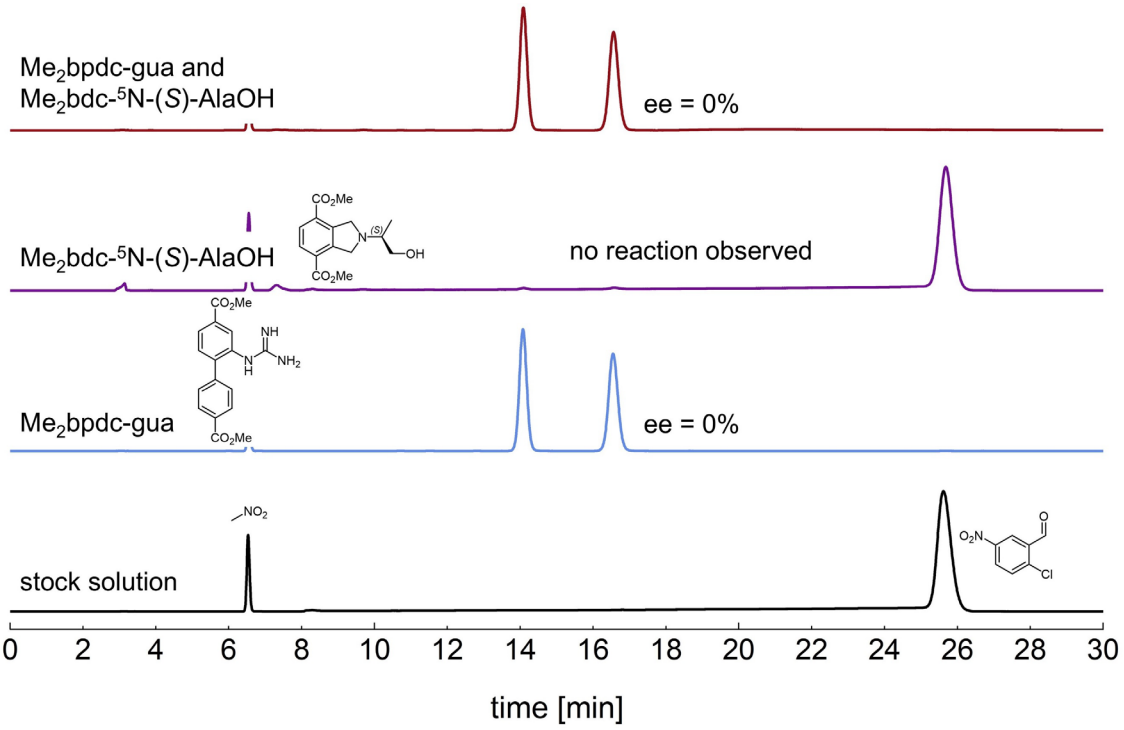

Figure 4.4 HPLC traces of the stock solution for the Henry reaction of 2-chloro-5-nitrobenzaldehyde with nitromethane in 1,4-dioxane (black) and the reaction solutions catalysed by Me_2bpdc-gua (blue), Me_2bdc-^{5}N-(*S*)-AlaOH (purple) and the mixture of both MOF linkers (red).

4.2.1.3 Reversal of ee by changing the stereochemistry of the chiral linker

The chiral linker serves as the exclusive source of chiral information RAI MOFs. Therefore, inverting its stereochemistry should in turn invert the stereochemistry of the reaction product. This is hypothesis (iv).

To test this hypothesis, H_2bdc-^{5}N-(*R*)-AlaOH was synthesised and integrated into the RAI MOF MUF-77_gua_^{5}N_10_(*R*). This catalyst was then used to catalyse the Henry reactions of various benzaldehydes with nitromethane and the ee's of the product mixtures were compared with those obtained using MUF-77_gua_^{5}N_10_(*S*) as the catalyst (**Table 4.1**).

Table 4.1 Measured ee values for Henry reactions of substituted benzaldehydes with nitromethane in 1,4-dioxane, catalysed by either MUF-77_gua_^{5}N_10_(*S*) and MUF-77_gua_^{5}N_10_(*R*). The RAI catalysts are represented by their chiral linkers.

	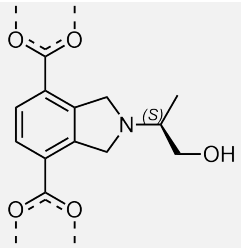	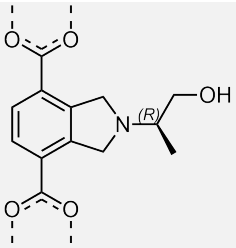
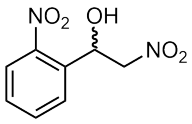	-41.0%	41.8%
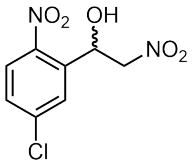	-78.0%	79.7%
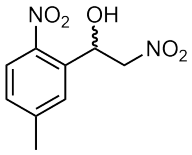	-83.4%	83.7%
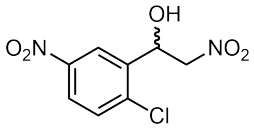	-65.9%	64.4%
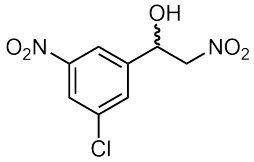	-75.1%	73.4%

Inverting the stereochemistry of the chiral linker lead an inversion of the enantioselectivity of the product. For example this held true for the Henry reaction of 5-methyl-2-nitrobenzaldehyde with nitromethane, where an ee of −83.4% was observed for bdc-^{5}N-(*S*)-AlaOH while bdc-^{5}N-(*R*)-AlaOH yielded an ee of +83.7 % (**Figure 4.5**). The inversion of the product ee was observed for a selection of five different benzaldehydes, highlighting that this principle is independent on the functionalisation of the reaction substrate. These results validate hypothesis (iv).

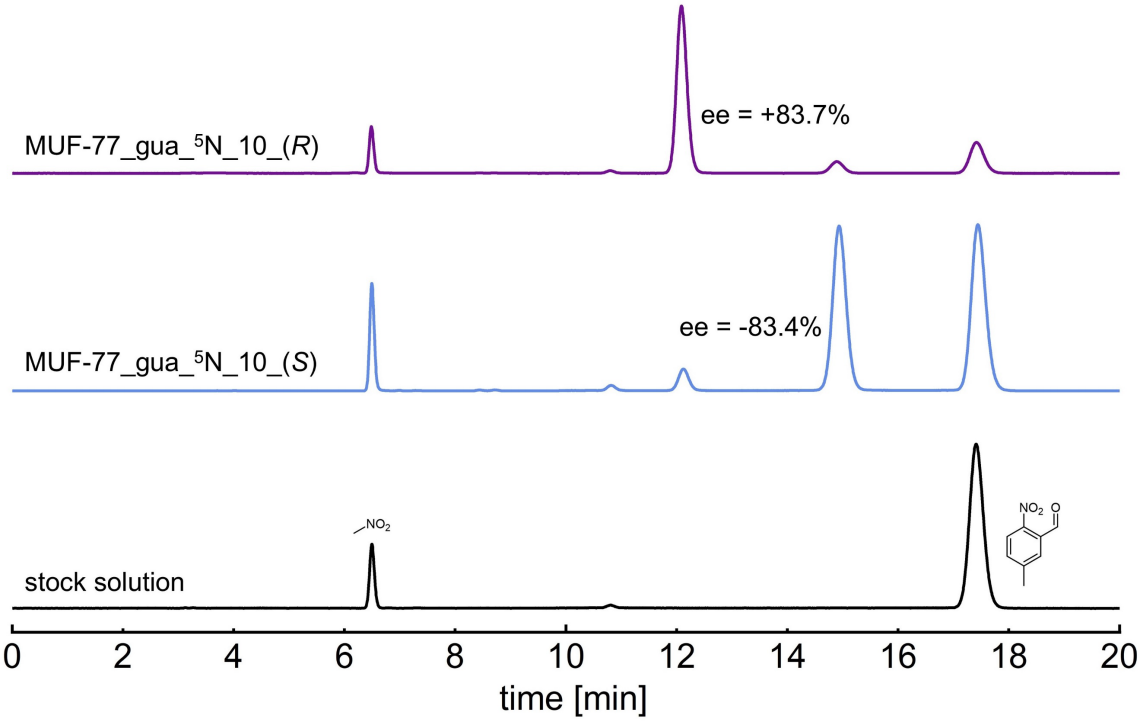

Figure 4.5 HPLC trace of the stock solution for the Henry reaction of 5-methyl-2-nitrobenzaldehyde with nitromethane in 1,4-dioxane (black) and of the reactions catalysed by MUF-77_gua_^{5}N_10_(*S*) (blue) and MUF-77_gua_^{5}N_10_ (*R*) (purple).

4.2.1.4 Influence of the external surface area of the MUF-77 crystals on the overall enantioselectivity

The usual assumption for heterogeneous MOF catalysis is that the catalysis takes place equally distributed throughout the entire MOF crystal. This underpins hypothesis (v), which will be valid as long as mass transport (diffusion) within a crystal is fast so that catalysis is not limited to the more accessible *exterior* surface of the crystals.[220, 221] If catalysis primarily takes place on the external crystal surface (**Figure 4.6** left), the product ee is expected to be lower than for catalysis that takes place in the internal pore spaces (**Figure 4.6** right). This is because the catalyst ligands at the external surface do not experience the well-defined environment of a pore and are unlikely to be in close contact with the chiral element.

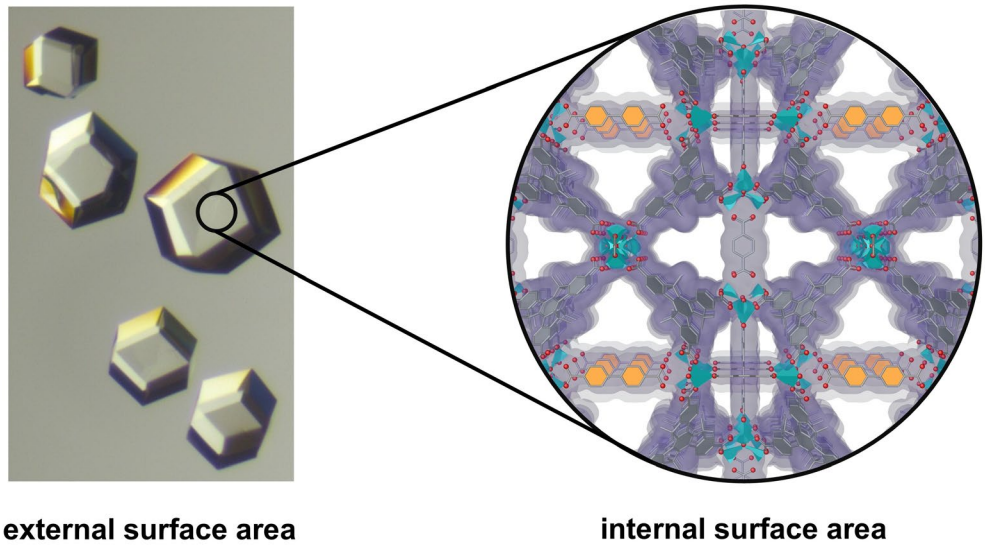

Figure 4.6 Schematic depiction of external and internal surface area of MUF-77 crystals. The filled space within the crystal framework is indicated as purple cloud.

This assumption was explored by artificially increasing the external surface area of a RAI-MUF-77 catalyst through crushing of the crystals. The external surface area is defined as the outermost layer of unit cells. For an average MUF-77 crystal with dimensions of 0.25 mm per side (assuming a cubic shape), only approximately 7.2×10^{-3} % of the unit cells constitute the external surface area. Crushing one large crystal into 100 smaller crystals with one tenth of the original dimensions increases this fraction of unit cells located on the crystal surface to approximately 3.3×10^{-2} %. Additionally, the combined external surface area of the 100 small crystals increases by a factor of 364% compared to that of one large crystal. If catalysis occurs predominantly on the external surface of the MOF crystals, this increase in external surface area was expected to result in a measurable decrease in ee.

The crystals from one synthesis batch of MUF-77_gua_^{5}N_10 (**Figure 3.17**) were equally separated into two vials and the MOF crystals in one of the vials were finely crushed by mechanical force using a glass rod. The Henry reaction of 5-methyl-2-nitrobenzaldehyde with nitromethane in 1,4-dioxane was then investigated for both samples.

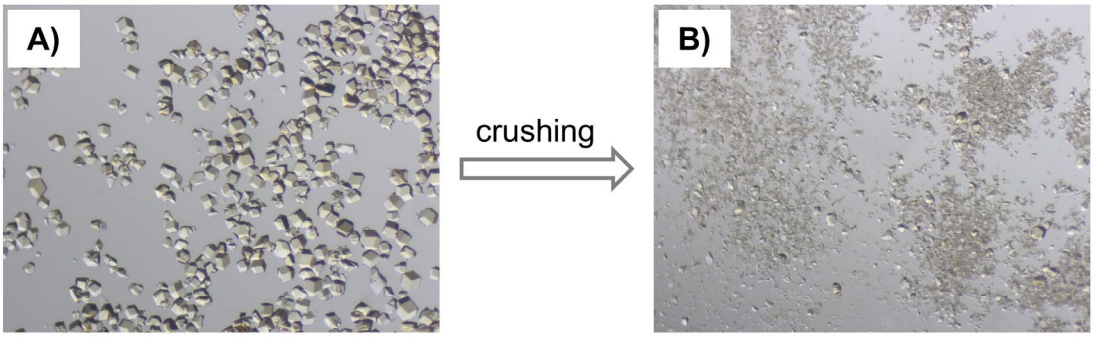

Figure 4.7 Photos of MUF-77_gua_^{5}N_10 crystals before and after crushing by mechanical force.

HPLC analysis showed that both samples yielded nearly identical |ee| values of 82.0% and 81.9%. This result was reassuring, as it suggested that we can use the assumption that catalysis occurs uniformly throughout the MOF crystals, with no overrepresentation of activity of catalyst units located at the external surface of the MOF crystals. These results validate hypothesis (v).

An additional point is that if catalyst was confined to the unit cells on the exterior surface of the crystals the catalyst units would have to be extraordinarily active to account for the product formation. This activity would need to exceed that typically observed for organocatalysts by several orders of magnitude.

4.2.2 RAI-MUF-77 catalyst performance

RAI-MUF-77 catalysts have shown high enantioselectivity for a variety of Henry reactions using different reaction conditions. However, additional qualities are important, such as:

(i) High reproducibility.
(ii) Recyclability.
(iii) Consistent enantioselectivity independent of conversion.
(iv) High catalytic activity and overall productivity.

4.2.2.1 Reproducibility of experiments

Essentially all chemical transformations must show high reproducibility to be considered practical. This also holds true for RAI catalysts. In the context of RAI-MOF catalysis, reproducibility can be evaluated through three key questions:

(i) How consistent is the ee when crystals from the **same MOF synthesis batch** are split into multiple vials for catalysis?

(ii) How reproducible is the ee across **multiple MOF synthesis batches**?

(iii) What is the **inherent variation** associated with the HPLC analysis?

The following sections address each of these questions using a representative example. However, it is assumed that these findings are applicable to all RAI-MUF-77 systems.

Consistency of ee when crystals from the same MOF synthesis are split into multiple vials for catalysis

The crystals within a given MOF synthesis batch are typically considered to be identical. Thus, if one batch of RAI-MOF catalyst is split into multiple samples and all samples are handled identically, it is expected that the obtained ee would be identical as well.

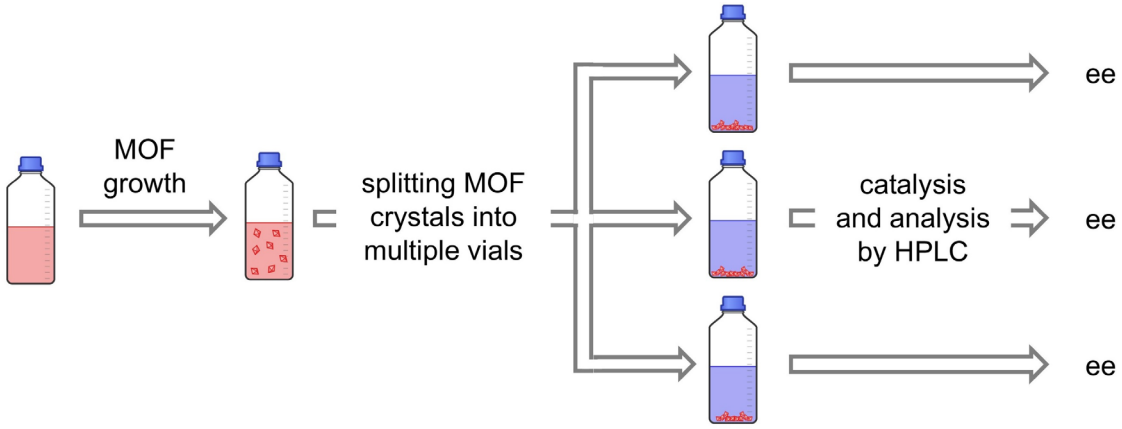

Figure 4.8 Schematic representation of the experimental procedure to test for reproducibility of ee when crystals from the same MOF synthesis are split into multiple vials for catalysis.

The crystals of a batch of MUF-77_gua_^{5}N_10 (**Figure 3.17**) were split into three vials and the Henry reaction of 5-methyl-2-nitrobenzaldehyde with nitromethane in 1,4-dioxane was performed separately in each vial (**Figure 4.8**). Pleasingly, the ee values were nearly identical (**Table 4.2**), with a mean of 82.1% and a standard deviation of 0.1%. This excellent result demonstrates that the catalytic properties of crystals from the same batch are virtually identical.

Table 4.2 Measured |ee| values for the Henry reaction of 5-methyl-2-nitrobenzaldehyde with nitromethane in 1,4-dioxane, catalysed by three samples from the same MOF synthesis batch of MUF-77_gua_^{5}N_10.

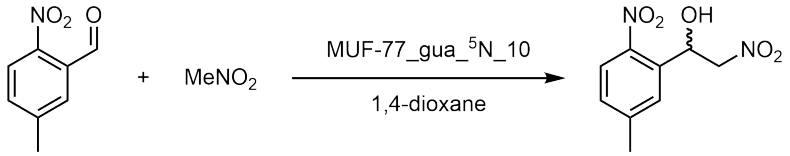

sample #	|ee|
sample 1	82.1%
sample 2	82.2%
sample 3	82.0%

Reproducible of ee across multiple MOF synthesis batches

MUF-77 formation is highly sensitive to a multitude of variables. Even slight changes in conditions such as temperature, reagent and additive ratios, or movement of the reaction vessel can significantly affect the success and rate of MOF formation and the crystal quality. These slight variations can directly impact RAI-MUF-77 catalyst performance, especially in terms of enantioselectivity. Therefore, a degree of variability in ee may be encountered between MOF catalysts from different synthesis batches. To minimise this variability, MOF synthesis conditions were kept as uniform as possible across batches.

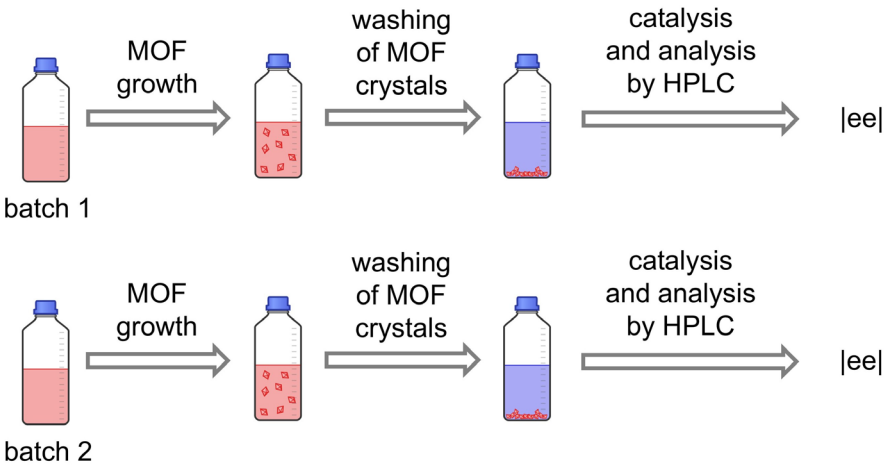

Figure 4.9 Schematic representation of the experimental procedure to test for reproducibility of ee across different batches of MOFs.

To test the reproducibility of the ee across different MOF syntheses, a small portion of each MOF batch was used to catalyse one reference Henry reaction. This allowed the ee of each MOF batch to be compared. A variety of benzaldehydes were selected as references that showed low, medium, and high ee values, to further explore whether the reproducibility varied

depending on the reaction substrate (**Table 4.3**). The catalyst used for this study was MUF-77_gua_^{5}N_10 (**Figure 3.17**). Notably, MOF syntheses were also performed using linkers that had themselves been prepared in separate synthesis batches, which covers an additional level of possible variability.

Satisfactorily, only minor variations in ee across the different MOF synthesis batches were observed, with standard deviations obtained between 0.95-3.0%. The standard deviations using benzaldehydes that show high mean ee, such as 5-methyl-2-nitrobenzaldehyde, were lower than those observed when catalysing benzaldehydes that show low or medium mean ee, such as 2-nitrobenzaldehyde.

Table 4.3 Measured |ee| values, their mean and calculated standard deviations (σ) for Henry reactions of substituted benzaldehydes with nitromethane in 1,4-dioxane, catalysed by different MOF synthesis batches of MUF-77_gua_^{5}N_10.

	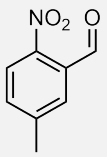	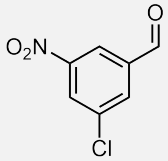	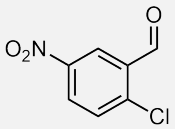	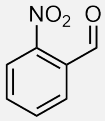
Measured |ee| for different MOF synthesis batches	83.0% 81.4% 82.8% 81.1% 83.6% 83.2% 83.5% 83.7% 83.4% 83.7% 81.9%	75.4% 75.4% 75.1% 73.4% 73.4% 75.7%	68.4% 66.7% 69.1% 65.9% 68.1% 61.5% 60.2% 64.1% 64.4% 63.3% 61.8%	41.0% 41.8% 45.7%
mean	82.8%	74.7%	64.9%	42.8%
σ	0.95%	1.05%	3.02%	2.52%

Overall, this set of experiments showed that catalysis using RAI-MOF catalysts is highly reproducible across different MOF synthesis batches, which is likely the most significant factor introducing discrepancies. Even though these experiments focused on one specific RAI catalyst, MUF-77_gua_^{5}N_10, the findings are expected to apply equally to all other RAI-MUF-77 systems.

Inherent measurement variability associated with the HPLC analysis

All ee values reported in this work were determined from HPLC chromatograms and are expected to accurately reflect the performance of the RAI-MOF catalysts. Therefore, understanding the inherent variability of this analytical method is essential to distinguish meaningful differences in ee from those arising due to instrument and measurement factors.

To assess this, a single Henry reaction product mixture was analysed ten consecutive times. To eliminate any influence from continued catalytic activity, the MOF crystals were removed from the sample before analysis, ensuring that any variation observed was solely due to the HPLC measurements. The ee was calculated for each measurement, and the standard deviation was used to quantify consistency.

The ten measurements had an average |ee| of 83.3%. Using the non-rounded raw data, the standard deviation of the ten measurements was calculated to be 0.02%, confirming the high precision of the HPLC measurements. This result gave reassurance that any observed variations and trends in ee values can be mainly attributed to differences in the RAI-MOF catalysts rather than to factors relating to HPLC measurements and integration of the chromatograms.

4.2.2.2 Recyclability of the RAI-MUF-77 catalysts

Catalysts increase the rate of reactions without themselves being consumed. This fundamental feature allows them to be reused multiple times. Catalyst separation from the reaction mixture is comparatively easy for solid-state heterogeneous catalysts, as solid/liquid or solid/gas phase separation can be achieved through simple filtration. In contrast, removing homogeneous catalysts is relatively challenging due their miscibility with the reaction mixture, requiring an extensive workup and significantly increasing the effort needed for catalyst recycling.

As the RAI-MUF-77 catalysts are solid-state heterogeneous catalysts, they are well-suited for recycling. However, potential issues such as framework degradation, pore collapse, or side reactions of the chiral or catalytic functional groups might render them inactive and/or not as enantioselective. The goal of this set of experiments was to test the recyclability of RAI-MUF-77 catalysts, focusing on the enantioselectivity of the catalysts upon reuse. Additionally, the conversion was qualitatively assessed using an internal standard as described in **section 4.4.2.2**.

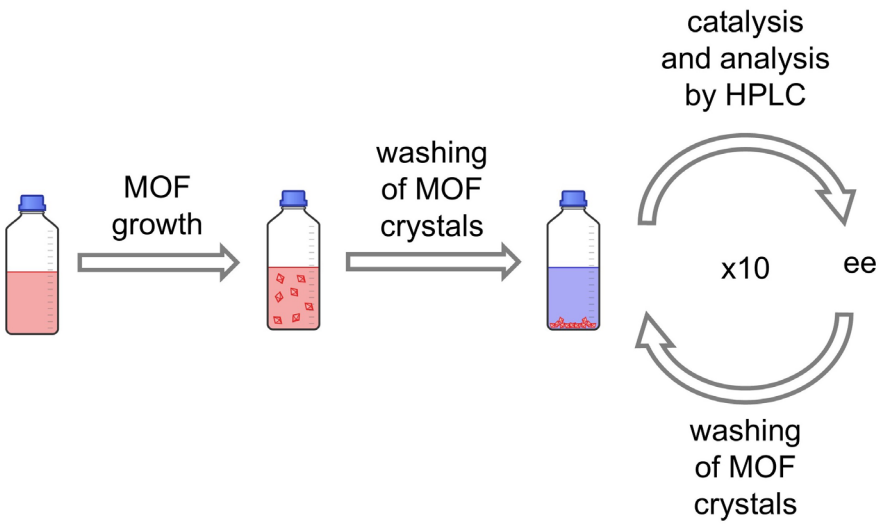

Figure 4.10 Schematic representation of the experimental procedure to test for recyclability of RAI-MOF catalysts.

MUF-77_gua_^{5}N_10 (**Figure 3.17**) was chosen for the recyclability experiment. The reaction of 5-methyl-2-nitrobenzaldehyde with nitromethane in 1,4-dioxane was selected as representative Henry reaction. In total ten recycling cycles were performed. Each recycling step consisted of performing the catalysis under standard conditions, analysis of the reaction mixture by HPLC and washing of the MOF (**Figure 4.10**).

The measured |ee| values for the fresh catalyst and all ten recycling experiments are shown in **Figure 4.11**. During the first two recycling steps, the |ee| values fluctuated only slightly around the |ee| obtained with the fresh, as-synthesised MOF. From recycling step three to ten, an overall gradual decrease in enantioselectivity was observed, with a total loss of approximately 4.1% after the last recycling step. Despite this small decrease in enantioselectivity, the results clearly demonstrate the excellent recyclability of RAI-MUF-77 catalysts.

This conclusion was further supported by the assessment of conversion. Virtually quantitative conversion was observed for the as-synthesised catalyst as well as during the first three recycling steps. From the fourth to the tenth recycling step, a gradual decline in conversion was noted, reaching approximately 40% in the tenth step. While the RAI-MUF-77 catalyst retained substantial catalytic activity throughout the extended recycling process, it is clear that this activity reduced over time.

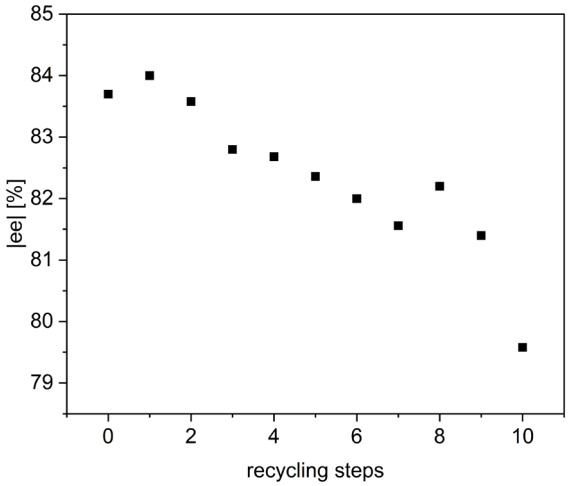

Figure 4.11 Measured |ee| values [%] from the recycling experiments using MUF-77_gua_^{5}N_10 as the catalyst for the Henry reaction of 5-methyl-2-nitrobenzaldehyde with nitromethane. The as-synthesised MOF is denoted as recycling step 0.

To validate the stability of the framework, the crystallinity of MUF-77_gua_^{5}N_10 was examined by PXRD after the tenth recycling step (**Figure 4.12**). The PXRD pattern of the recycled MOF confirmed that it maintained high crystallinity during recycling, as seen by the still sharp reflections up to 2θ = 25°. Only a slight broadening of the reflections occurred, predominantly in the low-angle region between 2-6° 2θ, potentially indicating a small loss in long-range order. This minor reduction in crystallinity may be responsible for the slight decrease in enantioselectivity observed after extended recycling. Overall, these results highlight the stability of the RAI-MUF-77 catalysts under the Henry reaction conditions and provided confidence that they would be recyclable for other reactions.

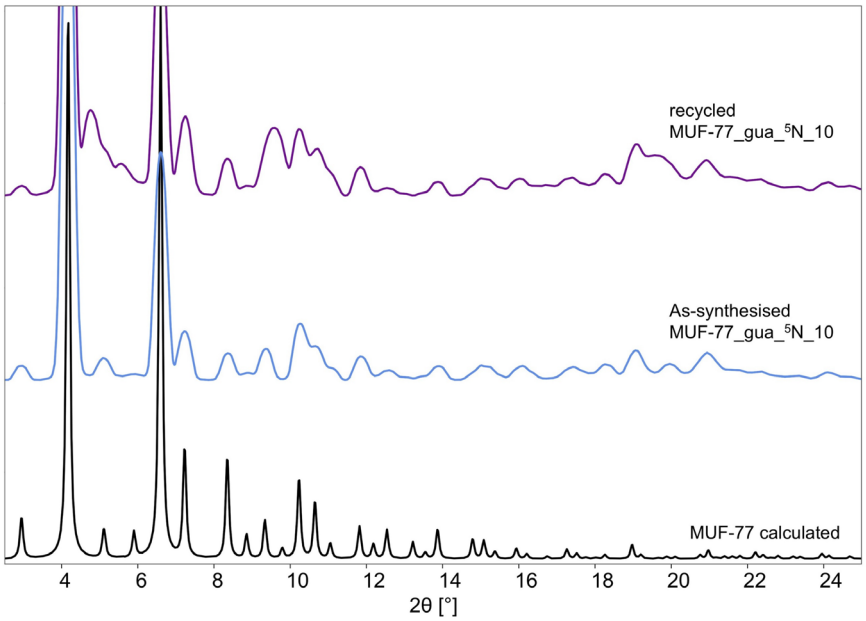

Figure 4.12 PXRD pattern of the as-synthesised MUF-77_gua_^{5}N_10, after ten recycling cycles and the calculated pattern of MUF-77. The intensities of the PXRD pattern are scaled up by a factor of three for visibility.

4.2.2.3 Quantification of catalyst performance in terms of traditional metrics and dependency of ee on conversion

Until now, the focus of all experiments and discussions was entirely on achieving the highest possible ee with the RAI-MUF-77 catalysts. However, the traditional catalyst performance metrics, turnover number (TON) and turnover frequency (TOF), are also important qualities, together providing a measure of catalyst activity. The dimensionless TON quantifies how many catalytic cycles each active site performs, while the TOF represents the rate of catalysis per site over time (with units of time^{-1}).[17, 222-224] These values are directly linked to one another through the reaction time:

$$TON = \frac{product\ formed}{active\ catalyst\ sites}$$

$$TOF\ [time^{-1}] = \frac{\Delta TON}{\Delta time}$$

Enzymes commonly exhibit exceptionally high TOF values of up to 10^7 s^{-1}. [17] In contrast, most industrial catalytic processes operate at lower TOFs, typically between 10^{-2} s^{-1} and 10^2 s^{-1}. For organocatalysis, the reported TOFs are generally much lower and are usually expressed in h^{-1} rather than s^{-1}. Nevertheless, these values can vary significantly depending on the reaction type. For instance, relatively high TOFs of around 10^3 h^{-1} have been reported for organocatalysed ring-opening polymerisations, while TOF values as low as 13.3 h^{-1} are discussed for aerobic oxidation of alcohols.[225, 226] As a general rule, TOF is a valuable metric for evaluating catalyst activity under defined conditions but is not meaningful for the comparison of different catalysts systems or especially different fields of catalysis.[224]

By determining TON and TOF metrics for RAI catalysts, the number of active sites present per catalysis are accounted and normalised for to deliver meaningful comparisons of catalytic activity for reactions with varying catalyst loading. Additionally, the ee of the reaction mixture is monitored to assess if any meaningful variation of ee depending on the TON, and with that the conversion, is observed.

Experimentally, this was achieved by monitoring the progress of a catalysis reaction over time *via* HPLC analysis. The consumption of the benzaldehyde was quantified using an internal standard for calibration. After catalysis, the RAI-MUF-77 crystals were washed, dried, and weighed to determine the number of catalyst units (which is the number of moles of catalytic ligands contained by the MOF crystals). After statistical analysis of the combined data, the TON and TOF at various time points (TON_t and TOF_t) were obtained (**section 4.4.2.4**). In parallel, the ee of the reaction mixture was tracked by integration of the appearing product peaks. As a

model system, the Henry reaction of 5-methyl-2-nitrobenzaldehyde with nitromethane in 1,4-dioxane catalysed by MUF-77_gua_^{5}N_10 (**Figure 3.17**) was selected.

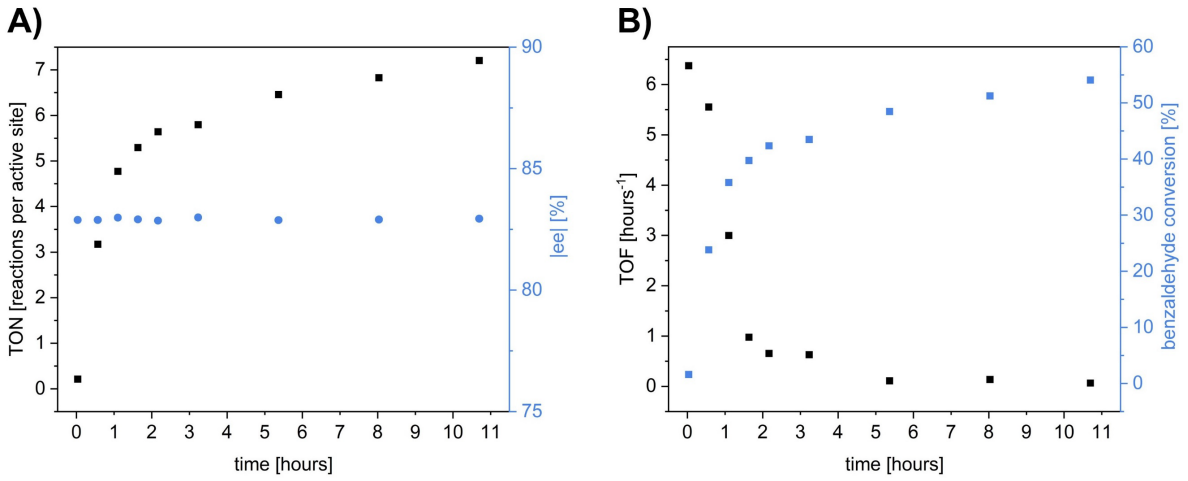

Figure 4.13 Calculated TON_t and |ee| values **A)** and TOF_t and benzaldehyde conversion **B)** of the Henry reaction of 5-methyl-2-nitrobenzaldehyde with nitromethane in 1,4-dioxane catalysed by MUF-77_gua_^{5}N_10 monitored over time.

The observed ee only varied negligibly over the reaction time and thus was independent of the conversion (or TON_t) (**Figure 4.13 A**). This finding is consistent with previous experiments (**experimental section Figure 4.21**), where similar ee values were observed regardless of whether the reaction reached low (between 1-5%) or full conversion. This highlighted the non-dependency of the ee on the reaction progress and also the accuracy of the HPLC measurements even for low conversions.

The MUF-77_gua_^{5}N_10 catalyst initially demonstrated good activity, with a steep rise in TON_t and TOF_t values exceeding 5 h^{-1} (**Figure 4.13 A**, **Figure 4.13 B**). However, between thirty minutes and one hour, the catalytic activity began to decline, eventually plateauing after approximately five hours. This trend was reflected by the plateauing of TON_t and the reduction in TOF_t to around 0.1 h^{-1} over time. After approximately eleven hours of reaction time, the final TON_t was calculated as 7.2 turnovers per active site, corresponding to a 54.1% conversion of the benzaldehyde based on the catalyst loading of 7.5% (determined retrospectively).

The observed catalyst deactivation and plateauing of activity was undesirable, so its root causes and methods to delay (or prevent it completely) were explored. The initial hypothesis was that the decline in TOF_t was partially caused by the decreasing concentration of benzaldehyde as the reaction progressed. As conversion increases, the TOF_t will drop and eventually reach zero once full conversion is achieved.[224] However, this large decrease in TOF_t was observed earlier than anticipated, at conversions around 30 – 45%, which left 70 – 55% benzaldehyde unreacted (**Figure 4.13 B**). This suggested that the decrease in activity was not

fully explained by the relationship of TOF_t and reaction progress. To further assess this, the reaction was repeated with a deliberately lower catalyst loading (retrospectively determined as 0.77%). The calculated TON_t and TOF_t (**experimental section Figure 4.20**) followed the same trend. TOF_t declined after reaching about 4% conversion, while 96% benzaldehyde was remaining. This reinforced the conclusion that changes in substrate availability were not the sole cause of the activity drop.

It started to appear more likely that the decrease of activity was related to the number of reaction cycles per active site (TON). In both experiments (normal and low catalyst loading), the decrease in TOF became evident after about five reactions per active site (TON of five). Possible explanations are that

- the guanidine moiety becomes 'poisoned' by gradual protonation over time.
- the product builds up relative to the number of active sites, causing the guanidine moiety to become 'blocked' by reaction products that bind to either the guanidine or the protonated guanidinium ions, overall hindering further catalytic cycles.

To investigate this hypothesis, further experiments were performed.

The effect of acid/base additives was explored. Since the catalyst unit comprises a guanidine functional group, it should be sensitive to these types of additives, potentially preventing the 'blocking-up'. Acetic acid and pyridine were chosen as the acidic and basic additives, respectively, as they did not cause any unwanted interference such as unwanted background reactions (**Chapter.3.2.8**). To assess the effect of each additive, while simultaneously reproducing the initial high activity of the catalyst alone, 1.0 equivalent of the respective additive (relative to benzaldehyde) was added immediately after the third sampling of the reaction mixture, approximately one hour into the reaction. The resulting time-resolved TON_t and TOF_t are shown in **Figure 4.14**.

The initial activity of the catalyst before the addition of additives is reproducible across the three catalyst runs (minor discrepancies in the TOF_t for the first measurement right after starting the catalysis can be attributed to slight variations in timing while starting the catalysis, which are elevated by the high initial activity of the catalysts).

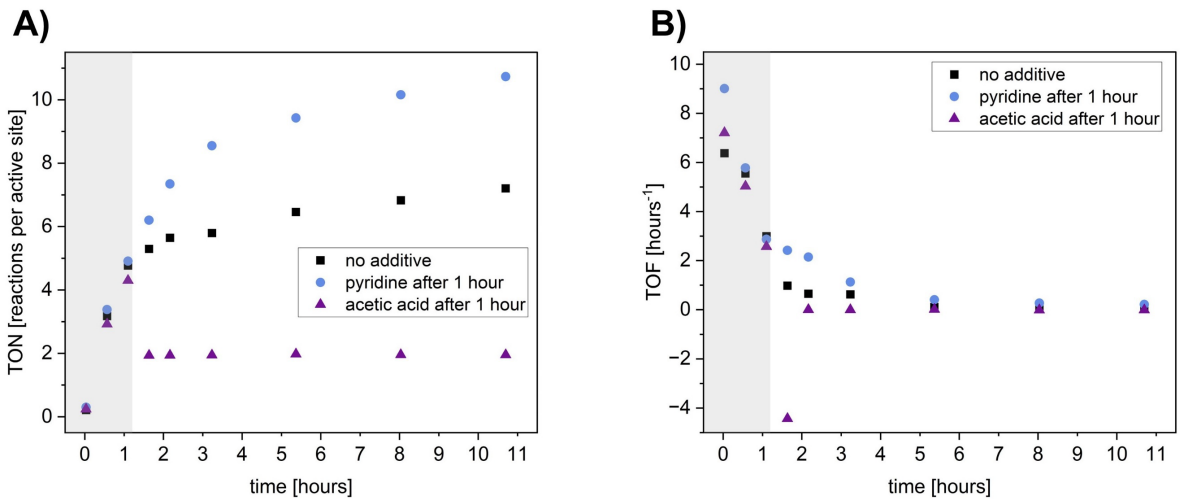

Figure 4.14 Calculated TON_t **A)** and TOF_t **B)** of the Henry reaction of 5-methyl-2-nitrobenzaldehyde with nitromethane in 1,4-dioxane catalysed by MUF-77_gua_^{5}N_10 without the addition of an additive (black) and with the addition of pyridine (blue) and acetic acid (purple) after about one hour. The time before the addition of an additive is highlighted by a grey background.

The addition of pyridine to the reaction mixture after one hour resulted in an increase of catalyst activity (**Figure 4.14 A)**, fourth data point (blue circles). This was reflected by the higher TON_t and TOF_t than the control reaction. In total, a 48.9% increase of TON after 10 hours was observed. A final TON of 10.7 turnovers per active site was reached, corresponding to a 77.9% conversion of the benzaldehyde based on the catalyst loading of 7.3% (determined retrospectively). Additionally, the TOF_t stabilised at around 0.2 h^{-1}, approximately twice the plateau value observed without the addition of pyridine.

These findings suggest that pyridine prevents the poisoning or blocking of the guanidine moiety to some extent, thereby enhancing catalytic activity. This is most likely related to the build-up of reaction products relative to the number of active sites, as pyridine (pK_a = 5.2)[227] is not a strong enough base to deprotonate the guanidine catalyst (pK_a around 13.7).[144] However, the exact mechanism underlying this effect remains uncertain, making this a working hypothesis.

It is worth noting here that these results and the working hypothesis align with the observations from the recyclability experiments (**section 4.2.2.2**). Effectively quantitative conversion was observed for the first few recycling steps, following a gradual decrease in conversion ending up at about 40% conversion in the tenth recycling step. This showed that the catalyst activity was maintained over ten recycling steps. Between each recycling step, the catalysts were washed three times with fresh solvent, effectively regenerating the catalyst by removing residual reaction products and leaving the catalytic units unblocked. This washing effectively regenerated the activity of the catalyst between each recycling.

Unexpectedly, the addition of acetic acid to the reaction mixture after one hour resulted in a reversal of the reaction back to the benzaldehyde (retro Henry reaction), indicated by a drop in the TON_t and a negative value for the TOF_t (**Figure 4.14 B)**, fourth data points (purple triangles). After this reversal, the mixture remained static, with no further changes in composition for the remainder of the reaction time. These results are reproducible. The reaction reversal was also attempted by adding acetic acid *after* removal of the RAI-MOF catalyst. This was done to determine whether acetic acid alone could promote the reverse reaction or whether the guanidine catalyst was involved. The reverse reaction did not proceed in the absence of the catalyst, confirming that the guanidine unit is essential. Overall, these experiments revealed that the addition of acidic additives to the reaction mixture reverses the Henry reaction in the presence of the guanidine catalyst.

In conclusion, this work demonstrated that the RAI-MOF catalyst, MUF-77_gua_^{5}N_10, initially shows high activity, which gradually plateaus, while maintaining consistent enantioselectivity throughout the entire reaction. The initial TOF values, ranging from 8 h^{-1} to 1 h^{-1} before plateauing, fall within the typical range observed for both organocatalysts and MOF catalysts.[228] The origin of the plateauing was investigated, and it could be shown that it was independent of the amount of benzaldehyde remaining. The study further revealed the high sensitivity of MUF-77_gua_^{5}N_10 to the addition of acid and base additives. Addition of pyridine increased the catalytic activity and delayed the plateauing of activity, resulting in overall higher TON. In contrast, the addition of acetic acid shifted the catalysis towards the retro-Henry reaction. The general trends observed for this system are expected to be applicable to all guanidine-based RAI-MUF-77 catalysts, with absolute values varying slightly by system. RAI-MUF-77 catalysts featuring bulkier chiral linkers are expected to show reduced activity due to lower diffusion rates caused by the higher pore filling.

4.2.3 Reaction mechanism within the MOF pore and origin of enantioselectivity

Up to this point, this work has focused on experimental efforts to maximise the enantioselectivity of the RAI-MUF-77 catalysts for the Henry reaction. By systematically optimising key variables, a high ee of 87.8% was achieved, corresponding to a product mixture containing 93.9% of the major and 6.1% of the minor enantiomer.

The goal of the following section is to propose a plausible explanation for the origin of this high enantioselectivity. This will be achieved by taking all experimentally obtained observations into consideration, structural analysis of the catalytic pore environments based on SCXRD data, and references from the literature. It is worth noting that no modelling based on density functional theory or related methods was performed, due to the complexity and size of the framework. Additionally, a discussion of the effect of the solvent and additives is avoided as this falls outside the scope of what can be achieved based on experimental results without the support of modelling.

Mechanistically, the Henry reaction proceeds *via* base catalysis (**Scheme 4.1**): nitromethane is deprotonated by a base, generating an anion that subsequently attacks the electrophilic carbonyl carbon of the aldehyde to create a carbon-carbon bond. This nucleophilic attack is the stereocontrolling step. The resulting intermediate is then protonated to yield the β-nitro alcohol product.

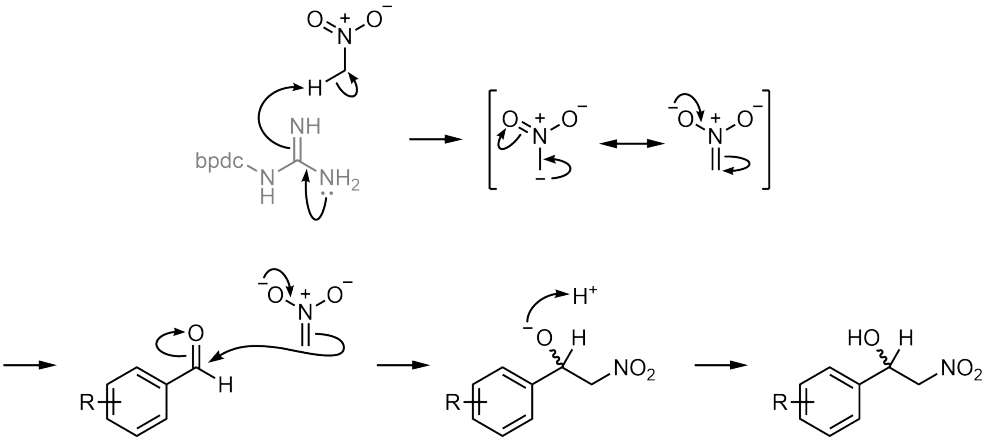

Scheme 4.1 Base catalysed Henry reaction mechanism.

A key step toward understanding the origin of the high enantioselectivity was to identify the specific pore in which the reaction takes place. MUF-77 contains three distinct pores: two larger pores and one smaller micropore (**Chapter 1.2.2**, **Figure 1.14**). Chiral induction must occur within the micropore, as it is the only pore that is shared by both linear linkers. In contrast, the large pores are either built entirely from chiral but non-catalytic bdc linkers, or from catalytic but achiral bpdc linkers. This makes it impossible for the chiral induction to occur within either of the two large pores. This conclusion is strongly supported by the findings

discussed in **Chapter 3.2.2**. The enantioselectivity of the RAI-MUF-77 catalysts was shown to be highly sensitive to the length of the alkyl chains on the truxene. These chains exclusively point into the large pores and, when having the right length (hexyl chains), effectively fill these pores. This directs the substrates into the small pores, where both catalytic and chiral functionalities are present. For this reason, the rest of the discussion will focus exclusively on the small pore.

Within the small pore, one guanidine moiety is present. It is responsible for initiating the reaction by deprotonating the nitromethane. Next, the nitronate likely coordinates with the guanidinium cation through hydrogen bonding (**Figure 4.15**). This coordination has been hypothesised for numerous catalysts and is often considered key to achieving high enantioselectivity. Such coordination through hydrogen bonding has been supported by its observation in SCXRD structures, where a bicyclic guanidinium cation was shown to interact directly with a nitroalkane anion.[147] This provides a plausible explanation for how the guanidine moiety both activates and positions the nitromethane for enantioselective attack on the benzaldehyde.

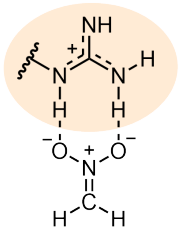

Figure 4.15 Schematic depiction of a nitromethane anion coordinating to a guanidinium cation through hydrogen bonding.

The one chiral linker present within the small pore is proposed to interact with the benzaldehyde *via* hydrogen bonding through its hydroxy group (**Chapter 3.2.1**). This interaction should position the benzaldehyde optimally for nucleophilic attack by the nitronate. This is supported by experimental observations: replacing the hydroxy group on the chiral linker with a non-hydrogen-bond donating functionality, such as a methyl or ether group, led to a complete loss in enantioselectivity. This shows that the hydroxy group and most likely the hydrogen bonding plays a critical role to achieve high enantioselectivity. The overall size of the chiral linker also influenced the interaction with the benzaldehyde. The highest enantioselectivity was achieved with the alaninol-derived functionality, which contains a small methyl substituent β to the hydroxy group. Larger groups close to the hydroxy moiety led to reduced ee values. This indicates that bulkier substituents interfere with optimal interaction between the benzaldehyde and hydroxy group, that likely prevent consistent spatial arrangement within the pore for the nucleophilic attack.

The strongest hydrogen bond between the chiral linker and benzaldehyde will occur between the hydroxyl group of the alaninol and the aldehyde oxygen. Similar hydrogen bonding interactions between a catalyst and aldehyde oxygen have been reported. For example in bifunctional guanidine-HBD catalysts, a hydrogen bond donor, such as thiourea or squaramide, coordinates to the aldehyde oxygen, arranging it optimally for an enantioselective attack by an activated nucleophile.[149, 229, 230]

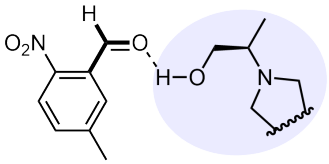

Figure 4.16 Schematic depiction of the chiral linker based on the amino alcohol alaninol interacting with 5-methyl-2-nitrobenzaldehyde through hydrogen bonding between the hydroxyl group of the chiral linker and the aldehyde oxygen.

The additional substituents on the aromatic ring of the benzaldehyde substrate were found to affect both reactivity and selectivity (**Chapter 3.2.4**). A nitro group was essential to activate the benzaldehyde so that it participates in the reaction. This is due to the strong electron-withdrawing effect exerted by nitro substituents. The identity of additional substituents was generally found to be less critical, with similar enantioselectivities observed, for example, for chloro, methyl, and bromo substituents. Yet, their position relative to the aldehyde and nitro group was important for the enantioselectivity. This suggests that these groups primarily influence the orientation of the benzaldehyde within the pore by noncovalent van der Waals interactions and/or steric repulsion. However, groups capable of strong hydrogen bonding, such as a hydroxy group, often reduced ee. This is likely attributed to competing hydrogen bonding interactions with the chiral linker.

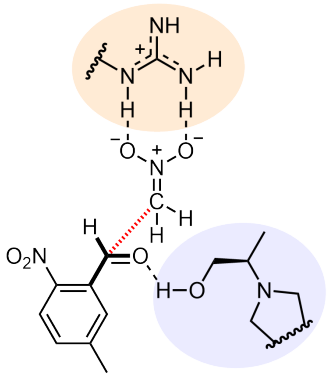

Figure 4.17 Depiction of a plausible transition state as the origin of enantioselectivity within the RAI-MUF-77 small pore.

Overall, these hypotheses provide a plausible explanation for the origin of enantioselectivity (**Figure 4.17**): both reaction substrates - nitromethane and the benzaldehyde - interact with one of the two distinct linkers within the pore. The nitronate coordinates to the guanidine catalyst, while the benzaldehyde is likely interacting through hydrogen bonding with the chiral linker.

These interactions are proposed to orient the substrates toward each other in a defined manner, thereby facilitating enantioselective product formation. A hypothetical representation of this stereocontrolling intermediate is presented to visualise the potential origin of enantioselectivity.

To test the feasibility of this arrangement within the confined space of the small pore, structural modelling was performed. This analysis serves as a preliminary validation that the proposed mechanism is at least structurally feasible within the small pore. However, without high-level computational analysis, this is simply a hypothetical static picture, and dynamic motion is not taken into account.

Using SCXRD data of MUF-77 as the starting point, representative orientations of the linker functionalities and both substrates were modelled to assess whether simultaneous coordination can potentially occur. Pleasingly, it is possible to fit both functionalities attached to the linear linkers into the MOF pore while still providing enough space for the reaction substrates to interact as hypothesised (**Figure 4.18**). This suggests that the mechanism proposed above is feasible.

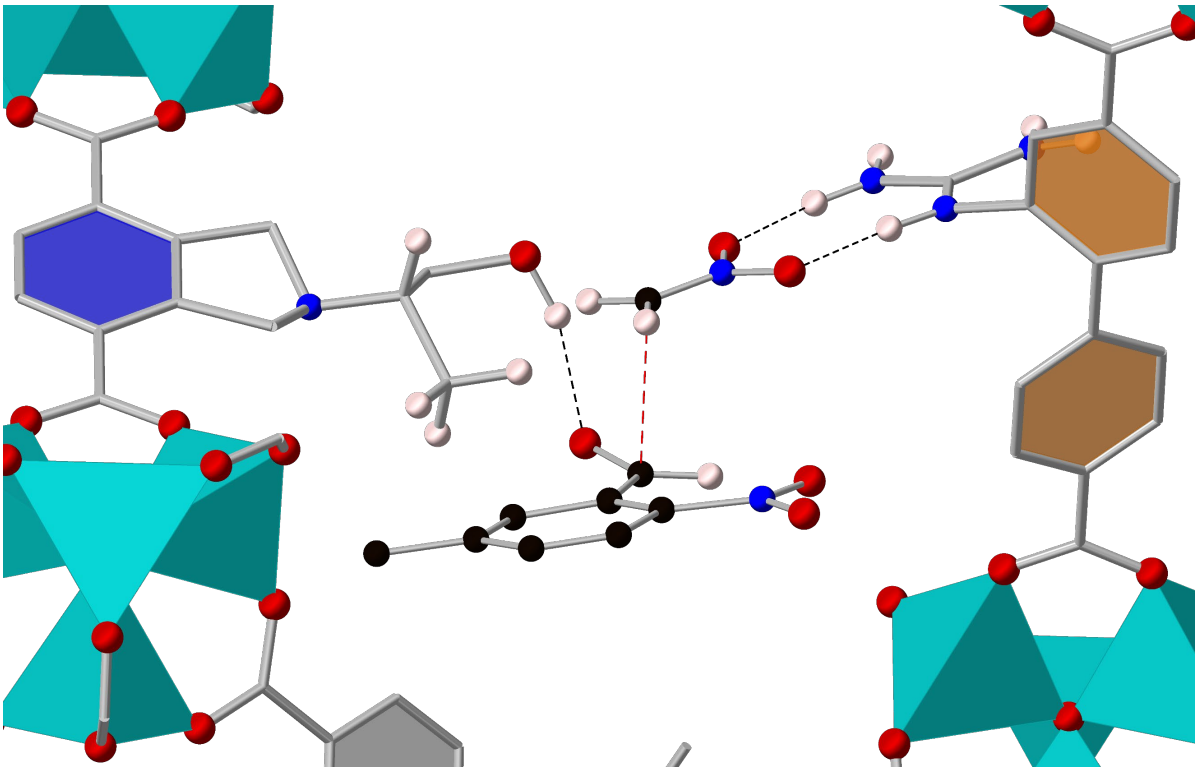

Figure 4.18 A software-generated snapshot of the nitronate and 5-methyl-2-nitrobenzaldehyde interacting with the guanidinium and ^{5}N-alaninol moieties in the small pore of RAI-MUF-77. Hydrogen bonds are shown as black dotted lines, while the potential trajectory for nucleophilic attack of the carbonyl carbon of the benzaldehyde by the nitronate is indicated by a red dotted line. The truxenes at the front and back of the pore are omitted for clarity.

It is important to note that confirming the structural feasibility of the proposed origin of enantioselectivity does not equate to predicting the absolute configuration of the major product. Without definitive knowledge of which enantiomer is preferentially formed, the current modelling serves only to support the plausibility of the hypothesis. The actual stereochemical outcome will be defined by which face of the benzaldehyde is attacked *or* the orientation of the aldehyde functionality at the moment of nucleophilic attack. However, due to the dynamic motion of the linker backbones, their functional moieties, and the reaction substrates, countless orientations within the pore can be imagined that could lead to either enantiomer. All of this is influenced by subtle variations in the pore environment, substrate functionalities, and solvent. Thus, high-level computational analysis would be an informative approach capable of providing a more precise picture of the orientation responsible for the observed enantioselectivity.

4.3 Conclusion

The set of experiments presented in this chapter verify several fundamental aspects of the RAI concept. Additionally, the origin of enantioselectivity within the RAI-MUF-77 catalysts was explored through theoretical considerations and a hypothetical mechanism for the Henry reaction within the MOF pores was proposed. Major milestones of this work included:

1. Verification of several fundamental assumptions that are central to the concept of RAI catalysis in MUF-77.
2. Demonstrating excellent reproducibility of ee within and across multiple RAI-MUF-77 syntheses batches.
3. Showcasing high catalyst recyclability over ten consecutive reaction cycles.
4. Determination of the TON and TOF for a representative RAI-MUF-77 catalyst and exploring its dependency to the addition of acid/base additives.
5. Proposing a feasible mechanism for the Henry reaction within the RAI-MUF-77 catalyst pores and an explanation of the origin of the observed enantioselectivity.

Taken together, these results cement RAI as a reliable method for designing and realising high performance asymmetric catalysts whose structural and mechanistic features can be understood with a high degree of precision.

4.4 Experimental section

4.4.1 MOF synthesis

All MOFs in this chapter were synthesised following one of the synthesis procedures described in **Chapter 2.4.3**. The synthesis method, along with the linker molar amounts and weights used for each MOF synthesis, are listed in **Table 4.4**. The linker ratios (truxene/bpdc/bdc) for each digested MOF sample are stated as determined by ^{1}H NMR.

Table 4.4 Linkers, weights and molar amounts used for the MOF synthesis of this work. The applied MOF synthesis method (#) and the measured linker ratio of the digested MOF as determined by NMR are stated.

MOF name code	#	truxene	H_2bpdc-R	H_2bdc-^{5}N-R	NMR ratio
$[Zn_4O(hhextt)_{1.33}(bpdc)_{0.5}(bdc\text{-}^5N\text{-}(S)\text{-}AlaOH)_{0.5}]$	3	H_3hhextt 3.9 mg 4.0 µmol	-H 1.2 mg 5.0 µmol	-(*S*)-AlaOH 2.5 mg 9.4 µmol	1.33/ 0.5/ 0.5
$[Zn_4O(hhextt)_{1.33}(bpdc\text{-}gua)_{0.5}(bdc)_{0.5}]$	3	H_3hhextt 3.9 mg 4.0 µmol	-gua 1.4 mg 4.7 µmol	-H 1.3 mg 7.8 µmol	1.33/ 0.5/ 0.5
MUF-77_gua_^{5}N_10_(*S*)	3	H_3hhextt 3.9 mg 4.0 µmol	-gua 1.4 mg 4.7 µmol	-(*S*)-AlaOH 2.5 mg 9.4 µmol	1.33/ 0.5/ 0.5
MUF-77_gua_^{5}N_10_(*R*)	3	H_3hhextt 3.9 mg 4.0 µmol	-gua 1.4 mg 4.7 µmol	-(*R*)-AlaOH 2.5 mg 9.4 µmol	1.33/ 0.5/ 0.5

4.4.2 RAI catalysis procedures

4.4.2.1 General RAI catalysis procedures

All Henry reaction stock solutions were prepared and handled as reported in **Chapter 3.4.3.1**. If not otherwise stated, the Henry reactions were performed using the standard RAI-MUF-77 catalysis procedure as described in **Chapter 2.4.7**. HPLC analysis of all reaction mixtures was performed using the conditions as reported in **Chapter 3.4.3.2**.

4.4.2.2 Internal standards for determination TON and TOF

Mesitylene was determined to be a suitable internal standard for the Henry reaction of 5-methyl-2-nitrobenzaldehyde with nitromethane, being inert to any reactions and not overlapping with the reaction substrates or product signals in HPLC. During the search for internal standards, an inherent impurity in the commercial benzaldehyde was identified to also be a viable reference, as it remained unchanged throughout the reaction. This was verified by the constant ratio of mesitylene to the inherent standard throughout catalysis (**Figure 4.19**). Using this inert, inherent impurity as internal standard offered the advantage of avoiding the need to add 1 vol% of mesitylene and thereby changing the solvent composition of the catalysis. It also enabled retrospective analysis of conversion for all previously performed Henry reactions using this benzaldehyde.

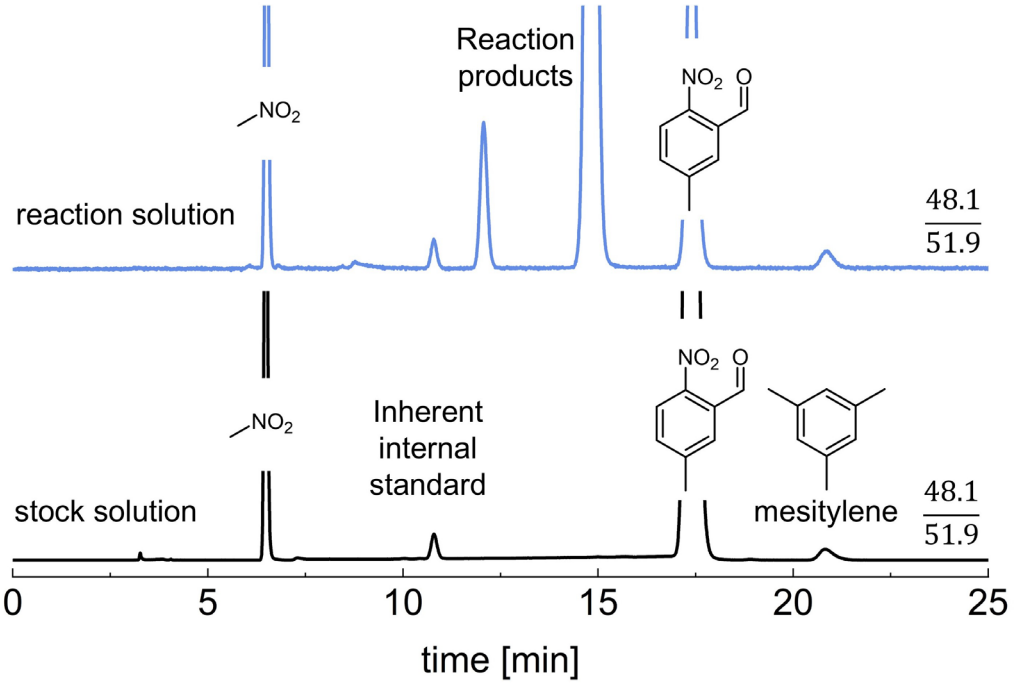

Figure 4.19 HPLC trace of the stock solution for the Henry reaction of 5-methyl-2-nitrobenzaldehyde with nitromethane in 1,4-dioxane with the addition of 1 vol% of mesitylene (black) and the reaction solution catalysed by MUF-77_gua_^{5}N_10 (blue). The ratio of inherent internal standard to mesitylene is stated.

4.4.2.3 Monitoring the progress of a catalysis over time

All kinetic measurements were performed for the Henry reaction of 5-methyl-2-nitrobenzaldehyde with nitromethane in 1,4-dioxane at standard concentrations (**Chapter 3.4.3.1**), catalysed by MUF-77_gua_^{5}N_10. To obtain a precise benzaldehyde/ internal standard ratio, the Henry reaction stock solution was measured three consecutive times directly prior to starting the kinetic measurements. To start the catalysis all washing solvent was removed from the RAI-MOF catalyst crystals and 60-80 µL of the Henry reaction stock solution was added. The first HPLC injection was taken 2 minutes after initiating the reaction, followed by consecutive measurements every 32 minutes for ten hours. For each measurement only 0.1 µL of the reaction mixture was taken to minimise changes in catalyst concentration, enabling the assumption of constant catalyst loading. The signals corresponding to the internal standard, unreacted substrates, and product enantiomers were integrated for each time point. After the reaction, the MOF crystals were washed with acetone (5 × 1 mL), dried under high vacuum for five hours at room temperature, and weighed using a TGA balance for maximum accuracy.

4.4.2.4 Calculation of the TON and TOF

The procedure for calculating the TON and TOF from the HPLC kinetic data is as follows:

(i) The HPLC integrals of the functionalised benzaldehydes (BA) are normalised using the integrals of the internal standards (IS) for each measurement at each time point.

$$[BA]_{t,norm} = \frac{[BA]_t}{[IS]_t}$$

(ii) To ensure high precision of the amount of benzaldehyde present at $t = 0$ the average of the multiple measured $[BA]_{t=0,norm}$ values for the stock solution is calculated.

$$[BA]_{t=0,norm,avg} = \frac{\sum[BA]_{t=0,norm}}{n}$$

(iii) The conversion of the benzaldehyde is calculated for each time point.

$$conversion[BA]_t = \left(\frac{\left([BA]_{t=0,norm,avg} - [BA]_{t,norm}\right)}{[BA]_{t=0,norm,avg}}\right) \cdot 100$$

(iv) The amount of product present at each time point $[product]_t$ is determined using the calculated $conversion[BA]_t$ and the known amount of benzaldehyde used in the catalysis.

$$product_t = mol\ of\ BA \cdot \left(\frac{conversion[BA]_t}{100}\right)$$

(v) The number of catalyst units present in the RAI-MUF-77 catalyst (*# catalyst units*) is calculated using the weight of the dried MOF crystals and the molecular weight of the MOF, calculated from its formula (e.g. the RAI-MOF catalyst $[Zn_4O(hhextt)_{1.33}(bpdc\text{-}gua)_{0.5}(bdc\text{-}^5N\text{-}(S)\text{-}AlaOH)_{0.5}]$ has a molecular weight of 1859.61 g/mol). The number of catalyst units present equals 50% of the amount of MOF present.

$$\#\ catalyst\ units = \left(\frac{mass\ of\ MOF\ crystals}{molecular\ weight\ of\ MOF}\right) \cdot 0.5$$

(vi) The TON for each time point (TON_t) is calculated using the amount of product present at each time point $[product]_t$ and the number of catalyst units present in the RAI-MUF-77 catalyst.

$$TON_t = \frac{product_t}{\#\ catalyst\ units}$$

(vii) The TOF for each time point (TOF_t) is calculated using the amount of product that is produced between two time points ($\Delta product_{t\text{-}(t\text{-}1)}$) and the time between the respective measurements (Δt).

$$TOF_t = \frac{(\Delta product_{\Delta t})}{(\Delta t \cdot \#\ catalyst\ units)}$$

4.4.2.5 Monitoring the progress of a catalysis over time: Low catalyst loading

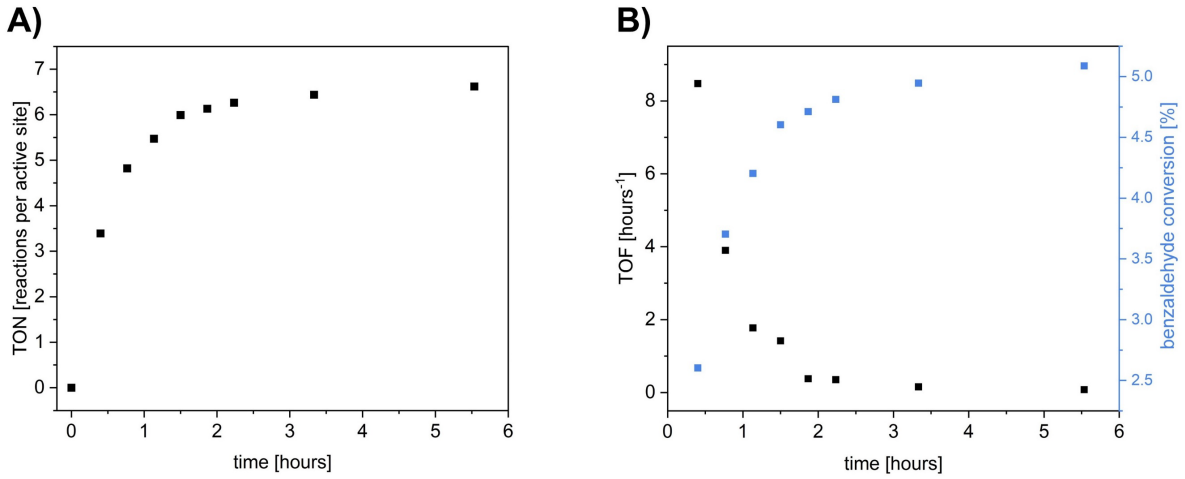

Figure 4.20 Calculated TON_t **A)** and TOF_t and benzaldehyde conversion **B)** of the Henry reaction of 5-methyl-2-nitrobenzaldehyde with nitromethane in 1,4-dioxane catalysed by MUF-77_gua_^{5}N_10 monitored over time. Catalyst loading was retrospectively calculated to be 0.77%.

4.4.2.6 Dependency of ee on conversion

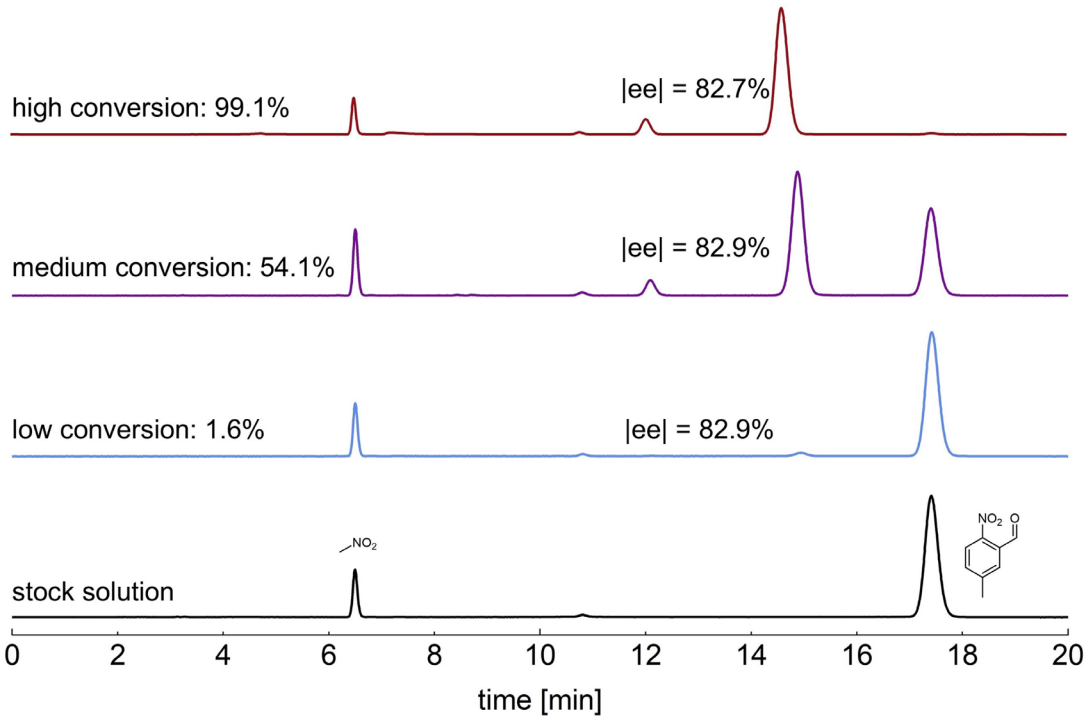

Figure 4.21 HPLC trace of the stock solution for the Henry reaction of 5-methyl-2-nitrobenzaldehyde with nitromethane in 1,4-dioxane (black) and the reaction solutions catalysed by MUF-77_gua_^{5}N_10 showing low (blue), medium (purple) and high (red) conversions. The calculated ee values are stated.

Chapter 5 - Summary and Perspectives

5.1 Thesis summary

This project developed and optimised a conceptually novel approach to asymmetric catalysis. Remote asymmetric induction (RAI) catalysis achieves stereocontrol through the spatially remote interaction of independent chiral and catalytic motifs. These moieties are separately designed and synthesised then brought into spatial proximity in the multicomponent metal-organic framework MUF-77. This framework served as a modular and well-defined structural platform for RAI catalyst development. The catalysts were evaluated and optimised across several aspects: reaction scope, enantioselectivity, validation of the foundational concepts and the overall catalyst performance. Through this systematic approach, a high-performing RAI-MOF catalyst was identified for the Henry reaction, yielding an enantioselectivity of up to 87.8%.

The first part of the project focused on exploring the reaction scope of RAI-catalysis. A structured step-by-step screening approach was developed, that began with the design and synthesis of achiral catalyst linkers and non-catalytic chiral linkers. Both types of linkers were then successfully co-integrated into the MUF-77 framework to generate a series of RAI-MOFs. These RAI catalysts were tested for their enantioselectivity across different reactions and conditions. The Henry reaction catalysed by RAI-MUF-77 catalysts consisting of a guanidine catalyst linker (bpdc-gua) and amino alcohol based chiral linkers (bdc-^{5}N-chiral) was identified as the most promising system to be explored in depth.

In the second phase of the project, the enantioselectivity and the substrate scope of RAI guanidine catalyst MOFs for the Henry reaction was maximised. This was achieved by altering a single variable at a time and monitoring the effect on the enantiomeric excess of the chiral product. The key variables that influenced the enantioselectivity were identified to be the functionalities on the chiral linker, alkyl chain length on the truxene, identity and backbone of the catalyst linker, solvent, functionalities attached to the benzaldehyde, presence of additives and reaction conditions.

From the 15 chiral linkers that were synthesised and tested, the bdc-^{5}N-(*S*)-AlaOH, featuring the amino alcohol alaninol as its chiral group, was the highest performing. The truxene functionalised with hexyl chains was identified to produce the highest ee values, which was attributed to optimal pore filling. Among 28 solvents, 1,4-dioxane proved to be the most effective. Screening 46 benzaldehyde derivatives, a high variation in ee was observed depending on the identity and substitution pattern of functionalities on the ring. 5-Methyl-2-nitrobenzaldehyde produced the highest ee. Modifications to the guanidine catalyst group, as

for example methylation, also strongly affected the efficiency of chiral induction. The addition of pyridine as an additive increased the enantioselectivity, while other additives had no effect. Finally, the reaction conditions also had a marginal effect. Lower concentrations and lower temperatures were correlated with higher enantioselectivity. Combining all optimised parameters delivered an enantioselectivity of 87.8%. Additional experiments using intentionally lower-performing variables confirmed that this result likely represents a global optimum for the current system.

In the final part of the project, the key hypotheses forming the foundation of the RAI concept were validated, and the performance of the catalyst was explored beyond the metric of enantioselectivity. It was shown that both linkers must be present and held together within the MOF framework for chiral induction to take place. Moreover, changing the stereochemistry of the chiral linker also changed the chiral information transferred to the product, validating the core concepts. Catalyst reproducibility and recyclability were shown to be excellent, with consistent enantioselectivities across different synthesis batches and high stability over ten reaction cycles. The catalyst's turnover number and turnover frequency were determined, and the influence of additives on these parameters was investigated. Lastly, the mechanism for the Henry reaction within the MOF pores was discussed. Based on experimental data and considering the spatial arrangements of the linker functionalities within the pores through structural analysis, a hypothesis was made for the transition state responsible for chiral induction *via* remote interaction of the catalyst, substrates, and chiral linker.

Collectively, these results establish RAI as a viable method of achieving asymmetric catalysis. Despite being a conceptually new approach, RAI catalysis has already proven capable of delivering high enantioselectivities. There also exists significant scope for future developments.

5.2 Outlook

The future of RAI-catalysis using MUF-77 as its platform can be summarised by three primary objectives:

(i) to build on the results presented in this work and further maximise the enantioselectivity of the MUF-77 RAI catalysts for the Henry reaction,

(ii) to explore whether reversing the roles of the two linear linkers - attaching the catalytic group to the shorter bdc linker and the chiral moiety to the longer bpdc linker - produces comparable or improved enantioselectivities; and

(iii) to expand the reaction scope of MUF-77 RAI-catalysis to be useful for a broad range of asymmetric transformations.

All of these objectives can be pursued using the same one variable at a time approach as discussed in this work. However, with the key parameters affecting enantioselectivity now clearly identified, adopting a 'design of experiments' approach presents a viable alternative. By systematically exploring multiple variables simultaneously, this approach could significantly reduce the experimental workload and accelerate the future of RAI-catalysis.

5.2.1 Maximising the ee

To further optimise the enantioselectivity of the RAI-MUF-77 catalysts for the Henry reaction, a goal could be set to consistently obtain enantioselectivities in excess of 95% across a broader substrate range. This could be pursued by systematically expanding the key variables that have been identified to influence the enantioselectivity in a pronounced way. This could primarily be achieved through the design of new MOF linkers. Some efforts to expand on the current system have already been performed, and the corresponding preliminary results are presented and discussed here. Other ligand designs are proposed, and their design rationale is discussed.

5.2.1.1 Catalyst linkers

During the work presented in **Chapter 3.2.5**, it was observed that the identity of the achiral guanidine catalyst linker had a pronounced effect on the enantioselectivity of the RAI-MUF-77 catalysts. To further investigate this, several new catalyst linkers were designed, and viable synthetic routes were developed, initially on paper (**Figure 5.1**).

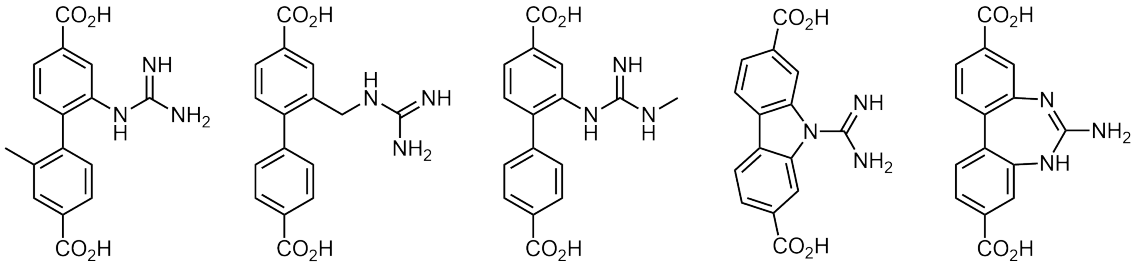

Figure 5.1 Depiction of proposed achiral guanidine catalysts to be synthesised and tested.

The linker H_2bpdc(Me)-gua (**A**) was designed based on the high-performing H_2bpdc-gua catalyst. Here, a methyl group is introduced on the second phenyl ring of the bpdc backbone. This will restrict the rotational freedom of the phenyl rings and enforce a different orientation of the catalytic guanidine group in the framework pore.

The opposite approach – increasing rotational freedom – inspired the design of the linker H_2bpdc-CH_2-gua (**B**). A methylene spacer is introduced between the bpdc backbone and the guanidine group. This will enable the catalytic group to sample a different range of spatial orientations, which may enhance interactions between the substrate and the chiral linker.

The design of H_2bpdc-gua(Me) (**C**) was inspired by the catalyst linker H_2bpdc-gua$(Me)_2$, which was discussed in **Chapter 3.2.5.1**. The key modification is that H_2bpdc-gua(Me) only features one methyl group attached to the guanidine group instead of two. This variation aims to establish whether the reduced enantioselectivities previously observed for the di-methylated variant were due to the double-substitution, or if even mono-substitution at the guanidine affects the stereo control in a similar manner.

The catalyst linker H_2bpdc-^{5}N-gua (**D**) was designed drawing from the well-established platform of carbazoles. This design is inspired by the high-performing H_2bpdc-gua catalyst, but with the two phenyl rings connected over the first nitrogen of the guanidine moiety. This small change makes the linker more symmetrical and rigid, giving the catalytic guanidine group a slightly different spatial orientation.

Similar to H_2bpdc-^{5}N-gua, in the catalyst linker H_2bpdc-^{7}N-secgua (**E**) the two phenyl rings are directly connected to one another through the guanidine group. However, in this case, the bridging involves two of the three nitrogen atoms. This modification again subtly alters the spatial arrangement of the catalytic functionality.

5.2.1.2 Chiral linkers with acid and ester functionalities

To date, all chiral linkers based on the H_2bdc-^{5}N-chiral linker structure were functionalised with amino alcohols or related motifs. None of the presented linkers featured a carboxyl group, as this was initially expected to impede the successful formation of MUF-77. However, concurrent research by other members of our research group has demonstrated that the incorporation of a carboxylic acid group on the H_2bdc-^{5}N-chiral backbone is compatible with MUF-77 formation. This advancement enables the inclusion of amino acids and other related structures into the RAI catalyst. Given their strong hydrogen bonding capacity, carboxyl-containing linkers are particularly attractive, as hydrogen bonding has proven essential for achieving enantioselectivity in this system. Building on this design principle, amino acid esters also were identified as feasible chiral motifs. Notable examples include H_2bdc-^{5}N-(*S*)-AlaCO_2H and H_2bdc-^{5}N-(*S*)-AlaCO_2R (R = methyl or *tert*-butyl). These linkers retain the same core structure as the highest performing linker H_2bdc-^{5}N-(*S*/*R*)-AlaOH but replace the alcohol with a carboxylic acid or ester group (**Figure 5.2**).

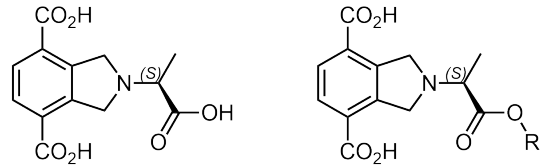

Figure 5.2 Depiction of H_2bdc-^{5}N-(*S*)-AlaCO_2H and H_2bdc-^{5}N-(*S*)-AlaCO_2R (R = methyl or *tert*-butyl) as the representative examples for H_2bdc-^{5}N-chiral linkers featuring carboxylic acid or ester groups.

Beyond alanine, these classes of chiral linkers are potentially extensible to all natural amino acids and structurally related motifs, with the condition that they are non-catalytic. Importantly, the identical synthetic route used for the amino alcohol-based linkers can be used to synthesise both classes of chiral linkers, which has been confirmed by work of other group members.

5.2.1.3 Truxene functionalisation

Throughout this work, all functionalised truxenes featured simple linear alkyl chains of varying lengths. It was shown that alkyl chain length significantly affects the enantioselectivity of the MUF-77 RAI catalysts, with hexyl-functionalised truxene being the most effective. This observation was attributed to the hexyl chains optimally filling the achiral but catalytic large pores present in MUF-77 and thus directing substrates to the small pores. In contrast, shorter chains leave these larger pores open to substrates, while longer chains may overfill the large pores and invade the small pores. Both of these effects would disrupt enantioselectivity. To

explore this observation further, other types of substituents beyond linear chains offer a promising approach. Two possible variations are shown in **Figure 5.3** that can be expanded to feature motifs of different sizes.

The first example (**Figure 5.3** left) replaces linear alkyl chains with branched variants, doubling the number of chain endings present within the pore. The second example (**Figure 5.3** right) replaces the linear alkyl chains with rings, which eliminates chain endings from the pores. In both cases, the overall number of carbon atoms remains similar to their linear analogues, but the steric bulk is concentrated near the truxene core rather than extending linearly into the pore centre. These truxenes will therefore help determine whether it is the total size of the functionalities (measured by atom count) or their spatial shape and orientation within the pores that more strongly influences enantioselectivity.

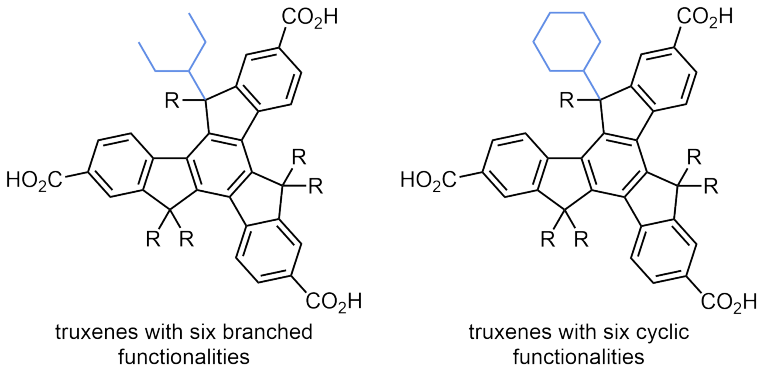

Figure 5.3 Depiction of possible truxenes featuring six branched or cyclic functionalities or three cyclic ones. For clarity, a single functionality is shown for each example in blue.

5.2.1.4 Different nitroalkanes as reagents for the Henry reaction

All Henry reactions discussed so far used nitromethane as a substrate. However, larger nitroalkane variants (**Figure 5.4 A**) are feasible alternatives and are expected to strongly influence the observed enantioselectivity.

A key requirement for these substrates is that the carbon atom bearing the nitro group must have at least one α-hydrogen to enable deprotonation and nucleophilic attack. This renders aromatic nitro compounds unsuitable. Nitroalkanes with non-identical substituents on this carbon atom, such as nitroethane or 1-nitropropane, lead to the formation of diastereomers (**Figure 5.4 B**). To avoid this added complexity, the two substituents on this carbon atom should be identical. 2-Nitropropane and nitrocyclohexane are examples of good substrates for future studies (**Figure 5.4 C**).

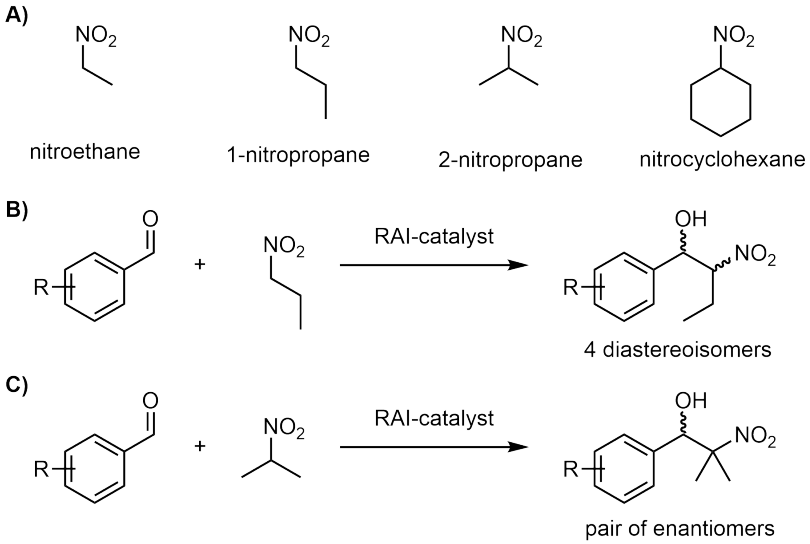

Figure 5.4 A) Possible nitroalkane substrates for the Henry reaction. **B)** The Henry reaction of functionalised benzaldehydes with 1-nitropropane to yield diastereoisomers. **C)** The Henry reaction of functionalised benzaldehydes with 2-nitropropane to yield a pair of enantiomers.

Preliminary experiments have been performed using 2-nitropropane and nitrocyclohexane to explore their effect on the enantioselectivity of the RAI catalyst. Two benzaldehydes were selected as representative examples: 2-chloro-5-nitrobenzaldehyde and 5-chloro-2-nitrobenzaldehyde. The catalysis was performed using the highest performing catalyst, MUF-77_gua_^{5}N_10 and at standard conditions.

Table 5.1 Measured ee values and qualitatively judged conversions for Henry reactions of substituted benzaldehydes with 2-nitropropane or nitrocyclohexane in 1,4-dioxane, catalysed by MUF-77_gua_^{5}N_10.

	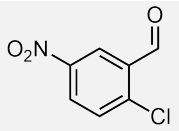	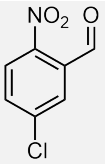
nitromethane	ee = 64.9% conversion: high	ee = 77.1% conversion: high
2-nitropropane	ee = not determined conversion: low	ee = not determined conversion: low
nitrocyclohexane	ee = 0% conversion: very low	ee = 0% conversion: very low

Both larger nitroalkanes yielded lower conversions than nitromethane. This was expected, as diffusion within the MOF pores of larger substrates is slower, thus decreasing the reaction

rate.[231] Nitrocyclohexane produced racemic product mixtures, showing that the bulky nitroalkane severely hindered stereocontrol.

Unexpected complications arose with 2-nitropropane. HPLC analysis revealed a complex mixture of overlapping peaks. Investigation using NMR showed the presence of 3% 1-nitropropane as an impurity in 2-nitropropane. 1-Nitropropane reacted disproportionately quickly, generating a mixture of diastereomeric products responsible for the additional HPLC signals. Attempts to separate the product mixture on HPLC were unsuccessful.

Given the impurity of 2-nitropropane, the study was paused. Nevertheless, further investigation using purified nitroalkanes is worth pursuing. Moreover, this outcome points to a compelling different direction for future work: exploring the diastereoselective capabilities of the MUF-77 RAI catalysts. This could potentially extend the scope of the RAI concept beyond enantioselectivity to broader stereochemical selectivity.

5.2.1.5 Different aldehydes or ketones as reagents for the Henry reaction

While all Henry reactions discussed so far have used functionalised benzaldehydes, aliphatic aldehydes could also potentially be used as substrates (**Figure 5.5 A**).[229] This change in substrate class is expected to greatly influence the enantioselectivity and would further test the substrate scope of RAI-catalysis. Additionally, ketones are also potential substrates, even though they remain underexplored in the organocatalysis literature.[232] Activated ketones featuring electron-withdrawing groups are likely the most suitable candidates (**Figure 5.5 B**), as these groups potentially help to overcome the inherently lower electrophilicity of ketones in nucleophilic addition reactions.[233]

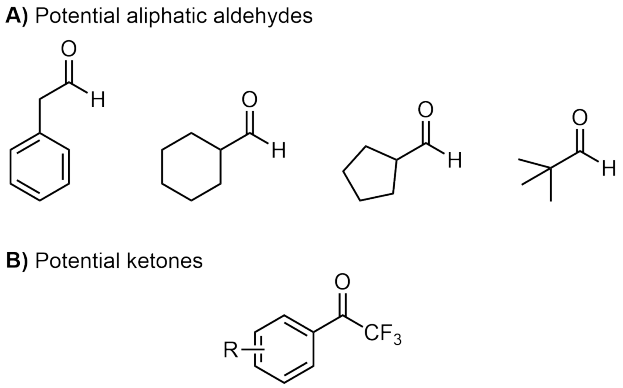

Figure 5.5 A) Potential aldehydes and **B)** ketones as substrates for the Henry reaction.

5.2.1.6 Identifying which product enantiomer is produced

Throughout this work, enantioselectivity was discussed without assigning absolute stereochemistry to the product enantiomers. The enantiomer that eluted first from the HPLC column was denoted as 'enantiomer 1', while the second was referred to as 'enantiomer 2'. This enabled discussion of the ee and allowed for comparison of enantioselectivity without the assignment of the exact stereochemistry. However, to support future high-level computational analysis, with the goal of identifying the exact origin of enantioselectivity, the absolute stereochemistry for at least the highest performing benzaldehyde should be determined.

In principle, comparison with the literature could allow stereochemical assignment, provided that the exact same HPLC conditions, including column type and mobile phase, were used. This, however, is rare, and for example, for the highest performing benzaldehyde, 5-methyl-2-nitrobenzaldehyde, no Henry product has even been reported so far.

An alternative and more feasible approach is to determine the stereochemistry of the enantiomers by SCXRD analysis. This requires large-scale catalysis producing exclusively one enantiomer, in sufficient quantity to grow single crystals. However, the Henry products in this study are typically oils. Therefore, to potentially obtain single crystals, a derivatisation step would be required. For example, the hydroxy group of the β-nitro alcohol could be derivatised into an ester. Importantly, this must be done with a sample as close to 100% ee as possible, otherwise there is a risk of crystallising a racemic mixture or selecting a crystal of the statistically less abundant enantiomer.

5.2.2 Reversing the roles of the two linear linkers

In the presented work, the longer linear linker bpdc was exclusively functionalised with achiral catalytic groups, while the shorter linear linker bdc was functionalised only with chiral moieties. An alternative would be to reverse these roles: functionalising the bdc linker with the catalytic group and the bpdc linker with the chiral group (**Figure 5.6 A**). This approach should in principle produce similar enantioselectivities and provide an important cross-validation of the design flexibility of the RAI concept.

This alternative strategy is currently being investigated by other members of our group. This work applies the reversed design to the MUF-77 framework, leading to the development of a new library of RAI catalysts. Selected examples of catalyst and chiral linkers investigated as part of this approach are shown in **Figure 5.6 B**.

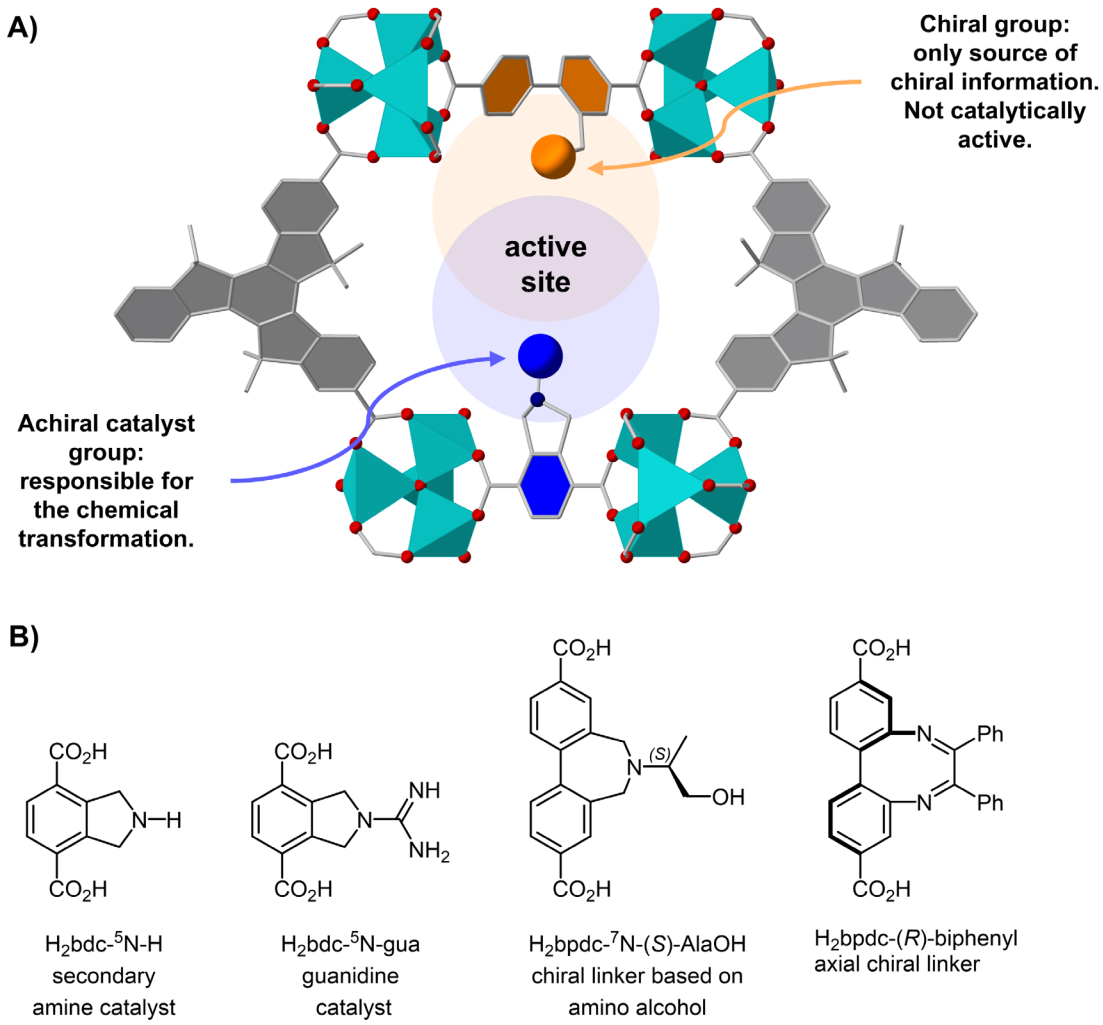

Figure 5.6 A) Schematic representation of an RAI active site in the tetrahedral micropores present in MUF-77, but with reversed roles of the linear linkers compared to this work. **B)** Examples of bdc-catalyst and bpdc-chiral linkers investigated in this approach to implement the RAI concept in MUF-77.

5.2.3 Expanding the scope of RAI MUF-77 catalysis

The third objective for the future is to extend the scope of the RAI concept. This can be approached in two ways:

(i) identifying new asymmetric reactions that are compatible with the currently available catalyst linkers; or

(ii) designing and synthesising novel catalyst linkers featuring functional groups not previously investigated with the RAI MUF-77 catalysts.

Both strategies have considerable potential, although individual limitations exist. Catalyst functional groups must be compatible with MOF synthesis conditions, and the reaction substrates should be sufficiently small to enter the pores of MUF-77.

For example, a promising inspiration comes from the organocatalysis literature on chiral phosphoric acids. These catalysts are used in numerous asymmetric transformations, including cycloadditions and the Pictet–Spengler reactions.[234-236] Using this inspiration for the design of phosphoric acid functionalised MOF linkers may unlock new asymmetric transformations for the RAI MUF-77 platform (**Figure 5.7 A**). These catalysts can be tested for their activity as homogeneous catalysis (e.g. the Pictet-Spengler reaction) and then further extended to explore MUF-77 framework formation and RAI activity (**Figure 5.7 B**).

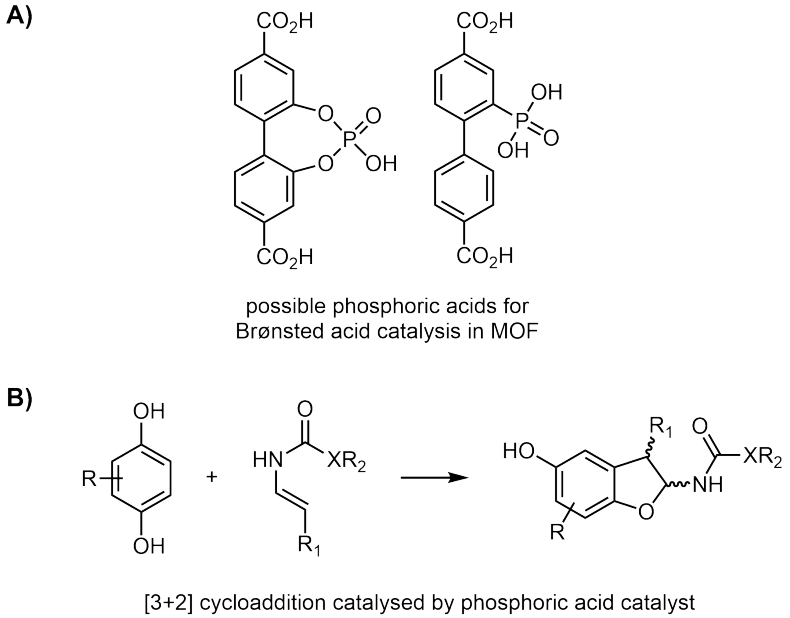

Figure 5.7 A) Depiction of potential phosphoric acid bpdc linkers. **B)** Example of a [3+2] cycloaddition reaction that is catalysed by phosphoric acids and represents a potential transformation to be explored using RAI catalysts.

By pursuing these three objectives the RAI concept may be significantly broadened and enhanced in terms of both scope and selectivity. Beyond this, the results of this work may serve as inspiration for future development of RAI catalysis on different structural platforms, including other MOFs or molecular cages.

References

(1) Catlow, C. R.; Davidson, M.; Hardacre, C.; Hutchings, G. J. Catalysis making the world a better place. *Philos. Trans. Royal Soc. A* **2016**, *374* (2061), 20150089.
(2) Beller, M.; Renken, A.; van Santen, R. A. *Catalysis: from principles to applications*; Wiley, 2012.
(3) Bonner, W. A. Chirality and life. *Origins of Life and Evolution of the Biosphere* **1995**, *25* (1-3), 175-190.
(4) Walsh, P. J.; Kozlowski, M. C. *Fundamentals of asymmetric catalysis*; University Science Books, 2009.
(5) Cahn, R. S.; Ingold, C.; Prelog, V. Specification of molecular chirality. *Angew. Chem. Int. Ed.* **1966**, *5* (4), 385-415.
(6) Inaki, M.; Liu, J.; Matsuno, K. Cell chirality: its origin and roles in left–right asymmetric development. *Philos. Trans. R. Soc. B* **2016**, *371* (1710), 20150403.
(7) Barron, L. D. Chirality and Life. *Space Sci. Rev.* **2008**, *135* (1-4), 187-201.
(8) Flügel, R. M. Chirality and Life. **2011**.
(9) Campos, K. R.; Coleman, P. J.; Alvarez, J. C.; Dreher, S. D.; Garbaccio, R. M.; Terrett, N. K.; Tillyer, R. D.; Truppo, M. D.; Parmee, E. R. The importance of synthetic chemistry in the pharmaceutical industry. *Science* **2019**, *363* (6424).
(10) Tiritan, M. E.; Fernandes, C.; Maia, A. S.; Pinto, M.; Cass, Q. B. Enantiomeric ratios: Why so many notations? *J. Chromatogr. A.* **2018**, *1569*, 1-7.
(11) Kagan, H. B. Is there a preferred expression for the composition of a mixture of enantiomers? *Recl. Trav. Chim. Pays-Bas* **1995**, *114* (4-5), 203-205.
(12) Gawley, R. E. Do the Terms "% ee" and "% de" Make Sense as Expressions of Stereoisomer Composition or Stereoselectivity? *J. Org. Chem.* **2006**, *71* (6), 2411-2416.
(13) Schurig, V. Terms for the Quantitation of a Mixture of Stereoisomers. In *Differentiation of Enantiomers I*, Schurig, V. Ed.; Springer International Publishing, 2013; pp 21-40.
(14) Yoon, T. P.; Jacobsen, E. N. Privileged Chiral Catalysts. *Science* **2003**, *299* (5613), 1691-1693.
(15) Meninno, S.; Lattanzi, A. Asymmetric organocatalytic journey into the world of three-membered rings. *Catal. Today* **2017**, *285*, 39-48.
(16) García Mancheño, O.; Waser, M. Recent Developments and Trends in Asymmetric Organocatalysis. *Eur. J. Org. Chem.* **2023**, *26* (1), e202200950.
(17) Vogel, P.; Lam, Y.-h.; Simon, A.; Houk, K. N. Organocatalysis: Fundamentals and Comparisons to Metal and Enzyme Catalysis. *Catalysts* **2016**, *6* (9), 128.
(18) Heitbaum, M.; Glorius, F.; Escher, I. Asymmetric Heterogeneous Catalysis. *Angew. Chem. Int. Ed.* **2006**, *45* (29), 4732-4762.

(19) Blake, C. C. F.; Koenig, D. F.; Mair, G. A.; North, A. C. T.; Phillips, D. C.; Sarma, V. R. Structure of Hen Egg-White Lysozyme: A Three-dimensional Fourier Synthesis at 2 Å Resolution. *Nature* **1965**, *206* (4986), 757-761.
(20) Ahrendt, K. A.; Borths, C. J.; MacMillan, D. W. C. New Strategies for Organic Catalysis: The First Highly Enantioselective Organocatalytic Diels−Alder Reaction. *J. Am. Chem. Soc.* **2000**, *122* (17), 4243-4244.
(21) Ohkuma, T.; Ooka, H.; Hashiguchi, S.; Ikariya, T.; Noyori, R. Practical enantioselective hydrogenation of aromatic ketones. *J. Am. Chem. Soc.* **1995**, *117* (9), 2675-2676.
(22) Iyer, P. V.; Ananthanarayan, L. Enzyme stability and stabilization—Aqueous and non-aqueous environment. *Process Biochem.* **2008**, *43* (10), 1019-1032.
(23) Chapman, J.; Ismail, A. E.; Dinu, C. Z. Industrial Applications of Enzymes: Recent Advances, Techniques, and Outlooks. *Catalysts* **2018**, *8* (6), 238.
(24) Whitesides, G. M.; Wong, C.-H. Enzymes as Catalysts in Synthetic Organic Chemistry. *Angew. Chem. Int. Ed. Engl.* **1985**, *24* (8), 617-638.
(25) Voet, D.; Voet, J. G. *Biochemistry*; John Wiley & Sons, 2010.
(26) Anfinsen, C. B. Principles that Govern the Folding of Protein Chains. *Science* **1973**, *181* (4096), 223-230.
(27) Bartlett, G. J.; Porter, C. T.; Borkakoti, N.; Thornton, J. M. Analysis of Catalytic Residues in Enzyme Active Sites. *J. Mol. Biol.* **2002**, *324* (1), 105-121.
(28) Hollmann, F.; Otten, L. G. Enantioselectivity of enzymes. *Wiley Encyclopedia of Chemical Biology* **2007**, 1-7.
(29) García-Urdiales, E.; Alfonso, I.; Gotor, V. Enantioselective Enzymatic Desymmetrizations in Organic Synthesis. *Chem. Rev.* **2005**, *105* (1), 313-354.
(30) Hedstrom, L. Serine Protease Mechanism and Specificity. *Chem. Rev.* **2002**, *102* (12), 4501-4524.
(31) Kashima, A.; Inoue, Y.; Sugio, S.; Maeda, I.; Nose, T.; Shimohigashi, Y. X-ray crystal structure of a dipeptide-chymotrypsin complex in an inhibitory interaction. *Eur. J. Biochem.* **1998**, *255* (1), 12-23.
(32) Silverman, R. B. *Organic chemistry of enzyme-catalyzed reactions*; Elsevier, 2002.
(33) Rasor, J. P.; Voss, E. Enzyme-catalyzed processes in pharmaceutical industry. *Appl. Catal. A: Gen.* **2001**, *221* (1), 145-158.
(34) Patel, R. N. Biocatalytic synthesis of chiral pharmaceutical intermediates. *Food Technol. Biotechnol.* **2004**, *42* (4), 305-325.
(35) Zhao, H. Recent advances in enzymatic carbon–carbon bond formation. *RSC Adv.* **2024**, *14* (36), 25932-25974.
(36) Liu, J.; Wu, S.; Li, Z. Recent advances in enzymatic oxidation of alcohols. *Curr. Opin. Chem. Biol.* **2018**, *43*, 77-86.

(37) Hall, M. Enzymatic strategies for asymmetric synthesis. *RSC Chem. Biol.* **2021**, *2* (4), 958-989.
(38) Sheldon, R. A.; Woodley, J. M. Role of Biocatalysis in Sustainable Chemistry. *Chem. Rev.* **2018**, *118* (2), 801-838.
(39) Fromm, H. J. The Effect of Temperature and pH on Enzyme Activity. In *Initial Rate Enzyme Kinetics*, Fromm, H. J. Ed.; Springer Berlin Heidelberg, 1975; pp 201-235.
(40) Smejkal, G. B.; and Kakumanu, S. Enzymes and their turnover numbers. *Expert Rev. Proteomics* **2019**, *16* (7), 543-544.
(41) Bornscheuer, U. T.; Huisman, G. W.; Kazlauskas, R. J.; Lutz, S.; Moore, J. C.; Robins, K. Engineering the third wave of biocatalysis. *Nature* **2012**, *485* (7397), 185-194.
(42) Renata, H.; Wang, Z. J.; Arnold, F. H. Expanding the Enzyme Universe: Accessing Non-Natural Reactions by Mechanism-Guided Directed Evolution. *Angew. Chem. Int. Ed.* **2015**, *54* (11), 3351-3367.
(43) Arnold, F. H. Design by directed evolution. *Acc. Chem. Res.* **1998**, *31* (3), 125-131.
(44) Eijsink, V. G. H.; Gåseidnes, S.; Borchert, T. V.; van den Burg, B. Directed evolution of enzyme stability. *Biomol. Eng.* **2005**, *22* (1), 21-30.
(45) Noyori, R. Asymmetric catalysis: science and opportunities (Nobel lecture). *Angew. Chem. Int. Ed.* **2002**, *41* (12), 2008-2022.
(46) Knowles, W. S. Asymmetric hydrogenations (Nobel lecture). *Angew. Chem. Int. Ed.* **2002**, *41* (12), 1998-2007.
(47) Sharpless, K. B. Searching for new reactivity (Nobel lecture). *Angew. Chem. Int. Ed.* **2002**, *41* (12), 2024-2032.
(48) Jacobsen, E. N.; Pfaltz, A.; Yamamoto, H. *Comprehensive asymmetric catalysis, Vol. 1*; Springer 2003.
(49) Steinlandt, P. S.; Zhang, L.; Meggers, E. Metal Stereogenicity in Asymmetric Transition Metal Catalysis. *Chem. Rev.* **2023**, *123* (8), 4764-4794.
(50) Wilkins, L. C.; Melen, R. L. Enantioselective main group catalysis: modern catalysts for organic transformations. *Coord. Chem. Rev.* **2016**, *324*, 123-139.
(51) Pramanik, M.; Guerzoni, M. G.; Richards, E.; Melen, R. L. Recent Advances in Asymmetric Catalysis Using p-Block Elements. *Angew. Chem. Int. Ed.* **2024**, *63* (9), e202316461.
(52) Pfaltz, A.; Drury, W. J. Design of chiral ligands for asymmetric catalysis: From C_2-symmetric P,P- and N,N-ligands to sterically and electronically nonsymmetrical P,N-ligands. *Proc. Natl. Acad. Sci.* **2004**, *101* (16), 5723-5726.
(53) Hartung, J.; Grubbs, R. H. Highly Z-Selective and Enantioselective Ring-Opening/Cross-Metathesis Catalyzed by a Resolved Stereogenic-at-Ru Complex. *J. Am. Chem. Soc.* **2013**, *135* (28), 10183-10185.

(54) Jacobsen, E. N.; Zhang, W.; Muci, A. R.; Ecker, J. R.; Deng, L. Highly enantioselective epoxidation catalysts derived from 1, 2-diaminocyclohexane. *J. Am. Chem. Soc.* **1991**, *113* (18), 7063-7064.
(55) Touge, T.; Hakamata, T.; Nara, H.; Kobayashi, T.; Sayo, N.; Saito, T.; Kayaki, Y.; Ikariya, T. Oxo-Tethered Ruthenium(II) Complex as a Bifunctional Catalyst for Asymmetric Transfer Hydrogenation and H_2 Hydrogenation. *J. Am. Chem. Soc.* **2011**, *133* (38), 14960-14963.
(56) Chen, Y.; Yekta, S.; Yudin, A. K. Modified BINOL ligands in asymmetric catalysis. *Chem. Rev.* **2003**, *103* (8), 3155-3212.
(57) Baleizão, C.; Garcia, H. Chiral Salen Complexes: An Overview to Recoverable and Reusable Homogeneous and Heterogeneous Catalysts. *Chem. Rev.* **2006**, *106* (9), 3987-4043.
(58) Tang, W.; Zhang, X. New Chiral Phosphorus Ligands for Enantioselective Hydrogenation. *Chem. Rev.* **2003**, *103* (8), 3029-3070.
(59) Fontecave, M.; Hamelin, O.; Ménage, S. Chiral-at-Metal Complexes as Asymmetric Catalysts. In *Chiral Diazaligands for Asymmetric Synthesis*, Lemaire, M., Mangeney, P. Eds.; Springer Berlin Heidelberg, 2005; pp 271-288.
(60) Zhang, L.; Meggers, E. Stereogenic‐Only‐at‐Metal Asymmetric Catalysts. *Chem. Asian J.* **2017**, *12* (18), 2335-2342.
(61) Dub, P. A.; Gordon, J. C. The role of the metal-bound N–H functionality in Noyori-type molecular catalysts. *Nat. Rev. Chem.* **2018**, *2* (12), 396-408.
(62) Shimizu, H.; Nagasaki, I.; Matsumura, K.; Sayo, N.; Saito, T. Developments in Asymmetric Hydrogenation from an Industrial Perspective. *Acc. Chem. Res.* **2007**, *40* (12), 1385-1393.
(63) Cozzi, P. G. Metal–Salen Schiff base complexes in catalysis: practical aspects. *Chem. Soc. Rev.* **2004**, *33* (7), 410-421.
(64) Cao, Z.-Y.; Brittain, W. D.; Fossey, J. S.; Zhou, F. Recent advances in the use of chiral metal complexes with achiral ligands for application in asymmetric catalysis. *Catal. Sci. Technol.* **2015**, *5* (7), 3441-3451.
(65) Yin, C.; Jiang, Y.-F.; Huang, F.; Xu, C.-Q.; Pan, Y.; Gao, S.; Chen, G.-Q.; Ding, X.; Bai, S.-T.; Lang, Q.; et al. A 13-million turnover-number anionic Ir-catalyst for a selective industrial route to chiral nicotine. *Nat. Commun.* **2023**, *14* (1), 3718.
(66) Sheldon, R. A. Fundamentals of green chemistry: efficiency in reaction design. *Chem. Soc. Rev.* **2012**, *41* (4), 1437-1451.
(67) Editorial. Price pressures on metals. *Nat. Catal.* **2019**, *2* (9), 735-735.
(68) García Mancheño, O.; Waser, M. Recent Developments and Trends in Asymmetric Organocatalysis. *Eur. J. Org. Chem.* **2023**, *26* (1).
(69) MacMillan, D. W. C. The advent and development of organocatalysis. *Nature* **2008**, *455* (7211), 304-308.

(70) Berkessel, A.; Gröger, H. *Asymmetric organocatalysis: from biomimetic concepts to applications in asymmetric synthesis*; John Wiley & Sons, 2006.
(71) Mukherjee, S.; Yang, J. W.; Hoffmann, S.; List, B. Asymmetric Enamine Catalysis. *Chem. Rev.* **2007**, *107* (12), 5471-5569.
(72) Min, C.; Seidel, D. Asymmetric Brønsted acid catalysis with chiral carboxylic acids. *Chem. Soc. Rev.* **2017**, *46* (19), 5889-5902.
(73) Palomo, C.; Oiarbide, M.; López, R. Asymmetric organocatalysis by chiral Brønsted bases: implications and applications. *Chem. Soc. Rev.* **2009**, *38* (2), 632-653.
(74) Dong, S.; Feng, X.; Liu, X. Chiral guanidines and their derivatives in asymmetric synthesis. *Chem. Soc. Rev.* **2018**, *47* (23), 8525-8540.
(75) Takemoto, Y. Development of chiral thiourea catalysts and its application to asymmetric catalytic reactions. *Chem. Pharm. Bull.* **2010**, *58* (5), 593-601.
(76) Connon, S. J. Organocatalysis mediated by (thio) urea derivatives. *Chem. Eur. J.* **2006**, *12* (21), 5418-5427.
(77) Okino, T.; Hoashi, Y.; Takemoto, Y. Enantioselective Michael Reaction of Malonates to Nitroolefins Catalyzed by Bifunctional Organocatalysts. *J. Am. Chem. Soc.* **2003**, *125* (42), 12672-12673.
(78) List, B.; Lerner, R. A.; Barbas, C. F. Proline-Catalyzed Direct Asymmetric Aldol Reactions. *J. Am. Chem. Soc.* **2000**, *122* (10), 2395-2396.
(79) Akiyama, T.; Itoh, J.; Yokota, K.; Fuchibe, K. Enantioselective Mannich‐Type Reaction Catalyzed by a Chiral Brønsted Acid. *Angew. Chem.* **2004**, *116* (12), 1592-1594.
(80) Ye, W.; Leow, D.; Goh, S. L. M.; Tan, C.-T.; Chian, C.-H.; Tan, C.-H. Chiral bicyclic guanidines: a concise and efficient aziridine-based synthesis. *Tetrahedron Lett.* **2006**, *47* (6), 1007-1010.
(81) Hargittai, I. The 2021 chemistry Nobel laureates and asymmetric organocatalysis. *Struct. Chem.* **2022**, *33* (1), 303-305.
(82) Brown, S. P.; Goodwin, N. C.; MacMillan, D. W. C. The First Enantioselective Organocatalytic Mukaiyama−Michael Reaction: A Direct Method for the Synthesis of Enantioenriched γ-Butenolide Architecture. *J. Am. Chem. Soc.* **2003**, *125* (5), 1192-1194.
(83) Pellissier, H. Asymmetric organocatalysis. *Tetrahedron* **2007**, *63* (38), 9267-9331.
(84) Giacalone, F.; Gruttadauria, M.; Agrigento, P.; Noto, R. Low-loading asymmetric organocatalysis. *Chem. Soc. Rev.* **2012**, *41* (6), 2406-2447.
(85) Murzin, D. Y.; Mäki‐Arvela, P.; Toukoniitty, E.; Salmi, T. Asymmetric heterogeneous catalysis: science and engineering. *Catal. Rev.* **2005**, *47* (2), 175-256.
(86) Ding, K.; Uozumi, Y. *Handbook of asymmetric heterogeneous catalysis*; Wiley Online Library, 2008.
(87) De Vos, D.; Vankelecom, I. F.; Jacobs, P. A. *Chiral catalyst immobilization and recycling*; John Wiley & Sons, 2008.

(88) Mallat, T.; Orglmeister, E.; Baiker, A. Asymmetric Catalysis at Chiral Metal Surfaces. *Chem. Rev.* **2007**, *107* (11), 4863-4890.
(89) de Rege, F. M.; Morita, D. K.; Ott, K. C.; Tumas, W.; Broene, R. D. Non-covalent immobilization of homogeneous cationic chiral rhodium–phosphine catalysts on silica surfaces. *Chem. Commun.* **2000**, (18), 1797-1798.
(90) Dioos, B. M. L.; Jacobs, P. A. CrIII(salen) impregnated on silica for asymmetric ring opening reactions and its recovery via desorption/re-impregnation. *Tetrahedron Lett.* **2003**, *44* (49), 8815-8817.
(91) Hu, A.; Yee, G. T.; Lin, W. Magnetically Recoverable Chiral Catalysts Immobilized on Magnetite Nanoparticles for Asymmetric Hydrogenation of Aromatic Ketones. *J. Am. Chem. Soc.* **2005**, *127* (36), 12486-12487.
(92) Zaera, F. Chiral Modification of Solid Surfaces: A Molecular View. *J. Phys. Chem. C.* **2008**, *112* (42), 16196-16203.
(93) Sunoj, R. B. Transition State Models for Understanding the Origin of Chiral Induction in Asymmetric Catalysis. *Acc. Chem. Res.* **2016**, *49* (5), 1019-1028.
(94) Kozlowski, M. C.; Dixon, S. L.; Panda, M.; Lauri, G. Quantum Mechanical Models Correlating Structure with Selectivity: Predicting the Enantioselectivity of β-Amino Alcohol Catalysts in Aldehyde Alkylation. *J. Am. Chem. Soc.* **2003**, *125* (22), 6614-6615.
(95) Ruth, M.; Gensch, T.; Schreiner, P. R. Contrasting Historical and Physical Perspectives in Asymmetric Catalysis: $\Delta\Delta G^{\neq}$ versus Enantiomeric Excess. *Angew. Chem. Int. Ed.*. **2024**, *63* (48), e202410308.
(96) Kaib, P. S. J.; Schreyer, L.; Lee, S.; Properzi, R.; List, B. Extremely Active Organocatalysts Enable a Highly Enantioselective Addition of Allyltrimethylsilane to Aldehydes. *Angew. Chem. Int. Ed.* **2016**, *55* (42), 13200-13203.
(97) Rein, J.; Rozema, S. D.; Langner, O. C.; Zacate, S. B.; Hardy, M. A.; Siu, J. C.; Mercado, B. Q.; Sigman, M. S.; Miller, S. J.; Lin, S. Generality-oriented optimization of enantioselective aminoxyl radical catalysis. *Science* **2023**, *380* (6646), 706-712.
(98) Wagen, C. C.; McMinn, S. E.; Kwan, E. E.; Jacobsen, E. N. Screening for generality in asymmetric catalysis. *Nat. Chem.* **2022**, *610* (7933), 680-686.
(99) Zheng, W.-F.; Chen, J.; Qi, X.; Huang, Z. Modular and diverse synthesis of amino acids via asymmetric decarboxylative protonation of aminomalonic acids. *Nat. Chem.* **2023**, *15* (12), 1672-1682.
(100) Cole-Hamilton, D. J. Homogeneous Catalysis--New Approaches to Catalyst Separation, Recovery, and Recycling. *Science* **2003**, *299* (5613), 1702-1706.
(101) Shende, V. S.; Saptal, V. B.; Bhanage, B. M. Recent Advances Utilized in the Recycling of Homogeneous Catalysis. *Chem. Rec.* **2019**, *19* (9), 2022-2043.

(102) Eddaoudi, M.; Kim, J.; Rosi, N.; Vodak, D.; Wachter, J.; O'Keeffe, M.; Yaghi, O. M. Systematic Design of Pore Size and Functionality in Isoreticular MOFs and Their Application in Methane Storage. *Science* **2002**, *295* (5554), 469-472.
(103) Batten, S. R.; Champness, N. R.; Chen, X.-M.; Garcia-Martinez, J.; Kitagawa, S.; Öhrström, L.; O'Keeffe, M.; Suh, M. P.; Reedijk, J. Terminology of metal–organic frameworks and coordination polymers (IUPAC Recommendations 2013). *Pure Appl. Chem.* **2013**, *85* (8), 1715-1724.
(104) Li, H.; Eddaoudi, M.; O'Keeffe, M.; Yaghi, O. M. Design and synthesis of an exceptionally stable and highly porous metal-organic framework. *Nature* **1999**, *402* (6759), 276-279.
(105) Qazvini, O. T.; Telfer, S. G. MUF-16: A Robust Metal–Organic Framework for Pre- and Post-Combustion Carbon Dioxide Capture. *ACS Appl. Mater. Interfaces* **2021**, *13* (10), 12141-12148.
(106) Qian, Q.; Asinger, P. A.; Lee, M. J.; Han, G.; Mizrahi Rodriguez, K.; Lin, S.; Benedetti, F. M.; Wu, A. X.; Chi, W. S.; Smith, Z. P. MOF-Based Membranes for Gas Separations. *Chem. Rev.* **2020**, *120* (16), 8161-8266.
(107) Li, J.-R.; Kuppler, R. J.; Zhou, H.-C. Selective gas adsorption and separation in metal–organic frameworks. *Chem. Soc. Rev.* **2009**, *38* (5), 1477.
(108) Kumar, P.; Deep, A.; Kim, K.-H. Metal organic frameworks for sensing applications. *Trends Anal. Chem.* **2015**, *73*, 39-53.
(109) Lustig, W. P.; Mukherjee, S.; Rudd, N. D.; Desai, A. V.; Li, J.; Ghosh, S. K. Metal–organic frameworks: functional luminescent and photonic materials for sensing applications. *Chem. Soc. Rev.* **2017**, *46* (11), 3242-3285.
(110) Chen, K.; Wu, C.-D. Designed fabrication of biomimetic metal–organic frameworks for catalytic applications. *Coord. Chem. Rev.* **2019**, *378*, 445-465.
(111) Zhu, L.; Liu, X.-Q.; Jiang, H.-L.; Sun, L.-B. Metal–organic frameworks for heterogeneous basic catalysis. *Chem. Rev.* **2017**, *117* (12), 8129-8176.
(112) Rogge, S. M.; Bavykina, A.; Hajek, J.; Garcia, H.; Olivos-Suarez, A. I.; Sepúlveda-Escribano, A.; Vimont, A.; Clet, G.; Bazin, P.; Kapteijn, F. Metal–organic and covalent organic frameworks as single-site catalysts. *Chem. Soc. Rev.* **2017**, *46* (11), 3134-3184.
(113) Chughtai, A. H.; Ahmad, N.; Younus, H. A.; Laypkov, A.; Verpoort, F. Metal–organic frameworks: versatile heterogeneous catalysts for efficient catalytic organic transformations. *Chem. Soc. Rev.* **2015**, *44* (19), 6804-6849.
(114) Chui, S. S.-Y.; Lo, S. M.-F.; Charmant, J. P. H.; Orpen, A. G.; Williams, I. D. A Chemically Functionalizable Nanoporous Material $[Cu_3(TMA)_2(H_2O)_3]_n$. *Science* **1999**, *283* (5405), 1148-1150.

(115) Cavka, J. H.; Jakobsen, S.; Olsbye, U.; Guillou, N.; Lamberti, C.; Bordiga, S.; Lillerud, K. P. A New Zirconium Inorganic Building Brick Forming Metal Organic Frameworks with Exceptional Stability. *J. Am. Chem. Soc.* **2008**, *130* (42), 13850-13851.
(116) Park, K. S.; Ni, Z.; Côté, A. P.; Choi, J. Y.; Huang, R.; Uribe-Romo, F. J.; Chae, H. K.; O'Keeffe, M.; Yaghi, O. M. Exceptional chemical and thermal stability of zeolitic imidazolate frameworks. *Proc. Natl. Acad. Sci. U.S.A.* **2006**, *103* (27), 10186-10191.
(117) Deng, H.; Doonan, C. J.; Furukawa, H.; Ferreira, R. B.; Towne, J.; Knobler, C. B.; Wang, B.; Yaghi, O. M. Multiple Functional Groups of Varying Ratios in Metal-Organic Frameworks. *Science* **2010**, *327* (5967), 846-850.
(118) Liu, L.; Konstas, K.; Hill, M. R.; Telfer, S. G. Programmed pore architectures in modular quaternary metal–organic frameworks. *J. Am. Chem. Soc.* **2013**, *135* (47), 17731-17734.
(119) Liu, L.; Telfer, S. G. Systematic ligand modulation enhances the moisture stability and gas sorption characteristics of quaternary metal–organic frameworks. *J. Am. Chem. Soc.* **2015**, *137* (11), 3901-3909.
(120) Knowles, R. R.; Jacobsen, E. N. Attractive noncovalent interactions in asymmetric catalysis: Links between enzymes and small molecule catalysts. *PNAS* **2010**, *107* (48), 20678-20685.
(121) Toste, F. D.; Sigman, M. S.; Miller, S. J. Pursuit of Noncovalent Interactions for Strategic Site-Selective Catalysis. *Acc. Chem. Res.* **2017**, *50* (3), 609-615.
(122) Neel, A. J.; Hilton, M. J.; Sigman, M. S.; Toste, F. D. Exploiting non-covalent π interactions for catalyst design. *Nature* **2017**, *543* (7647), 637-646.
(123) Davis, H. J.; Phipps, R. J. Harnessing non-covalent interactions to exert control over regioselectivity and site-selectivity in catalytic reactions. *Chem. Sci.* **2017**, *8* (2), 864-877.
(124) Pelletier, J. r. m. D.; Basset, J.-M. Catalysis by design: well-defined single-site heterogeneous catalysts. *Acc. Chem. Res.* **2016**, *49* (4), 664-677.
(125) Hong, L.; Sun, W.; Yang, D.; Li, G.; Wang, R. Additive effects on asymmetric catalysis. *Chem. Rev.* **2016**, *116* (6), 4006-4123.
(126) Liu, L.; Zhou, T.-Y.; Telfer, S. G. Modulating the performance of an asymmetric organocatalyst by tuning its spatial environment in a metal–organic framework. *J. Am. Chem. Soc.* **2017**, *139* (39), 13936-13943.
(127) Zhu, C.; Mao, Q.; Li, D.; Li, C.; Zhou, Y.; Wu, X.; Luo, Y.; Li, Y. A readily available urea based MOF that act as a highly active heterogeneous catalyst for Friedel-Crafts reaction of indoles and nitrostryenes. *Catal. Commun.* **2018**, *104*, 123-127.
(128) Shirokawa, S.-i.; Kamiyama, M.; Nakamura, T.; Okada, M.; Nakazaki, A.; Hosokawa, S.; Kobayashi, S. Remote Asymmetric Induction with Vinylketene Silyl N,O-Acetal. *J. Am. Chem. Soc.* **2004**, *126* (42), 13604-13605.

(129) Hosokawa, S. Remote asymmetric induction reactions using a E, E-vinylketene silyl N, O-acetal and the wide range stereocontrol strategy for the synthesis of polypropionates. *Acc. Chem. Res.* **2018**, *51* (5), 1301-1314.
(130) Lewis, C. A.; Gustafson, J. L.; Chiu, A.; Balsells, J.; Pollard, D.; Murry, J.; Reamer, R. A.; Hansen, K. B.; Miller, S. J. A Case of Remote Asymmetric Induction in the Peptide-Catalyzed Desymmetrization of a Bis(phenol). *J. Am. Chem. Soc.* **2008**, *130* (48), 16358-16365.
(131) Lee, S. J.; Telfer, S. G. Multicomponent Metal‐Organic Frameworks. *Angew. Chem.* **2023**, *135* (44).
(132) Dondoni, A.; Massi, A. Asymmetric organocatalysis: from infancy to adolescence. *Angew. Chem. Int. Ed.* **2008**, *47* (25), 4638-4660.
(133) Yang, H.; Carter, R. G. N-(p-Dodecylphenylsulfonyl)-2-pyrrolidinecarboxamide: A Practical Proline Mimetic for Facilitating Enantioselective Aldol Reactions. *Org. Lett.* **2008**, *10* (20), 4649-4652.
(134) Kano, T.; Yamaguchi, Y.; Tokuda, O.; Maruoka, K. anti-Selective Direct Asymmetric Mannich Reactions Catalyzed by Axially Chiral Amino Sulfonamide as an Organocatalyst. *J. Am. Chem. Soc.* **2005**, *127* (47), 16408-16409.
(135) Hechavarria Fonseca, M. T.; List, B. Catalytic Asymmetric Intramolecular Michael Reaction of Aldehydes. *Angew. Chem. Int. Ed.* **2004**, *43* (30), 3958-3960.
(136) Erkkilä, A.; Majander, I.; Pihko, P. M. Iminium Catalysis. *Chem. Rev.* **2007**, *107* (12), 5416-5470.
(137) Windle, C. L.; Müller, M.; Nelson, A.; Berry, A. Engineering aldolases as biocatalysts. *Curr. Opin. Chem. Biol.* **2014**, *19*, 25-33.
(138) Machajewski, T. D.; Wong, C.-H. The Catalytic Asymmetric Aldol Reaction. *Angew. Chem. Int. Ed.* **2000**, *39* (8), 1352-1375.
(139) List, B. Enamine Catalysis Is a Powerful Strategy for the Catalytic Generation and Use of Carbanion Equivalents. *Acc. Chem. Res.* **2004**, *37* (8), 548-557.
(140) Lun, D. J.; Waterhouse, G. I. N.; Telfer, S. G. A General Thermolabile Protecting Group Strategy for Organocatalytic Metal−Organic Frameworks. *J. Am. Chem. Soc.* **2011**, *133* (15), 5806-5809.
(141) Zhou, T.-Y.; Auer, B.; Lee, S. J.; Telfer, S. G. Catalysts confined in programmed framework pores enable new transformations and tune reaction efficiency and selectivity. *J. Am. Chem. Soc.* **2019**, *141* (4), 1577-1582.
(142) Deshpande, R. K.; Minnaar, J. L.; Telfer, S. G. Thermolabile Groups in Metal–Organic Frameworks: Suppression of Network Interpenetration, Post-Synthetic Cavity Expansion, and Protection of Reactive Functional Groups. *Angew. Chem. Int. Ed.* **2010**, *49* (27), 4598-4602.
(143) Cobb, A. J. A.; Longbottom, D. A.; Shaw, D. M.; Ley, S. V. 5-Pyrrolidin-2-yltetrazole as an asymmetric organocatalyst for the addition of ketones to nitro-olefins. *Chem. Commun.* **2004**, (16), 1808.

(144) Albert, A.; Goldacre, R.; Phillips, J. 455. The strength of heterocyclic bases. *J. Chem. Soc.* **1948**, 2240.
(145) Chinchilla, R.; Nájera, C.; Sánchez-Agulló, P. Enantiomerically pure guanidine-catalysed asymmetric nitroaldol reaction. *Tetrahedron: Asymmetry* **1994**, *5* (7), 1393-1402.
(146) Ube, H.; Terada, M. Enantioselective Henry (nitroaldol) reaction catalyzed by axially chiral guanidines. *Bioorg. Med. Chem. Lett.* **2009**, *19* (14), 3895-3898.
(147) van Aken, E.; Wynberg, H.; van Bolhuis, F. Nitroalkanes in C–C bond forming reactions: a crystal structure of a complex of a guanidine catalyst and a nitroalkane substrate. *Chem. Commun.* **1992**, (8), 629-630.
(148) Hosoya, K.; Odagi, M.; Nagasawa, K. Guanidine organocatalysis for enantioselective carbon-heteroatom bond-forming reactions. *Tetrahedron Lett.* **2018**, *59* (8), 687-696.
(149) Sohtome, Y.; Takemura, N.; Takada, K.; Takagi, R.; Iguchi, T.; Nagasawa, K. Organocatalytic Asymmetric Nitroaldol Reaction: Cooperative Effects of Guanidine and Thiourea Functional Groups. *Chem. Asian J.* **2007**, *2* (9), 1150-1160.
(150) Liu, X.; Lin, L.; Feng, X. Amide-based bifunctional organocatalysts in asymmetric reactions. *Chem. Commun.* **2009**, (41), 6145.
(151) Sohtome, Y.; Nagasawa, K. Dynamic asymmetric organocatalysis: cooperative effects of weak interactions and conformational flexibility in asymmetric organocatalysts. *Chem. Commun.* **2012**, *48* (63), 7777.
(152) Misaki, T.; Takimoto, G.; Sugimura, T. Direct Asymmetric Aldol Reaction of 5H-Oxazol-4-ones with Aldehydes Catalyzed by Chiral Guanidines. *J. Am. Chem. Soc.* **2010**, *132* (18), 6286-6287.
(153) Mirabdolbaghi, R.; Hassan, M.; Dudding, T. Design and synthesis of a chiral seven-membered ring guanidine organocatalyst applied to asymmetric vinylogous aldol reactions. *Tetrahedron: Asymmetry* **2015**, *26* (10), 560-566.
(154) Ye, W.; Jiang, Z.; Zhao, Y.; Goh, S. L. M.; Leow, D.; Soh, Y. T.; Tan, C. H. Chiral Bicyclic Guanidine as a Versatile Brønsted Base Catalyst for the Enantioselective Michael Reactions of Dithiomalonates and β‐Keto Thioesters. *Adv. Synth. Catal.* **2007**, *349* (16), 2454-2458.
(155) Thai, K.; Gravel, M. Design, synthesis, and application of chiral electron-poor guanidines as hydrogen-bonding catalysts for the Michael reaction. *Tetrahedron: Asymmetry* **2010**, *21* (6), 751-755.
(156) Pan, Y.; Zhao, Y.; Ma, T.; Yang, Y.; Liu, H.; Jiang, Z.; Tan, C. H. Enantioselective Synthesis of α‐Fluorinated β‐Amino Acid Derivatives by an Asymmetric Mannich Reaction and Selective Deacylation/Decarboxylation Reactions. *Chem. Eur. J.* **2010**, *16* (3), 779-782.

(157) Fu, X.; Loh, W. T.; Zhang, Y.; Chen, T.; Ma, T.; Liu, H.; Wang, J.; Tan, C. H. Chiral Guanidinium Salt Catalyzed Enantioselective Phospha‐Mannich Reactions. *Angew. Chem.* **2009**, *121* (40), 7523-7526.
(158) Leow, D.; Tan, C. H. Chiral Guanidine Catalyzed Enantioselective Reactions. *Chem. Asian J.* **2009**, *4* (4), 488-507.
(159) Chou, H. C.; Leow, D.; Tan, C. H. Recent Advances in Chiral Guanidine‐Catalyzed Enantioselective Reactions. *Chem. Asian J.* **2019**, *14* (21), 3803-3822.
(160) Nataj, S. M. M.; Kaliaguine, S.; Fontaine, F.-G. Post-synthetic modification of Zr-MOFs using guanidine for cyclic carbonate formation catalysis. *Catal. Today* **2023**, *422*, 114216.
(161) Mohammadi, L.; Vaezi, M. R. Palladium Nanoparticle-Decorated Porous Metal–Organic-Framework (Zr)@Guanidine: Novel Efficient Catalyst in Cross-Coupling (Suzuki, Heck, and Sonogashira) Reactions and Carbonylative Sonogashira under Mild Conditions. *ACS Omega* **2023**, *8* (18), 16395-16410.
(162) Zhang, Y.; Ning, L.; Zhu, T.; Xie, Z.; Dong, S.; Feng, X.; Liu, X. Chiral guanidine catalyzed cyclization reactions of 1,3-enynes for lactone synthesis: switchable H-bond catalysis. *Org. Chem. Front.* **2024**, *11* (10), 2897-2904.
(163) Almaşi, D.; Alonso, D. A.; Gómez-Bengoa, E.; Nájera, C. Chiral 2-Aminobenzimidazoles as Recoverable Organocatalysts for the Addition of 1,3-Dicarbonyl Compounds to Nitroalkenes. *J. Org. Chem.* **2009**, *74* (16), 6163-6168.
(164) Davis, A. P.; Dempsey, K. J. Synthesis and investigation of a hindered, chiral, bicyclic guanidine. *Tetrahedron: Asymmetry* **1995**, *6* (11), 2829-2840.
(165) Auvil, T. J.; Schafer, A. G.; Mattson, A. E. Design Strategies for Enhanced Hydrogen‐Bond Donor Catalysts. *Eur. J. Org. Chem.* **2014**, *2014* (13), 2633-2646.
(166) Parvin, T.; Yadav, R.; Choudhury, L. H. Recent applications of thiourea-based organocatalysts in asymmetric multicomponent reactions (AMCRs). *Org. Biomol. Chem.* **2020**, *18* (29), 5513-5532.
(167) Curran, D. P.; Kuo, L. H. Altering the Stereochemistry of Allylation Reactions of Cyclic .alpha.-Sulfinyl Radicals with Diarylureas. *J. Org. Chem.* **1994**, *59* (12), 3259-3261.
(168) Vera, S.; García‐Urricelqui, A.; Mielgo, A.; Oiarbide, M. Progress in (Thio)urea‐ and Squaramide‐Based Brønsted Base Catalysts with Multiple H‐Bond Donors. *Eur. J. Org. Chem.* **2023**, *26* (7).
(169) Sigman, M. S.; Jacobsen, E. N. Schiff Base Catalysts for the Asymmetric Strecker Reaction Identified and Optimized from Parallel Synthetic Libraries. *J. Am. Chem. Soc.* **1998**, *120* (19), 4901-4902.
(170) Geng, X. Y.; Du, D. M. Bifunctional Squaramide‐Catalyzed Asymmetric Michael/Cyclization Reactions of 3‐Hydroxychromenones with Isatylidenemalononitriles. *ChemistrySelect* **2024**, *9* (20).

(171) Kobayashi, Y.; Taniguchi, Y.; Hayama, N.; Inokuma, T.; Takemoto, Y. A Powerful Hydrogen‐Bond‐Donating Organocatalyst for the Enantioselective Intramolecular Oxa‐Michael Reaction of α,β‐Unsaturated Amides and Esters. *Angew. Chem.* **2013**, *125* (42), 11320-11324.
(172) Robak, M. T.; Trincado, M.; Ellman, J. A. Enantioselective Aza-Henry Reaction with an N-Sulfinyl Urea Organocatalyst. *J. Am. Chem. Soc.* **2007**, *129* (49), 15110-15111.
(173) Siu, P. W.; Brown, Z. J.; Farha, O. K.; Hupp, J. T.; Scheidt, K. A. A mixed dicarboxylate strut approach to enhancing catalytic activity of a de novo urea derivative of metal–organic framework UiO-67. *Chem. Commun.* **2013**, *49* (93), 10920.
(174) Alegre-Requena, J. V.; Marqués-López, E.; Herrera, R. P.; Díaz, D. D. Metal–organic frameworks (MOFs) bring new life to hydrogen-bonding organocatalysts in confined spaces. *CrystEngComm* **2016**, *18* (22), 3985-3995.
(175) Das, A.; Anbu, N.; Sk, M.; Dhakshinamoorthy, A.; Biswas, S. Highly Active Urea-Functionalized Zr(IV)-UiO-67 Metal–Organic Framework as Hydrogen Bonding Heterogeneous Catalyst for Friedel–Crafts Alkylation. *Inorg. Chem.* **2019**, *58* (8), 5163-5172.
(176) Rao, P. C.; Mandal, S. Potential Utilization of Metal‐Organic Frameworks in Heterogeneous Catalysis: A Case Study of Hydrogen‐Bond Donating and Single‐Site Catalysis. *Chem. Asian J.* **2019**, *14* (23), 4087-4102.
(177) McGuirk, C. M.; Katz, M. J.; Stern, C. L.; Sarjeant, A. A.; Hupp, J. T.; Farha, O. K.; Mirkin, C. A. Turning On Catalysis: Incorporation of a Hydrogen-Bond-Donating Squaramide Moiety into a Zr Metal–Organic Framework. *J. Am. Chem. Soc.* **2015**, *137* (2), 919-925.
(178) Reyes, E.; Uria, U.; Vicario, J. L.; Carrillo, L. The Catalytic, Enantioselective Michael Reaction. In *Organic Reactions*, pp 1-898.
(179) List, B.; Pojarliev, P.; Martin, H. J. Efficient Proline-Catalyzed Michael Additions of Unmodified Ketones to Nitro Olefins. *Org. Lett.* **2001**, *3* (16), 2423-2425.
(180) Kozachenko, A. G.; Matrosov, E. I.; Kabachnik, M. I. Acid-base interactions in nitromethane. *Bull. Acad. Sci. USSR, Div. Chem. Sci.* **1976**, *25* (7), 1411-1414.
(181) Yamashita, Y.; Yasukawa, T.; Yoo, W.-J.; Kitanosono, T.; Kobayashi, S. Catalytic enantioselective aldol reactions. *Chem. Soc. Rev.* **2018**, *47* (12), 4388-4480.
(182) Li, A.; Ye, L.; Yang, X.; Wang, B.; Yang, C.; Gu, J.; Yu, H. Reconstruction of the Catalytic Pocket and Enzyme–Substrate Interactions To Enhance the Catalytic Efficiency of a Short‐Chain Dehydrogenase/Reductase. *ChemCatChem* **2016**, *8* (20), 3229-3233.
(183) Holliday, G. L.; Mitchell, J. B. O.; Thornton, J. M. Understanding the Functional Roles of Amino Acid Residues in Enzyme Catalysis. *J. Mol. Biol.* **2009**, *390* (3), 560-577.
(184) Stock, N.; Biswas, S. Synthesis of Metal-Organic Frameworks (MOFs): Routes to Various MOF Topologies, Morphologies, and Composites. *Chem. Rev.* **2012**, *112* (2), 933-969.
(185) Sheldrick, G. M. SHELXT – Integrated space-group and crystal-structure determination. *Acta Crystallogr. A* **2015**, *71* (1), 3-8.

(186) Dolomanov, O. V.; Bourhis, L. J.; Gildea, R. J.; Howard, J. A. K.; Puschmann, H. OLEX2: a complete structure solution, refinement and analysis program. *J. Appl. Crystallogr.* **2009**, *42* (2), 339-341.
(187) Burrows, A. D.; Frost, C. G.; Mahon, M. F.; Richardson, C. Post-Synthetic Modification of Tagged Metal-Organic Frameworks. *Angew. Chem. Int. Ed.* **2008**, *120* (44), 8610-8614.
(188) Yuan, S.; Lu, W.; Chen, Y.-P.; Zhang, Q.; Liu, T.-F.; Feng, D.; Wang, X.; Qin, J.; Zhou, H.-C. Sequential Linker Installation: Precise Placement of Functional Groups in Multivariate Metal–Organic Frameworks. *J. Am. Chem. Soc.* **2015**, *137* (9), 3177-3180.
(189) Nagata, S.; Sato, H.; Sugikawa, K.; Kokado, K.; Sada, K. Conversion of azide to primary amine via Staudinger reaction in metal–organic frameworks. *CrystEngComm* **2012**, *14* (12), 4137.
(190) Garro-Helion, F.; Merzouk, A.; Guibe, F. Mild and selective palladium (0)-catalyzed deallylation of allylic amines. Allylamine and diallylamine as very convenient ammonia equivalents for the synthesis of primary amines. *J. Org. Chem.* **1993**, *58* (22), 6109-6113.
(191) Siu, P. W.; Brown, Z. J.; Farha, O. K.; Hupp, J. T.; Scheidt, K. A. A mixed dicarboxylate strut approach to enhancing catalytic activity of a de novo urea derivative of metal–organic framework UiO-67. *Chem comm* **2013**, *49* (93), 10920.
(192) Qiao, Z.; Wang, Q.; Zhang, F.; Wang, Z.; Bowling, T.; Nare, B.; Jacobs, R. T.; Zhang, J.; Ding, D.; Liu, Y.; et al. Chalcone–Benzoxaborole Hybrid Molecules as Potent Antitrypanosomal Agents. *J. Med. Chem.* **2012**, *55* (7), 3553-3557.
(193) Yamamoto, K.; Tamura, T.; Henmi, K.; Kuboyama, T.; Yanagisawa, A.; Matsubara, M.; Takahashi, Y.; Suzuki, M.; Saito, J.-i.; Ueno, K.; et al. Development of Dihydrodibenzooxepine Peroxisome Proliferator-Activated Receptor (PPAR) Gamma Ligands of a Novel Binding Mode as Anticancer Agents: Effective Mimicry of Chiral Structures by Olefinic E/Z-Isomers. *J. Med. Chem.* **2018**, *61* (22), 10067-10083.
(194) Lai, Y.-H.; Yap, A. H.-T. Synthesis and rigid conformers of 14,15-dimethyl-2,11-dithia[3.3](1,3)(1,4)cyclophane and 12,13-dimethyl[2.2](1,3)(1,4)cyclophane. *J. Chem. Soc., Perkin trans.* **1993**, (7), 1373.
(195) Fontán, N.; Vaz, B.; Álvarez, R.; De Lera, Á. R. A conjunctive diiodoheptaene for the synthesis of C2-symmetric carotenoids. *ChemComm* **2013**, *49* (26), 2694.
(196) Padmanaban, M.; Müller, P.; Lieder, C.; Gedrich, K.; Grünker, R.; Bon, V.; Senkovska, I.; Baumgärtner, S.; Opelt, S.; Paasch, S.; et al. Application of a chiral metal–organic framework in enantioselective separation. *ChemComm* **2011**, *47* (44), 12089.
(197) Nickerl, G.; Henschel, A.; Grünker, R.; Gedrich, K.; Kaskel, S. Chiral Metal‐Organic Frameworks and Their Application in Asymmetric Catalysis and Stereoselective Separation. *Chem. Ing. Tech.* **2011**, *83* (1-2), 90-103.

(198) Murray, P. M.; Bellany, F.; Benhamou, L.; Bučar, D.-K.; Tabor, A. B.; Sheppard, T. D. The application of design of experiments (DoE) reaction optimisation and solvent selection in the development of new synthetic chemistry. *Org. Biomol. Chem.* **2016**, *14* (8), 2373-2384.
(199) Dyson, P. J.; Jessop, P. G. Solvent effects in catalysis: rational improvements of catalysts via manipulation of solvent interactions. *Catal. Sci. Technol.* **2016**, *6* (10), 3302-3316.
(200) Kayal, R.; Baldinelli, L.; Harden, I.; Neese, F.; Bistoni, G. Understanding and quantifying the impact of solute–solvent van der Waals interactions on the selectivity of asymmetric catalytic transformations. *Chem. Sci.* **2025**, *16* (6), 2700-2709.
(201) Tsuyusaki, R.; Nakashima, K.; Shimomura, M.; Kawada, M.; Matsushima, Y.; Hirashima, S.-i.; Miura, T. Highly efficient, asymmetric, and organocatalyst-based Henry reactions between α,β-unsaturated trifluoromethyl ketone and nitromethane. *Tetrahedron Lett.* **2023**, *117*, 154375.
(202) Bhadra, S.; Yamamoto, H. Substrate Directed Asymmetric Reactions. *Chem. Rev.* **2018**, *118* (7), 3391-3446.
(203) Mei, H.; Xiao, X.; Zhao, X.; Fang, B.; Liu, X.; Lin, L.; Feng, X. Catalytic Asymmetric Henry Reaction of Nitroalkanes and Aldehydes Catalyzed by a Chiral N,N′-Dioxide/Cu(I) Complex. *J. Org. Chem.* **2015**, *80* (4), 2272-2280.
(204) Boruwa, J.; Gogoi, N.; Saikia, P. P.; Barua, N. C. Catalytic asymmetric Henry reaction. *Tetrahedron Asymm* **2006**, *17* (24), 3315-3326.
(205) Palomo, C.; Oiarbide, M.; Laso, A. Recent Advances in the Catalytic Asymmetric Nitroaldol (Henry) Reaction. *Eur. J. Org. Chem.* **2007**, *2007* (16), 2561-2574.
(206) Hammett, L. P. The Effect of Structure upon the Reactions of Organic Compounds. Benzene Derivatives. *J. Am. Chem. Soc.* **1937**, *59* (1), 96-103.
(207) Hansch, C.; Leo, A.; Taft, R. A survey of Hammett substituent constants and resonance and field parameters. *Chem. Rev.* **1991**, *91* (2), 165-195.
(208) Lineberry, A. M.; Benjamin, E. T.; Davis, R. E.; Kassel, W. S.; Wheeler, K. A. Structural Studies of Racemates and Quasiracemates: Chloro, Bromo, and Methyl Adducts of 2-Phenoxypropionic Acid. *Cryst. Growth Des.* **2008**, *8* (2), 612-619.
(209) Akhtar, M.; Gani, D. Synthesis of the isosteric L-valine analogues (2r,3s)- and (2r,3r)-3-bromobutyrine. *Tetrahedron* **1987**, *43* (22), 5341-5349.
(210) Patani, G. A.; LaVoie, E. J. Bioisosterism: A Rational Approach in Drug Design. *Chem. Rev.* **1996**, *96* (8), 3147-3176.
(211) Odagi, M.; Nagasawa, K. Exploring Guanidinium Organocatalysts for Hypoiodite‐Mediated Reactions. *Chem. Rec.* **2023**, *23* (7).
(212) Kapp, T. G.; Fottner, M.; Maltsev, O. V.; Kessler, H. Small Cause, Great Impact: Modification of the Guanidine Group in the RGD Motif Controls Integrin Subtype Selectivity. *Angew. Chem. Int. Ed.* **2016**, *55* (4), 1540-1543.

(213) Mobinikhaledi, A.; Forughifar, N.; Mohtasabi, S.; Shalbaf, H. Synthesis of Some of New Substituted 2-(Phenyl)-1,3-dimethyl- and -1,1,3,3-tetramethylguanidines. *Phosphorus, Sulfur, Silicon Relat. Elem.* **2003**, *178* (10), 2235-2240.
(214) Kreher, R. P.; Hildebrand, T. Struktur und Reaktivität von isoanellierten heterocyclischen Systemen mit 4nπ- und (4n+2)π-Elektronen, XIV [1]: Tri- und tetracyclische Hetarene mit lokalisierten oder delokalisierten PyrroI-Strukturen / Structure and Reactivity of Isoannellated Heterocyc. *Z. Naturforsch. B* **1988**, *43* (1), 125-131.
(215) Suzuki, T.; Fujisawa, M.; Takagi, S.; Kimura, T. Excessenthalpies of water+1,4-dioxane at 278.15, 298.15, 318.15 and 338.15 K. *J. Therm. Anal. Calorim.* **2006**, *85* (3), 545-550.
(216) Banerjee, S.; Vanka, K. The Role of Aromatic Alcohol Additives on Asymmetric Organocatalysis Reactions: Insights from Theory. *Chem. Asian J.* **2024**, *19* (4), e202300997.
(217) Chen, M.; Sun, J. How Understanding the Role of an Additive Can Lead to an Improved Synthetic Protocol without an Additive: Organocatalytic Synthesis of Chiral Diarylmethyl Alkynes. *Angew. Chem.* **2017**, *129* (39), 12128-12132.
(218) Horcajada, P.; Salles, F.; Wuttke, S.; Devic, T.; Heurtaux, D.; Maurin, G.; Vimont, A.; Daturi, M.; David, O.; Magnier, E.; et al. How Linker's Modification Controls Swelling Properties of Highly Flexible Iron(III) Dicarboxylates MIL-88. *J. Am. Chem. Soc.* **2011**, *133* (44), 17839-17847.
(219) Moorthy, J. N.; Singhal, N. Facile and Highly Selective Conversion of Nitriles to Amides via Indirect Acid-Catalyzed Hydration Using TFA or AcOH−H_2SO_4. *J. Org. Chem.* **2005**, *70* (5), 1926-1929.
(220) Wang, C.; Zheng, M.; Lin, W. Asymmetric Catalysis with Chiral Porous Metal–Organic Frameworks: Critical Issues. *J. Phys. Chem* **2011**, *2* (14), 1701-1709.
(221) Johnson, B. A.; Beiler, A. M.; McCarthy, B. D.; Ott, S. Transport Phenomena: Challenges and Opportunities for Molecular Catalysis in Metal–Organic Frameworks. *J. Am. Chem. Soc.* **2020**, *142* (28), 11941-11956.
(222) Bligaard, T.; Bullock, R. M.; Campbell, C. T.; Chen, J. G.; Gates, B. C.; Gorte, R. J.; Jones, C. W.; Jones, W. D.; Kitchin, J. R.; Scott, S. L. Toward Benchmarking in Catalysis Science: Best Practices, Challenges, and Opportunities. *ACS Catal.* **2016**, *6* (4), 2590-2602.
(223) Hassanzadeh-Afruzi, F. Turn over number (TON) and turn over frequency (TOF) studies for heterogeneous micro and nanocomposite catalysts. In *Heterogeneous Micro and Nanoscale Composites for the Catalysis of Organic Reactions*, Maleki, A. Ed.; Elsevier, 2022; pp 223-232.
(224) Kozuch, S.; Martin, J. M. L. "Turning Over" Definitions in Catalytic Cycles. *ACS Catal.* **2012**, *2* (12), 2787-2794.
(225) Zhang, W.; Shan, S.-Y.; Dai, J.; Cai, Z.; Zhu, J.-B. Well-controlled Organocatalytic Ring-opening Polymerization of Seven-membered Cyclic Carbonates with Cyclohexyl Fusion. *Chem. Res. Chinese. U.* **2024**, *40* (5), 856-862.

(226) She, Y.; Chen, X.; Wang, M.; Liu, A.; Wang, X.; Gao, D.; Hu, K.; Hu, M. Heterogeneous solvent-metal-free aerobic oxidation of alcohol under ambient conditions catalyzed by TEMPO-functionalized porous poly(ionic liquid)s. *RSC Adv.* **2024**, *14* (28), 20199-20209.
(227) Gero, A.; Markham, J. J. Studies on pyridines: I. The basicity of pyridine bases. *J. Org. Chem.* **1951**, *16* (12), 1835-1838.
(228) García-García, P.; Müller, M.; Corma, A. MOF catalysis in relation to their homogeneous counterparts and conventional solid catalysts. *Chem. Sci.* **2014**, *5* (8), 2979.
(229) Sohtome, Y.; Hashimoto, Y.; Nagasawa, K. Guanidine-Thiourea Bifunctional Organocatalyst for the Asymmetric Henry (Nitroaldol) Reaction. *Adv. Synth. Catal* **2005**, *347* (11-13), 1643-1648.
(230) Fu, X.; Tan, C.-H. Mechanistic considerations of guanidine-catalyzed reactions. *Chem. Commun.* **2011**, *47* (29), 8210-8222.
(231) Gu, J.-M.; Kim, W.-S.; Huh, S. Size-dependent catalysis by DABCO-functionalized Zn-MOF with one-dimensional channels. *Dalton Trans.* **2011**, *40* (41), 10826.
(232) Alvarez-Casao, Y.; Marques-Lopez, E.; Herrera, R. P. Organocatalytic Enantioselective Henry Reactions. In *Symmetry*, 2011; Vol. 3, pp 220-245.
(233) Bandini, M.; Sinisi, R.; Umani-Ronchi, A. Enantioselective organocatalyzed Henry reaction with fluoromethyl ketones. *Chem. Commun.* **2008**, (36), 4360-4362.
(234) Shoja, A.; Zhai, J.; Reid, J. P. Comprehensive Stereochemical Models for Selectivity Prediction in Diverse Chiral Phosphate-Catalyzed Reaction Space. *ACS Catal.* **2021**, *11* (19), 11897-11905.
(235) Woldegiorgis, A. G.; Suleman, M.; Lin, X. Asymmetric Cycloaddition/Annulation Reactions by Chiral Phosphoric Acid Catalysis: Recent Advances. *Eur. J. Org. Chem.* **2022**, *2022* (34), e202200624.
(236) Sewgobind, N. V.; Wanner, M. J.; Ingemann, S.; de Gelder, R.; van Maarseveen, J. H.; Hiemstra, H. Enantioselective BINOL-Phosphoric Acid Catalyzed Pictet−Spengler Reactions of N-Benzyltryptamine. *J. Org. Chem.* **2008**, *73* (16), 6405-6408.

Appendix

Appendix Chapter 2

Linker synthesis

Chiral linkers based on the structure: H_2bdc-OX-(*S*/*R*)-R

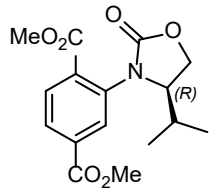

Me$_2$bdc-OX-(*R*)-4-*i*Pr

The title compound was prepared from backbone 1 (1.2 g, 4.5 mmol, 1.0 eq.) and (*R*)-4-isopropyl-2-oxazolidinone (761.4 mg, 5.9 mmol, 1.3 eq.) according to the general procedure. Me$_2$bdc-OX-(*R*)-4-*i*Pr (850.0 mg, 2.7 mmol, 59%) was obtained as a slightly yellow oil after silica-gel column chromatography (cyclohexane/EtOAc gradient from 9:1 to 7:3). The ^{1}H NMR spectrum agrees with literature data.[196]

^{1}H NMR (500 MHz, $CDCl_3$) δ (ppm) 8.01-8.01 (m, 2H), 7.91 (s, 1H), 4.52 (t, *J* = 8.2 Hz, 1H), 4.35-4.27 (m, 2H), 3.95 (s, 3H), 3.92 (s, 3H), 2.08-2.01 (m, 1H), 1.03 (d, *J* = 6.8 Hz, 3H), 0.89 (d, *J* = 7.0 Hz, 3H).

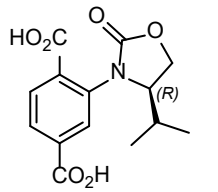

H$_2$bdc-OX-(*R*)-4-*i*Pr

The title compound was prepared from Me$_2$bdc-OX-(*R*)-4-*i*Pr (850.0 mg, 2.7 mmol, 1.0 eq.) according to the general ester hydrolysis procedure. H_2bdc-OX-(*R*)-4-*i*Pr was obtained as a yellow, powdery solid (744.1mg, 2.5 mmol, 96%). The ^{1}H NMR spectrum agrees with literature data.[196]

^{1}H NMR (500 MHz, *d6*-DMSO) δ (ppm) 13.44 (br, 2H), 7.97-7.92 (m, 2H), 7.86 (d, *J* = 1.4 Hz, 1H), 4.47-4.39 (m, 2H), 4.27 (dd, *J* = 8.1, 5.8 Hz, 1H), 1.92-1.86 (m, 1H), 0.89 (d, *J* = 6.8 Hz, 3H), 0.81 (d, *J* = 6.9 Hz, 3H).

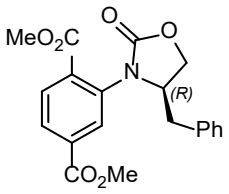

Me$_2$bdc-OX-(*R*)-4-Bn

The title compound was prepared from backbone 1 (1.1 g, 4.0 mmol, 1.0 eq.) and (*R*)-4-benzyloxazolidi-2-one (708.4 mg, 4.0 mmol, 1.0 eq.) according to the general procedure. Me$_2$bdc-OX-(*R*)-4-Bn (923.5 mg, 2.5 mmol, 63%) was obtained as a slightly yellow oil after silica-gel column chromatography (cyclohexane/EtOAc gradient from 9:1 to 7:3). The ^{1}H NMR spectrum agrees with literature data.[196]

^{1}H NMR (500 MHz, $CDCl_3$) δ (ppm) 8.02 (s, 2H), 7.93 (s, 1H), 7.25-7.09 (m, 5H), 4.69- 4.63 (m, 1H), 4.46 (t, *J* = 8.6 Hz, 1H), 4.25 (dd, *J* = 8.7, 6.7 Hz, 1H), 3.96 (s, 3H), 3.94 (s, 3H), 3.10 (dd, *J* = 13.6, 4.7 Hz, 1H), 2.91 (dd, *J* = 13.6, 9.9 Hz, 1H).

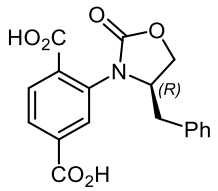

H_2bdc-OX-(*R*)-4-Bn

The title compound was prepared from Me_2bdc-OX-(*R*)-4-Bn (923.5 mg, 2.5 mmol, 1.0 eq.) according to the general ester hydrolysis procedure. H_2bdc-OX-(*R*)-4-Bn was obtained as a yellow, powdery solid (710.6 mg, 2.1 mmol, 83%). The ^{1}H NMR spectrum agrees with literature data.[1]

^{1}H NMR (500 MHz, D_2O) δ (ppm) 7.80 (dd, *J* = 8.0, 1.6 Hz, 1H), 7.68 (d, *J* = 1.6 Hz, 1H), 7.62 (d, *J* = 8.0 Hz, 1H), 7.27-7.17 (m, 5H), 4.76-4.70 (m, 1H), 4.56 (t, *J* = 8.6 Hz, 1H), 4.35 (dd, *J* = 8.7, 6.6 Hz, 1H), 3.05 (dd, *J* = 13.8, 6.0 Hz, 1H), 2.95 (dd, *J* = 13.8, 8.0Hz, 1H). ^{13}C NMR (126 MHz, D_2O) δ (ppm) 174.38, 173.84, 159.40, 138.94, 137.82, 136.12, 132.19, 129.61, 129.13, 128.71, 128.62, 128.54, 126.79, 68.88, 59.56, 38.44.

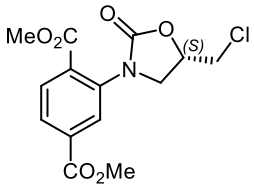

Me_2bdc-OX-(*S*)-5-MeCl

The title compound was prepared from backbone 1 (1.0 g, 3.7 mmol, 1.0 eq.) and (*S*)-5-(chloromethyl)oxazolidine-2-one (799.8 mg, 5.9 mmol, 1.6 eq.) according to the general procedure. Me_2bdc-OX-(*S*)-5-MeCl (859.0 mg, 2.6 mmol, 71%) was obtained as a slightly yellow oil after silica-gel column chromatography (cyclohexane/EtOAc gradient from 9:1 to 7:3).

^{1}H NMR (500 MHz, $CDCl_3$) δ (ppm) 8.03-7.98 (m, 2H), 7.95 (d, *J* = 1.2 Hz, 1H), 4.94-4.89 (m, 1H), 4.23 (t, *J* = 8.9 Hz, 1H), 3.98 (dd, *J* = 8.7, 5.3 Hz, 1H), 3.95 (s, 3H), 3.91 (s, 3H), 3.85 (d, *J* = 6.0 Hz, 2H). ^{13}C NMR (126 MHz, $CDCl_3$) δ (ppm) 165.66, 165.40, 155.61, 137.13, 134.34, 131.76, 131.67, 128.52, 127.98, 72.49, 52.93, 52.80, 50.79, 44.16. MS (ESI) calculated for $[M+Na]^+$ $(C_{14}H_{14}N_1O_6Cl_1Na_1)^+$ m/z 350.04, found m/z 350.07.

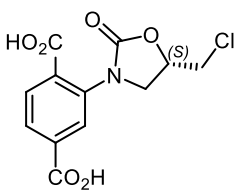

H_2bdc-OX-(*S*)-5-MeCl

The title compound was prepared from Me_2bdc-OX-(*S*)-5-MeCl (859.0 mg, 2.6 mmol, 1.0 eq.) according to the general ester hydrolysis procedure. H_2bdc-OX-(*S*)-5-MeCl was obtained as a slightly yellow, powdery solid (650.2 mg, 2.2 mmol, 83%).

^{1}H NMR (500 MHz, *d6*-DMSO) δ (ppm) 13.43 (brs, 2H), 7.96-7.92 (m, 3H), 5.00-4.95 (m, 1H), 4.19 (t, *J* = 8.8 Hz, 1H), 3.99 (dd, *J* = 11.8, 4.3 Hz, 1H), 3.94 (dd, *J* =

11.8, 5.8 Hz, 1H), 3.85 (dd, *J* = 8.8, 5.8 Hz, 1H). ^{13}C NMR (126 MHz, *d6*-DMSO) δ (ppm) 166.48, 165.98, 155.15, 136.77, 134.43, 132.65, 131.07, 127.89, 127.70, 72.54, 49.79, 45.64. HRMS (FTMS + p ESI Full) calculated for $[M]^-$ $(C_{12}H_9N_1O_6Cl)^-$ m/z 298.0113, found m/z 298.0125.

Chiral linkers based on the structure: H_2bdc-^{5}N-(*S*/*R*)-R^1-R^2

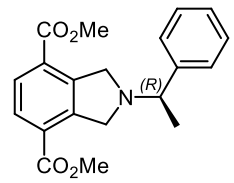

Me_2bdc-^{5}N-(*R*)-CH_3-Ph

The title compound was prepared from backbone 2 (199.4 mg, 524.7 µmol, 1.0 eq.) and (*R*)-(+)-α-methylbenzylamine (80.0 mg, 660.2 µmol, 1.3 eq.) according to general procedure **I**. Me_2bdc-^{5}N-(*R*)-CH_3-Ph (120.1 mg, 353.9 µmol, 67%) was obtained as a slightly yellow oil after silica-gel column chromatography (cyclohexane/EtOAc; 2/1; v/v; 0.5% TEA).

^{1}H NMR (500 MHz, $CDCl_3$) δ (ppm) 7.89 (s, 2H), 7.42-7.39 (m, 2H), 7.36-7.33 (m, 2H), 7.28-7.25 (m, 2H), 4.36-4.17 (m, 4H), 3.87 (s, 6H), 3.75 (brs, 1H), 1.56 (d, *J* = 5.8 Hz, 3H). ^{13}C NMR (126 MHz, $CDCl_3$) δ (ppm) 166.21, 144.74, 144.36, 128.73, 128.54, 128.41, 127.37, 64.99, 58.02, 52.31, 23.06. HRMS (FTMS + p ESI Full) calculated for $[M+H]^+$ $(C_{20}H_{22}N_1O_4)^+$ m/z 340.1543, found m/z 340.1538.

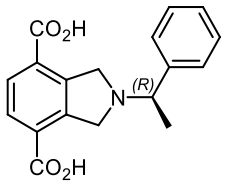

H_2bdc-^{5}N-(*R*)-CH_3-Ph

The title compound was prepared from Me_2bdc-^{5}N-(*R*)-CH_3-Ph (120.1 mg, 353.9 µmol, 1.0 eq.) according to the general ester hydrolysis procedure. H_2bdc-^{5}N-(*R*)-CH_3-Ph precipitated at pH 5.5 as a fine, slightly beige solid (95.0 mg, 305.1 µmol, 86%).

^{1}H NMR (500 MHz, *d6*-DMSO) δ (ppm) 7.84 (s, 2H), 7.41-7.26 (m, 5H), 4.18 (d, *J* = 14.5 Hz, 2H), 4.07 (d, *J* = 14.4 Hz, 2H), 3.76-3.73 (m, 1H), 1.41 (d, *J* = 6.5 Hz, 3H). ^{13}C NMR (126 MHz, *d6*-DMSO) δ (ppm) 166.68, 143.27, 128.84, 128.54, 128.47, 127.07, 126.97, 63.82, 57.51, 23.12. HRMS (FTMS + p ESI Full) calculated for $[M]^-$ $(C_{18}H_{16}N_1O_4)^-$ m/z 310.1074, found m/z 310.1076.

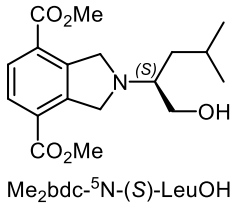

Me_2bdc-^{5}N-(*S*)-LeuOH

The title compound was prepared from backbone 2 (504.5 mg, 1.3 mmol, 1.0 eq.) and (*S*)-(+)-leucinol (201.0 mg, 1.7 mmol, 1.3 eq.) according to general procedure **II**. Me_2bdc-^{5}N-(*S*)-LeuOH (351.8 mg, 1.1 mmol, 79%) was obtained as a slightly yellow oil after silica-gel column chromatography (cyclohexane/EtOAc; 1/2; v/v; 0.5% TEA).

^{1}H NMR (500 MHz, MeOD-*d*$_4$) δ (ppm) 7.81 (s, 2H), 4.32 (s, 4H), 3.90 (s, 6H), 3.75-3.68 (m, 2H), 2.83 (brs, 1H), 1.77-1.73 (m, 1H), 1.55-1.49 (m, 1H), 1.44-1.42 (m, 1H), 0.99 (d, *J* = 6.5 Hz, 6H). ^{13}C NMR (500 MHz, MeOD-*d*$_4$) δ (ppm) 167.12, 144.77, 129.47, 129.32, 62.86, 62.42, 56.90, 52.76, 38.87, 26.49, 24.02, 22.83. HRMS (FTMS + p ESI Full) calculated for $[M+H]^+$ $(C_{18}H_{25}N_1O_5)^+$ m/z 336.1805, found m/z 336.1805.

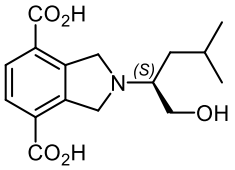

H_2bdc-^{5}N-(*S*)-LeuOH

The title compound was prepared from Me_2bdc-^{5}N-(*S*)-LeuOH (351.8 mg, 1.1 mmol, 1.0 eq.) according to the general ester hydrolysis procedure. H_2bdc-^{5}N-(*S*)-LeuOH precipitated at pH 4.0 as a fine, slightly beige solid (193.7 mg, 630.2 µmol, 60%).

^{1}H NMR (500 MHz, D_2O/NaOD) δ (ppm) 7.68 (s, 2H), 4.37-4.30 (m, 4H), 3.92-3.85 (m, 2H), 2.96-2.92 (m, 1H), 1.85-1.77 (m, 1H), 1.63-1.53 (m, 2H), 1.05 (d, *J* = 6.5 Hz, 6H). ^{13}C NMR (126 MHz, D_2O/NaOD) δ (ppm) 175.63, 139.68, 133.95, 127.11, 61.95, 61.82, 55.92, 37.66, 25.06, 23.20, 21.59. HRMS (FTMS) calculated for $[M]^-$ $(C_{16}H_{20}N_1O_5)^-$ m/z 306.1336, found m/z 306.1348.

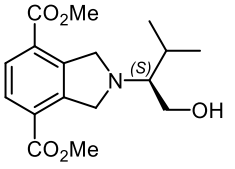

Me_2bdc-^{5}N-(*S*)-ValOH

The title compound was prepared from backbone 2 (503.7 mg, 1.3 mmol, 1.0 eq.) and (*S*)-(+)-valinol (177.8 mg, 1.7 mmol, 1.3 eq.) according to general procedure **I**. Me_2bdc-^{5}N-(*S*)-ValOH (290.2 mg, 902.4 µmol, 68%) was obtained as a slightly yellow oil after silica-gel column chromatography (CH_3CN, 0.5% TEA).

^{1}H NMR (500 MHz, MeOD-*d*$_4$) δ (ppm) 7.88 (s, 2H), 4.43 (s, 4H), 3.91 (s, 6H), 3.86 (dd, *J* = 11.7, 3.5 Hz, 1H), 3.75 (dd, *J* = 11.7, 5.9 Hz, 1H), 2.58-2.55 (m, 1H), 2.13-2.07 (m, 1H), 1.07 (d, *J* = 6.9 Hz, 3H), 1.00 (d, *J* = 6.9 Hz, 3H). ^{13}C NMR (126 MHz, MeOD-*d*$_4$) δ (ppm) 167.33, 145.08, 129.45, 129.41, 70.41, 61.57, 58.07, 52.73, 30.35, 20.98, 18.44.

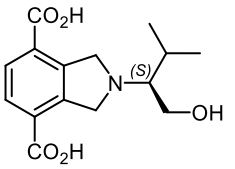

H_2bdc-^{5}N-(*S*)-ValOH

The title compound was prepared from Me_2bdc-^{5}N-(*S*)-ValOH (290.2 mg, 902.4 µmol, 1.0 eq.) according to the general ester hydrolysis procedure. H_2bdc-^{5}N-(*S*)-ValOH precipitated at pH 4.0 as a fine, slightly beige solid (210.3 mg, 717.0 µmol, 79%).

^{1}H NMR (500 MHz, D_2O/NaOD) δ (ppm) 7.61 (s, 2H), 4.27 (s, 4H), 3.91 (dd, *J* = 12.3, 3.3 Hz, 1H), 3.77 (dd, *J* = 12.3, 5.0 Hz, 1H), 2.65-2.62 (m, 1H), 2.27-2.21 (m, 1H), 1.08 (d, *J* = 6.9 Hz, 3H), 0.95 (d, *J* = 7.0 Hz, 3H). ^{13}C NMR (126 MHz, D_2O/NaOD) δ (ppm) 175.59, 139.51, 133.82,

126.99, 70.74, 60.72, 57.18, 28.54, 19.62, 16.10. HRMS (FTMS + p ESI Full) calculated for $[M]^-$ $(C_{15}H_{18}N_1O_5)^-$ m/z 292.1179, found m/z 292.1184.

Model reactions

Acetone aldol reaction

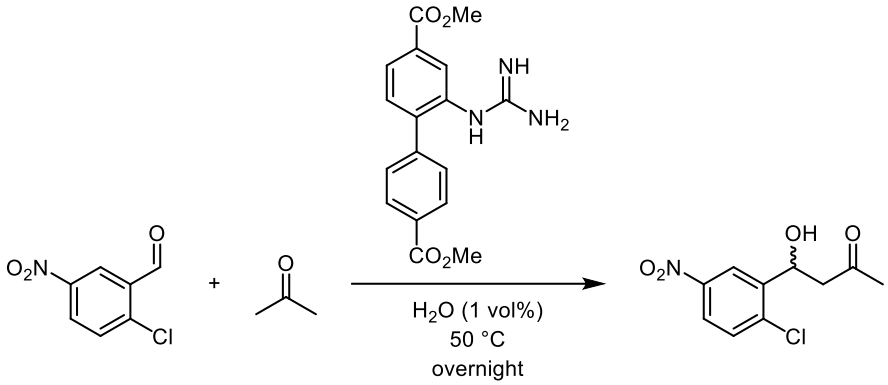

Scheme 2.1 Reaction scheme for the synthesis of the aldol reaction product of 2-chloro-5-nitrobenzaldehyde with acetone.

2-Chloro-5-nitrobenzaldehyde (7.4 mg, 40.0 mmol, 1.0 eq.) was dissolved in acetone (990.0 µL) and water (10.0 µL; 1 vol%). Me_2bpdc-gua (0.2 mg, 2.0 mol%) was added, and the reaction solution was heated to 50 °C overnight. The solvent was removed under reduced pressure, and the crude product was purified by passing through a silica plug, eluting with acetone. The pure product was obtained as a white solid (8.8 mg, 36.1 mmol, 91%).

^{1}H NMR (500 MHz, $CDCl_3$) δ (ppm) 8.54 (d, *J* = 2.7 Hz, 1H), 8.09 (dd, *J* = 8.7, 2.8 Hz, 1H), 7.50 (d, *J* = 8.7 Hz, 1H), 5.52 (dt, *J* = 9.8, 2.5 Hz, 1H), 3.74 (d, *J* = 3.1 Hz, 1H), 3.02 (dd, *J* = 18.0, 2.3 Hz, 1H), 2.67 (dd, *J* = 18.0, 9.8 Hz, 1H), 2.24 (s, 3H). ^{13}C NMR (126 MHz, $CDCl_3$) δ (ppm) 208.71, 147.31, 142.39, 137.79, 130.44, 123.52, 122.99, 66.31, 49.51, 30.74.

TLC: n-hexane/EtOAc (1/1, V/V); R_f = 0.40. HPLC: reverse phase system; Lux Amylose column; 0.5 mL/min; CH_3CN/H_2O (55/45, V/V); λ = 280 nm; e1 = 11.9 min; e2 = 14.4 min.

Friedel-Crafts reaction

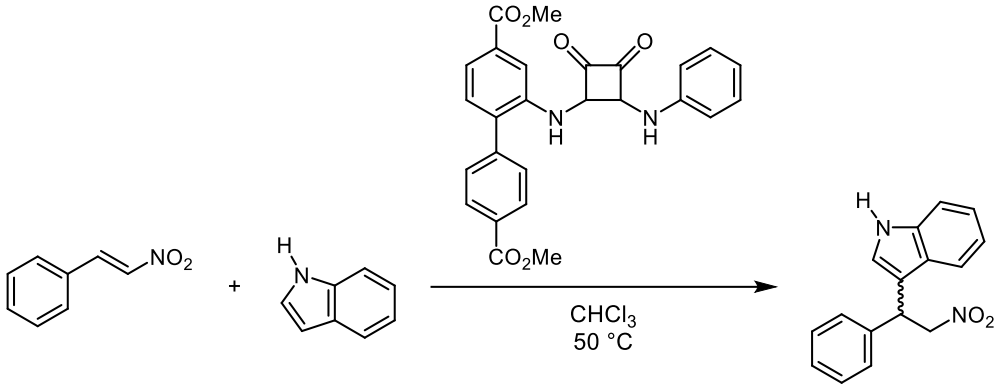

Scheme 2.2 Reaction scheme for the synthesis of the Friedel-Crafts reaction product of β-nitrostyrene with indole.

The TLC and HPLC conditions were developed by Dr. Jose Quinsaat. The reaction was performed according to the procedure reported by Zhang *et al.*[2] β-Nitrostyrene (6.0 mg, 40.0 µmol, 1.0 eq.) and indole (9.4 mg, 80.0 µmol, 2.0 eq.) were dissolved in $CHCl_3$ (1.0 mL). The linker precursor Me_2bpdc-Sq-Ph (0.4 mg, 2.0 mol%) was added as the homogeneous catalyst and the reaction was heated to 50 °C. The reaction progress was monitored by ^{1}H NMR. The TLC and HPLC conditions were developed without purification of the crude product.

TLC: n-hexane/EtOAc (7/3, V/V); R_f = 0.42. HPLC: reverse phase system; Lux Cellulose column; 0.6 mL/min; CH_3OH/H_2O (95/5, V/V); λ = 254 nm; e1 = 16.8 min; e2 = 22.8 min.

Baylis Hillman

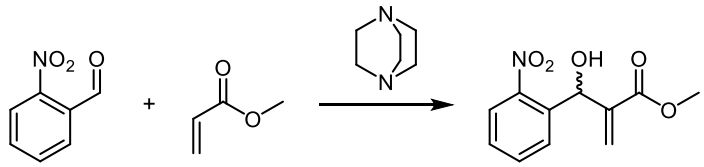

Scheme 2.3 Reaction scheme for the synthesis of the aldol reaction product of 2-chloro-5-nitrobenzaldehyde with acetone.

The reaction was performed according to the procedure reported by Maher et. al.[3] *o*-Nitrobenzaldehyde (76.6 mg, 506.9 µmol, 1.0 eq.) was dissolved in methyl acrylate (140.0 µL, 1.5 mmol, 3.1 eq.). DABCO (57.0 mg, 508.1 mmol, 1.0 eq.) was added and the reaction stirred at room temperature for 24 hours. The crude product was purified by silica gel column chromatography (cyclohexane/EtOAc; 60/40) to yield the pure product as a cloudless oil (103.8 mg, 437.6 µmol, 86%). The ^{1}H NMR spectrum agrees with literature data.[3]

^{1}H NMR (500 MHz, $CDCl_3$) δ (ppm) 7.95 (d, *J* = 8.1 Hz, 1H), 7.75 (d, *J* = 7.8 Hz, 1H), 7.65 (t, *J* = 7.6 Hz, 1H), 7.47 (t, *J* = 7.7 Hz, 1H), 6.37 (s, 1H), 6.21 (d, *J* = 4.6 Hz, 1H), 5.73 (s, 1H), 3.73 (s, 3H), 3.40 (d, *J* = 4.8 Hz, 1H).

TLC: n-hexane/EtOAc (6/4, V/V); R_f = 0.21. HPLC: normal phase system; Chiralcel OD-H column; 1.0 mL/min; n-hexane/2-PrOH (90/10, V/V); λ = 254 nm; e1 = 13.3 min; e2 = 14.8 min.

Michael_1 reaction

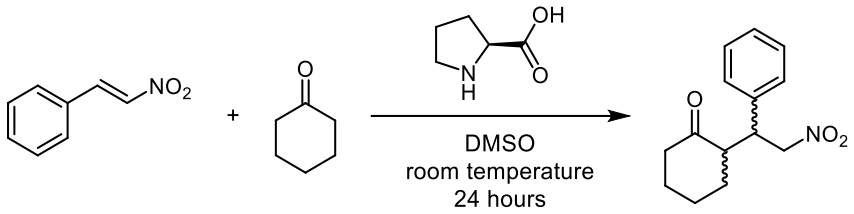

Scheme 2.4 Reaction scheme for the synthesis of the Michael_1 product of β-nitrostyrene with cyclohexanone.

The reaction was performed according to the procedure reported by List et al.[4] β-Nitrostyrene (150.0 mg, 1.0 mmol, 1.0 eq.) and L-proline (20.0 mg, 173.7 µmol, 17.0 mol%) were dissolved in DMSO (8.0 mL). Cyclohexanone (2.0 mL, 19.3 mmol, 19.2 eq.) was added and the reaction mixture was stirred at room temperature for 24 hours. The reaction was quenched by the addition of an aqueous NH_4Cl solution, and the mixture was extracted with EtOAc (3 × 10 mL). The combined organic phases were washed with water (1 × 10 mL) and removed under reduced pressure. The crude product was purified by silica gel column chromatography (cyclohexane/EtOAc; 4/1) and recrystallised in diethyl ether to yield the pure product as colourless crystals (184.6 mg, 746.5 µmol, 74%). The ^{1}H NMR spectrum agrees with literature data.[5]

^{1}H NMR (500 MHz, $CDCl_3$) δ (ppm) 7.34-7.28 (m, 3H), 7.17 (d, *J* = 7.6 Hz, 2H), 4.93 (dd, *J* = 12.5, 4.5 Hz, 1H), 4.64 (dd, *J* = 12.3, 10.0 Hz, 1H), 3.76 (dt, *J* = 9.8, 4.5 Hz, 1H), 2.69 (dt, *J* = 11.6, 5.0 Hz, 1H), 2.49-2.46 (m, 1H), 2.42-2.36 (m, 1H), 2.10-2.06 (m, 1H), 1.80-1.67 (m, 3H), 1.28-1.21 (m, 2H).

TLC: n-hexane/EtOAc (4/1, V/V); R_f = 0.24. HPLC: normal phase system; Chiralpak AS-H column; 1.0 mL/min; n-hexane/2-PrOH (80/20, V/V); λ = 210 nm; e1 = 17.7 min; e2 = 25.3 min.

Michael_2 reaction

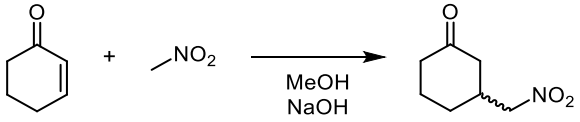

Scheme 2.5 Reaction scheme for the synthesis of the Michael_2 product of 2-cyclohexen-1-one with nitromethane.

2-Cyclohexen-1-one (120.0 µL, 1.2 mmol, 1.0 eq.) and nitromethane (650.0 µL, 12.1 mmol, 9.8 eq.) were dissolved in MeOH (15 mL). Aqueous NaOH solution (1 M, 50.0 µL, 4.0 mol%) was added, and the reaction mixture was stirred overnight at room temperature. The solvent was removed under reduced pressure and the residue was extracted with $CHCl_3$. The organic phase was isolated, and removal of the solvent yielded the pure product as a colourless oil (96.3 mg, 612.7 µmol, 49%). NMR matches literature spectra.[6]

^{1}H NMR (500 MHz, $CDCl_3$) δ (ppm) 4.39-4.31 (m, 2H), 2.69-2.60 (m, 1H), 2.51-2.42 (m, 2H), 2.32-2.25 (m, 1H), 2.19-2.09 (m, 2H), 2.00-1.96 (m, 1H), 1.78-1.68 (m, 1H), 1.55-1.47 (m, 1H).

TLC: n-hexane/EtOAc (2/1, V/V); R_f = 0.40, product spot visible with $KMnO_4$ stain. HPLC: normal phase system; Chiralpak AD-H column; 1.0 mL/min; n-hexane/2-PrOH (85/15, V/V); λ = 210 nm; e1 = 29.5 min; e2 = 33.5 min.

Pictet-Spengler reaction

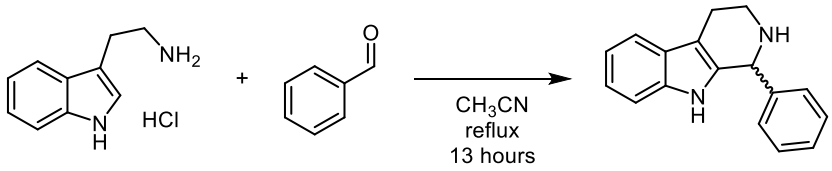

Scheme 2.6 Reaction scheme for the synthesis of the Pictet-Spengler product of tryptamine hydrochloride and benzaldehyde.

The TLC and HPLC conditions were developed by Mohana Arul. Tryptamine hydrochloride (78.0 mg, 489.9 µmol, 1.0 eq.) was dissolved in dry CH_3CN (10 mL) and benzaldehyde (52.0 mg, 490.0 µmol, 1.0 eq.) was added. The reaction mixture was refluxed for 13 hours. After cooling to room temperature solids were removed by filtration and the solvent was removed under reduced pressure. The residue was dissolved in a K_2CO_3 (10wt%) solution (5 mL) and refluxed overnight. After cooling to room temperature, the reaction mixture was extracted with EtOAc (3 × 10 mL) and the combined organic phases were removed under reduced pressure. The crude product was recrystalised in ethanol to yield the product as a white solid. The 1H NMR spectrum agrees with reported spectra.[7]

^{1}H NMR (500 MHz, D_2O) δ (ppm) 7.50-7.44 (m, 4H), 7.37-7.35 (m, 2H), 7.23 (d, *J* = 8.1 Hz, 1H), 7.11-7.08 (m, 1H), 7.04-7.01 (m, 1H), 5.85 (s, 1H), 360-3.55 (m, 1H), 3.53-3.47 (m, 1H), 3.22-3.16 (m, 1H), 3.13-3.05 (m, 1H).

TLC: CH_2Cl_2/methanol (8/2, V/V); R_f = 0.45. HPLC: normal phase system; Chiralcel OD-H column; 1.0 mL/min; n-hexane/2-PrOH (80/20, V/V); λ = 280 nm; e1 = 10.1 min; e2 = 13.8 min.

MOFs

Achiral MUF-77 catalysts and chiral but non catalytic MUF-77

PXRD

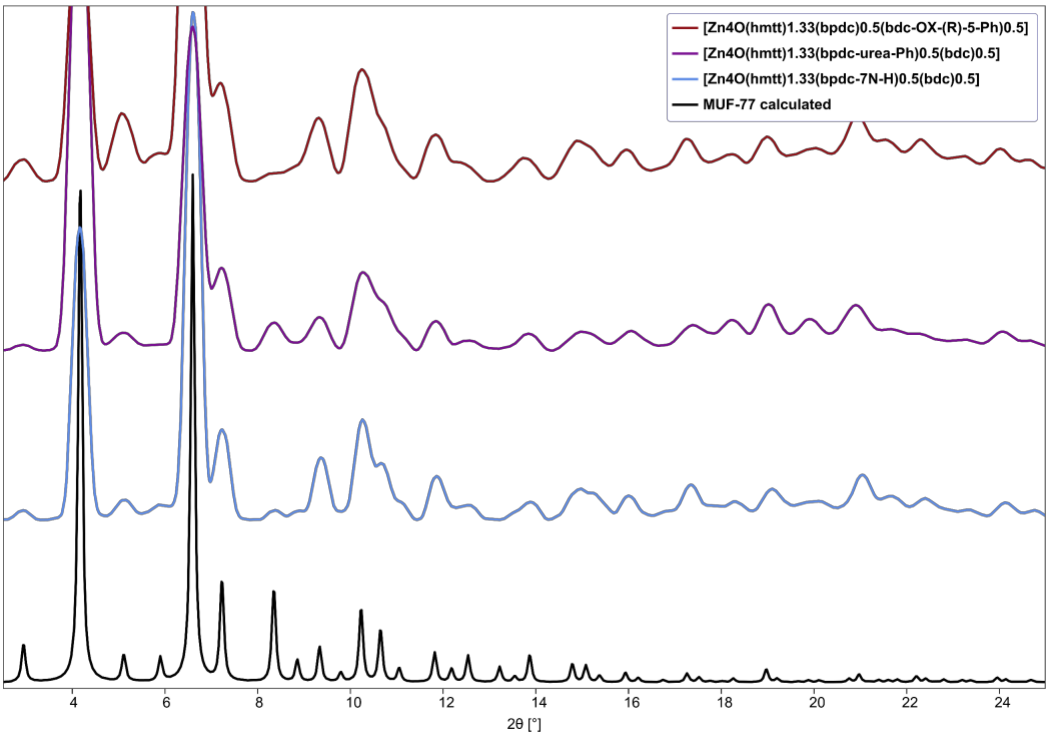

Figure 2.1 PXRD pattern of achiral MUF-77 catalysts and chiral but non catalytic MUF-77 compared to the calculated pattern of MUF-77. The pattern are scaled by a factor of three for better visibility.

MOF NMRs

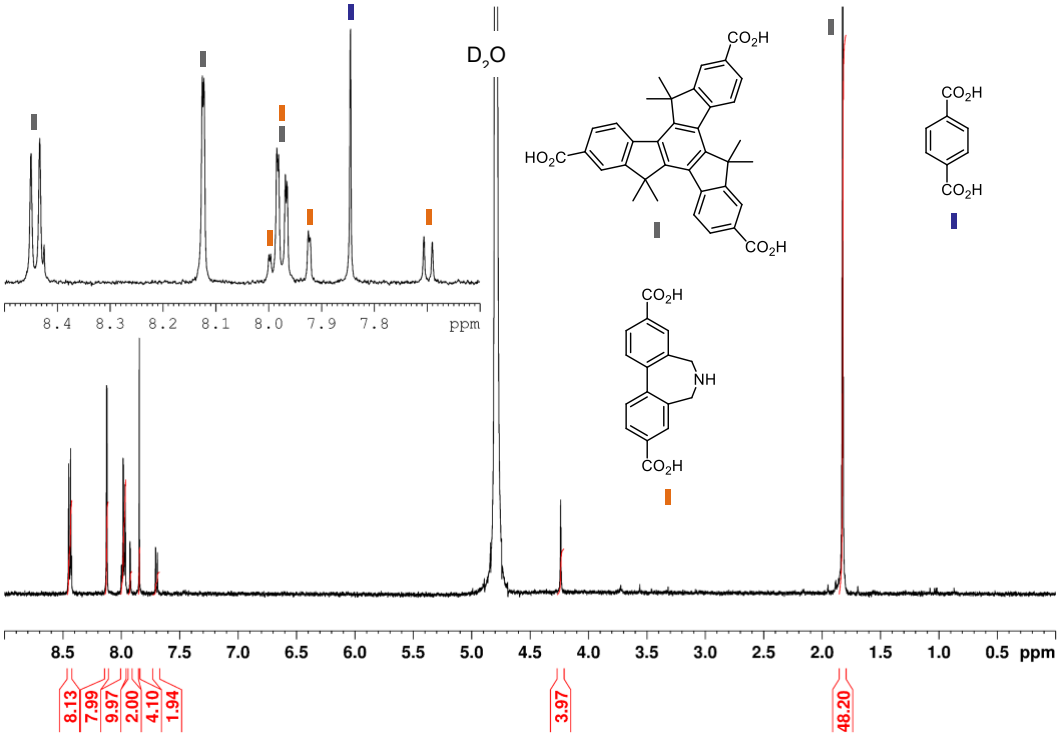

Figure 2.2 ^{1}H NMR of digested $[Zn_4O(hmtt)_{1.33}(bpdc\text{-}^{7}N\text{-}H)_{0.5}(bdc)_{0.5}]$ in D_2O/NaOD.

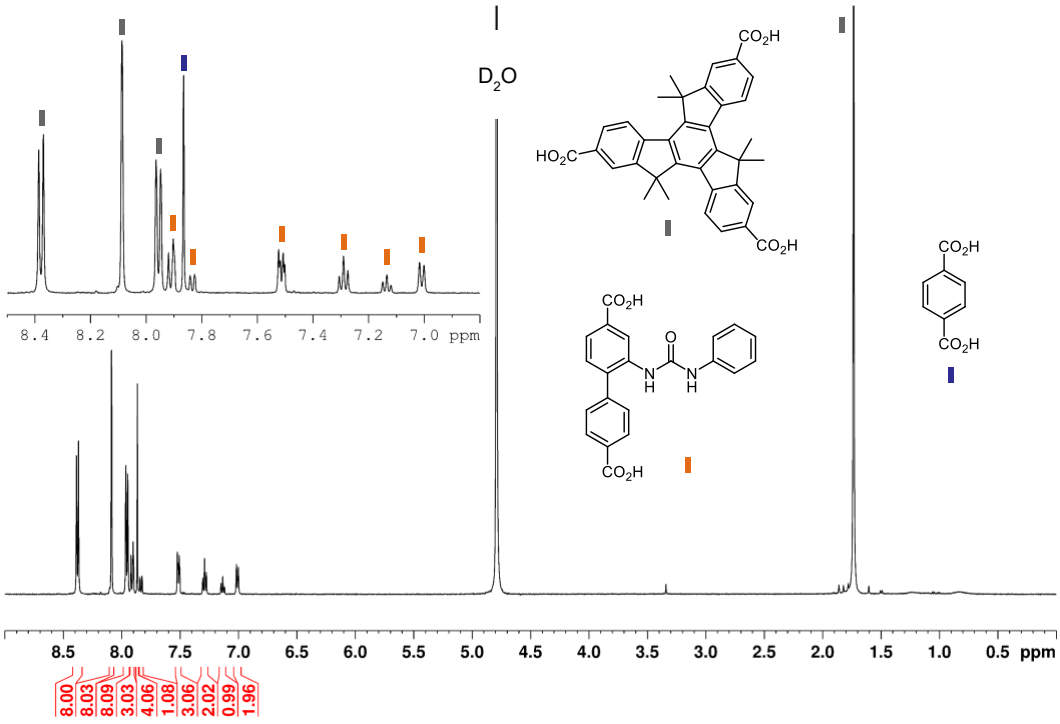

Figure 2.3 ^{1}H NMR of digested $[Zn_4O(hmtt)_{1.33}(bpdc\text{-}urea\text{-}Ph)_{0.5}(bdc)_{0.5}]$in D_2O/NaOD.

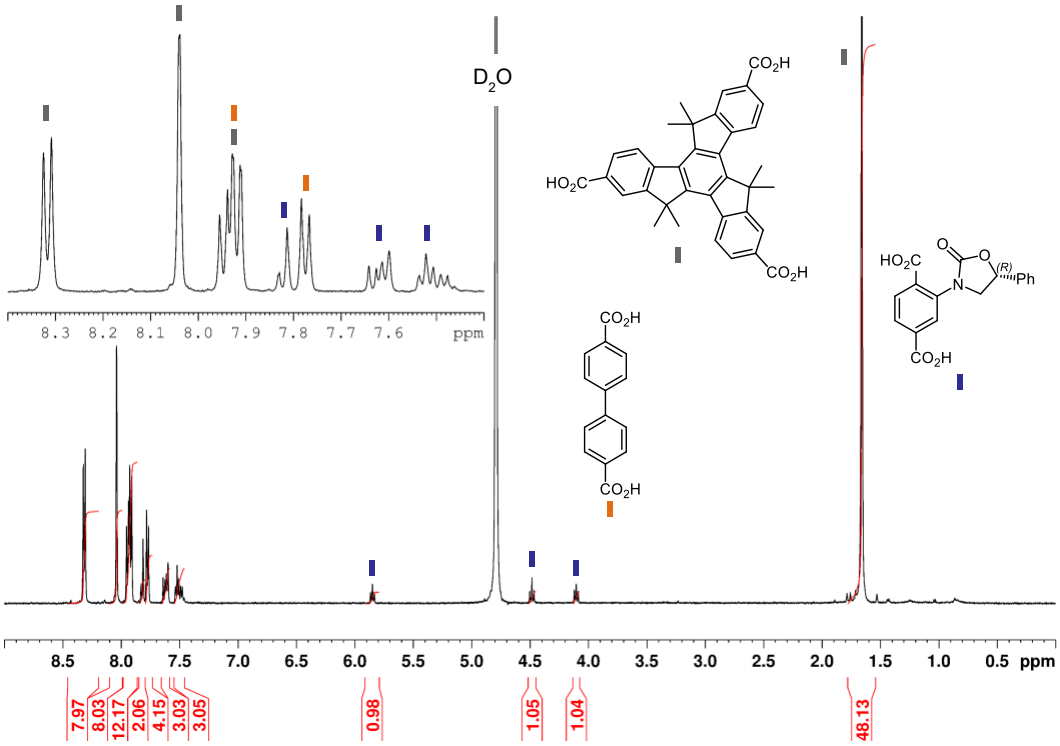

Figure 2.4 ^{1}H NMR of digested $[Zn_4O(hmtt)_{1.33}(bpdc)_{0.5}(bdc\text{-}OX\text{-}(R)\text{-}5\text{-}Ph)_{0.5}]$ in D_2O/NaOD.

RAI-MOFs

MUF-77_^{7}N-H_Ox

NMR

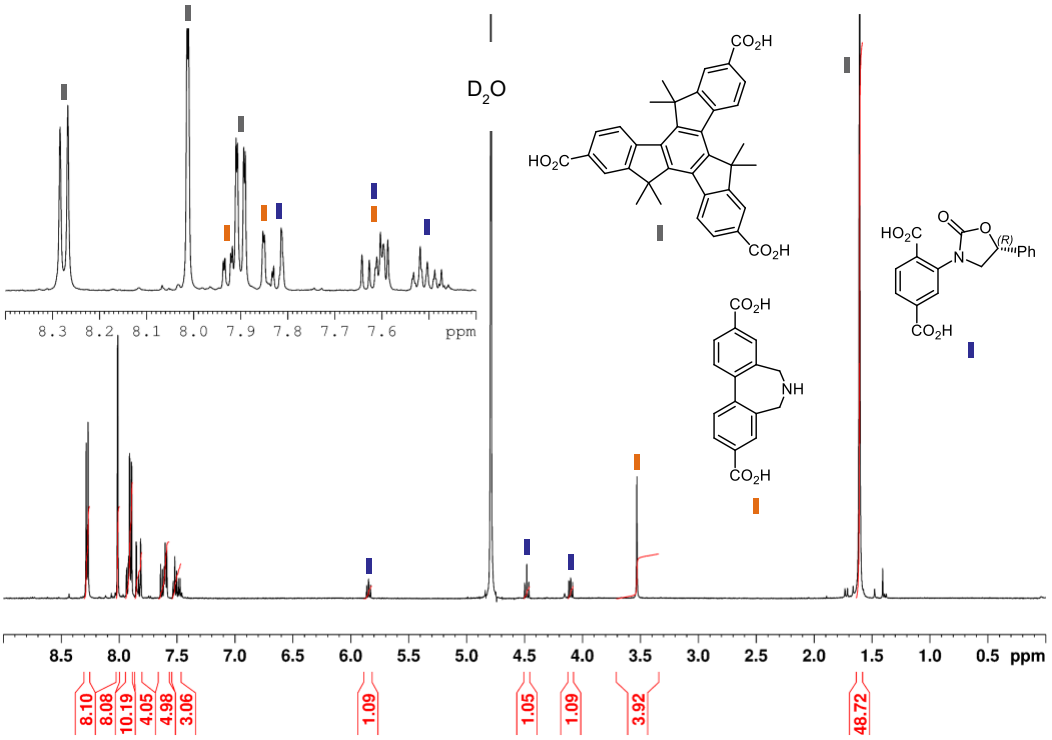

Figure 2.5 ^{1}H NMR of digested MUF-77_^{7}N-H_Ox_2 in D_2O/NaOD.

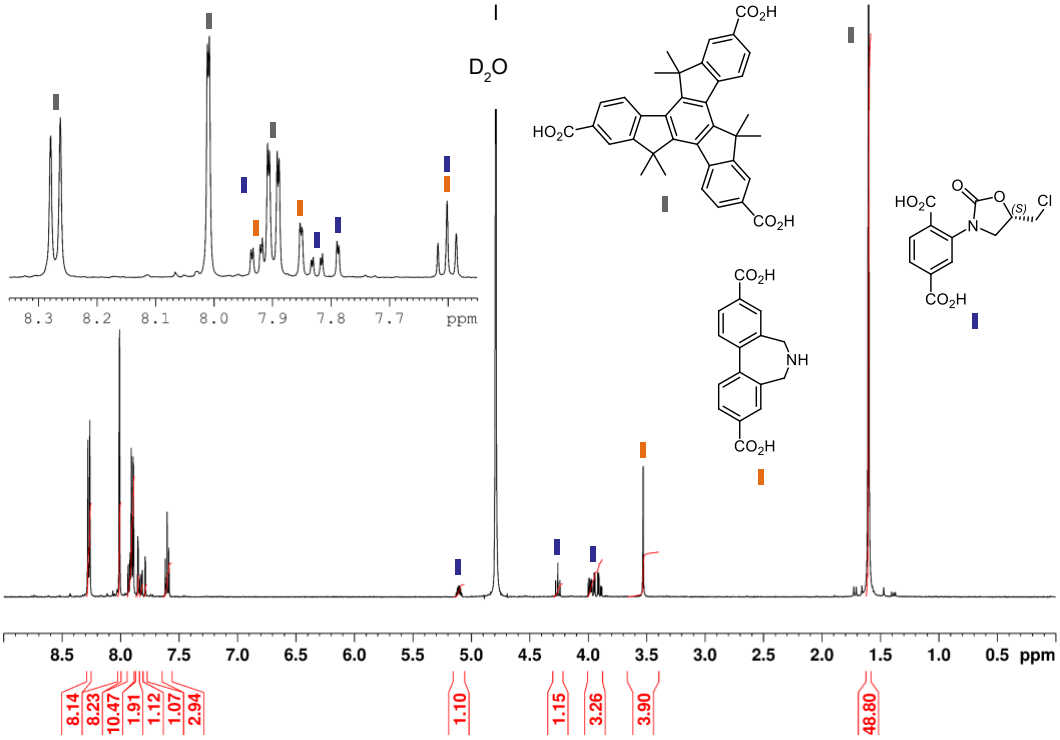

Figure 2.6 ^{1}H NMR of digested MUF-77_^{7}N-H_Ox_3 in D_2O/NaOD.

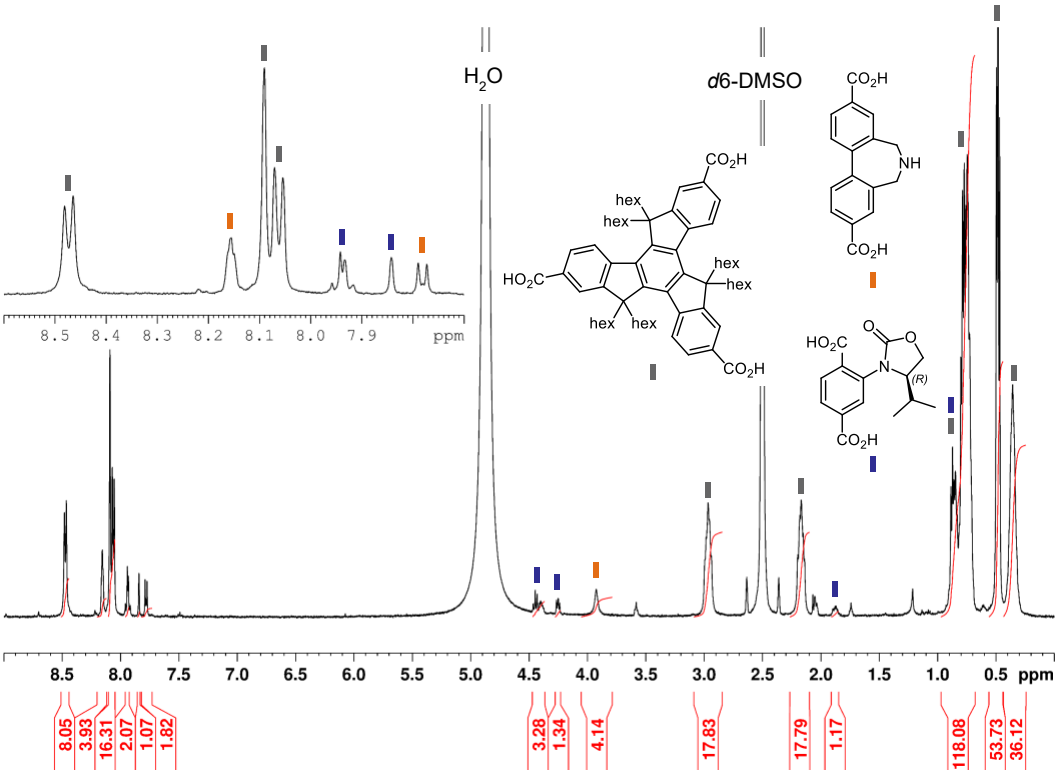

Figure 2.7 ^{1}H NMR of digested MUF-77_^{7}N-H_Ox_4 in *d6*-DMSO/DCl.

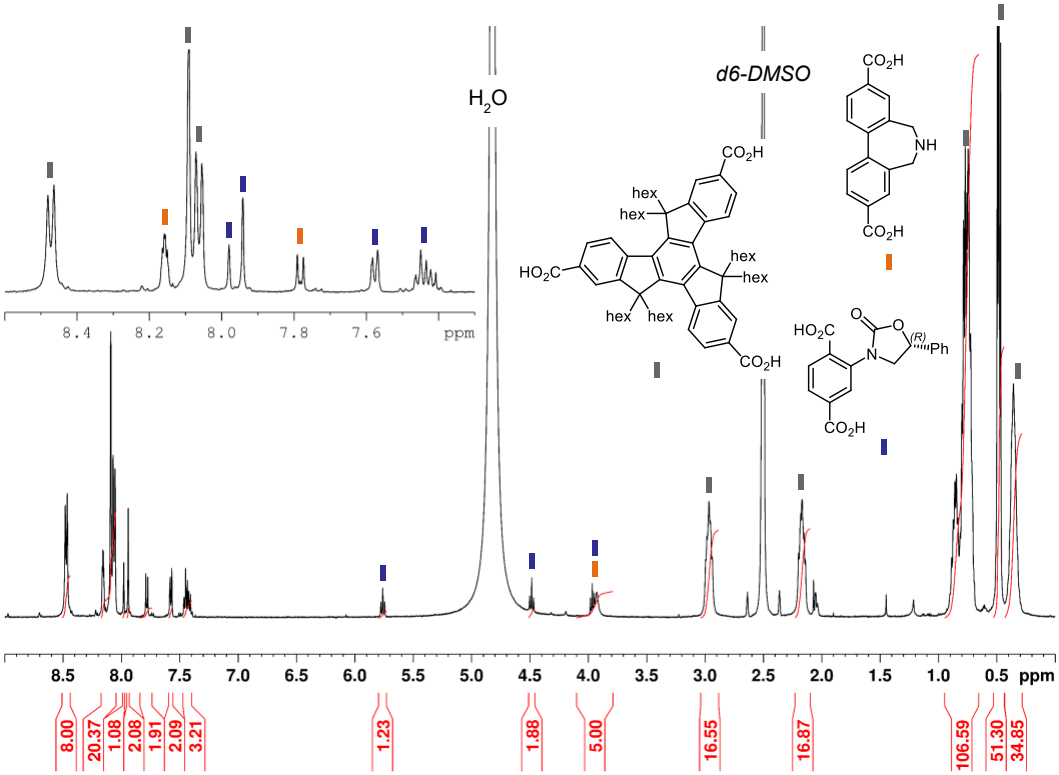

Figure 2.8 ^{1}H NMR of digested MUF-77_^{7}N-H_Ox_5 in *d6*-DMSO/DCl.

MUF-77_urea_OX

PXRD

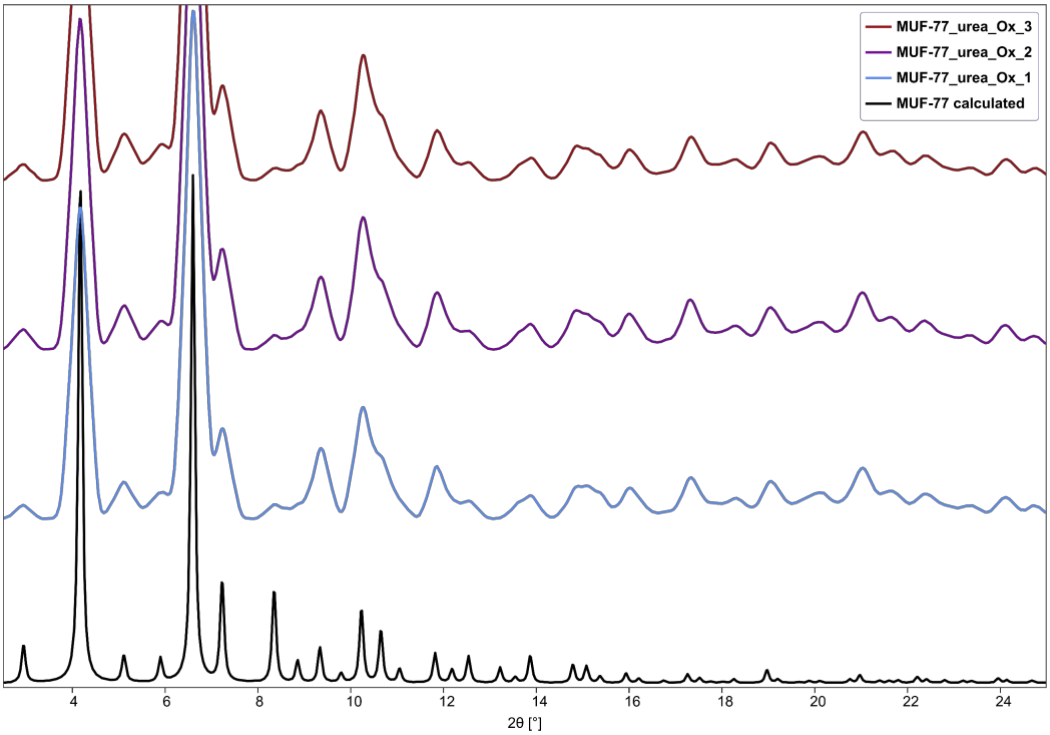

Figure 2.9 PXRD pattern of MUF-77_urea_Ox_1-3 compared to the calculated pattern of MUF-77. The pattern are scaled by a factor of three for better visibility.

NMR

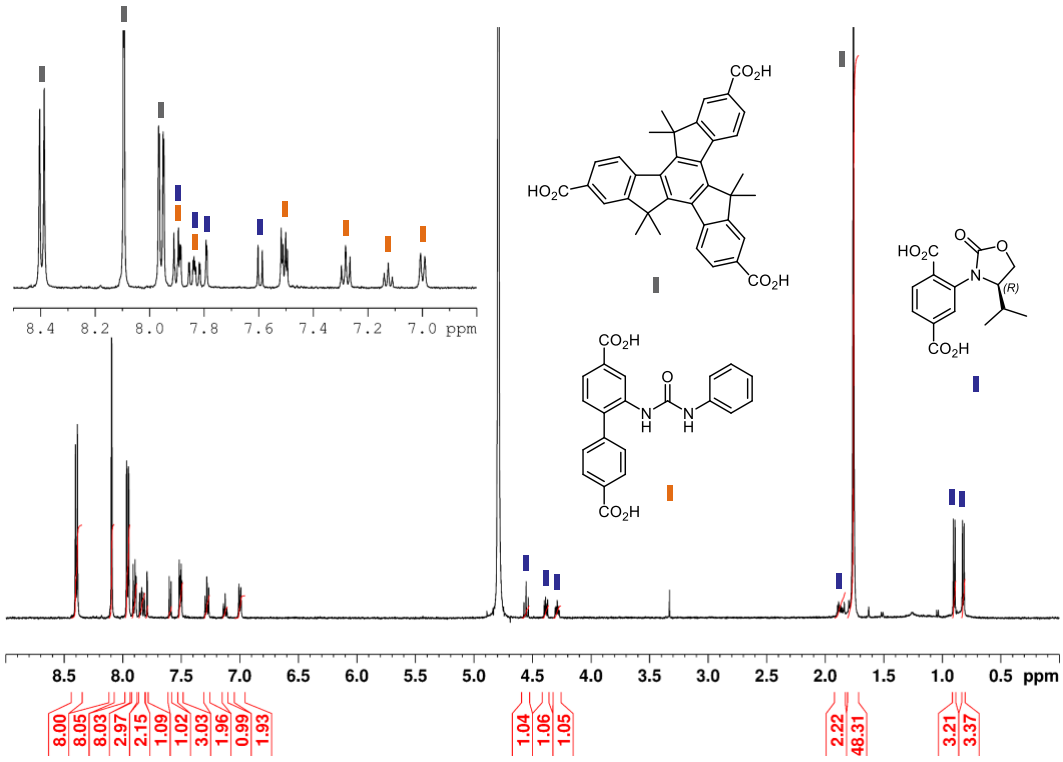

Figure 2.10 ^{1}H NMR of digested MUF-77_urea_Ox_1 in D_2O/NaOD.

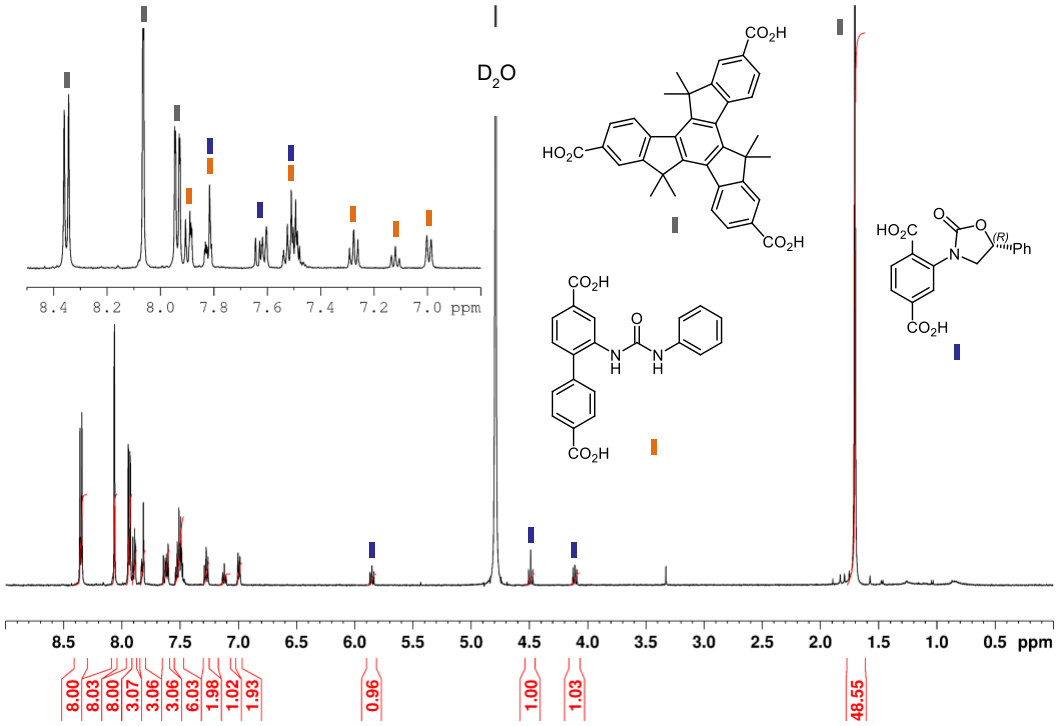

Figure 2.11 ^{1}H NMR of digested MUF-77_urea_Ox_2 in D_2O/NaOD.

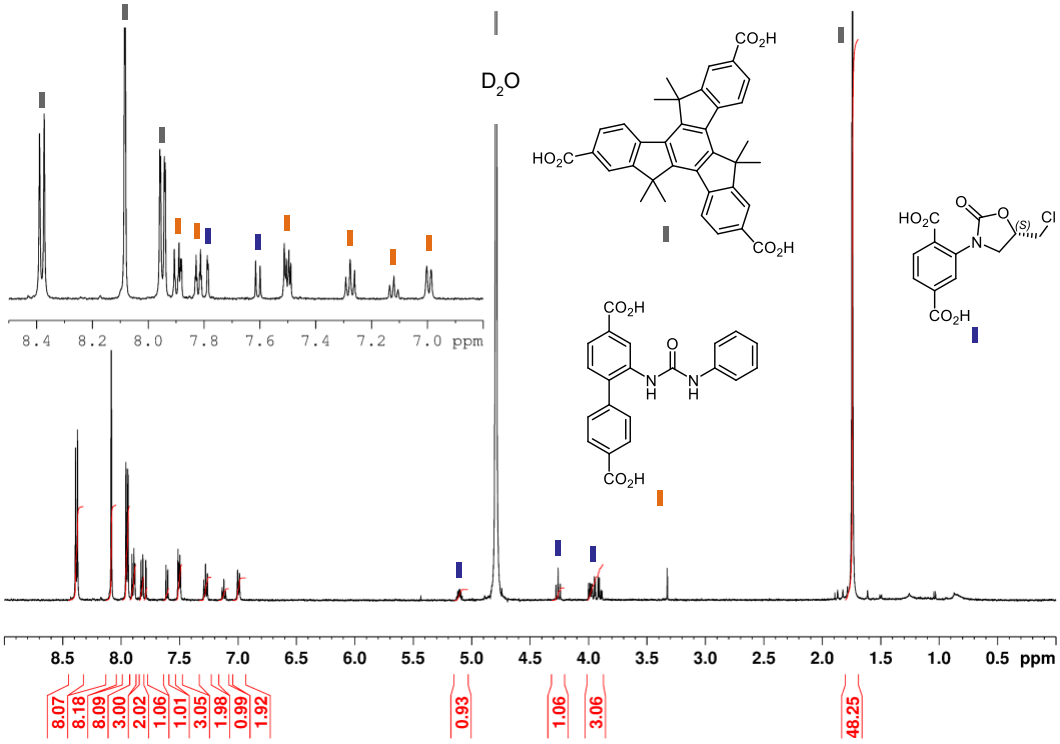

Figure 2.12 ^{1}H NMR of digested MUF-77_urea_Ox_3 in D_2O/NaOD.

MUF-77/7_gua_OX

PXRD

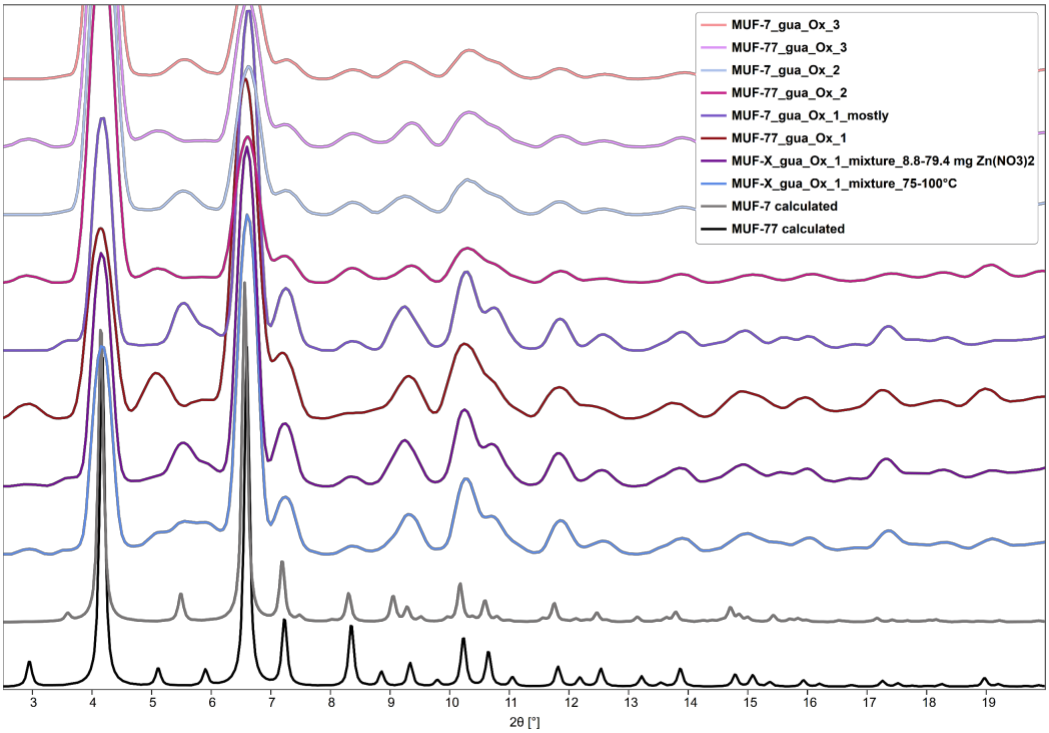

Figure 2.13 PXRD pattern of MUF-X_gua_Ox_1-3 compared to the calculated pattern of MUF-77 and MUF-7. The pattern are scaled by a factor of three for better visibility.

NMR

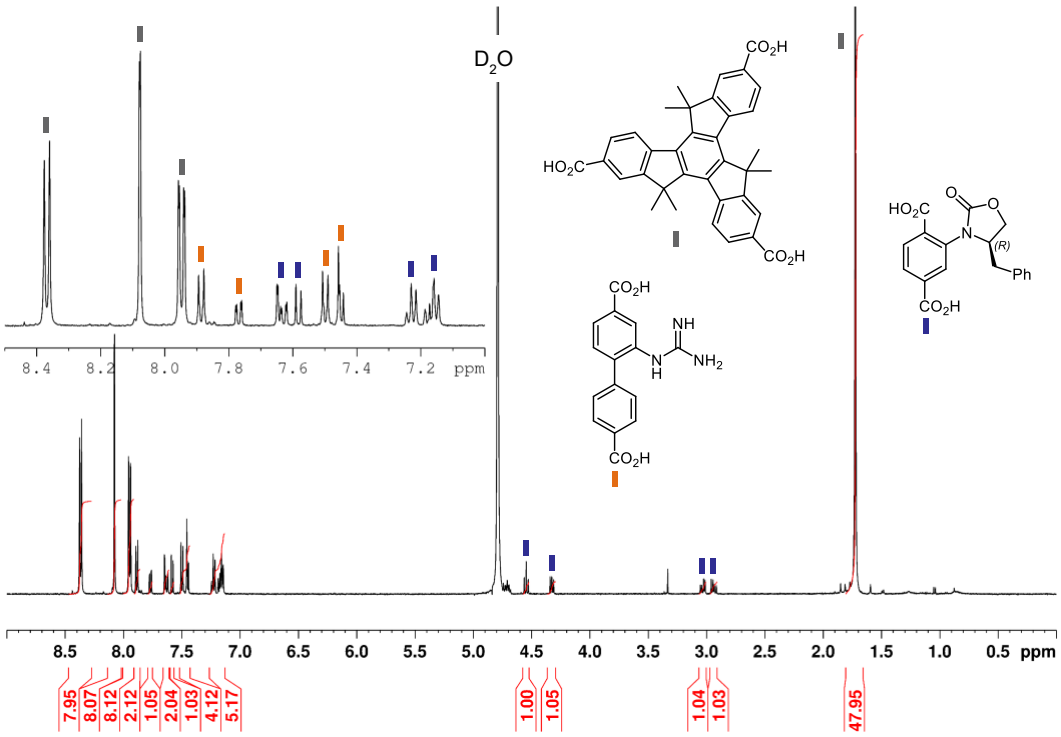

Figure 2.14 ^{1}H NMR of digested MUF-77/7_gua_Ox_1 in D_2O/NaOD.

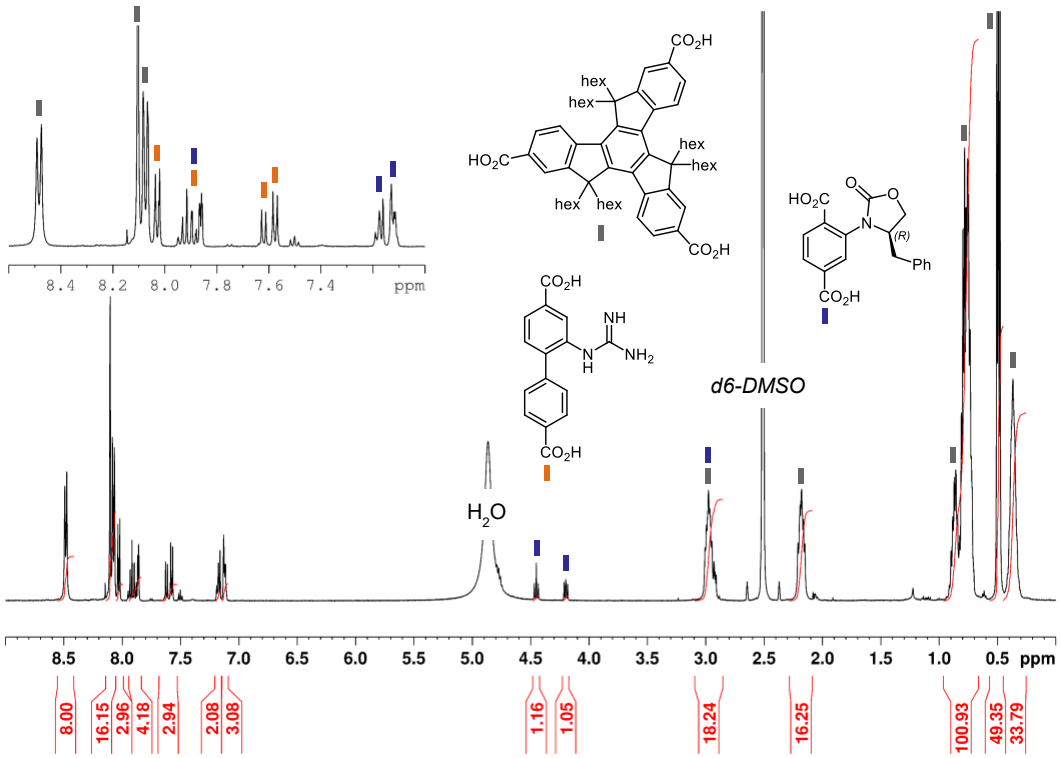

Figure 2.15 ^{1}H NMR of digested MUF-77/7_gua_Ox_2 in D_2O/NaOD.

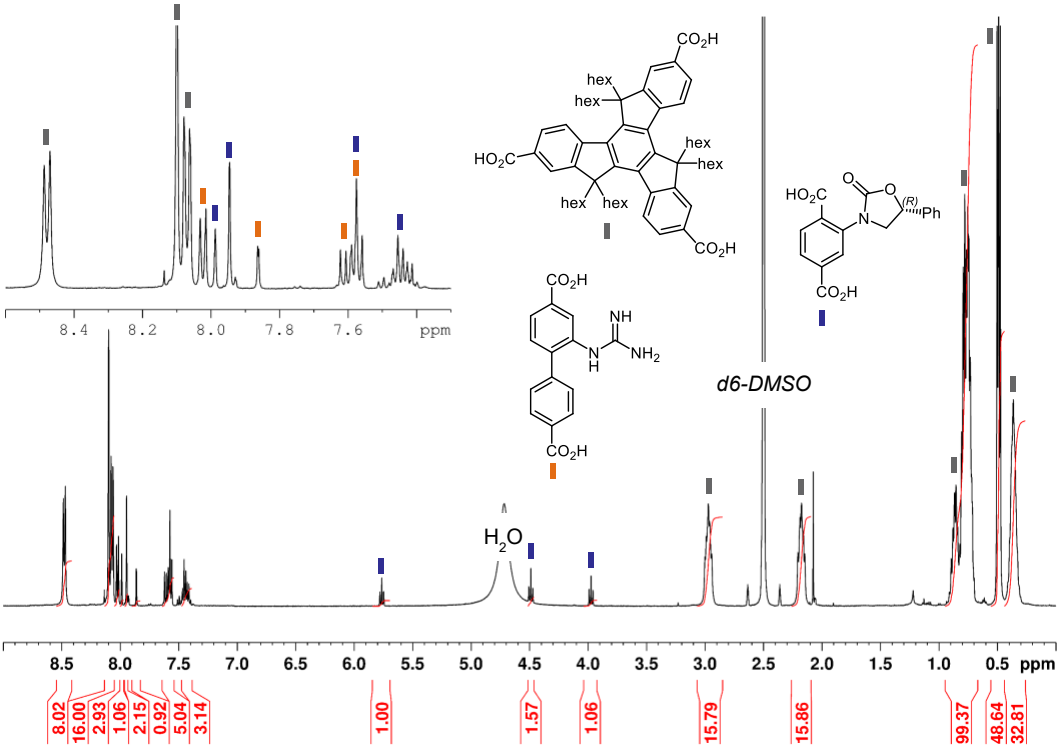

Figure 2.16 ^{1}H NMR of digested MUF-77/7_gua_Ox_3 in D_2O/NaOD.

MUF-77_gua_^{5}N

PXRD

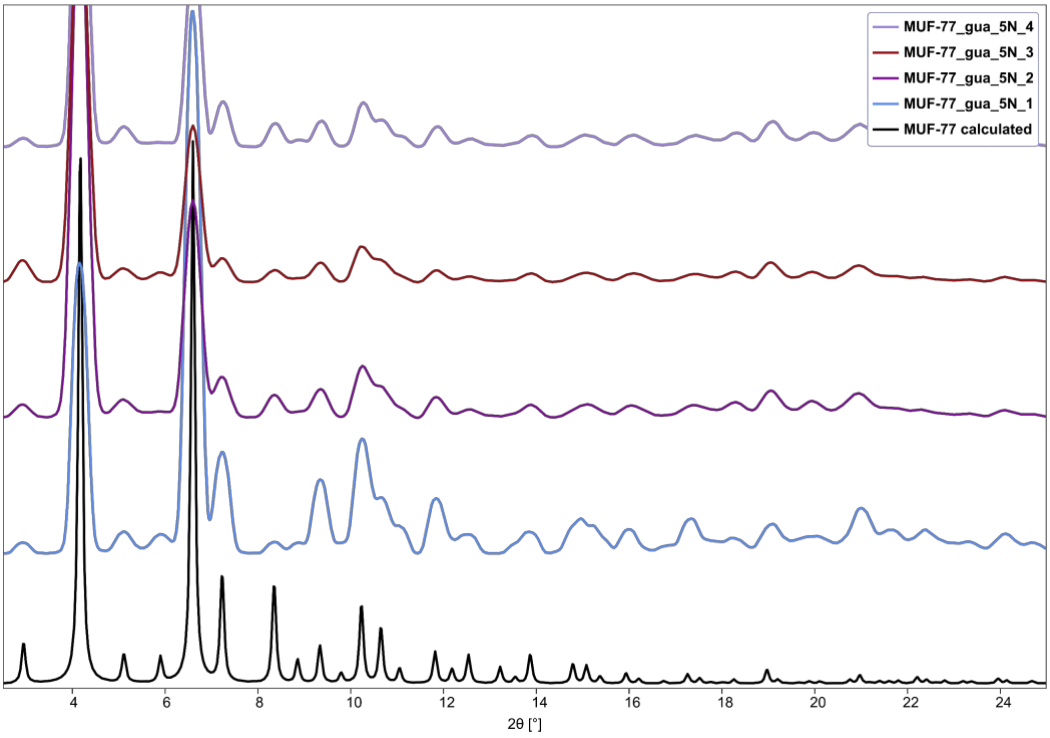

Figure 2.17 PXRD pattern of MUF-77_gua_^{5}N_1-4 compared to the calculated pattern of MUF-77. The pattern are scaled by a factor of three for better visibility.

NMR

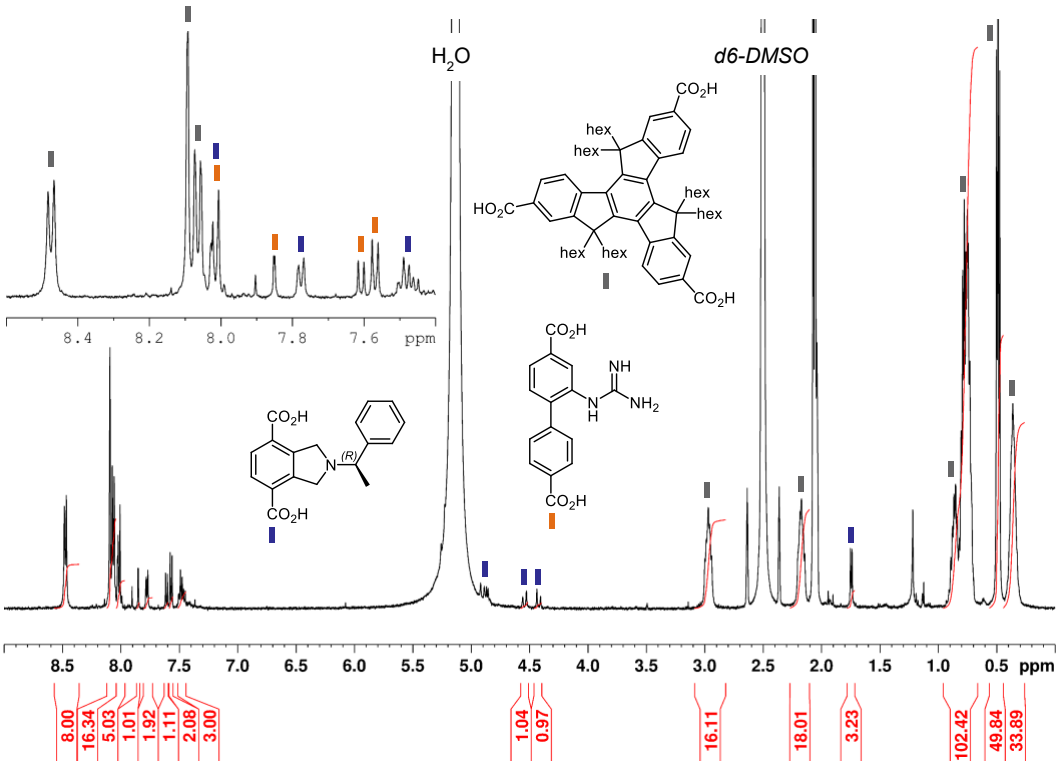

Figure 2.18 ^{1}H NMR of digested MUF-77_gua_^{5}N_1 in *d6*-DMSO/DCl.

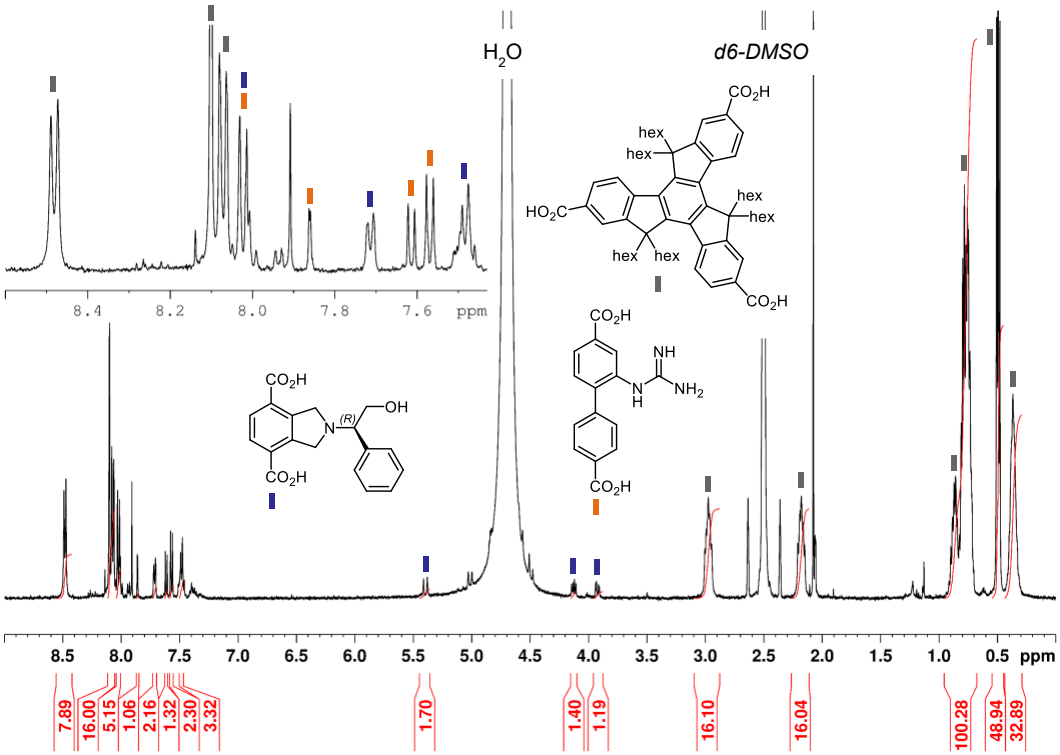

Figure 2.19 ^{1}H NMR of digested MUF-77_gua_^{5}N_2 in *d6*-DMSO/DCl.

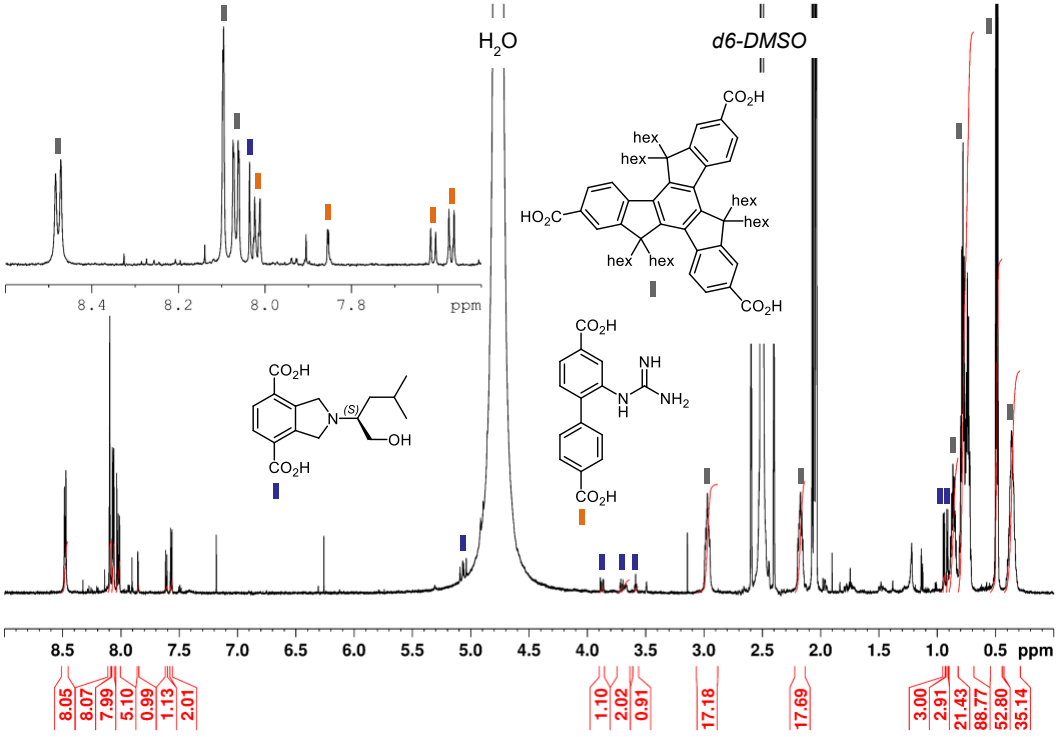

Figure 2.20 ^{1}H NMR of digested MUF-77_gua_^{5}N_3 in *d6*-DMSO/DCl.

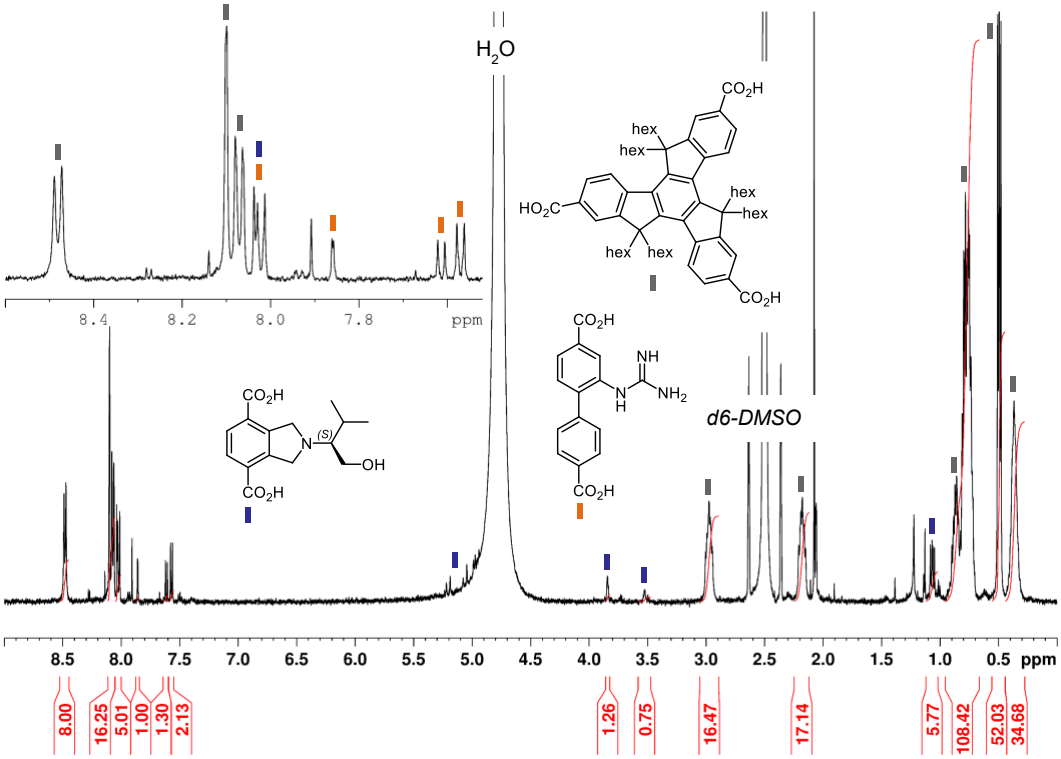

Figure 2.21 ^{1}H NMR of digested MUF-77_gua_^{5}N_4 in *d6*-DMSO/DCl.

Linker synthesis: NMR spectra

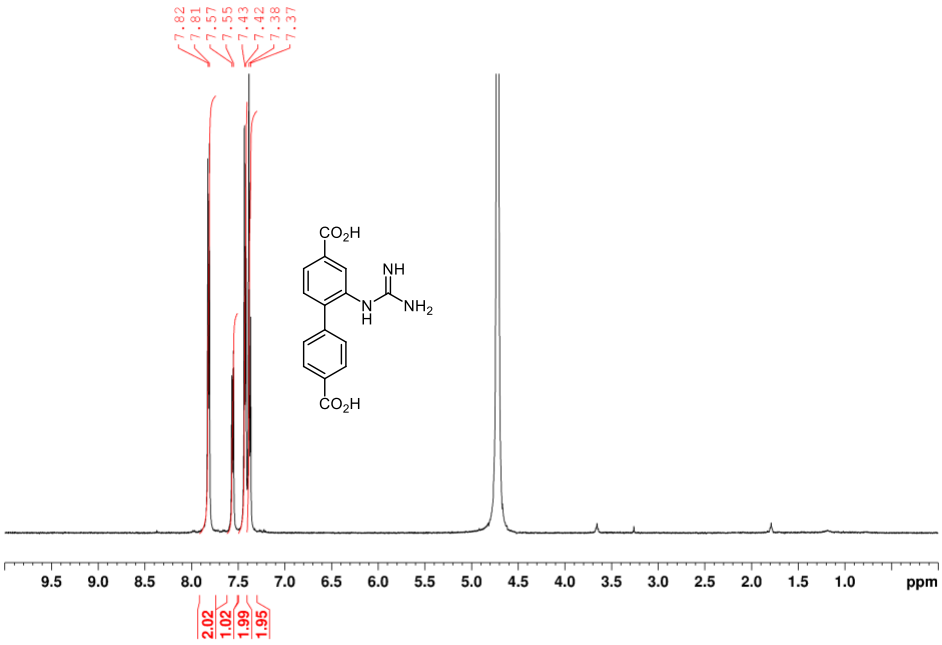

Figure 2.22 ^{1}H NMR spectrum of H_2bpdc-gua in D_2O/NaOD.

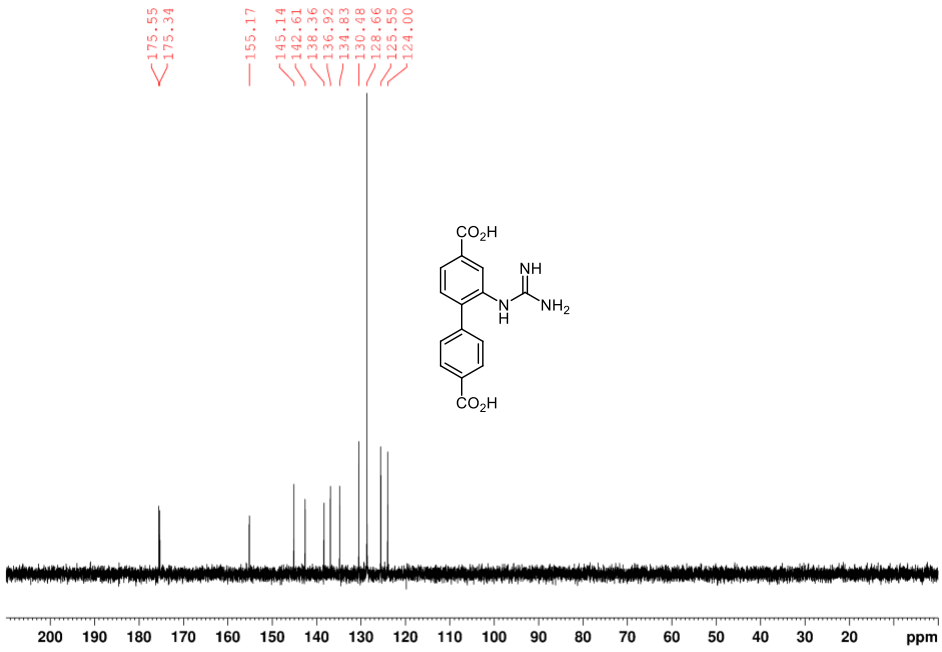

Figure 2.23 ^{13}C NMR spectrum of H_2bpdc-gua in D_2O/NaOD.

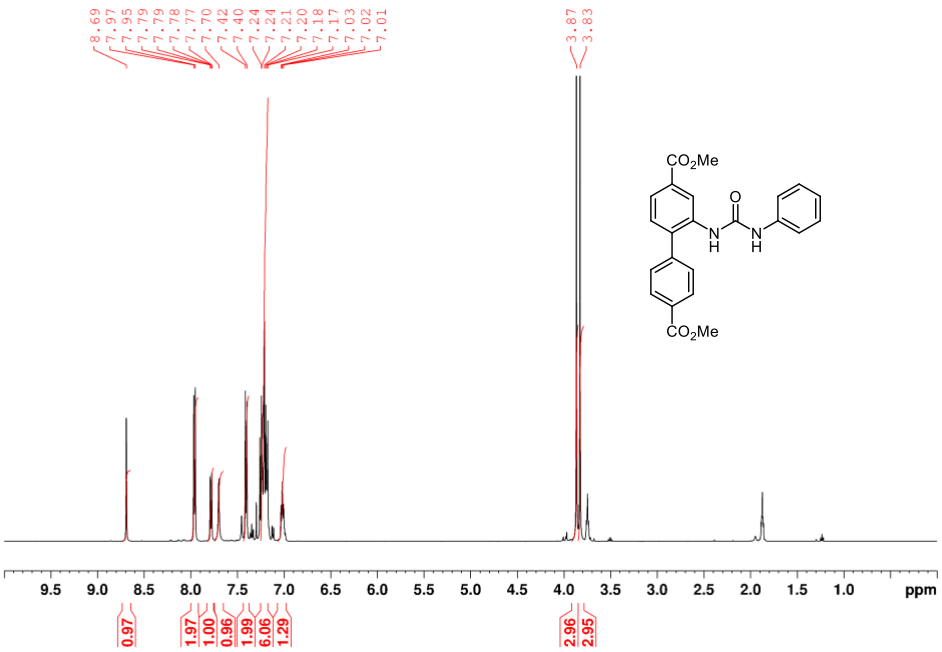

Figure 2.24 ^{1}H NMR spectrum of Me$_2$bpdc-urea-Ph in CDCl$_3$.

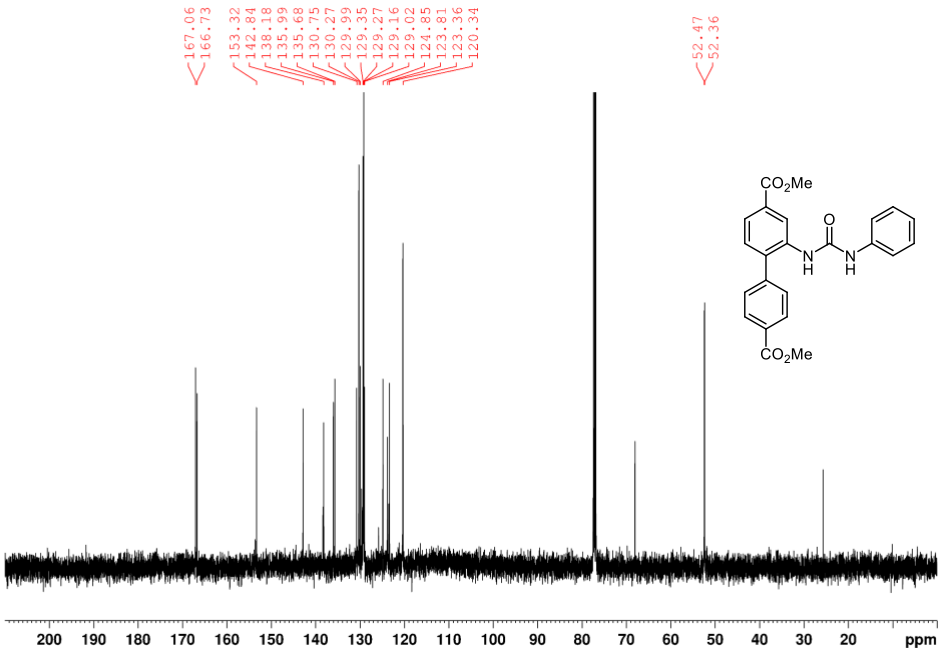

Figure 2.25 ^{13}C NMR spectrum of Me$_2$bpdc-urea-Ph in CDCl$_3$.

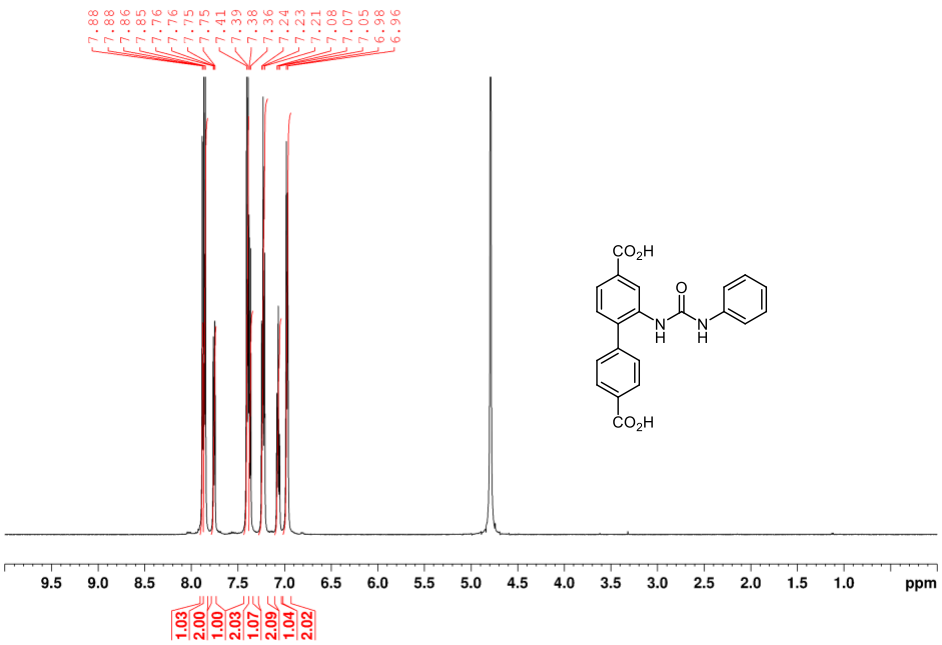

Figure 2.26 ^{1}H NMR spectrum of H_2bpdc-urea-Ph in D_2O/NaOD.

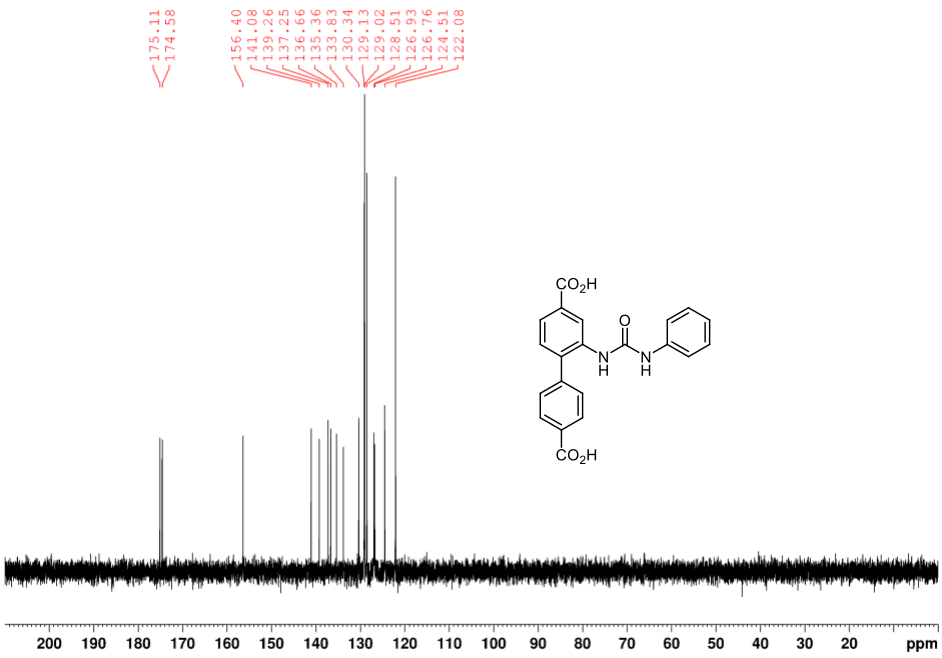

Figure 2.27 ^{13}C NMR spectrum of H_2bpdc-urea-Ph in D_2O/NaOD.

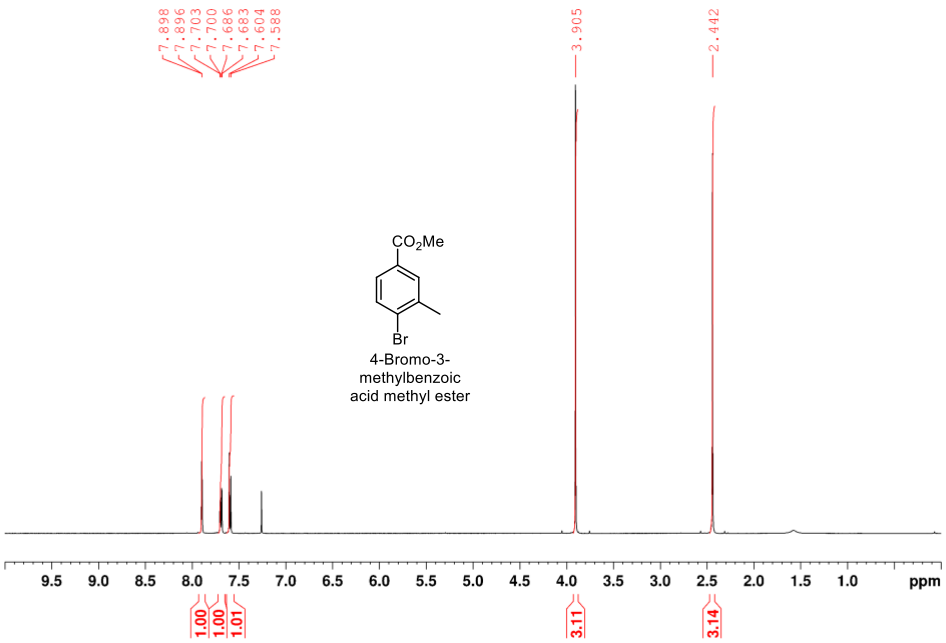

Figure 2.28 ^{1}H NMR spectrum of 4-bromo-3-methylbenzoic acid methyl ester in $CDCl_3$.

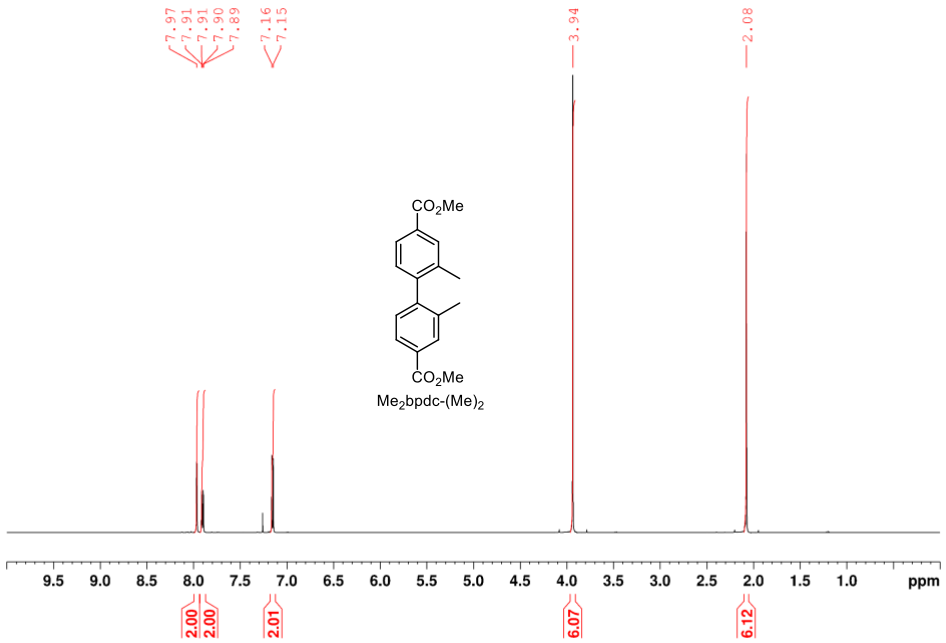

Figure 2.29 ^{1}H NMR spectrum of $Me_2bpdc\text{-}(Me)_2$ in $CDCl_3$.

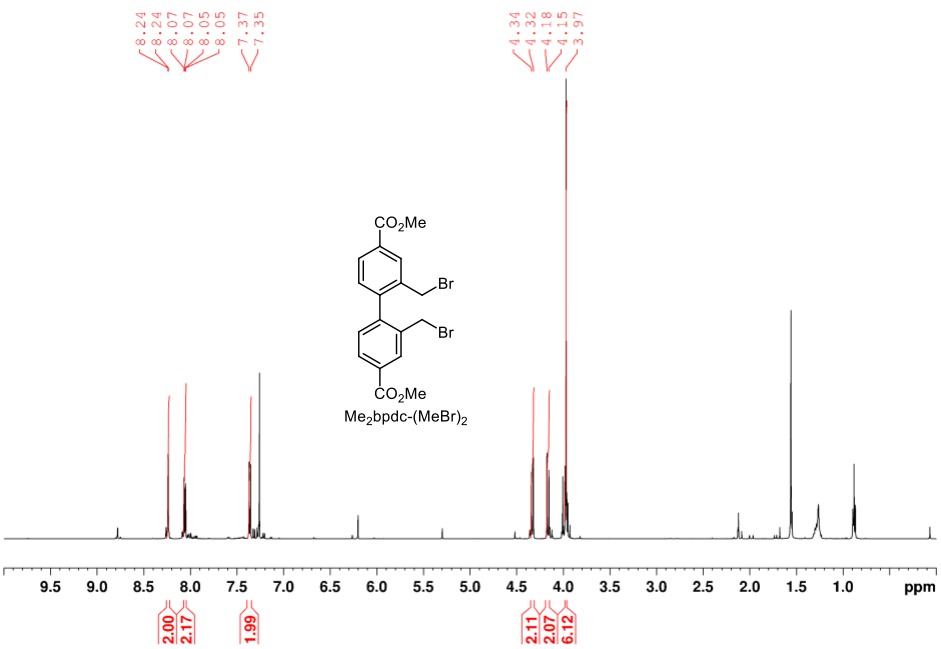

Figure 2.30 ^{1}H NMR spectrum of Me$_2$bpdc-(MeBr)$_2$ in CDCl$_3$.

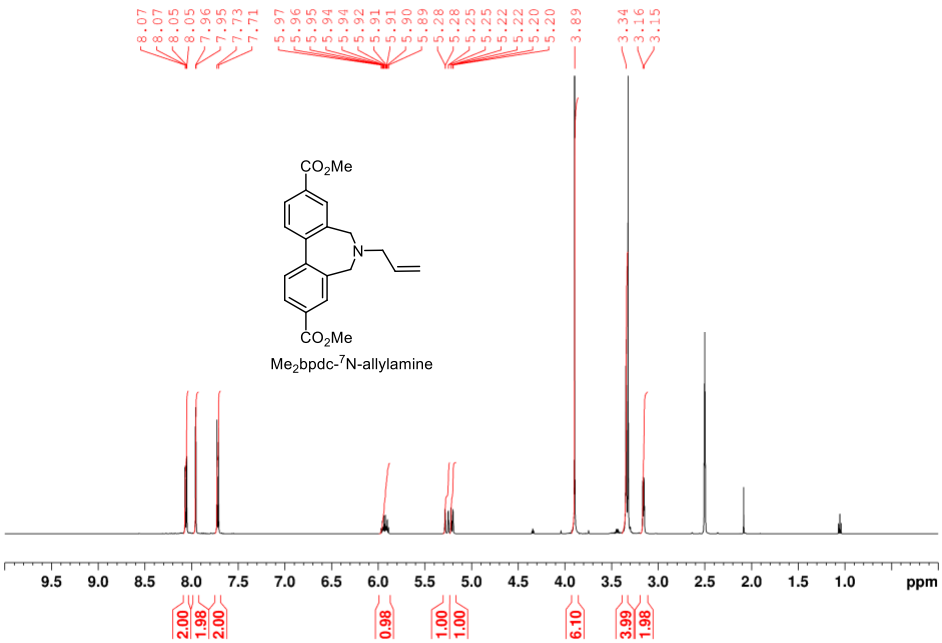

Figure 2.31 ^{1}H NMR spectrum of Me$_2$bpdc-^{7}N-allylamine in *d6*-DMSO.

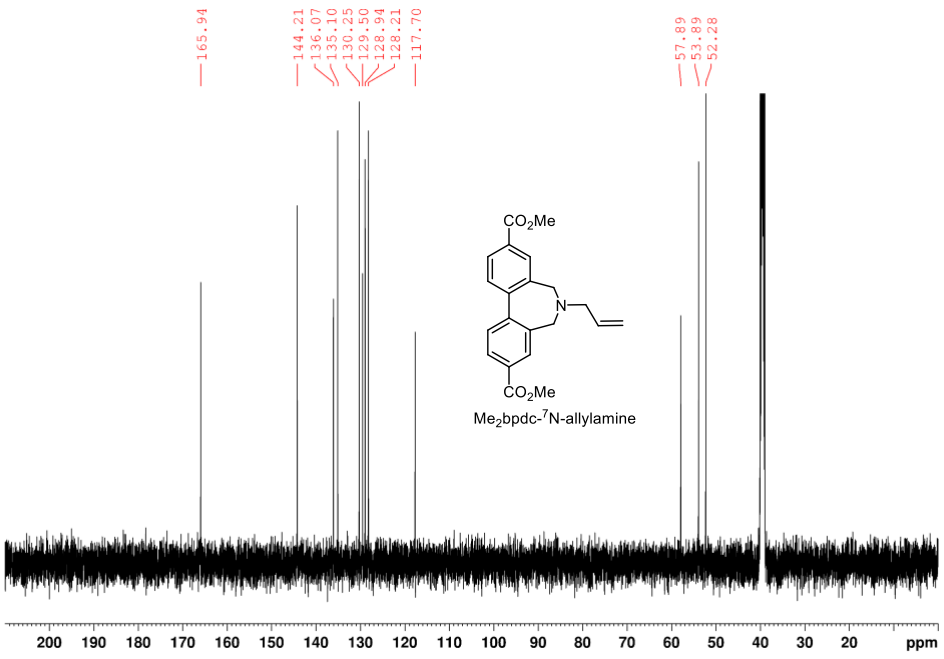

Figure 2.32 ^{13}C NMR spectrum of Me$_2$bpdc-^{7}N-allylamine in *d6*-DMSO.

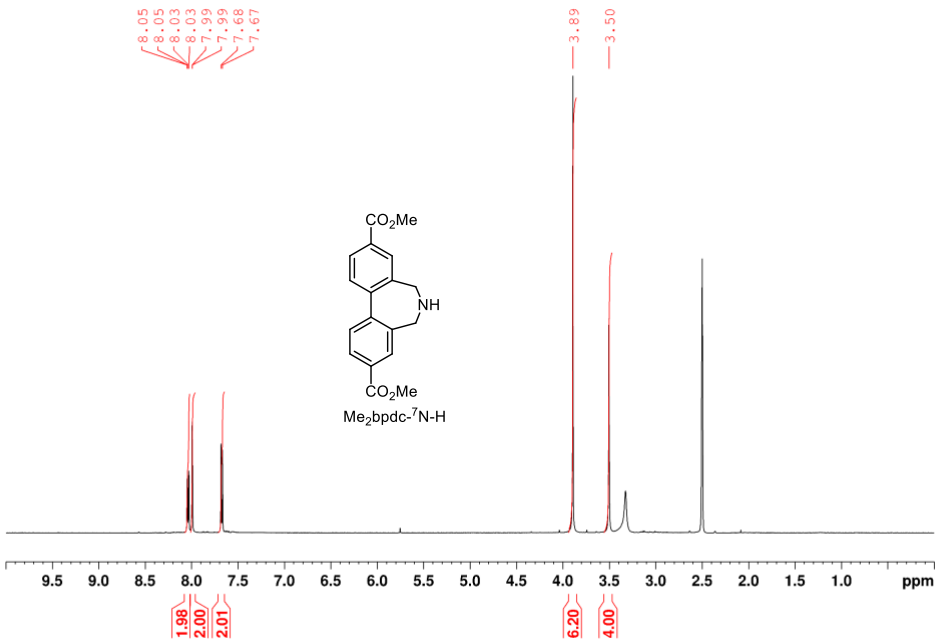

Figure 2.33 ^{1}H NMR spectrum of Me$_2$bpdc-^{7}N-H in *d6*-DMSO.

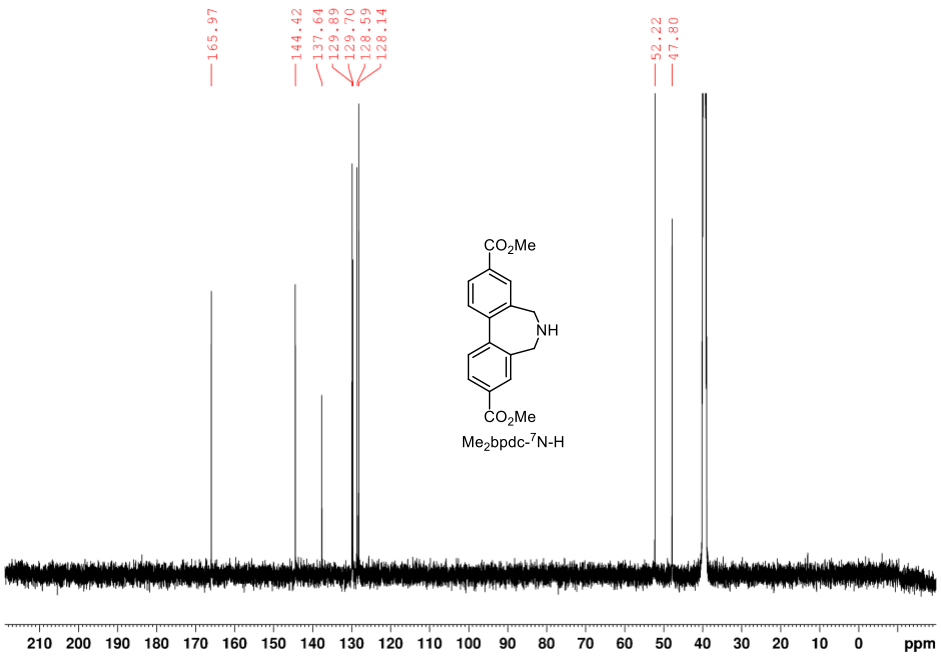

Figure 2.34 ^{13}C NMR spectrum of Me$_2$bpdc-^{7}N-H in *d6*-DMSO.

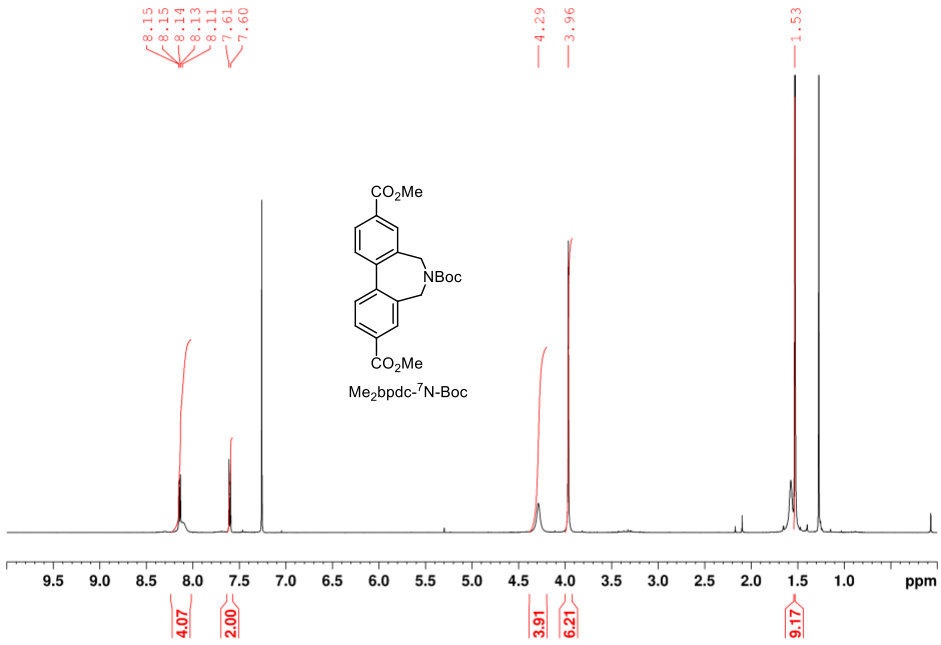

Figure 2.35 ^{1}H NMR spectrum of Me$_2$bpdc-^{7}N-Boc in CDCl$_3$.

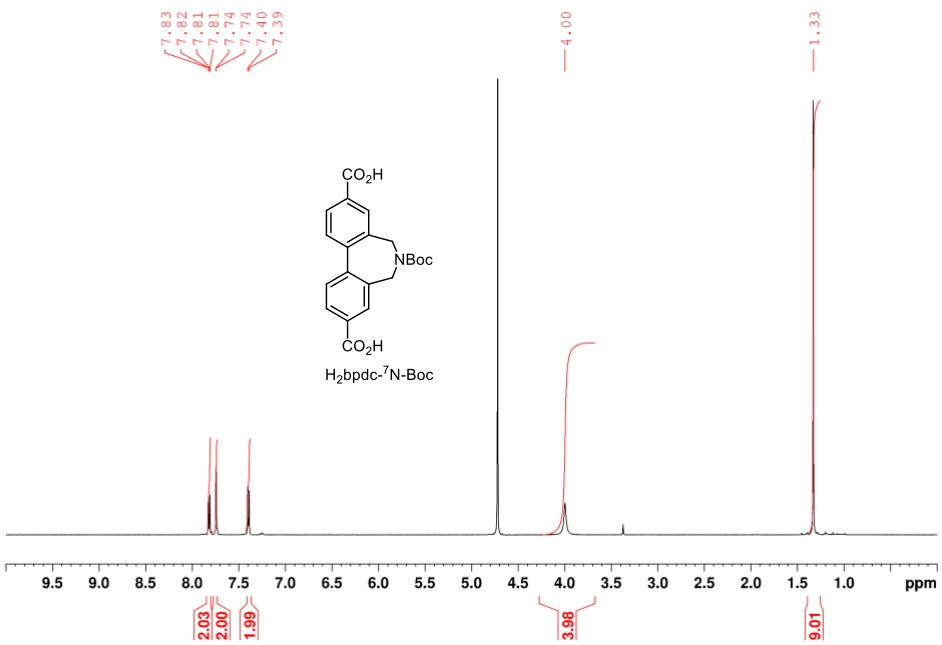

Figure 2.36 ^{1}H NMR spectrum of H$_2$bpdc-^{7}N-Boc in D$_2$O/NaOD.

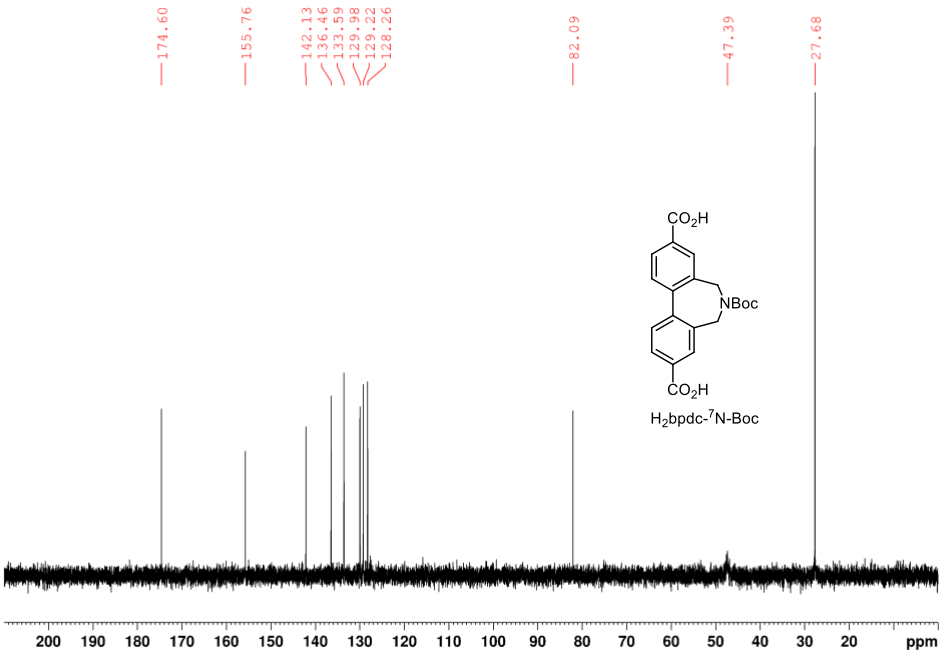

Figure 2.37 ^{13}C NMR spectrum of H$_2$bpdc-^{7}N-Boc in D$_2$O/NaOD.

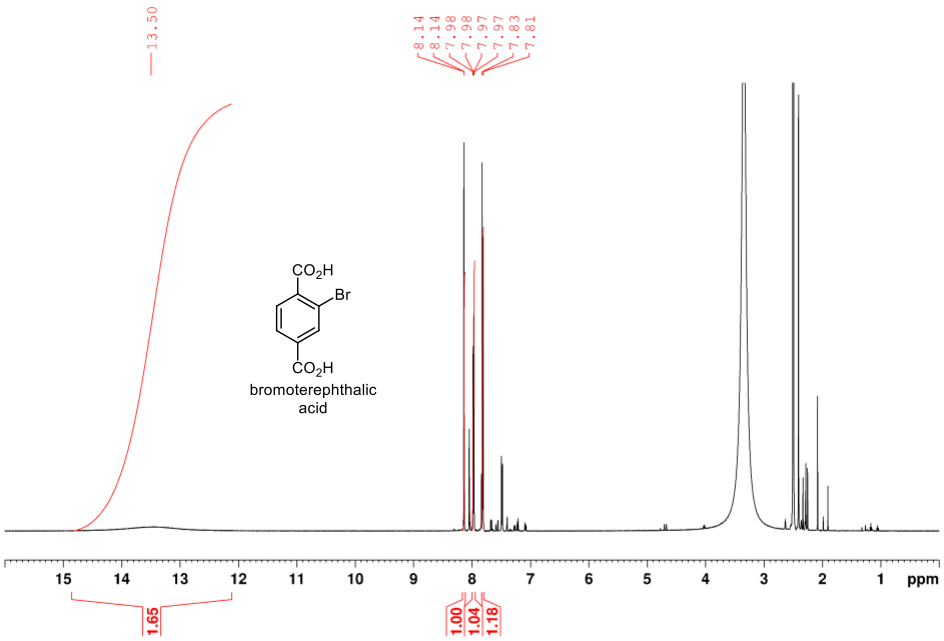

Figure 2.38 ^{1}H NMR spectrum of bromoterephthalic acid in *d6*-DMSO.

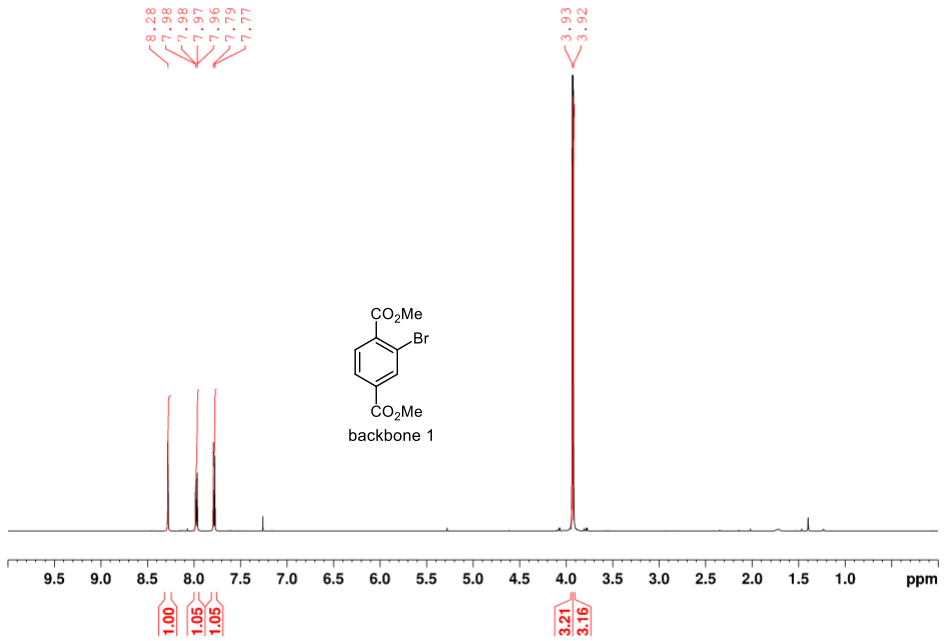

Figure 2.39 ^{1}H NMR spectrum of backbone 1 in $CDCl_3$.

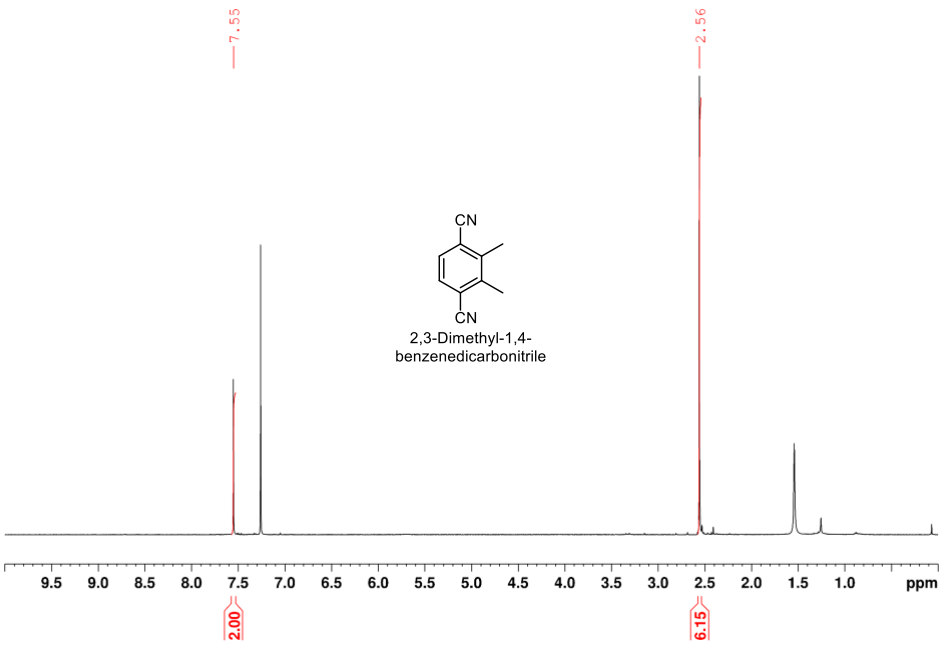

Figure 2.40 ^{1}H NMR spectrum of 2,3-dimethyl-1,4-benzenedicarbonitrile in $CDCl_3$.

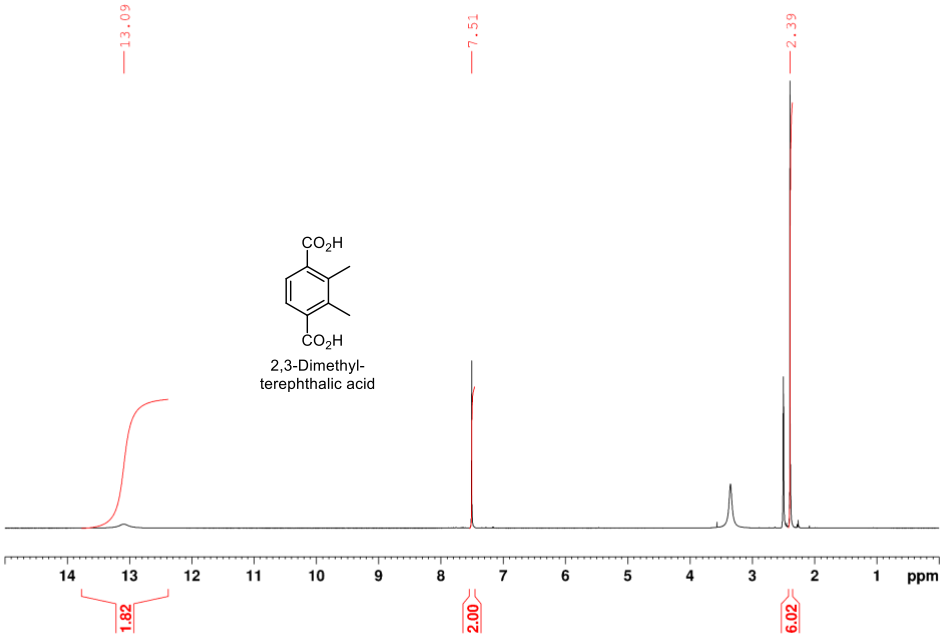

Figure 2.41 ^{1}H NMR spectrum of 2,3-dimethyl-terephthalic acid in *d6*-DMSO.

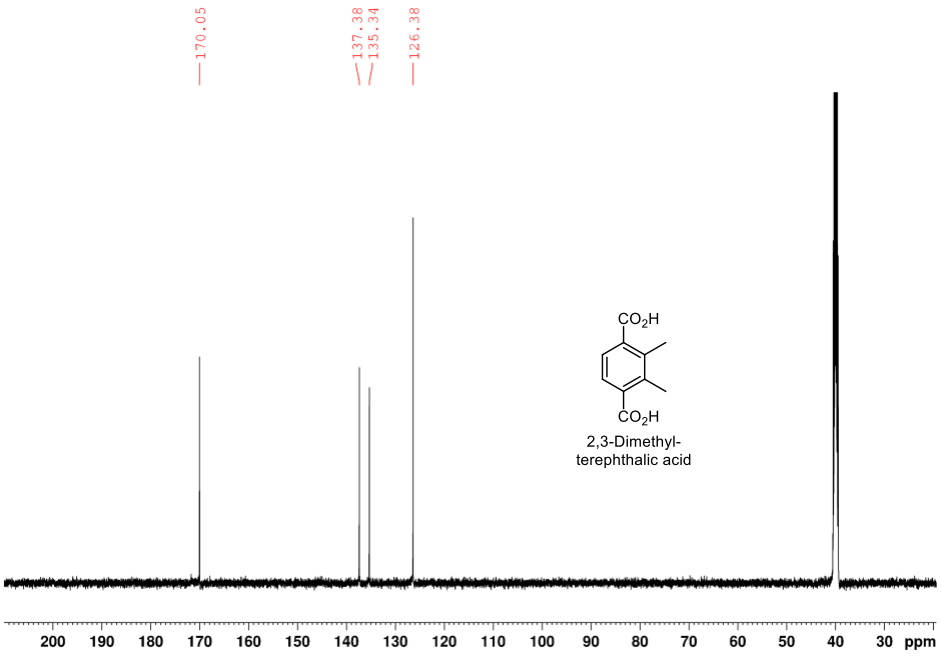

Figure 2.42 ^{13}C NMR spectrum of 2,3-dimethyl-terephthalic acid in *d6*-DMSO.

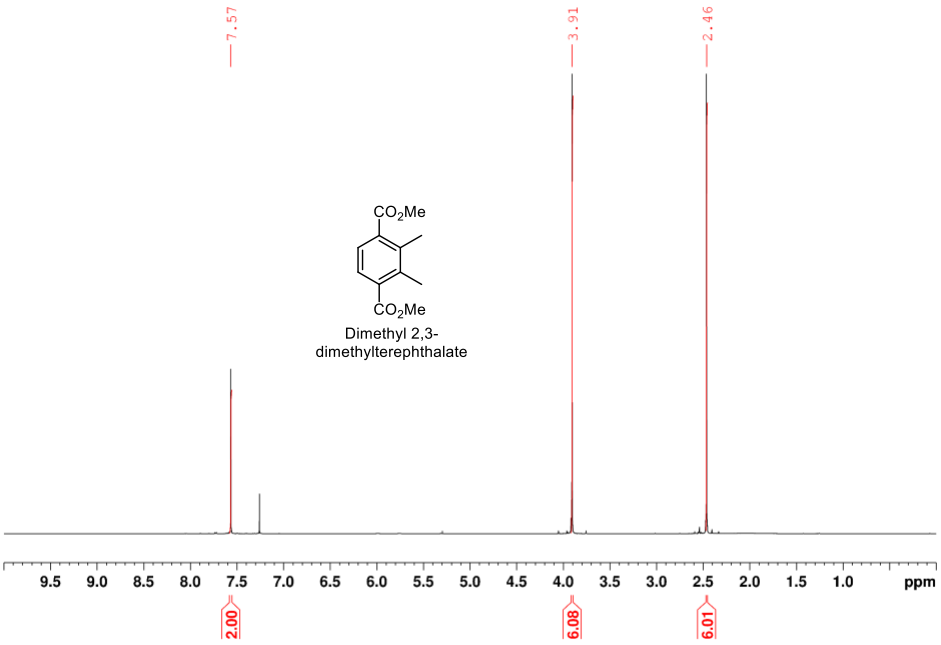

Figure 2.43 ^{1}H NMR spectrum of dimethyl 2,3-dimethylterephthalate in $CDCl_3$.

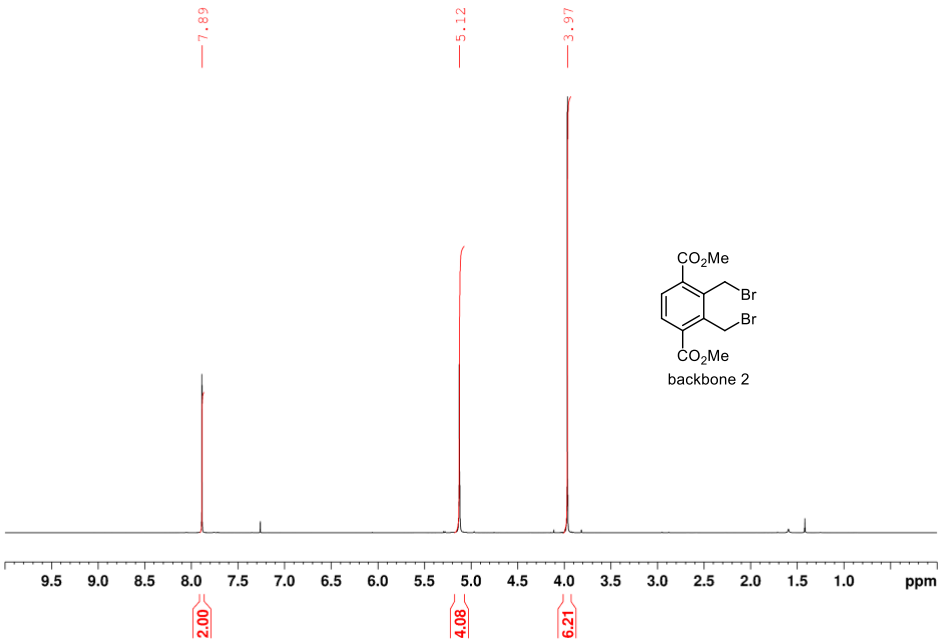

Figure 2.44 ^{1}H NMR spectrum of backbone 2 in $CDCl_3$.

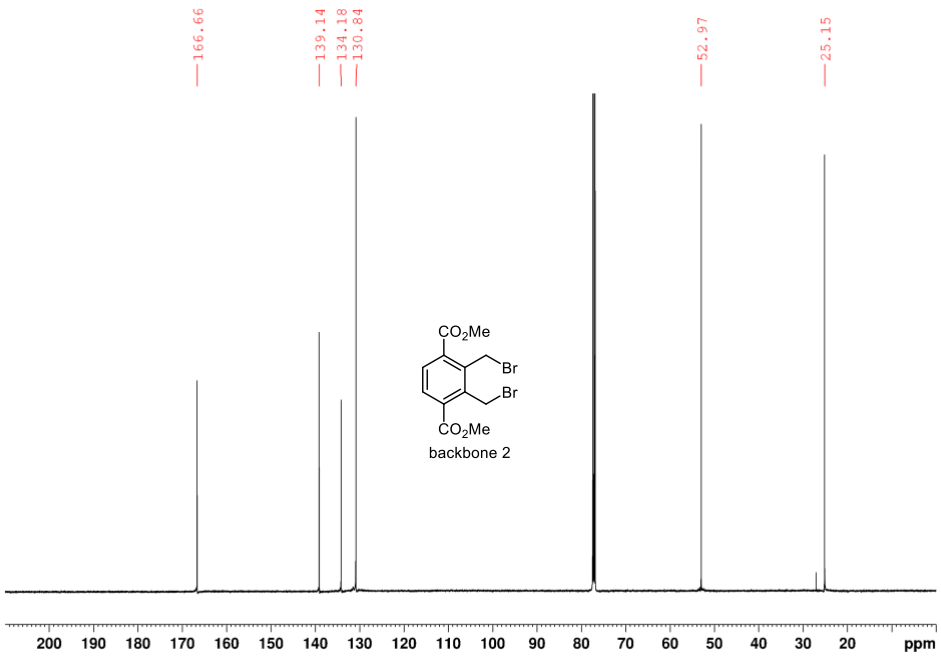

Figure 2.45 ^{13}C NMR spectrum of backbone 2 in $CDCl_3$.

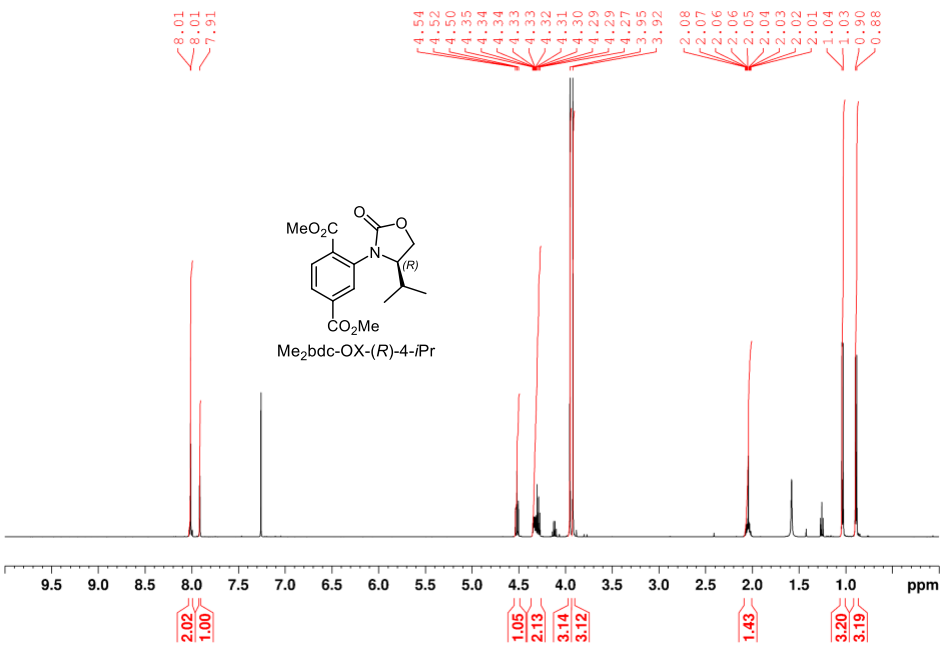

Figure 2.46 ^{1}H NMR spectrum of Me$_2$bdc-OX-(*R*)-4-*i*Pr in CDCl$_3$.

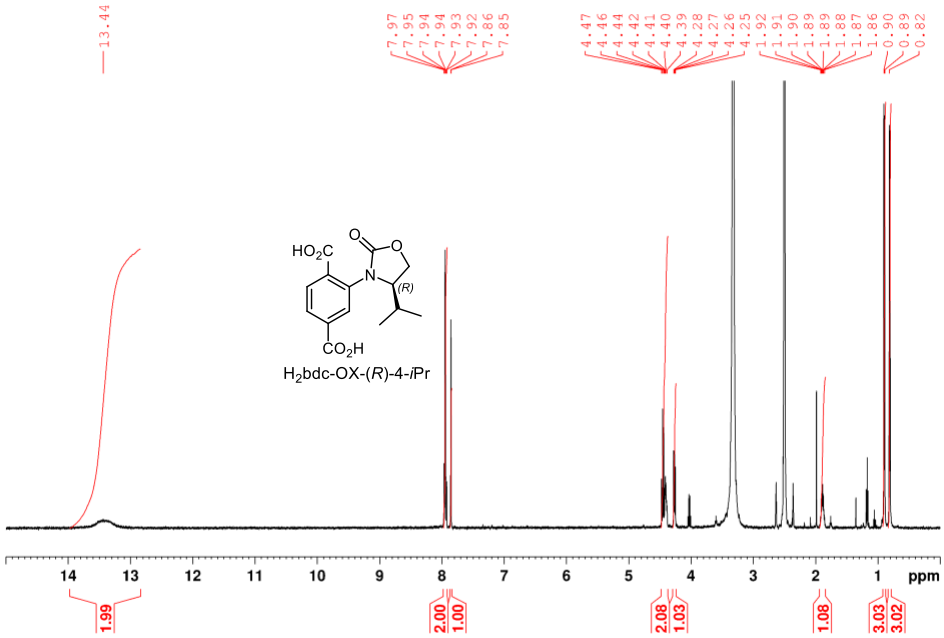

Figure 2.47 ^{1}H NMR spectrum of H$_2$bdc-OX-(*R*)-4-*i*Pr in *d6*-DMSO.

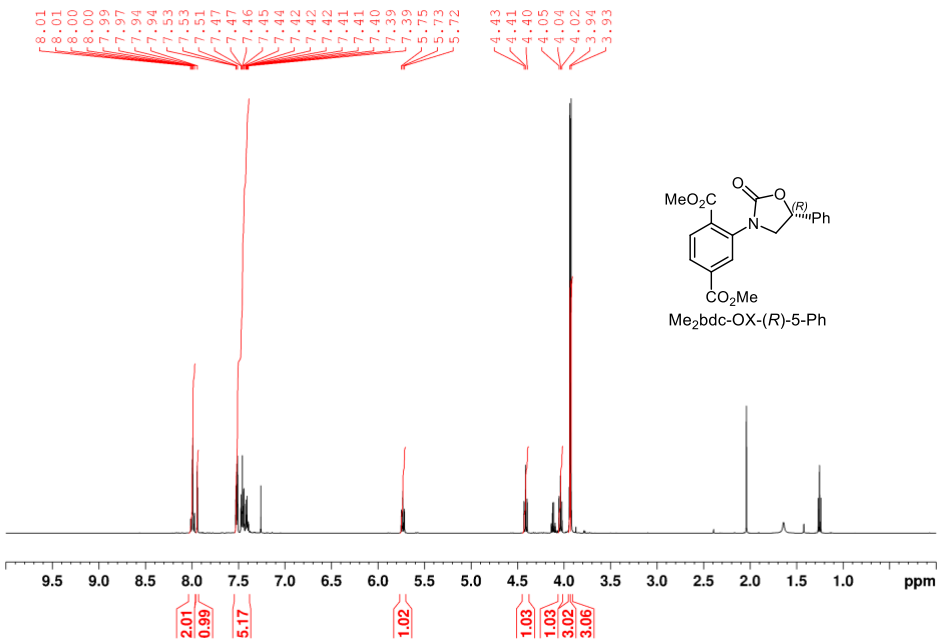

Figure 2.48 ^{1}H NMR spectrum of Me$_2$bdc-OX-(*R*)-5-Ph in CDCl$_3$.

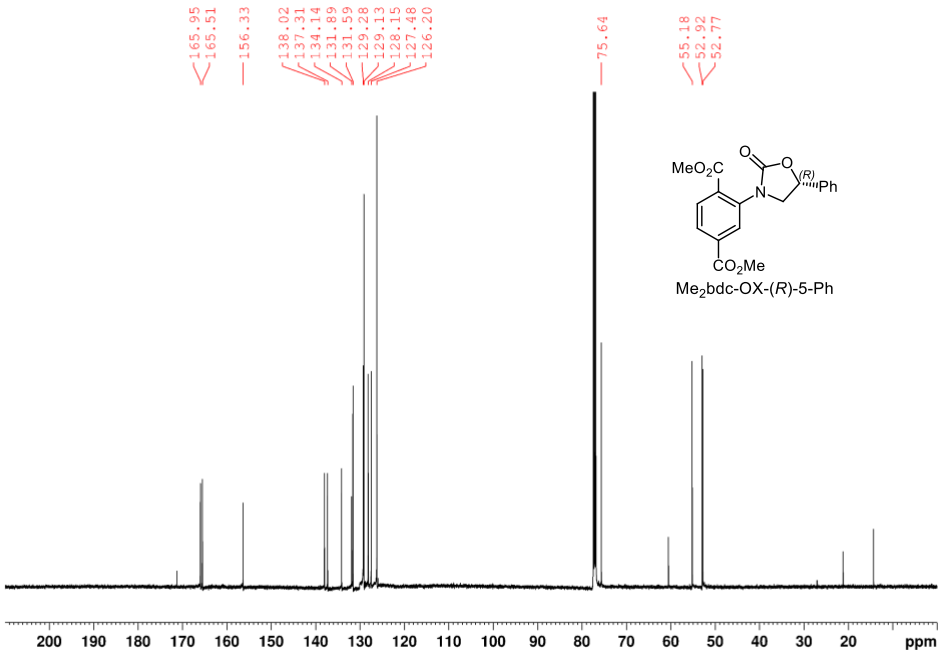

Figure 2.49 ^{13}C NMR spectrum of Me$_2$bdc-OX-(*R*)-5-Ph in CDCl$_3$.

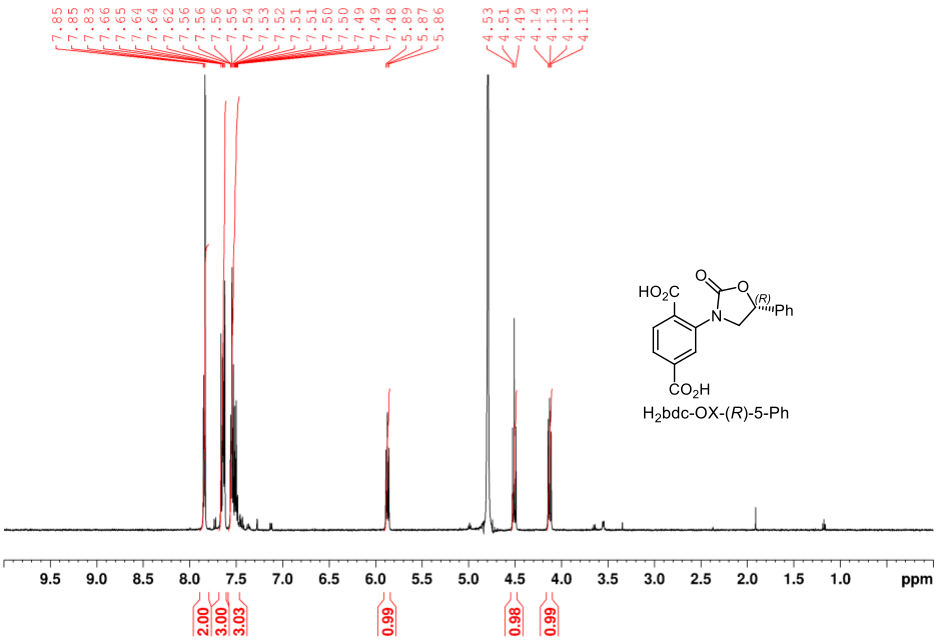

Figure 2.50 ^{1}H NMR spectrum of H$_2$bdc-OX-(*R*)-5-Ph in D$_2$O/NaOD.

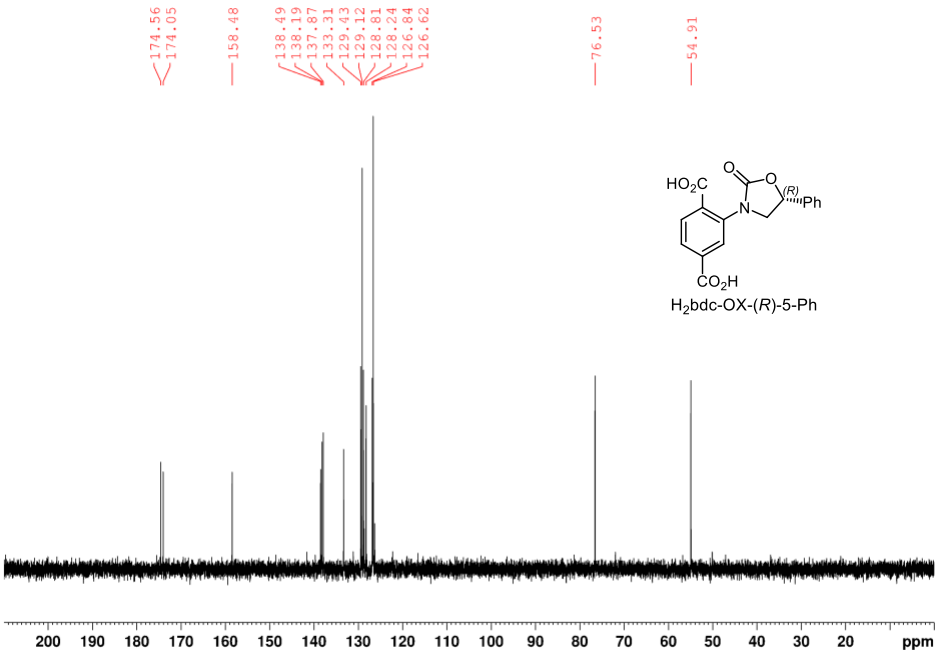

Figure 2.51 ^{13}C NMR spectrum of H$_2$bdc-OX-(*R*)-5-Ph in D$_2$O/NaOD.

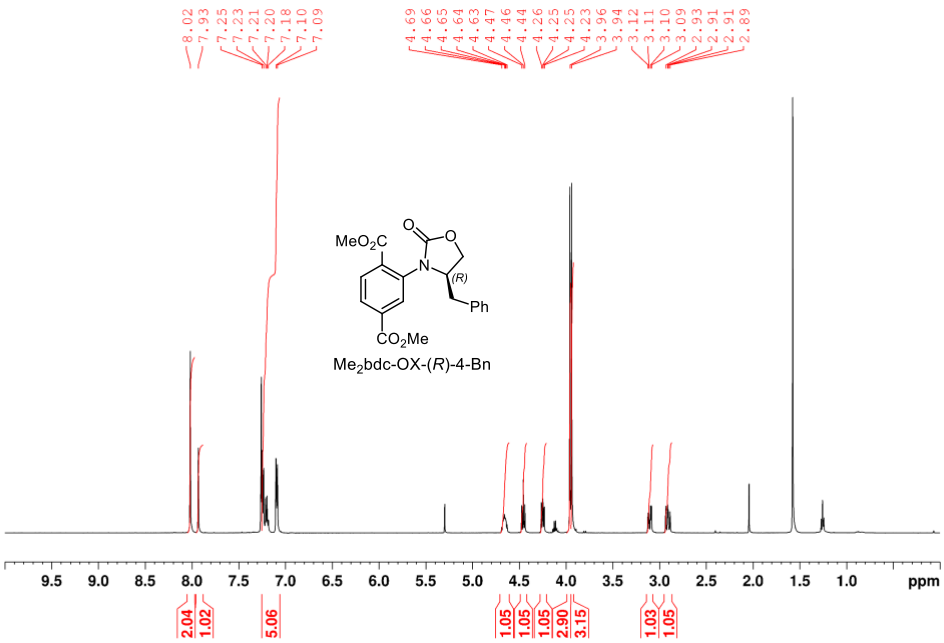

Figure 2.52 ^{1}H NMR spectrum of Me_2bdc-OX-(*R*)-4-Bn in $CDCl_3$.

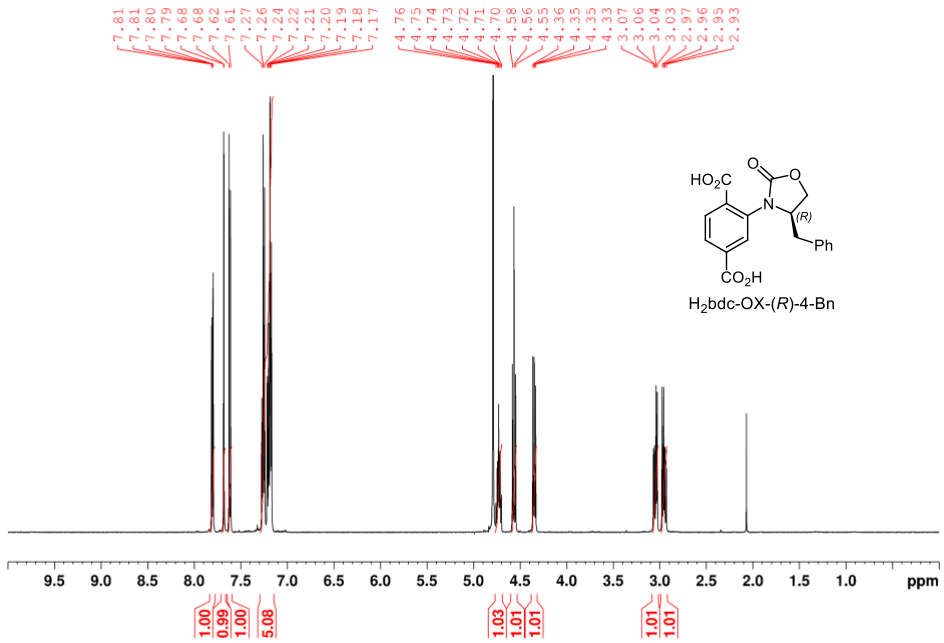

Figure 2.53 ^{1}H NMR spectrum of H_2bdc-OX-(*R*)-4-Bn in D_2O/NaOD.

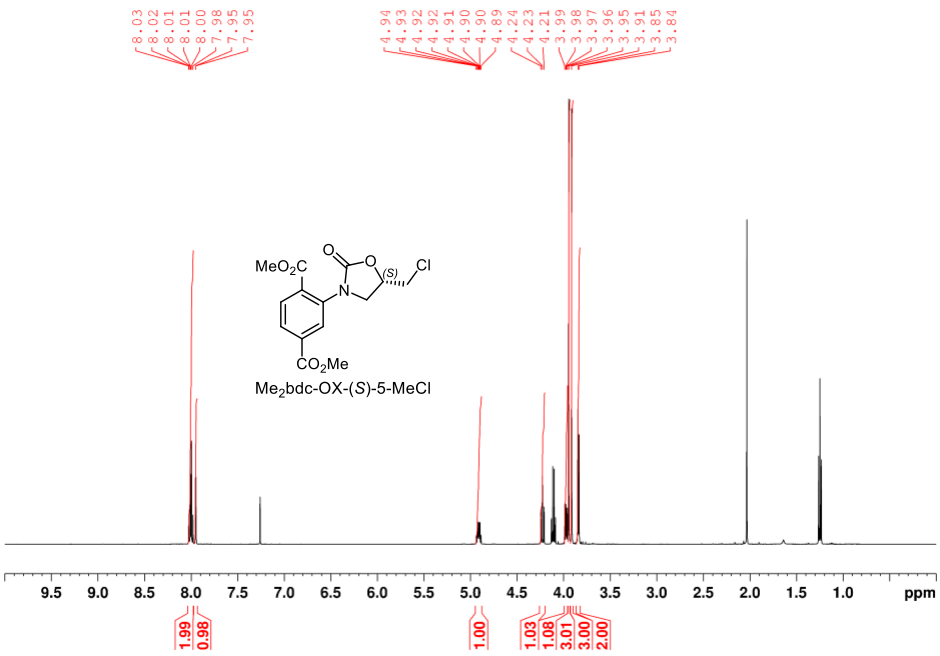

Figure 2.54 ^{1}H NMR spectrum of Me$_2$bdc-OX-(*S*)-5-MeCl in CDCl$_3$.

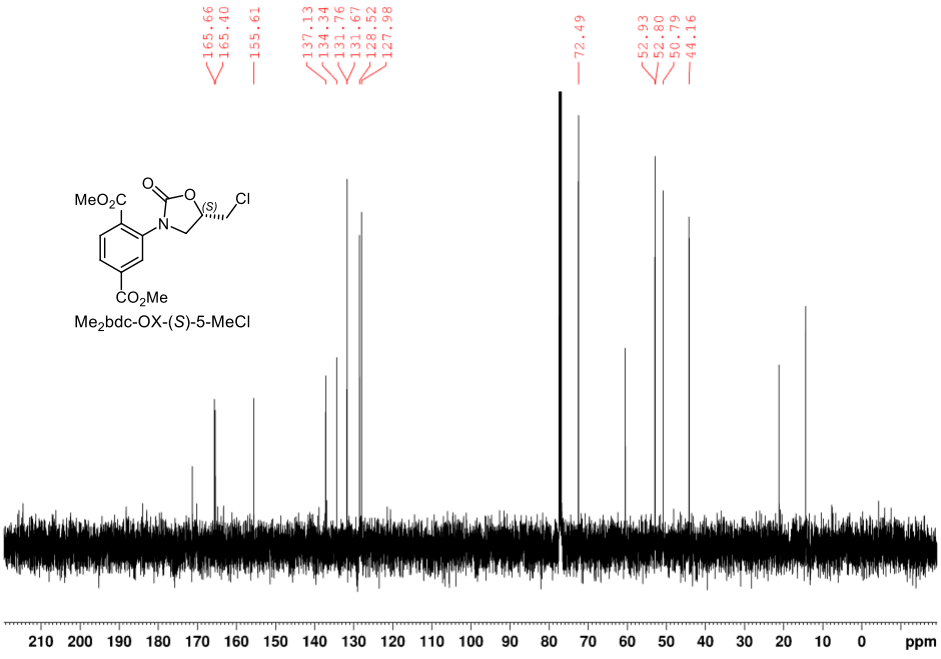

Figure 2.55 ^{13}C NMR spectrum of Me$_2$bdc-OX-(*S*)-5-MeCl in CDCl$_3$.

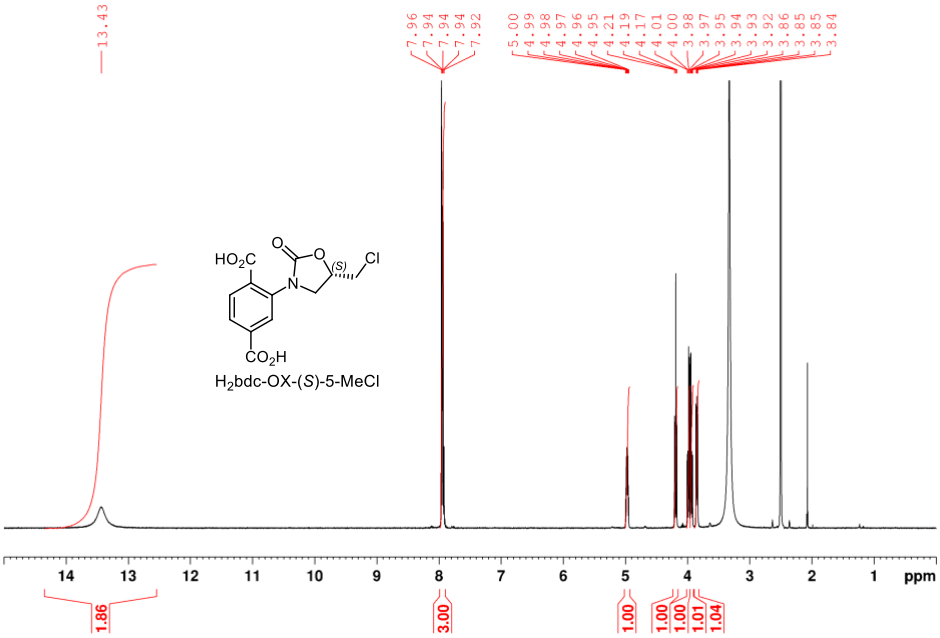

Figure 2.56 ^{1}H NMR spectrum of H2bdc-OX-(*S*)-5-MeCl in *d6*-DMSO.

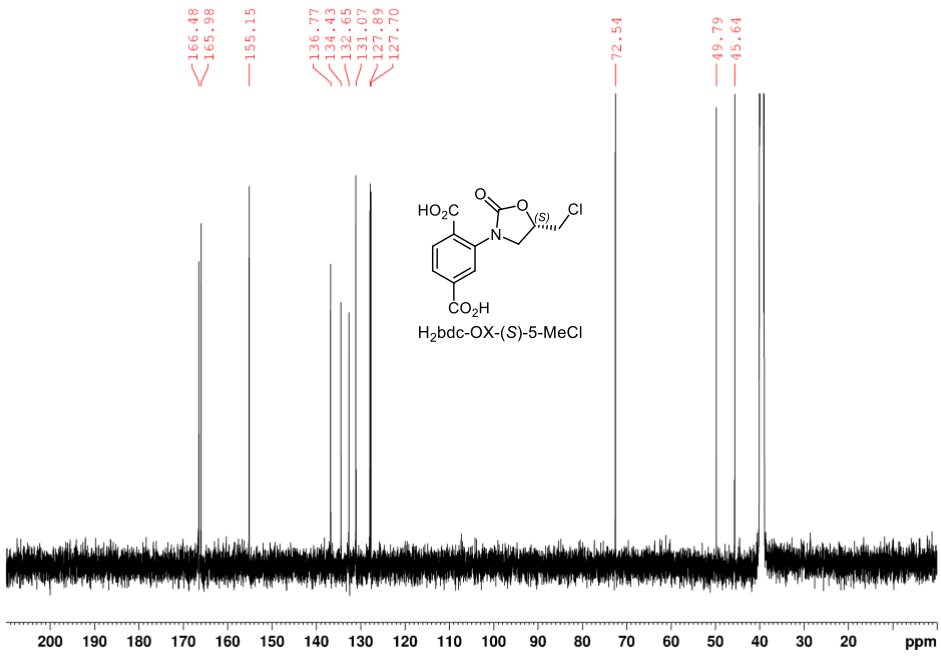

Figure 2.57 ^{13}C NMR spectrum of H2bdc-OX-(*S*)-5-MeCl in *d6*-DMSO.

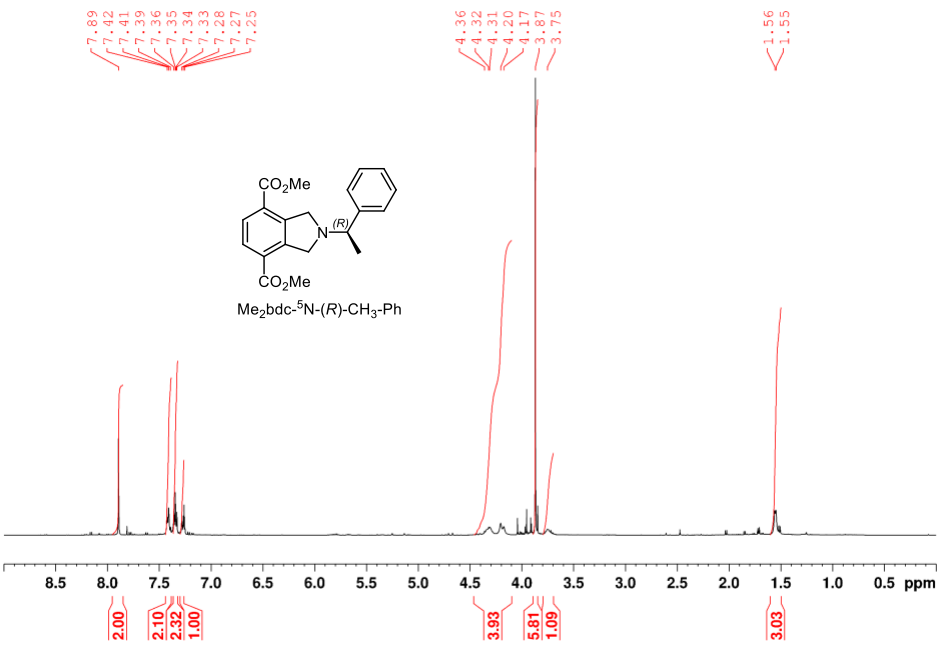

Figure 2.58 ^{1}H NMR spectrum of Me$_2$bdc-^{5}N-(*R*)-CH$_3$-Ph in CDCl$_3$.

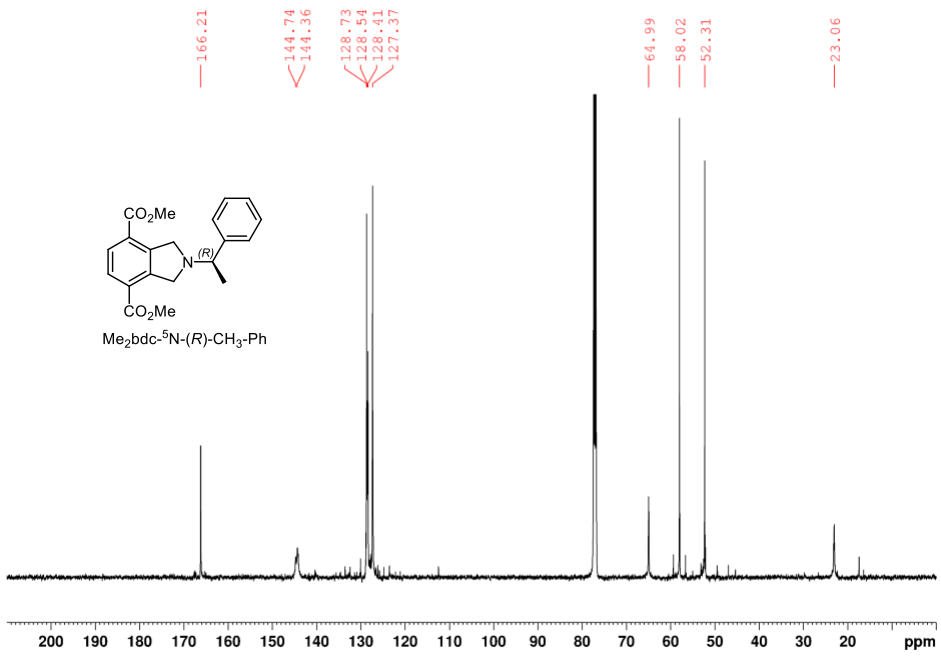

Figure 2.59 ^{13}C NMR spectrum of Me$_2$bdc-^{5}N-(*R*)-CH$_3$-Ph in CDCl$_3$.

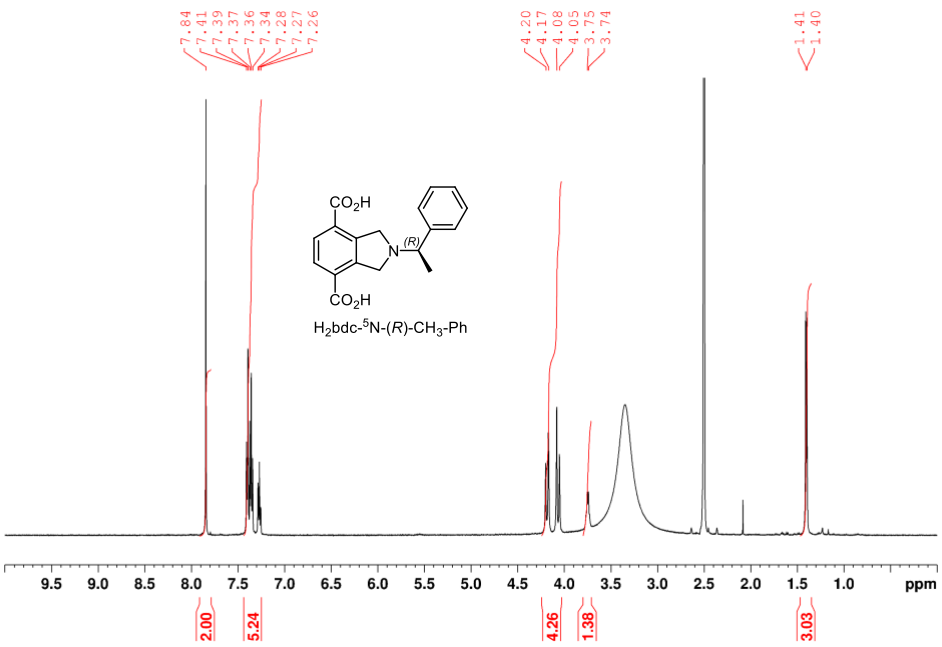

Figure 2.60 ^{1}H NMR spectrum of H2bdc-^{5}N-(*R*)-CH3-Ph in *d6*-DMSO.

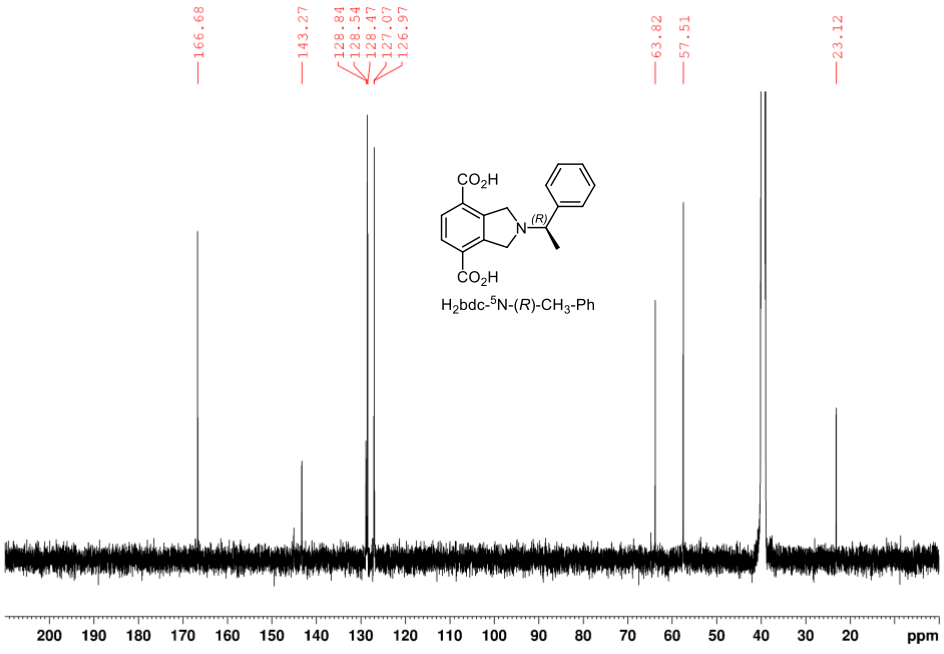

Figure 2.61 ^{13}C NMR spectrum of H2bdc-^{5}N-(*R*)-CH3-Ph in *d6*-DMSO.

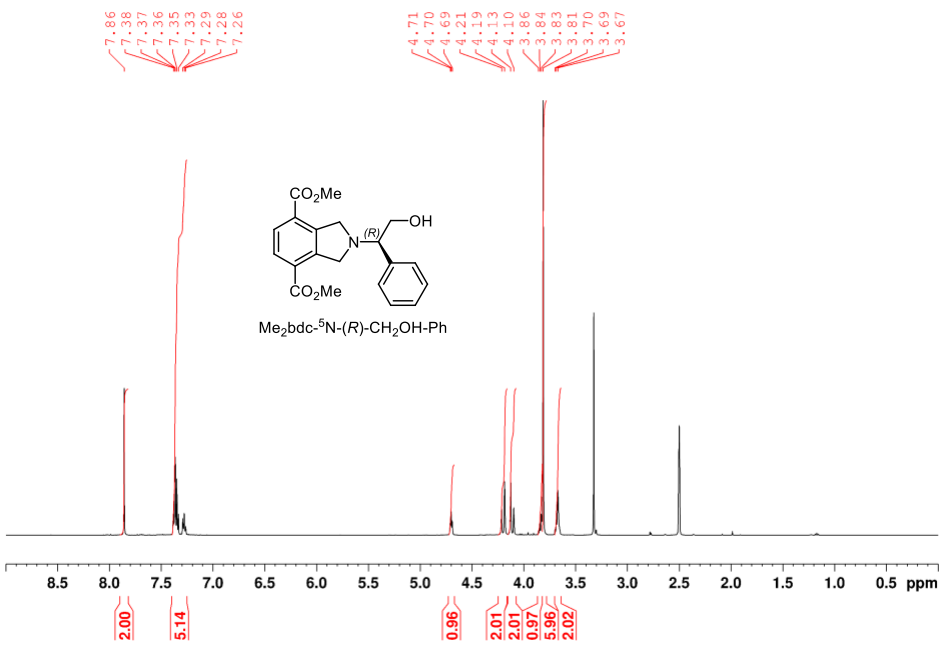

Figure 2.62 ^{1}H NMR spectrum of Me$_2$bdc-^{5}N-(*R*)-CH$_2$OH-Ph in *d6*-DMSO.

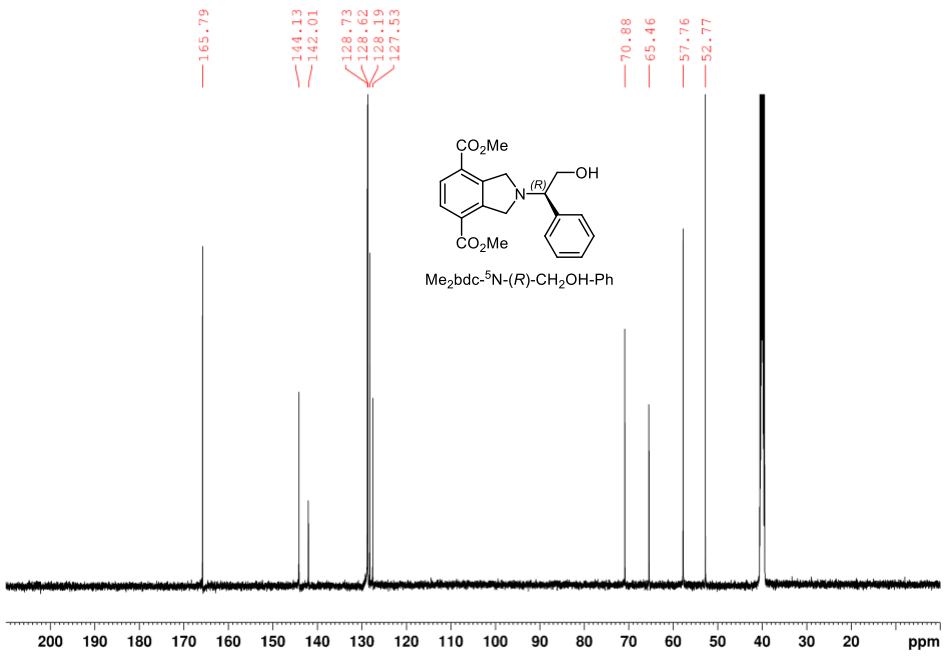

Figure 2.63 ^{13}C NMR spectrum of Me$_2$bdc-^{5}N-(*R*)-CH$_2$OH-Ph in *d6*-DMSO.

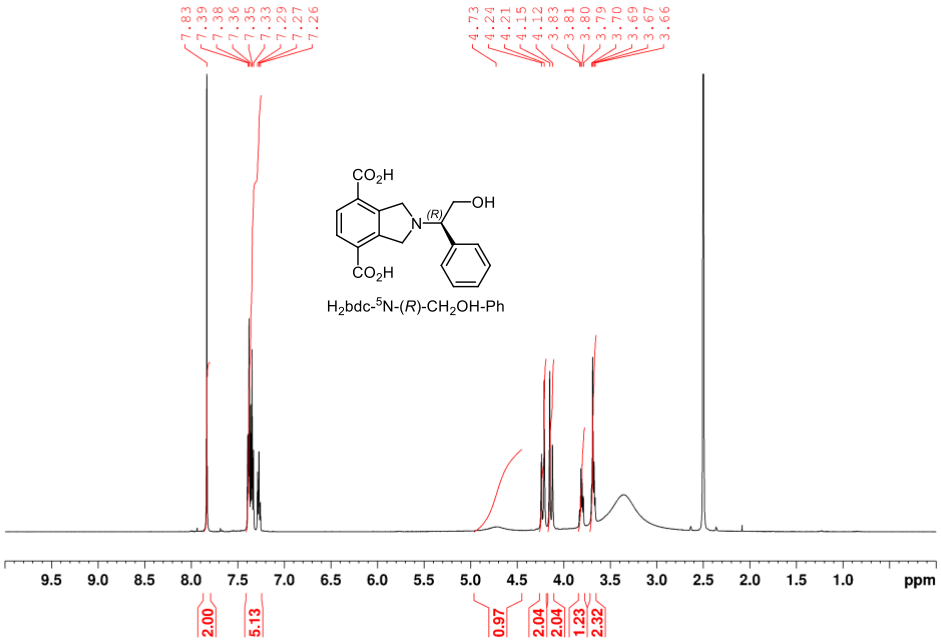

Figure 3.1 ^{1}H NMR spectrum of H_2bdc-^{5}N-(*R*)-CH_2OH-Ph in *d6*-DMSO.

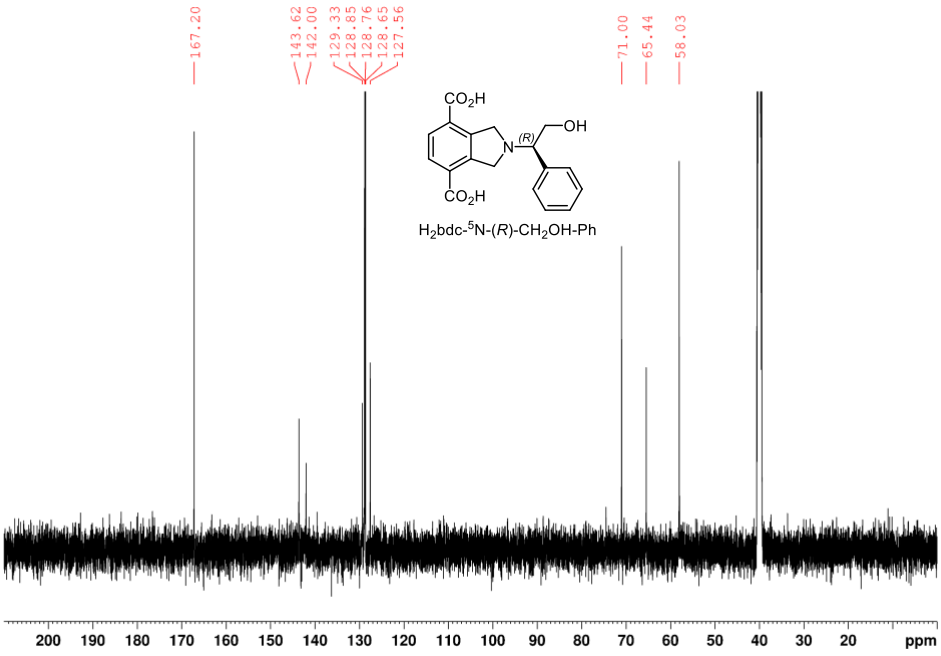

Figure 3.2 ^{13}C NMR spectrum of H_2bdc-^{5}N-(*R*)-CH_2OH-Ph in *d6*-DMSO.

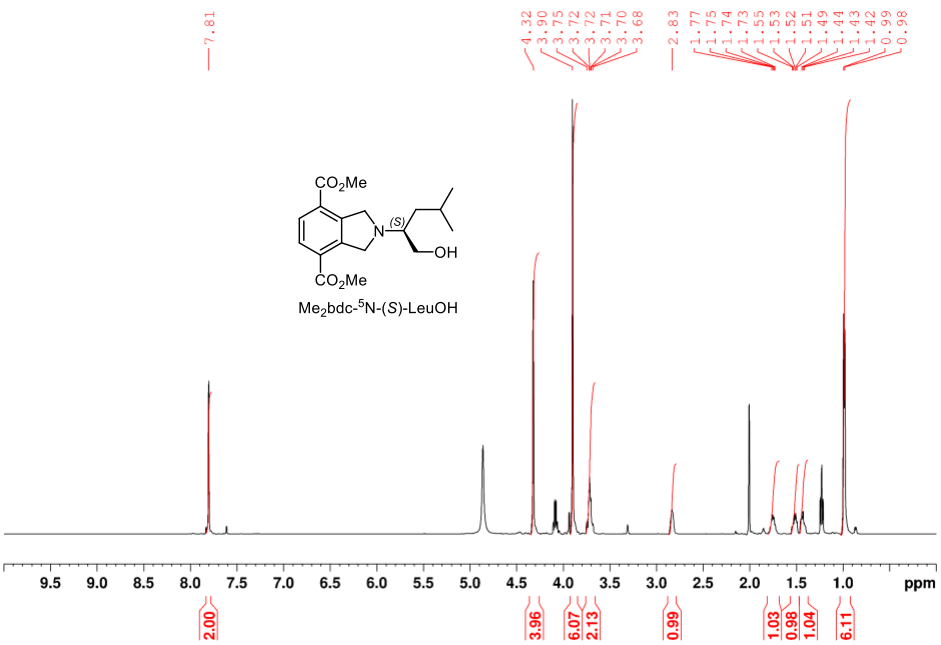

Figure 3.3 ^{1}H NMR spectrum of Me$_2$bdc-^{5}N-(*S*)-LeuOH in MeOD-*d*$_4$.

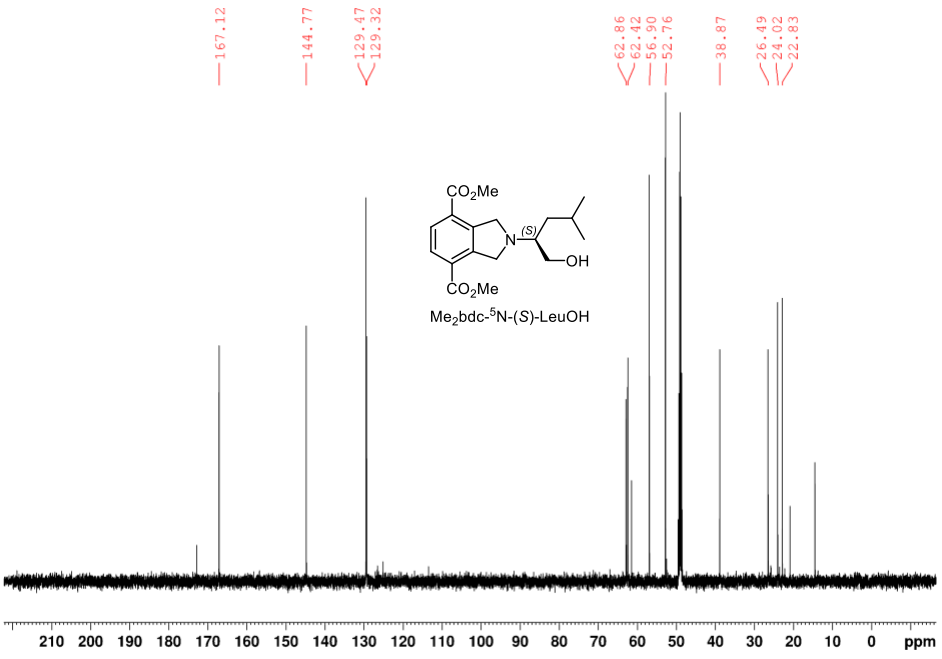

Figure 3.4 ^{13}C NMR spectrum of Me$_2$bdc-^{5}N-(*S*)-LeuOH in MeOD-*d*$_4$.

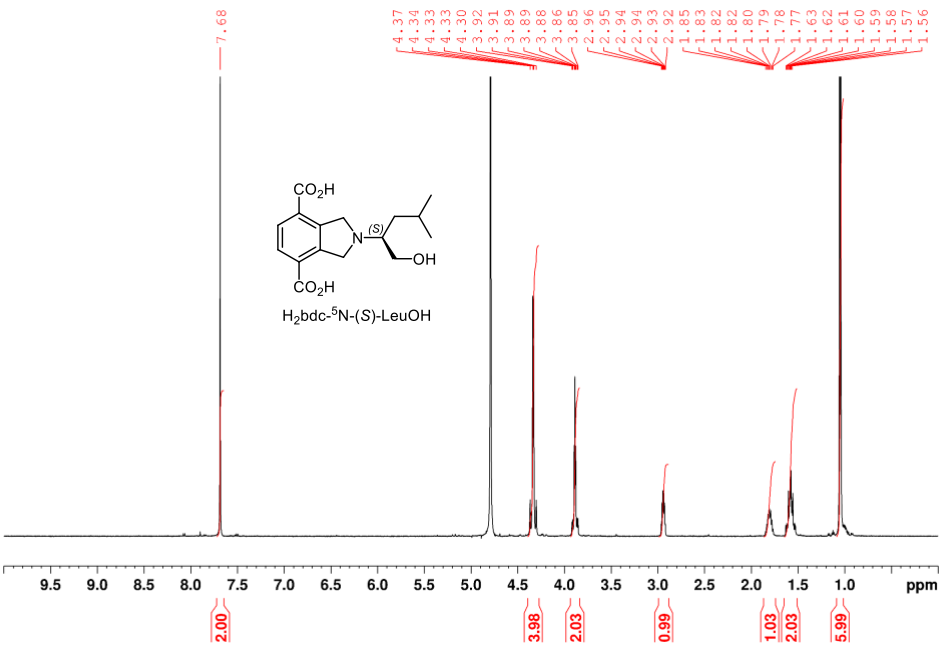

Figure 3.5 ^{1}H NMR spectrum of H2bdc-^{5}N-(*S*)-LeuOH in D2O/NaOD.

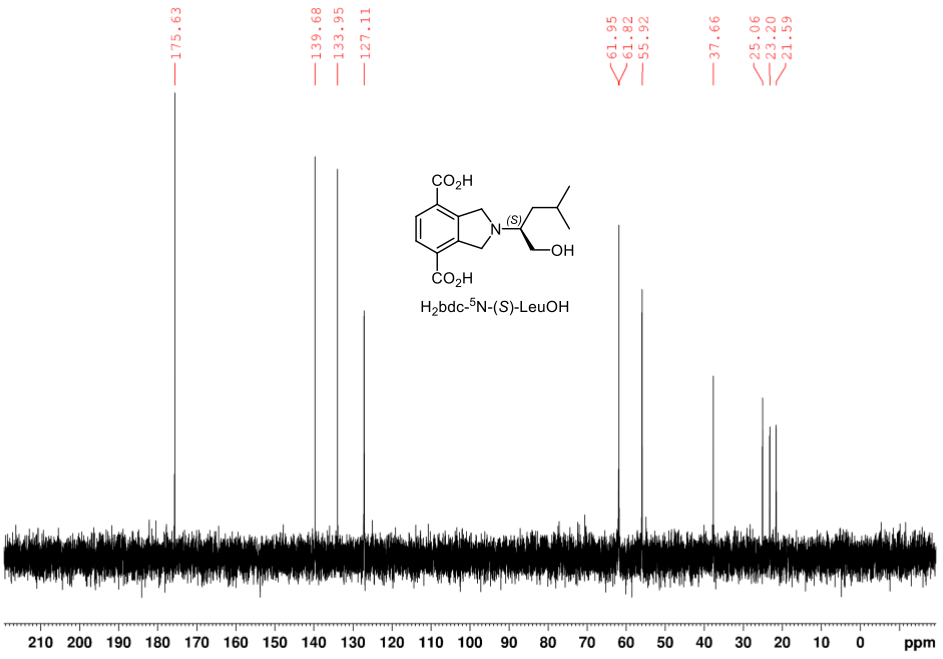

Figure 3.6 ^{13}C NMR spectrum of H2bdc-^{5}N-(*S*)-LeuOH in D2O/NaOD.

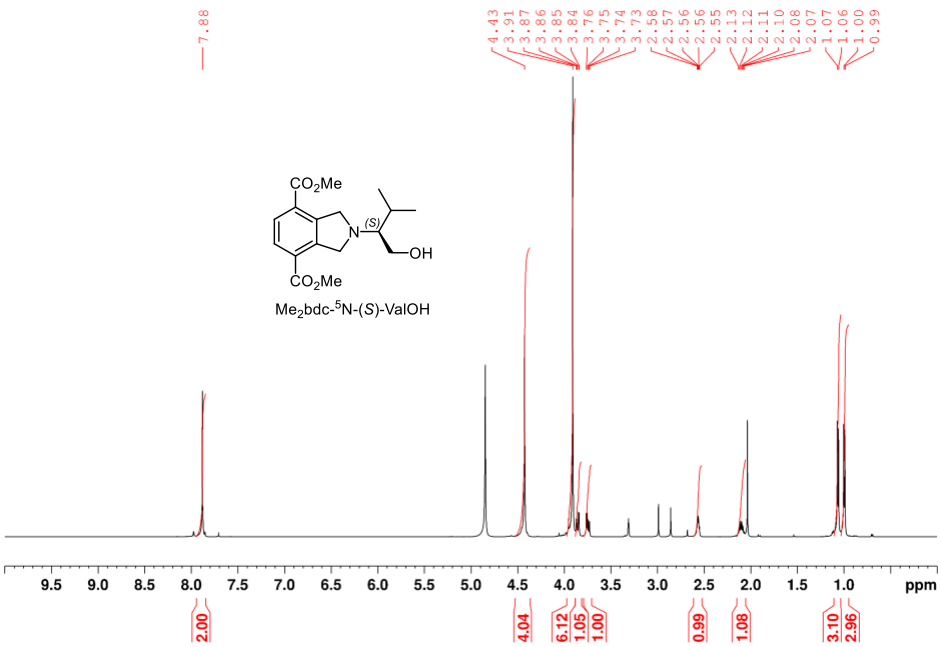

Figure 3.7 ^{1}H NMR spectrum of Me$_2$bdc-^{5}N-(*S*)-ValOH in MeOD-*d*$_4$.

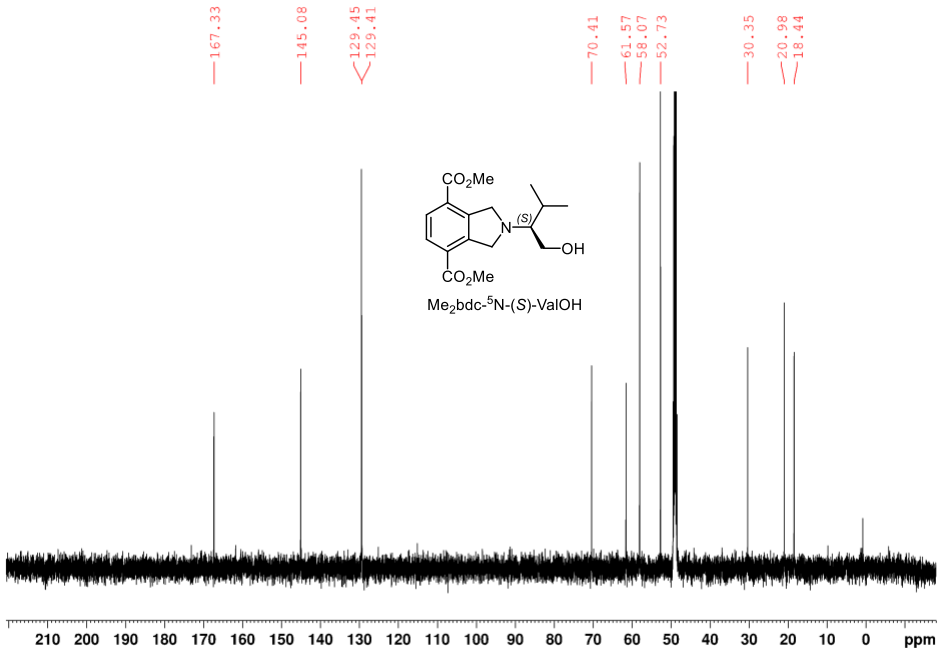

Figure 3.8 ^{13}C NMR spectrum of Me$_2$bdc-^{5}N-(*S*)-ValOH in MeOD-*d*$_4$.

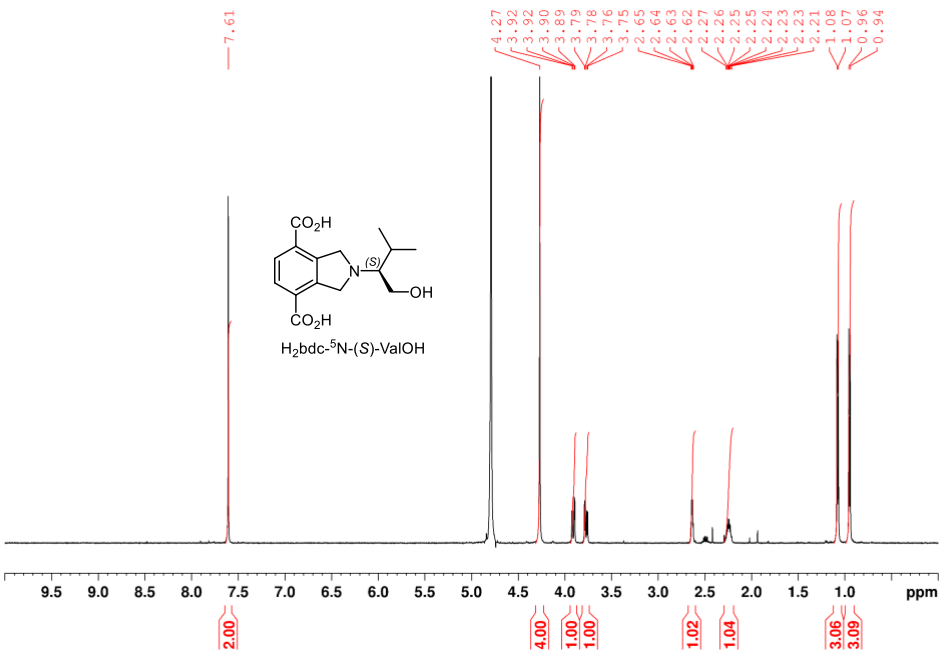

Figure 3.9 ^{1}H NMR spectrum of H$_2$bdc-^{5}N-(*S*)-ValOH in D$_2$O/NaOD.

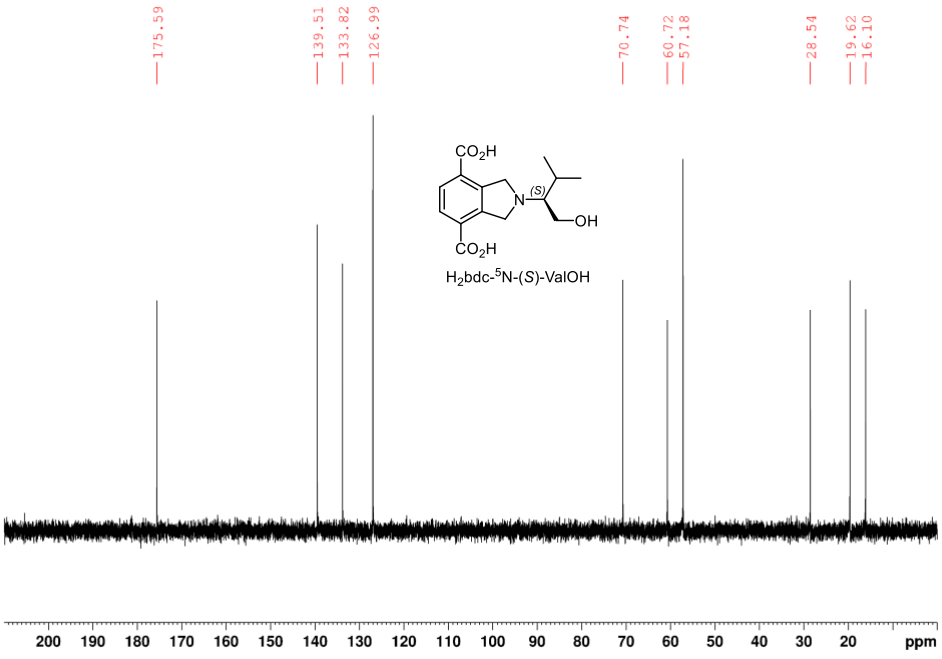

Figure 3.10 ^{13}C NMR spectrum of H$_2$bdc-^{5}N-(*S*)-ValOH in D$_2$O/NaOD.

TGA data

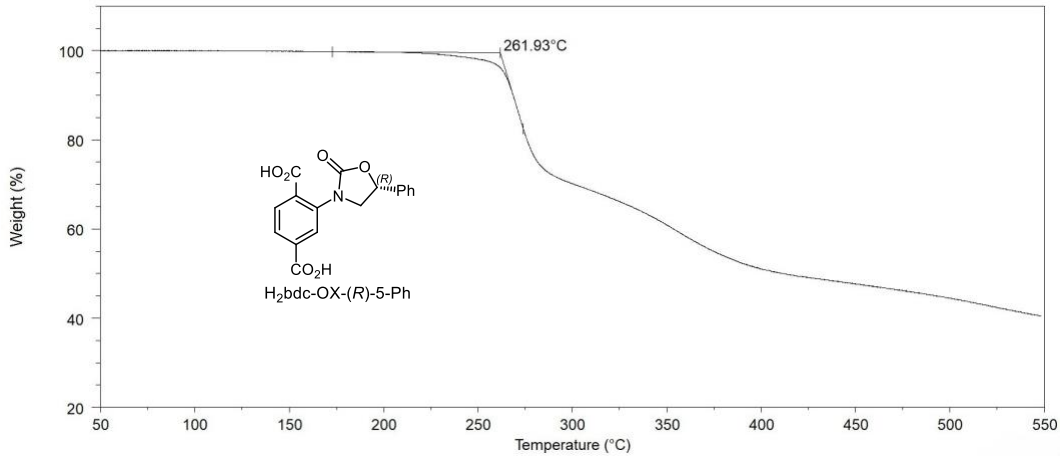

Figure 3.11 TGA measurement of H_2bdc-OX-(*R*)-5-Ph.

Model reactions

Aldol reaction

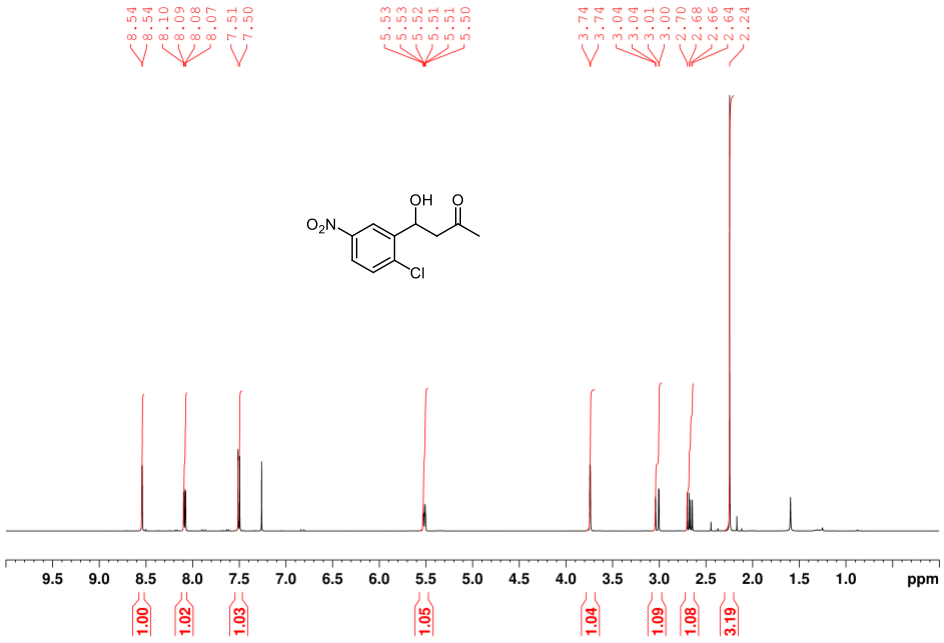

Figure 3.12 ^{1}H NMR spectrum of the aldol product of 2-chloro-5-nitrobenzaldehyde with acetone in $CDCl_3$.

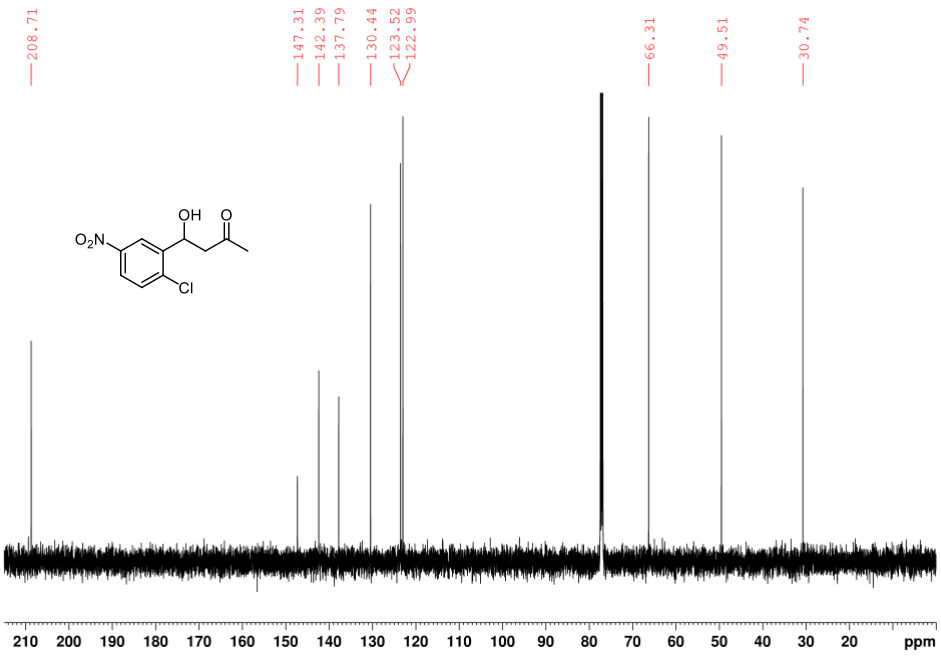

Figure 3.13 ^{13}C NMR spectrum of the aldol product of 2-chloro-5-nitrobenzaldehyde with acetone in $CDCl_3$.

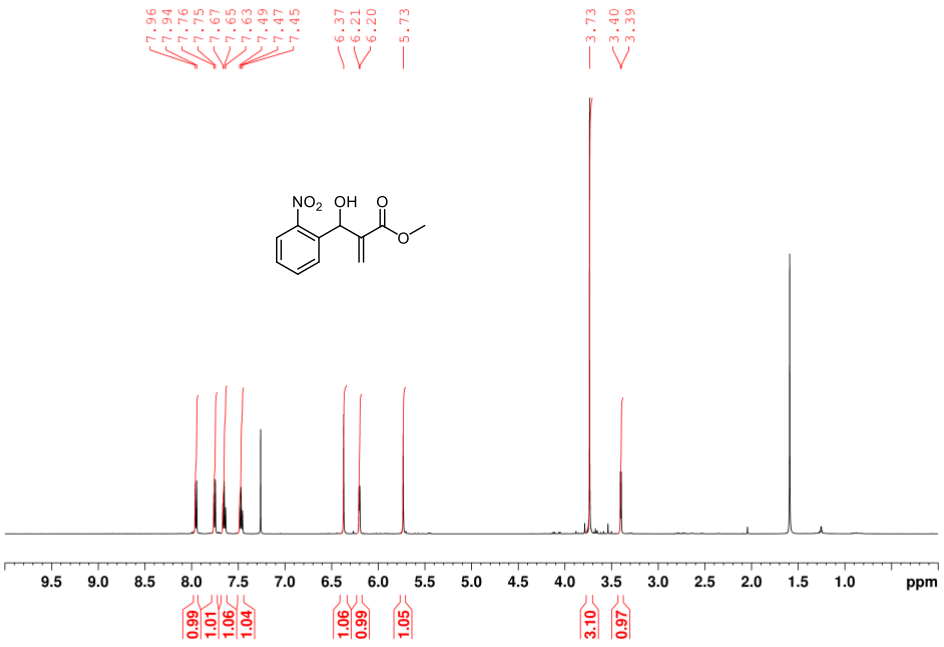

Figure 3.14 ^{1}H NMR spectrum of the Baylis Hillman product of *o*-nitrobenzaldehyde with methylacrylate in $CDCl_3$.

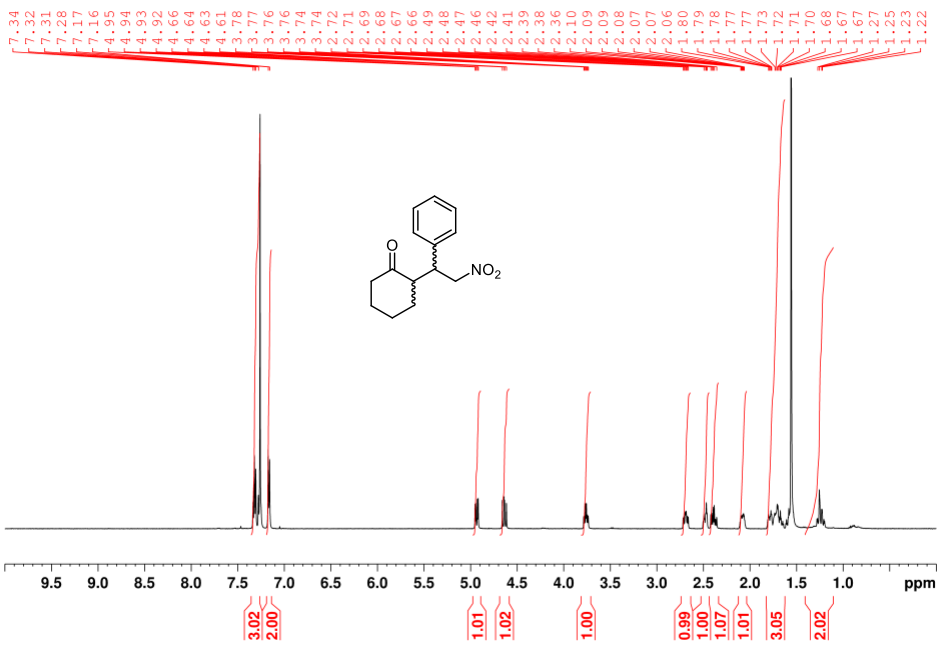

Figure 3.15 ^{1}H NMR spectrum of the Michael_1 product of β-nitrostyrene with cyclohexanone in $CDCl_3$.

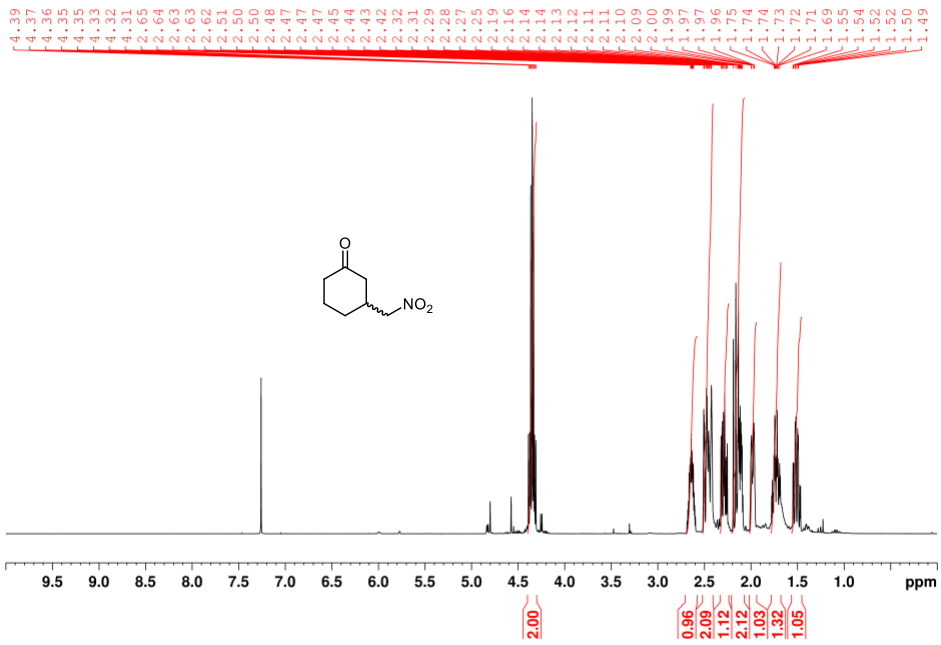

Figure 3.16 ^{1}H NMR spectrum of the Michael_2 product of 2-cyclohexen-1-one with nitromethane in $CDCl_3$.

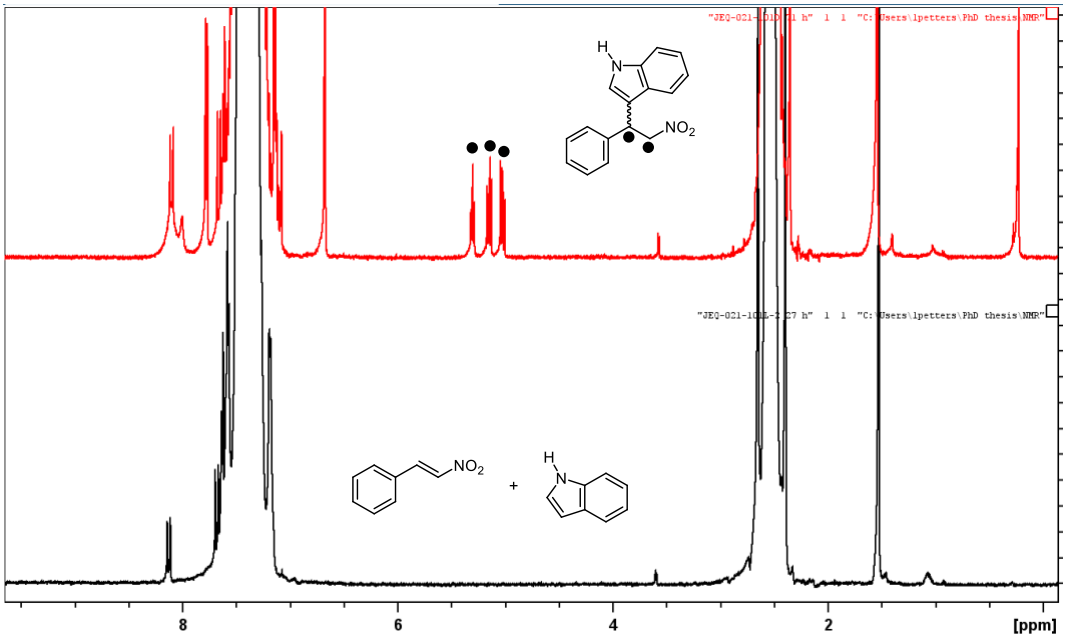

Figure 3.17 ^{1}H NMR spectrum of a stock solution for the Friedel-Crafts reaction containing β-nitrostyrene and indole (black spectra) and a reaction solution where the product signals are highlighted by black spheres. The NMR solvent for both spectra was $CDCl_3$.

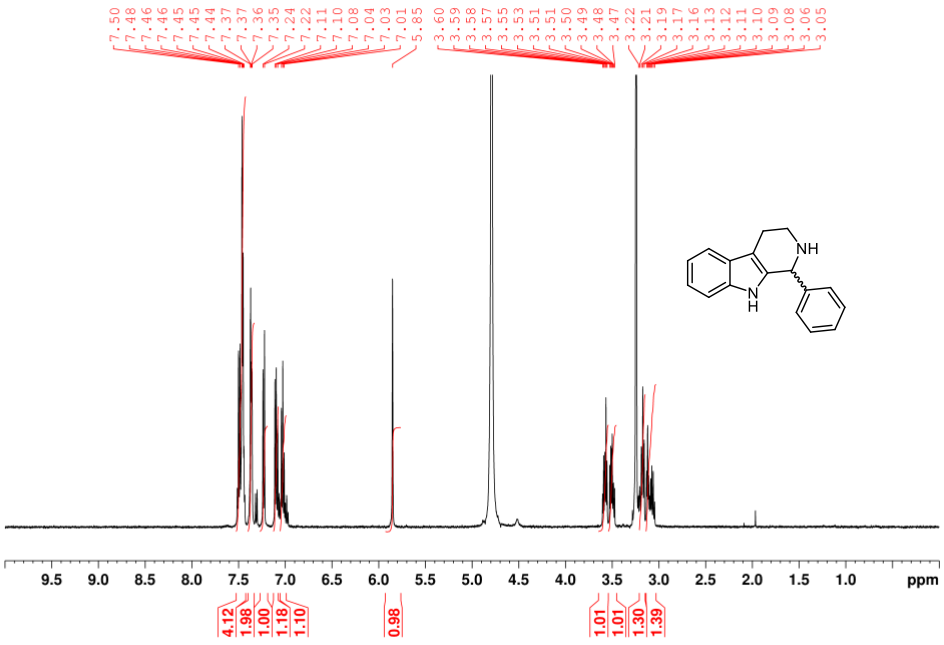

Figure 3.18 ^{1}H NMR spectrum of the Pictet-Spengler product of tryptamine hydrochloride with benzaldehyde in D_2O.

Appendix Chapter 3

Linker synthesis

Truxenes: H_3hheptt

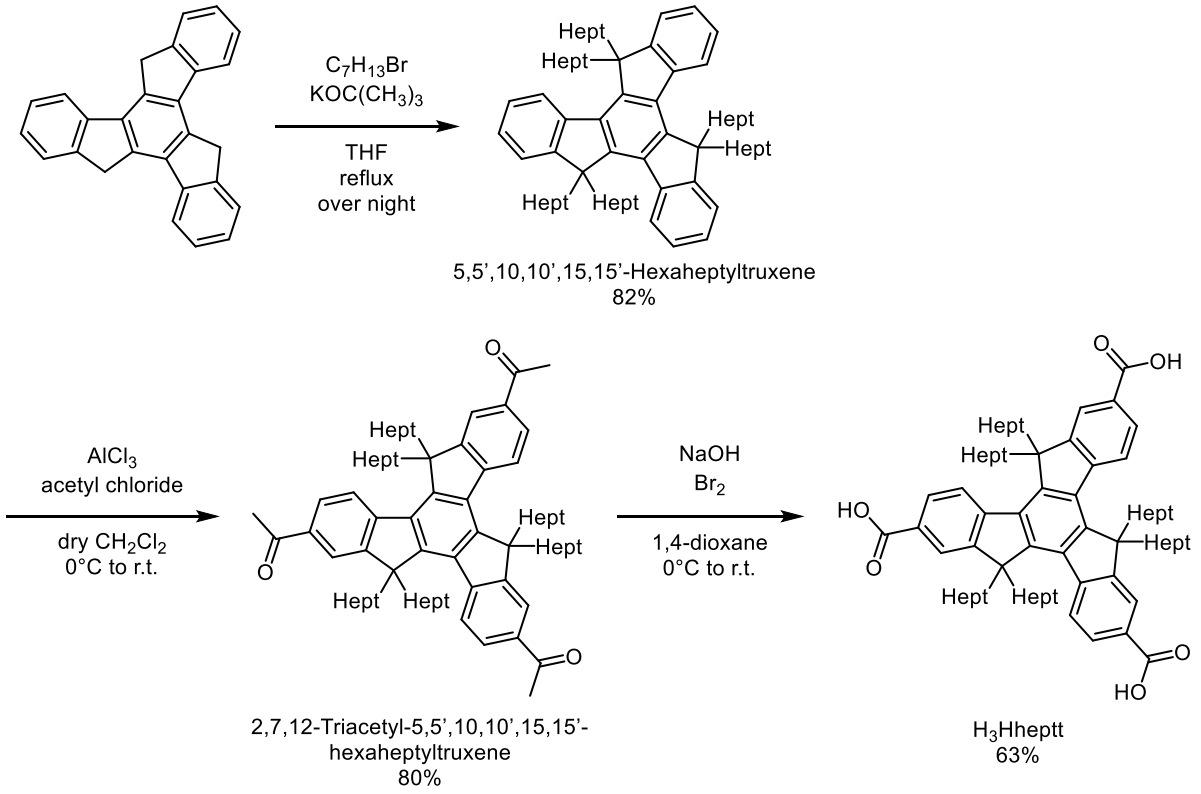

Scheme 3.1 Reaction scheme for the synthesis of H_3hheptt.

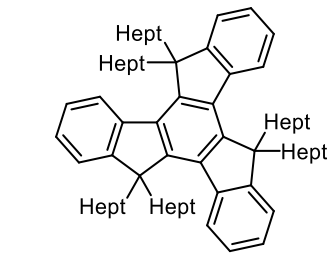

Truxene (3.1 g, 8.9 mmol, 1.0 eq.) and potassium *tert*-butoxide (18.1 g, 161.3 mmol, 18.1 eq.) were suspended in dry THF (150 mL) under an argon atmosphere and cooled to 0 °C. 1-Bromoheptane (19.1 g, 106.9 mmol, 12.0 eq.) was added to the cold solution over 30 minutes. The reaction mixture was allowed to warm up to room temperature and then was refluxed at 80 °C overnight. After cooling to room temperature, the dark green suspension was filtered, and solids were washed with THF (2 × 50 mL). The combined solvent was removed under reduced pressure. The dark green residue was dissolved in CH_2Cl_2 (250 mL) and washed with 0.5 M HCl solution (2 × 100 mL), saturated $NaHCO_3$ solution (2 × 100 mL), water (2 × 100 mL) and dried over $MgSO_4$. Removal of the solvent yielded a green solid that was recrystalised in EtOAc to yield 5,5',10,10',15,15'-Hexaheptyltruxene as a white crystalline solid (6.7 g, 7.3 mmol, 82%).

^{1}H NMR (500 MHz, $CDCl_3$) δ (ppm) 8.37 (d, *J* = 7.3 Hz, 3H), 7.46 (dd, *J* = 7.2, 1.3 Hz, 3H), 7.40-7.34 (m, 6H), 2.99-2.93 (m, 6H), 2.10-2.05 (m, 6H), 1.05-0.98 (m, 12H), 0.93-0.82 (m, 36H), 0.66 (t, *J* = 7.3 Hz, 18H), 0.54-0.48 (m, 12H). ^{13}C NMR (126 MHz, $CDCl_3$) δ (ppm) 153.65, 144.85, 140.36, 138.35, 126.32, 125.94, 124.64, 122.18, 55.57, 36.88, 31.52, 29.77, 28.89, 26.93, 23.92, 22.48, 13.90.

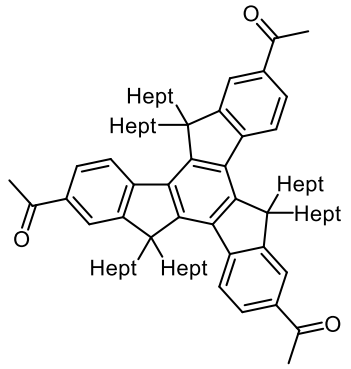

2,7,12-Triacetyl-5,5',10,10',15,15'-hexaheptyltruxene

$AlCl_3$ (3.1 g, 23.4, mmol, 13.5 eq.) was weight into a flame dried round bottom flask under an argon atmosphere. While cooling to 0 °C, acetyl chloride (15 mL) is slowly added. The mixture is stirred at 0 °C for 30 minutes. A solution of 5,5',10,10',15,15'-Hexaheptyltruxene (1.6 g, 1.7 mmol, 1.0 eq.) in dry CH_2Cl_2 (15mL) was then dropwise added to the stirring $AlCl_3$/acetyl chloride solution at 0 °C. The reaction mixture was stirred for 10 min at 0 °C and further stirred at room temperature for 4 hours. The mixture was poured onto an ice/water slurry (100 mL). The resulting suspension was stirred at room temperature overnight. The aqueous suspension was extracted with CH_2Cl_2 and the organic phase was washed with a saturated $NaHCO_3$ solution. The solvent was removed under reduced pressure to afford the crude product as a yellow solid. The crude product was recrystalised in EtOH to yield 2,7,12-Triacetyl-5,5',10,10',15,15'-hexaheptyltruxene as yellow needles (1.5 g, 1.4 mmol, 80%).

^{1}H NMR (500 MHz, $CDCl_3$) δ (ppm) 8.46 (d, *J* = 8.4 Hz, 3H), 8.09 (d, *J* = 1.5 Hz, 3H), 8.04 (dd, *J* = 8.3, 1.4 Hz, 3H), 2.97-2.91 (m, 6H), 2.72 (s, 9H), 2.22-2.16 (m, 6H), 1.02-0.95 (m, 12H), 0.94-0.79 (m, 36H), 0.63 (t, *J* = 7.4 Hz, 18H), 0.52-0.39 (m, 12H). ^{13}C NMR (126 MHz, $CDCl_3$) δ (ppm) 197.94, 153.86, 148.32, 144.47, 137.84, 135.45, 127.53, 124.44, 121.62, 56.13, 36.75, 31.41, 29.58, 28.80, 26.80, 23.96, 22.42, 13.83.

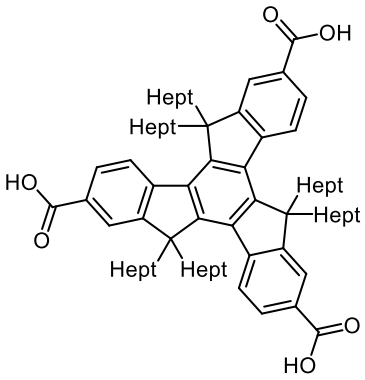

H_3Hheptt

NaOH (5.5 g, 136.8, mmol, 99.1 eq.) was dissolved in water (25 mL) and cooled to 0 °C. Bromine (10.2 g, 63.8 mmol, 46.2 eq.) was added dropwise and the solution was stirred at 0 °C for 15 minutes. 2,7,12-Triacetyl-5,5',10,10',15,15'-hexaheptyltruxene (1.46 g, 1.38, mmol, 1.0 eq.) was dissolved in 1,4-dioxane (20 mL) and added to the NaOH/Br_2 solution at 0 °C. The reaction solution was allowed to warm to room temperature and then was heated to 70 °C for 3 hours. After

cooling to room temperature, a solution of $NH_2OH \cdot HCl$ (5.80 g) in water (10 mL) was added. The organic phase was removed under reduced pressure resulting in the formation of a yellow solid. The reaction mixture was acidified to pH < 1 with 3 M HCl. The solid was isolated by filtration, washed with excess water and dried under vacuum. The solid was suspended and refluxed in a mixture of dichloroethane (20 mL) and THF (1 mL) for 10 minutes. After hot filtration, H_3hheptt was obtained as a white powder (920.1 mg, 865.0 µmol, 63%).

^{1}H NMR (500 MHz, DMSO-*d6*/DCl) δ (ppm) 8.48 (d, *J* = 8.4 Hz, 3H), 8.09 (s, 3H), 8.07 (d, *J* = 8.6 Hz, 3H), 2.99-2.94 (m, 6H), 2.19-2.14 (m, 6H), 0.92-0.75 (m, 48H), 0.54 (t, *J* = 7.3 Hz, 18H), 0.41-0.32 (m, 12H). ^{13}C NMR (126 MHz, DMSO-*d6*/DCl) δ (ppm) 167.37, 153.13, 147.04, 143.49, 137.67, 129.12, 128.25, 124.38, 123.04, 55.59, 35.85, 30.66, 28.89, 28.21, 23.41, 21.92, 13.57. HRMS (FTMS + p ESI Full) calculated for $[M]^-$ $(C_{72}H_{101}O_6)^-$ m/z 1061.7593, found m/z 1061.7631.

Chiral linkers: H_2bdc-^{5}N-(*S*/*R*)-R^1-R^2

All H_2bdc-^{5}N-(*S*/*R*)-R^1-R^2 chiral linkers were synthesised according to the procedures described in **Chapter 2.4.2.4**.

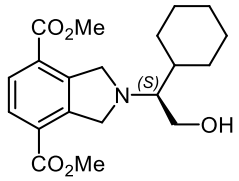

Me_2bdc-^{5}N-(*S*)-CH_2OH-cycloHex

The title compound was prepared from backbone 2 (497.5 mg, 1.3 mmol, 1.0 eq.) and (*S*)-2-amino-2-cyclohexylethanol (422.8 mg, 3.0 mmol, 2.3 eq.) according to general procedure **I**. Me_2bdc-^{5}N-(*S*)-CH_2OH-cycloHex (364.2 mg, 1.0 mmol, 77%) was obtained as a slightly yellow oil after silica-gel column chromatography (cyclohexane/EtOAc gradient from 4/1 to 2/1; 0.5% TEA).

^{1}H NMR (500 MHz, $CDCl_3$) δ (ppm) 7.96 (s, 2H), 4.53 (s, 4H), 3.93 (s, 6H), 3.78 (dd, *J* = 10.5, 4.7 Hz, 1H), 3.49 (dd, *J* = 10.5, 8.7 Hz, 1H), 2.80-2.76 (m, 1H), 1.82-1.66 (m, 6H), 1.23-1.09 (m, 5H).

Me_2bdc-^{5}N-(*S*)-CH_2OH-cycloHex was hydrolysed without further purification or analysis.

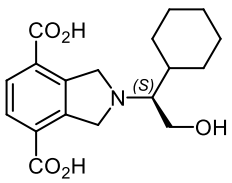

H_2bdc-^{5}N-(*S*)-CH_2OH-cycloHex

The title compound was prepared from Me_2bdc-^{5}N-(*S*)-CH_2OH-cycloHex (364.2 mg, 1.0 mmol, 1.0 eq.) according to the general ester hydrolysis procedure. H_2bdc-^{5}N-(*S*)-CH_2OH-cycloHex precipitated at pH 4.0 as a fine, slightly beige solid (198.1 mg, 594.2 µmol, 59%).

^{1}H NMR (500 MHz, D_2O/NaOD) δ (ppm) 7.59 (s, 2H), 4.25 (s, 4H), 3.92 (dd, *J* = 12.2, 3.6 Hz, 1H), 3.77 (dd, *J* = 12.2, 5.0 Hz, 1H), 2.62-2.59 (m, 1H), 1.90-1.68 (m, 6H), 1.35-1.24 (m, 3H), 1.18-1.07 (m, 2H). ^{13}C NMR (126 MHz, D_2O/NaOD) δ (ppm) 172.73, 136.63, 130.94, 124.07, 67.48, 58.34, 54.21, 36.47, 27.54, 24.40, 23.56, 23.39, 23.31. HRMS (FTMS + p ESI Full) calculated for $[M]^-$ $(C_{18}H_{22}N_1O_5)^-$ m/z 332.1492, found m/z 332.1510.

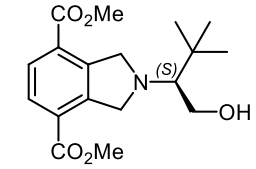

Me_2bdc-^{5}N-(*S*)-CH_2OH-*t*Bu

The title compound was prepared from backbone 2 (541.2 mg, 1.4 mmol, 1.0 eq.) and (2*S*)-2-amino-3,3-dimethyl-1-butanol (250.3 mg, 2.1 mmol, 1.5 eq.) according to general procedure **I**. Me_2bdc-^{5}N-(*S*)-CH_2OH-*t*Bu (250.1 mg, 745.4 µmol, 52%) was obtained as a yellow oil after silica-gel column chromatography (cyclohexane/EtOAc gradient from 4/1 to 2/1; 0.5% TEA).

^{1}H NMR (500 MHz, $CDCl_3$) δ (ppm) 7.93 (s, 2H), 4.74 (d, *J* = 13.4 Hz, 2H), 4.65 (d, *J* = 13.5 Hz, 2H), 3.91 (s, 6H), 3.87-3.83 (m, 2H), 2.86 (dd, *J* = 10.1, 4.3 Hz, 1H), 1.03 (s, 9H).

Me_2bdc-^{5}N-(*S*)-CH_2OH-*t*Bu was used for the next step without further purification or analysis.

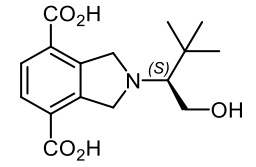

H_2bdc-^{5}N-(*S*)-CH_2OH-*t*Bu

The title compound was prepared from Me_2bdc-^{5}N-(*S*)-CH_2OH-*t*Bu (250.1 mg, 745.4 µmol, 1.0 eq.) according to the general ester hydrolysis procedure. H_2bdc-^{5}N-(*S*)-CH_2OH-*t*Bu precipitated at pH 4.2 as a slightly beige solid and was recrystalised in ethanol to a yield a white solid (82.3 mg, 267.8 µmol, 36%).

^{1}H NMR (500 MHz, D_2O/NaOD) δ (ppm) 7.59 (s, 2H), 4.49-4.42 (m, 4H), 4.03-3.96 (m, 2H), 2.79 (dd, *J* = 7.0, 4.3 Hz, 1H), 1.02 (s, 9H). ^{13}C NMR (126 MHz, D_2O/NaOD) δ (ppm) 175.64, 139.86, 133.76, 126.94, 70.85, 59.59, 57.24, 34.42, 27.55. HRMS (FTMS + p ESI Full) calculated for $[M]^-$ $(C_{16}H_{20}N_1O_5)^-$ m/z 306.1336, found m/z 306.1355.

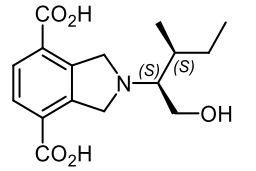

H_2bdc-^{5}N-(*S*)-isoLeuOH

The title compound was prepared from backbone 2 (504.1 mg, 1.3 mmol, 1.0 eq.) and (*S*)-isoleucinol (194.2 mg, 1.7 mmol, 1.3 eq.) according to general procedure **II**. Ester hydrolysis was observed during the standard conditions. H_2bdc-^{5}N-(*S*)-isoLeuOH (280.3 mg, 912.0 µmol, 69%) was obtained as a slightly yellow, powdery solid after acidification of the water phase to pH 4.3.

^{1}H NMR (500 MHz, D_2O/NaOD) δ (ppm) 7.60 (s, 2H), 4.25 (s, 4H), 3.90 (dd, *J* = 12.4, 3.1 Hz, 1H), 3.75 (dd, *J* = 12.3, 5.4 Hz, 1H), 2.75-2.73 (m, 1H), 2.00-1.92 (m, 1H), 1.54-1.44 (m, 1H), 1.41-1.32 (m, 1H), 0.99 (t, *J* = 7.4 Hz, 3H), 0.92 (d, *J* = 7.0 Hz, 3H). ^{13}C NMR (126 MHz, D_2O/NaOD) δ (ppm) 175.59, 139.54, 133.82, 126.98, 69.42, 61.03, 57.29, 35.78, 27.02, 13.37, 11.74. HRMS (FTMS) calculated for $[M]^-$ $(C_{16}H_{20}N_1O_5)^-$ m/z 306.1336, found m/z 306.1342.

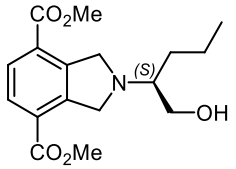

Me_2bdc-^{5}N-(*S*)-CH_2OH-$(CH_2)_2CH_3$

The title compound was prepared from backbone 2 (516.1 mg, 1.4 mmol, 1.0 eq.) and (*S*)-2-aminopentan-1-ol (211.3 mg, 2.1 mmol, 1.5 eq.) according to general procedure **I**. Me_2bdc-^{5}N-(*S*)-CH_2OH-$(CH_2)_2CH_3$ (227.9 mg, 709.1 µmol, 52%) was obtained as a slightly yellow oil after silica-gel column chromatography (cyclohexane/EtOAc gradient from 2/1 to 1/2; 0.5% TEA).

^{1}H NMR (500 MHz, $CDCl_3$) δ (ppm) 7.94 (s, 2H), 4.43-4.37 (m, 4H), 3.93 (s, 6H), 3.74 (dd, *J* = 10.8, 4.2 Hz, 1H), 3.52 (dd, *J* = 11.2, 7.9 Hz, 1H), 2.96-2.90 (m, 1H), 1.66-1.59 (m, 1H), 1.50-1.39 (m, 2H), 1.38-1.30 (m, 1H), 0.96, (t, *J* = 7.2 Hz, 3H). ^{13}C NMR (126 MHz, $CDCl_3$) δ (ppm) 166.25, 143.86, 128.73, 128.49, 62.09, 61.97, 55.03, 52.43, 29.06, 20.19, 14.56. HRMS (FTMS + p ESI Full) calculated for $[M+H]^+$ $(C_{17}H_{24}N_1O_5)^+$ m/z 322.1649, found m/z 322.1640.

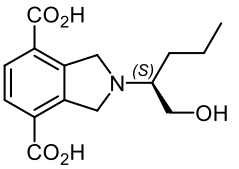

H_2bdc-^{5}N-(*S*)-CH_2OH-$(CH_2)_2CH_3$

The title compound was prepared from Me_2bdc-^{5}N-(*S*)-CH_2OH-$(CH_2)_2CH_3$ (227.9 mg, 709.1 µmol, 1.0 eq.) according to the general ester hydrolysis procedure. Me_2bdc-^{5}N-(*S*)-CH_2OH-$(CH_2)_2CH_3$ precipitated at pH 4.5 as a fine, white solid (124.1 mg, 423.1 µmol, 60%).

^{1}H NMR (500 MHz, D_2O/NaOD) δ (ppm) 7.58 (s, 2H), 4.22 (s, 4H), 3.82 (dd, *J* = 12.0, 4.4 Hz, 1H), 3.77 (dd, *J* = 12.0, 5.0 Hz, 1H), 2.78-2.74 (m, 1H), 1.72-1.57 (m, 2H), 1.47-1.34 (m, 2H), 0.95, (t, *J* = 7.3 Hz, 3H). ^{13}C NMR (126 MHz, D_2O/NaOD) δ (ppm) 175.51, 139.41, 133.82, 127.02, 64.05, 61.46, 56.38, 30.78, 18.32, 13.69. HRMS (FTMS + p ESI Full) calculated for $[M]^-$ $(C_{15}H_{18}N_1O_5)^+$ m/z 292.1179, found m/z 292.1194.

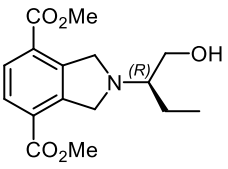

Me_2bdc-^{5}N-(*R*)-CH_2OH-CH_2CH_3

The title compound was prepared from backbone 2 (514.5 mg, 1.4 mmol, 1.0 eq.) and (*R*)-2-aminobutan-1-ol (163.0 mg, 1.8 mmol, 1.4 eq.) according to general procedure **I**. Me_2bdc-^{5}N-(*R*)-CH_2OH-CH_2CH_3 (264.8 mg, 861.6 µmol, 64%) was obtained

as a slightly yellow oil after silica-gel column chromatography (EtOAc/methanol gradient from 1/0 to 9.5/0.5; 0.5% TEA).

^{1}H NMR (500 MHz, MeOD-*d*$_4$) δ (ppm) 7.82 (s, 2H), 4.30 (s, 4H), 3.90 (s, 6H), 3.75 (d, *J* = 4.7 Hz, 2H), 2.63-2.59 (m, 1H), 1.78-1.71 (m, 1H), 1.70-1.62 (m, 1H), 1.01 (t, *J* = 7.4 Hz, 3H). ^{13}C NMR (126 MHz, MeOD-*d*$_4$) δ (ppm) 167.16, 144.67, 129.55, 129.38, 66.82, 62.09, 57.63, 52.76, 22.60, 10.69 HRMS (FTMS + p ESI Full) calculated for $[M+H]^+$ $(C_{16}H_{21}N_1O_5)^+$ m/z 308.1492, found m/z 308.1489.

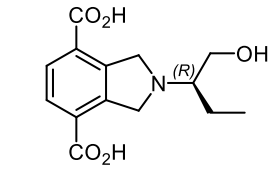

H_2bdc-^{5}N-(*R*)-CH_2OH-CH_2CH_3

The title compound was prepared from Me_2bdc-^{5}N-(*R*)-CH_2OH-CH_2CH_3 (264.8 mg, 861.6 µmol, 1.0 eq.) according to the general ester hydrolysis procedure. H_2bdc-^{5}N-(*R*)-CH_2OH-CH_2CH_3 precipitated at pH 4.0 as a white solid (185.3 mg, 662.4 µmol, 77%).

^{1}H NMR (500 MHz, D_2O/NaOD) δ (ppm) 7.58 (s, 2H), 4.21 (s, 4H), 3.84 (dd, *J* = 11.9, 4.3 Hz, 1H), 3.76 (dd, *J* = 11.9, 5.4 Hz, 1H), 2.71-2.67 (m, 1H), 1.83-1.75 (m, 1H), 1.71-1.62 (m, 1H), 0.96 (t, *J* = 7.5 Hz, 3H). ^{13}C NMR (176 MHz, D_2O/NaOD) δ (ppm) 175.54, 139.35, 133.80, 126.99, 65.55, 60.72, 56.51, 21.29, 8.87. HRMS (FTMS + p ESI Full) calculated for $[M]^-$ $(C_{14}H_{16}N_1O_5)^-$ m/z 278.1023, found m/z 278.1034.

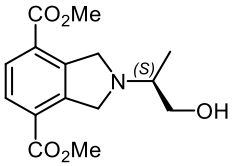

Me_2bdc-^{5}N-(*S*)-AlaOH

The title compound was prepared from backbone 2 (544.8 mg, 1.4 mmol, 1.0 eq.) and (*S*)-alaninol (140.0 mg, 1.9 mmol, 1.3 eq.) according to general procedure **I**. Me_2bdc-^{5}N-(*S*)-AlaOH (265.6 mg, 908.5 µmol, 63%) was obtained as a slightly yellow oil after silica-gel column chromatography (EtOAc/methanol gradient from 1/0 to 9.5/0.5; 0.5% TEA).

^{1}H NMR (500 MHz, $CDCl_3$) δ (ppm) 7.94 (s, 2H), 4.40-4.32 (m, 4H), 3.93 (s, 6H), 3.70 (dd, *J* = 10.8, 4.3 Hz, 1H), 3.52 (dd, *J* = 10.8, 7.0 Hz, 1H), 3.10-3.04 (m, 1H), 2.58 (brs, 1H), 1.16 (d, *J* = 6.6 Hz, 3H). ^{13}C NMR (126 MHz, $CDCl_3$) δ (ppm) 166.25, 143.92, 128.72, 128.47, 64.61, 57.97, 55.15, 52.43, 12.47. HRMS (FTMS + p ESI Full) calculated for $[M+H]^+$ $(C_{15}H_{20}N_1O_5)^+$ m/z 294.1336, found m/z 294.1330.

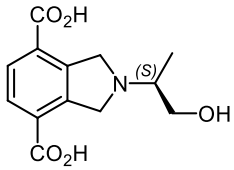

H_2bdc-^{5}N-(*S*)-AlaOH

The title compound was prepared from Me_2bdc-^{5}N-(*S*)-AlaOH (265.6 mg, 908.5 µmol, 1.0 eq.) according to the general ester hydrolysis procedure. H_2bdc-^{5}N-(*S*)-AlaOH precipitated at pH 4.0 as a white solid (155.3 mg, 585.4 µmol, 65%).

^{1}H NMR (500 MHz, D_2O/NaOD) δ (ppm) 7.58 (s, 2H), 4.20 (s, 4H), 3.84 (dd, *J* = 11.4, 4.0 Hz, 1H), 3.57 (dd, *J* = 11.3, 6.6 Hz, 1H), 2.90-2.84 (m, 1H), 1.23 (d, *J* = 6.5 Hz, 3H). ^{13}C NMR (126 MHz, D_2O/NaOD) δ (ppm) 175.51, 139.32, 133.84, 127.03, 64.34, 59.84, 56.39, 15.04. HRMS (FTMS + p ESI Full) calculated for $[M]^-$ $(C_{13}H_{14}N_1O_5)^-$ m/z 264.0866, found m/z 264.0869.

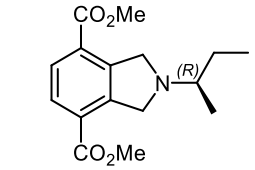

Me_2bdc-^{5}N-(*R*)-CH_2CH_3-CH_3

The title compound was prepared from backbone 2 (207.6 mg, 546.3 µmol, 1.0 eq.) and (*S*)-2-aminobutane (50.5 mg, 690.5 µmol, 1.3 eq.) according to general procedure **I**. Me_2bdc-^{5}N-(*R*)-CH_2CH_3-CH_3 (102.8 mg, 352.8 µmol, 65%) was obtained as a slightly yellow oil after silica-gel column chromatography (EtOAc; 0.5% TEA).

^{1}H NMR (500 MHz, MeOD-*d*$_4$) δ (ppm) 7.87 (s, 2H), 4.24 (s, 4H), 3.91 (s, 6H), 2.65-2.58 (m, 1H), 1.84-1.77 (m, 1H), 1.48-1.39 (m, 1H), 1.18 (d, *J* = 6.4 Hz, 3H) 0.98 (t, *J* = 7.4 Hz, 3H). ^{13}C NMR (500 MHz, MeOD-*d*$_4$) δ (ppm) 165.76, 143.16, 128.36, 128.15, 60.23, 56.55, 51.43, 27.13, 15.92, 9.13. HRMS (FTMS + p ESI Full) calculated for $[M+H]^+$ $(C_{16}H_{22}N_1O_4)^+$ m/z 292.1543, found m/z 292.1538.

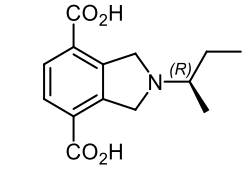

H_2bdc-^{5}N-(*R*)-CH_2CH_3-CH_3

The title compound was prepared from Me_2bdc-^{5}N-(*R*)-CH_2CH_3-CH_3 (102.8 mg, 352.8 µmol, 1.0 eq.) according to the general ester hydrolysis procedure. H_2bdc-^{5}N-(*R*)-CH_2CH_3-CH_3 precipitated at pH 4.3 as a white solid (74.8 mg, 284.1 µmol, 81%).

^{1}H NMR (500 MHz, D_2O/NaOD) δ (ppm) 7.56 (s, 2H), 4.14 (s, 4H), 2.69-2.65 (m, 1H), 1.80-1.75 (m, 1H), 1.43-1.39 (m, 1H), 1.16 (d, *J* = 6.4 Hz, 3H) 0.92 (t, *J* = 7.4 Hz, 3H). ^{13}C NMR (500 MHz, D_2O/NaOD) δ (ppm) 175.62, 139.66, 133.82, 126.91, 60.14, 56.40, 26.82, 16.44, 9.26. HRMS (FTMS + p ESI Full) calculated for $[M]^-$ $(C_{14}H_{16}N_1O_4)^-$ m/z 262.1074, found m/z 262.1085.

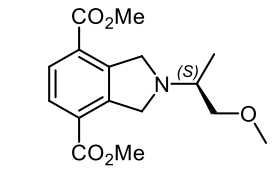

Me_2bdc-^{5}N-(*S*)-CH_2OCH_3-CH_3

The title compound was prepared from backbone 2 (513.2 mg, 1.4 mmol, 1.0 eq.) and (*S*)-1-methoxy-2-propylamine (160.0 mg, 1.8 mmol, 1.3 eq.) according to general procedure **I**. Me_2bdc-^{5}N-(*S*)-CH_2OCH_3-CH_3 (273.5 mg, 889.9 µmol, 66%) was obtained as a slightly yellow oil after silica-gel column chromatography (cyclohexane/EtOAc gradient from 2/1 to 1/1; 0.5% TEA).

^{1}H NMR (500 MHz, DMSO-*d6*) δ (ppm) 7.87 (s, 2H), 4.23 (s, 4H), 3.86 (s, 6H), 3.51 (dd, *J* = 9.5, 5.1 Hz, 1H), 3.31-3.30 (m, 1H), 3.29 (s, 3H), 2.96-2.91 (m, 1H), 1.12 (d, *J* = 6.4 Hz, 3H). ^{13}C NMR (126 MHz, DMSO-*d6*) δ (ppm) 165.39, 143.64, 128.15, 127.77, 75.54, 58.31, 56.24, 55.89, 52.29, 15.41 HRMS (FTMS + p ESI Full) calculated for $[M+H]^+$ $(C_{16}H_{22}N_1O_4)^+$ m/z 292.1543, found m/z 292.1538.

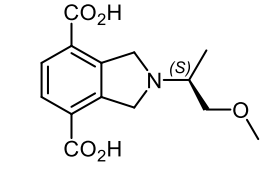

H_2bdc-^{5}N-(*S*)-CH_2OCH_3-CH_3

The title compound was prepared from Me_2bdc-^{5}N-(*S*)-CH_2OCH_3-CH_3 (273.5 mg, 889.9 µmol, 1.0 eq.) according to the general ester hydrolysis procedure. H_2bdc-^{5}N-(*S*)-CH_2OCH_3-CH_3 precipitated at pH 4.5 as a white solid (210.0 mg, 751.9 µmol, 85%).

^{1}H NMR (500 MHz, D_2O/NaOD) δ (ppm) 7.60 (s, 2H), 4.21 (s, 4H), 3.69 (dd, *J* = 10.2, 4.8 Hz, 1H), 3.49 (dd, *J* = 10.2, 6.0 Hz, 1H), 3.41 (s, 3H), 3.04-2.98 (m, 1H), 1.22 (d, *J* = 6.5 Hz, 3H). ^{13}C NMR (500 MHz, D_2O/NaOD) δ (ppm) 175.49, 139.43, 133.86, 127.07, 75.38, 58.35, 57.36, 56.26, 15.18. HRMS (FTMS + p ESI Full) calculated for $[M]^-$ $(C_{14}H_{16}N_1O_5)^-$ m/z 278.1023, found m/z 278.1028.

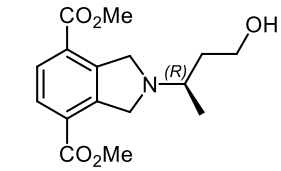

Me_2bdc-^{5}N-(*R*)-$(CH_2)_2OH$-CH_3

The title compound was prepared from backbone 2 (499.3 mg, 1.3 mmol, 1.0 eq.) and (*R*)-3-Aminobutan-1-ol (161.5 mg, 1.8 mmol, 1.4 eq.) according to general procedure **I**. Me_2bdc-^{5}N-(*R*)-$(CH_2)_2OH$-CH_3 (210.0 mg, 683.3 µmol, 52%) was obtained as a slightly yellow oil after silica-gel column chromatography (EtOAc/methanol gradient from 1/0 to 9.5/0.5; 0.5% TEA).

^{1}H NMR (500 MHz, MeOD-d_4) δ (ppm) 7.90 (s, 2H), 4.33-4.27 (m, 4H), 3.92 (s, 6H), 3.77-3.66 (m, 2H), 3.00-2.94 (m, 1H), 1.67-1.61 (m, 1H), 1.23 (d, *J* = 3.4 Hz, 3H). ^{13}C NMR (500 MHz, MeOD-d_4) δ (ppm) 167.15, 144.45, 129.77, 129.57, 60.38, 57.34, 57.02, 52.81, 38.12, 17.26. HRMS (FTMS + p ESI Full) calculated for $[M+H]^+$ $(C_{16}H_{22}N_1O_5)^+$ m/z 308.1492, found m/z 308.1482.

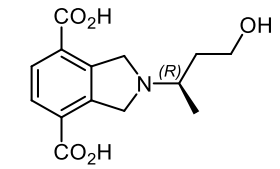

H_2bdc-^{5}N-(*R*)-$(CH_2)_2$OH-CH_3

The title compound was prepared from Me_2bdc-^{5}N-(*R*)-$(CH_2)_2$OH-CH_3 (210.0 mg, 683.3 µmol, 1.0 eq.) according to the general ester hydrolysis procedure. H_2bdc-^{5}N-(*R*)-$(CH_2)_2$OH-CH_3 precipitated at pH 4.8 as a slightly beige solid (139.3 mg, 498.8 µmol, 73%).

^{1}H NMR (500 MHz, D_2O/NaOD) δ (ppm) 7.67 (s, 2H), 4.54-4.47 (m, 4H), 3.81-3.76 (m, 1H), 3.74-3.69 (m, 1H), 3.29-3.26 (m, 1H), 2.14-2.08 (m, 1H), 1.77-1.71 (m, 1H), 1.30 (d, *J* = 6.5 Hz, 3H). ^{13}C NMR (500 MHz, D_2O/NaOD) δ (ppm) 174.61, 137.22, 133.92, 128.08, 58.47, 57.15, 56.38, 35.13, 15.83. HRMS (FTMS + p ESI Full) calculated for $[M]^-$ $(C_{14}H_{16}N_1O_5)^-$ m/z 278.1023, found m/z 278.1031.

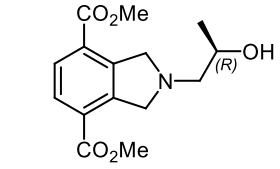

Me_2bdc-^{5}N-CH_2CH-(*R*)-CH_3-OH

The title compound was prepared from backbone 2 (497.2 mg, 1.3 mmol, 1.0 eq.) and (2*R*)-1-Amino-2-propanol (151.7 mg, 2.0 mmol, 1.5 eq.) according to general procedure **I**. Me_2bdc-^{5}N-CH_2CH-(*R*)-CH_3-OH (160.2 mg, 545.5 µmol, 42%) was obtained as a slightly yellow oil after silica-gel column chromatography (cyclohexane/EtOAc gradient from 2/1 to 1/1; 0.5% TEA).

^{1}H NMR (500 MHz, DMSO-*d6*) δ (ppm) 7.89 (s, 2H), 4.48 (d, *J* = 4.1 Hz, 1H), 4.42 (s, 4H), 3.86 (s, 6H), 3.83-3.78 (m, 1H), 2.67 (dd, *J* = 12.0, 6.7 Hz, 1H), 2.62 (dd, *J* = 12.0, 5.5 Hz, 1H), 1.10 (d, *J* = 6.2 Hz, 3H). ^{13}C NMR (126 MHz, $CDCl_3$) δ (ppm) 165.46, 143.92, 128.23, 127.82, 64.94, 63.15, 59.40, 52.34, 21.70. MS (ESI) calculated for $[M+H]^+$ $(C_{15}H_{20}N_1O_5)^+$ m/z 294.13, found m/z 294.21.

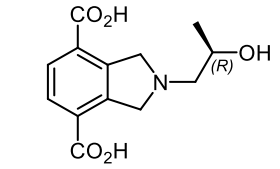

H_2bdc-^{5}N-CH_2CH-(*R*)-CH_3-OH

The title compound was prepared from Me_2bdc-^{5}N-CH_2CH-(*R*)-CH_3-OH (160.2 mg, 545.5 µmol, 1.0 eq.) according to the general ester hydrolysis procedure. H_2bdc-^{5}N-CH_2CH-(*R*)-CH_3-OH precipitated at pH 4.4 as a white solid (112.6 mg, 424.5 µmol, 78%).

^{1}H NMR (500 MHz, D_2O/NaOD) δ (ppm) 7.57 (s, 2H), 4.17 (s, 4H), 4.09-4.05 (m, 1H), 2.87-2.78 (m, 2H), 1.23 (d, *J* = 6.5 Hz, 3H). ^{13}C NMR (126 MHz, D_2O/NaOD) δ (ppm) 175.50, 139.56, 133.85, 127.02, 65.95, 62.58, 59.02, 20.71. HRMS (FTMS + p ESI Full) calculated for $[M]^-$ $(C_{13}H_{14}N_1O_5)^-$ m/z 364.866, found m/z 264.0871.

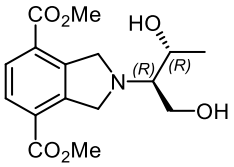

Me$_2$bdc-^{5}N-(*R*)-ThrOH

The title compound was prepared from backbone 2 (309.7 mg, 814.9 µmol, 1.0 eq.) and (2*R*,3*R*)-2-aminobutane-1,3-diol (221.6 mg, 2.1 mmol, 2.6 eq.) according to general procedure **I**. Me$_2$bdc-^{5}N-(*R*)-ThrOH (160.3 mg, 494.8 µmol, 61%) was obtained as a slightly yellow oil after silica-gel column chromatography (CH_3CN, 0.5% TEA).

^{1}H NMR (500 MHz, DMSO-*d6*) δ (ppm) 7.89 (s, 2H), 4.45-4.43 (m, 6H), 3.86-3.84 (m, 7H), 3.75-3.65 (m, 2H), 2.68-2.65 (m, 1H), 1.10 (d, *J* = 6.5 Hz, 3H). ^{13}C NMR (126 MHz, $CDCl_3$) δ (ppm) 165.49, 144.15, 128.01, 127.75, 66.91, 65.68, 58.96, 56.13, 52.29, 19.88. HRMS (FTMS + p ESI Full) calculated for $[M+H]^+$ $(C_{16}H_{21}N_1O_6)^+$ m/z 324.1442, found m/z 324.1435.

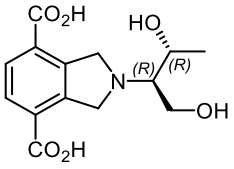

H$_2$bdc-^{5}N-(*R*)-ThrOH

The title compound was prepared from Me$_2$bdc-^{5}N-(*R*)-ThrOH (160.3 mg, 494.8 µmol, 1.0 eq.) according to the general ester hydrolysis procedure. H$_2$bdc-^{5}N-(*R*)-ThrOH precipitated at pH 3.5 as a fine, slightly beige solid (95.3 mg, 322.7 µmol, 65%).

^{1}H NMR (500 MHz, D_2O/NaOD) δ (ppm) 7.60 (s, 2H), 4.31 (s, 4H), 4.27-4.22 (m, 1H), 3.99 (dd, *J* = 12.1, 4.2 Hz, 1H), 3.88 (dd, *J* = 12.1, 5.4 Hz, 1H), 2.89-2.86 (m, 1H), 1.24 (d, *J* = 6.5 Hz, 3H). ^{13}C NMR (126 MHz, D_2O/NaOD) δ (ppm) 175.50, 139.28, 133.83, 127.06, 68.64, 66.97, 59.83, 56.72, 17.15. HRMS (FTMS + p ESI Full) calculated for $[M]^-$ $(C_{14}H_{16}N_1O_6)^-$ m/z 294.0972, found m/z 294.0984.

Synthesis of functionalised benzaldehydes

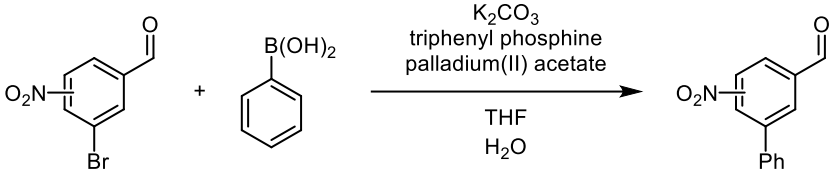

Scheme 3.2 Schematic reaction scheme for the synthesis of phenyl functionalised benzaldehydes.

The synthesis of phenyl functionalised benzaldehydes was performed according to the procedure reported by Waldvogel et. al.[8] Bromo-nitrobenzaldehyde (1.0 eq.) and phenylboronic acid (1.1 eq.) were dissolved in THF (2.5 mL). A solution of K_2CO_3 (2.2 eq.) in water (5.0 mL) was added and the reaction mixture was degassed and stirred under an argon atmosphere. Triphenylphosphine (0.1 eq.) and palladium(II) acetate (0.1 eq.) were added, and the reaction mixture was stirred at 65 °C overnight. After cooling to room temperature, solids were removed by filtration through celite and washed with water (10 mL) and EtOAc (10 mL). The mixture

was extracted with EtOAc (2 × 20 mL), and the combined organic phases were dried over $MgSO_4$. The crude product was purified using silica-gel column chromatography (cyclohexane/EtOAc gradient from 1:0 to 9:1).

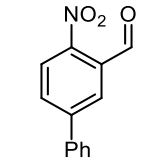

Benzaldehyde **24**

The title compound was prepared from 5-Bromo-2-nitrobenzaldehyde (297.6 mg, 1.3 mmol, 1.0 eq.) according to the procedure described above. Benzaldehyde **24** (231.7 mg, 1.0 mmol, 79%) was obtained as a white solid. The ^{1}H NMR spectrum agrees with literature data.[8]

^{1}H NMR (500 MHz, $CDCl_3$) δ (ppm) 10.52 (s, 1H), 8.22 (d, *J* = 8.5 Hz, 1H), 8.15 (d, *J* = 2.1 Hz, 1H), 7.94 (dd, *J* = 8.5, 2.1 Hz, 1H), 7.67-7.65 (m, 2H), 7.54-7.47 (m, 3H).

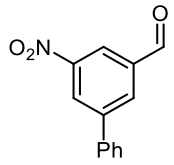

Benzaldehyde **33**

The title compound was prepared from 5-Bromo-3-nitrobenzaldehyde (241.6 mg, 1.1 mmol, 1.0 eq.) according to the procedure described above. Benzaldehyde **33** (127.5 mg, 561.1 µmol, 53%) was obtained as a white solid.

^{1}H NMR (500 MHz, $CDCl_3$) δ (ppm) 10.18 (s, 1H), 8.69 (td, *J* = 14.3, 1.4 Hz, 2H), 8.43 (t, *J* = 1.4 Hz, 1H), 7.69-7.68 (m, 2H), 7.56-7.48 (m, 3H). ^{13}C NMR (126 MHz, $CDCl_3$) δ (ppm) 189.91, 149.46, 144.34, 137.98, 137.49, 132.88, 129.58, 129.45, 127.34, 126.97, 123.09.

Henry reaction products

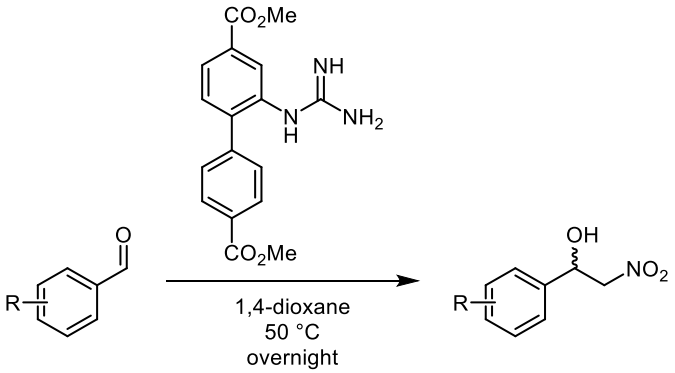

Scheme 3.3 Schematic reaction scheme for the synthesis of representative Henry reaction products.

Three Henry reaction products of representative benzaldehydes were isolated to confirm the HPLC conditions (**Scheme** 3.3). The selected benzaldehyde (40.0 µmol) was dissolved in 1,4-dioxane (893 µL) and nitromethane (107 µL, 2.0 mmol, 50.0 eq.), and Me2bpdc-gua (1.3 mg, 4.0 µmol, 0.1 eq.) was added as a homogeneous catalyst. The reaction mixture was

heated at 50 °C overnight. The solvent was removed under reduced pressure. The crude product was passed through a short plug of silica (100% acetone) to yield the Henry reaction product.

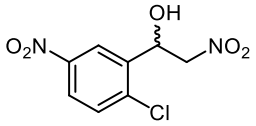

Yield: 9.5 mg, 38.5 µmol, 97%.

^{1}H NMR (500 MHz, $CDCl_3$) δ (ppm) 8.61 (d, *J* = 2.7 Hz, 1H), 8.18 (dd, *J* = 8.7, 2.7 Hz, 1H), 7.59 (d, *J* = 8.8 Hz, 1H), 5.88 (dd, *J* = 9.4, 1.9 Hz, 1H), 4.71 (dd, *J* = 13.9, 2.2 Hz, 1H), 4.48 (dd, *J* = 13.9, 9.4 Hz, 1H), 3.33 (brs, 1H). ^{13}C NMR (126 MHz, $CDCl_3$) δ (ppm) 147.43, 138.08, 137.81, 130.92, 124.84, 123.45, 78.76, 67.45.

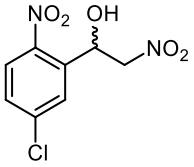

Yield: 9.6 mg, 38.9 µmol, 98%.

^{1}H NMR (500 MHz, $CDCl_3$) δ (ppm) 8.08 (d, *J* = 8.8 Hz, 1H), 7.98 (d, *J* = 2.2 Hz, 1H), 7.52 (dd, *J* = 8.8, 2.2 Hz, 1H), 6.09 (dd, *J* = 8.8, 2.2 Hz, 1H), 4.86 (dd, *J* = 13.9, 2.2 Hz, 1H), 4.52 (dd, *J* = 13.9, 8.8 Hz, 1H), 3.30 (brs, 1H). ^{13}C NMR (126 MHz, $CDCl_3$) δ (ppm) 145.29, 141.56, 136.19, 129.96, 129.24, 126.80, 79.88, 66.65.

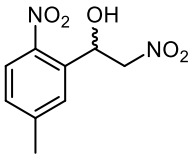

Yield: 8.5 mg, 37.6 µmol, 94%.

^{1}H NMR (500 MHz, $CDCl_3$) δ (ppm) 8.01 (d, *J* = 8.4 Hz, 1H), 7.74 (d, *J* = 1.4 Hz, 1H), 7.32 (dd, *J* = 8.4, 1.4 Hz, 1H), 6.07 (dd, *J* = 9.1, 2.2 Hz, 1H), 4.86 (dd, *J* = 13.9, 2.3 Hz, 1H), 4.53 (dd, *J* = 13.9, 9.1 Hz, 1H), 3.19 (brs, 1H), 2.49 (s, 3H). ^{13}C NMR (126 MHz, $CDCl_3$) δ (ppm) 146.03, 133.94, 130.18, 129.05, 125.35, 80.05, 67.10, 21.73. HRMS (FTMS + p ESI Full) calculated for $[M+H]^+$ $(C_9H_{10}N_2O_5)^+$ m/z 225.0506, found m/z 225.0509.

Verification of peak identity in HPLC for the Henry reaction

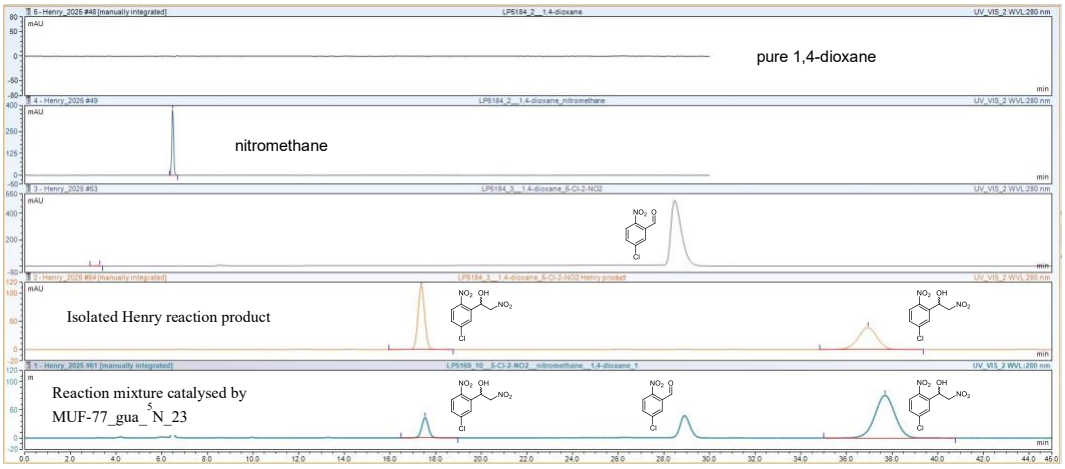

Figure 3.1 HPLC traces of nitromethane, 5-chloro-2-nitrobenzaldehyde, the purified racemic Henry reaction product and a catalysis reaction mixture of a MUF-77_gua_^{5}N catalyst.

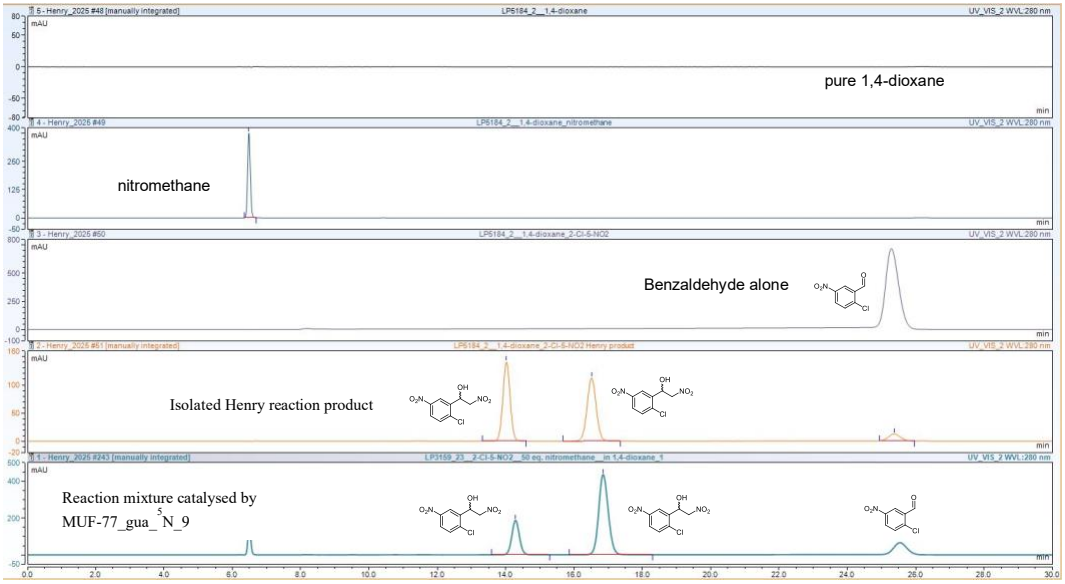

Figure 3.2 HPLC traces of nitromethane, 2-chloro-5-nitrobenzaldehyde, the purified racemic Henry reaction product and a catalysis reaction mixture of a MUF-77_gua_^{5}N catalyst.

MOFs

PXRD

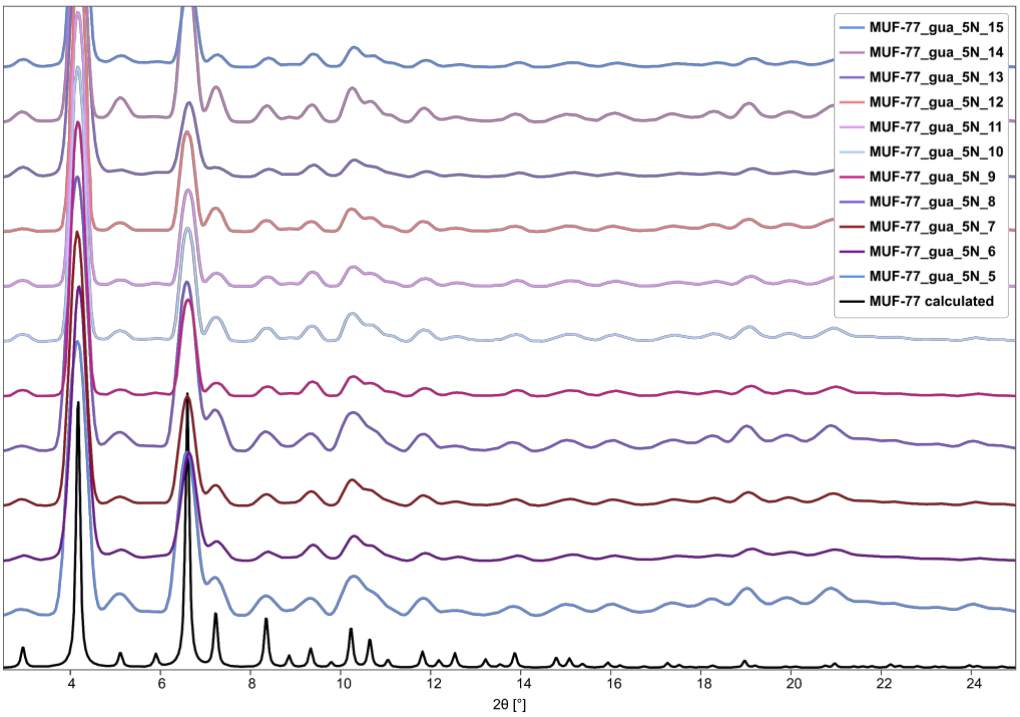

Figure 3.3 PXRD pattern of MUF-77_gua_^{5}N_5-15 compared to the calculated pattern of MUF-77. The pattern are scaled by a factor of three for better visibility.

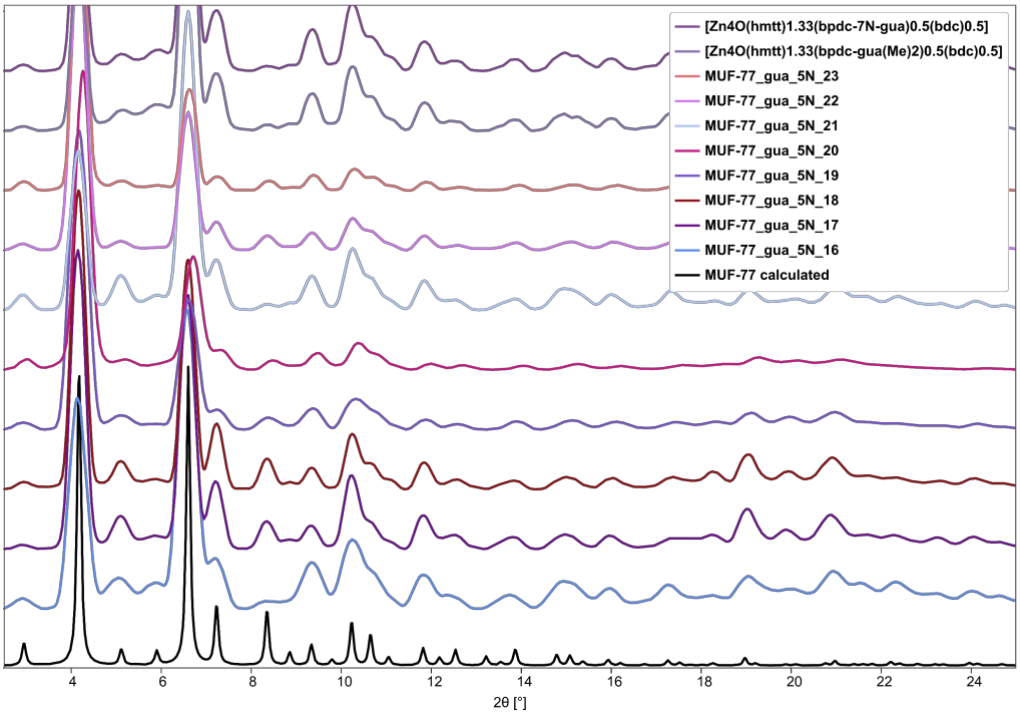

Figure 3.4 PXRD pattern of MUF-77_gua_^{5}N_16-23 and two achiral catalyst MOFs compared to the calculated pattern of MUF-77. The pattern are scaled by a factor of three for better visibility.

MOF NMRs

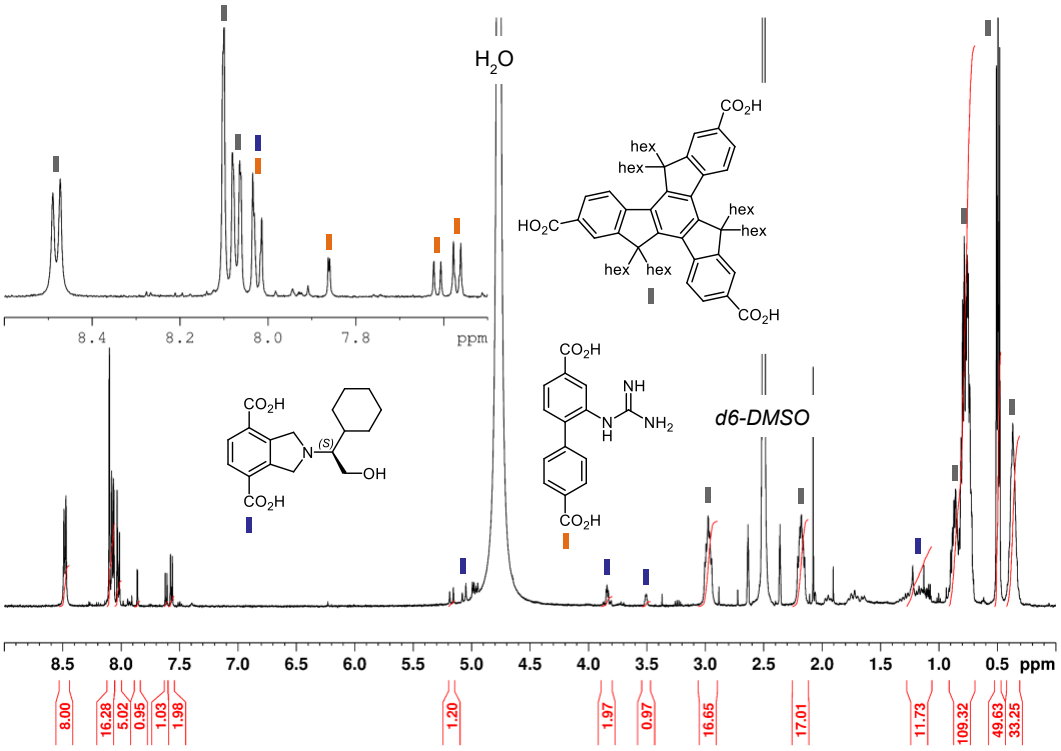

Figure 3.5 ^{1}H NMR of digested MUF-77_gua_^{5}N_5 in *d6*-DMSO/DCl.

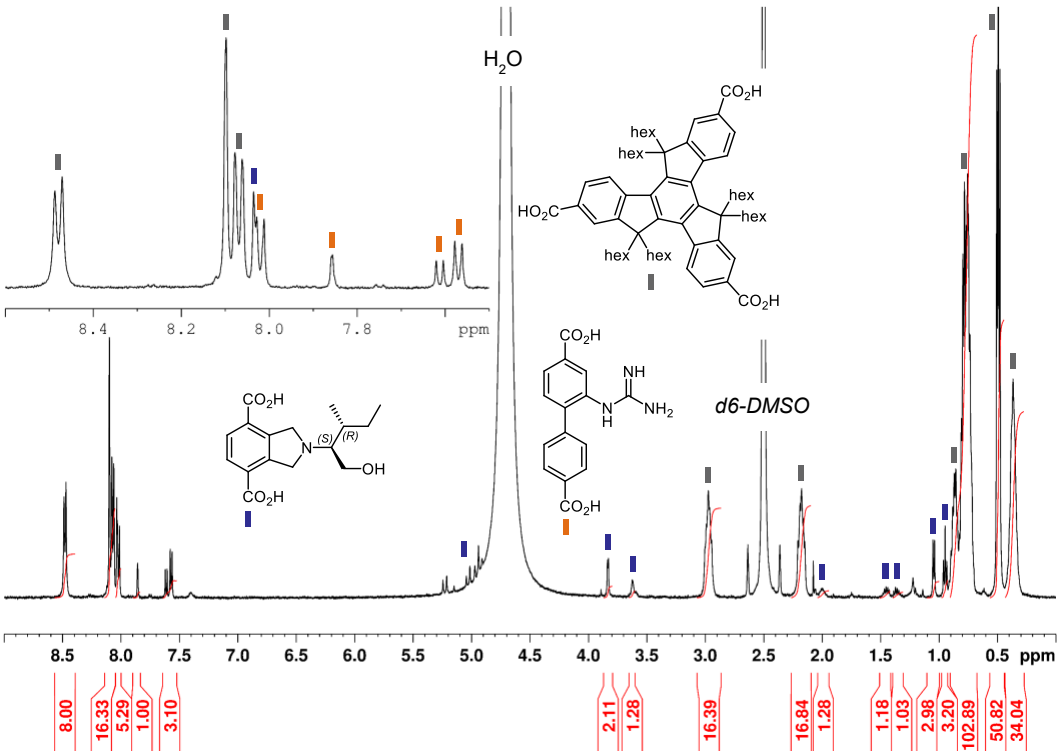

Figure 3.6 ^{1}H NMR of digested MUF-77_gua_^{5}N_7 in *d6*-DMSO/DCl.

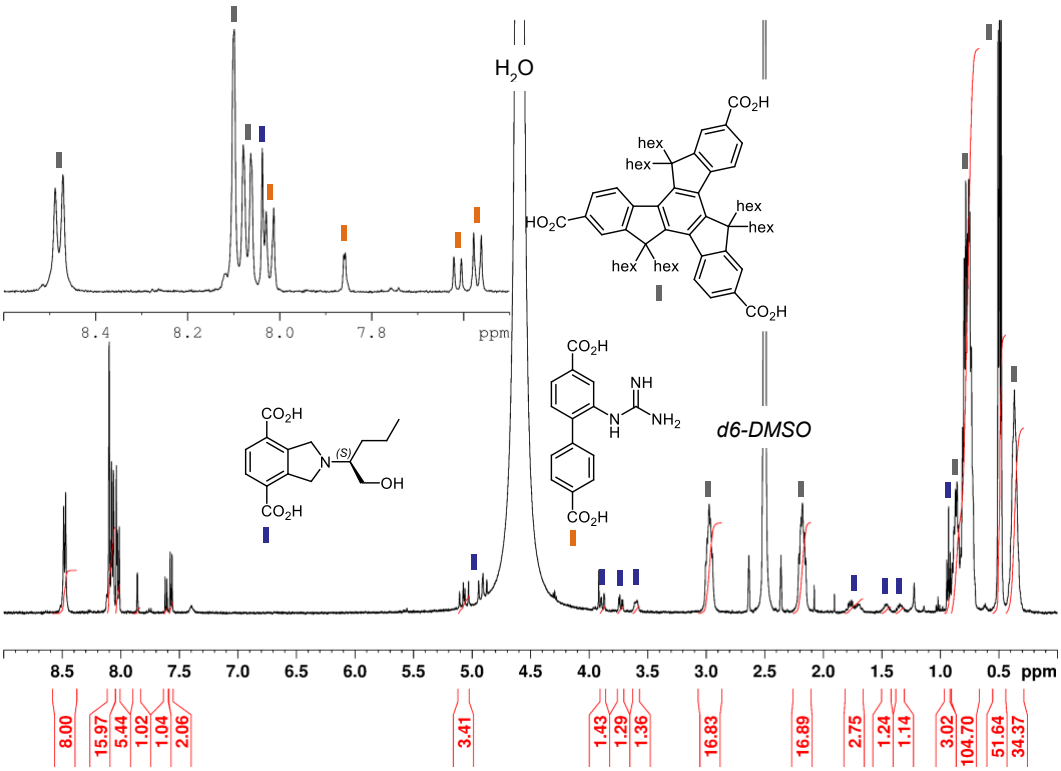

Figure 3.7 ^{1}H NMR of digested MUF-77_gua_^{5}N_8 in *d6*-DMSO/DCl.

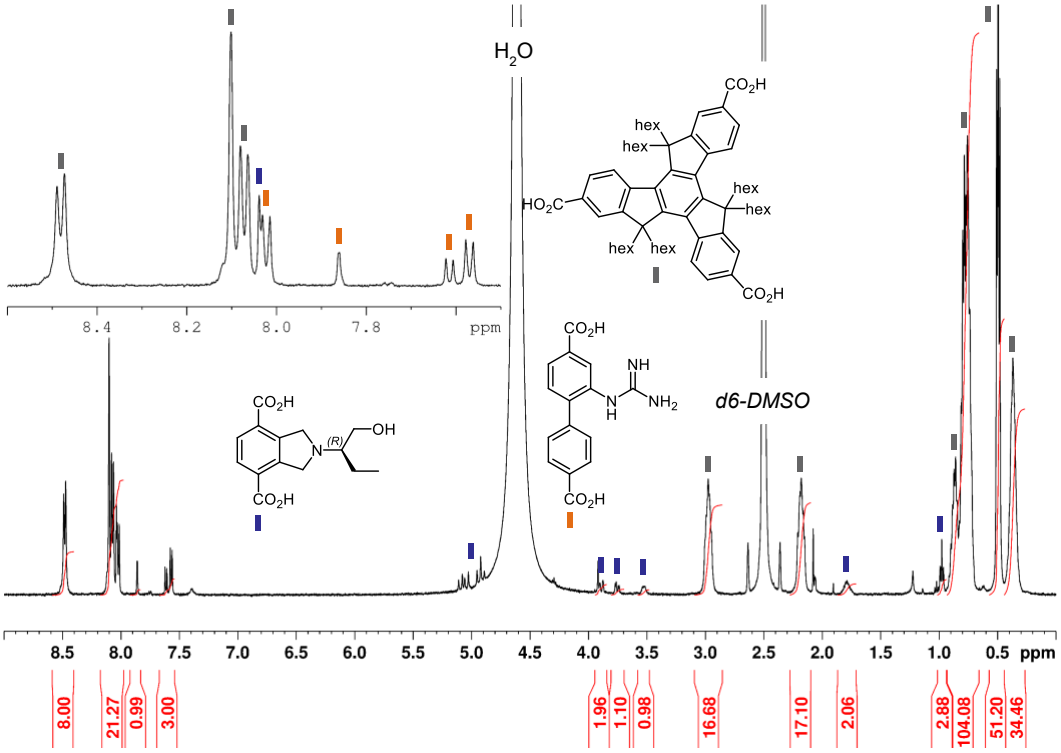

Figure 3.8 ^{1}H NMR of digested MUF-77_gua_^{5}N_9 in *d6*-DMSO/DCl.

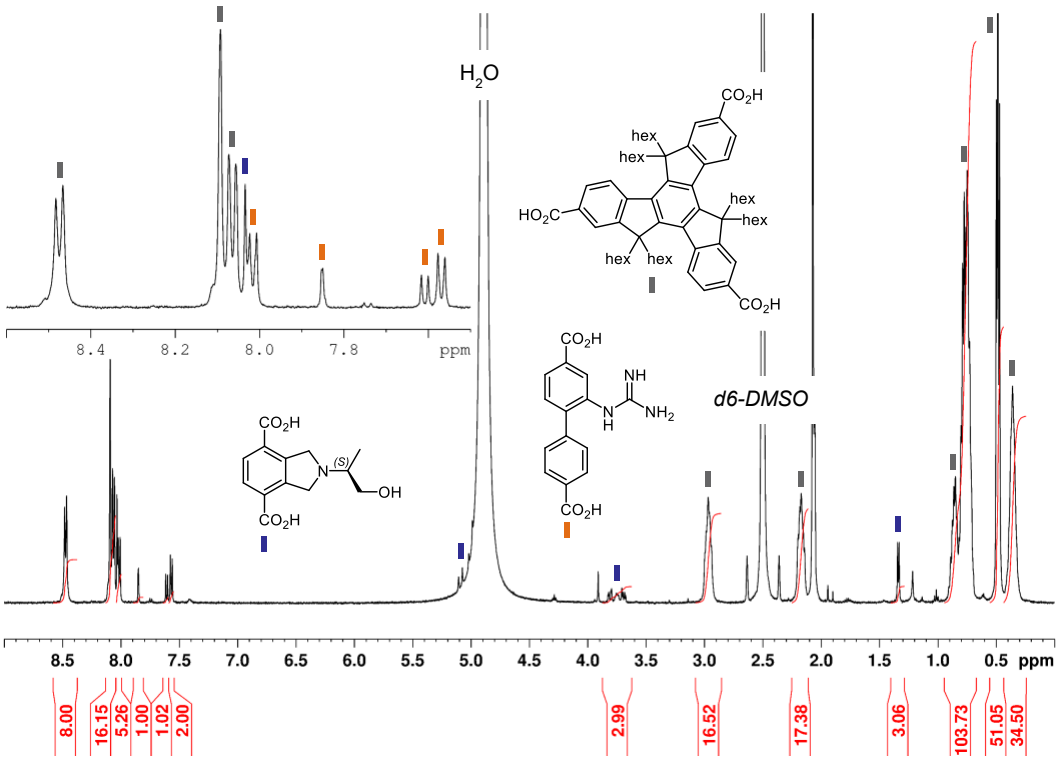

Figure 3.9 ^{1}H NMR of digested MUF-77_gua_^{5}N_10 in *d6*-DMSO/DCl.

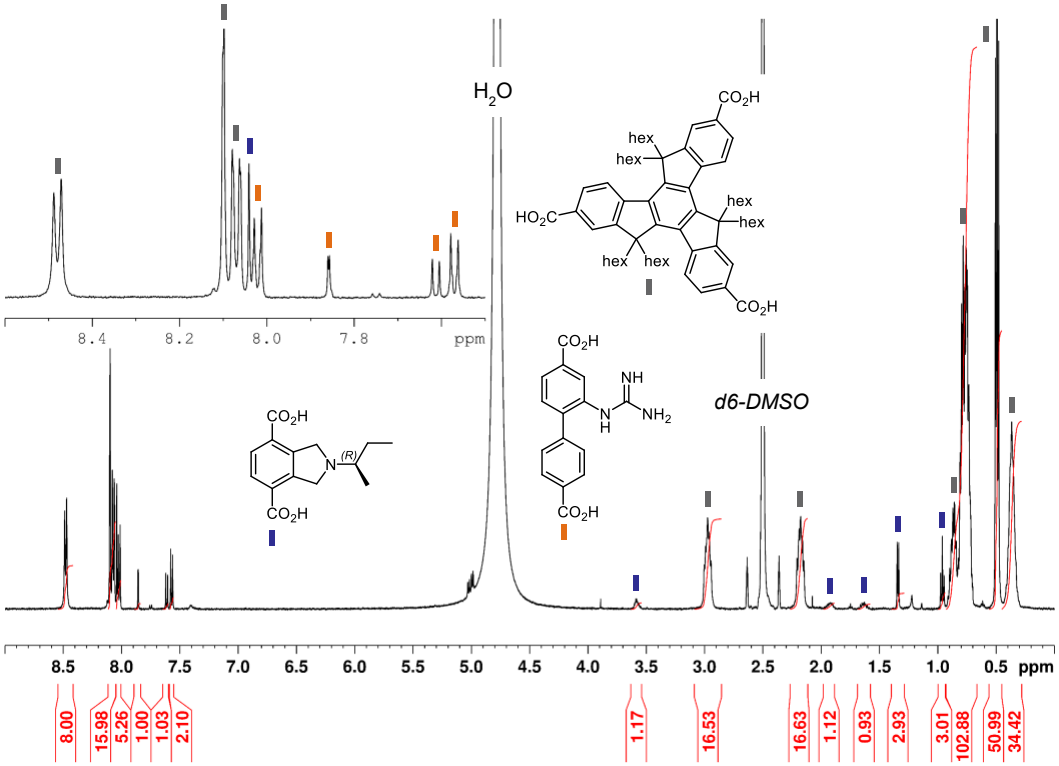

Figure 3.10 ^{1}H NMR of digested MUF-77_gua_^{5}N_11 in *d6*-DMSO/DCl.

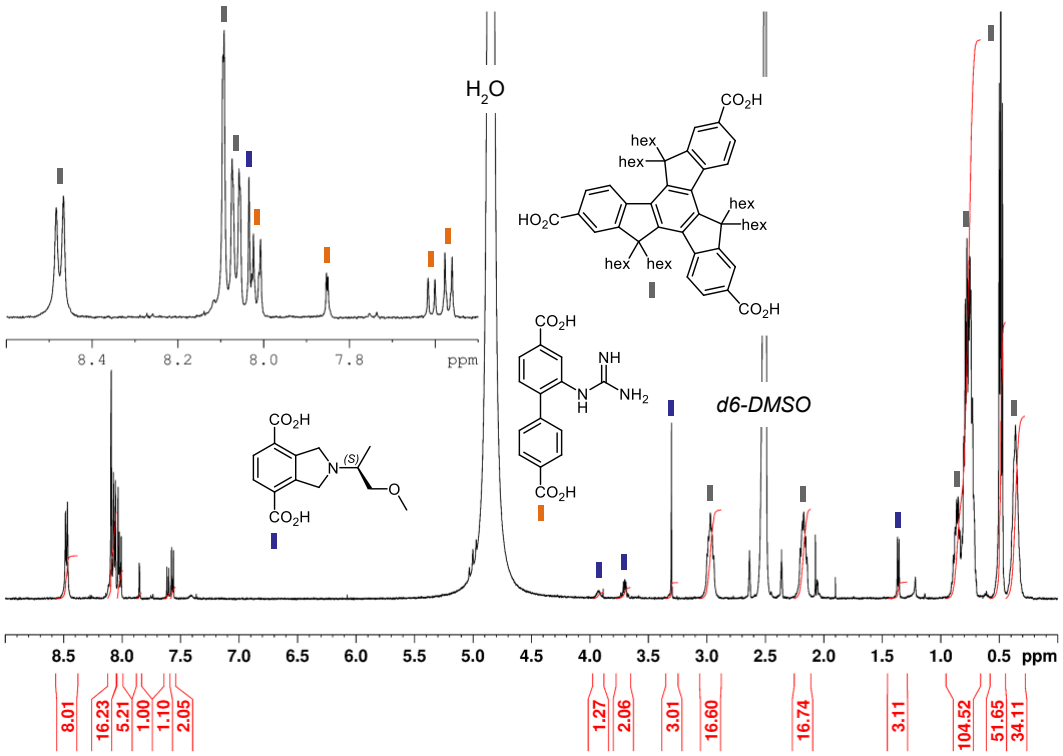

Figure 3.11 ^{1}H NMR of digested MUF-77_gua_^{5}N_12 in *d6*-DMSO/DCl.

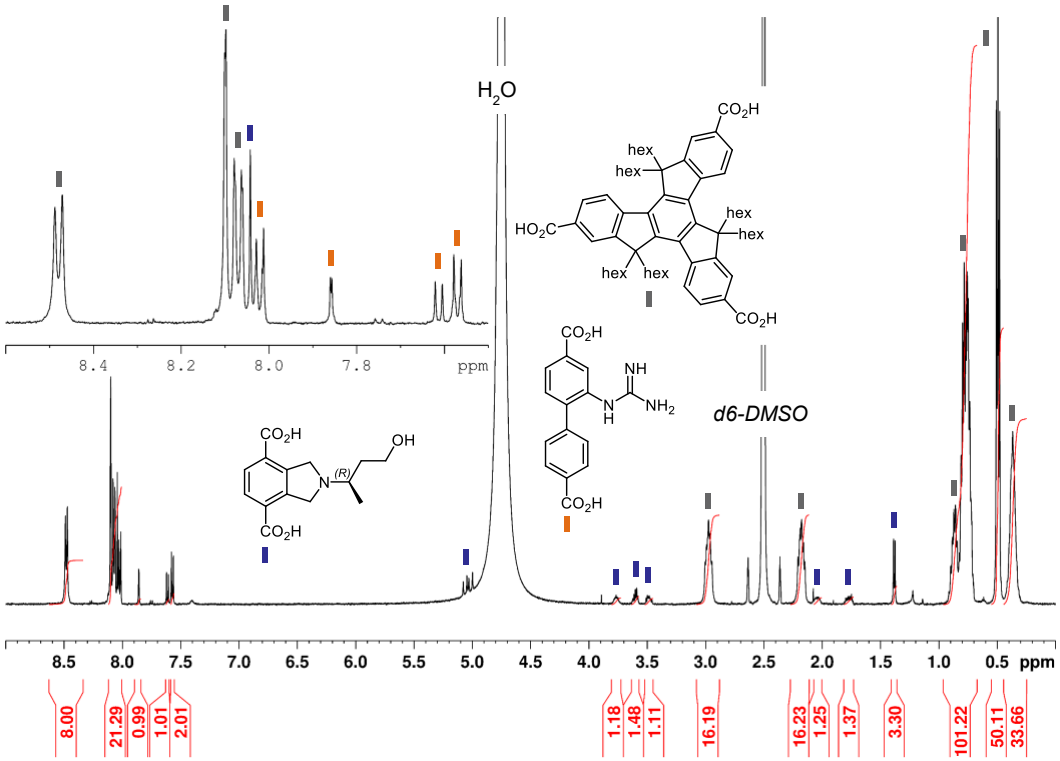

Figure 3.12 ^{1}H NMR of digested MUF-77_gua_^{5}N_13 in *d6*-DMSO/DCl.

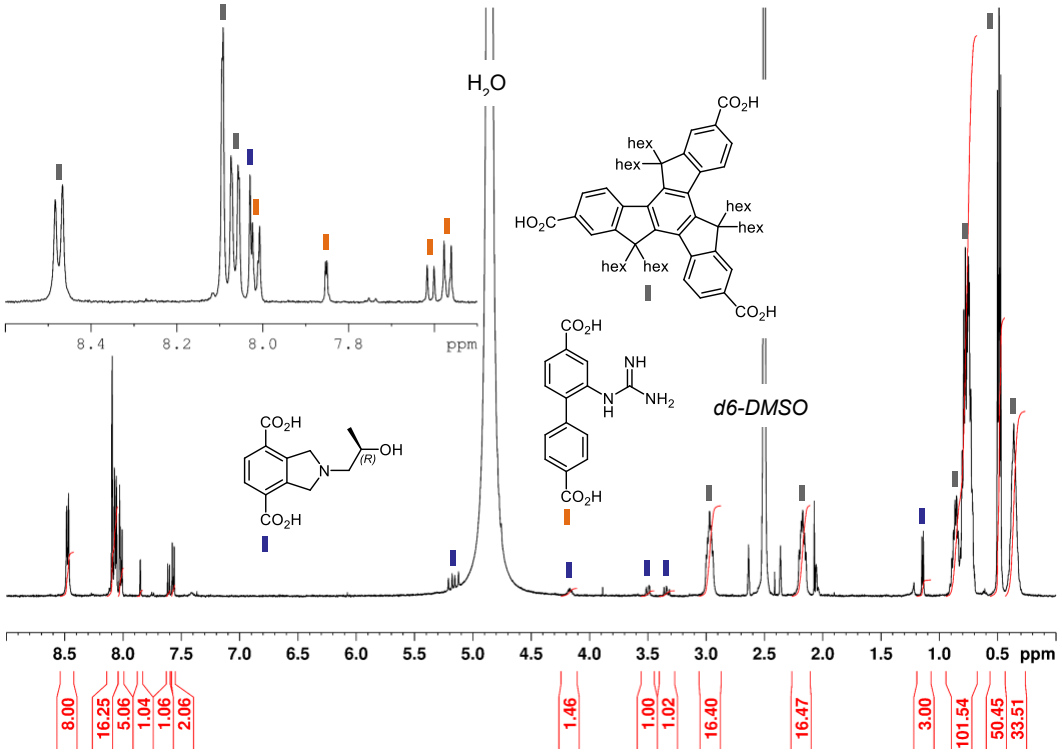

Figure 3.13 ^{1}H NMR of digested MUF-77_gua_^{5}N_14 in *d6*-DMSO/DCl.

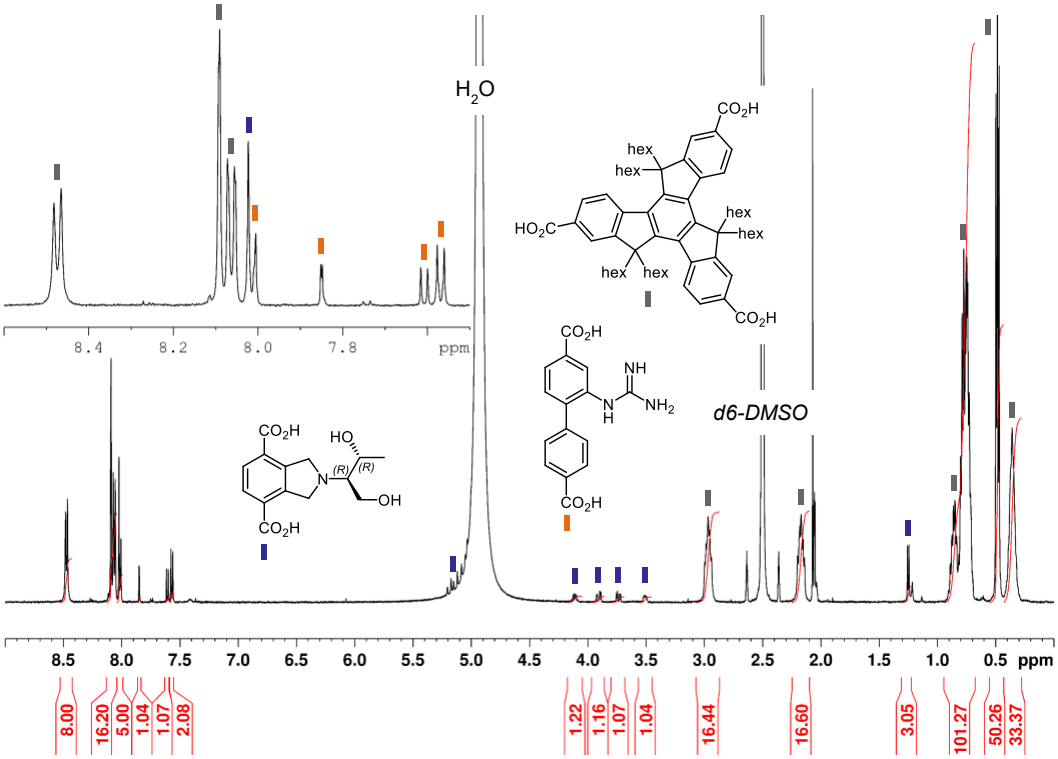

Figure 3.14 ^{1}H NMR of digested MUF-77_gua_^{5}N_15 in *d6*-DMSO/DCl.

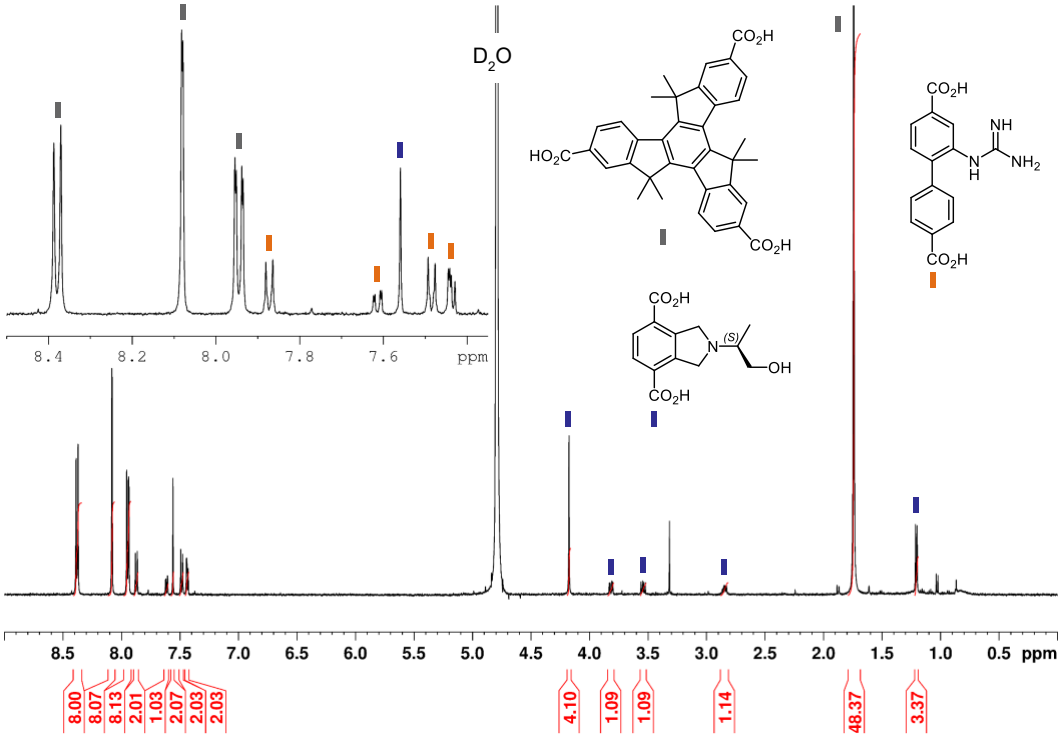

Figure 3.15 ^{1}H NMR of digested MUF-77_gua_^{5}N_16 in D_2O/NaOD.

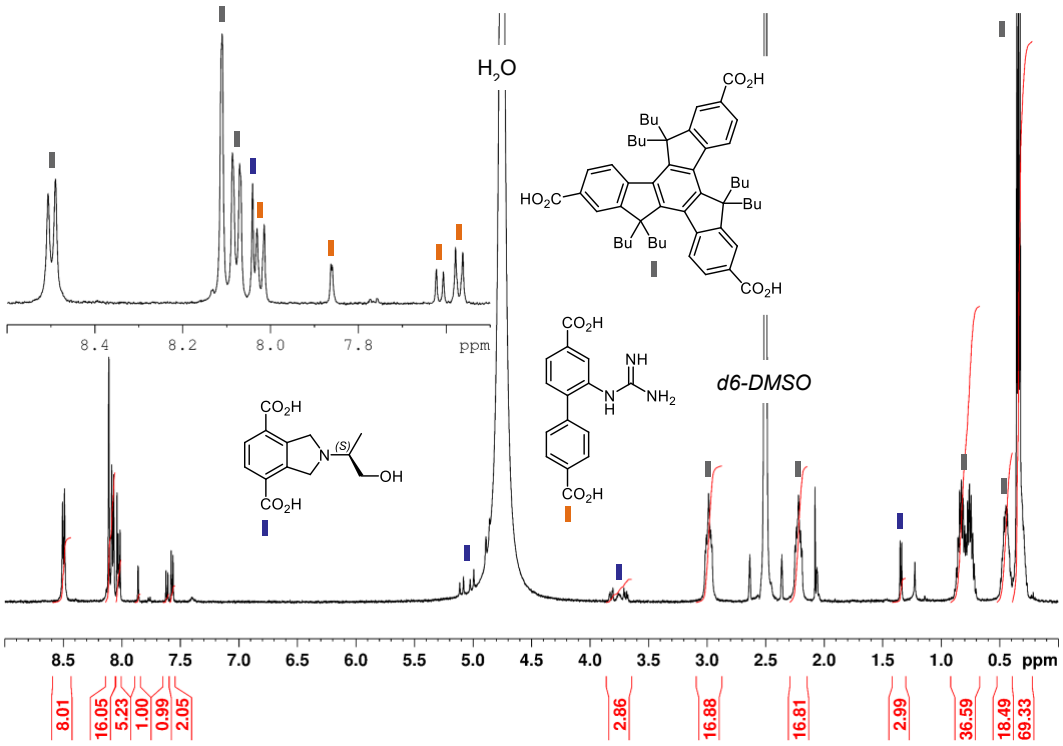

Figure 3.16 ^{1}H NMR of digested MUF-77_gua_^{5}N_17 in *d6*-DMSO/DCl.

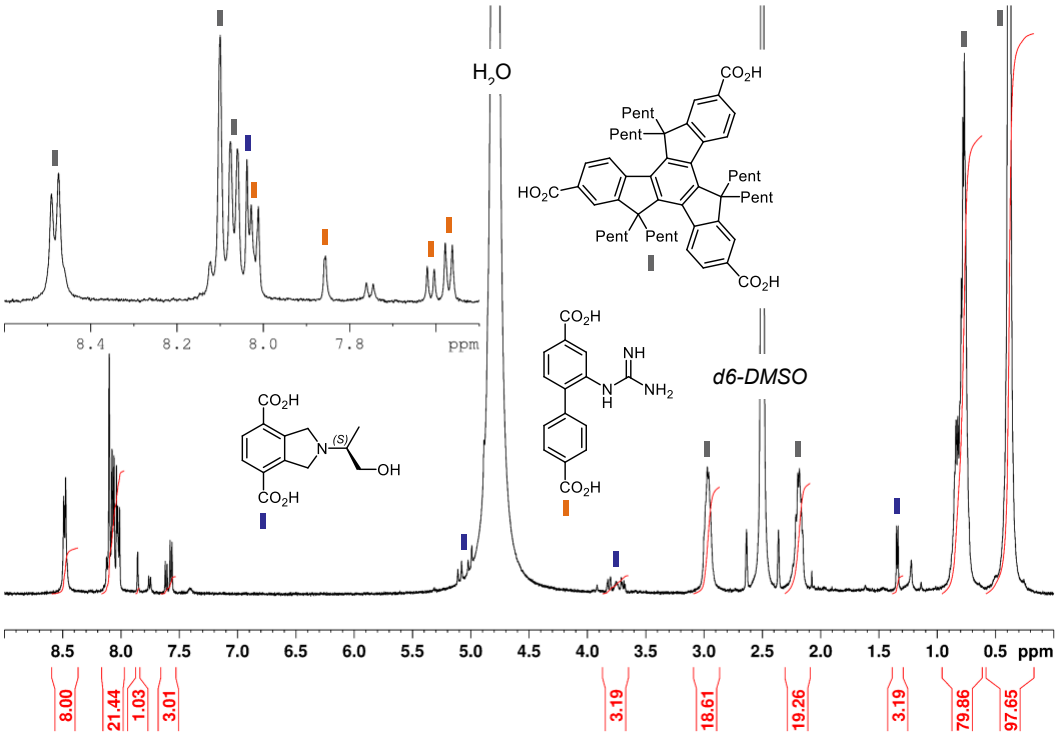

Figure 3.17 ^{1}H NMR of digested MUF-77_gua_^{5}N_18 in *d6*-DMSO/DCl.

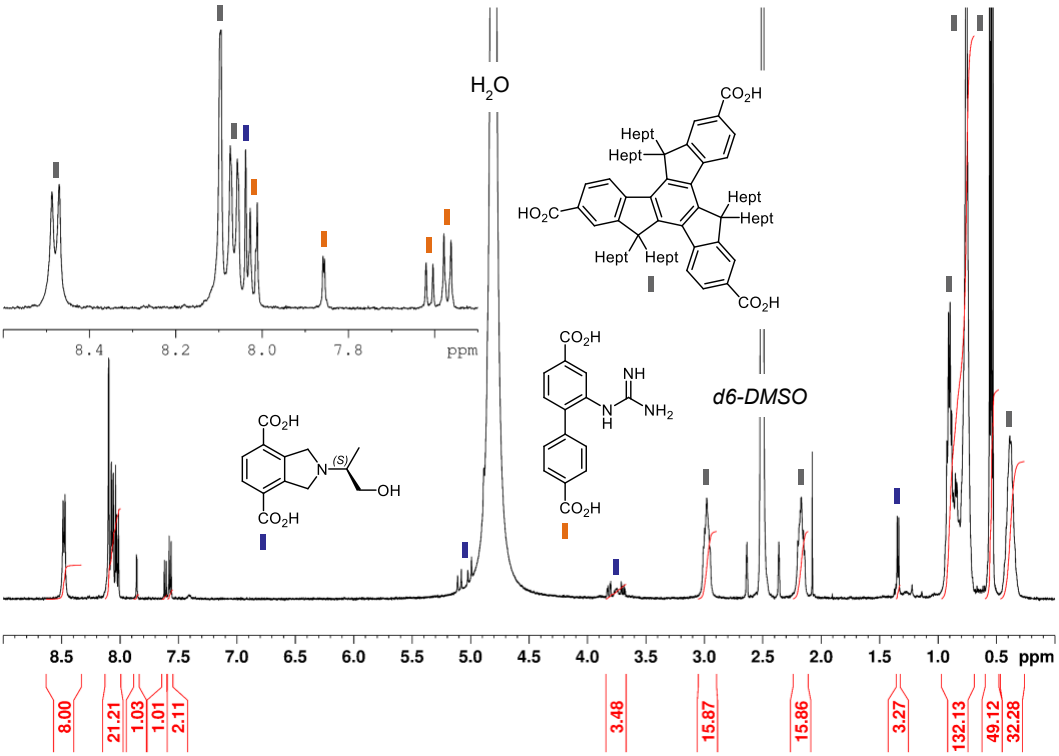

Figure 3.18 ^{1}H NMR of digested MUF-77_gua_^{5}N_19 in *d6*-DMSO/DCl.

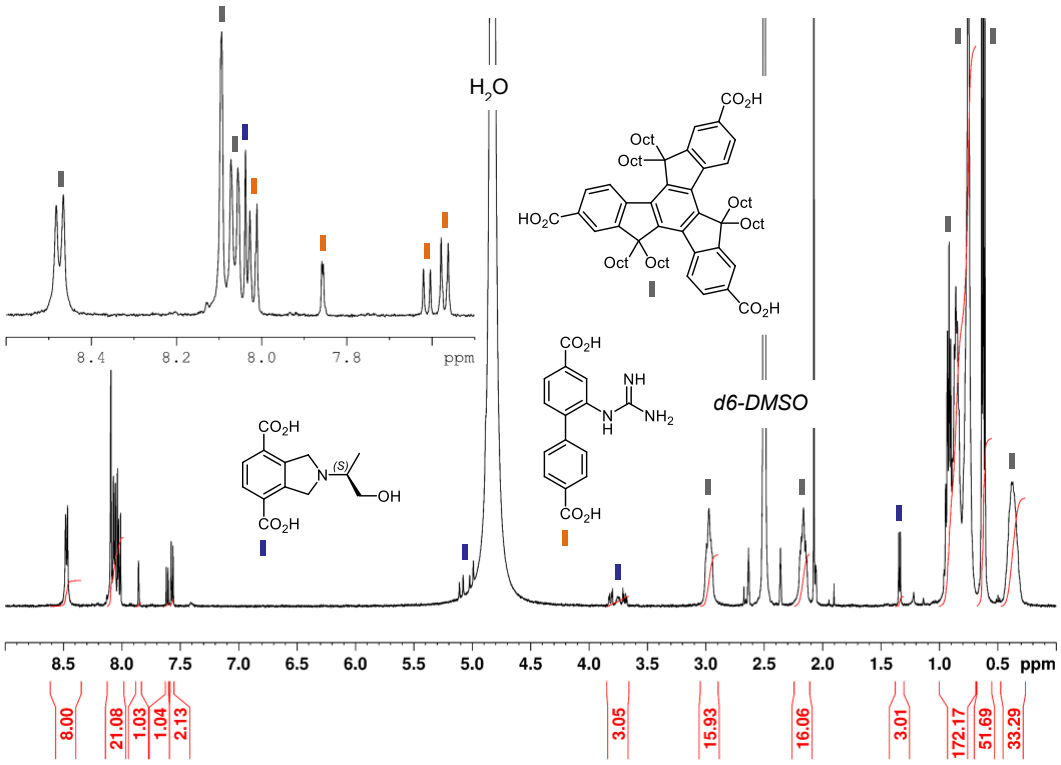

Figure 3.19 ^{1}H NMR of digested MUF-77_gua_^{5}N_20 in *d6*-DMSO/DCl.

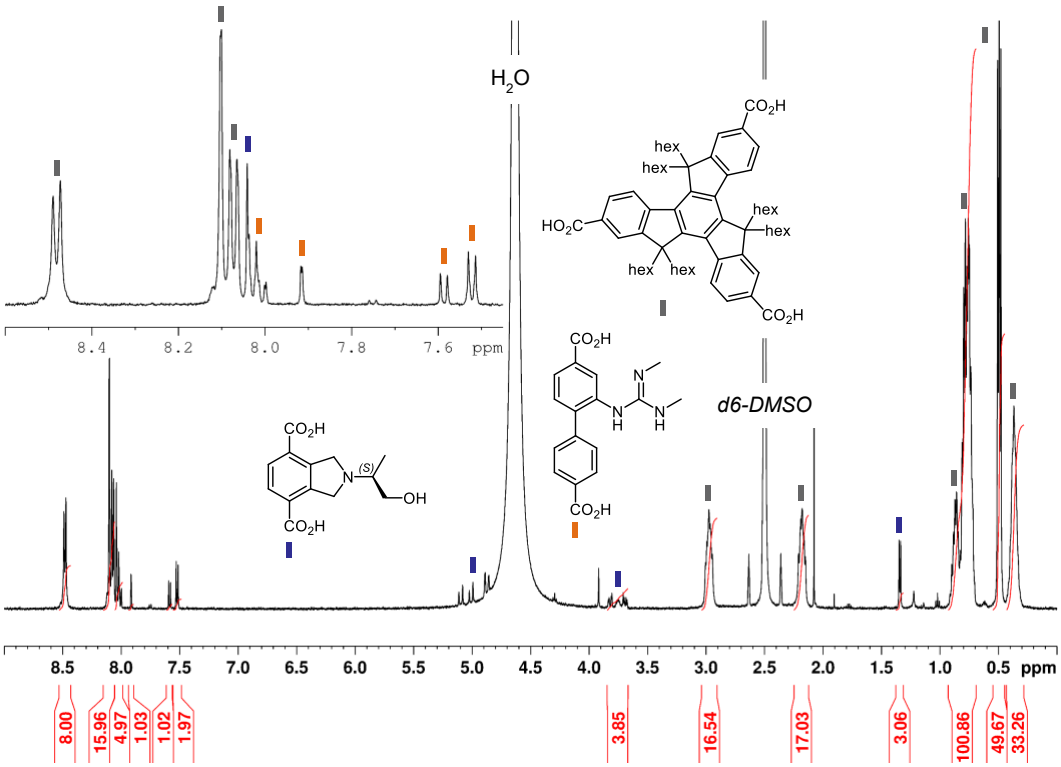

Figure 3.20 ^{1}H NMR of digested MUF-77_gua_^{5}N_21 in *d6*-DMSO/DCl.

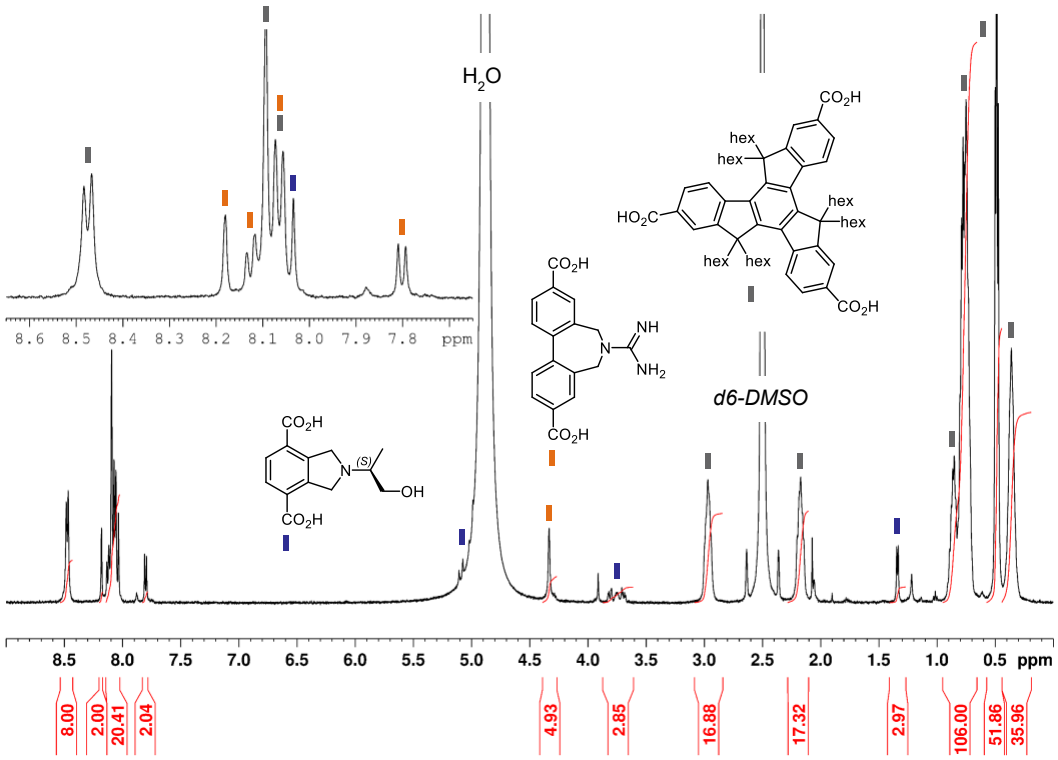

Figure 3.21 ^{1}H NMR of digested MUF-77_gua_^{5}N_22 in *d6*-DMSO/DCl.

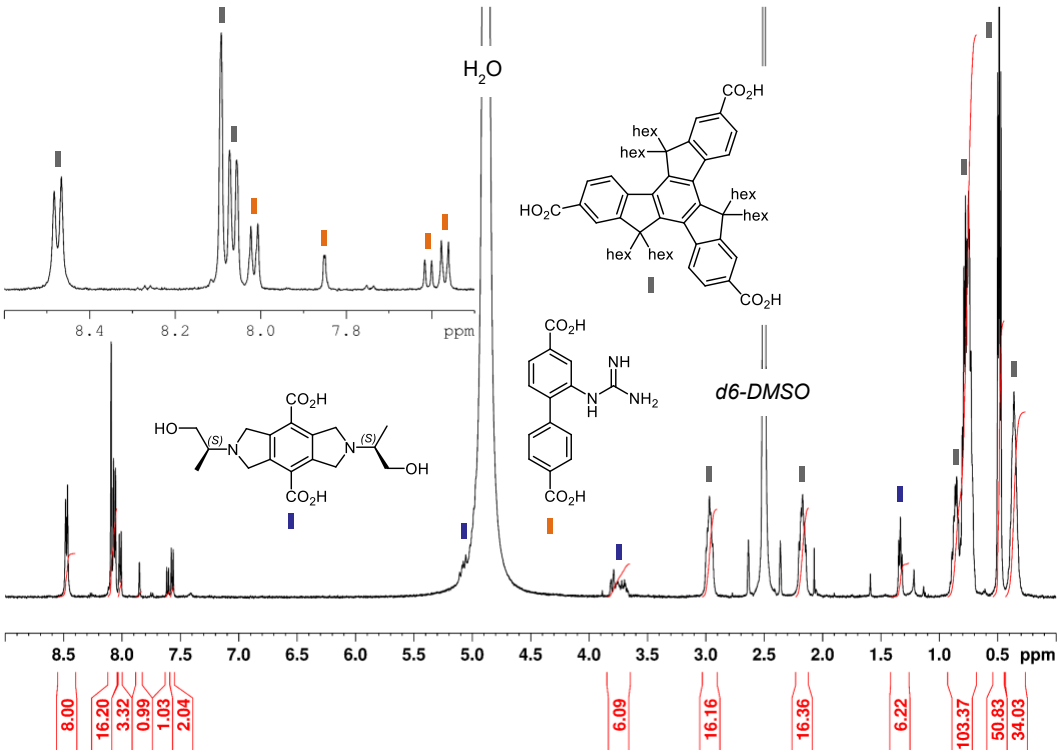

Figure 3.22 ^{1}H NMR of digested MUF-77_gua_^{5}N_23 in *d6*-DMSO/DCl.

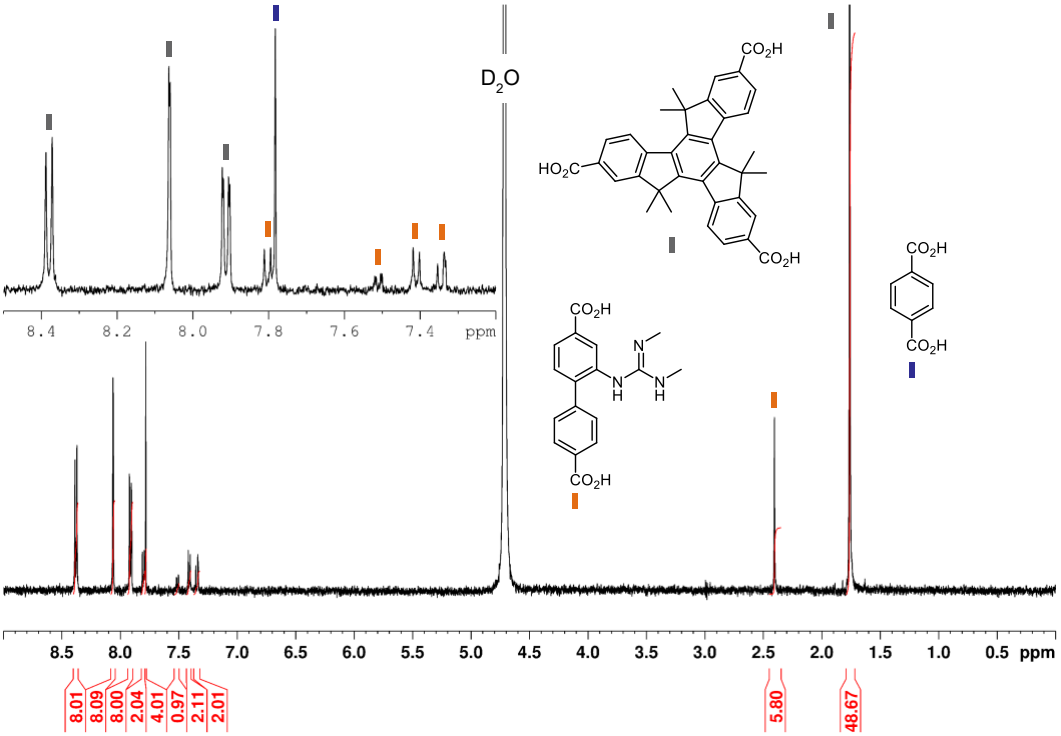

Figure 3.23 ^{1}H NMR of digested $[Zn_4O(hmtt)_{1.33}(bpdc\text{-}gua(Me)_2)_{0.5}(bdc)_{0.5}]$ in D_2O/NaOD.

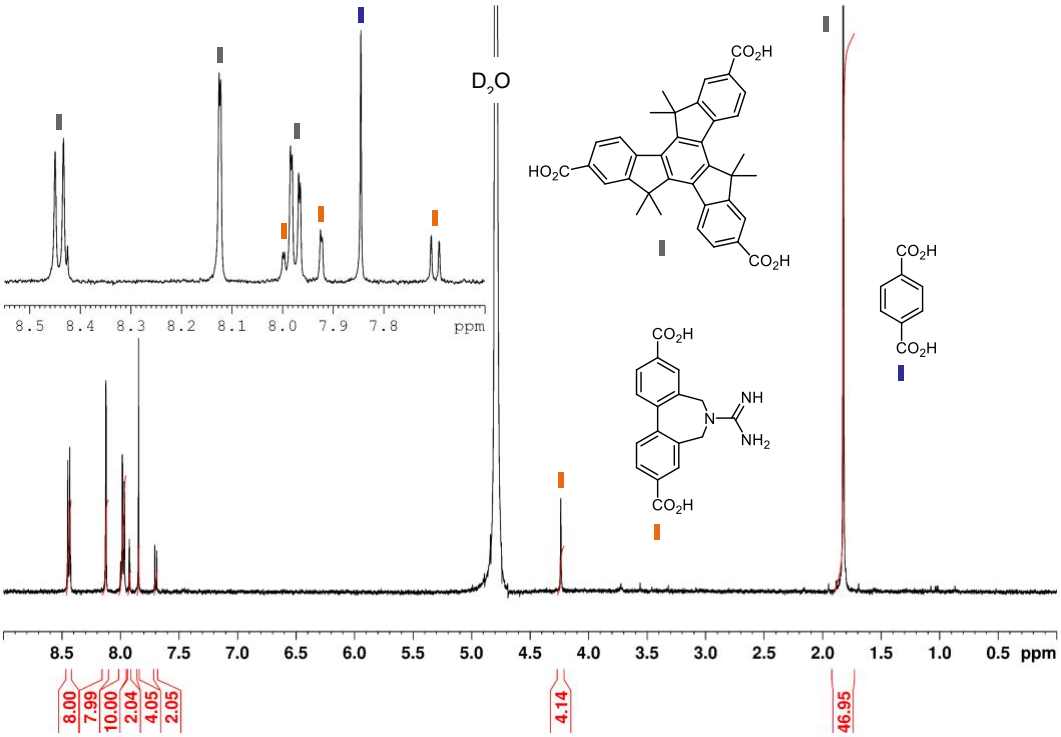

Figure 3.24 ^{1}H NMR of digested $[Zn_4O(hmtt)_{1.33}(bpdc\text{-}^{7}N\text{-}gua)_{0.5}(bdc)_{0.5}]$ in D_2O/NaOD.

Linker synthesis: NMR data

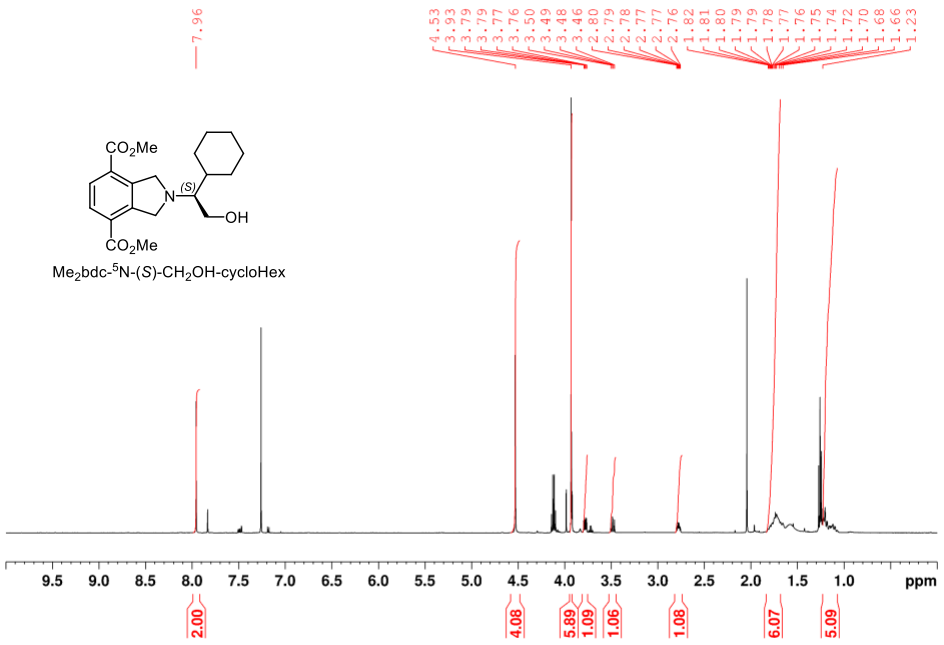

Figure 3.25 ^{1}H NMR spectrum of Me_2bdc-^{5}N-(*S*)-CH_2OH-cycloHex in $CDCl_3$.

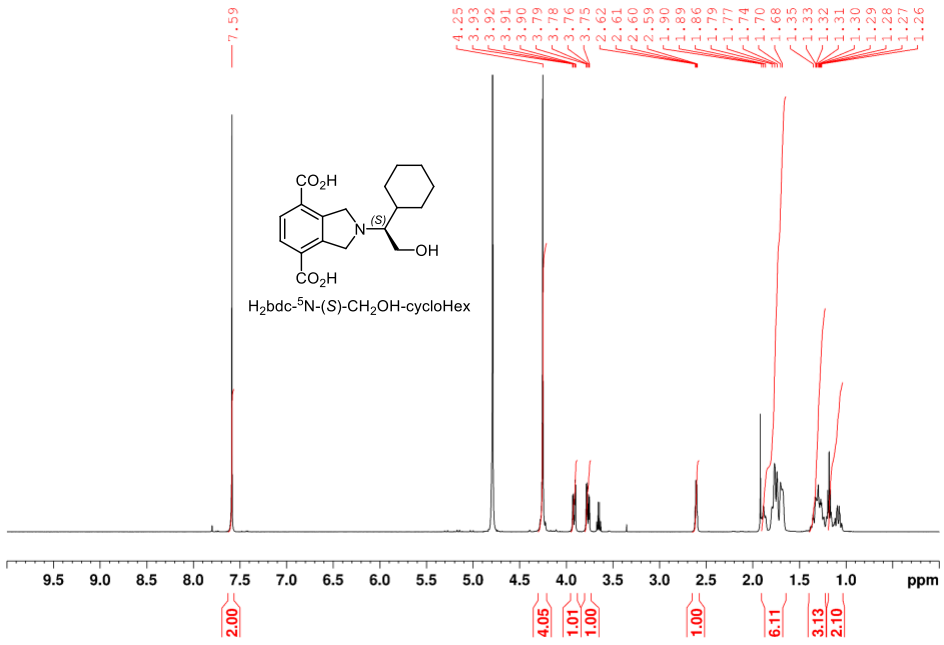

Figure 3.26 ^{1}H NMR spectrum of H_2bdc-^{5}N-(*S*)-CH_2OH-cycloHex in D_2O/NaOD.

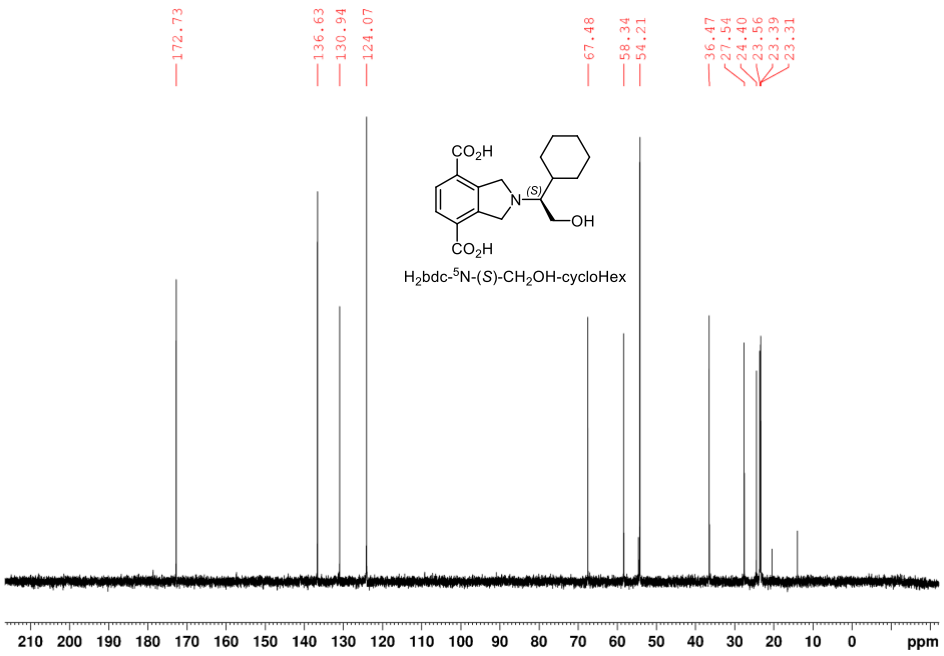

Figure 3.27 ^{13}C NMR spectrum of H$_2$bdc-^{5}N-(*S*)-CH$_2$OH-cycloHex in D$_2$O/NaOD.

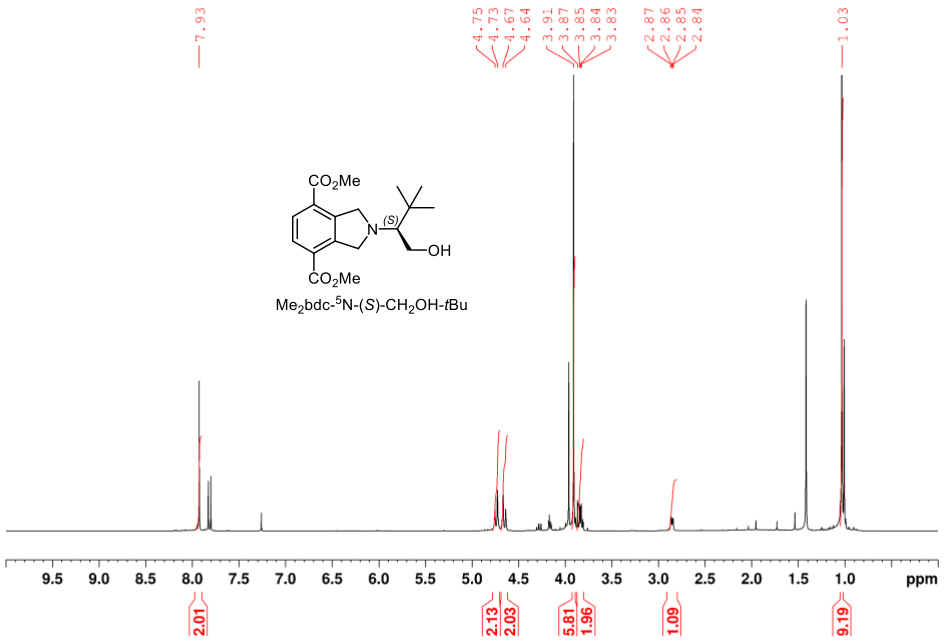

Figure 3.28 ^{1}H NMR spectrum of Me$_2$bdc-^{5}N-(*S*)-CH$_2$OH-*t*Bu in CDCl$_3$.

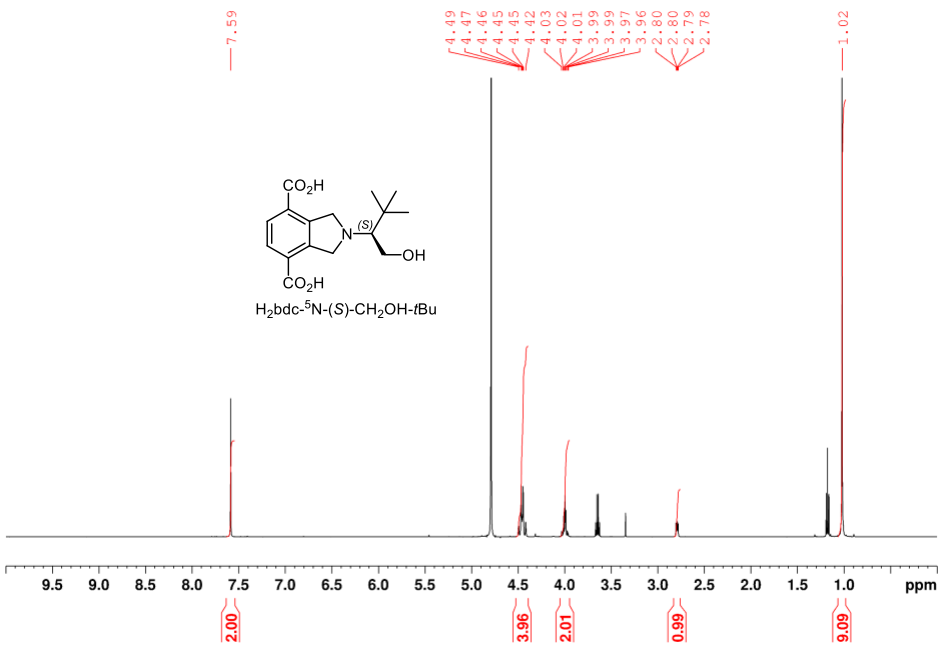

Figure 3.29 ^{1}H NMR spectrum of H$_2$bdc-^{5}N-(*S*)-CH$_2$OH-*t*Bu in D$_2$O/NaOD.

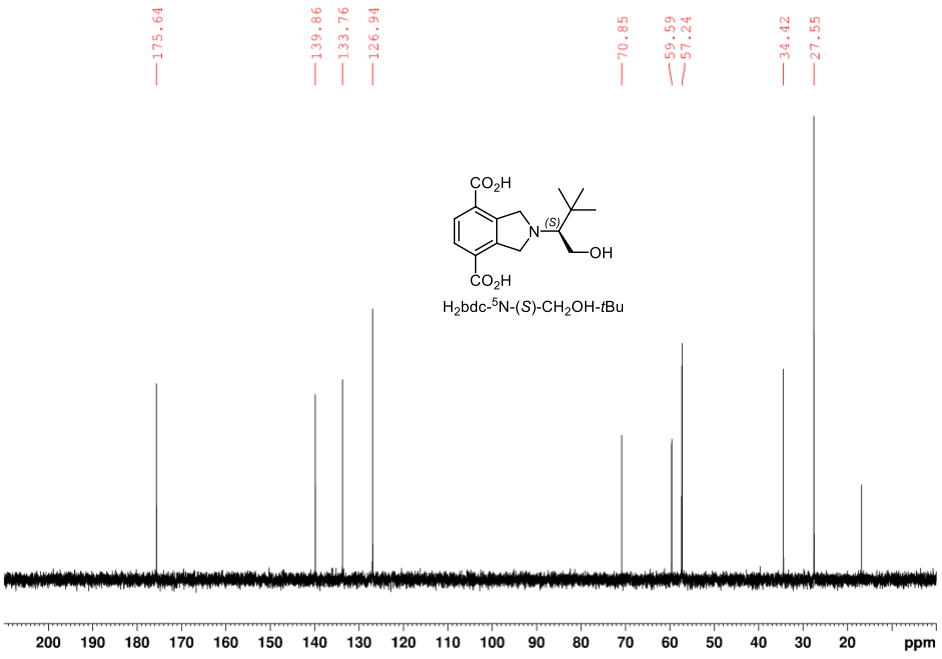

Figure 3.30 ^{13}C NMR spectrum of H$_2$bdc-^{5}N-(*S*)-CH$_2$OH-*t*Bu in D$_2$O/NaOD.

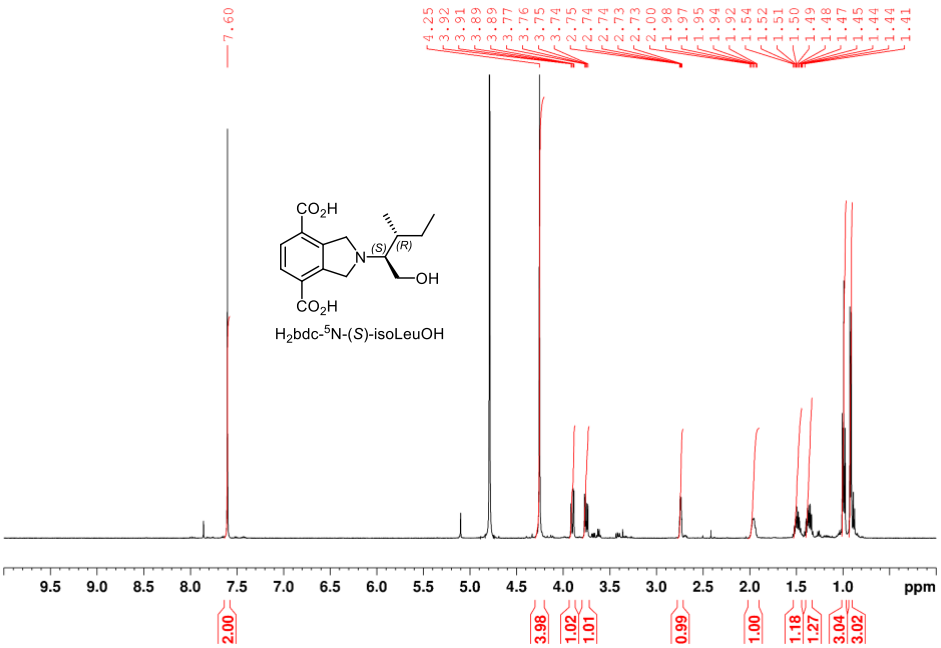

Figure 3.31 ^{1}H NMR spectrum of H2bdc-^{5}N-(*S*)-isoLeuOH in D2O/NaOD.

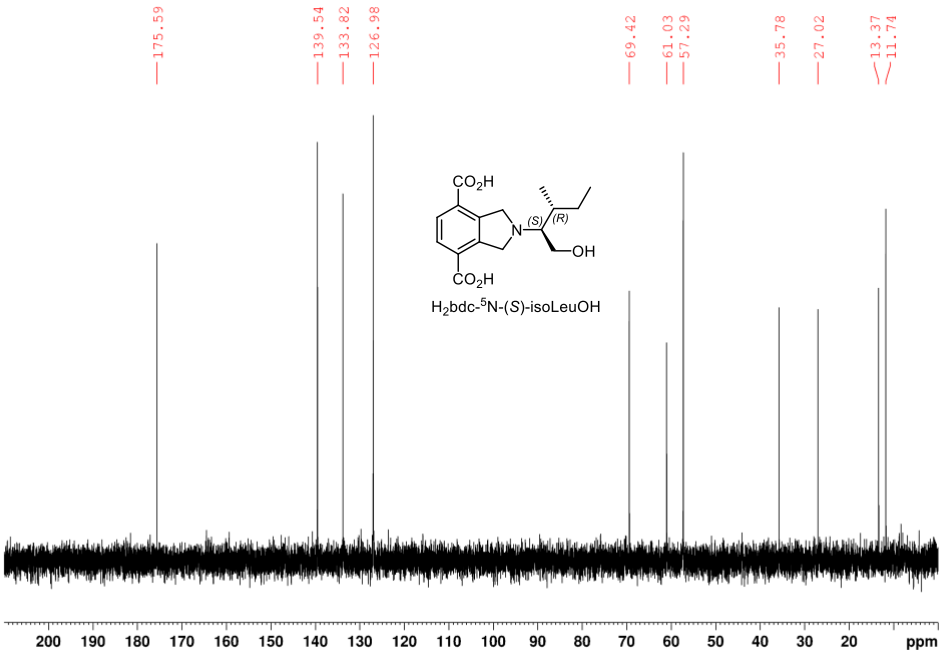

Figure 3.32 ^{13}C NMR spectrum of H2bdc-^{5}N-(*S*)-isoLeuOH in D2O/NaOD.

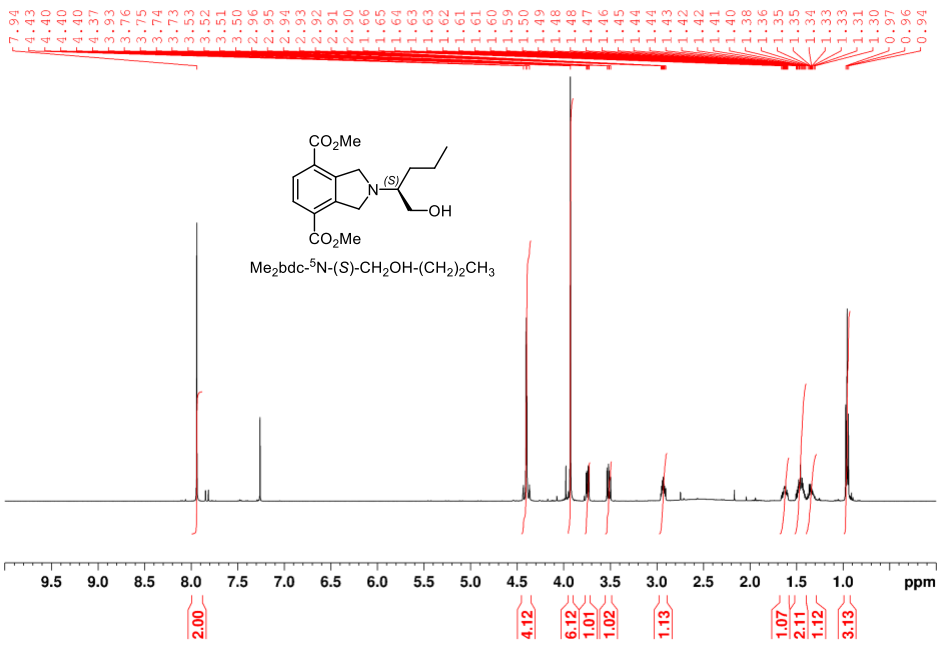

Figure 3.33 ^{1}H NMR spectrum of Me$_2$bdc-^{5}N-(*S*)-CH$_2$OH-(CH$_2$)$_2$CH$_3$ in CDCl$_3$.

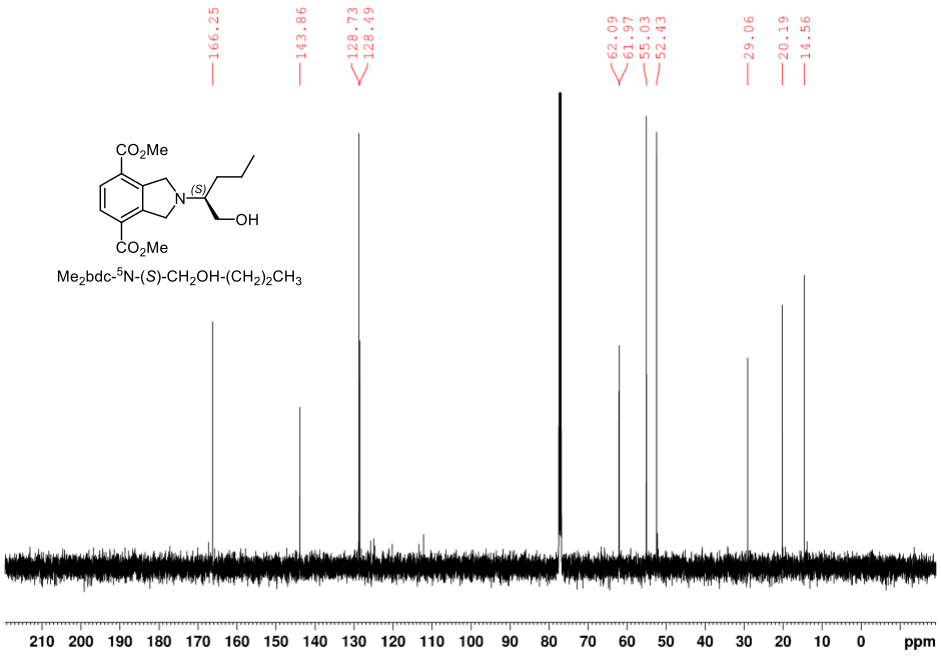

Figure 3.34 ^{13}C NMR spectrum of Me$_2$bdc-^{5}N-(*S*)-CH$_2$OH-(CH$_2$)$_2$CH$_3$ in CDCl$_3$.

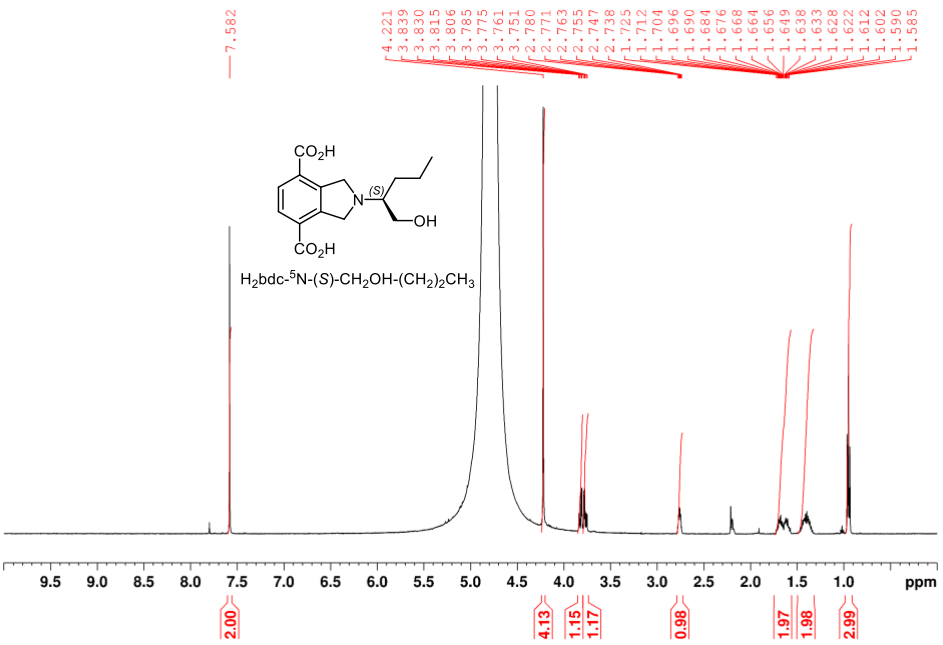

Figure 3.35 ^{1}H NMR spectrum of H$_2$bdc-^{5}N-(*S*)-CH$_2$OH-(CH$_2$)$_2$CH$_3$ in D$_2$O/NaOD.

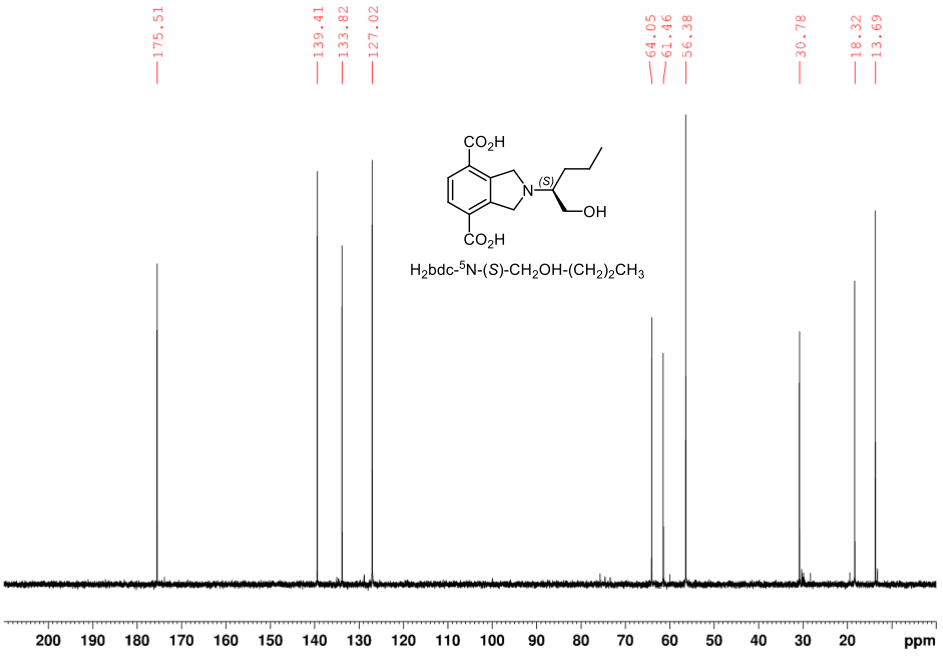

Figure 3.36 ^{13}C NMR spectrum of H$_2$bdc-^{5}N-(*S*)-CH$_2$OH-(CH$_2$)$_2$CH$_3$ in D$_2$O/NaOD.

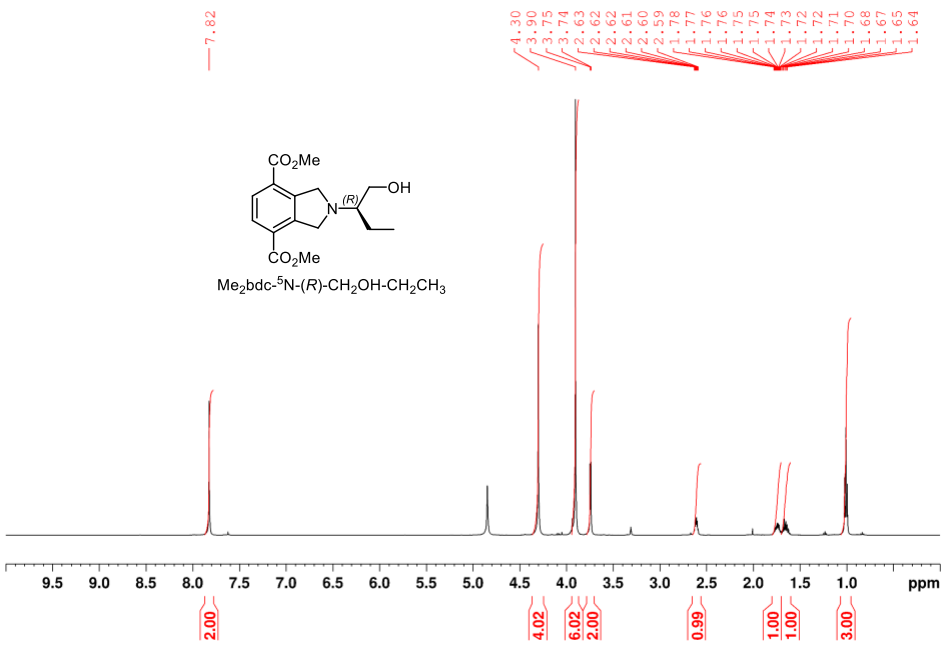

Figure 3.37 ^{1}H NMR spectrum of Me$_2$bdc-^{5}N-(*R*)-CH$_2$OH-CH$_2$CH$_3$ in MeOD-*d*$_4$.

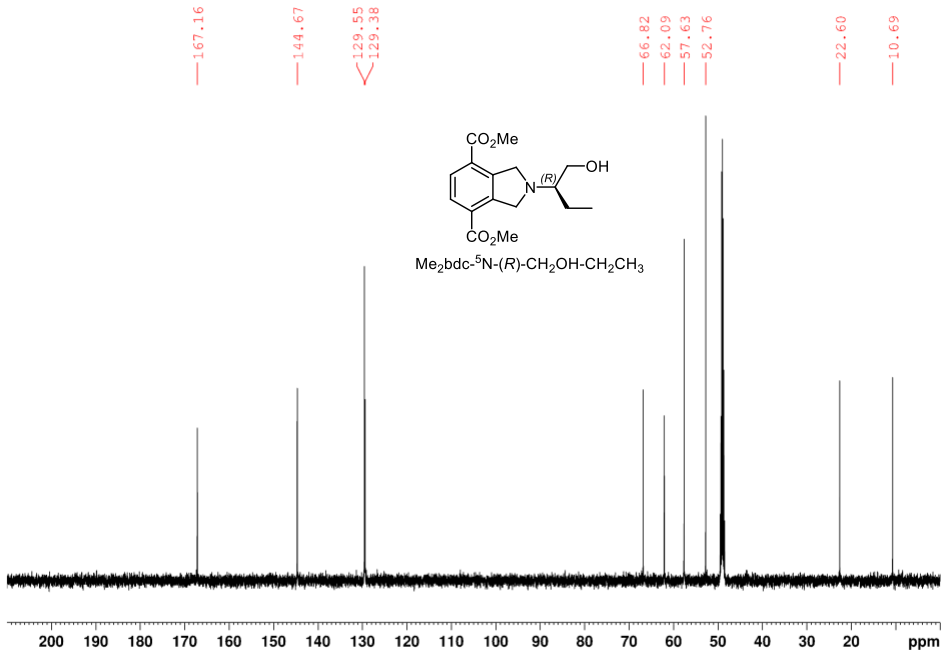

Figure 3.38 ^{13}C NMR spectrum of Me$_2$bdc-^{5}N-(*R*)-CH$_2$OH-CH$_2$CH$_3$ in MeOD-*d*$_4$.

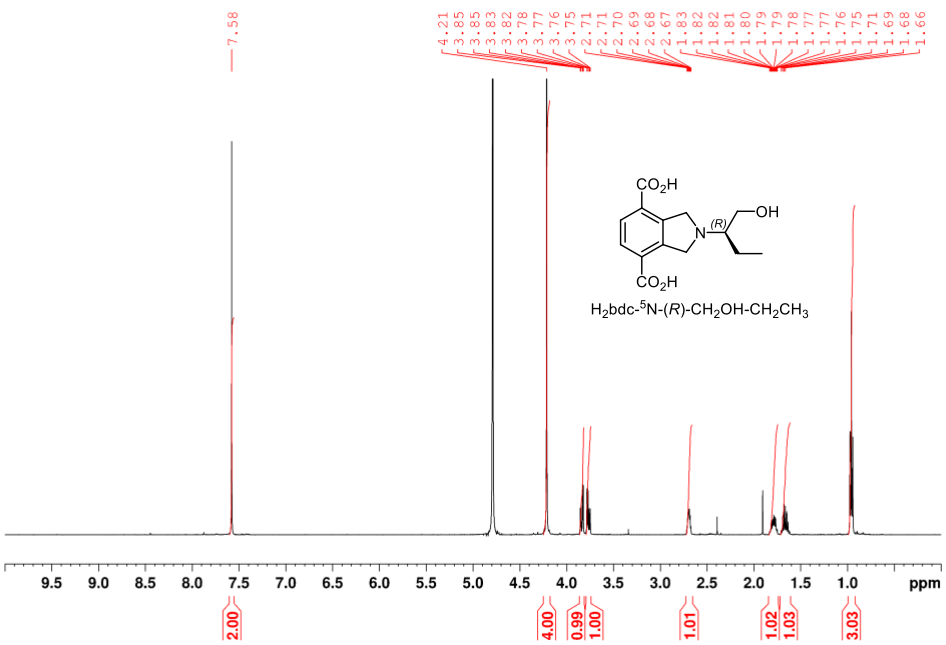

Figure 3.39 ^{1}H NMR spectrum of H2bdc-^{5}N-(*R*)-CH2OH-CH2CH3 in D2O/NaOD.

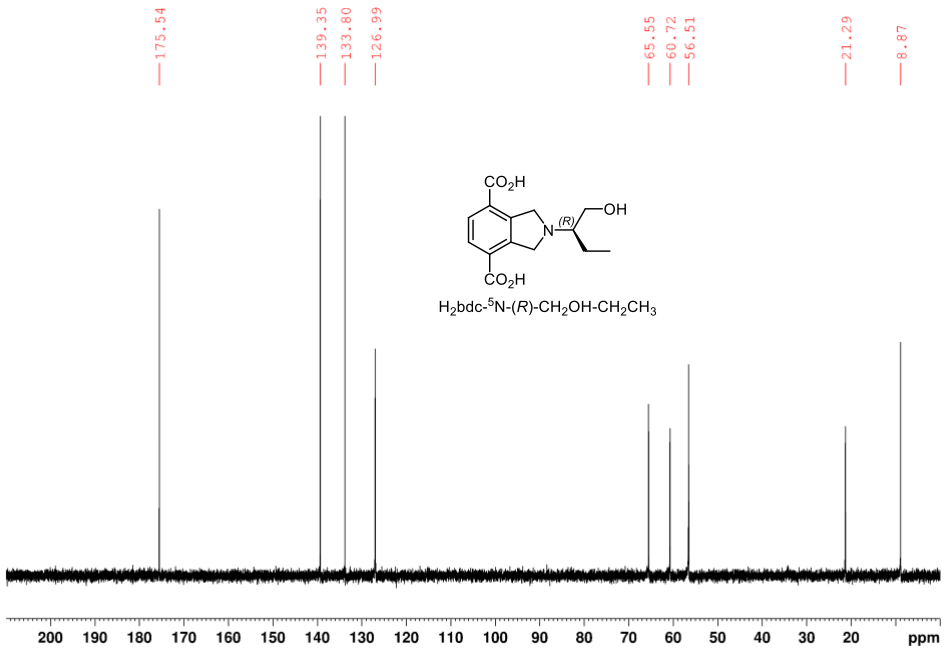

Figure 3.40 ^{13}C NMR spectrum of H2bdc-^{5}N-(*R*)-CH2OH-CH2CH3 in D2O/NaOD.

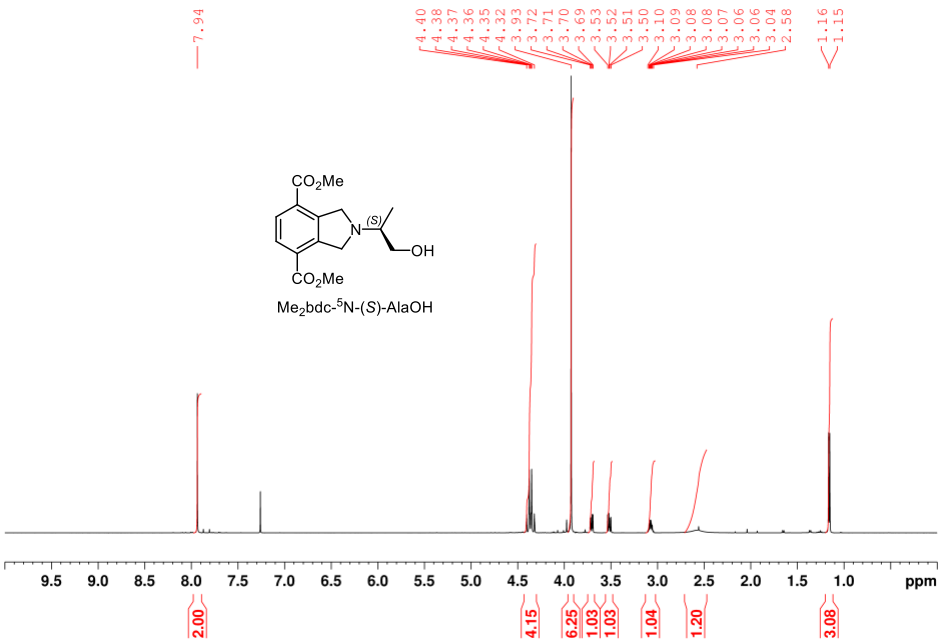

Figure 3.41 ^{1}H NMR spectrum of Me$_2$bdc-^{5}N-(*S*)-AlaOH in CDCl$_3$.

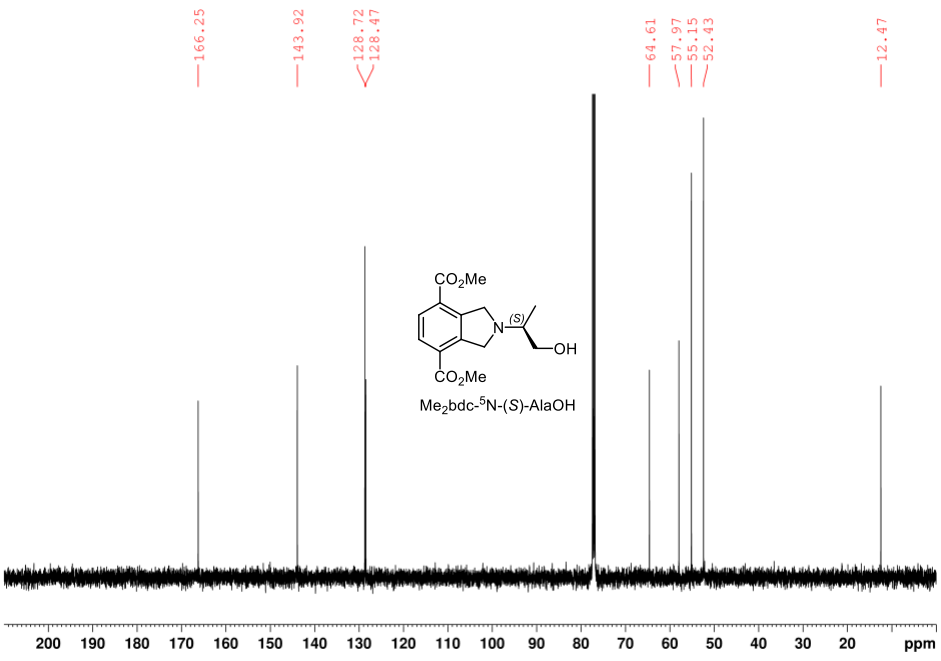

Figure 3.42 ^{13}C NMR spectrum of Me$_2$bdc-^{5}N-(*S*)-AlaOH in CDCl$_3$.

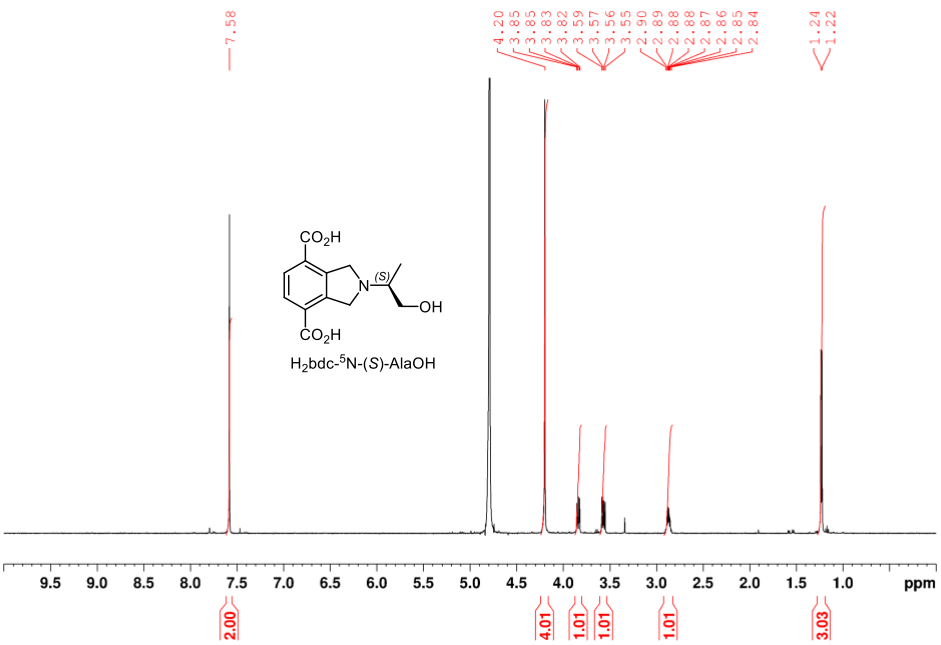

Figure 3.43 ^{1}H NMR spectrum of H$_2$bdc-^{5}N-(*S*)-AlaOH in D$_2$O/NaOD.

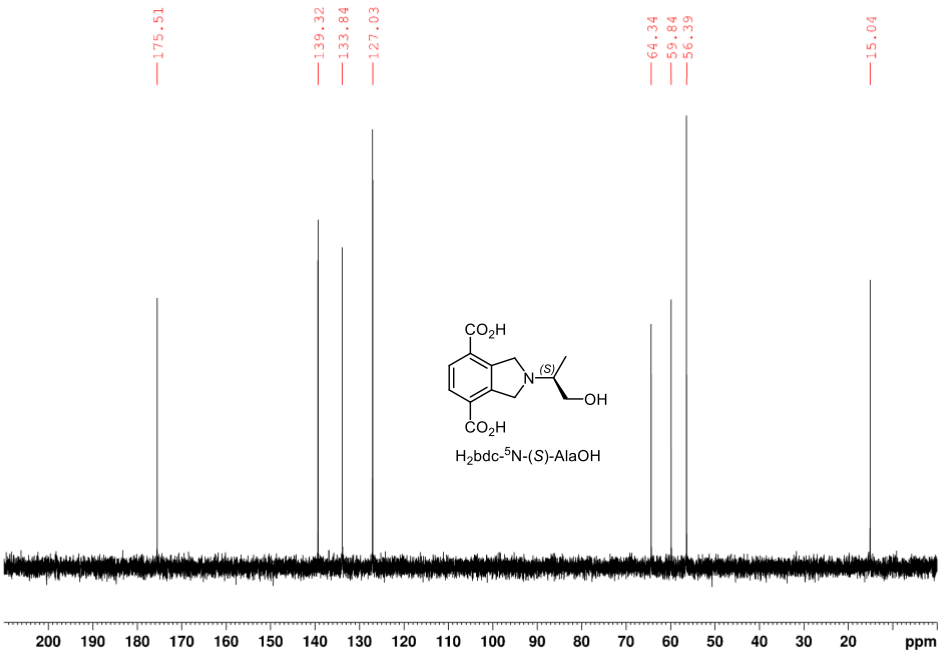

Figure 3.44 ^{13}C NMR spectrum of H$_2$bdc-^{5}N-(*S*)-AlaOH in D$_2$O/NaOD.

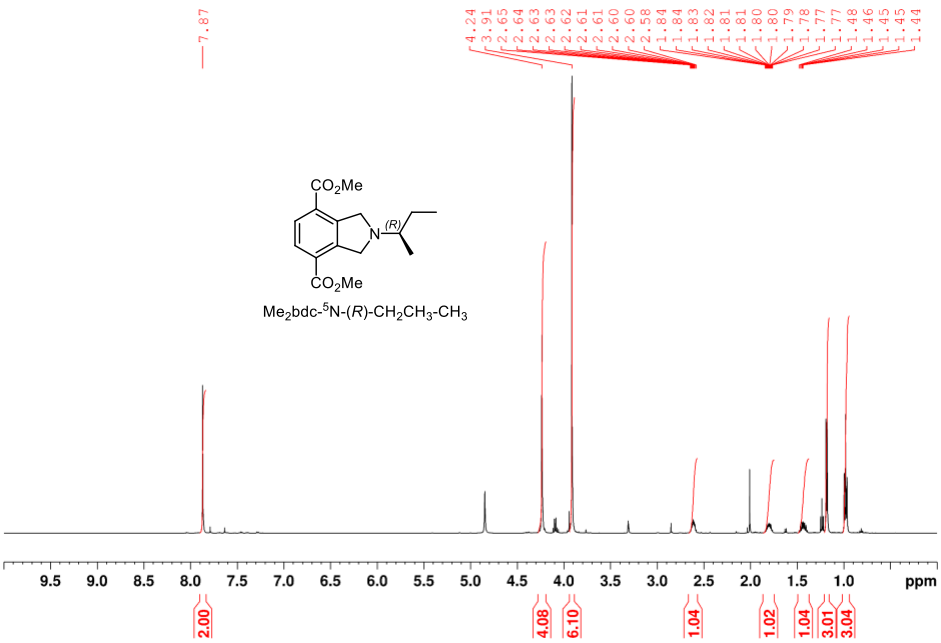

Figure 3.45 ^{1}H NMR spectrum of Me$_2$bdc-^{5}N-(*R*)-CH$_2$CH$_3$-CH$_3$ in MeOD-*d*$_4$.

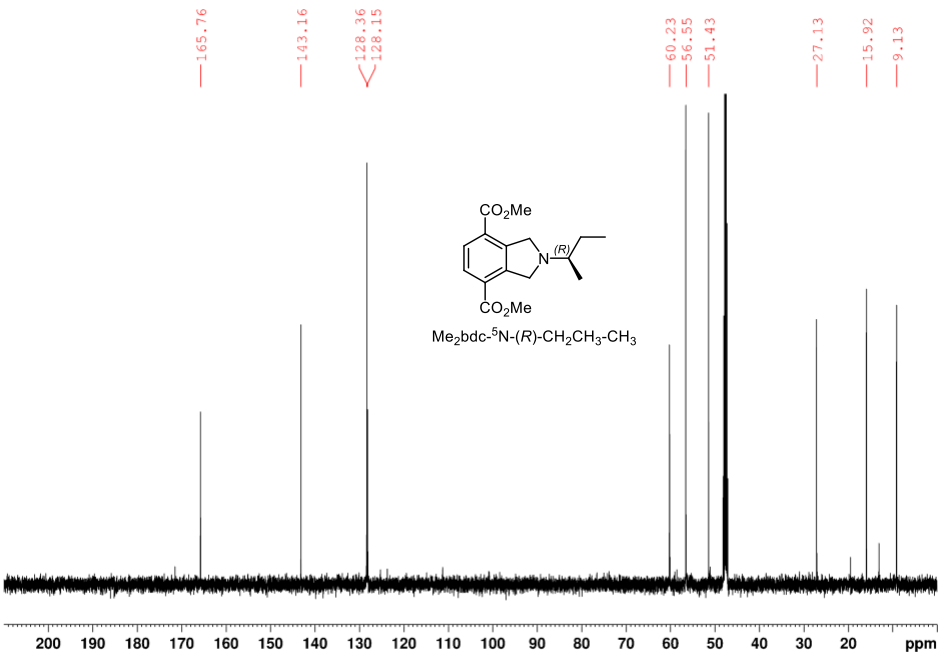

Figure 3.46 ^{13}C NMR spectrum of Me$_2$bdc-^{5}N-(*R*)-CH$_2$CH$_3$-CH$_3$ in MeOD-*d*$_4$.

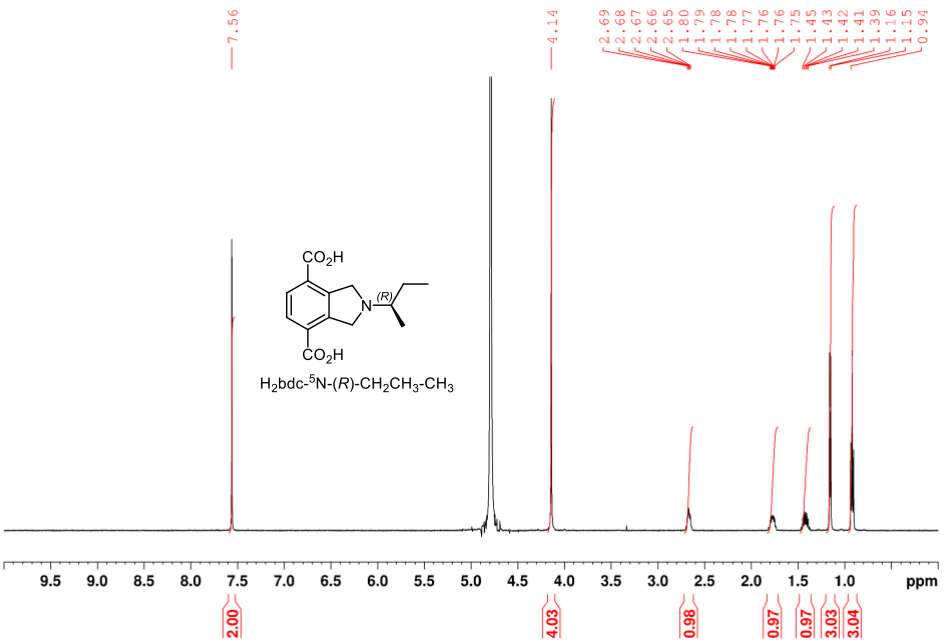

Figure 3.47 ^{1}H NMR spectrum of H_2bdc-^{5}N-(*R*)-CH_2CH_3-CH_3 in D_2O/NaOD.

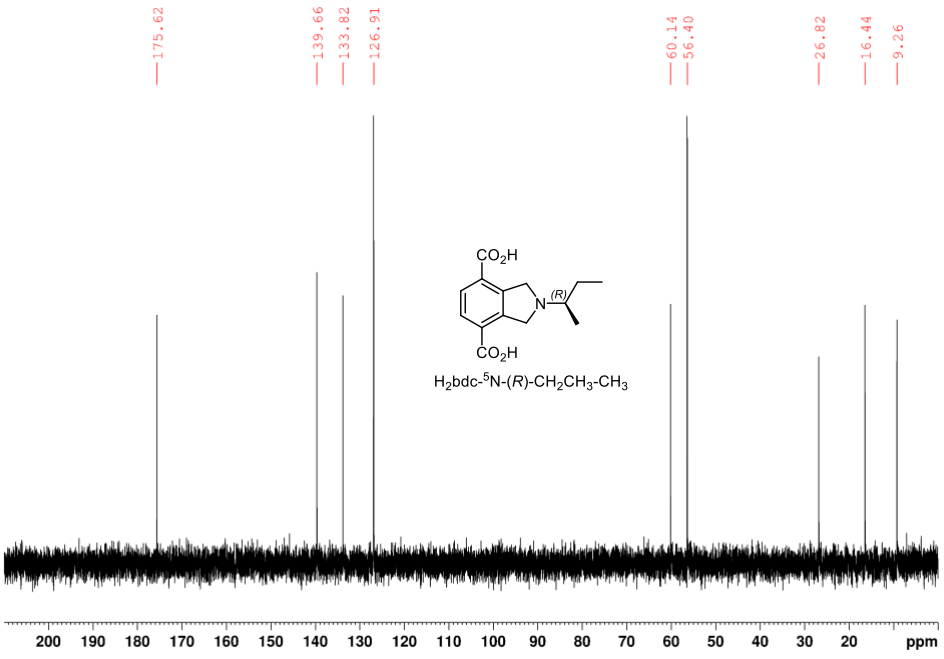

Figure 3.48 ^{13}C NMR spectrum of H_2bdc-^{5}N-(*R*)-CH_2CH_3-CH_3 in D_2O/NaOD.

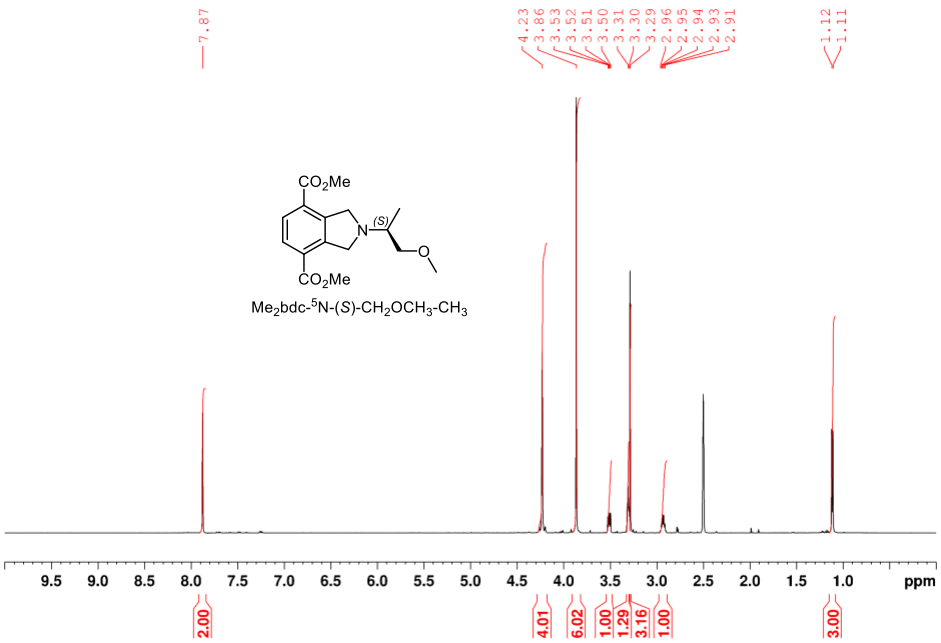

Figure 3.49 ^{1}H NMR spectrum of Me$_2$bdc-^{5}N-(*S*)-CH$_2$OCH$_3$-CH$_3$ in DMSO-*d6*.

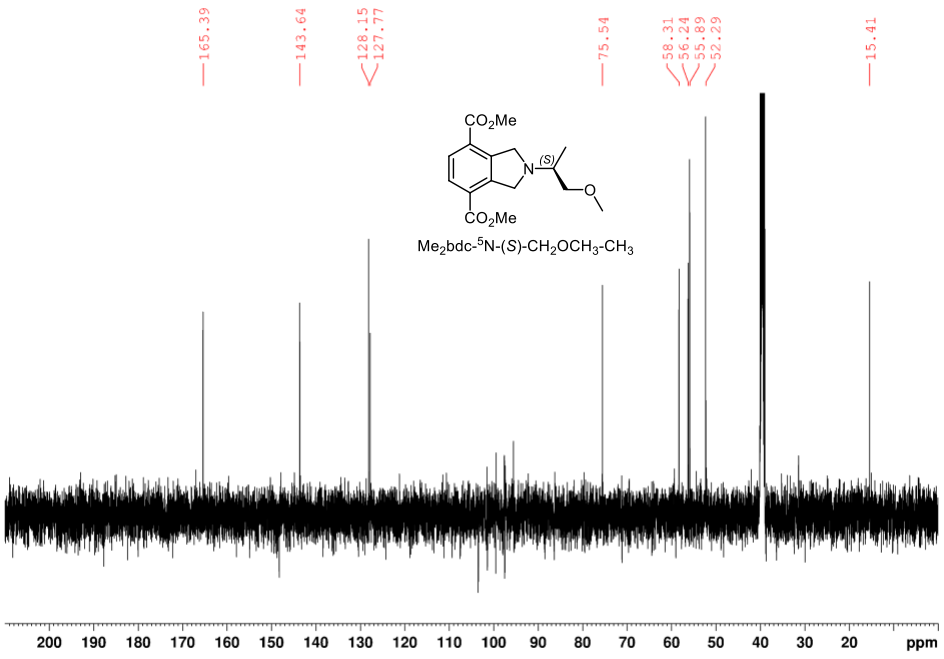

Figure 3.50 ^{13}C NMR spectrum of Me$_2$bdc-^{5}N-(*S*)-CH$_2$OCH$_3$-CH$_3$ in DMSO-*d6*.

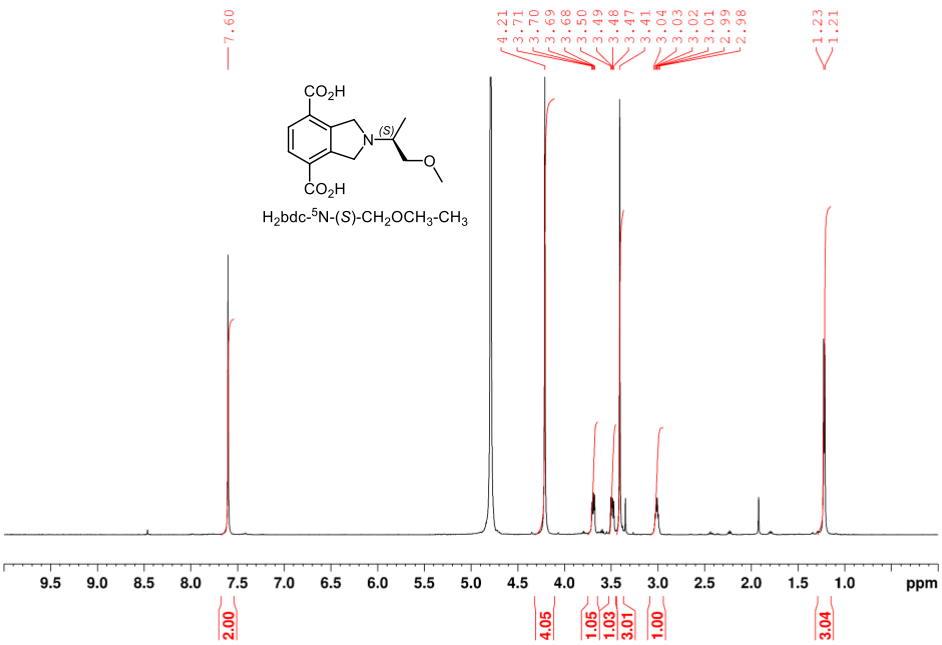

Figure 3.51 ^{1}H NMR spectrum of H2bdc-^{5}N-(*S*)-CH2OCH3-CH3 in D2O/NaOD.

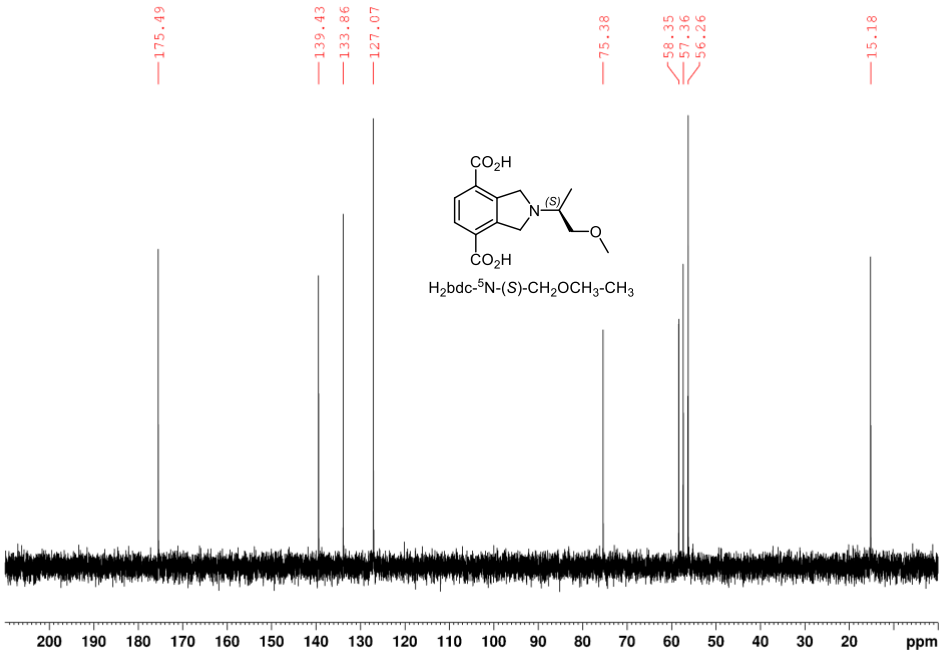

Figure 3.52 ^{13}C NMR spectrum of H2bdc-^{5}N-(*S*)-CH2OCH3-CH3 in D2O/NaOD.

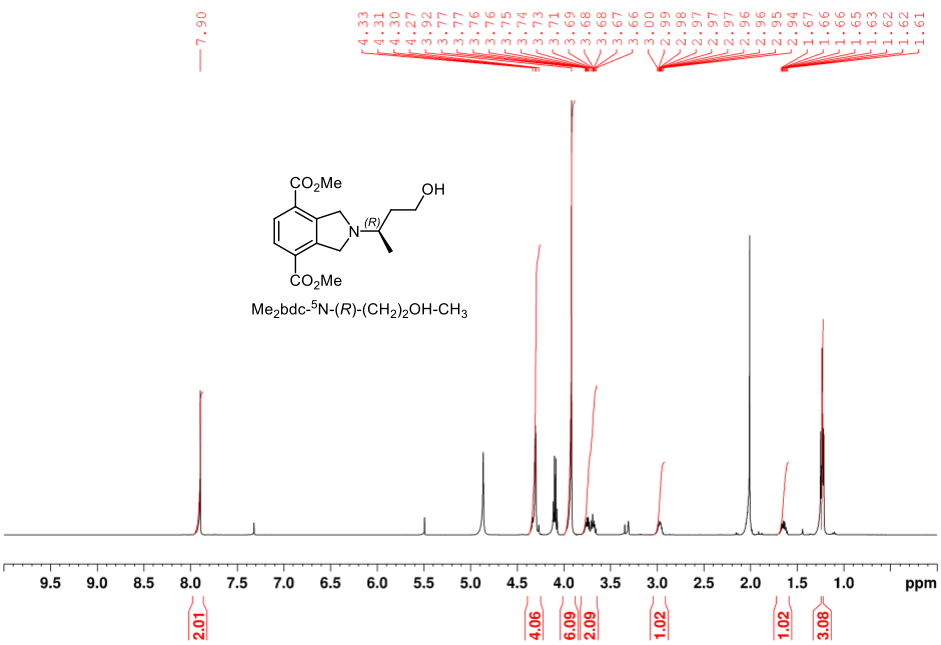

Figure 3.53 ^{1}H NMR spectrum of Me$_2$bdc-^{5}N-(*R*)-(CH$_2$)$_2$OH-CH$_3$ in MeOD-*d*$_4$.

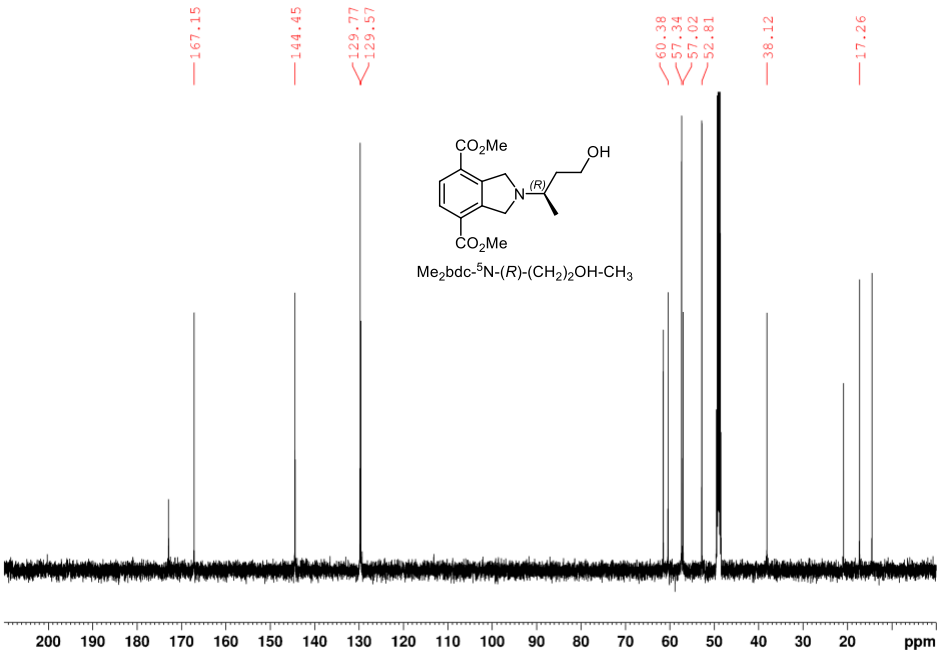

Figure 3.54 ^{13}C NMR spectrum of Me$_2$bdc-^{5}N-(*R*)-(CH$_2$)$_2$OH-CH$_3$ in MeOD-*d*$_4$.

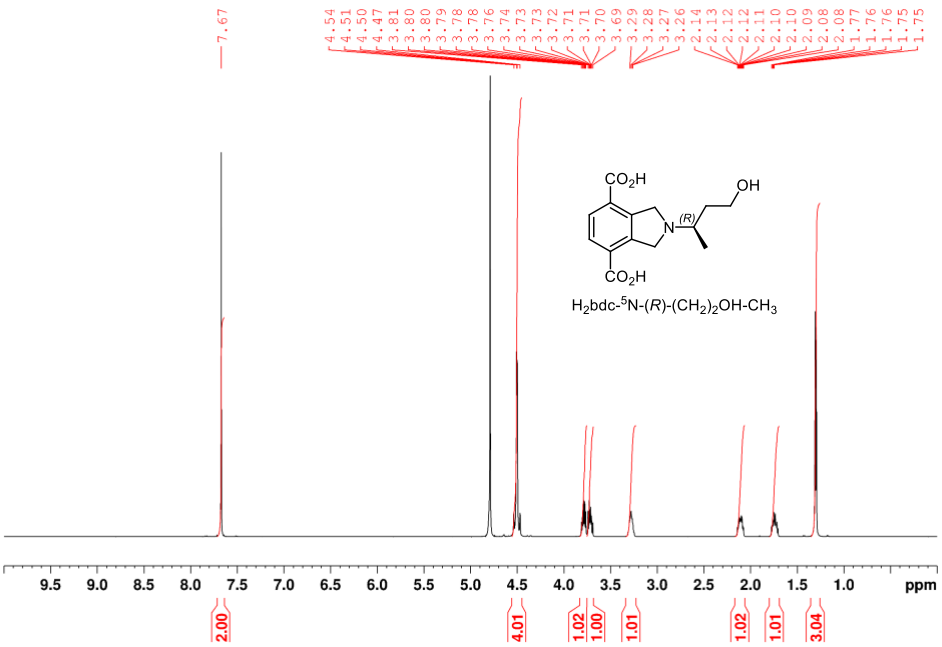

Figure 2.1 ^{1}H NMR spectrum of H_2bdc-^{5}N-(*R*)-$(CH_2)_2$OH-CH_3 in D_2O/NaOD.

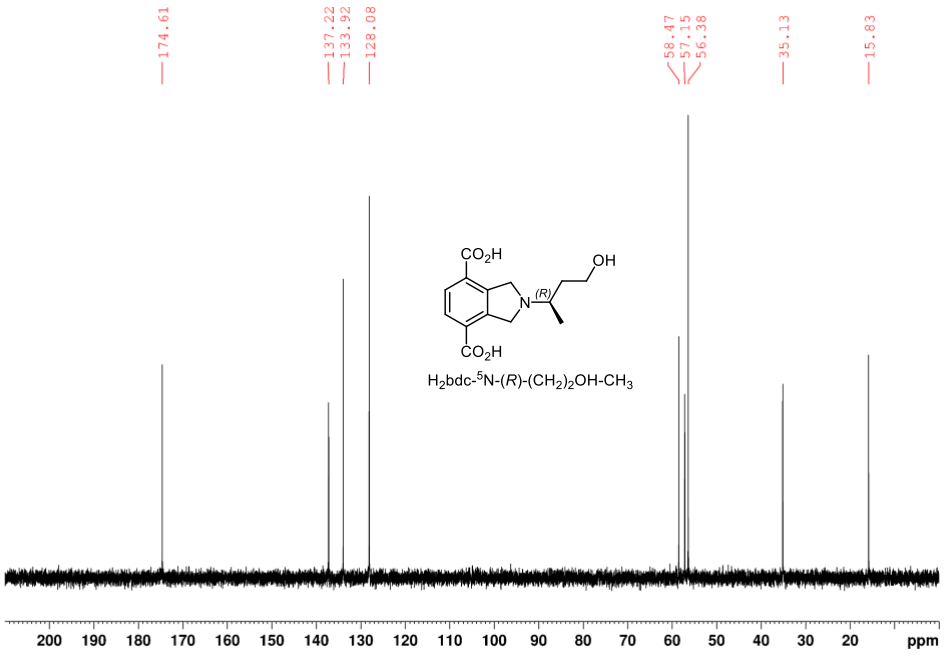

Figure 2.2 ^{13}C NMR spectrum of H_2bdc-^{5}N-(*R*)-$(CH_2)_2$OH-CH_3 in D_2O/NaOD.

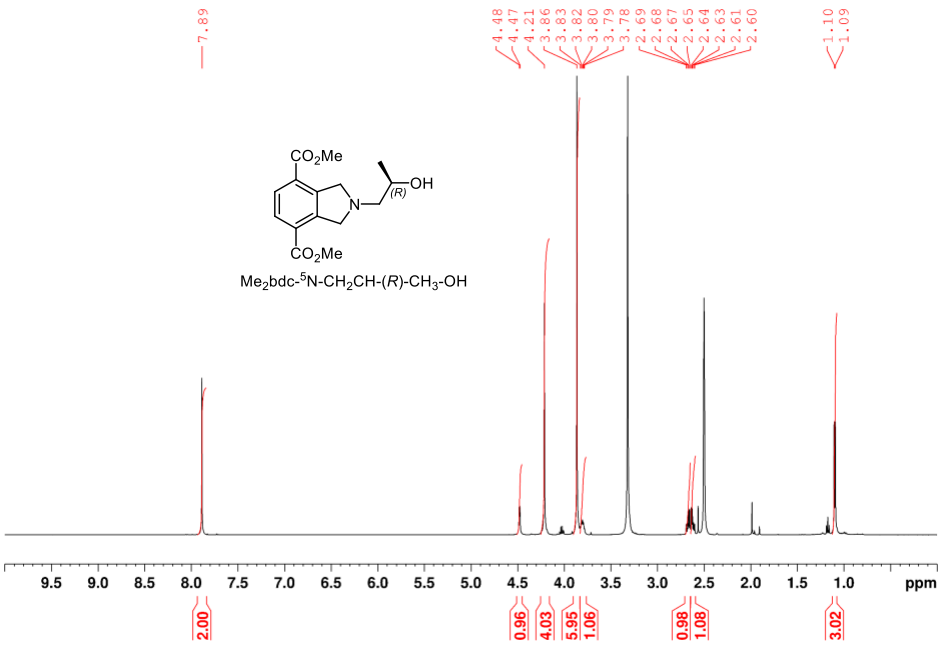

Figure 2.3 ^{1}H NMR spectrum of Me$_2$bdc-^{5}N-CH$_2$CH-(*R*)-CH$_3$-OH in DMSO-*d6*.

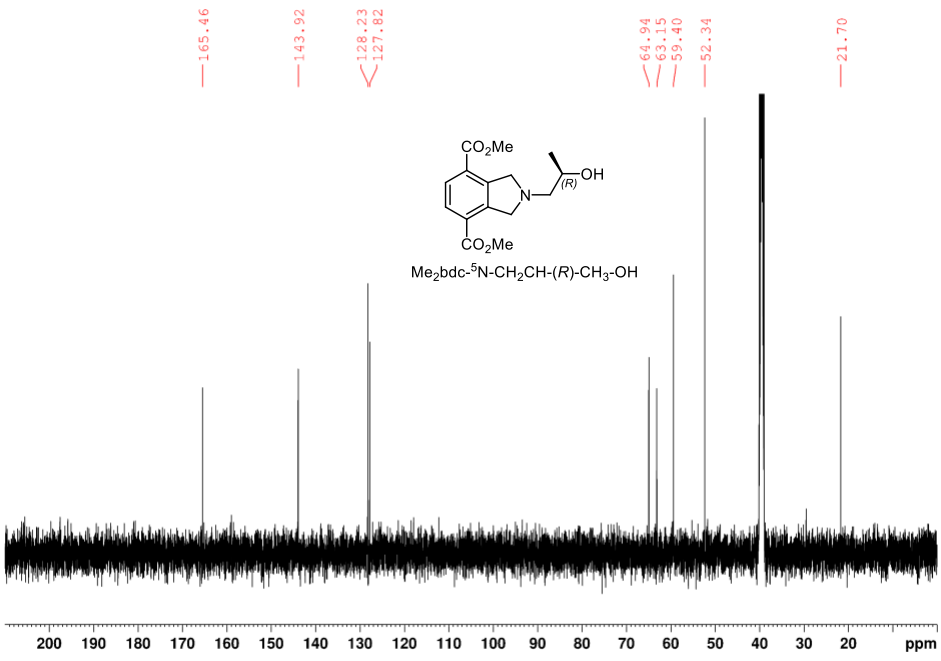

Figure 2.4 ^{13}C NMR spectrum of Me$_2$bdc-^{5}N-CH$_2$CH-(*R*)-CH$_3$-OH in DMSO-*d6*.

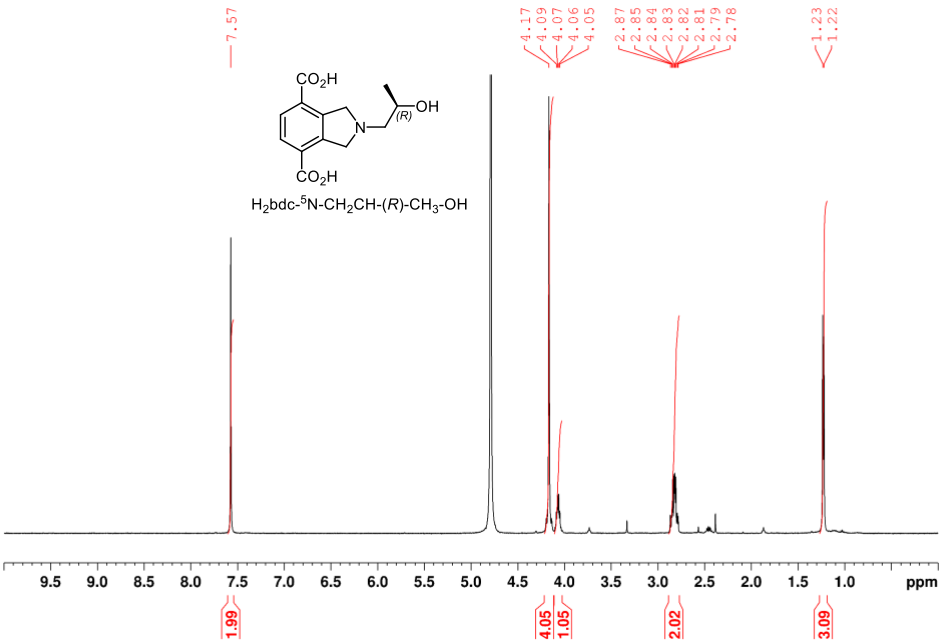

Figure 2.5 ^{1}H NMR spectrum of H$_2$bdc-^{5}N-CH$_2$CH-(*R*)-CH$_3$-OH in D$_2$O/NaOD.

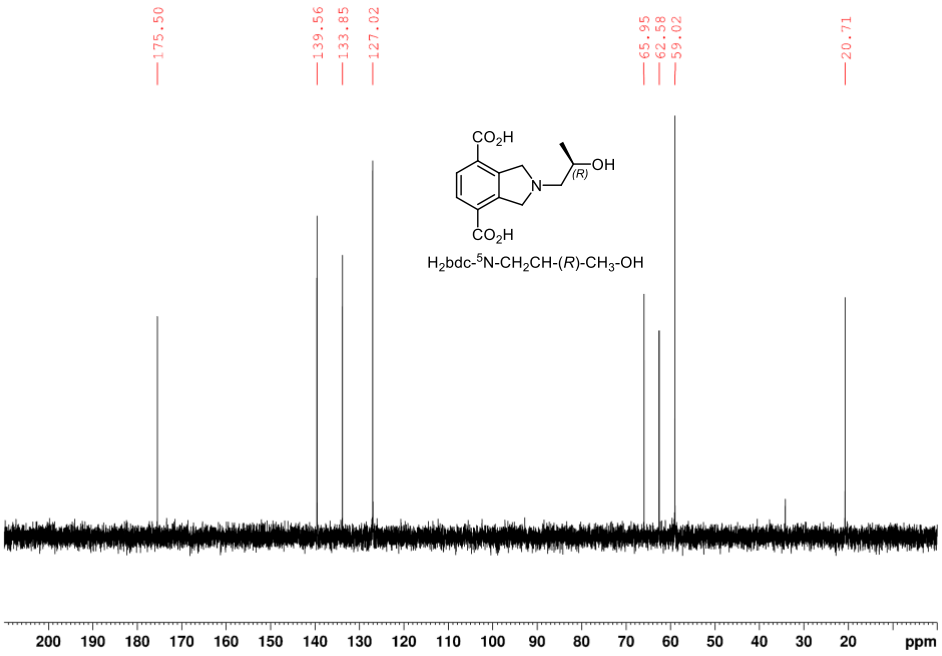

Figure 2.6 ^{13}C NMR spectrum of H$_2$bdc-^{5}N-CH$_2$CH-(*R*)-CH$_3$-OH in D$_2$O/NaOD.

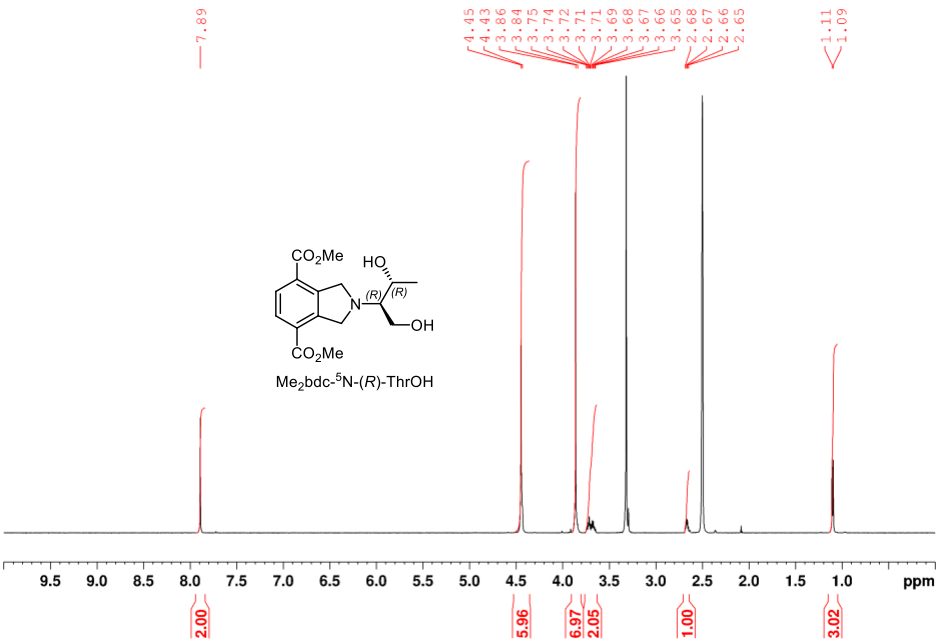

Figure 2.7 ^{1}H NMR spectrum of Me$_2$bdc-^{5}N-(*R*)-ThrOH in DMSO-*d6*.

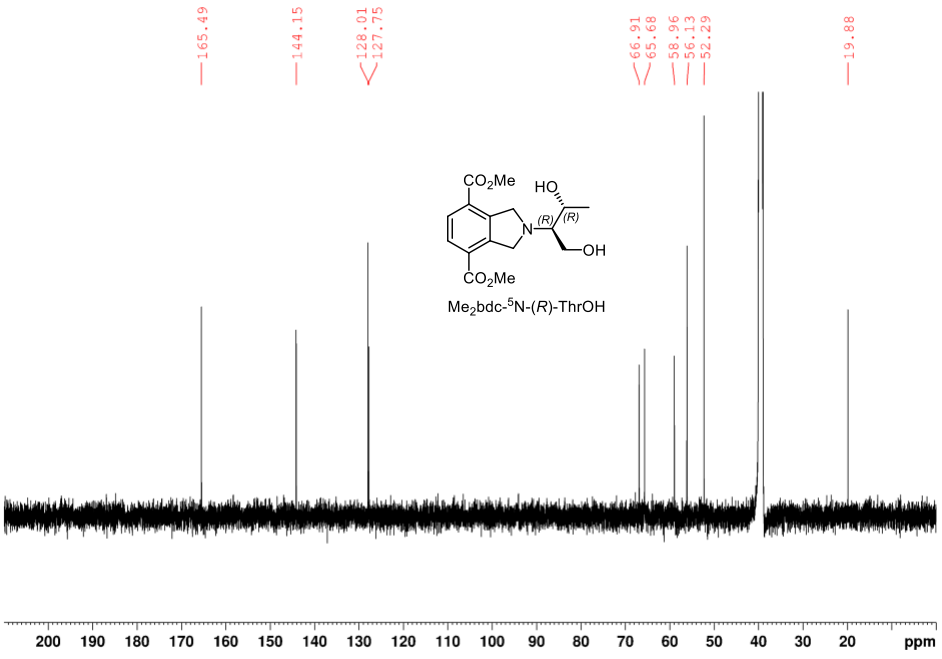

Figure 2.8 ^{13}C NMR spectrum of Me$_2$bdc-^{5}N-(*R*)-ThrOH in DMSO-*d6*.

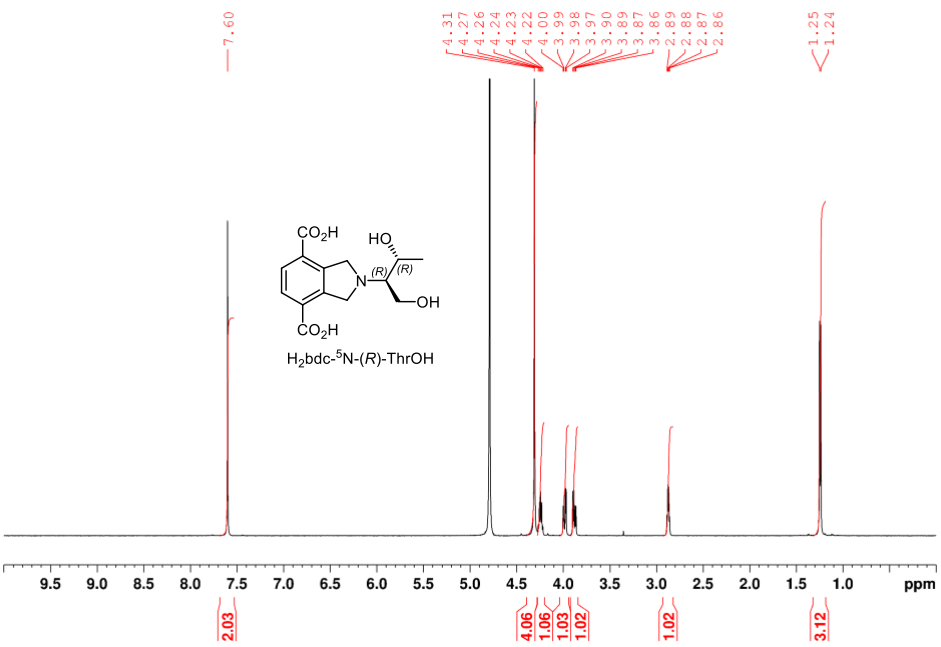

Figure 2.9 ^{1}H NMR spectrum of H$_2$bdc-^{5}N-(*R*)-ThrOH in D$_2$O/NaOD.

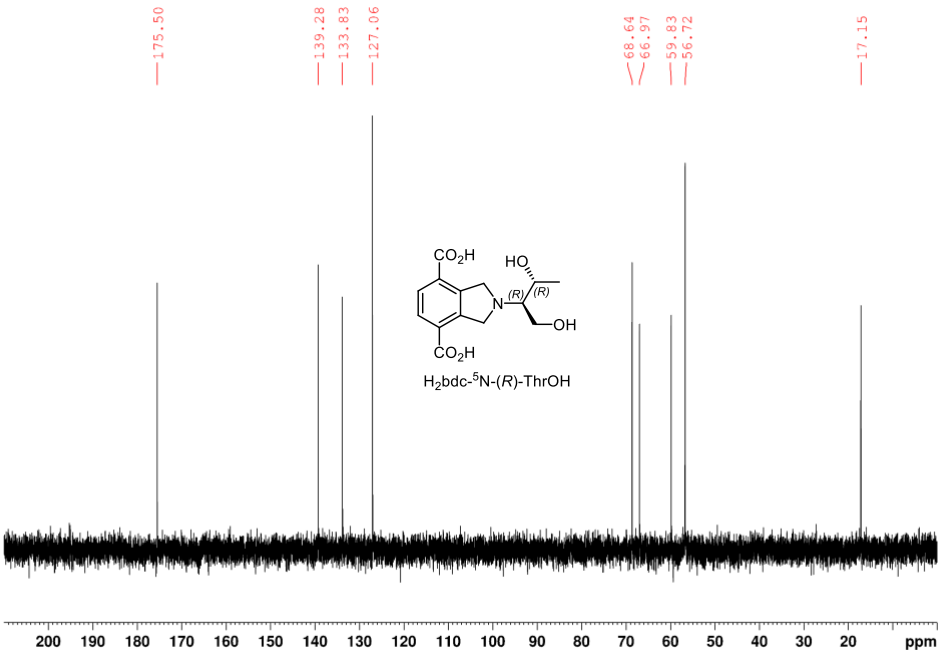

Figure 2.10 ^{13}C NMR spectrum of H$_2$bdc-^{5}N-(*R*)-ThrOH in D$_2$O/NaOD.

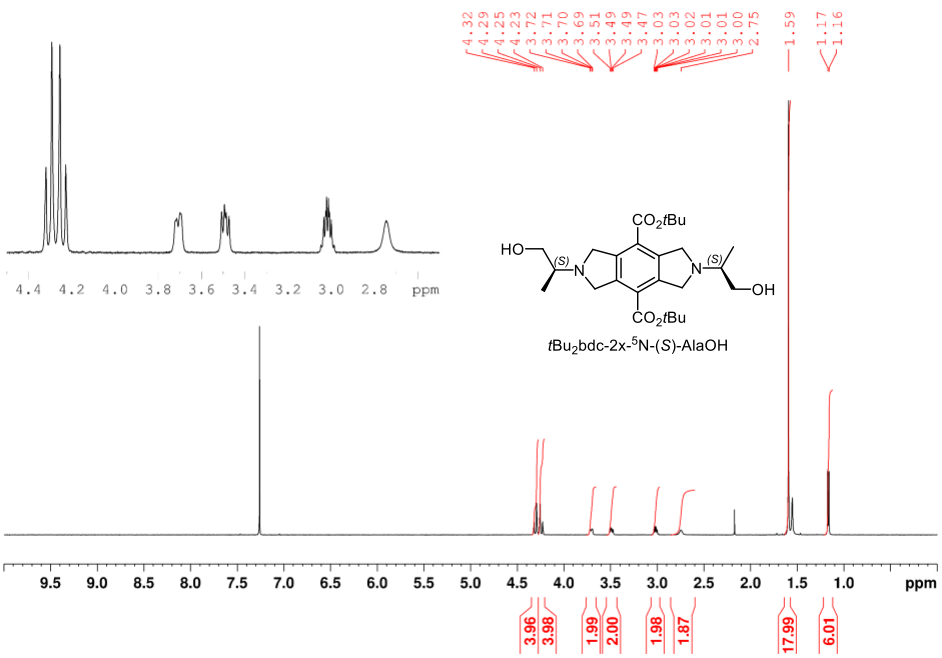

Figure 2.11 ^{1}H NMR spectrum of *t*Bu2bdc-2x-^{5}N-(*S*)-AlaOH in $CDCl_3$.

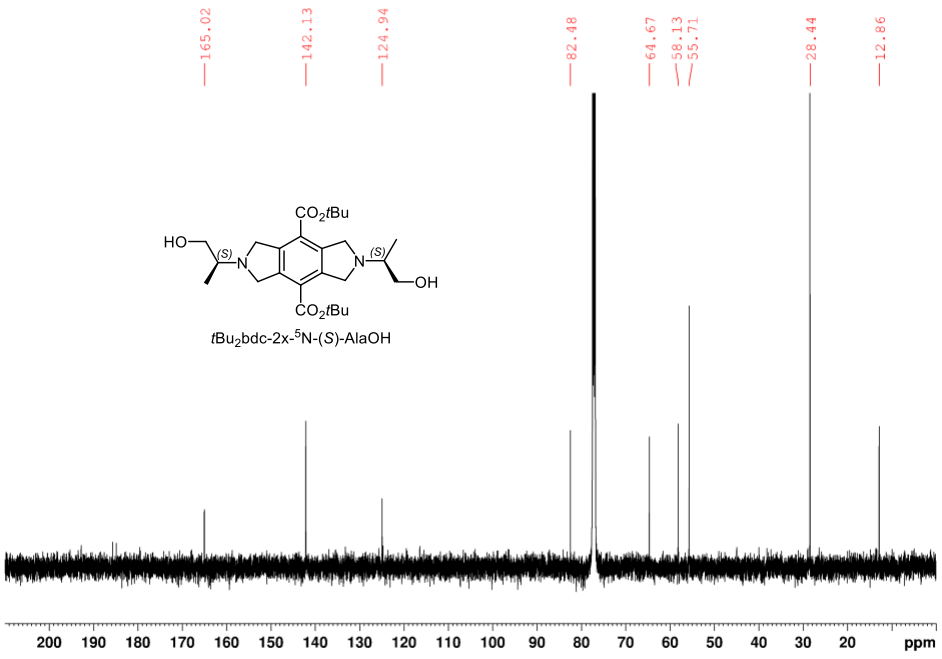

Figure 2.12 ^{13}C NMR spectrum of *t*Bu2bdc-2x-^{5}N-(*S*)-AlaOH in $CDCl_3$.

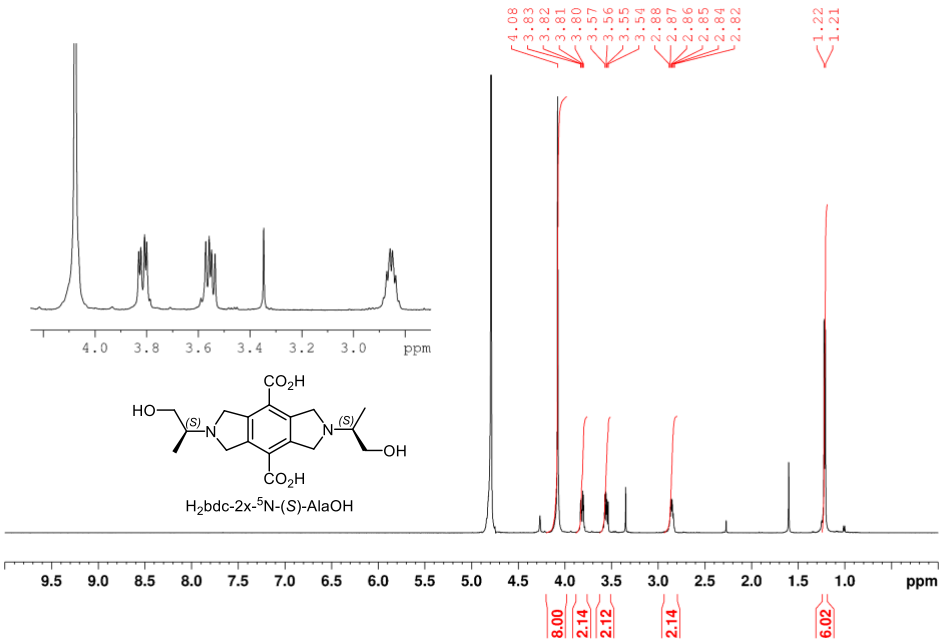

Figure 2.13 ^{1}H NMR spectrum of H$_2$bdc-2x-^{5}N-(*S*)-AlaOH in D$_2$O/NaOD.

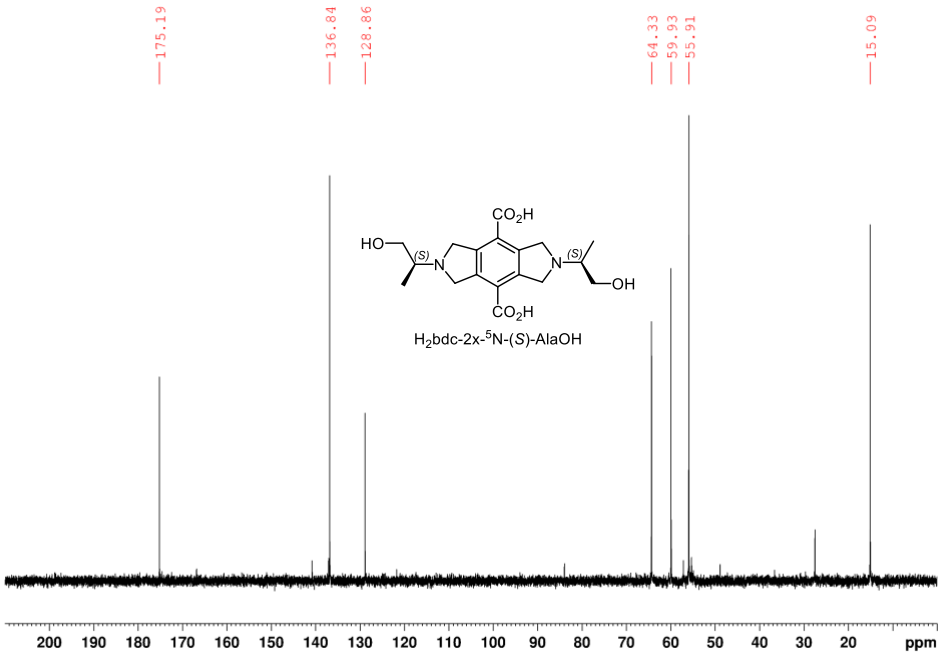

Figure 2.14 ^{13}C NMR spectrum of H$_2$bdc-2x-^{5}N-(*S*)-AlaOH in D$_2$O/NaOD.

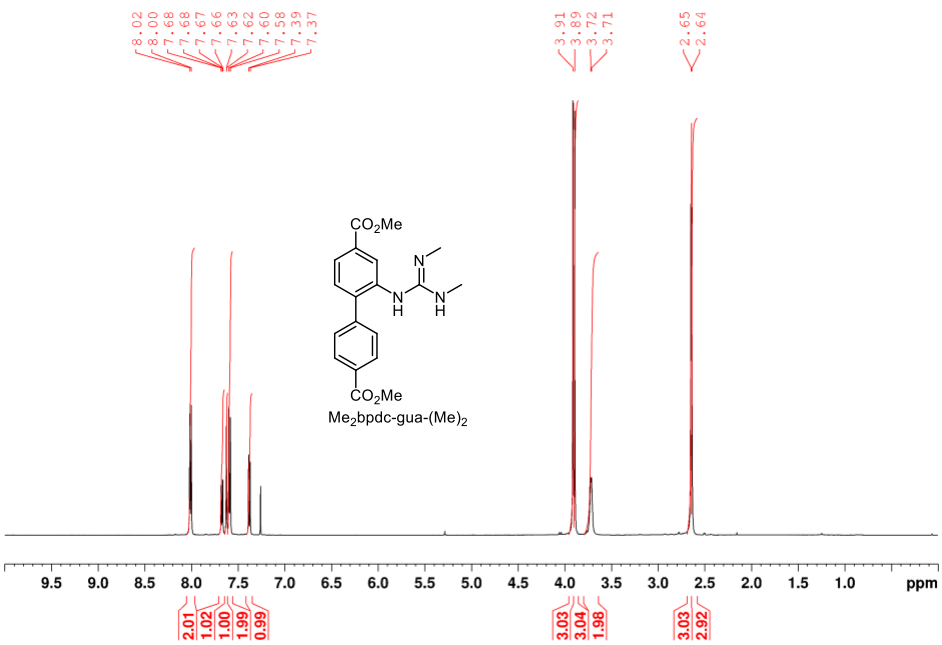

Figure 2.15 ^{1}H NMR spectrum of Me2bpdc-gua(Me)2 in CDCl3.

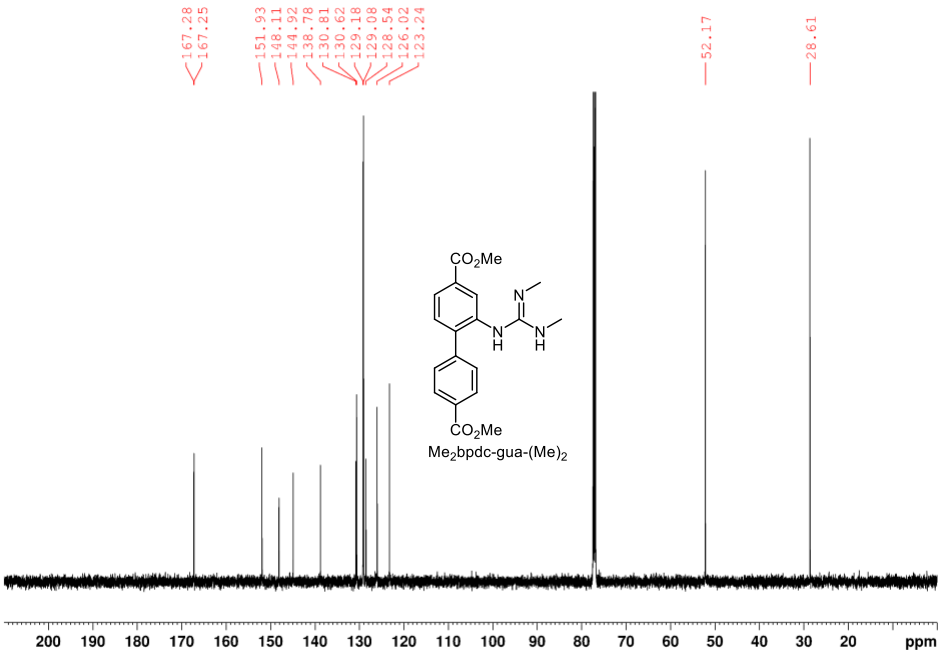

Figure 2.16 ^{13}C NMR spectrum of Me2bpdc-gua(Me)2 in CDCl3.

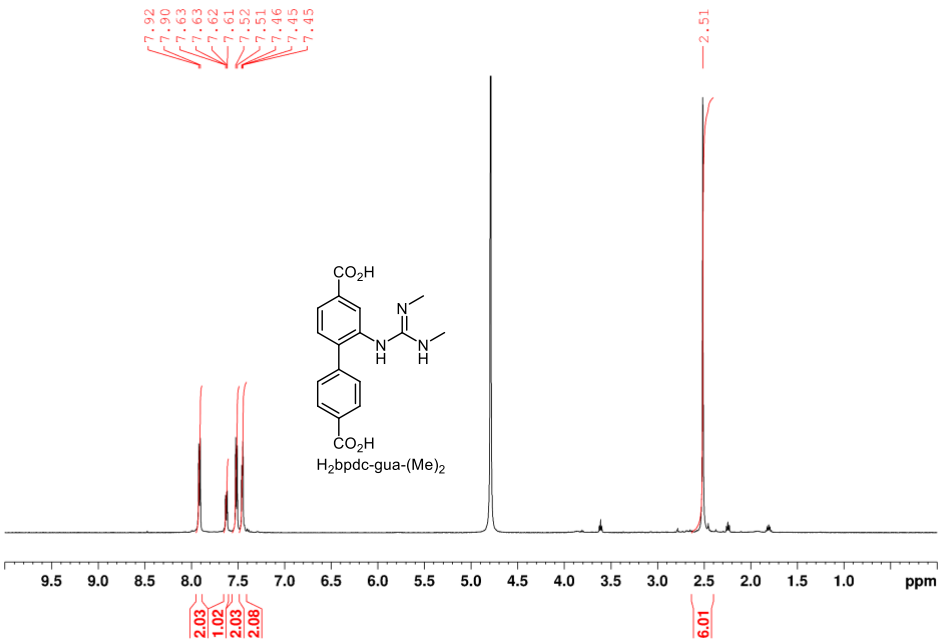

Figure 2.17 ^{1}H NMR spectrum of H_2bpdc-gua(Me)$_2$ in D_2O/NaOD.

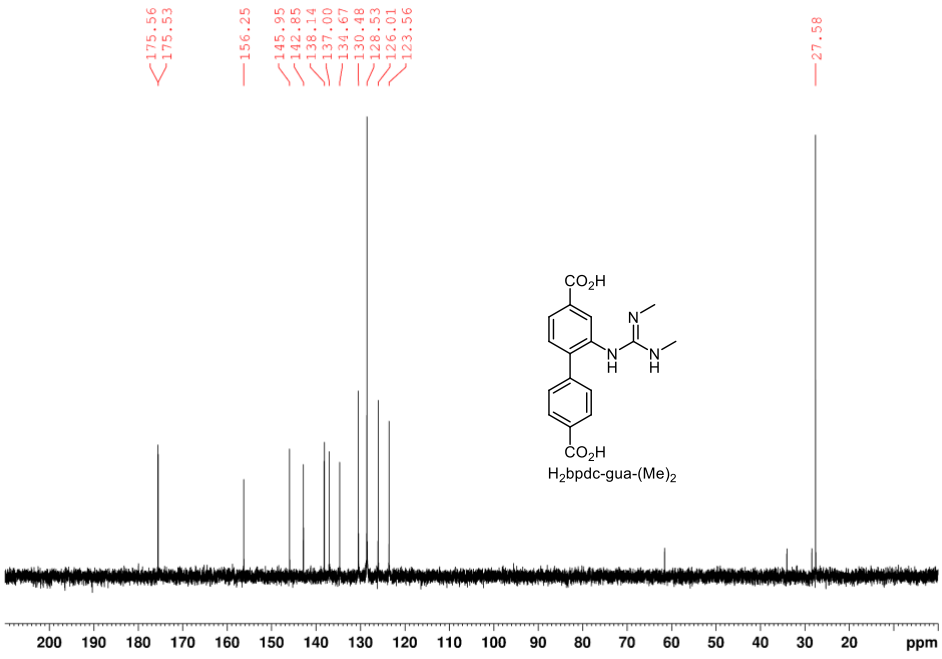

Figure 2.18 ^{13}C NMR spectrum of H_2bpdc-gua(Me)$_2$ in D_2O/NaOD.

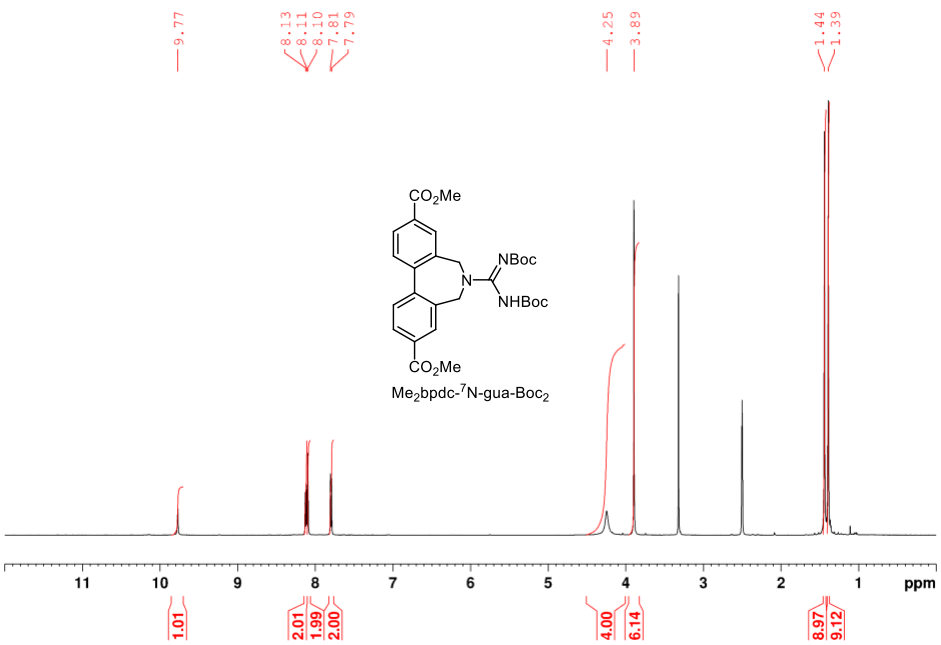

Figure 2.19 ^{1}H NMR spectrum of Me$_2$bpdc-^{7}N-gua-Boc$_2$ in *d6*-DMSO.

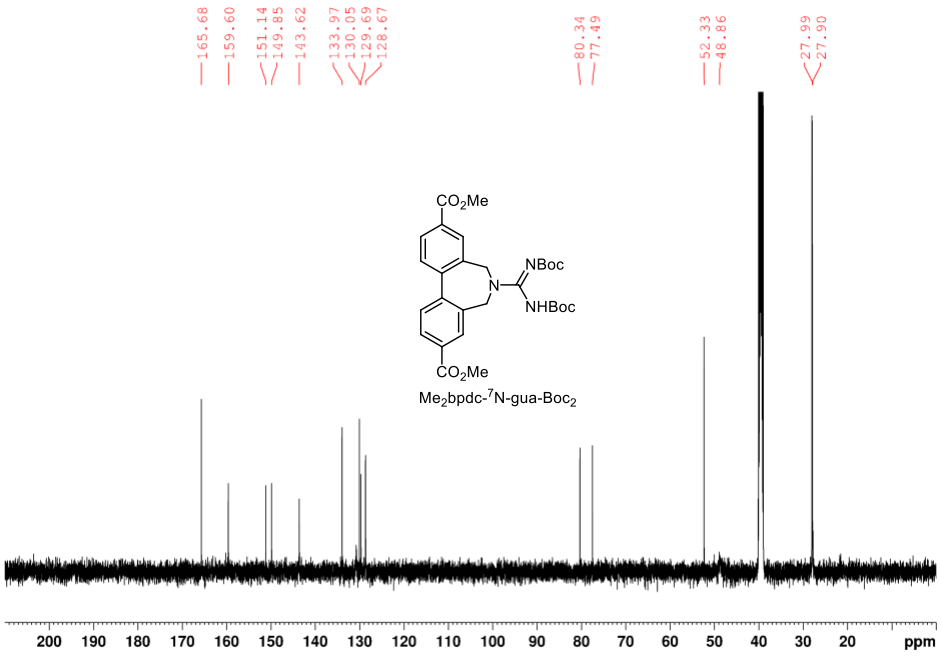

Figure 2.20 ^{13}C NMR spectrum of Me$_2$bpdc-^{7}N-gua-Boc$_2$ in *d6*-DMSO.

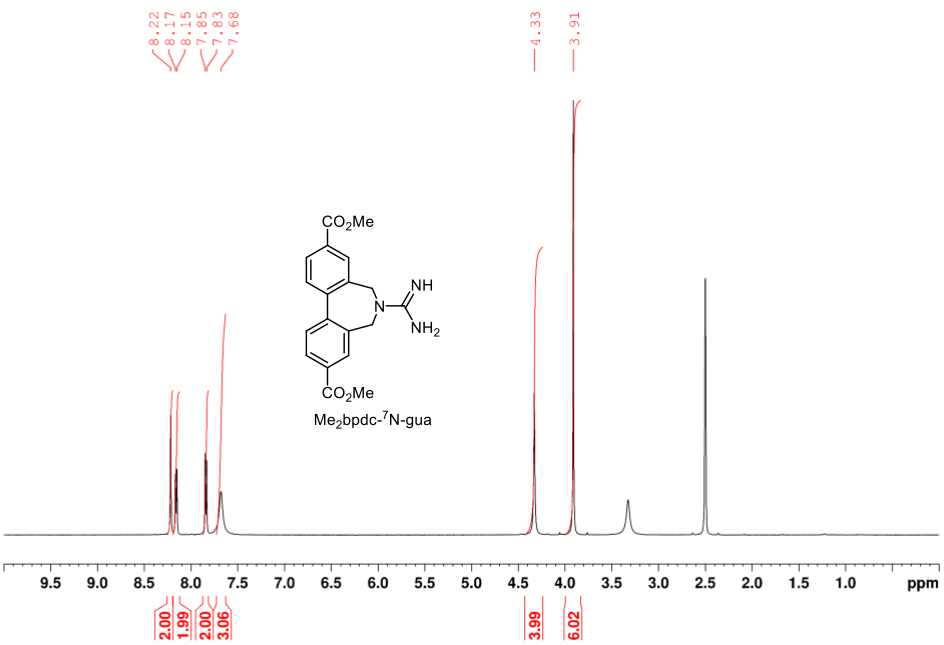

Figure 2.21 ^{1}H NMR spectrum of Me$_2$bpdc-^{7}N-gua in *d6*-DMSO.

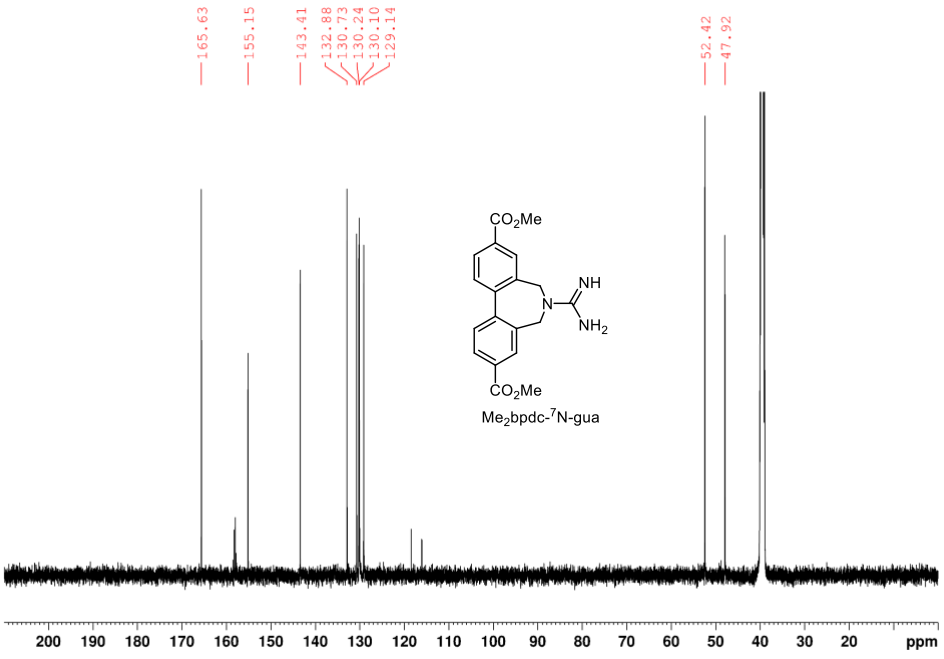

Figure 2.22 ^{13}C NMR spectrum of Me$_2$bpdc-^{7}N-gua in *d6*-DMSO.

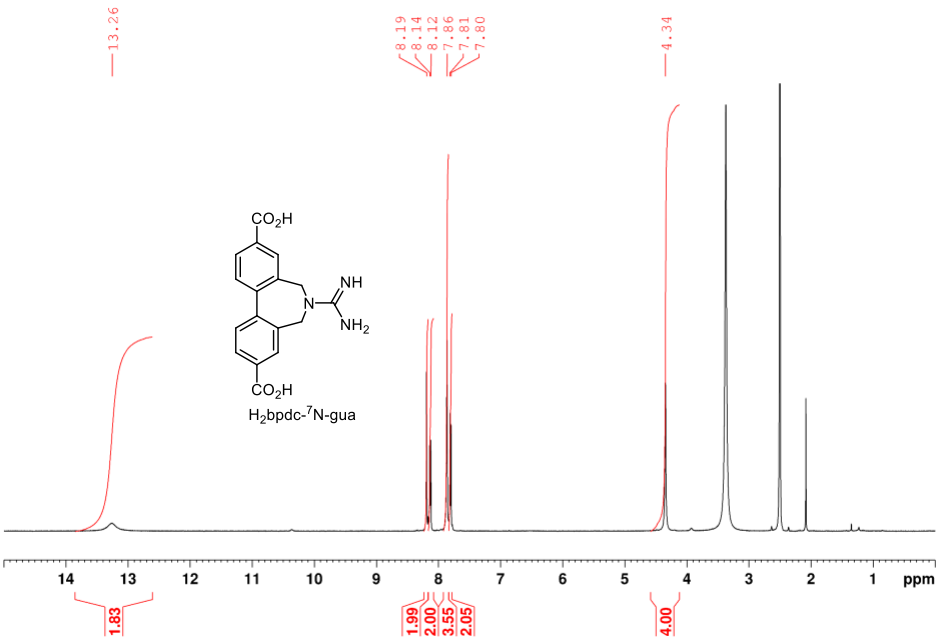

Figure 2.23 ^{1}H NMR spectrum of H2bpdc-^{7}N-gua in *d6*-DMSO.

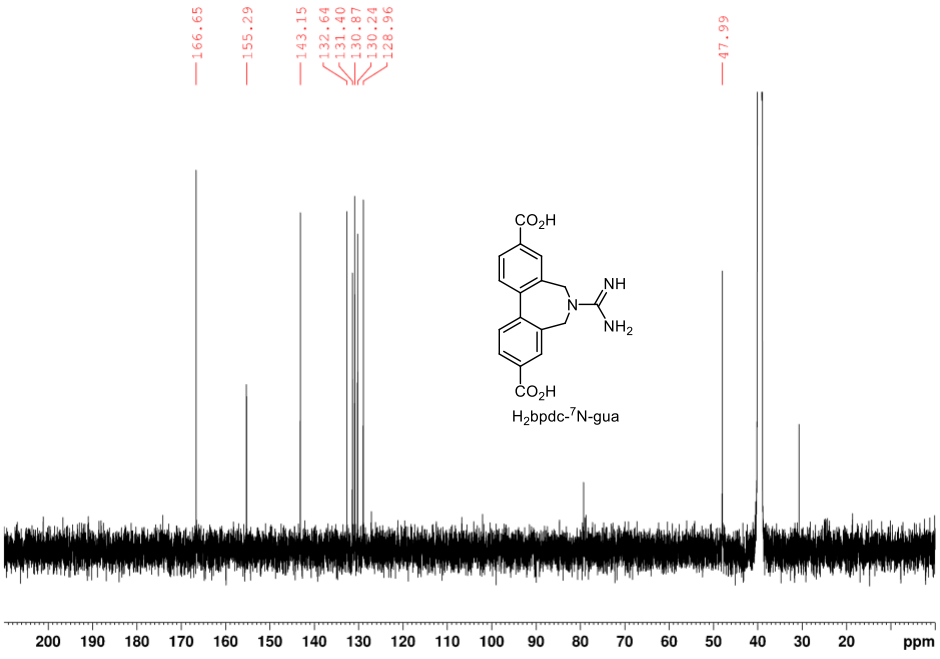

Figure 2.24 ^{13}C NMR spectrum of H2bpdc-^{7}N-gua in *d6*-DMSO.

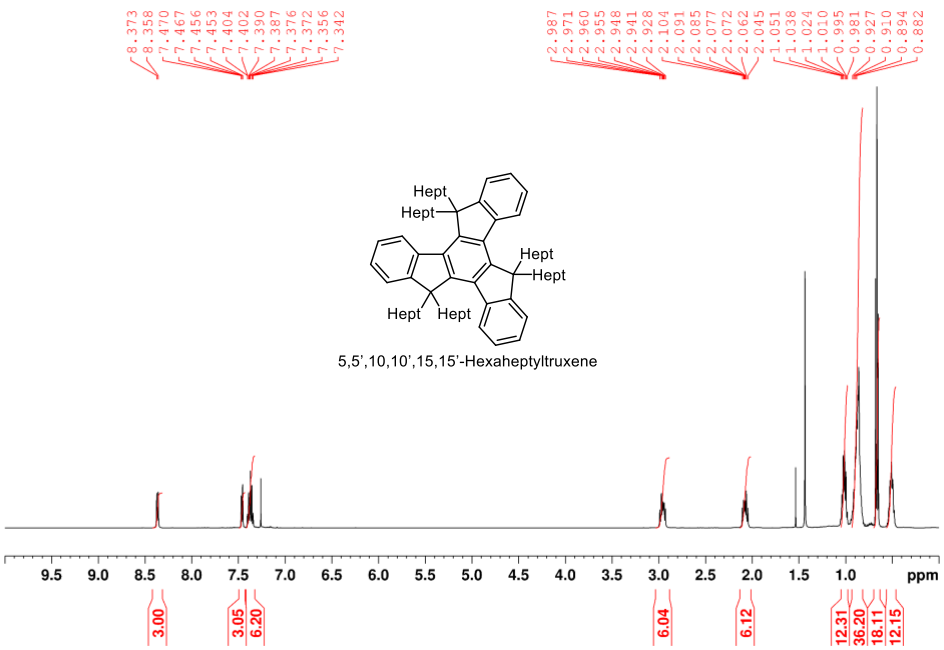

Figure 2.25 ^{1}H NMR spectrum of 5,5',10,10',15,15'-hexaheptyltruxene in $CDCl_3$.

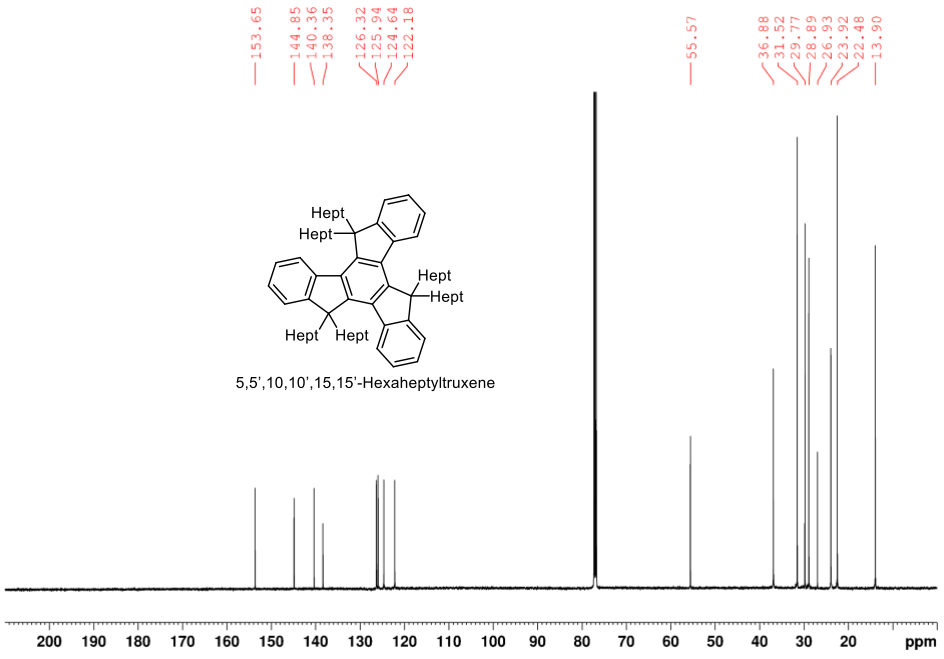

Figure 2.26 ^{13}C NMR spectrum of 5,5',10,10',15,15'-hexaheptyltruxene in $CDCl_3$.

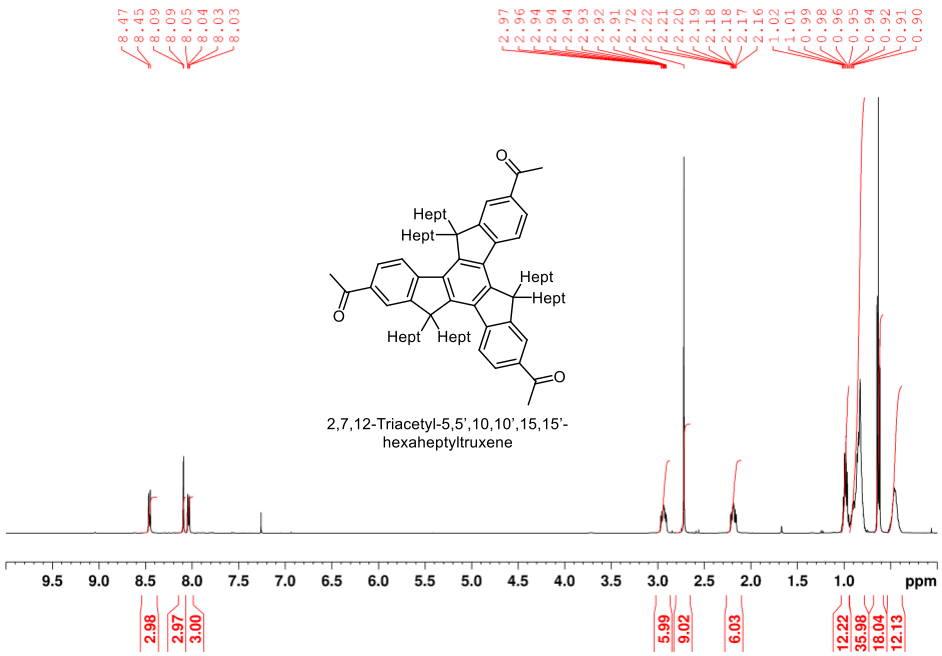

Figure 2.27 ^{1}H NMR spectrum of 2,7,12-triacetyl-5,5',10,10',15,15'-hexaheptyltruxene in $CDCl_3$.

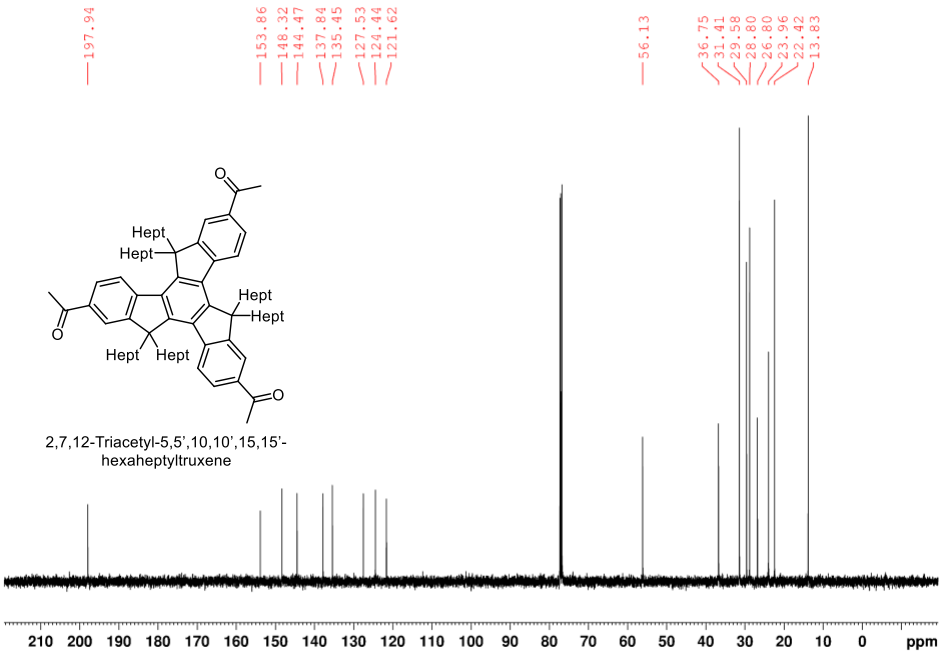

Figure 2.28 ^{13}C NMR spectrum of 2,7,12-triacetyl-5,5',10,10',15,15'-hexaheptyltruxene in $CDCl_3$.

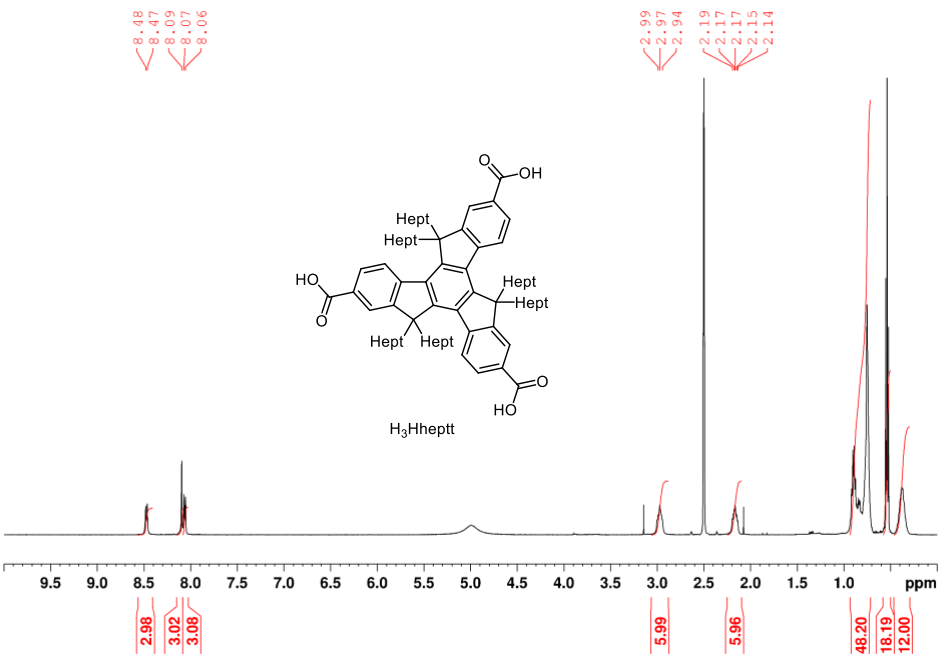

Figure 2.29 ^{1}H NMR spectrum of H$_3$hheptt in *d6*-DMSO/DCl.

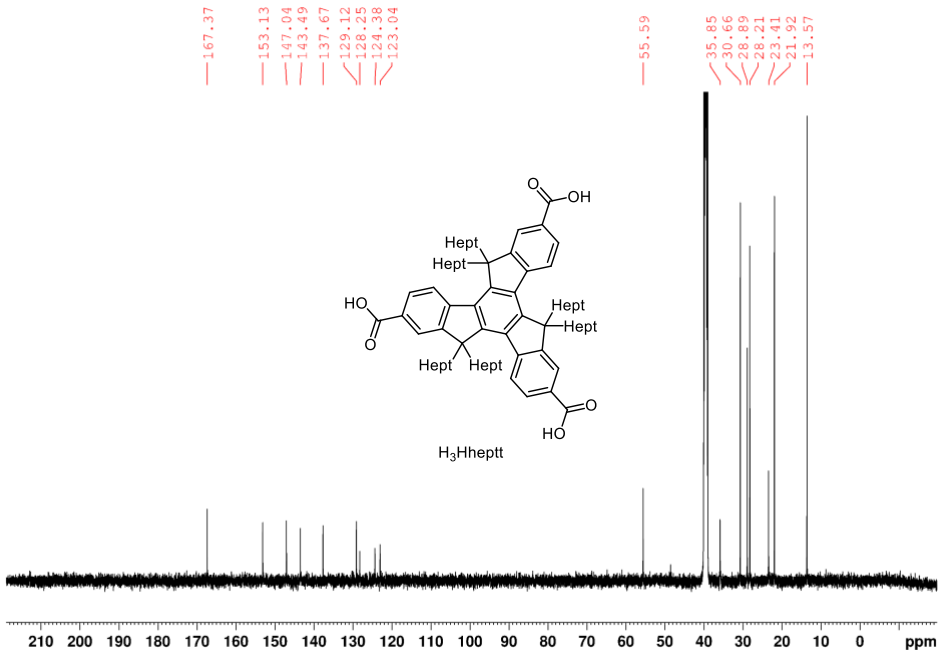

Figure 2.30 ^{13}C NMR spectrum of H$_3$hheptt in *d6*-DMSO/DCl.

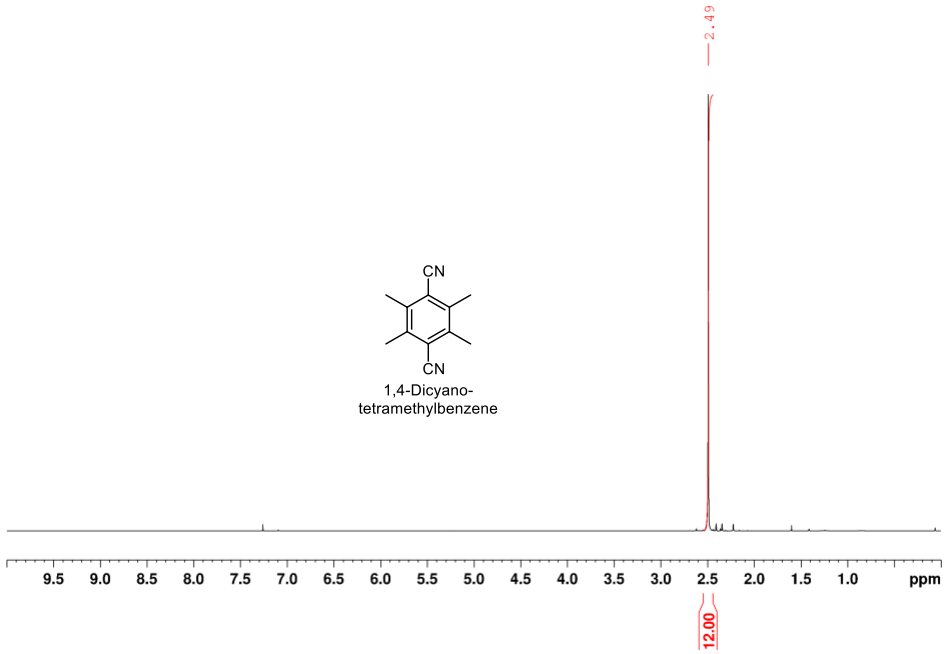

Figure 2.31 ^{1}H NMR spectrum of 1,4-dicyano-tetramethylbenzene in $CDCl_3$.

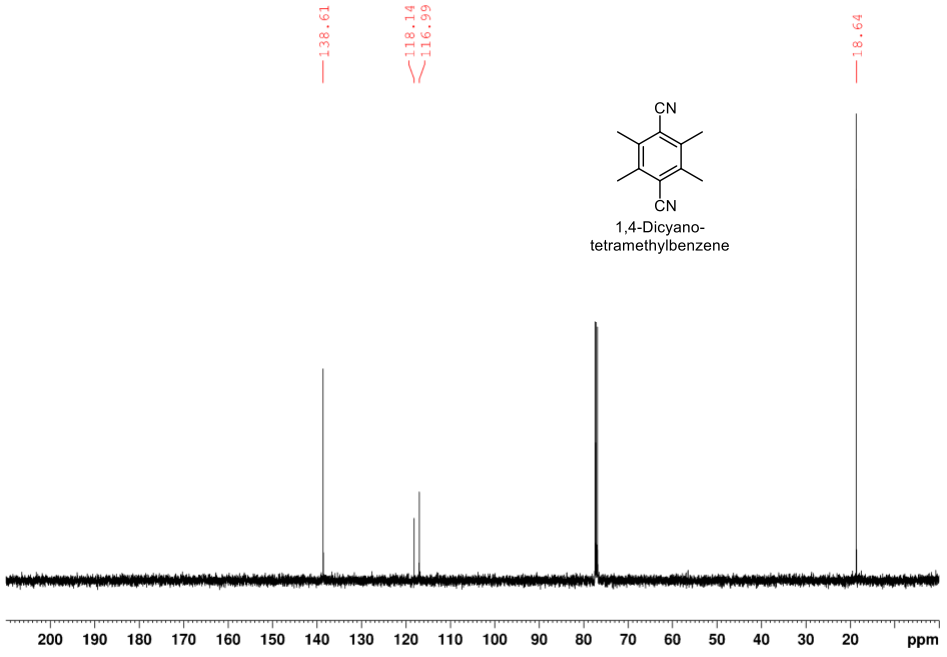

Figure 2.32 ^{13}C NMR spectrum of 1,4-dicyano-tetramethylbenzene in $CDCl_3$.

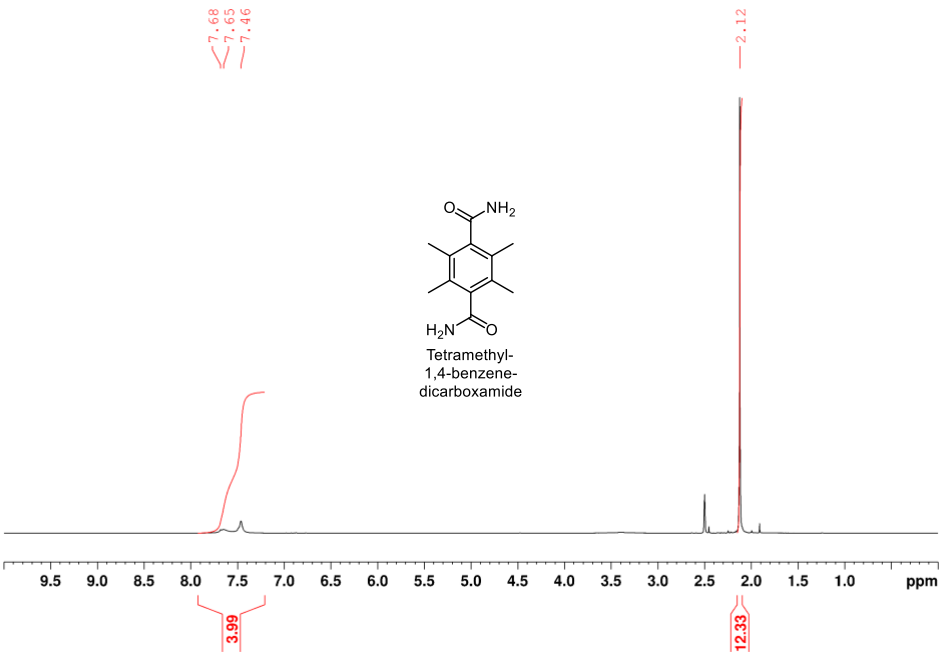

Figure 2.33 ^{1}H NMR spectrum of tetramethyl-1,4-benzenedicarboxamide in *d6*-DMSO.

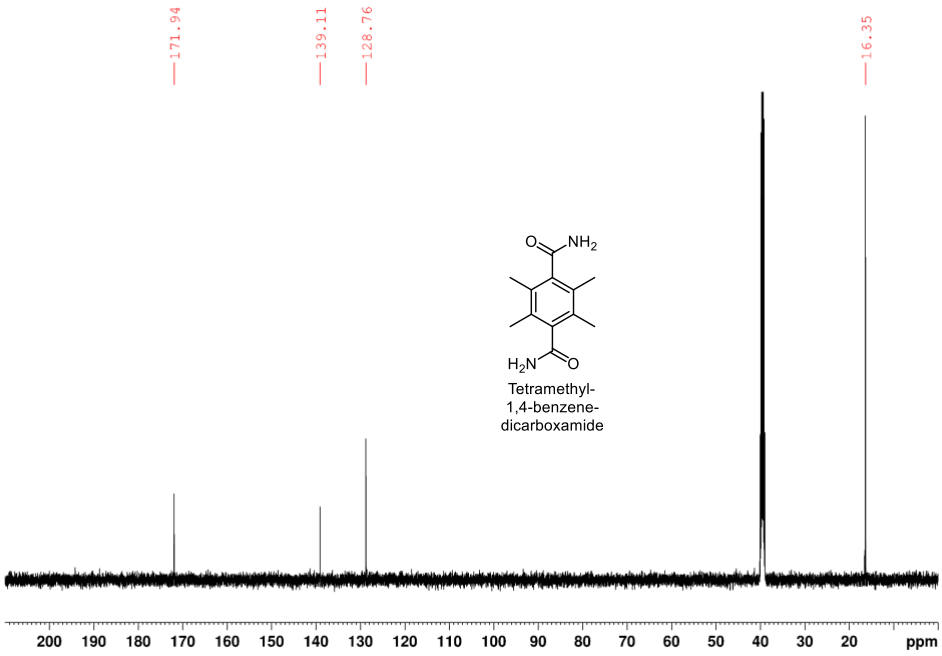

Figure 2.34 ^{13}C NMR spectrum of tetramethyl-1,4-benzenedicarboxamide in *d6*-DMSO.

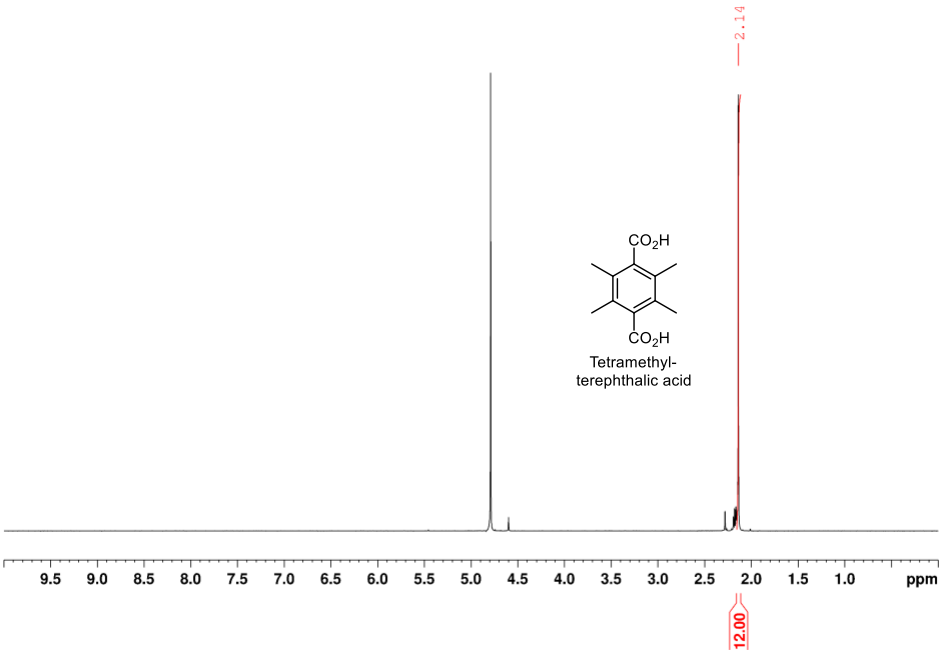

Figure 2.35 ^{1}H NMR spectrum of tetramethyl-terephthalic acid in D_2O/NaOD.

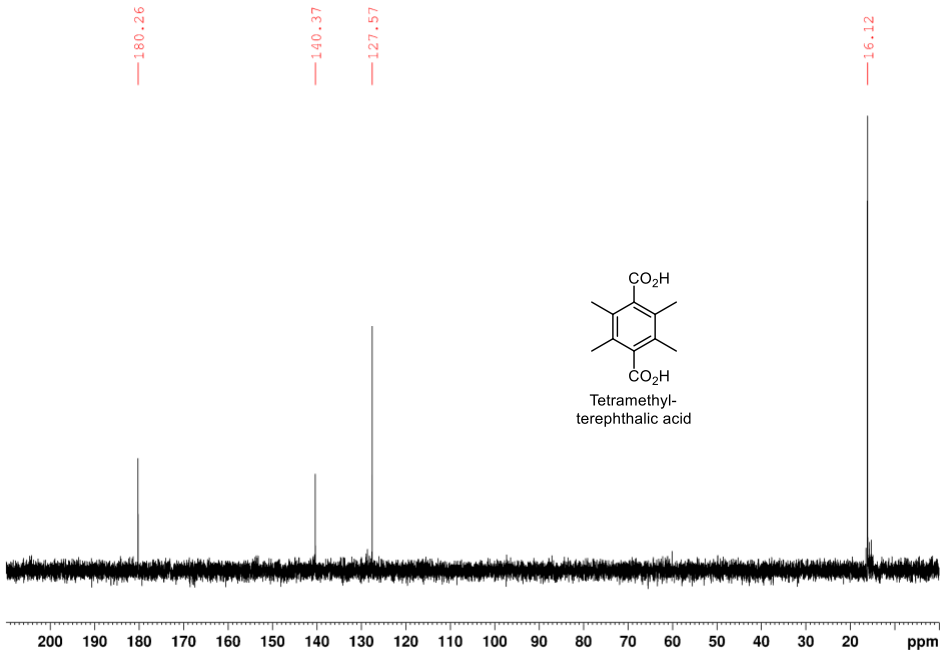

Figure 2.36 ^{13}C NMR spectrum of tetramethyl-terephthalic acid in D_2O/NaOD.

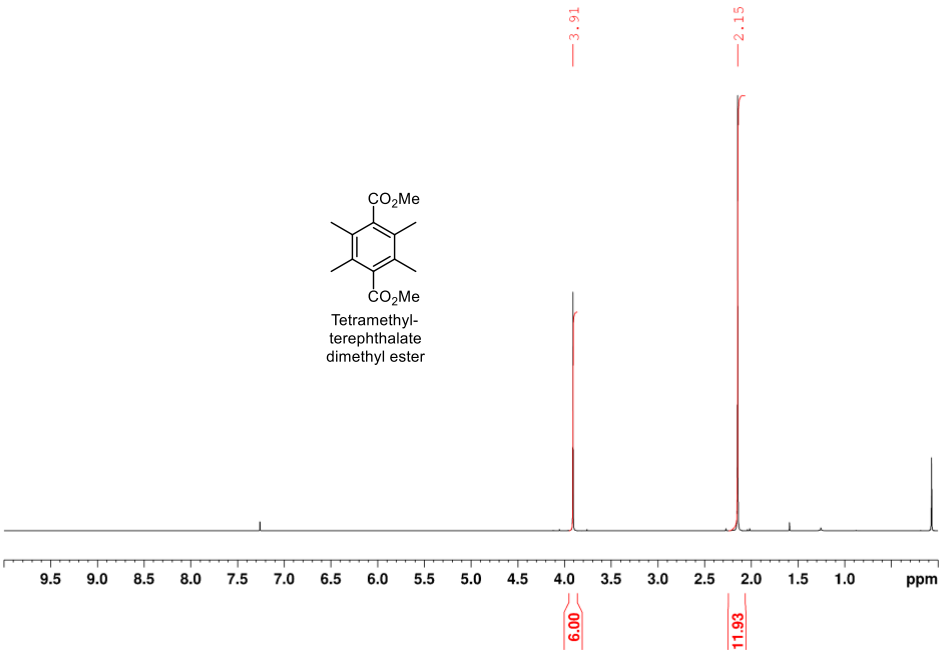

Figure 2.37 ^{1}H NMR spectrum of tetramethyl-terephthalate dimethyl ester in $CDCl_3$.

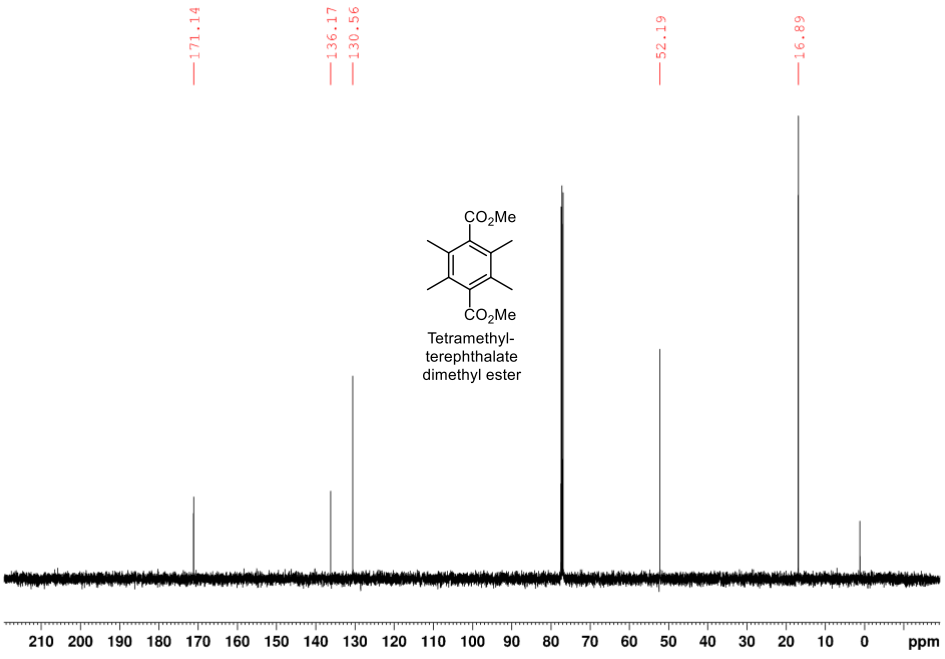

Figure 2.38 ^{13}C NMR spectrum of tetramethyl-terephthalate dimethyl ester in $CDCl_3$.

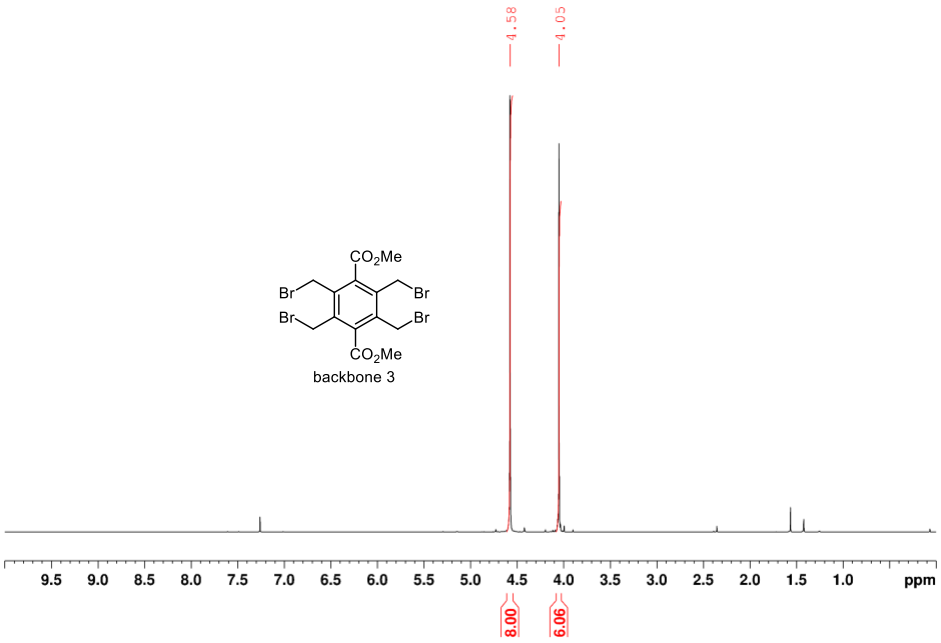

Figure 2.39 ^{1}H NMR spectrum of backbone 3 in $CDCl_3$.

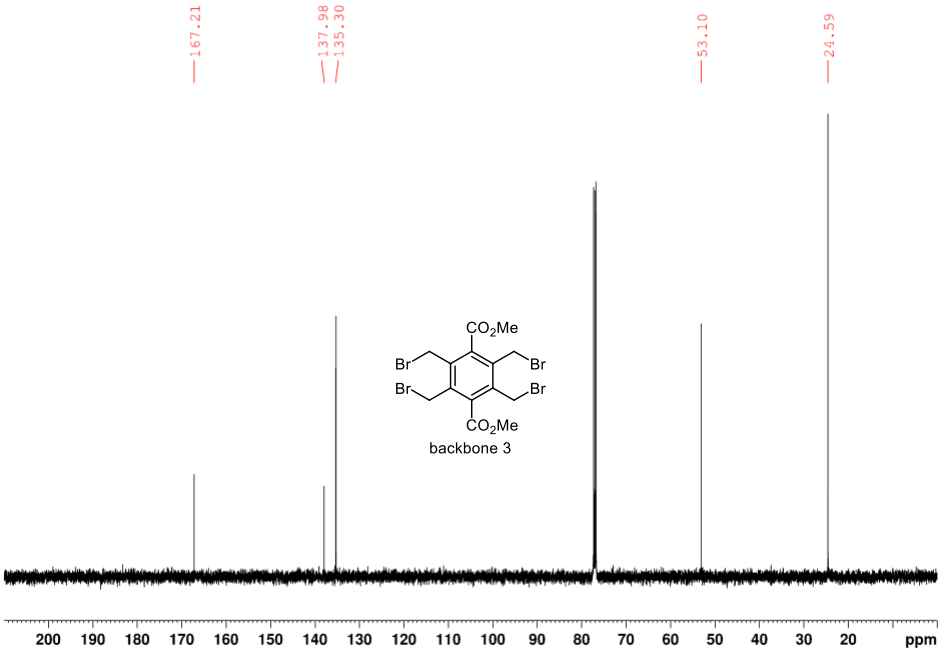

Figure 2.40 ^{13}C NMR spectrum of backbone 3 in $CDCl_3$.

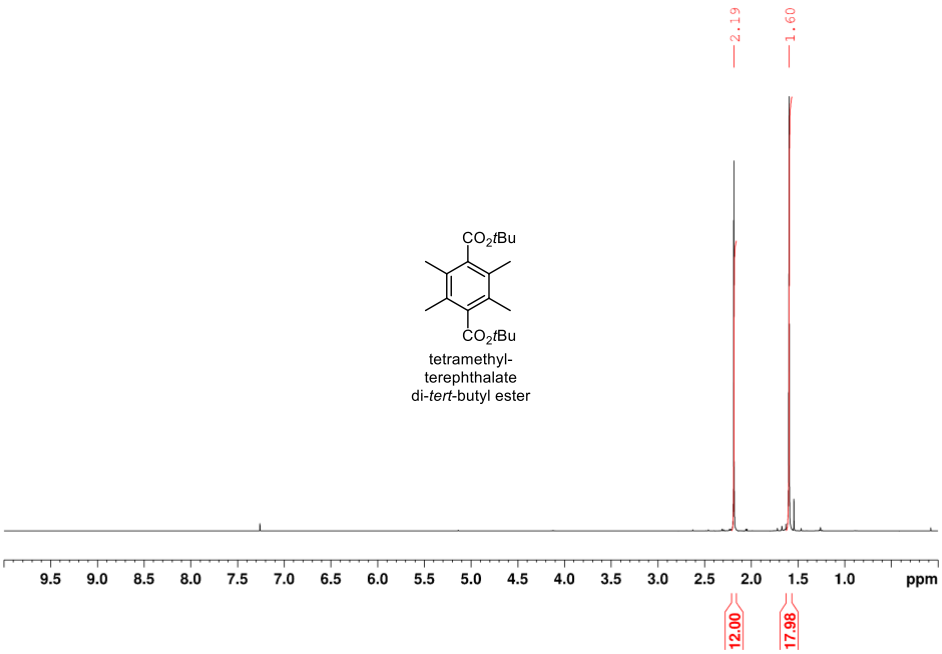

Figure 2.41 ^{1}H NMR spectrum of tetramethyl-terephthalate di-*tert*-butyl ester in $CDCl_3$.

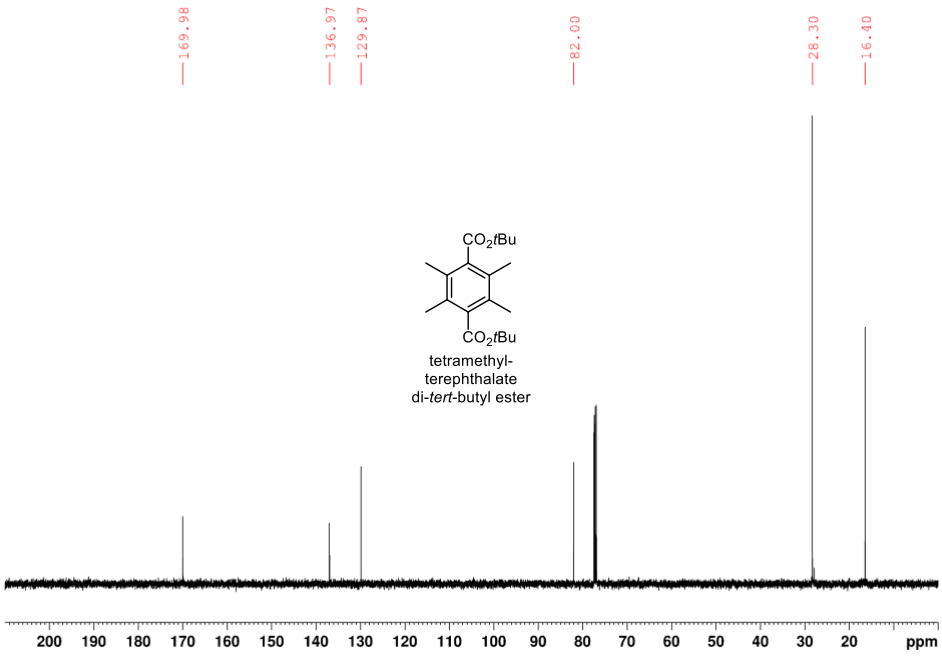

Figure 2.42 ^{13}C NMR spectrum of tetramethyl-terephthalate di-*tert*-butyl ester in $CDCl_3$.

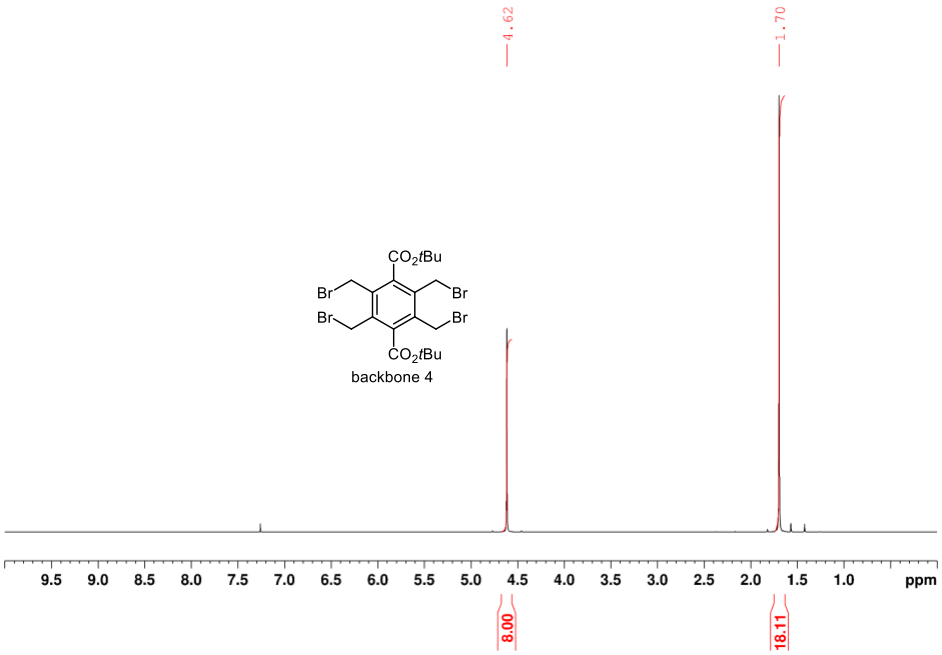

Figure 2.43 ^{1}H NMR spectrum of backbone 4 in $CDCl_3$.

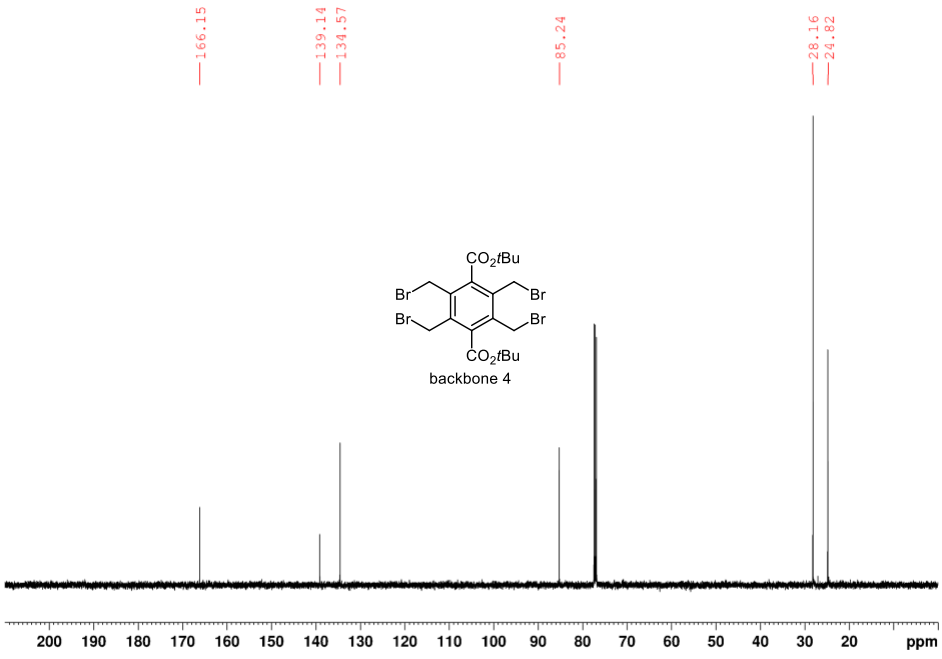

Figure 2.44 ^{13}C NMR spectrum of backbone 4 in $CDCl_3$.

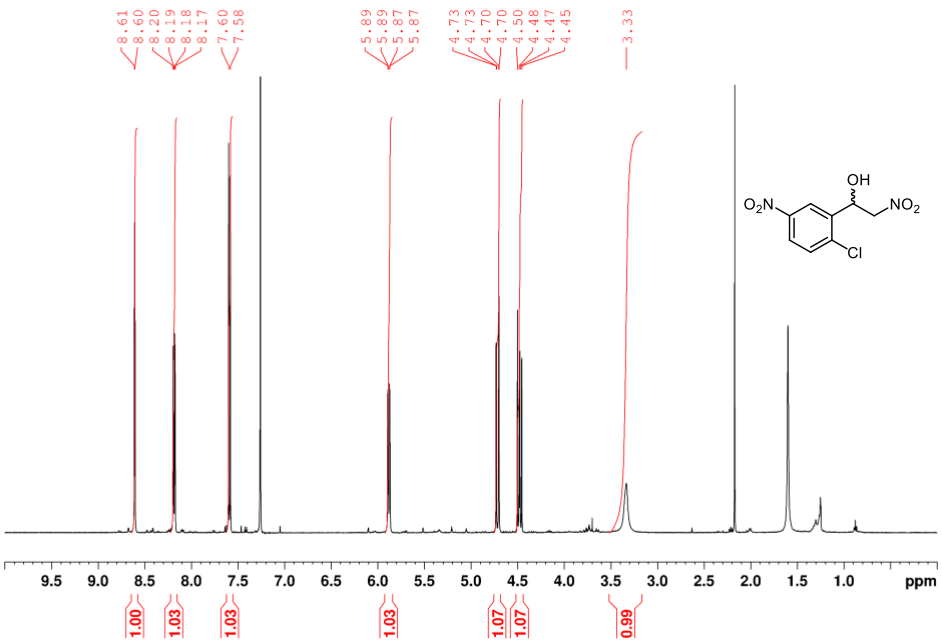

Figure 2.45 ^{1}H NMR spectrum of the Henry product of 6-chloro-3-nitrobenzaldehyde in $CDCl_3$.

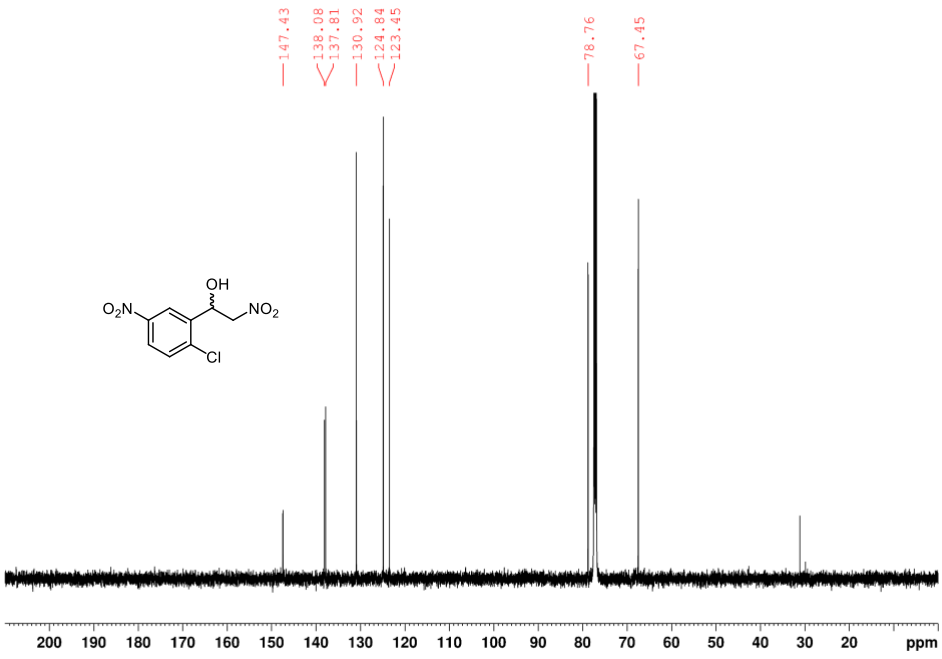

Figure 2.46 ^{13}C NMR spectrum of the Henry product of 6-chloro-3-nitrobenzaldehyde in $CDCl_3$.

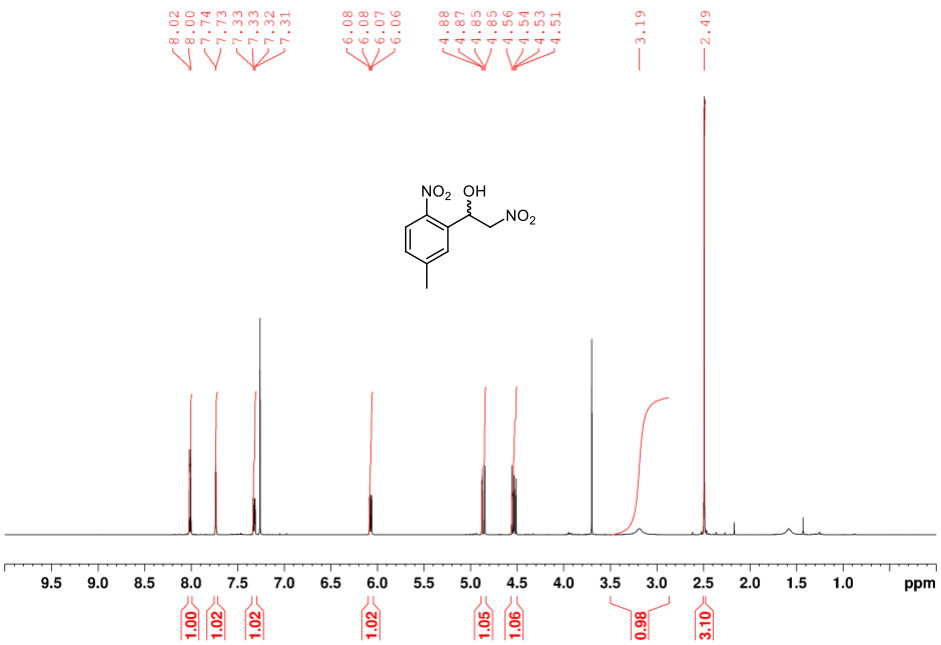

Figure 2.47 ^{1}H NMR spectrum of the Henry product of 5-methyl-2-nitrobenzaldehyde in $CDCl_3$.

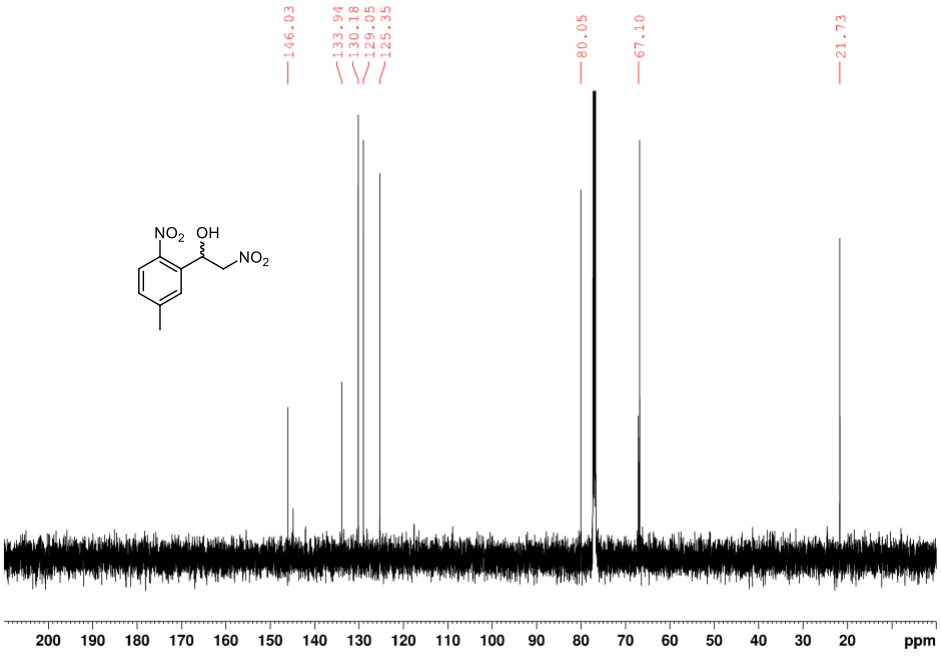

Figure 2.48 ^{13}C NMR spectrum of the Henry product of 5-methyl-2-nitrobenzaldehyde in $CDCl_3$.

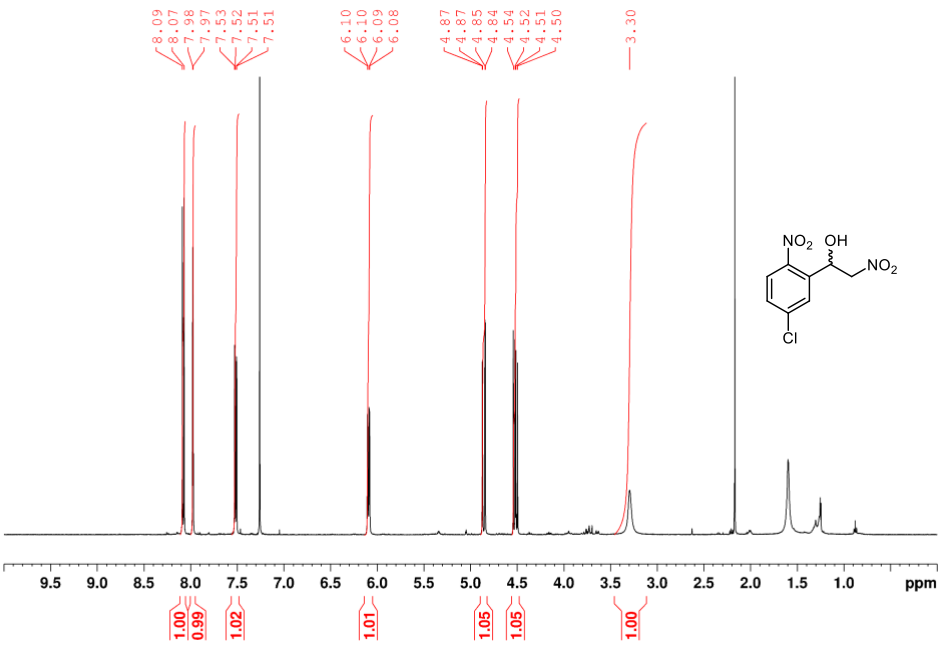

Figure 2.49 ^{1}H NMR spectrum of the Henry product of 5-chloro-2-nitrobenzaldehyde in $CDCl_3$.

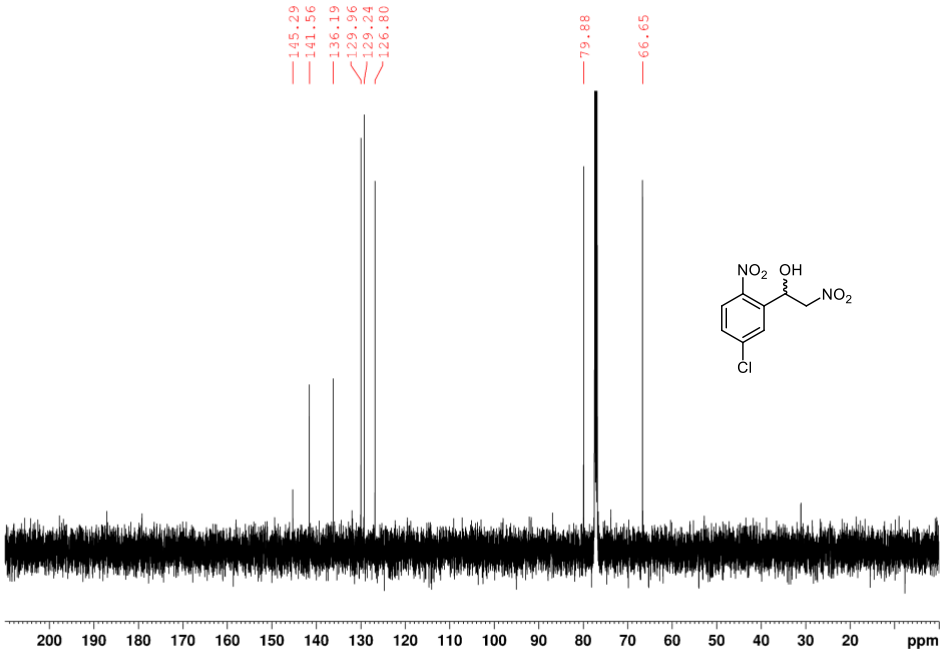

Figure 2.50 ^{13}C NMR spectrum of the Henry product of 5-chloro-2-nitrobenzaldehyde in $CDCl_3$.

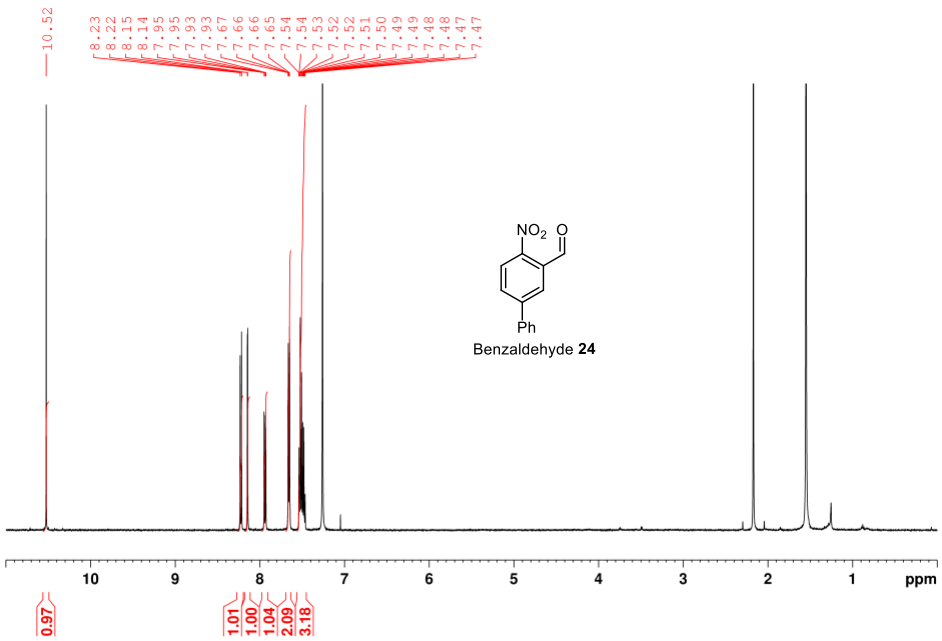

Figure 2.51 ^{1}H NMR spectrum of benzaldehyde **24** in $CDCl_3$.

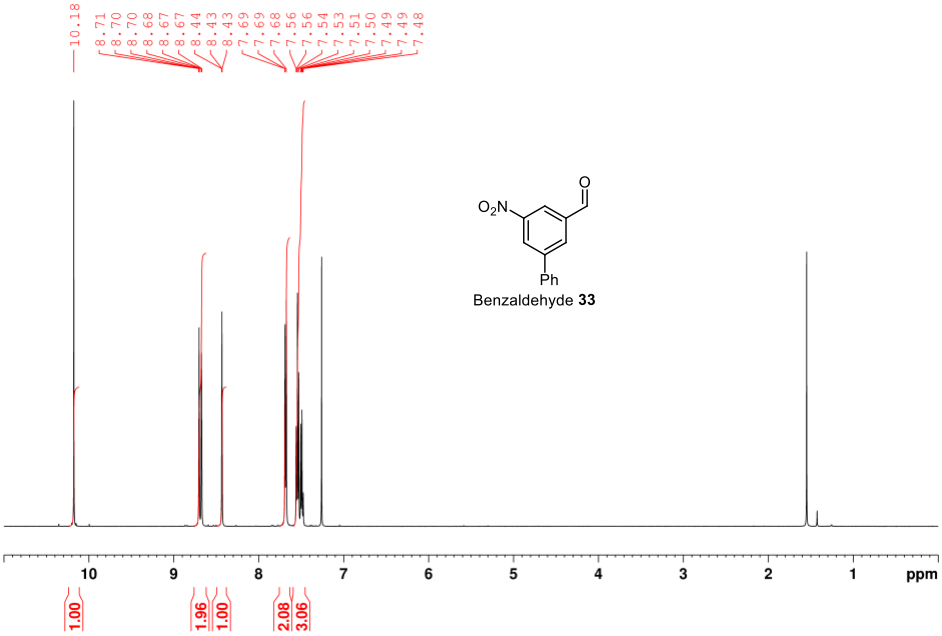

Figure 2.52 ^{1}H NMR spectrum of benzaldehyde **33** in $CDCl_3$.

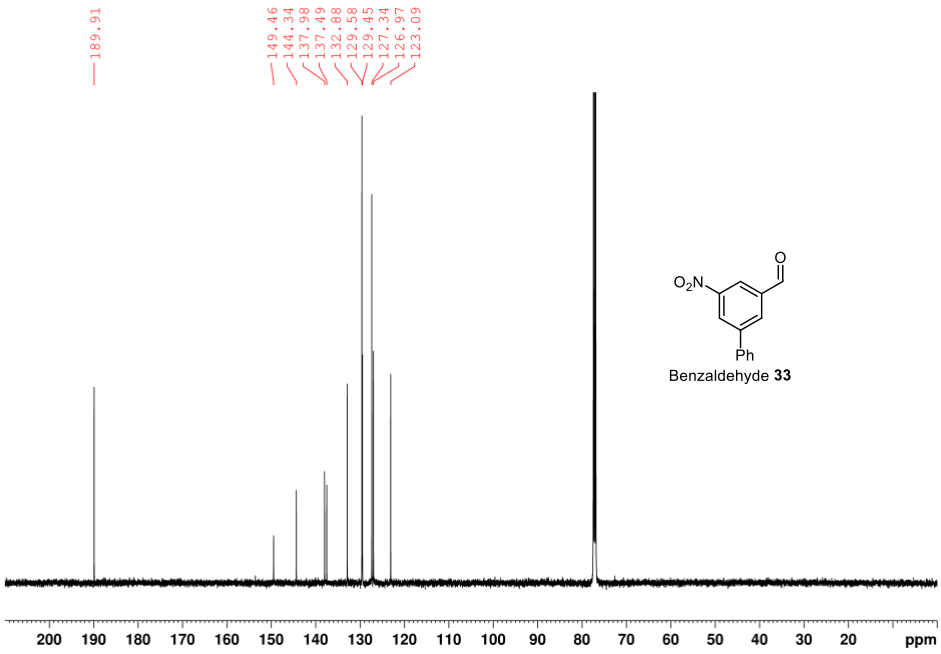

Figure 2.53 ^{13}C NMR spectrum of benzaldehyde **33** in $CDCl_3$.

Appendix Chapter 4

Linker synthesis

All H_2bdc-^{5}N-(*S*/*R*)-R^1-R^2 linkers were synthesised according to the procedures described in **Chapter 2.4.2.4** (**Scheme 2.7**).

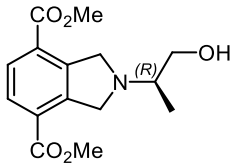

Me_2bdc-^{5}N-(*R*)-AlaOH

The title compound was prepared from backbone 2 (528.0 mg, 1.4 mmol, 1.0 eq.) and (*R*)-alaninol (145.0 mg, 1.9 mmol, 1.4 eq.) according to general procedure **I**. Me_2bdc-^{5}N-(*R*)-AlaOH (266.5 mg, 908.6 µmol, 65%) was obtained as a slightly yellow oil after silica-gel column chromatography (EtOAc/methanol gradient from 1/0 to 9.5/0.5; 0.5% TEA).

^{1}H NMR (500 MHz, MeOD-*d*$_4$) δ 7.91 (s, 2H), 4.37-4.31 (m, 4H), 3.92 (s, 6H), 3.75 (dd, *J* = 11.1, 4.7 Hz, 1H), 3.60 (dd, *J* = 11.1, 6.2 Hz, 1H), 2.88-2.82 (m, 1H), 1.25 (d, *J* = 6.3 Hz, 3H). ^{13}C NMR (126 MHz, MeOD-*d*$_4$) δ 167.24, 144.49, 129.74, 129.59, 65.78, 61.44, 57.88, 52.79, 15.58. HRMS (FTMS + p ESI Full) calculated for $[M+H]^+$ $(C_{15}H_{20}N_1O_5)^+$ m/z 294.1336, found m/z 294.1333.

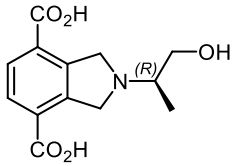

H_2bdc-^{5}N-(*R*)-AlaOH

The title compound was prepared from Me_2bdc-^{5}N-(*R*)-AlaOH (266.5 mg, 908.6 µmol, 1.0 eq.) according to the general ester hydrolysis procedure. H_2bdc-^{5}N-(*R*)-AlaOH precipitated at pH 4.0 as a white solid (186.7 mg, 703.8 µmol, 77%).

^{1}H NMR (500 MHz, D_2O/NaOD) δ 7.58 (s, 2H), 4.19 (s, 4H), 3.83 (dd, *J* = 11.3, 4.2 Hz, 1H), 3.56 (dd, *J* = 11.3, 6.8 Hz, 1H), 2.88-2.85 (m, 1H), 1.23 (d, *J* = 6.8 Hz, 3H). ^{13}C NMR (700 MHz, D_2O/NaOD) δ 175.51, 139.30, 133.82, 127.02, 64.33, 59.84, 56.39, 15.05. HRMS (FTMS + p ESI Full) calculated for $[M]^-$ $(C_{13}H_{14}N_1O_5)^-$ m/z 264.0866, found m/z 264.0871.

MOFs

PXRD

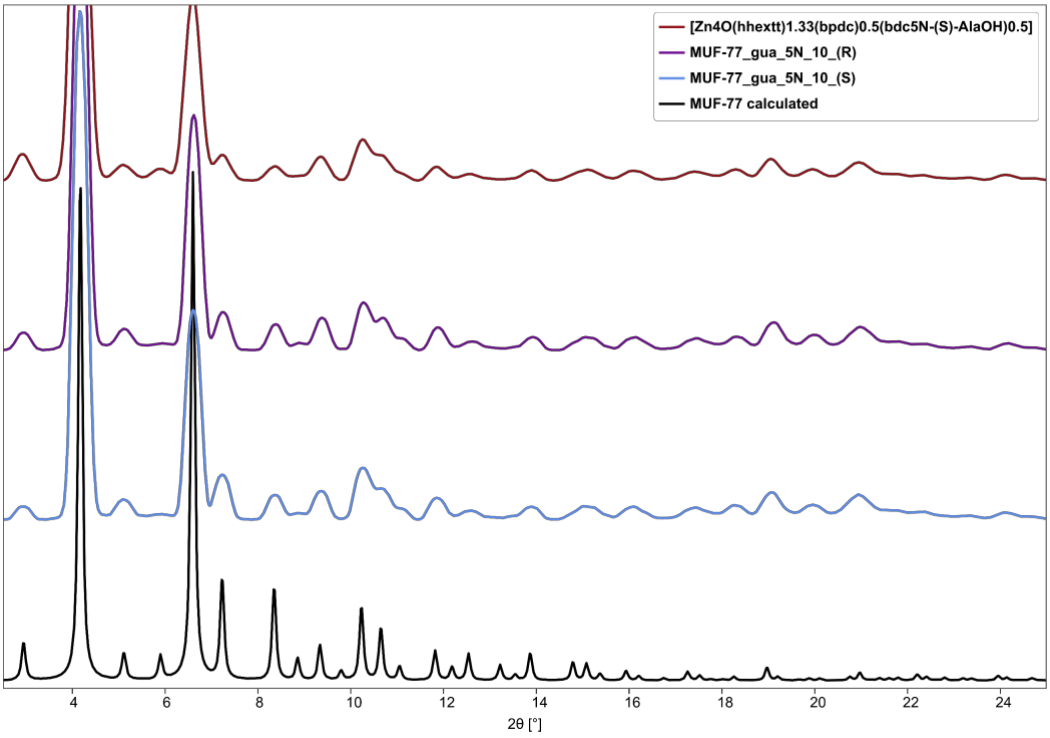

Figure 2.1 PXRD pattern of MUF-77_gua_^{5}N_10_(*S*) and (*R*) and $[Zn_4O(hhextt)_{1.33}(bpdc)_{0.5}(bdc^{5}N\text{-}(S)\text{-}AlaOH)_{0.5}]$ compared to the calculated pattern of MUF-77. The pattern are scaled by a factor of three for better visibility.

NMR

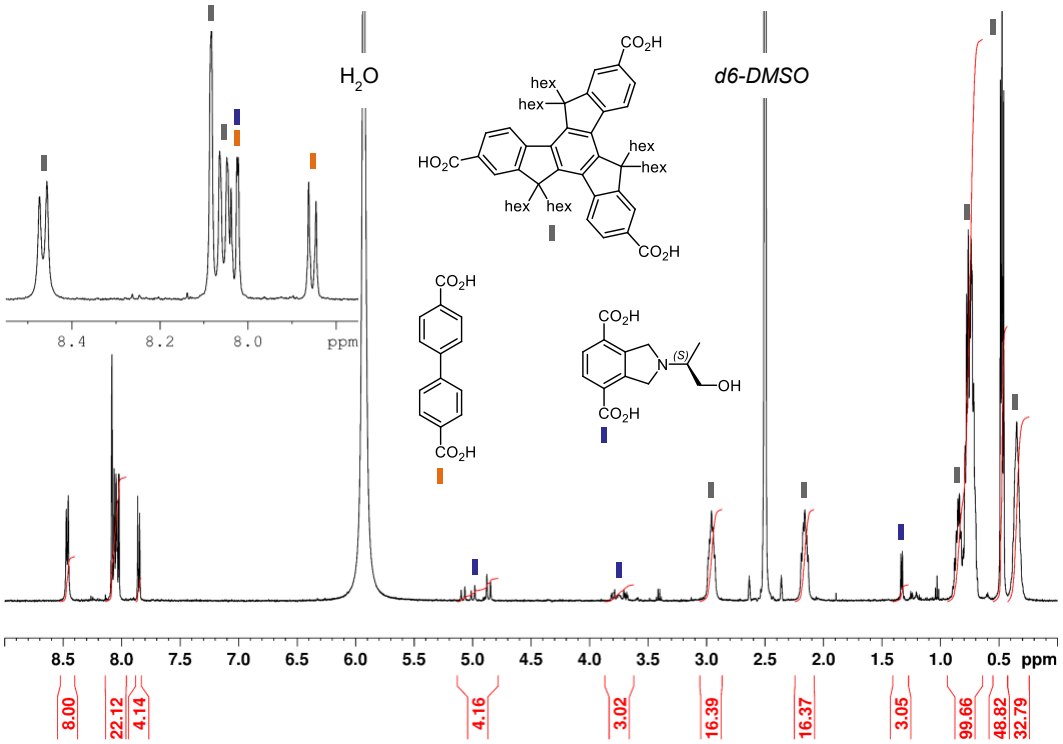

Figure 2.2 ^{1}H NMR of digested $[Zn_4O(hhextt)_{1.33}(bpdc)_{0.5}(bdc^{5}N\text{-}(S)\text{-}AlaOH)_{0.5}]$ in *d6*-DMSO/DCl.

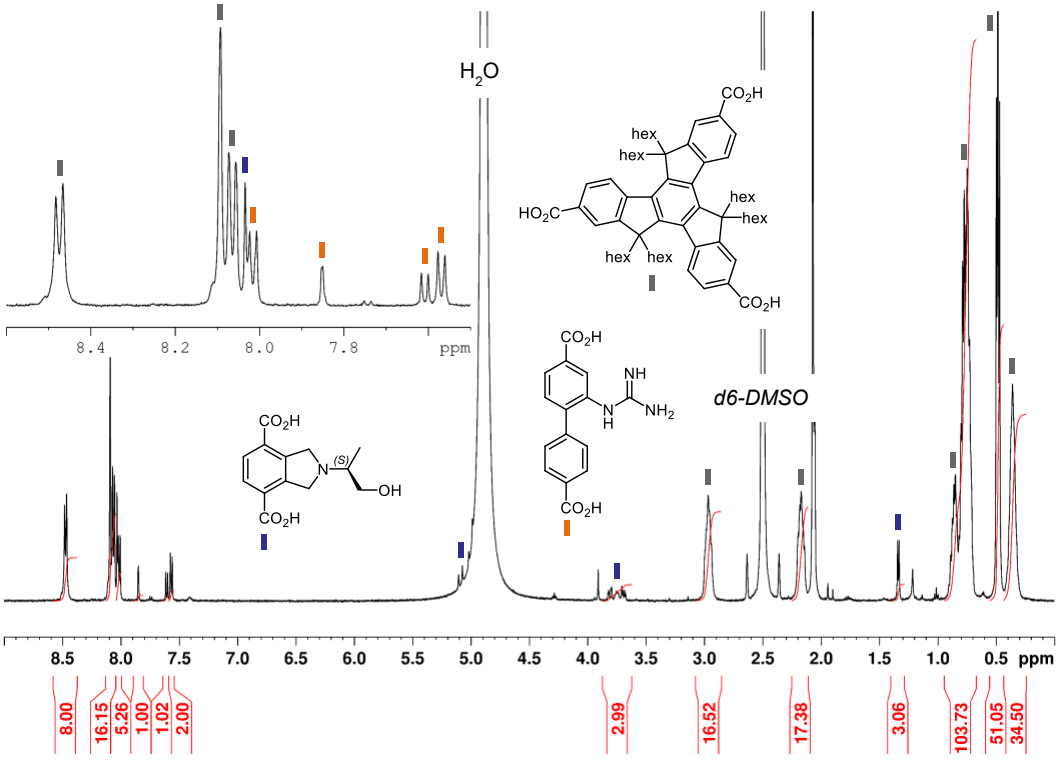

Figure 2.3 ^{1}H NMR of digested MUF-77_gua_^{5}N_10_(*S*) in *d6*-DMSO/DCl.

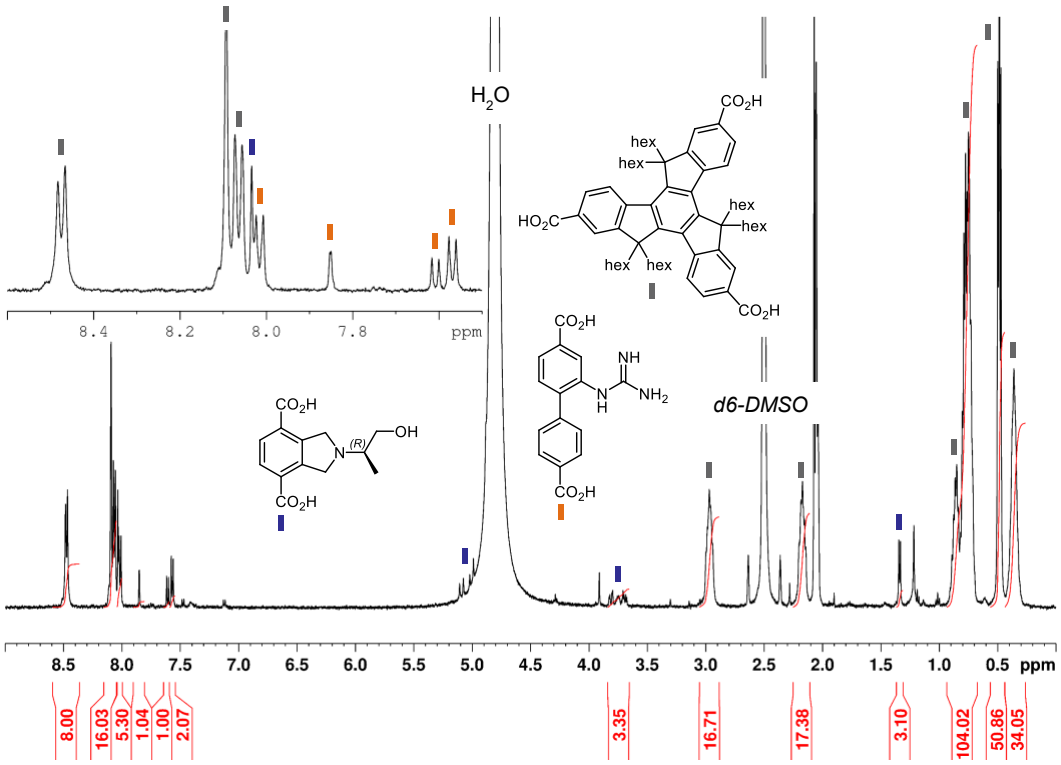

Figure 2.4 ^{1}H NMR of digested MUF-77_gua_^{5}N_10_(*R*) in *d6*-DMSO/DCl.

Linker synthesis: NMR data

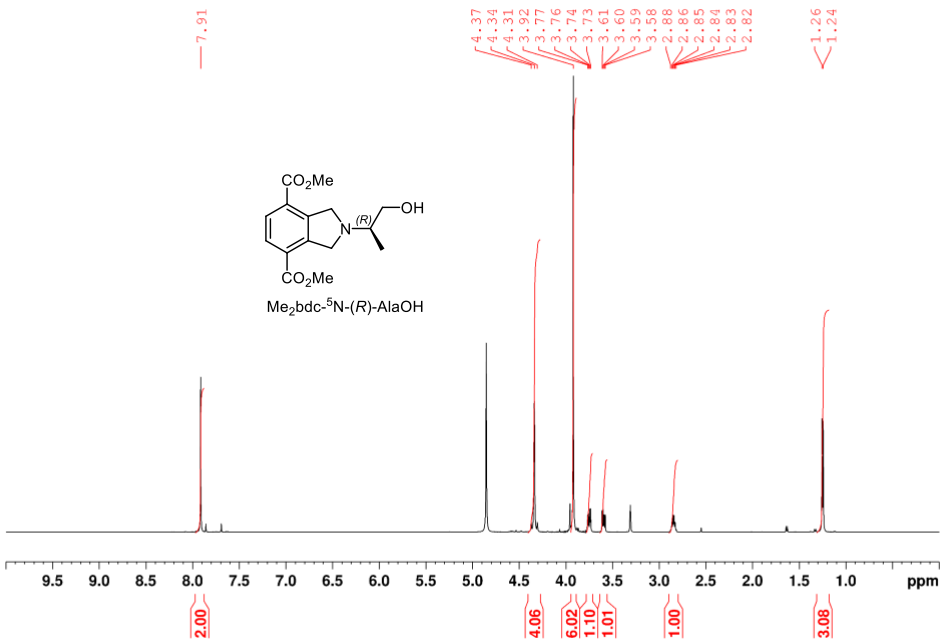

Figure 2.5 ^{1}H NMR spectrum of Me$_2$bdc-^{5}N-(*R*)-AlaOH in MeOD-*d*$_4$.

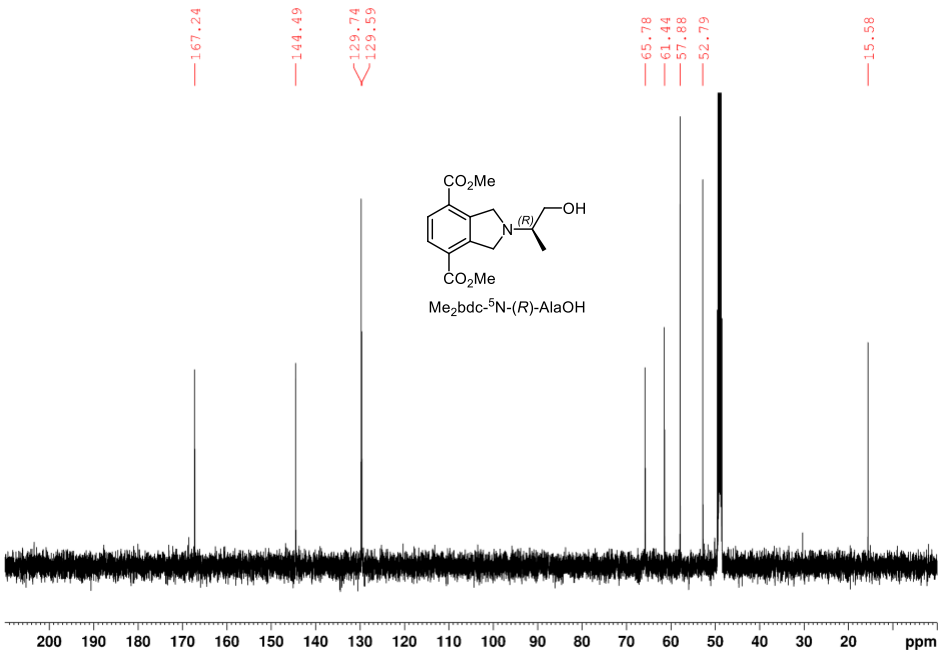

Figure 2.6 ^{13}C NMR spectrum of Me$_2$bdc-^{5}N-(*R*)-AlaOH in MeOD-*d*$_4$.

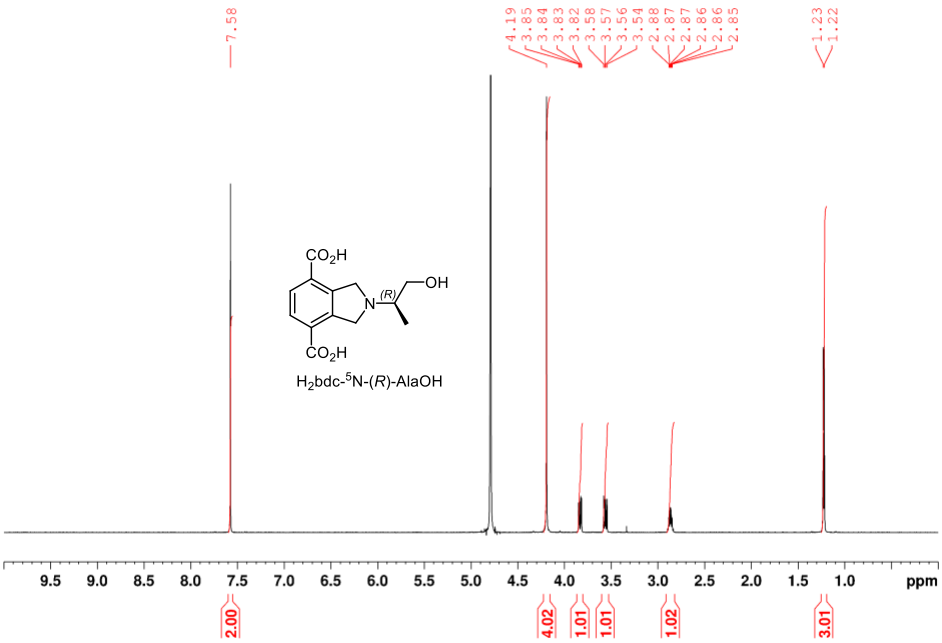

Figure 2.7 ^{1}H NMR spectrum of H$_2$bdc-^{5}N-(*R*)-AlaOH in D$_2$O/NaOD.

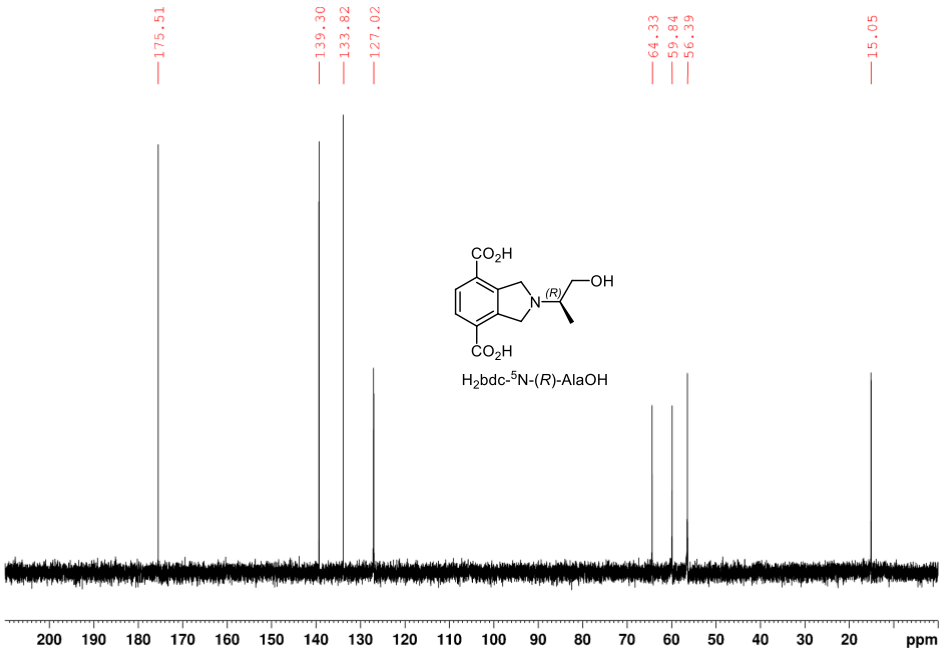

Figure 2.8 ^{13}C NMR spectrum of H_2bdc-^{5}N-(*R*)-AlaOH in D_2O/NaOD.

(1) Padmanaban, M.; Müller, P.; Lieder, C.; Gedrich, K.; Grünker, R.; Bon, V.; Senkovska, I.; Baumgärtner, S.; Opelt, S.; Paasch, S.; et al. Application of a chiral metal–organic framework in enantioselective separation. *ChemComm* **2011**, *47* (44), 12089.
(2) Zhang, X.; Zhang, Z.; Boissonnault, J.; Cohen, S. M. Design and synthesis of squaramide-based MOFs as efficient MOF-supported hydrogen-bonding organocatalysts. *ChemComm* **2016**, *52* (55), 8585-8588.
(3) Maher, D. J.; Connon, S. J. Acceleration of the DABCO-promoted Baylis–Hillman reaction using a recoverable H-bonding organocatalyst. *Tetrahedron Lett.* **2004**, *45* (6), 1301-1305.
(4) List, B.; Pojarliev, P.; Martin, H. J. Efficient Proline-Catalyzed Michael Additions of Unmodified Ketones to Nitro Olefins. *Org. Lett.* **2001**, *3* (16), 2423-2425.
(5) Kaur, A.; Singh, K. N.; Sharma, E.; Shilpy; Rani, P.; Sharma, S. K. Pyrrolidine-carbamate based new and efficient chiral organocatalyst for asymmetric Michael addition of ketones to nitroolefins. *Tetrahedron* **2018**, *74* (42), 6137-6143.
(6) Pansare, S. V.; Lingampally, R. Synthesis and evaluation of guanidinyl pyrrolidines as bifunctional catalysts for enantioselective conjugate additions to cyclic enones. *Org. Biomol. Chem.* **2009**, *7* (2), 319-324.
(7) Huang, Y.-Q.; Song, H.-J.; Liu, Y.-X.; Wang, Q.-M. Dehydrogenation of N-Heterocycles by Superoxide Ion Generated through Single-Electron Transfer. *Chem. Eur. J.* **2018**, *24* (9), 2065-2069.
(8) Winter, J.; Prenzel, T.; Wirtanen, T.; Schollmeyer, D.; Waldvogel, S. R. Direct Electrochemical Synthesis of 2,3-Disubstituted Quinoline N-oxides by Cathodic Reduction of Nitro Arenes. *Chem. Eur. J.* **2023**, *29* (12), e202203319.